DRAFT
EIC PDR
December 2, 2024

Electron Ion Collider
Preliminary Design Report

Contributors:

E-C. Aschenauer[1], R. Ent[2], S. Joosten[3], M. Żurek[3], ADD NAMES AND INSTITUTIONS

[1]Brookhaven National Laboratory, USA
[2]Thomas Jefferson National Accelerator Facility, USA
[3]Argonne National Laboratory, USA

Contents

List of Figures

List of Tables

multi-chapters

Chapter 0

Style Guide

The following is the Style guild as developed for the full design report. This is the guide the accelerator team is following and it will make merging the documents together much easier if everyone uses this guide.

0.1 Chapter Abstract

Summary: Each chapter begins with a stand-alone single "punch line" page that serves as a chapter abstract. Rather than simply duplicating the Table of Contents outline of the subject matter of the chapter, a well-constructed abstract will lay out the key ideas and conclusions that chapter editors wish to convey to readers. The Executive Summary will also describe these key ideas, in a modestly longer form (perhaps $\sim 250 - 1000$ words per chapter). This sample **non-EIC** chapter abstract emphasizes key ideas such as the separation of pre-existing and new subsystems, and the level of technical risk.

The Cryogenic System consists of the cryoplant that provides cooling for cryomodules; the test and instruments cryoplant that provides cooling for test stands and liquid helium for instruments; cryoplant that provides 16 K helium cooling for the target hydrogen moderators, and the distribution system that connects the linac cryoplant to cryomodules. The linac cryoplant and test/instrument cryoplant share common gas management and storage systems. The target cryoplant system is completely separate due to potential for tritium contamination.

The Vacuum System provides vacuum for the linac beam line, target system and instrument lines. It uses well established technology and procedures based on experience at similar facilities, including RHIC, Tevatron, and LHC. It has low technical risk.

Test Stands provide testing and validation of both RF equipment (klystrons and modulators) and cryomodules. Cryogenic connection to cryomodules in the test stands will prototype similar connections in the linac tunnel. The test stand program accommodates the unavoidable uncertainty in EIC construction schedule by allowing for RF equipment testing in a temporary location if necessary. Cryomodule testing will be carried out at the EIC site. All cryomodules will be tested at nominal temperatures and RF power levels before tunnel installation.

0.2 Wordsmithing

0.2.1 Passive voice

Authors should avoid the passive voice as much as possible – as in this sentence. This rule is sometimes made to be broken – as in this sentence :). The crucial point is that authors should not use passive voice to avoid identifying the specific individual or group of individuals within the EIC organization which is/are (or will be) responsible for fulfilling some specific function. It's not good enough to say, "Quality management will be implemented". The purpose of the Design Report is to explain for EIC itself, and for readers outside of EIC, who will implement quality management, and how they will do it. Excessive use of passive voice is not just bad writing. It communicates confusion or uncertainty about the path from aspiration to reality.

0.2.2 Verb tenses

The simplest way to make everything consistent is to apply a general rule:

> Use past tense for things that happened in the past, present tense for things that are happening now, and future tense for things that will happen in the future.

If the designs call for something to happen, they call for it in the present tense. But it will happen in the future tense. Avoid inconsistent usage across chapters, across authors, and even within the same paragraph by a single author.

0.2.3 Apostrophes

Decades are written as in the 1960s and 1970s, NOT as in the 1980's or 1990's.

0.2.4 Capitalization and names

0.2.4.1 Pieces of EIC

For example, linac, accelerator, target station, test stand. For the sake of consistency these terms will not be capitalized.

0.2.4.2 Internal phrases

Correct capitalization for specific "internal" EIC phrases and names will be accumulated here. For example:

> Pre-construction Phase NOT Pre-Construction phase
> Decommissioning Phase NOT De-commissioning phase
> Work Packages NOT Work-packages

0.2.4.3 Discipline-specific approaches or "guiding principles" or buzz phrases

Such as design integration, systems engineering, defense in depth. Recommend capitalizing none of them, but the important thing is to be consistent.

0.2.4.4 Formal group names

When authors identify the parts of the EIC organization who will be responsible for doing something, then capitalize the formal names of that groups from the org chart. Recommend avoiding informal terms such as "test stand personnel", where possible.

0.2.4.5 Headings

The titles of sections and subsections should have only the first letter capitalized.

0.2.5 Captions

Write Figure and Table captions in a self-contained way, to carry a complete self-contained description of the figure. Define symbology in all figures, either in the text or (preferably) in the caption. Captions always end with a period. Use the format:

```
\caption[Short caption for List of Tables or Figures.]{Long caption to carry a complete
self-contained description of the figure or table, in the chapter text.}
```

0.2.6 Spelling

The Design Report follows American spelling rules. For example, with "z" not "s", and "program" not "programme":

emphasize not emphasise
meter not metre

0.2.6.1 Exceptions to U.S. spelling

1. (None so far).

0.2.6.2 Capitalization

The words "Figure", "Table", "Chapter" and "Section" should always be capitalized in the text if they occur with a number. For example, Figure 3.8 occurs in Chapter 3 and Table 5.5 is in Section 5.1.3, but there are many other figures and tables in other section, subsections and chapters.

0.2.7 Commas

The incorrect placement of a comma can change the meaning of a sentence. For example, compare "Let's eat Mom" and "Let's eat, Mom". And compare "Scientists, who conduct important research, are well respected in the community" with "Scientists who conduct important research are well respected in the community".

Commas go where there is a natural pause in a long sentence, where additional information has been added to a sentence and where, if removed, the sentence would still make sense. They are used when listing items – between each item on the list. They are used where two shorter sentences are made into one (usually with the addition of "and"), but still consist of two separate parts. And they are used after "lead" words [however, therefore, consequently, in fact].

0.2.7.1 Commas in numbers

Write 2.4 million and not 2,4 million (as in some parts of Europe).

No commas in numbers below 10,000 – thus, write 1240 and 9999, but 12,400 and 99,999.

0.2.8 Plurals and possessives

For example, use

WPs not WP's (plural)
EIC's not EIC' (possessive)

0.2.9 Abbreviations

0.2.9.1 Textual treatment of Figures and Tables

The words "Figure" and "Table" should always be capitalized in the text. Include a reference or discussion of all Tables and Figures in the main text of the chapter. For example, "Figure 3.8 shows thus-and-such". The abbreviations Fig. and Tab. should not be used.

0.2.9.2 Radio frequency

The phrase "radio frequency" is always two words and is never hyphenated or capitalized, whether used as an adjective or as a noun. Thus, the two radio frequencies used in the radio frequency system are 352.21 MHz and 704.42 MHz. The upper case abbreviation "RF" is acceptable in many circumstances.

0.2.9.3 etc., et cetera

It is acceptable to use "e.g." within parentheses, but not outside. For example, Jack and Jill met many animals (e.g. Reynard the Fox) when going down the hill. It is also correct to say that Jack and Jill met many animals, for example Reynard the Fox, but no tortoise. Similar rules apply for "i.e.".

The periods (i.e. the full stops) should not be dropped, for example "ie" or "eg".

It is incorrect to use ok, o.k., or okay.

The following are acceptable:

e.g.
etc.
i.e.
RF (in many circumstances)

0.2.10 Hyphenation of multi-word adjectival phrases

In general, hyphenate an adjectival phrase where the second part is a past (-ed) or present (-ing) participle of a verb. Consider the following illustrative (nonsensical) paragraph:

> This chapter describes the *beam physics design* of the *neutron-generating* spallation target. Following a brief overview, the chapter presents a detailed description of the *beam physics* of EIC, which drive the accelerator design. The accelerator consists of several sections: the ion source, *normal-conducting* linac, *superconducting* linac and *beam transport* sections. The chapter also describes the *radio frequency* system.

Simplified advice available online includes: *"When two or more words are combined to form a modifier immediately preceding a noun, join the words by hyphens if doing so will significantly aid the reader in recognizing the compound adjective."* Not so simple are phrases like "high-power proton beam" where "proton beam" itself is a single idea. Some judgement is involved ....

For the sake of consistency, the editors have created and are expanding a spreadsheet of words and phrases specifying hyphenation policy for the Design Repoprt. Here are somewhat-arbitrary rules for whether or not to hyphenate some common multi-word phrases, *when they are used as an adjective, a noun, or as a verb*. Alphabetically:

1D, 2D, 3D, 4D
accelerator-driven
back up (verb)
back-flow (noun adj)
backscattering
backup (adj noun)
baseline (adj or noun)
beam dynamics
beam guide
beam instrumentation

beam physics
beampipe
beam port
beam time
beam transport
beamline
bispectral
bottom-up approach
broadband
by-product
clamshell clamshell-style
clean room
cold box
co-chair (noun)
contact-less
cool-down (noun or adj)
coordinate
cost-saving
cross reference (noun)
cross-reference (verb)
cross section
cryo-building
cryo-pump
cryo-system
cryomodule
cryoplant
debunched
decision making (noun)
decommissioning
de-excitation
deionised
down-mix
downtime
eigenmode (noun adj)
equipartitioning
failover
failsafe
feed box
feedthrough
follow up (verb)
follow-up (adj and noun)
hands-on (adj)
high level
high-β
high-current (adj)
high-power
high-resolution
hot cell
in situ (italicize)
innermost
inrush

interdependency
interlayer
intra-layer
intra-nuclear
Joule-Thomson valve
layout (noun)
life-cycle (noun)
line-of-sight
long-pulse
lookup
Lorentz detuning (noun)
Lorentz-detuning (adj)
low-resolution
magnetoresistance
medium-β
metadata
micropattern
microphonics
midpoint
middleware
multi-component
multi-layer
multi-pacting
multi-particle
multi-resistant
nanoparticle
nano-sized
nanostructure
neutron-generating
noninvasive (seen both ways in different dictionaries)
normal-conducting
on-board
ongoing
on-site (adj)
outermost
outgassing
overarching
phase space (noun)
phase-space (adj)
pinpoint
plug-in
post mortem (noun or adj)
pre-cools
premoderator
prequalification
radio frequency
radionuclide
radiotoxic
ramp up (verb)
ramp-up (noun)
read-back

ready-made
requalification
roadmap
safety-critical
short-pulse
short-term
shut off (noun verb)
shut-off (adj)
space charge (noun)
space-charge (adj)
staff-based
start-up
state-of-the-art
storm water
stripline
sub-atmospheric
subcomponent
sub-cool
sub-millimeter
sub-second
superconducting
switchyard
systemwide
thermo-mechanical
thermo-plastic
thermo-responsive
thermosyphon
time-frame
time scale
time-saving
time-stamp (noun and verb)
timeline
timesaving (adj and noun)
tool-set
top level
trade-off
tunable
tune up (verb)
tune-up (adj and noun)
twofold
uniaxial
uninterruptible
un-irradiated
up-mix
uptime
von Mises
waste water (noun)
waveguide
work flow (noun)
work-flow (adj)
workspace

world-leading
X-ray (upper case X)
zigzag (noun or adj)

0.2.11 Double letters

In UK spelling, both ”focussing” and ”focusing” are considered to be correct. In the Design Report we use single ”s” spelling in all cases.

Note the ’double “l” rule for UK English – label becomes labelled, travel becomes travelled, et cetera. Not so with U.S. English in the Design Report.

0.2.12 Mathematical symbols, subscripts and superscripts

Mathematical symbols are written in math-mode, even when they are embedded in text. For example, a longitudinal dimension L is often called a length. Descriptive subscripts and superscripts, as in L_{acc} or $L^{overhead}$, are not written in Roman font. They appear to be italics, no matter how long or short they are.

0.2.13 Quotation marks

LaTeX is fussy about some things, like quotation marks. Sooner or later an author, a chapter editor, or a general editor must pay attention. This the correct way to put “a certain piece of text” inside quotation marks. The following ”certain piece of text” is incorrect.

0.2.14 Citations, references and the bibliography

Please use inspire hep bibtex entries and notation whenever possible.

Don’t use a “pointer” (for example [4]) in place of naming a reference [7]. That is, use “Joe Blow [4] describes thus and such,” NOT, “[4] describes thus and such”. There should be a space in the text before the citation, so “Joe Blow[4]” is wrong. Multiple citations should be placed with the same square brackets. In the LaTeX vernacular, use `Joe Blow~\cite{Blow2011}` or `Joe Blow~\cite{Blow2011,Smith2012}`.

We are using `bibtex` to handle the references, which are gathered into one `bib` file per chapter, although all references appear in a single bibliography at the end of the Design Report.

During the editing process we are (currently by default) using the LaTeXpackage `showkeys`, which flags references (to Tables, Figures, sections and subsections) and citations (to references) above the text, or in the margin. This should aid in generating cross-references, for example, even though it is rather ugly. It will be turned off in the final stages of editing, before printing. (Comments and feedback, please!)

0.2.15 Miscellaneous

0.2.15.1 "Calculations show that . . . "

This usage, with no indication who carried out the calculations, provides no way for a reader to check the work, or to build upon it in the future. Citations of internal documents, or of individuals to contact to get more information would be helpful for readers, and would also convey a greater sense of credibility. For example, "Relativistic Heavy Ion Collider (2021), unpublished calculations by members of the XYZ working group. Contact Sven Larsson (sven.larsson@bnl.gov) for details."

0.2.15.2 "Should", "must", and reference to future studies

In general, authors should convey the conviction that EIC will do what it should do. In those cases where there is an ongoing internal debate, the Design Report should convey the sense that such debates will be resolved on the basis of a reasoned and careful assessment of the evidence. Only write about future studies in those limited cases where it is needed to show "that we know what we are doing".

0.2.15.3 "Enable"

Incorrect usage:

> "Neutrons pass easily through most materials, enabling the study of large or bulk samples and buried interfaces."

Correct usage:

> "In addition, as the BLM system will be a major tool for beam tune-up, it should also be designed in a way that enables it to pin-point the loss location as precisely as possible."

The point is that the direct object of enable is made capable of doing something – roughly a synonym for empower. You enable the direct object to do something (enable it to pin-point . . .). You could rewrite the first sentence to say, "enabling the study of large or bulk samples . . . to take place." Then it would be correct – although more unwieldy than just saying "making possible the study of . . . "

0.2.15.4 Reporting technical results without a clear statement of their import

In general, it is a mistake to assume that "the numbers speak for themselves". Using words to summarize the meaning of results helps readers to understand them; it also signals that the authors understand the implications of the results they report.

0.2.15.5 Excessive and inconsistent use of lists

Sometimes the use of lists is appropriate, but often there are too many in a draft. Authors should rework most lists into narrative form. For the remaining lists, authors should follow editorial guide-

lines to ensure consistent style across the entire Design Report.

After minimizing the number of lists, Design Report editors will convert most of the remaining lists to enumerated lists. The first letter of each item will be upper case, even when the items in the list are not formulated as complete sentences. Items will generally end with a semi-colon unless the phrases are very short, in which case a comma will be used. The last item in the list will be followed by a period. In those cases in which each item in a list consists of multiple sentences, items will be ended with a period.

0.2.15.6 Cross-references

Should be added throughout the whole Design Report, but only down to `\subsection` level, so that cross-references can be found and numbered in the Table of Contents. This implies that subsections should be reasonably balanced in length – not too many pages long.

0.2.15.7 Isotopes

Write ^{3}He, for example, not 3He or He-3.

0.2.15.8 *** asterisks in comments

Sometimes a comment is inserted in a sentence, perhaps indicating that something needs to happen later, such as add a value, a citation, or more text. In this case please include (at least) 3 asterisks in a row *** so that text searches (for example `grep *** *.f`) are made easier. ALSO CONSIDER WRITING IN UPPER CASE***.

0.3 Dimensions and units

Systeme Internationale (SI) units will be used wherever possible. For example, use MPa instead of bar. Some exceptions are inevitable, for example Kilpatrick units. Unusual units should be briefly explained, on their first introduction.

When in doubt, the `siunitx` package does the Right Thing, for example using:

- `\si{\units}` lower case si
- `\SI{numbers}{\units}` upper case SI

A longitudinal dimension – or length – L should be written in one of these ways:

- $L = 100$ m `$L = 100$~m`
- $L = 100$ µm `$L = 100$~\si{\micro\metre}`
- $L = 100$ km `$L = $ \SI{100}{km}`
- $L = 10^2$ km `$L = $ \SI{e2}{km}`

so that the dimension ("m" or "µm" or "km") is not in italics, and is separated from the numerical value by a non-breakable space – for example "~" in LaTeX vernacular. Do not write $L = 100$m, $100m$ or 100 m. Note that text and mathematical equals signs are different in length (= and $=$): always use the latter.

Powers of ten are written in one of these ways:

- 3.14×10^{39} `$3.14 \times 10^{39}$`
- 3.14×10^{39} `\SI{3.14e39}{}`

Complex dimensions may be written in one of these ways:

- $F = 42\,\mathrm{J\,cm^{-2}\,s^{-1}}$ `$F = 42$~J cm$^{-2}$ s$^{-1}$`
- $F = 42\,\mathrm{J\,cm^{-2}\,s^{-1}}$ `$F=$ \SI{42}{J.cm^{-2}.s^{-1}}`

Exceptionally, percentages are written without a space – 42% is correct but 42 % is not. In LaTeX vernacular a % sign is the beginning of a comment, so it is necessary to say \% ...

Temperatures are written as 273 K or 100°C or 101°C, without a space between the number and the °C unit symbol.

Angles are preferably written $\theta = 7.5$ degrees, although 7.5° is acceptable.

0.4 Numbering – chapters, sections, and subsections

In the `\documentclass{report}` style, a "section" (such as this, with the numeric label 0.4) has two numbers associated with it.

0.4.1 This is the heading of a subsection

A "subsection" (like this, 0.4.1) is labelled by 3 numbers, namely "chapter_number.section_number.subsection_number". Sections and subsections begin with a bold face font.

0.4.1.1 A subsubsection heading like this has no period at the end

In bold font, it has no numerical label, and sits separately from the text that immediately follows, even if there is no white space between `\subsubsection{}` and the first word of the text. It does not appear in the Table of Contents.

This paragraph heading ends with a period. Subsequent text remains in the same paragraph. The editors will use their judgement to prevent the excessive use of paragraph headings and boldface text.

0.4.2 More formatting rules and standards

0.4.2.1 Clearpages and Pagebreaks

As a rule there is NO `\clearpage` or `\pagebreak` before a new section (or subsection), and hence no white space.

0.5 Equations, Tables, Figures, and plots

0.5.1 Equations

Start with a simple equation, like Equation 1:

$$H = \frac{\sqrt{3\left\langle x^4\right\rangle \left\langle x'^4\right\rangle + 9\left\langle x^2x'^2\right\rangle^2 - 12\left\langle xx'^3\right\rangle \left\langle x^3x'\right\rangle}}{2\left\langle x^2\right\rangle \left\langle x'^2\right\rangle - 2\left\langle xx'\right\rangle^2} \tag{1}$$

Avoid ending a sentence with an equation, in order to avoid deciding whether or not to put a period after the equation.

Here is a simple equation array:

$$\begin{aligned} M_{virg}(\sigma) &= M_{virg0} + k_{virg}.\sigma \\ M_{rel}(\sigma) &= M_{rel0} + k_{rel}.\sigma \end{aligned} \tag{2}$$

0.5.2 Tables

- Table 1 is a relatively complicated multi-column table, while Table 2 is a standard 3-column parameter table.
- Table 3 shows how to make a table exportable, for example to the Parameter Tables appendix.
- The source text for Table 4 shows how to enable text filling in columns.
- Table 5 shows 2 ways to squeeze tables, with the `\scalebox{}` and `\phantom{}` commands.
- Table 6 shows a third way, using `\tabcolsep{}`.

The vertical spacing of Table rows is set in "preamble.tex" by the line `\renewcommand{\arraystretch}{1.0}`.

0.5.3 Converting between LaTeX and Excel table formats

More than one free utility enables table conversion with a drag-and-drop interface. E.g.:

Excel to LaTeX try `https://tableconvert.com/excel-to-latex`

LaTeX to Excel try `https://tableconvert.com/latex-to-excel`

Facility	Location	Status	First oper.	Power [MW]	Instruments	Integrated flux [10^{14}cm^{-2}]	Peak flux [10^{15}cm^{-2}s^{-1}]
ESS	Lund	Pre-constr.	2019	5	22	–	40
J-PARC	Tokai	Re-furbish	2009			–	

Table 1: A standard Table looks like this, using "toprule", "midrule" and "bottomrule" separation lines.

Parameter	Unit	Value
Energy	GeV	2.5
Current	mA	50
Pulse length	ms	2.86
Pulse repetition frequency	Hz	14
Average power	MW	5
Peak power	MW	125

Table 2: Long version of caption for top-level parameters.

Parameter	Unit	Value
Energy	GeV	2.5

Table 3: A parameter table made available for export, for example to Appendix E "Parameter Tables", using input from a /Tables subdirectory file.

System	Subsystem	Test
Target	Shaft and drive	Run at up to 25 Hz.
	Target segments	Leak test at pressure.
	Target Safety System	Demonstrate trip signals generated for all defined cases.
Primary helium loop	Pump, heat exchanger, filter	Pressure and flow tests without target.
	Full loop with target	Full operational test without heat.

Table 4: A table with fixed third column width, enabling text filling.

Nuclide	**Decay time** [years]						
	0	6	40	100	1000	10^4	10^5
^{3}H	0.9	83.4	96.4	72	0	0	0
^{14}C	0	0	0	0	0.3	0.6	0
^{36}Cl	0	0	0	0	0	0	0.7
^{39}Ar	0	0	0	0.1	0.7	0	0
^{154}Dy	0	0	0	0	0	0.2	4.3
^{163}Ho	0	0	0	0.7	29.7	53.4	0

Table 5: Two ways to squeeze tables, with the "scalebox" and "phantom" commands.

Nuclide	**Decay time** [years]						
	0	6	40	100	1000	10^4	10^5
^{137}La	0	0	0	0	1.4	8.7	57.6
^{148}Gd	0	0.2	0.9	11.6	0.1	0	0
^{150}Gd	0	0	0	0	0	0.3	5.6
^{154}Dy	0	0	0	0	0	0.2	4.3
^{157}Tb	0	0.1	0.6	9.3	7.2	0	0
^{154}Dy	0	0	0	0	0	0.2	4.3
^{163}Ho	0	0	0	0.7	29.7	53.4	0

Table 6: A third way to squeeze tables, with the "tabcolsep".

0.5.4 Figures

Many figures, like Figure 1, are non-graphical images – perhaps a photograph, drawing or sketch.

Figure 1: This is an example of a non-graphical figure. We need to address the means by which we can give "all" graphs the same look and feel.

0.5.5 Plots

It is clear that for the ePIC detector sections we will mostly be using ROOT and Python, while the accelerator team most likely will be using a different package; so as soon as a figure style is agreed on, we will need to make style packages for ROOT and Python so all figures in the manuscript look stylistically the same.

As teams develop initial plots, please be sure to each the codes available so that they can be remade in a common style.

0.6 Italics and bold face type

In general, retsrain the use of *italics* and **bold face**.

Long quotations will be set in italics. Italics will also be used (sparingly) for traditional purposes of emphasis (e.g. "when she was good, she was *very* good.")

Occasionally, authors wish to draw attention to the subject matter being addressed in a block of text. Usually, this should be done by headings and subheadings. In those limited instances in which use of altered type face is appropriate within the body text, the editors will use bold face, rather than italics. One such situation is for short introductory phrases at the beginning of paragraph-long items in an enumerated list.

0.7 Issues that this Style Guide does not yet address

This Style Guide addresses "consistency of style" issues. Here is a numerical list of issues that could or should be significantly expanded:

1. the use of pronouns
2. specialized terminology
3. acronyms
4. the use of italics
5. the use of digits (e.g. 1) where written numbers are more appropriate
6. the overuse of capital letters (Boron vs. boron, User vs. user, etc.).
7. balancing the length of sections and subsections
8. global glossary
9. Lists
10. Plots (see placeholder 0.5.5)

Chapter 2

Physics Goals and Requirements

2.1 EIC Context and History

The Electron-Ion Collider is a major new research facility to advance the longterm vision for Nuclear Physics to discover and understand the emergent phenomena of Quantum Chromo-Dynamics (QCD). The developing of the physics case for the EIC has been a tremendous community effort over the last few decades.

A joint report on the EIC Science case was put together at the Institute for Nuclear Theory (INT) in 2010 [8]. This set the base for the following release in 2014 of a White Paper (WP) [9] outlining the fundamental questions that would have been addressed at the EIC. In the following year, the US 2015 Long Range Plan for Nuclear Science recommended a high-energy high-luminosity polarized EIC as the highest priority for new facility construction.

In 2016, the worldwide fast growing community of scientists interested in the EIC organized itself under the EIC Users Group (EICUG) [www.eicug.org].

In 2017, the National Academy of Sciences, Engeneering, and Medicine (NAS) assessed the science case of the EIC as "compelling, fundamental, and timely". Quoting from the NAS report [10] released in 2018, the EIC can uniquely address three profound questions about nucleons—neutrons and protons—and how they are assembled to form the nuclei of atoms:

- How does the mass of the nucleon arise?
- How does the spin of the nucleon arise?
- What are the emergent properties of dense systems of gluons?

In December 2019, following the extremely positive assessment by the NAS, the US Department of Energy (DoE) established EIC Critical Design 0 (CD0), a "mission need" declaration", formally starting the EIC Project.

At about the same time, in late 2019, the EICUG led an intensive, year-long consideration of the EIC physics measurements and scientific equipment. This initiative yielded the EICUG Yellow Report (YR) [7] defining the detector requirements needed to deliver the science case endorsed by the NAS report and highlighted in the WP and all the subsequent studies and publications. The YR

provided the basis for further development of concepts for experimental equipment best suited for EIC science needs.

The ePIC Collaboration, established in July 2022 at the EICUG Meeting at Stony Brook University. ePIC was born as a merger of two pre-conceptual designs, ECCE [11] and ATHENA [12] and is a general purpose detector to deliver the whole EIC core science program.

The propose of this chapter study key measurements in order to demonstrate that our current detector design, is capable of delivering on its mission.

Processes taken into consideration are chosen for both their relevance to the core science and the specific challenges that they pose to the detector.

All the studies contained in this pre-TDR are based on a full GEANT4 simulation of the ePIC detector and reconstruction tools as available in the October 2024 simulation campaign. As the development of both simulation and tools progresses, we will repeat our studies for the final TDR.

In some instances, our ability to demonstrate the detector performance for a relevant measurement might be hampered by the absence of a needed tool that was yet to be developed/finalized. When this occurs, it must not be taken as that the detector cannot accomplish a certain measurement or that we are overlooking certain physics. Our goal is to be able to show those results by the final version of the TDR (90% design completion).

There are many studies performed by the ePIC's Physics Working Groups that will not enter this selection but that are absolutely relevant for the EIC core science and beyond. Furthermore, many details that went into the physics studies, both on the analysis and the impact on the current knowledge, will be omitted for the purpose of this TDR. The ePIC collaboration plans to separately publish a "science paper" containing all the missing information that cannot be given within the present document.

2.2 The Science Goals of the EIC and the Machine Parameters.

We will add more on science goals and machine parameters here by version 1

2.3 Reconstruction Tools and Special Probes

2.3.1 Kinematic reconstruction

The DIS scattering event can be described by two kinematic variables, typically the momentum transfer squared, Q^2, and scaling variable, x_B. Although it is possible to completely reconstruct neutron-current inclusive event kinematics from only the scattered electron, this does not always result in the best resolution. To optimize resolution, multiple reconstruction methods can be employed, using various combinations of scattered electron and hadronic final state (HFS) information:

- **Electron method**: uses only scattered electron
- $e\Sigma$ **method**: uses both scattered electron and HFS
- **Double-angle method (DA)**: uses both scattered electron and HFS

- **Jacquet-Blondel method (JB)**: uses only HFS

For more details on these three methods see Sec.8.1.1 of the YR [7]. Generally, these methods differ in the calculation of Q^2 and inelasticity y, then the scaling variable is calculated as $x_B = Q^2/sy$. Note that while JB typically does not give the best resolution, it is the only reconstruction method possible for charged-current interactions (where the outgoing DIS lepton is a neutrino).

Figure 2.1 shows the y resolution at ePIC as a function of x_B and Q^2 for 18 GeV on 275 GeV ep collisions. As can be seen, the optimal reconstruction method changes with kinematics. These resolutions result from reconstructing the electron momentum strictly from tracking detectors. The resolution could be further improved by using the electromagnetic calorimeter clusters to reconstruct the electron energy. This is particularly important for electrons scattered into the backwards ECAL.

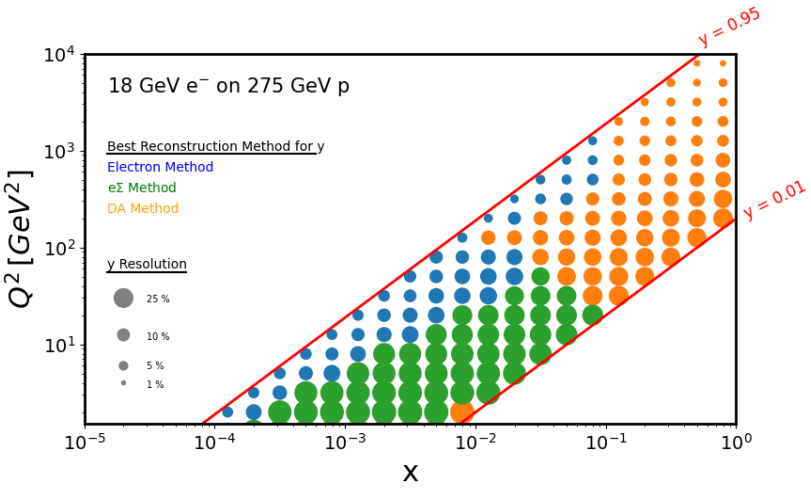

Figure 2.1: y Resolutions.

2.3.2 Electron identification and event selection

Regardless of reconstruction method used, it is important to identify the scattered electron in the event final state. It can be challenging to separate the electron signal from the large π^- background present in DIS collisions. A rudimentary electron identification algorithm has been already developed in ePIC and applied to inclusive analyses.

The first step is to separate final state electrons from pions. This is done by applying a cut on E/p, where p is the track momentum and E is the ECAL cluster energy matched to that track. Electrons will typically deposit all of their energy in the ECAL and have $E/p \approx 1$, while pions will pass through the ECAL and peak at $E/p < 1$. The current analysis uses a cut of $0.7 < E/p < 1.3$, which accounts for smearing due to electron energy and momentum resolutions.

The next step is to identify the scattered DIS electron, as other electrons may be present in the final state. All negative tracks satisfying our E/p requirement are used to calculate $\delta_h = \sum_i (E_i - p_{z,i})$, where the sum i runs over all final-state hadrons. Note that the electron candidate must be excluded in the summation. For the DIS electron, $\delta_h \approx 2E_e$, while for other particles $\delta_h < 2E_e$. The current analysis chooses the electron candidate with the highest δ_h.

This rudimentary algorithm is actively being improved, namely by incorporating signals from PID detectors (hpDIRC, pfRICH, TOF), applying cuts on shower shape parameters of the calorimeter clusters, and using a more rigorous treatment of δ_h instead of simply taking the largest value.

Further, kinematic cuts are applied to ensure DIS kinematics and avoid regions of poor resolution and large backgrounds:

- $Q^2 > 2\,\mathrm{GeV}^2$
- $W^2 > 10\,\mathrm{GeV}^2$
- $0.1 < y < 0.95$

2.3.3 Jets: a versatile probe

As demonstrated in the YR [7], jets are an important observable, bringing both complimentary and unique insight to many of the EIC science goals. In order to comprehensively evaluate the impact that they can have, jet reconstruction has been integrated into the ePIC reconstruction framework, EICrecon. It utilizes the FastJet package to implement various jet definitions. The default settings, which are used for jets saved to the shared output trees and included in the analyses below, include the Anti-k_T algorithm, E-scheme recombination, a resolution of 1.0, and a minimum jet transverse momentum of 1 GeV/c. In addition, constituents were required to have transverse momenta greater than 200 MeV/c to be included in the clustering.

Due to the lack of mature algorithms for integrating information from tracking, calorimetry, and particle identification subsystems, the reconstructed jets used to benchmark the ePIC detector performance and evaluate physics impact are clustered exclusively from charged particle tracks.

The primary metrics for evaluating the quality of jet reconstruction at ePIC are the jet energy scale (JES) and jet energy resolution (JER). These quantities were calculated by comparing the energies of matched particle-level and reconstructed jets. Because the reconstruction currently uses track-only jets and we are primarily interested in quantifying the effects of the detector, only stable charged particles were used when clustering the particle-level jets. For each particle-level jet, the closest reconstructed jet in $\eta - \phi$ space was considered the matching jet as long as $\Delta R = \sqrt{\Delta\eta^2 + \Delta\phi^2}$ was less than 0.1. The quantity: [(reco - particle)/particle] jet energy was found for each set of matching jets and fit with a triple Gaussian function. A triple Gaussian was used to try to take into account the tails of the distribution. The mean of fit is taken as the JES while the sigma is taken as the JER. To get a more differential picture of the jet performance, this procedure was performed as a function of particle-level jet energy for three pseudorapidity ranges as shown in Fig. 2.2.

2.4 The EIC Science (ePIC performance for key observables)

2.4.1 Origin of Nucleon Mass

Nucleons are made of quarks bound together by massless gluons. The Higgs mechanism can only explain the source of the quark masses. Nevertheless, the masses of valence quarks account only for $\sim 1\%$ of a nucleon's mass and thus cannot explain the mass of all the visible matter in the universe. The reminder of the proton mass must originate from the field energy of quarks and gluons in the sea.

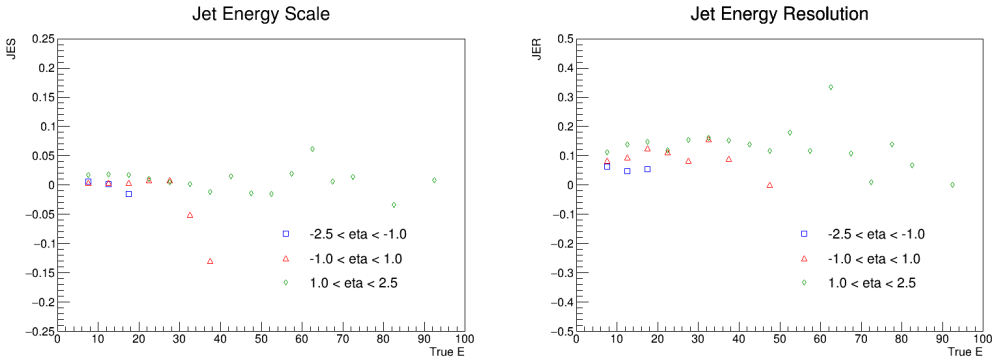

Figure 2.2: PLACEHOLDER (Left) Jet energy scale and (Right) jet energy resolution as a function of particle-level jet energy for backward (blue squares), mid (red triangles), and forward (green diamonds) rapidities.

The most accessible description of hadrons in terms of their constituent partons is by parton distribution functions (PDFs), representing the fractional (longitudinal) momentum carried by each parton flavor. The inclusive DIS cross section is sensitive to PDFs through the structure functions F_1 and F_2, which are linear combinations of the PDFs.

Tomographic images of quarks and gluons, also achievable at ePIC, will be discussed in Sec.2.4.3.

2.4.1.1 Inclusive neutral current cross sections

To extract neutral-current cross sections, corrections for acceptance and bin migration are defined by comparing reconstructed events to generated events. These corrections are then applied to the reconstructed events. Note that since the same reconstructed events are used for both the corrections and cross section extraction, this by definition yields the cross sections of the underlying event generator.

The projected neutral-current reduced cross sections for three center of mass energies are shown in Figures 2.3-2.5. These use the electron identification and event selection criteria as described in Sec: 2.3.2. However, at this stage the kinematics have been reconstructed using the electron method only. The statistical uncertainties are estimated assuming an integrated luminosity of 10 fb^{-1} for each center of mass energy.

2.4.1.2 Upsilon production

The production of the three Υ states in the electron channel was simulated in electron-proton collisions at a center-of-mass energy of 18×275 GeV. The Monte Carlo samples were generated using eSTARlight, covering a range of $10^{-3} < Q^2 < 10\ GeV^2$, with no restrictions on W. The Υ states

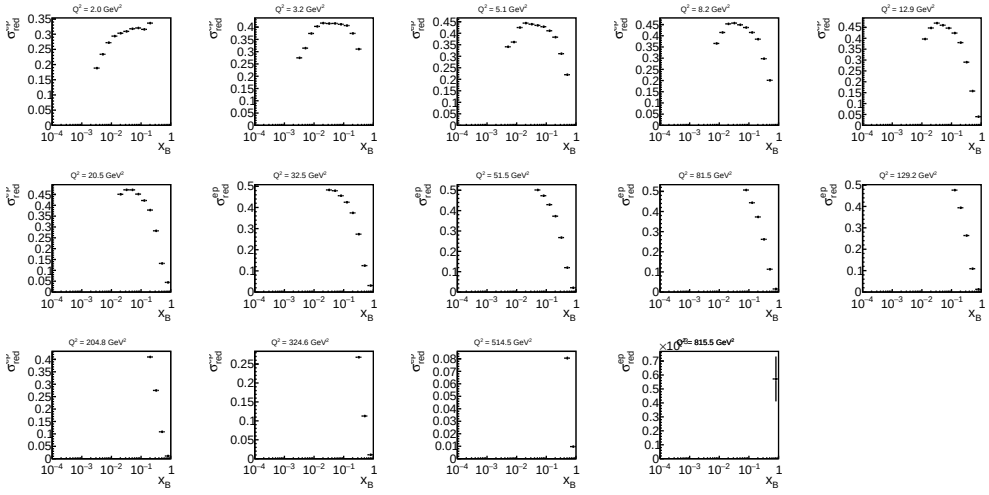

Figure 2.3: Projected *ep* neutral current reduced cross sections at 5x41 GeV. Statistical uncertainties assume an integrated luminosity of 10 fb^{-1}.

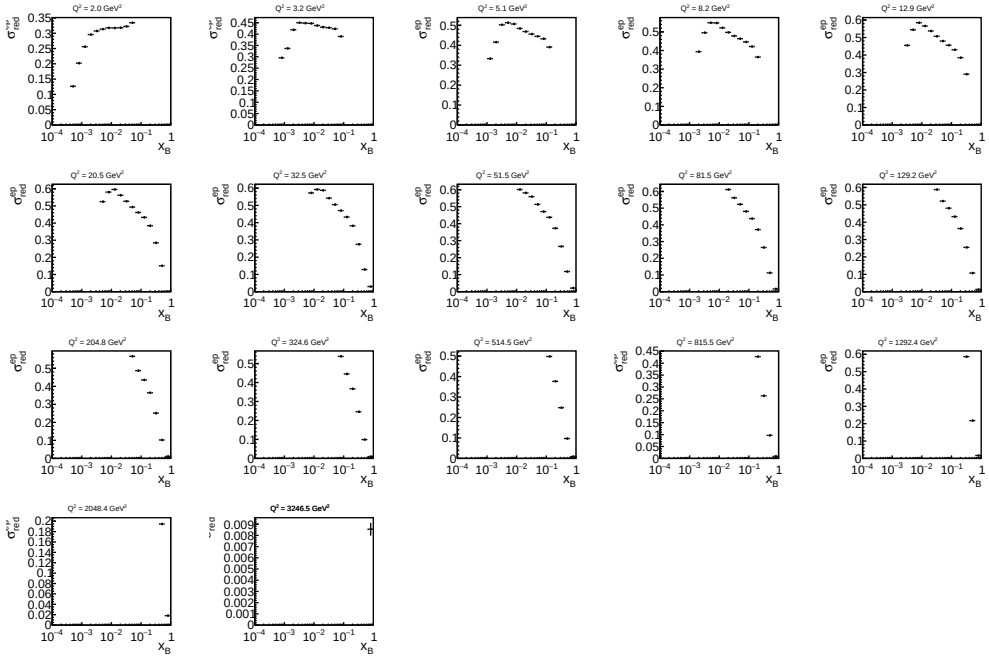

Figure 2.4: Projected *ep* neutral current reduced cross sections at 10x100 GeV. Statistical uncertainties assume an integrated luminosity of 10 fb^{-1}.

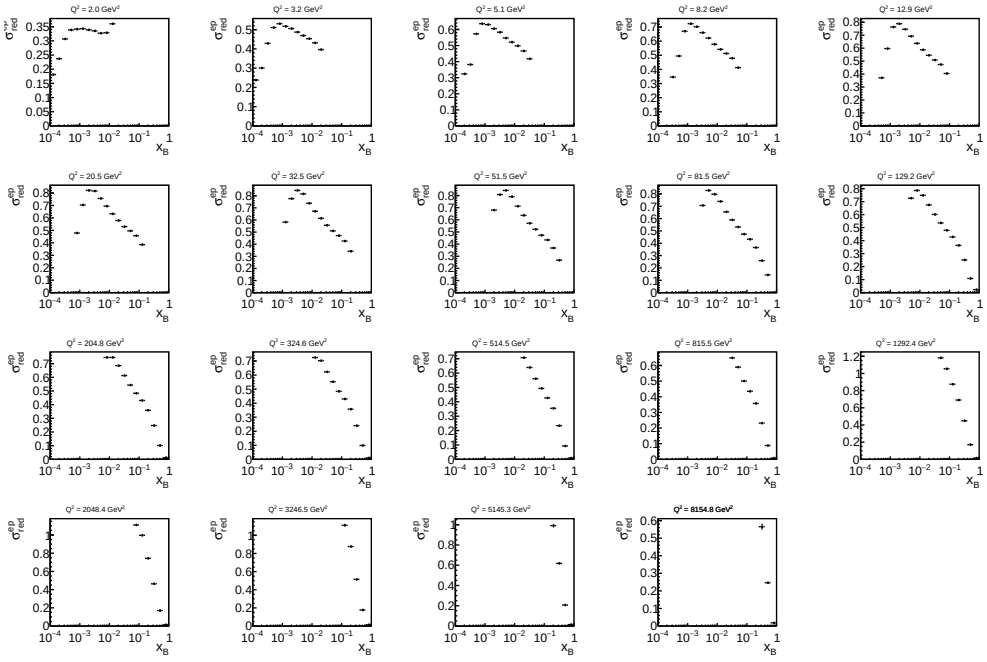

Figure 2.5: Projected ep neutral current reduced cross sections at 18x275 GeV. Statistical uncertainties assume an integrated luminosity of 10 fb^{-1}.

were produced according to their relative ratio based on [13] and then combined. The reconstruction of these Monte Carlo samples was simulated using EICRECON version 1.15.0. The figure showcases the momentum resolution of the ePIC tracking system in terms of separating the three Υ states, which is presented across various rapidity regions for the reconstructed Υ states. The top left plot in Figure 2.6 represents the resolution for all rapidity regions combined, while the other plots present results for specific intervals: $-3 < y < -1$, $-1 < y < 0$, $0 < y < 1$, $1 < y < 2$, and $2 < y < 4$. In the forward region, corresponding to $2 < y < 4$, a degradation in resolution was observed. However, in a similar study done by the muon channel (not shown), it is found to have an improvement on the resolution of approximately 1 to 8 % due to reduced final state radiation.

2.4.2 Origin of Nucleon Spin

Thanks to the availability of polarized electron and hadron beams at the EIC, inclusive DIS can be used to probe the contribution of nucleon spin from quark helicity. Double-spin asymmetries between different relative electron/hadron polarization states are sensitive to polarized PDFs through the spin structure function $A_1 \propto g_1 = \sum_q e_q^2(\Delta q - \Delta\overline{q})$. The gluon contribution to nucleon spin is inferred by the Q^2 dependence of the spin structure functions, therefore it is critical for the measurements to cover a wide range of kinematics.

The projected proton double-spin asymmetries A_1^p for three center of mass energies are shown in Figure 2.7. The statistical uncertainties are estimated assuming an integrated luminosity of 10 fb^{-1} for each center of mass energy, equally split between the the beam polarization configurations required for the asymmetry measurement. The reconstruction, event selection, and kinematic cuts are described in Sec. 2.3.2.

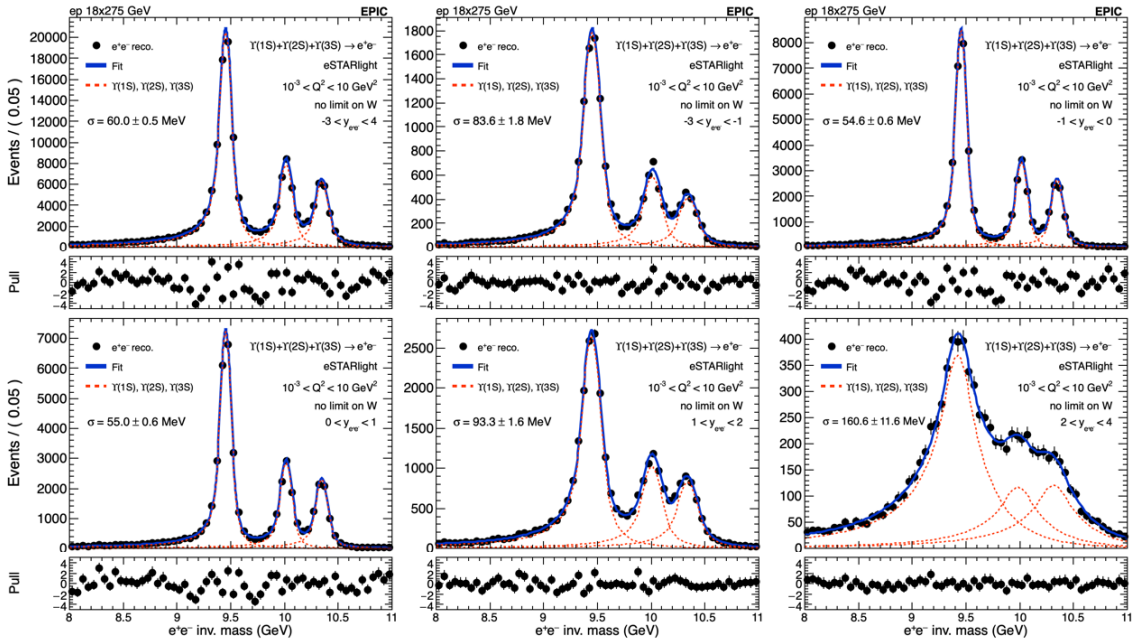

Figure 2.6: The reconstructed mass distribution of the Υ three states in the electron channel from the electron-proton collisions at $18 \times 275\ GeV$, utilizing the tracker with realistic seeding. The top left plot shows the invariant mass distribution of the Υ three states in the rapidity range from -3 to 4. The other plots display invariant mass distribution for specific rapidity intervals: (top middle) $-3 < y < -1$, (top right) $-1 < y < 0$, (bottom left) $0 < y < 1$, (bottom middle) $1 < y < 2$, and (bottom right) $2 < y < 4$. The resolution of the Υ three states is indicated on each plot as σ.

2.4.3 Multi-Dimensional Imaging of the Nucleon

One-dimensional PDFs reveal the distribution of longitudinal parton momenta in the direction of the nucleon momentum. Nevertheless, a fast moving nucleon has still sizable transverse spatial dimensions.

The 3D parton structure of hadrons in momentum space is encoded in transverse momentum dependent parton distributions (TMDs). The non-perturbative quantities that encode the spatial distributions in the transverse plane are called generalized parton distributions (GPDs).

2.4.3.1 Imaging in Momentum Space

Using semi-inclusive DIS, it is possible to extract information on the three-dimensional momentum structure of the nucleon by making use of transverse momentum dependent fragmentation functions. These in turn provide sensitivity to the flavor and the transverse momentum of partons in the nucleon. Already with an un-polarized nucleon the ePIC experiment can provide flavor-separated transverse-momentum dependent PDFs over a large range in x and Q^2, and for transverse momenta that reach from the low, TMD-dominated region into the perturbative region. The wide range of scales, as shown in Fig.2.8 will also solve the existing uncertainties in the TMD evolution where non-perturbative contributions require experimental input.

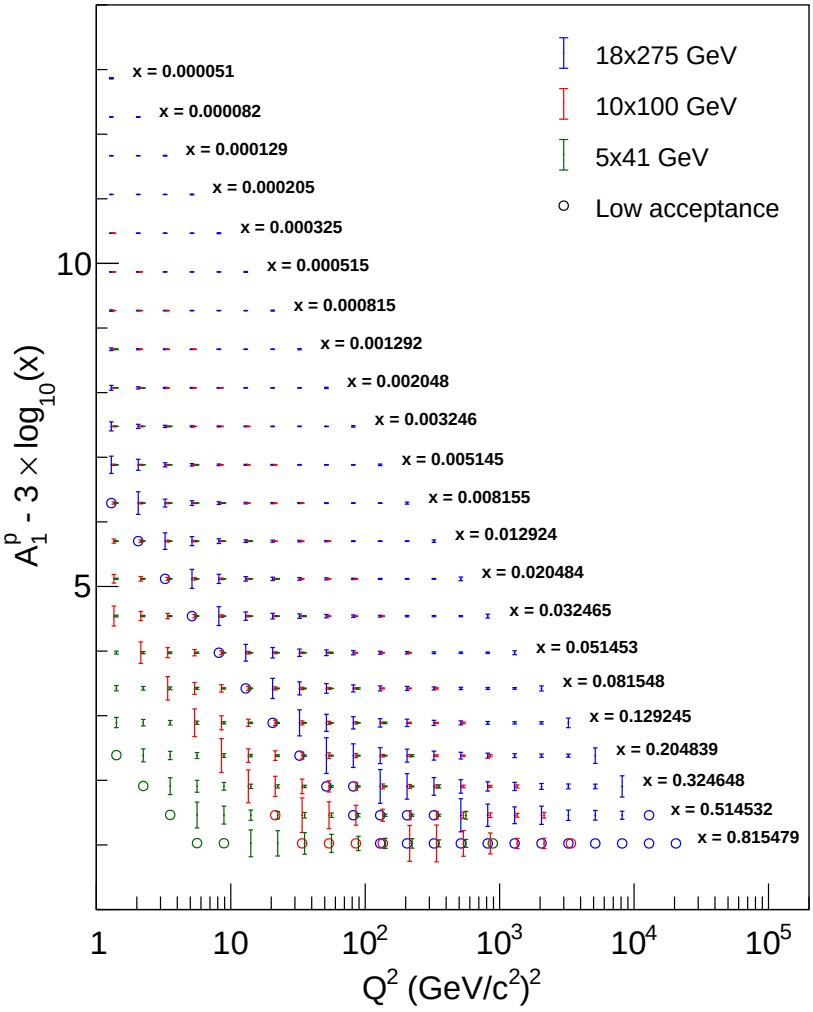

Figure 2.7: Projected measurements of A_1^p.

These unpolarized TMD PDFs also serve as the unpolarized baseline for any polarized TMD observable which are obtained as single or double spin asymmetries. The most relevant are the Sivers function [14, 15] and the quark transversity [] which is obtained together with either the Collins fragmentation function [] or a di-hadron fragmentation function []. Examples of the expected uncertainties on these asymmetries are displayed in Fig. 2.9 where one can see that over a larger range of phase space very precise uncertainties can be obtained. Those will in turn then provide flavor-separated Transversity extractions and their first moments, the tensor charges. These tensor charges are of particular interest as they can relate to interactions outside the standard model. Lattice-QCD can model the tensor charges very well and any differences with the measurements would provide a hint for BSM physics.

Collins asymmetries of identified hadrons in jets are also sensitive to the Collins Fragmentation Function (FF), which describes the azimuthal distribution of hadrons fragmented by a transversely polarized quark as a function of the parent quark momentum fraction carried by the hadron (z) and the hadron momentum transverse to the quark direction (κ_T). Figure 2.10 illustrates projected statistical precision for Collins asymmetry measurements of charged π, K and p in jets as a function

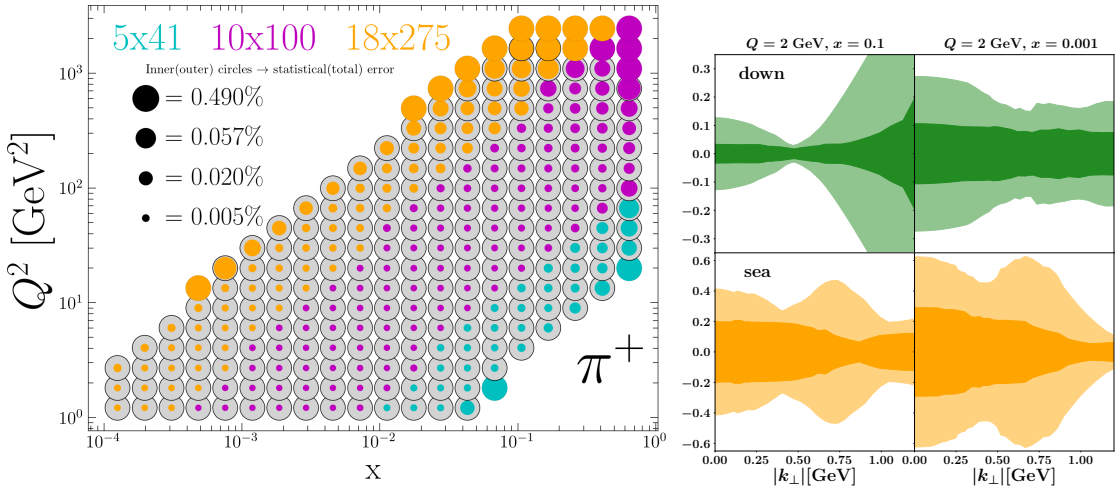

Figure 2.8: Left: Expected statistical and total uncertainty of un-polarized TMD PDFs for π^+ in the $Q^2 - x_B$ plane. The inner (colored) circle shows the statistical uncertainty, while the outer circle provides the total uncertainty for each $Q^2 - x_B$ bin. The color shows the beam energy configuration which provides the highest statistics in a specific bin. Right panel: Expected uncertainties of valence down (green) and sea quark (orange) TMD PDFs at $x = 0.1$ (left) and $x = 0.001$ (right) as obtained based on the MAP24 [1] global TMD fit. The lighter shaded regions show the uncertainties based on existing data while the darker shaded regions show the expected uncertainties after including ePIC data.

of hadron z and jet p_T. An absolute statistical uncertainty of less than *XXX* can be achieved for jet $p_T = 20$ GeV/c for protons. When integrated over jet $5.0 < p_T < 51.9$ GeV/c, the statistical uncertainty becomes negligible for the range of $0.1 < z < 0.8$. These high precision measurements will provide stringent constraints for quark transversity in the proton.

2.4.3.2 Imaging in Transverse Position Space

GPDs can be extracted via measurements of exclusive reactions. E.g. the exclusive production of a real photon via deeply virtual Compton scattering (DVCS) or of a meson, while the proton remains intact. Exclusivity requires all the final-state particles to be detected.

DVCS events have been simulated using the EpIC Monte Carlo generator [16] with a minimum Q^2 of 1 GeV^2. The analysis of such events provides a good test of a large number of subsystems within the ePIC detector, namely the scattered electron and final state photon are detected in either the central barrel or endcaps, and the scattered proton is detected in the far forward region within the B0 spectrometer or the Roman Pot detectors.

DVCS candidate events were identified by applying a series of cuts on the individual final state particles, as well as on the properties of the full reaction. The cuts applied were as follows:

- exactly 1 photon, scattered electron and scattered proton were reconstructed in the final state.
- the reconstructed electron and photon have momenta no more than 10% higher than the corresponding beam momentum; for this study, that corresponds to a maximum of 11 GeV for scatterd electrons and 110 GeV for scattered protons.

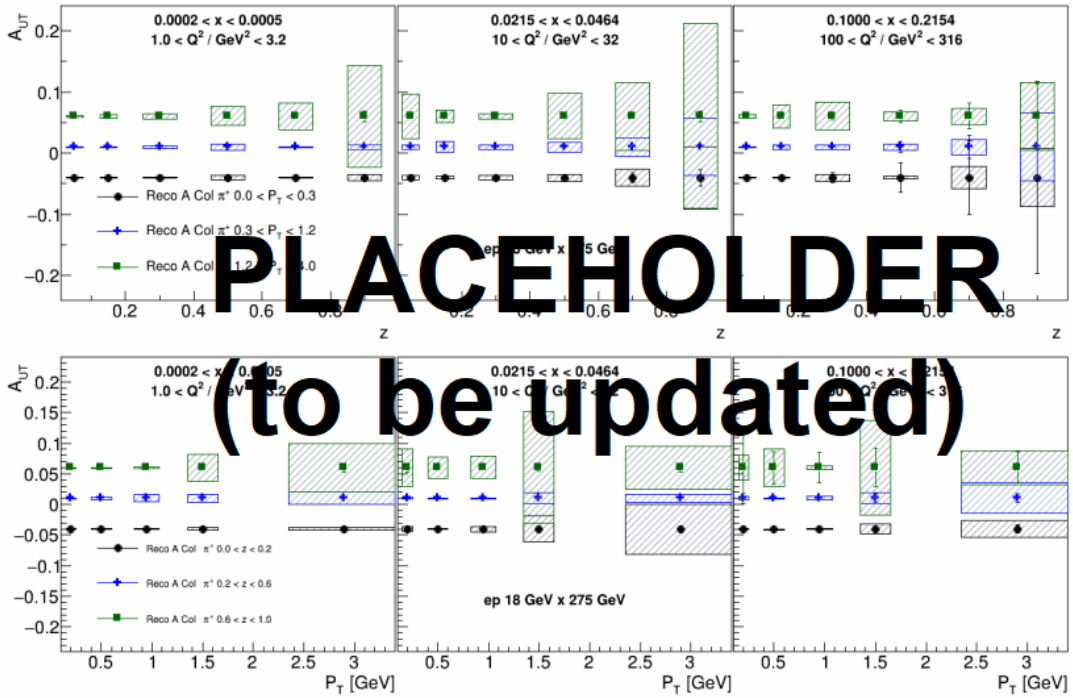

Figure 2.9: Expected uncertainties in three example x-Q^2 bins for the Collins asymmetries as a function of the momentum fraction z in three bins of hadron transverse momentum relative to the virtual photon direction.

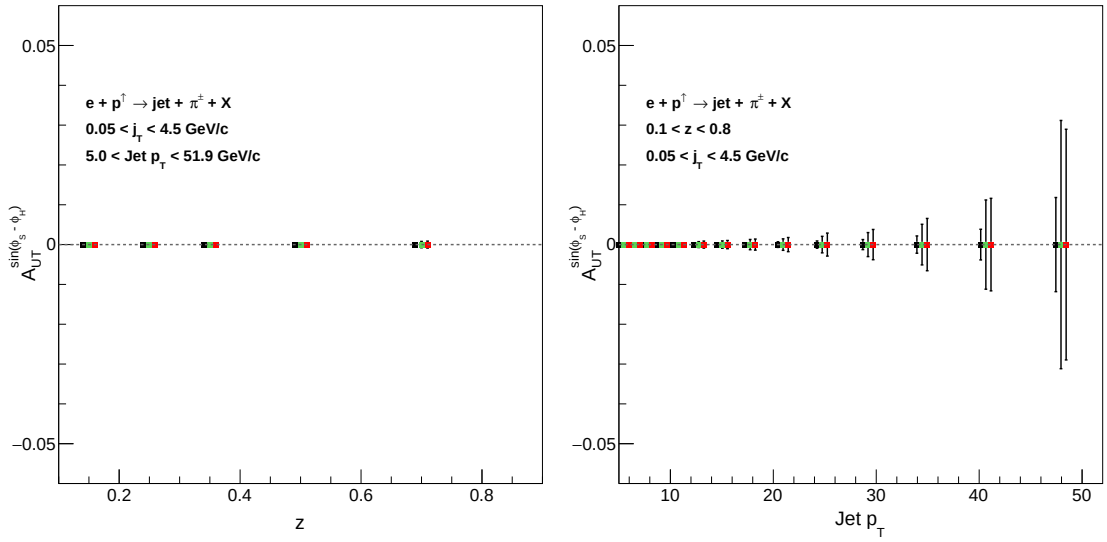

Figure 2.10: Projected statistical precision, indicated by vertical bars around data points, for measurements of Collins asymmetries of identified hadrons in jets as a function of hadron z (left) and jet p_T (right). In case the vertical bars are invisible, they are smaller than the marker size. This figure will be updated

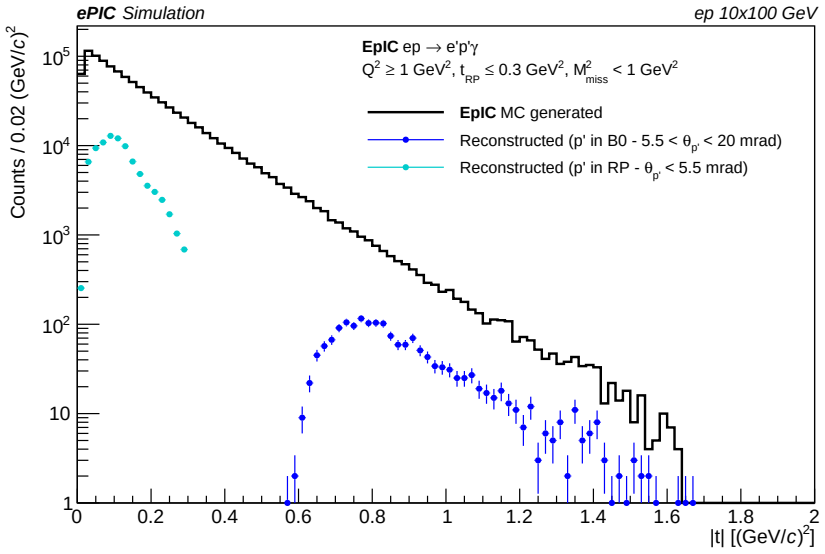

Figure 2.11: Generated and reconstructed t-distributions for fully-exclusive DVCS events.

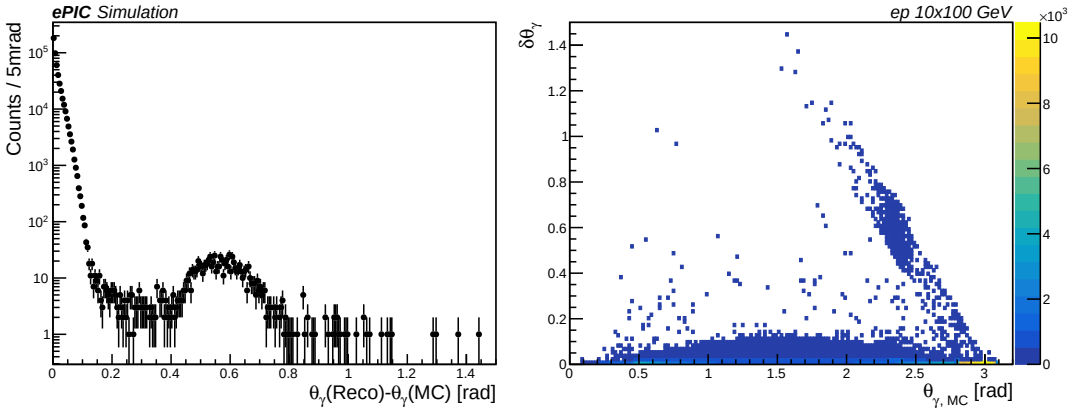

Figure 2.12: Reconstructed minus generated track θ for all reconstructed DVCS photons (left), well as as a function of the generated photon θ (right). Note that the left plot is on a logarithmic scale.

- track θ cuts for the reconstructed proton (where θ is defined as the angle from the positive z-axis to the track of interest) to ensure the track matches the acceptance of the detector expected. Tracks reconstructed in the Roman Pots are required to have $\theta < 5.5$ mrad; tracks in the B0 spectrometer are required to have $5.5 < \theta < 20$ mrad.
- a minimum Q^2 of 1 GeV^2, to match the conditions of the initially generated events.
- a maximum t for events with the proton detected in the Roman Pots of 0.3 GeV^2.
- a maximum missing mass of the full final state, M^2_{miss} of 1 GeV^2.

As mentioned, a key parameter on which the DVCS process depends is the Mandelstam variable t

of the reaction. The generated and reconstructed distributions of t, calculated for events with full exclusivity (exactly one reconstructed electron, proton and photon), are shown in figure 2.11. As well as studying the underlying physics process, DVCS can be used to test the performance of the ePIC subdetectors. Figure 2.12 shows the angular resolution of the barrel calorimeters, calculated using the detected DVCS photon. Of particular note from figure 2.12 are the following points:

- the angular reconstruction of the barrel is, on the whole, very good. No more than 0.5% of all photons are reconstructed more than 5° from their generated track, and more than 75% are reconstructed to within 1°.
- the significant majority of the generated photons are detected in the electron endcap calorimeter, in the range $2.8 < \theta < 3.1$ rad.

2.4.4 Properties of Nuclear Matter

2.4.4.1 Gluon Saturation

One of the three central questions highlighted in the National Academy of Science report on Electron-Ion Collider (EIC) science is to understand the properties of high parton density matter and the onset of gluon saturation. A critical observable for understanding the dynamics of gluonic matter is the spatial distribution of gluons within nuclei, particularly in systems likely to be in the saturation regime at high energy.

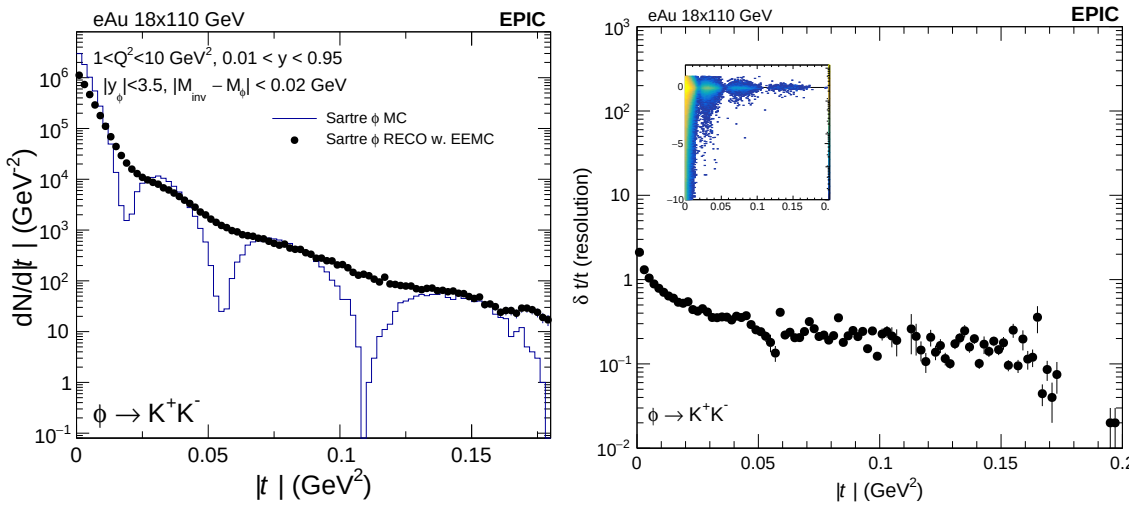

Figure 2.13: Left: differential distribution of the momentum transfer $|t|$ of coherent ϕ meson electroproduction in electron-gold collisions with 18x110 GeV. The Monte Carlo model is provided by Sartre and the reconstructed distribution is obtained from full ePIC simulation with the official August 2024 simulation campaign. Right: the momentum transfer t reconstruction resolution as a function of the true t.

To achieve gluon imaging of nuclei, exclusive and diffractive vector meson electroproduction involving electron-heavy nuclei collisions has been proposed [9]. In Fig. 2.13 (left), the differential

	Signal efficiency	Background efficiency
3 tracks	0.97383	0.914885
J/ψ mass window	0.898815	0.827045
Veto signals in B0	0.898805	0.429656
Veto signals in OMD	0.898805	0.29286
Veto signals in ZDC	0.898795	0.013776

Table 2.1: Event composition in incoherent J/ψ production before and after full event selection

cross section for ϕ meson production is shown for electron-gold collisions at an energy configuration of 18x110 GeV. The input is derived from the Monte Carlo model Sartre, and the reconstructed distribution is obtained after a full ePIC simulation based on the version from August 2024. The reconstruction is achieved by detecting a scattered electron in the backward calorimeter and reconstructing the two kaons from ϕ decay using tracking data.

As shown, the diffractive structure is barely visible in the reconstructed data due to insufficient momentum transfer (t) resolution. The main limitation stems from the electron reconstruction, where the momentum resolution is hampered by the small scattering angle relative to the electron beamline. The magnetic field in this region is insufficient to provide the necessary lever arm for achieving the required momentum resolution. More specifically, Fig. 2.13 (right) presents the momentum transfer t reconstruction resolution as a function of true t. Efforts to improve the resolution are ongoing.

On the other hand, the incoherent vector meson production needs to be vetoed in the event in order to suppress its contamination to the coherent process. This is enabled by the far-forward detector system (B0, Roman Pot, Off-Momentum Detector, zero-degree calorimeter). By vetoing signals in the forward detectors one can reject up to two orders of magnitude of the incoherent background. Table 2.1 summarizes the fraction of signal and background events after each veto.

The t spectra of coherent and incoherent (before veto) are shown in Fig. 2.14 left, and the residue distribution of incoherent production events (that pass event selection) are shown in Fig. 2.14 right. Therefore, the vetoing power is sufficient to supress the incoherent production down to a level below the first diffractive minimum but not quite for the second and third minima.

2.4.4.2 Nuclear Modifications of Parton Distribution Functions

Add text here.

2.4.4.3 Passage of Color Charge Through Cold QCD Matter

[Rongrong: performance of D^0 reconstruction with ePIC is currently under study. It is not clear if it will be available for pre-TDR, but definitely will be included in TDR.]

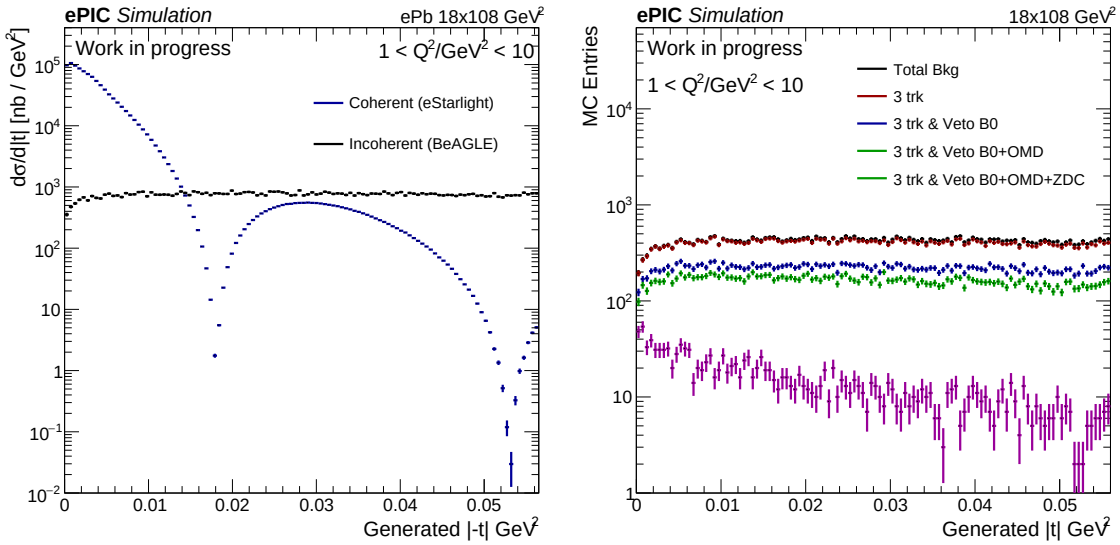

Figure 2.14: Left: Differential cross-section of momentum transfer t distribution for coherent (blue) and incoherent (black) exclusive J/ψ production in ePb collisions. Right: Differential measurement of t and the residue distributions after each veto based on the far-forward detector system.

Chapter 8

Experimental Systems

8.1 Experimental Equipment Requirements Summary

The YR table (Fig. 8.1) is being reviewed and an updated table with accompanying text will be included in the draft Version1.

Table 10.6: This matrix summarizes the high level requirements for the detector performance. The interactive version of this matrix can be obtained through the Yellow Report Physics Working Group WIKI page (https://wiki.bnl.gov/eicug/index.php/Yellow_Report_Physics_Common).

η	Nomenclature			Tracking				Electrons and Photons			π/K/p		HCAL		Muons
Paste				Resolution	Allowed	minimum-pT	Si-Vertex	Resolution σ/E	PID	min E	p-Range	Separati	Resolution σ/E	Energy	
-6.9 to -5.8			low-Q2 tagger	σE/E < 1.5%; 10-6 < Q2 < 10-2 GeV2											
-5.0 to -4.5						300 MeV pions									
-4.5 to -4.0			Instrumentation to separate charged particles from photons			300 MeV pions		2%/√E(+1-3%)		50 MeV					
-4.0 to -3.5	↓ p/A	Auxiliary De								50 MeV			~50%/√E + 6%		
-3.5 to -3.0										50 MeV					
-3.0 to -2.5			Backward Detector	σpT/pT ~ 0.1%@0.5%			σ_xy ~ 30⊕pT μm +40 μm			50 MeV					
-2.5 to -2.0				σpT/pT 0.05%@0.5%			σ_xy ~ 30⊕pT μm +20 μm	2%/√E(+1-3%)		50 MeV	≤ 7 GeV/c		~45%/√E+6%		muons useful for bkg. improve resolution
-2.0 to -1.5								2%/√E(+1-3%)		50 MeV					
-1.5 to -1.0								2%/√E(+1-3%)	π suppression up to 1:1E-4	50 MeV					
-1.0 to -0.5			Barrel	σpT/pT ~0.05%⊕pT⊕0.5%	~5% or less X		dxyz ~ 20 μm, d0(z) ~d0(r0) ~ 20/pTGeV μm ⊕ 5 μm			50 MeV	≤ 10 GeV/c		~85%/√E+7%	~600 MeV	
-0.5 to 0.0										50 MeV			~85%/√E+7%		
0.0 to 0.5										50 MeV			~85%/√E+7%		
0.5 to 1.0		Central Detector								50 MeV	≤ 15 GeV/c	≥ 3 σ	~85%/√E+7%		
1.0 to 1.5			Forward Detectors	σpT/pT ~0.05%⊕pT⊕1.0%		<500MeV pions, 135MeV kaons	σ_xy ~ 30⊕pT μm +20 μm			50 MeV	≤ 30 GeV/c				
1.5 to 2.0										50 MeV	≤ 50 GeV/c				
2.0 to 2.5										50 MeV					
2.5 to 3.0				σpT/pT ~ 0.1%⊕pT⊕2.0%			σ_xy ~ 30⊕pT μm +40 μm	(10-12)%/√E(+1-3%)	3σ e/π	50 MeV	≤ 30 GeV/c		35%/√E		
3.0 to 3.5							σ_xy ~ 30⊕pT μm +60 μm			50 MeV	≤ 45 GeV/c				
3.5 to 4.0			Instrumentation to separate charged particles from photons	Tracking capabilities are desirable for forward tagging						50 MeV					
4.0 to 4.5	↑ e	Auxiliary Detectors								50 MeV			35%/√E (goal), <80%/√E (acceptable)*, 3mrad/√E (goal)		
4.5 to 5.0			Neutron Detection			300 MeV pions		4.5%/√E for photon energy > 20 GeV	<= 3 cm granularity	50 MeV					
>6.2			Proton Spectrometer	σintrinsic(R)/R < 1%; Acceptance: 0.2 < pt < 1.2 GeV/c											

Figure 8.1: Table presenting the Experimental Equipment Requirements Summary in the YR. At present, the table is not updated and it is here as a mere space holder.

8.2 General Detector Considerations and Operations Challenges

8.2.1 General Design Considerations

This section will discuss the detector challenges with cross-reference to the appropriate sections. The Sec.s to refer to are related to machine parameters (not in chapter 8), 8.1 "Experimental Equipment requirement Summary", 8.2.2 "Background and Rates" and 8.2.3 "Radiation Level". At present, all these sections are not available. Therefore, for Version0, a mere list of topics that will be covered is provided.

Discussion of challenges related to:

- Physics requirements (ref. to Sec. 8.1);
- Beams rates, polarization, luminosities (ref. to Sec.s in the machine chapters);
- Integration with the machine and hermeticity (ref. to Sec.s in the machine chapters, ref. to Sec. 8.1);
- Rates and multiplicity (ref. to Sec.c in the machine chapters, to Sec. 8.2.2);
- Radiation hardness (Ref. to Sec. 8.2.3).

8.2.2 Backgrounds and Rates

Add text here.

8.2.3 Radiation Level

Add text here.

8.3 The ePIC Detector

8.3.1 Introduction

The Context The development of the EIC science and the experimental equipment required to successfully implement the science as documented in the NSAC and NAS reports has been driven by an international EIC community, formalized in 2016 in the EIC User Group [17], at present (September 2024) formed by more than 1500 members from almost 300 institutions and 40 countries. Several conceptual general-purpose detectors had been elaborated. A next step effort was required by the EIC project approval with the signature of CD0 in December 2019. The User Group engaged in advancing the state of documented physics studies, which dictate the detector requirements, and consolidate the general-purpose detector concept matching these requirements. This effort resulted in the EIC Yellow Report completed in early 2021 and then published in Nuclear Physics A [18]. This document guided the two proposals for a general-purpose detector elaborated in 2021, which resulted in further progress in the conceptual detector design. In 2022, a merging process of the communities presenting the two proposals and of the two conceptual approaches resulted in the formation of the ePIC Collaboration [19] (July 2022) and in baselining of the ePIC

detector as EIC project detector. At present (September 2024), ePIC has more than 850 members from 177 Institutions and 25 countries, confirming the international vocation of the community pursuing the EIC science and detector.

The Detector THIS DETECTOR DESCRIPTION IS AN INTRODUCTION TO THE WHOLE SECTION 8.3. IT WILL BE REVISED WHEN THE SUBSYSTEM MATERIAL IS UPLOADED TO ENSURE A BETTER CONSISTENCY OF THE SECTION 8.3.

The detector challenges and the technologies matching these challenges are discussed in Sec. 8.2.1. The resulting design of the ePIC detector consists in a Central Detector (CD) surrounding the Interaction Point 6 (IP6) making optimal use of the space available at the Interaction Region (IR) complemented by equipment situated along the outgoing beam lines, the Far Detectors (FD), which complete the phase-space coverage.

Figure 8.2 illustrates the CD kinematic coverage; Fig. 8.3 presents a schematic overview of the CD structure. The overall CD length is imposed by the constrain of the IR design. The asymmetric beam energies reflect in an asymmetric design of the detector and, together with the requirements from physics, imposes the choice of the different detector technologies that have been adopted. The setup is designed around the solenoid providing the magnetic field for the momentum analysis. The adoption of a solenoid shapes the CD in a barrel region where the subsystem have pseudo-cylindrical layouts and two endcap regions, the forward one equipping the region around the outgoing ion beam and the backward endcap around the outgoing electron beam. The barrel subsystems cover, approximately, the pseudorapidity η region (-1.5, 1.5), while the endcaps equip the regions up to pseudorapidity $|3.5 - 4.0|$, the upper bound being dictated by the beampipe layout. The separation in barrel and endcap region is not rigid with exceptions where the optimization of the detector design suggests it. For instance, the most inner layers of the tracking system have acceptance well beyond $\eta < |1.5|$, the barrel Cherenkov PID counter and the barrel electromagnetic calorimeter extends in the backward endcap.

The CD subsystems have a layered structure, from inside to outside: tracking subsystems, particle identification devices, electromagnetic calorimeters, solenoid coils in the barrel, and hadronic calorimeters.

The reference operation condition of the new **MARCO magnet** (Sec. 8.3.2), specifically designed for ePIC, is with 1.7 T field intensity and it can provide up to 2 T. It has good homogeneity in the central region and provides projective field lines in the forward endcap to match the requirements posed by the usage of a gaseous radiator in the forward RICH. The solenoid axis coincides with the electron beam line in the IR to limit the synchrotron radiation from the beam electrons. This results in helicoidal trajectories of the beam ions, due to the crossing angle of the two beams.

The **tracking system** (Sec. 8.3.3) is the most inner subsystem in order to ensure the minimum distortion of the trajectories by the material crossed by the particles. It consists of pseudo cylindrical layers completed by discs in the endcaps. The low material budget (Fig. 8.4) is guaranteed by the selected tracker technologies, with the thin ITS3 MAPS, even in support-less arrangement in the most inner layers, and MPGDs for the most external layers. The two tracker technologies support each other thanks to key complementary characteristics. MAPS sensors offer extremely fine space resolution, but poor timing information in the order of a few microsecond range. In-time hits can be selected combining MAPS information with the measurements in the MPGDs, which have time resolution of 10-20 ns. Further space and time information will be provided by the time-of-flight layers in the barrel and the forward endcap and by the first layer of the barrel imaging electromagnetic calorimeter equipped with AstroPix MAPS sensors. The minimization of the material budget is one of the ingredients allowing fine resolution for momentum determination and vertex recon-

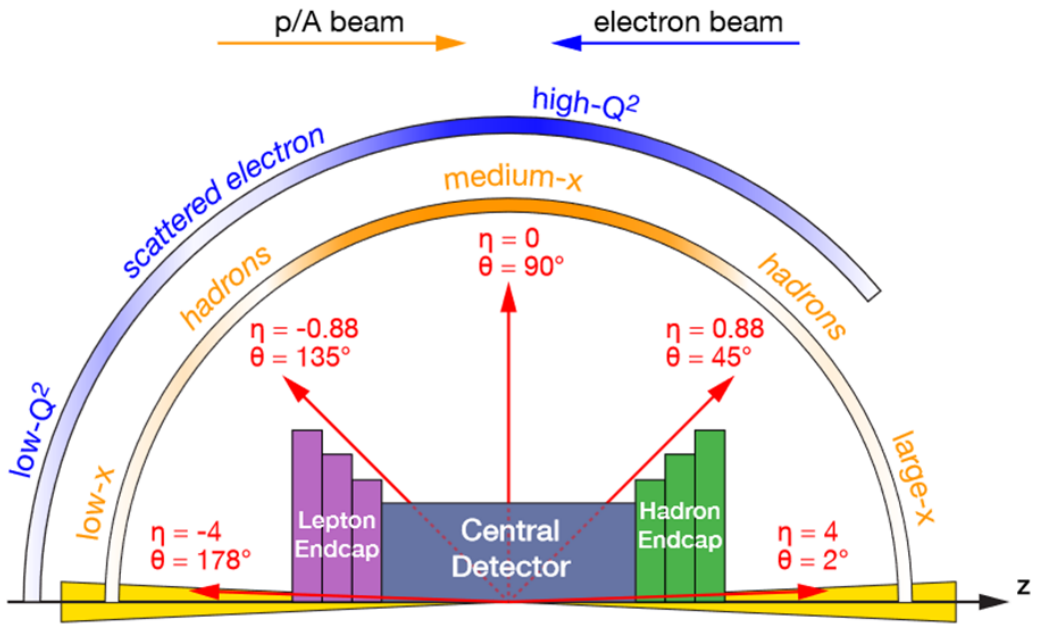

Figure 8.2: A schematic showing how hadrons and the scattered electron for different x - Q^2 are distributed over the detector rapidity coverage. THIS FIGURES IS A PLACE HOLDER: IT IS FROM YR AND REQUIRES REVISION.

struction. To this end, fine intrinsic resolution is requested for the trackers and it is provided by the ITS3 MAPS. The momentum resolution is affected by the available lever arm and the solenoidal configuration of the magnetic field, the latter having its largest impact on the very forward and backward trajectories.

The tracking information is also a key ingredient for the performance of the Cherenkov imaging devices; in particular, very fine resolution of the particle direction is needed for the barrel DIRC. The most external tracker layers in the barrel, positioned in front of the DIRC, further support this requirement.

The **particle identification subsystems** (Sec. 8.3.4) surround the tracking systems. Their mission is twofold: (i) supporting the electromagnetic calorimeters by complementing the pion/electron separation to ensure the high purity of the electron sample; (ii) identifying hadrons, as needed by a large fraction of the physics program. The coverage of the wide kinematic domain imposes the adoption of a variety of technologies with time-of-flight measurements complementing Cherenkov imaging devices. Time-of-flight dedicated layers by AC-LGADs are present in the barrel and in the forward endcap, the barrel layer being by strip sensor elements to reduce the material budget, while the forward endcap layer is by pixelized AC-LGADs. In the backward endcap, the fine time-resolution provided by the photosensors of the Cherenov counter, which are sitting in the endcap acceptance, provide timing information via the Cherenkov light generated in the sensor window. The Cherenkov imaging counter in the backward endcap is a proximity focusing RICH with aerogel radiator and extended proximity gap to increase the resolution and, correspondingly, enlarging the momentum range for particle identification. As already underlined, the use of fine-time resolution HRPPDs by MCP technology as photosensors also provides timing information. The whole detector components are positioned in the acceptance, in front of the electromagnetic

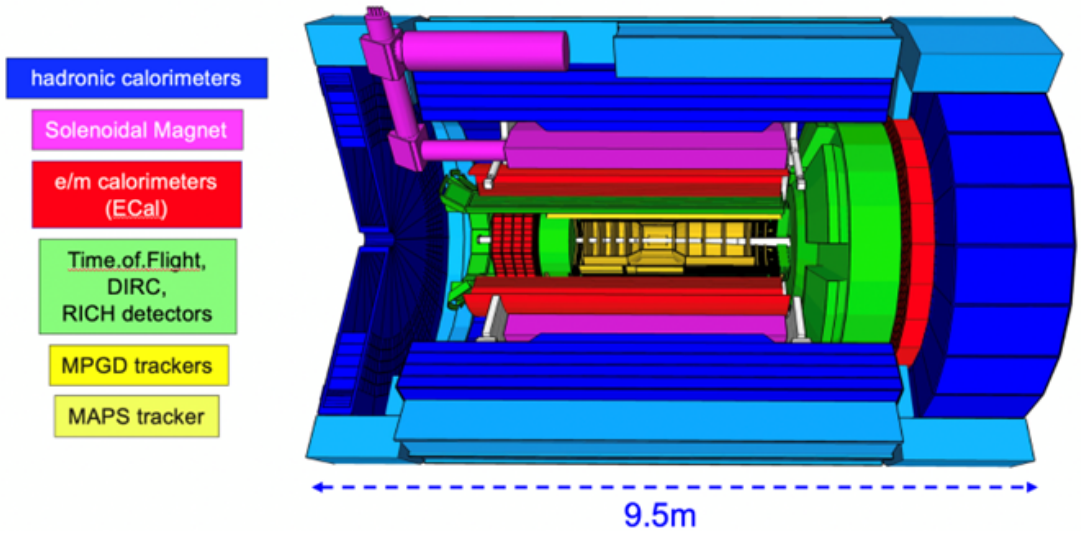

Figure 8.3: A schematic showing the ePIC central detector subsystems. THIS FIGURES IS A PLACE HOLDER

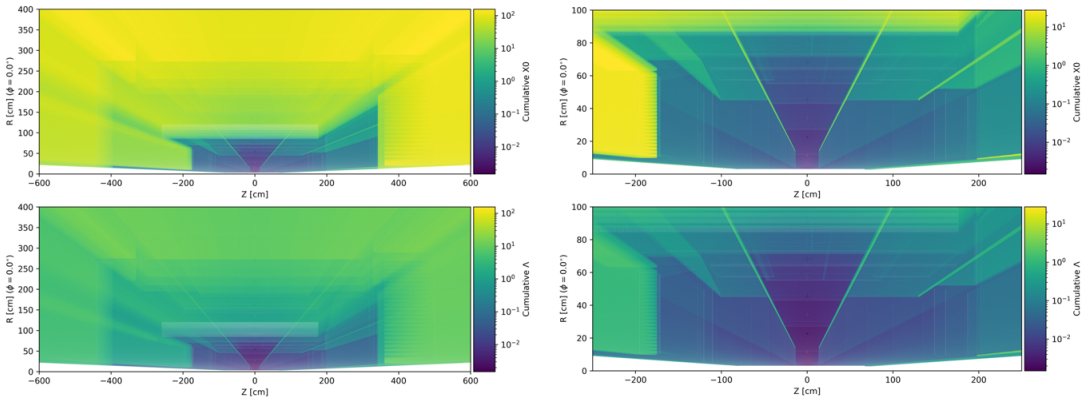

Figure 8.4: Cumulative material budget in radiation lengths (top row) and interaction lengths (bottom row) for the whole CD (left column) and zooming at the CD tracking region (right column). THIS FIGURES IS A PLACE HOLDER BECAUSE IT HAS TO BE COMPLETED WITH SUBSYSTEM CONTOURS AND REQUIRES GRAPHICAL IMPROVEMENTS.

calorimeter. This layout is compatible with the overall detector design; in fact, the bulky elements, namely the sensors with readout electronics and services are just in front of the calorimeter acting as a pre-shower element. In the barrel, a high performance DIRC is used, this choice being dictated by the reduced space. The DIRC fused silica bars, acting as radiator and as photon lightguides, make possible positioning the image expansion elements and the read-out electronics with its services in the backward region, outside the acceptance cone. The dual radiator RICH (Sec) in the forward endcap is equipped with two radiators, aerogel and gas, therefore acting as a couple of Cherenkov imaging counters dedicated to particle identification in two different momentum ranges, while economizing in space and single photon sensors. It is a focusing RICH with spherical mirrors as focusing elements. The photosensors and related services are placed outside the acceptance thank

to appropriate mirror orientation.

The electromagnetic calorimeters (Sec. 8.3.5) are external to the particle identification devices and, once more, the different technologies are imposed by the physics requirements, the kinematic ranges and the overall constrains. The budget of the material in front of the calorimeters is low and mainly concentrated near to the calorimeter front face. The backward endcap electromagnetic calorimeter is by fine granularity lead tungstate crystal offering very fine energy resolution. In the barrel, the electromagnetic calorimeter has a hybrid architecture combining imaging layers by AstroPix MAPS and sampling calorimetry by lead and scintillating fibers with sampling layer between the imaging layers and in the most external calorimeter portion. The layout is pseudo cylindrical with the read-out equipment at the cylinder edges minimizing the space requirement in the crowded barrel area. The electromagnetic calorimetry in the forward region is by sampling calorimetry with scintillating fibers inserted in matrices of tungsten powder embedded in epoxy. This calorimeter offer a near to 1 ratio of the signal amplitude response for electrons and hadrons and, therefore, it is design to operate in duet with the hadronic calorimeter place immediately behind.

All the **hadron calorimeters** (Sec. 8.3.6) are by iron as converter and scintillating active elements, even if with very different implementations. The forward endcap calorimeter is by SiPM-on-tile technology, with finer granularity in the central zone, near to the beam pipe, to cope with the higher rates. The barrel calorimeter, placed behind the solenoid coils, acts as a tail catcher. The backward endcap calorimeter ... (to be completed: layout in evolution).

All the calorimeter subsystem in the ePIC detector make use of SiPMs as photosensors, even if of different size and pixelization, with common approach for the readout chain.

The global layout of the FDs (Sec.s 8.3.7 and 8.3.8) is illustrated in a artistic view in Fig. 8.5.

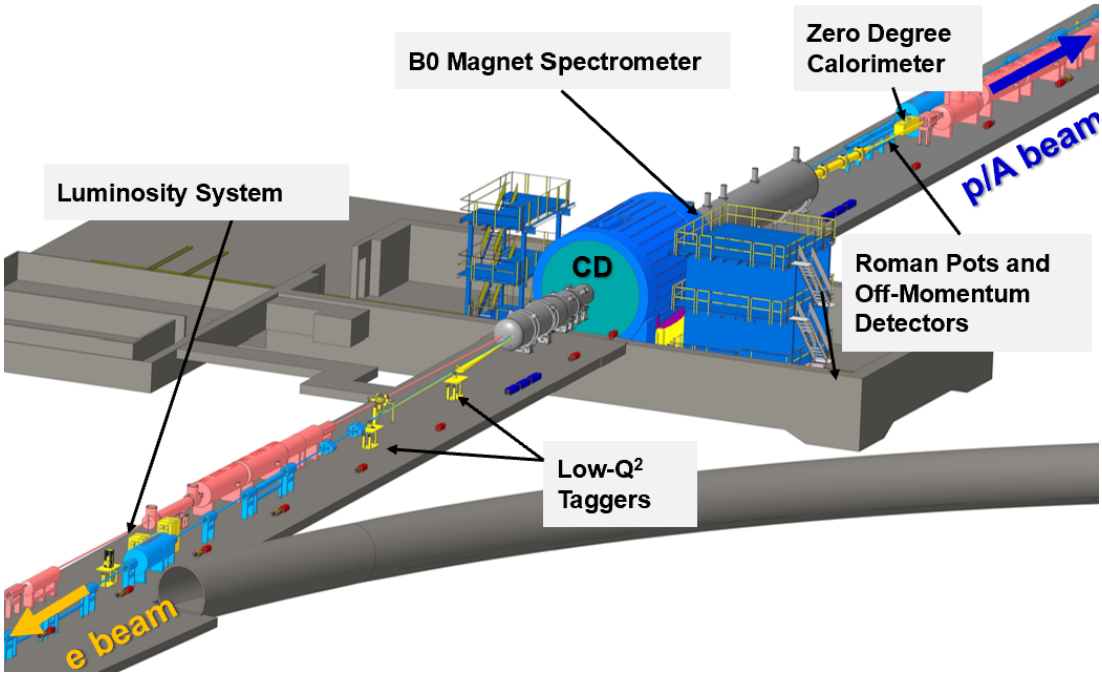

Figure 8.5: A schematic showing the ePIC far detector subsystems. THIS FIGURES IS A PLACE HOLDER

The **forward FDs** include tracking and electromagnetic calorimetry inserted in the first dipole of the ion beam line B0, off-momentum detector trackers and roman-pot trackers and a zero-degree-calorimeter. The technology for the trackers is by AC-LGADs, which have good radiation hardness. The B0 electromagnetic calorimeter is by lead tungstate crystals. The zero-degree-calorimeter is formed by a long SiPM-on-tile module with fine granularity adequate for photon and neutron detection. A crystal layer can be inserted in front of it for those studies that require the detection of low energy photons.

The **luminosity system** is part of the backward FD. Based on the measurement of the photons from the Betha-Heitler process at IP, it consists of a high-rate calorimeter for direct photon detection and a couple of pair spectrometers to detect the electrons and positrons generated by the Betha-Heitler photons in the exit window. The high-rate calorimeter and the calorimeters in the pair spectrometers are by tungstate and scintillating fibers. Tracking in the pair spectrometer is by AC-LGADs. The **low-Q^2** taggers consist in tracking stations followed by an electromagnetic calorimeter. The selected technologies must cope with extremely high rate in this kinematic region. Therefore, tracking is by TimePix4 and calorimetry by tungstate and scintillating fibers.

Integral elements of the detector are the **electronic read-out chain**, the data acquisition system (Sec. 8.3.10) and the **software implementation and computing model** (Sec. 8.3.11). The overall underlining model that has guided the selection of the components and the design of the read-out/DAQ/software/computing architecture is the streaming readout concept. Streaming readout has been selected to simplify the readout scheme as no triggers are required and to increase the information selection flexibility, to improve the event building from the holistic detector information, to improve, via continuous dataflow, the knowledge of backgrounds and, therefore, enhances the control over systematics. In this approach, already at the front-end level, the ASICs, which are intimate related to the sensors and their performance, have been selected with architectures compatible with their usage in streaming readout mode.

Independent setups are designed to measure and monitor the **beam polarization** (Sec. 8.3.9). Rapid, precise beam polarization measurements will be crucial for meeting the goals of the EIC physics program as the uncertainty in the polarization propagates directly into the uncertainty for relevant observables as asymmetries. The basic requirements for beam polarimetry are non-destructive with minimal impact on the beam lifetime, uncertainty at the 1% level, the capacity of measuring the beam polarization for each bunch in the ring with rapid, quasi-online analysis in order to provide timely feedback for accelerator setting up. The electron beam polarimetry will be based on the well established Compton polarimeter techniques, where the polarized electrons scatter from 100% circularly polarized laser photons. This approach offers the advantage that both longitudinal and transversal polarizations are measured. Hadron polarimetry has been successfully performed on RHIC polarized proton beams for nearly two decades. Through continual development a relative systematic uncertainty ¡1.5% was achieved for the most recent RHIC polarized proton run. As the only hadron polarimeter system at a high energy collider it is the natural starting point for hadron polarimetry at the EIC. Hadron polarization will be measured via a transverse single spin left right asymmetry in the pp interaction on targets by plastic material (H-C composition), where the experimental challenge is the control of the background events.

Technological Synergistic Aspects of the Detector Design The synergistic aspects of the ePIC detector have been carefully maximized in view of the optimal usage of the workforce and the financial resources. This is illustrated by the following examples.

SiPM sensors, recently introduced in calorimetry applications, are adopted for all the electromagnetic and hadronic calorimeters in ePIC. They offer a cost-effective technology that can operate in magnetic field, can provide wide dynamic range when the sensor type is properly chosen to tune

the response parameters, and present low noise level by applying appropriate thresholding. The use of a common technology makes possible to access the effect of the radiation by a single effort and the use of the same front-end ASIC CALOROC.

Also the calorimetry reconstruction software is synergistic for the overall set of subsystems.

In electromagnetic calorimetry, the sampling approach with tungsten and scintillating fiber is adopted for the forward endcap calorimeter and in FDs: calorimetry in B0, luminosity system and low-Q^2 taggers.

In hadron calorimetry, the SiPM-on-tile technology is used for the forward endcap calorimeter and its insert in the central area, as well as for the zero-degree calorimeter.

In particle identification by Cherenkov imaging counters, MCP-based photosensors are used for the backward endcap RICH and the barrel DIRC, that can be read by the same read-out ASIC HGCROC (information to be crosschecked). The backward endcap RICH and the forward endcap RICH use aerogel as radiator and the quality assessment station will be used for both batches. The reconstruction software in both RICHes has large communalities and it is based on the same ray-tracing algorithm.

AC-LGADs form the time-of-flight layers and are used for tracking in the forward FD in B0, off momentum detectors and roman pots, and selected for the pair spectrometers of the luminosity system.

In tracking by MAPS, the different sensors of the inner layers, the outer layers and the forward and backward disks are all evolutions of the ITS3 sensor, therefore all based on stitching the same readout chip element.

The same hybrid MPGD architecture with a preamplifying GEM layer followed by a μRWELL is used in the most outer tracker in the barrel and the most external discs in the endcaps. All MPGDs, namely the hybrid MPGDs and the cylindrical Micromegas in the barrel are coupled to the same front-end ASIC: SALSA.

A single integrated effort is at the basis of the tracking reconstruction with the use of the software package AC.

8.3.2 Magnet

Requirements

Requirements from physics: Add text here.

Requirements from Radiation Hardness: Add text here.

Requirements from Data Rates: Add text here.

Justification

Device concept and technological choice: Add text here.

Subsystem description:

General device description: Add text here.

Sensors: Add text here.

FEE: Add text here.

Other components: Add text here.

Requirements from Data Rates: Add text here.

Implementation

Services: Add text here.

Subsystem mechanics and integration: Add text here.

Calibration, alignment and monitoring: Add text here.

Status and remaining design effort:

R&D effort: Add text here.

E&D status and outlook: Add text here.

Other activity needed for the design completion: Add text here.

Status of maturity of the subsystem: Add text here.

Environmental, Safety and Health (ES&H) aspects and Quality Assessment (QA planning: Add text here.

Construction and assembly planning: Add text here.

Collaborators and their role, resources and workforce: Add text here.

Risks and mitigation strategy: Add text here.

Additional Material Add text here.

8.3.3 Tracking

Add text here.

8.3.3.1 The silicon trackers

Requirements

Requirements from physics: The Silicon Vertex Tracker (SVT) needs to meet stringent performance requirements, set by the EIC science program, on acceptance and resolutions for charged-particle trajectories. At a high level, the SVT needs to precisely measure the scattered electron and charged hadrons produced in the electron-ion beam collisions. The scattered ion, if it remains intact, is outside of the SVT acceptance. The SVT also needs to measure charged decay-particles from hadrons containing heavy quarks and from vector meson decays. It is to aid in particle-identification a) through determination of the displacement of the geometrical origin of the decay particles (secondary vertex) from the collisison point (event vertex) via precision reconstruction of both vertices and b) by providing directional and impact information on charged-particle trajectories through the outer gaseous tracking subsystems and into the outer particle-identification subsystems.

Table 8.1 contains the resolution requirements on the particle momentum measurement at the event vertex for different ranges in pseudorapidity and on the determination of the radial distance of closest approach of the particle trajectory to the event vertex with its dependence on transverse momentum. The SVT is the innermost subsystem of the ePIC central detector. Constraints from the

η **range**	dp/p [%]	$\mathbf{DCA}_r$ [μm]
$(-3.5, -2.5)$	$0.10 \times p \oplus 2.0$	$30/p_T \pm 40$
$(-2.5, -1.0)$	$0.05 \times p \oplus 1.0$	$30/p_T \pm 20$
$(-1.0, 1.0)$	$0.05 \times p \oplus 0.5$	$20/p_T \pm 5$
$(\ 1.0, 2.5)$	$0.05 \times p \oplus 1.0$	$30/p_T \pm 20$
$(\ 2.5, 3.5)$	$0.10 \times p \oplus 2.0$	$30/p_T \pm 40$

Table 8.1: Physics requirements on the relative momentum measurement, dp/p at the event vertex for different ranges in pseudorapidity, η, and on the determination of the radial distance of closest approach, DCA_r, of the particle trajectory to the event vertex with its dependence on tranverse momentum, p_T.

overall detector size and the outer subsystems limit the active volume of the SVT to $-105 < z <$ 135 cm and a radius of approximately 42 cm. In combination with the 1.7 T solenoidal field, this leads to a requirement on the point resolution of better than 10 μm as well as the need to minimize traversed material by limiting the number of detection surfaces and minimizing their radiation lengths.

Requirements from Radiation Hardness: We have evaluated the radiation levels in the SVT using the current knowledge of the beam configuration and beam backgrounds from beam gas interactions and synchrotron radiation. Figure 8.6 shows the current estimates for fluence (in 1 MeV n_{eq} cm^{-2}) and dose (in rad). The black lines indicate the approximate locations of the SVT detection surfaces. These radiation maps have been estimated for the beam configuration with the highest luminosity and include contributions from hadron and electron beam gas interactions. The results assume that the machine and detector run at 100% efficiency for 6 months per year over a period of 10 years. This is to obtain a conservative estimate. Even under these assumptions,

the radiation levels in the SVT will be low to moderate. The majority of the SVT will see fluence levels well below 10^{11} n_{eq} cm^{-2}. Innermost central layers and layers in the hadron going direction will experience slightly higher fluence between 10^{11} and 10^{12} n_{eq} cm^{-2}, with some small regions reaching above 10^{12} n_{eq} cm^{-2}. The dose rate map indicates that areas close to the beam pipe will experience a total ionising dose between ten and a few hundred krad, while the rest of the SVT remains below 10 krad.

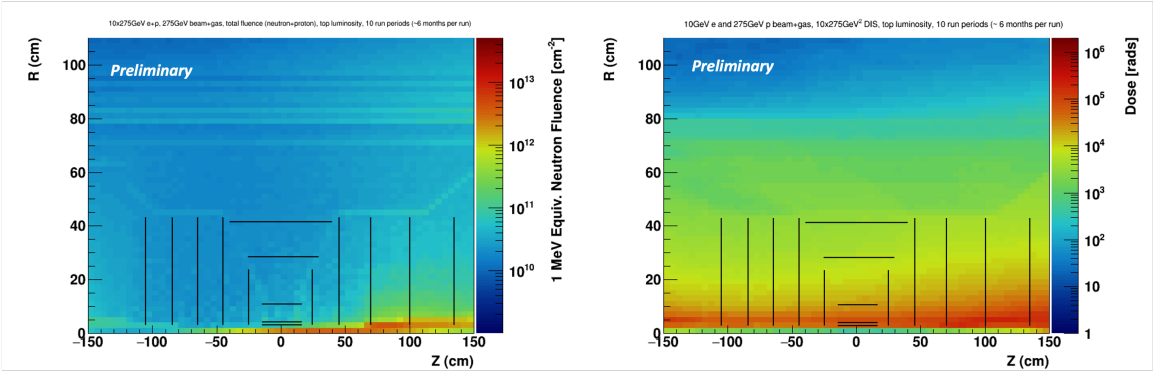

Figure 8.6: Maps of simulated fluence (left) and total ionising dose (right) over the ePIC tracking envelope. This is a conservative estimate assuming 10 years of running at top luminosity with 100% efficient accelerator and detector. The black lines indicate the approximate location of the ePIC SVT detector layers.

Requirements from Data Rates: EIC physics rates are expected to be below 0.5 MHz. That is, only a small fraction of the EIC beam crossings produces a physics event and physics event pileup from within a single beam crossing is negligible. The dominant fraction of these events originate from a region, $|z| < 80 - 100$ mm, surrounding the nominal interaction point. We thus estimate that event pileup within the SVT is determined by its readout frame or integration window of 2 μs or a small multiple thereof. Within this window, SVT will also accumulate hits from noise and beam backgrounds. We estimate that the associated hit load and data volume will exceed that from physics events. Hit occupancies will be low in view of the high SVT granularity. We estimate a hit probability per pixel per readout frame of $\mathcal{O}(10^{-7})$ and a typical total data rate at the level of 15 Gbps. The sensor and readout chain need to be efficient under these conditions.

Justification

Device concept and technological choice: To meet the stringent requirements on charged-particle tracking and vertexing, we have designed the SVT to provide a well-integrated, large acceptance, high granularity, and low-mass tracking and vertexing subsystem. The SVT has four regions covering a total active area of approximately 8.5 m^2. An Inner Barrel (IB) and Outer Barrel (OB), made of three and two detecting layers respectively, cover the mid-central pseudorapidity range and have an active volume that extends radially to approximately 42 cm. Endcaps, each with five detecting annuli surrounding the beampipe, are placed on either side of the nominal interaction point with their active area constrained to $-105 < z < 135$ cm and an outer radius equal to that of the OB. The Electron Endcap (EE) is positioned in the direction of the electron beam and has acceptance for a large fraction of the scattered electrons, while the Hadron Endcap (HE) pro-

vides acceptance for many of the hadrons produced in physics collisions. Figure 8.7 shows The SVT regions and geometrical layout.

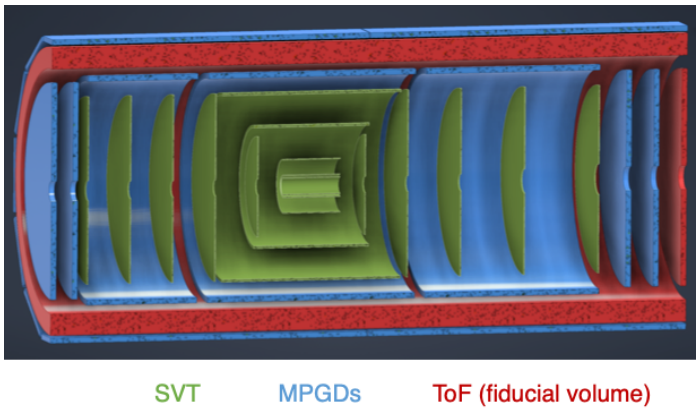

Figure 8.7: Schematic layout of the ePIC SVT showing the central region consisting of the inner and outer barrel made of three and two cylindrical layers, respectively, together with the endcap regions made of five annuli each. The figure also shows the surrounding Micro Pattern Gas Detector (MPGD) layers and the envelope of the Time of Flight PID detector.

We designed the SVT to cover the required pseudorapidity range and to reach spatial resolutions as low as ≤ 5 μm through a combination of high granularity (~ 20 μm pixel pitch), low power sensor design (≤ 40 mW cm^{-2}), and lightweight support structures, cooling, and electrical services. Our development aims at achieving 0.05% X/X_0 in the IB, 0.25% X/X_0 in the innermost OB layer and in the disks, and 0.55% X/X_0 in the outermost OB layer. We selected a sensor technology based of the ALICE-ITS3 development [20] to meet our requirements. This is a new generation, large area Monolithic Active Pixel Sensor (MAPS) in a commercial 65 nm CMOS imaging process.

Subsystem description:

General device description: Tables 8.2 and 8.3 show the positioning and size of the SVT detecting layers, together with their material budget target. We designed the IB to provide precise vertex reconstruction, while also contributing to momentum measurement. This is achieved with a combination of very thin layers at optimised radii. The IB will use the ALICE ITS3 wafer scale sensor [20] with a suitable adaptation of the ITS3 ultra-thin detector concept to the large EIC beam pipe diameter. The IB design has three layers of silicon sensors thinned below 50 μm and bent around the beam pipe, with minimal mechanical support, air cooling, and no electrical services in the active area, to reach the very low material budget target of $X/X_0 = 0.05\%$. The innermost layer is positioned as close as possible to the beam pipe, taking into account the constraints coming from the large beam pipe radius and the requirements from beam pipe bake-out, which will be performed with the IB installed. The position of the second layer is chosen to maximise vertex resolution. The outermost layer of the IB aims at maintaining the very low material budget at a radius of 120 mm and serves both vertexing and sagitta measurements. The OB, EE and HE will be equipped with the EIC Large Area Sensor (LAS), a modified version of the ITS3 sensor, optimized for high yield, low cost, large area coverage. These sensors will be mounted on lightweight support structures, in the form of staves for the OB and disks for the endcaps, with integrated cooling and electrical interfaces for power, data and slow control. The OB layers and the endcap disks are

positioned to provide high precision measurements over a large level arm to improve momentum resolution and optimize acceptance at large pseudorapidity. The inner openings of the disks will accommodate beam pipe bake-out constraints as well as beam pipe divergence. These translate into six different inner opening geometries over ten disks.

Region	**Layer**	**radius** [mm]	**length** [mm]	X/X_0
IB	L0	36	270	0.05%
	L1	48	270	0.05%
	L2	120	270	0.05%
OB	L3	270	540	0.25%
	L4	420	840	0.55%

Table 8.2: Radius, length and material budget of the SVT IB and OB layers.

Region	**Disk**	**z** [mm]	$\mathbf{r}_{out}$ [mm]	X/X_0	**Region**	**Disk**	**z** [mm]	$\mathbf{r}_{out}$ [mm]	X/X_0
EE	ED0	-250	240	0.25%	HE	HD0	250	240	0.25%
	ED1	-450	415	0.25%		HD1	450	415	0.25%
	ED2	-650	421	0.25%		HD1	700	421	0.25%
	ED3	-850	421	0.25%		HD3	1000	421	0.25%
	ED4	-1050	421	0.25%		HD4	1350	421	0.25%

Table 8.3: Position along the beam pipe, outer radius and material budget for the SVT layers in the EE and HE regions.

Sensors: The SVT will be constructed with MAPS sensors, that integrate sensing and front-end electronics functionalities in one device. The ePIC SVT will use MAPS sensors developed in a 65 nm CMOS imaging process based-off the ALICE ITS3 development [20]. This technology enables a high granularity and low power consumption design, and offers stitching on 300 mm wafers for the development of large area sensors. These characteristics are key to delivering a high precision detector through high spatial resolution and minimized material budget.

The SVT IB will use the ALICE ITS3 sensor, called MOSAIX. A sketch of MOSAIX on a wafer is shown in figure 8.8. MOSAIX is composed of an active matrix of Repeated Sensor Units (RSUs). Twelve RSUs are stitched along the length of the sensor. The sensor will be three, four, and five RSUs wide for L0, L1 and L2 respectively. Each RSU is further divided into 12 tiles that can be switch off independently in case of faults to improve yield over such large area device. A row of twelve RSUs, together with the left and right endcap (LEC, REC) is called a segment. The LEC contains circuits for power, slow control and data. The REC is used for power only to ensure a uniform power distribution over the full sensor length. Data links for each segment can be configured with 3 links, plus one spare, at 10.24 Gb/s or 6 links, plus 2 spares, at 5.12 Gbps. For each segment, seven electrical links provide clock, synchronisation and control signals, referred to here as slow control signals. The clock runs at 40 MHz, while the other control signals will run at 5 Mbps. MOSAIX has different power

domains for analogue and digital circuitry at 1.2 V, plus two more domains for specific blocks, one at 1.2 V and one at 1.8 V [20]. The sensor's bias voltage will be in a range between -1.2 and -4.8 V.

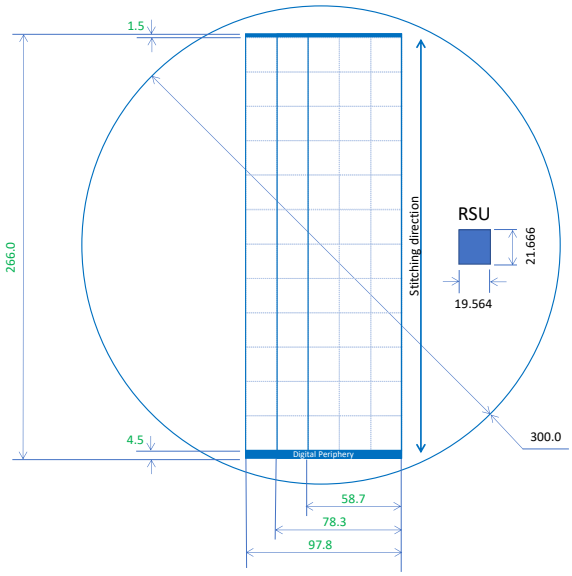

Figure 8.8: Sketch of the MOSAIX sensor on a 300 mm wafer showing the size of the RSU, LEC, REC and of the full sensor for the three different widths.

The SVT OB and endcaps cover an area of approximately 8 m^2. Considerations based on yield, cost, integration, and coverage require the use of a sensor with a smaller size. These regions will use the MOSAIX sensor with modifications to reduce the size. This sensor would still be large in traditional terms and is therefore referred to as the EIC Large Area Sensor (EIC-LAS). The EIC-LAS will be one RSU wide and either 5 or 6 RSUs long. In addition to reducing the size of the sensor, the EIC-LAS will see a reduction of the number of data links to match the lower SVT data rate, reducing material and easing integration aspects. To further ease the integration of the EIC-LAS in the OB and endcaps, EIC-LAS sensors will be powered in series by a constant current and a dedicated communication protocol will be used to reduce the number of slow control links from the counting room to the sensor. These features will be provided by a supporting ASIC, referred to as the Ancillary ASIC (AncASIC).

FEE: One AncASIC will be used per EIC-LAS. This chip includes three main features. It integrates the SLDO regulator for serial powering. This regulator will generate the voltages needed by the EIC-LAS from the input current. This design is adapted from the original SLDO design for the upgrades of the ATLAS and CMS pixel detectors at the HL-LHC. One AncASIC will integrate four SLDO regulators. The AncASIC will also contain a Negative Voltage Generator (NVG) block. The NVG is a diode-based charge-pump circuit (Dickson-type charge pump voltage multiplier). It will generate the sensor's negative bias voltage from one of the regulated power supply at 1.2 V generated by the SLDO. The third block is the Slow Control (SC). Slow control signals from the counting room will be transmitted over I2C for multiple EIC-LAS sensors over one link. The SC block will decode them into the MOSAIX format (i.e. into seven links). The AncASIC will be produced in a 110 nm SOI process offering multiple MPW per year and the required transistors' ratings for the SLDO and NVG.

Other components: All components of the SVT detector are designed with the goal of achieving the low material budget target, while providing a robust, high precision system. Traditionally the bulk of the material in silicon detectors is contributed by the powering system. The SVT will adopt a current based power distribution scheme, so called serial powering, for the OB and disks. Groups of up to four EIC-LAS sensors are powered in series by a constant current, with the electronics low voltage generated close to the sensors by the SLDO regulators in the AncASIC. This scheme reduces cabling material and provides the only viable powering solution to fit within the available space for services in the ePIC detector. For the smaller IB system, a traditional voltage based, direct powering scheme is foreseen. Data, slow control signals and power are routed over aluminium-based flexible printed circuits (FPC) between the SVT active elements (MOSAIX, EIC-LAS, AncASIC) and the readout (RDO) boards. Four different RDO boards are used in the SVT. The interface board receives data from the sensors for transmission to the counting room. The control board receives slow control signals from the counting room to be transmitted to the AncASIC. Lightweight communication between these RDO boards and the counting room is achieved by use of optical fibers. An aggregator board achieves a reduction of the optical fiber lines through multiplexing via FPGA to match the number of fibers to the available channels of the FELIX data acquisition board in the counting room. The electro-optical interface components used on the interface and control boards are the lpGBT [21] and VTRx+ [22] devices developed by CERN. The power board provides interface for power distribution for sensors and Anc-ASIC as well as RDO boards. Whilst the functionality of the RDO boards and FPC remains the same, different designs will be needed for IB, OB and disks to accommodate the different powering schemes, number of data links, and sensors grouping. The preferred cooling solution for the SVT detector is air cooling, baselined for the two innermost layers of the IB and under study elsewhere. The OB, EE and HE are designed to allow air flow through the low mass staves and disks, made of carbon composite material, that support the sensors.

Performance We have simulated track finding and reconstruction within the ePIC software framework to quantify momentum and vertexing resolutions. Figure 8.9 shows the simulated relative momentum resolution for single charged pions versus their total momentum for different pseudorapidity regions, together with the requirements. The simulations show that the momentum resolutions are substantially met over most of the SVT acceptance. The performance in the range of smallest pseudorapidity, $-3.5 < \eta < -2.5$, is limited by constraints on the SVT lever arm from ePIC's outer subsystems in this region and overall detector size. Figure 8.10 shows the simulated radial distance of closest approach, DCA_r, for the reconstructed trajectories of simulated charged pions to the event origin versus pion transverse momentum in different pseudorapidity regions, together with the requirements. The simulations show that the requirements on DCA_r are substantially substantially met over the SVT acceptance.

We have performed beamtests at FNAL with a single-RSU sensor, called babyMOSS, from ITS3 Engineering Run 1. In these tests, two times three sensors were arranged in a telescope and exposed to the test beam. A seventh sensor, the Device Under Test (DUT), was placed at the center of the telescope and its angle with respect to the incident beam was varied in the horizontal plane of the telescope. Figure 8.11 shows a close-up of the telescope and results for the cluster extent as a function of the incident beam angle onto the DUT from data and simulations. The results demonstrate that the geometrical effect from the angle dominates over diffusion and otherwise confirm the expected point resolution.

Implementation

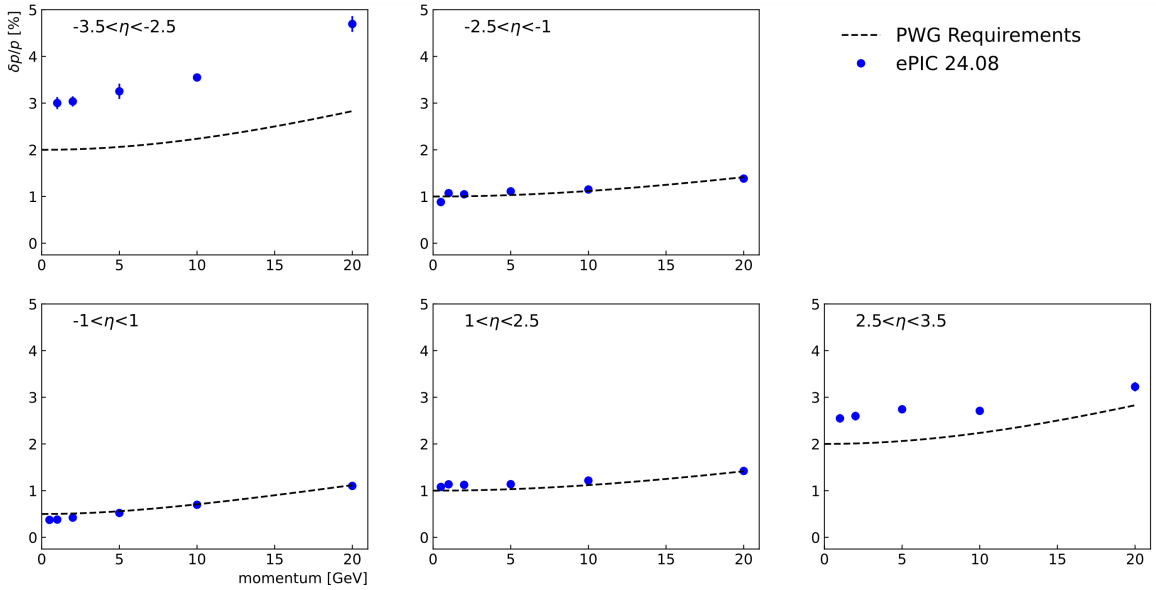

Figure 8.9: Relative momentum resolution versus total momentum for charged pions (points) together with physics requirements (curves) in different pseudorapidity ranges as indicated. The results are based on full GEANT simulations using the ePIC software stack and ACTS-based track finding and reconstruction using optimized parameters.

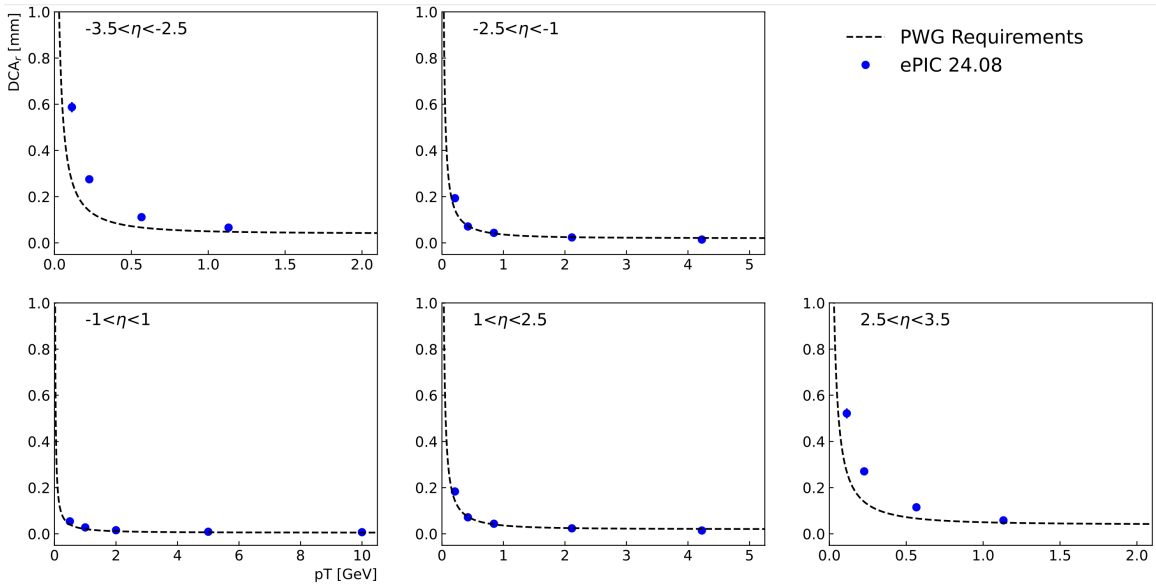

Figure 8.10: Distance of closest approach in the radial direction between reconstructed charged pion trajectories and the event origin versus transverse pion momentum (points) together with physics requirements (curves) in different pseudorapidity ranges as indicated. The results are based on full GEANT simulations using the ePIC software stack and ACTS-based track finding and reconstruction using optimized parameters.

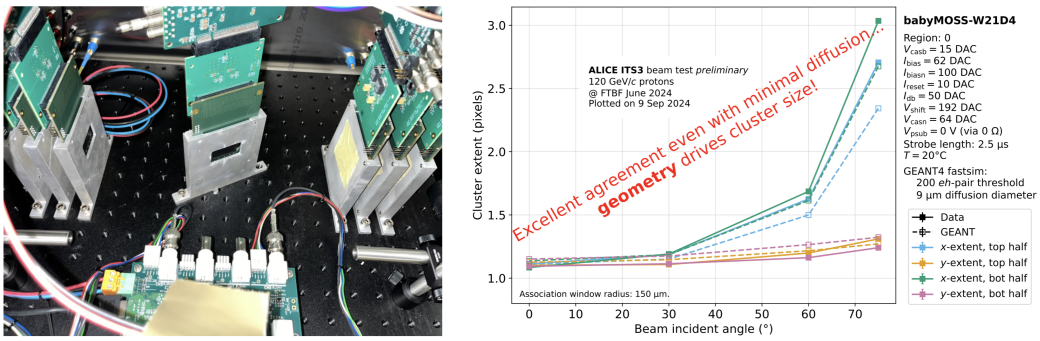

Figure 8.11: A close-up of a beam telescope constructed from two times three single-RSU sensors from ITS3 Engineering Run 1 with a seventh sensor (DUT) under an angle at the center of the telescope (left) and (right) results from beamtests at FNAL and from simulations for the cluster extent as a function of the beam incident angle onto the DUT.

Services: Services to the SVT are of two types: electrical/fiber-optical services and cooling. Electrical/fiber-optical services to the SVT comprise power, data and slow control. For the IB (MOSAIX sensor and direct powering), electrical services will be by MOSAIX segment. For the OB and endcaps (EIC-LAS and serial powering), they will be by group of up to four EIC-LAS. A summary of the data, slow control and power lines needed in the different regions of the SVT is given in Table 8.4. The table illustrates the reduction in power lines using serial powering versus

Region	Sensor	Electrical services group	# power lines/group	# slow control links/group	# data links/group
IB	MOSAIX	MOSAIX segment	10	7	8
OB	EIC-LAS	Up to 4 EIC-LAS	2	3	4
ED	EIC-LAS	Up to 4 EIC-LAS	2	3	4

Table 8.4: Summary of power and readout services for the different regions of the sPIC SVT (slow control and data links are differential pairs of wires).

direct powering. In the IB each MOSAIX segments will need ten lines (including the return line) to serve the four power domains of the electronics plus the sensor bias. For each segment, the full MOSAIX current will be transmitted. In the OB and endcaps two lines (including the return line) will be needed to deliver the same power to up four EIC-LAS (i.e. four segments). The current flowing on these lines will be the current needed by only one EIC-LAS, reducing the current being transmitted to the detector of up to a factor four, and correspondingly reducing cables cross section and material budget.

Figure 8.12 shows the data and slow control distribution for a group of four EIC-LAS. Each data line connects to one input of a VTRx+ on the interface board. Given the high speed of the data transmission, this board will be placed at the end of each stave and disk for signal integrity. The VTRx+ transmits the data of a group of up to four EIC-LAS over a bundle of optical fibers to the

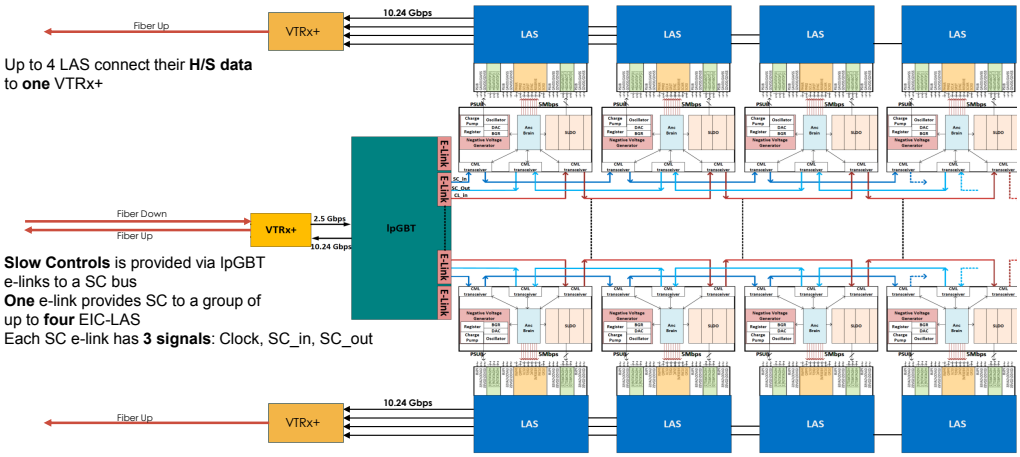

Figure 8.12: Schematic overview of data and slow control lines to a group of four EIC-LAS.

counting room (each VTRx+ has a pigtail bundling up to 5 optical fibers). Slow control signals are transmitted over optical fibers to the control board, placed along the support structure. Once converted into electrical signals, one lpGBT elink provides the slow control signals to up to four AncASICs. Each lpGBT has 16 elinks, meaning that each control board will serve multiple groups of EIC-LAS. The slow control signals are transmitted between the control board and the AncASIC either in a daisy-chain architecture (as shown in the figure) or via multi-drop. The exact configuration is still being evaluated. The AncASIC converts the incoming I2C protocol to the MOSAIX protocol expected by the EIC-LAS. As the OB and endcaps are powered in series, each EIC-LAS is on a different ground potential. A dedicated communication scheme is thus needed. Data lines will be AC-coupled. For the slow control, a standard DC transmission is also being investigated with the ground difference between EIC-LAS sensors being accommodated.

Flexible printed circuits (FPCs) are required to electrically connect MOSAIX sensors, EIC-LAS sensors and AncASIC chips to the interface and control boards. In the IB the FPC will connect to the REC and LEC of the MOSAIX sensor. In the OB and disks, it will run along staves and disks respectively, serving groups of EIC-LAS sensors, connecting to the AncASIC. The FPCs must have a low mass in order to maintain the low material budget of the SVT. It is therefore advantageous to select conductive tracks made of aluminium (X_0 = 8.9 cm) instead of traditional copper (X_0 = 1.4 cm). Dielectrics like polyimide (X_0 = 28.57 cm) are the default solution for the manufacturing technologies of aluminium-based FPCs deployed in scientific experiments. The selection of the dielectric material is dependent on its loss-tangent properties versus the frequency of the signals to be transmitted. Typically the most stringent requirements to signal attenuation are set by the high-speed data transmission lines. In case of the ePIC SVT, it is envisaged that data links can transmit signals as fast as 10.24 Gb/s for a length of $\sim$50 cm. The baseline configuration for the FPCs assumes a stack-up made of two aluminium conductive layers (each $\sim$15 μm thick) separated by a polyimide dielectric substrate ($\sim$35 μm), and then additional polyimide cover layers ($\sim$35 μm combined thickness) to insulate the conductive tracks from external electrical shorts. This cross section ($\sim$100 μm in total) would equate to a combined material budget of $\sim$0.06% X_0. The combination of serial powering, slow control daisy-chained/multi-drop configuration and impedance matching at 100 Ω for clock, control lines and data, enables a reduction of the number of signals to be propagated. This is particularly important for staves and disks where the FPCs overlap the sensitive area of the MAPS. By combining these power and signal distribution techniques, it is estimated that the minimum width for the FPC can as narrow as 6 mm. This is $\sim$1/3 of the width of the LAS

(∼19 mm).

The transmission of the signals to the counting room will see a further stage of processing. The data fiber-optic lines will be aggregated in the aggregator board which has multiple fiber inputs, an FPGA for extracting the payload from these fibers, and one fiber output towards the FELIX board, thus reducing the number of fiber inputs at the Data Acquisition FELIX boards. It is estimated that approximately 5000 data fiber links run from the sensors to the aggregator board. Assuming an aggregation factor of 10, there will be approximately 500 fibers towards the DAQ FELIX boards, which can be accommodated by 11 FELIX boards (assuming each FELIX board will have 48 fiber inputs).

Cooling adds to the service load, including the target radiation lengths in the SVT active areas. The preferred cooling solution for the SVT detector is air cooling, baselined for the two innermost layers of the IB and under study elsewhere, with liquid cooling in strategic places as necessary. We will operate the sensors at or near room temperature ($\sim 25\,^{\circ}$C), which requires a lower coolant temperature. Thermal performance of the cooling is measured with $\Delta T = T_{sensor} - T_{inletairorcoolant}$. Our target for thermal tests and simulations is ΔT of $10\,^{\circ}$C, although this is not a strict requirement.

For the inner layers of the IB, the baseline is air cooling with thermally conductive foam near the LEC. Measurements from ALICE ITS3 show this is reasonable to cool the MOSAIX sensor. Air will be forced between L0 and L1. To cool L2, the possibility for natural convection with liquid cooling near the LEC is under study. The air inlet and outlet are under design, with the bulk of the material to be placed on the hadron-going side of the detector.

In addition to cooling during operation, the IB will need to be kept cool during beam-pipe bake-out. The aim is for no additions to the operational cooling, i.e. no additional material (e.g. insulators) or changes (i.e. liquid instead of air). ANSYS studies at Jlab and LBNL have shown that there is a path forward to keep the detector cool. Climate chamber studies at LBNL and CERN have shown no failures up to $50\,^{\circ}$C.

The target for both the OB staves and the EE and HE disks is air cooling. We are targeting a maximum air velocity of 12 m/s within the structures of the staves and disks. Current estimates are approximately 1700 m^3h^{-1} total air split between the staves and disks. This will require compressed air to mitigate the otherwise excessive size of the air tubes coming into the detector and pressure regulation inside the detector. Studies are ongoing to reduce these numbers, including the use of thermally conductive materials (e.g. carbon foam) to help with heat dissipation. The SVT will be interlocked to turn off in the case of failure of its cooling system, including conditions so as to prevent pressurising the system beyond its design values.

Subsystem mechanics and integration: The inner barrel (IB) layers will be made of two symmetric half-layers, which will be the basic assembly elements of the detector. The two innermost layers (L0 and L1) will be based on four MOSAIX sensors (two for each half-layer), while the outermost layer (L2) will contain eight MOSAIX sensors (four for each half-layer). All the sensors equipping a given half-layer will be placed one next to the other to fully cover the half-layer surface and bent on a cylindrical shape at the corresponding radius (c.f. table 8.2).

Each IB half-layer will consist of the following components: the MOSAIX sensors, a local support structure mainly made in carbon foam shaped as a frame along the edges of the sensors, two sets of FPCs wire-bonded to the sensor peripheries for powering and data/control transmission. The sensor cooling will be air-flow based and delivered through appropriate ducts that will be part of the local support structure and matched to the global mechanics described below.

The IB global support will be the main structure supporting the MOSAIX sensors already assem-

bled in half-barrels. The current design foresees a cylindrical frame structure for each layer, supported by two conical endcaps, one for L0-L1 and a second for L2, the last including a flange for connection to the other half-cone and to the OB. The material is currently fixed in a carbon fiber composite, whose thickness will be approximately 0.5 mm. FPC and cables from the e-side are routed along the inner surface of the conical support. A half-cylindrical shell made of polyamide is placed outside and close to L2 for general protection of the barrel and to constrain the airflow on the surface of L2. Air is distributed through conveyors in the volumes between L0 and L1 and between L2 and the outer shell. The current design of the cables (power lines) which run from e-side to h-side need that the longerons of the local mechanics have also the role of cable trays, the requirement of rigidity and the U-shape for cables routing suggesting carbon fiber composite as a preferred material choice, while alternatives are being considered. Figure 8.13 shows CAD representations of the IB support.

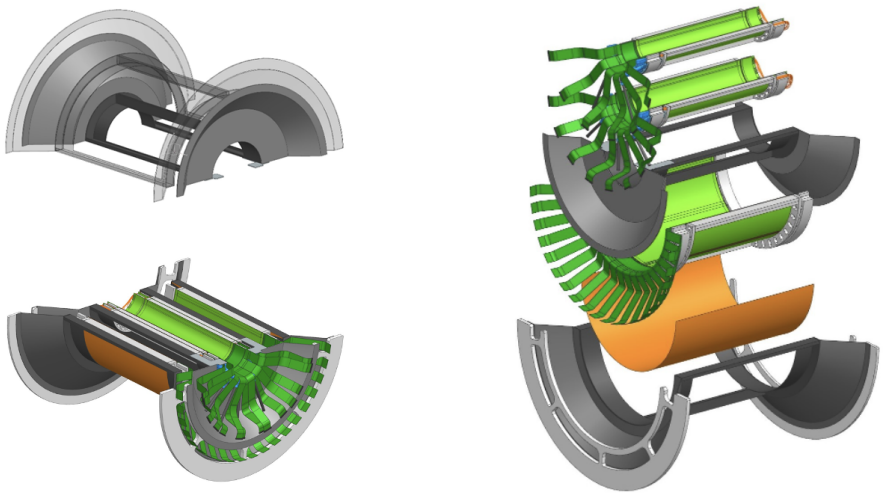

Figure 8.13: Top left: CAD representation of the frame supporting the IB. Bottom left: IB half-barrel CAD view with sensors and cable routing. Right: Exploded CAD view of IB from the h-side and the e-side. The orange element is the kapton shield. In blue the air conveyors are shown.

For the OB, EE, and HE, we introduced a modular approach in the SVT design to simplify the assembly process of these complex detector elements. A modular approach reduces complexity by breaking down the system into sub-units (i.e. detector modules) that we will pre-assemble and pre-test and then mount/interlink in the final staves or disks. The advantage is that defects in sub-units like detector modules are detected earlier in the production flow. This makes it easier to re-work problems and/or discard faulty components earlier in the production flow. A modular approach also reduces debugging complexity of the final product like a stave or disk. Overall introducing a modular approach in the design of the OBs and Disks increases the predictability of the production rate of the SVT in the production phase. It mitigates risks of delays by design and it increases confidence in planning for the production phase.

The goal in the definition of a detector module is to identify a coherent sub-unit from a functional prospective, and to shape it into a design-for-manufacturing unit. Electrical and mechanical constraints shape the implementation of the module.

The first point to consider is that the deployment of Large Areas Sensors (LASes) in the ePIC SVT represents an unprecedented technological evolution in the field of particle trackers, without any

previous, directly applicable example. The concept of a LAS is an evolution of the concept of previous detector modules where individual dies were combined into a module. The LAS combines directly via stitching multiple repeated sensor units into a single large area silicon die. A LAS is itself an evolution of the traditionally assembled detector modules with many single dies. Despite this, the LAS operation depends on the ancillary ASIC (AncASIC). Therefore an electrically coherent unit is represented by a LAS and its AncASIC.

The two components (i.e. LAS and AncAsic) of this electrically coherent unit need to be electrically connected via flexible printed circuits boards and micro-electronics interconnection techniques. This electrically coherent unit needs to be supported by a mechanical frame to be interfaced with cooling systems and to meet handling requirements.

The design of a module for the outer barrel envisions two LAS with their respective two AncAsic, once for each LAS. The mechanical frame is made of a thin film of polyimide that holds together all the module components.

The design of a module for the disks envisages one LAS and one AncAsic and a mechanical frame made of a carbon fibre plate.

We will test modules standalone after their assembly and before their assembly into staves or disks.

The outer barrel (OB) layers will be segmented in staves. The staves are composite structures using carbon fibre (CF) skins, a central CF I-beam spar and cross-ribs made of K9 foam. The side walls will be formed by the FPCs. The structure has openings where modules will be placed. During module mounting the modules are glued on top of these openings, forming a closed hollow structure with large second moment of area, and thus high stiffness. The closed structure provides a contained channel for the forced flow of air through the stave, that will remove the heat from the sensors and ancillary ASICs. In addition to their structural function, the cross-ribs made of highly thermally-conductive K9 foam are placed underneath high-power density components (the left endcap of the EIC-LAS and the AncASIC) to improve the transfer of the heat into the air coolant flow.

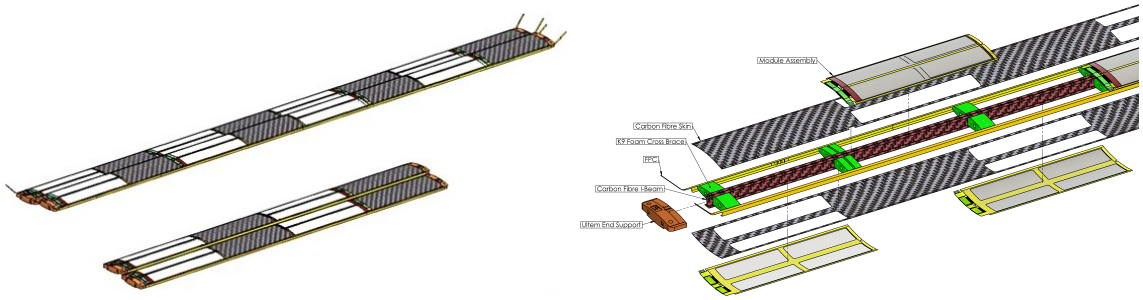

Figure 8.14: Left: OB staves for L3 and L4. Two staves per layer are shown. Right: Exploded view of an OB stave.

Each stave is one OB module (two EIC-LAS) wide, and has modules on both facings, staggered in z so that the active areas of the modules provide overlap for tracks from the vertex. L4 staves will hold 4 modules on each facing, or 8 modules in total, while L3 staves will have half that number. The dimensions of the staves are dictated by the layout of the SVT and we achieve the required coverage with LAS made up of 6 RSUs in L3 and 5 RSUs in L4, respectively. L3 will consist of two halves with 44 staves in total in a castellated layout to cover the full azimuth. L4 will consist of two halves and have 70 staves. Our initial FEA analysis of the modal frequencies finds $f_1 = 91.6$ Hz.

The staves will connect mechanically at their ends to segmented half-cones that are part of the SVT

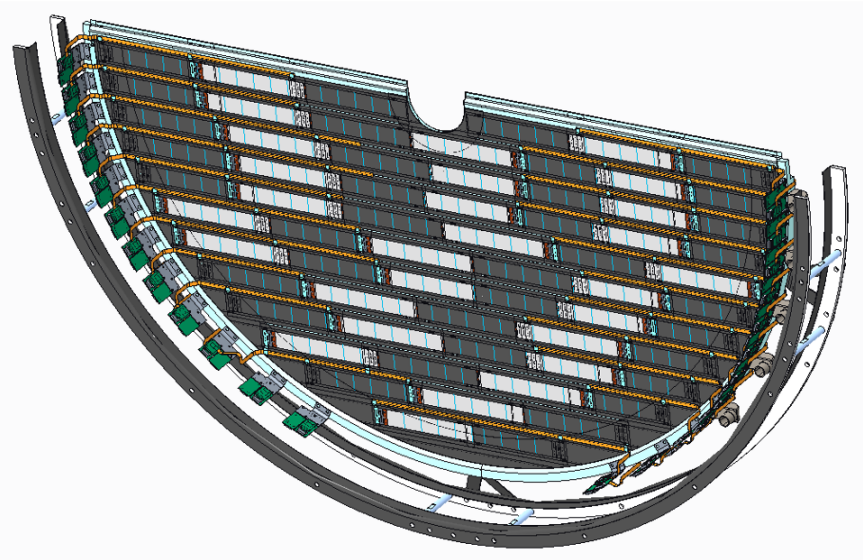

Figure 8.15: CAD model of the preliminary (half-) disk design. Modules are shown in alternatingly inward (dark gray) and outward (white) facing orientations. Common bus FPCs are shown in orange. RDOs (green) are arranged on the outside of the disk ring, inside of the interface to the SVT global support structure.

support structure. This interface still needs to be detailed, but will constrain stave rotations at the support, while allowing for limited misalignment of the support cones and thermal expansion of components. The interface will also contain the couplings of the air channel inputs to the supply distribution. The cones interface at their outer radius with a support tube surrounding the entire SVT, including its services, and also connect to the the global support structure of the IB and the innermost disks.

The EE and HE disks are a two-sided design with a corrugated carbon composite core. The purpose of the corrugation is to add strength without adding too much mass. The corrugated channels can be used for air flow to cool the disks. It also gives options for sensor layout to maximize overlaps of inactive area. Modules with one EIC-LAS will be tiled over the valleys of the corrugation on either side of the disk, creating overlap along the long axis of the sensor. Modules will be placed in an alternating inward and outward facing orientation along the corrugation which ensures that an active area of the neighboring sensor covers the insensitive LEC.

Each disk will have a ring at the outer radius that will sandwich the corrugated core to provide mechanical support, a mounting point for the RDOs, and an inlet for air cooling. Those rings will then connect mechanically to either the SVT support cone (ED0-1, HD0-1) or support cylinder (ED2-4, HD2-4). This design is currently being optimized in conjunction with the global mechanics. A CAD model of the disk design is shown in Figure 8.15.

Calibration, alignment and monitoring: Calibration procedures are needed to optimize the settings for the pixels in the ITS3 and EIC-LAS sensors. We anticipate these to be similar to those used for the existing ITS2, MLR1, and ER1 sensors, and consist in data-taking scans where one injects a charge into groups of pixels and varies their settings. We have made initial estimates of the time required to perform such scans and anticipate that such scans can be done in a parallel fashion in approximately half an hour with the final readout system.

Alignment procedures are needed to achieve the required resolutions. We will survey the IB (half-) layers, staves, and disks with precision coordinate measuring machines during their construction and will pursue a global survey during installation. Final alignment will be track-based.

Monitoring will include sensor settings and other slow-control data, including temperatures, as well as analysis in near-realtime of residuals in alignment and other observables.

Status and remaining design effort:

R&D effort: The development of the MOSAIX sensor is well underway. Two submissions have already taken place in 2020 and 2022. The former, so called MLR1, included numerous test structures for technology exploration and to develop prototype circuit blocks for future sensors. The latter, ER1, contained exploratory designs to study stitching principles, methodology and yield. The submission of the MOSAIX sensors (ER2) aiming to satisfy ITS3 requirements is planned for beginning of 2025. ePIC designers are integrated in the MOSAIX design team and contributing to the development of logic libraries, and circuitry for data transmission over the full sensor length between RSUs. The final submission (ER3) will be the MOSAIX production version for the ITS3 detector and the ePIC SVT IB.

Work on the EIC-LAS has started in terms of defining the required modifications. Design work will start once the design database is available upon signature of the necessary CERN-EIC agreement.

The AncASIC is in development with good progress on all functional blocks. Multi-Project Wafer (MPW) runs are foreseen until the full chip will be ready for production in 2026.

E&D status and outlook – IB: We have developed a preliminary design for the two innermost (L0 and L1) half-layers of the IB and its global support mechanics. Different solutions have been explored for bending and assembly of each half-layer: connecting two sensors in a single object and following a "half-layer" based procedure has been considered largely preferable mainly due to advantages from overlaps with the ITS3 building concept. Once the two half-layers have been individually built, they are assembled in a L0-L1 half-barrel. Blank silicon pieces with dimensions corresponding to the final MOSAIX sensors have been used to advance the design of the L0-L1 assembly and build the first half-barrel prototypes. In parallel, a preliminary design of the whole SVT IB mechanics, including an external shell to L2, has been also developed and a first mock-up has been produced.

We will evolve the designs for the half-barrel assembly and for the global mechanics, towards properly engineered realistic ones. The next half-barrel assembly to be built has to integrate as much as possible all the basic components of the final detector (although in a prototyping shape) and allow for thermo-mechanical studies to finalize the cooling design. Test campaigns in a climate chamber and in a wind tunnel facility for ageing and cooling studies are planned. Building of a first L2 half-layer prototype, based on the guidance from the L0-L1 assembly experience, is also scheduled to happen in parallel.

For the SVT IB global mechanics, we will use carbon fiber composites as the main material for the support, given the low mass and excellent mechanical properties. In the coming months an engineered version is planned, with the goal of both verifying possible space conflicts within the global mechanics and matching with the SVT IB assembly procedures.

E&D status and outlook – OB: We are currently prototyping the curved surface stave design for L4 to evaluate tooling and assembly procedures, as well as the performance of the design. These prototypes will be equipped with mechanical dummy sensors (40 μm unpatterned silicon) for mechanical studies, and thermo-mechanical dummy sensors (40 μm silicon

encapsulated in 25 μm and 50 μm thick Kapton layers with a 5 μm thick Cu trace layer). In particular, we will verify/measure

- Manufacturability (co-cure), mechanical integrity and good compaction of carbon fibre,
- Mechanical response spectrum up to 500 Hz and associated Q values,
- Deformations with air flow up to 20 m/s,
- Surface temperatures with thermo-mechanical dummy sensors powered up to 40 W per stave,
- Thermo-mechanical deformations with thermo-mechanical dummy sensors powered up to 40 W per stave.

The results from these studies will guide us in the finalisation of the stave design. In the

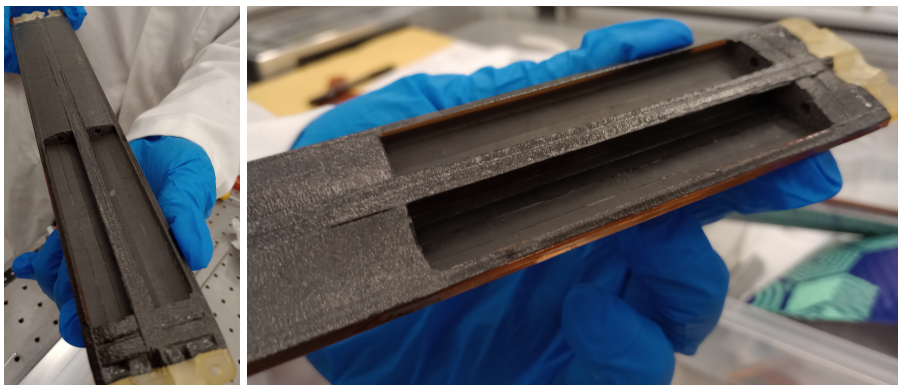

Figure 8.16: First L4 quarter length stave prototype.

first phase we are prototyping the stave design with the curved facings, as this is the more challenging to construct.

Interfaces to the support cones will be designed in parallel with the design work on these structures.

E&D status and outlook – Disks: Work continues on the design and layout of the disks. We are finalizing the carbon fiber layouts for both the corrugated core and the flat module sheets. The first prototype was made using carbon fiber veil for the face sheets and corrugation and had a density of 500 gsm. However, the veil is not ideal for thermal performance and can be challenging to lay up on the corrugated tooling. New prototypes are being made with K13CU unidirectional carbon fiber, which has a much improved thermal conductivity.

The initial test piece has been tested for thermal performance using copper trace heaters. The prototype is shown in Figure 8.17. The measured ΔT is well within 10 °C for the EIC-LAS RSUs, but is high for the LEC, though trending in the right direction with increased air flow, and depends on the design dissipation. The thus far high values of ΔT for the LEC region can be due to many factors, including the low thermal conductivity of the carbon fiber veil and the overall thinness of the contact surface. We are studying mitigation possibilities using pyrolytic graphite sheets (PGS), which have a large in-plane thermal conductivity (upwards of 800 W/m·K) and significantly improve the thermal performance of the prototype. Results are shown in the right of Figure 8.17. The new face sheets made with K13CU have similiar thermal conductivity to the PGS and initial tests are promising. A new, full prototype is being assembled with the K13CU carbon fiber..

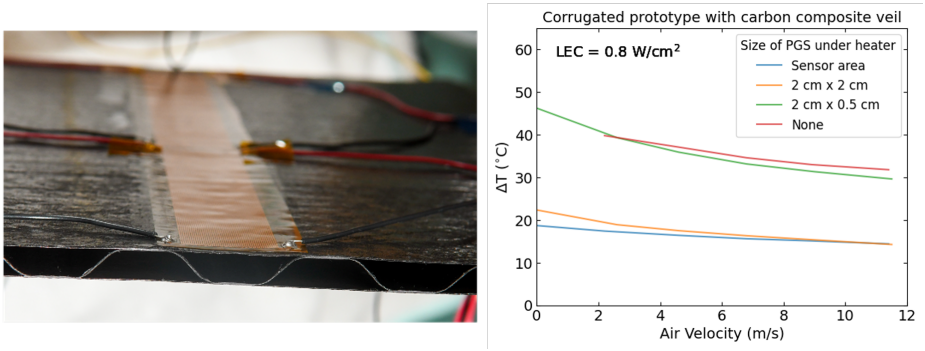

Figure 8.17: (Left) First test piece of the carbon composite corrugated disc core made in the LBNL composite shop. Heaters with two different heating zones that can mimic the sensor power density are placed on the carbon composite facesheet and are used for thermal measurements. (Right) Observed ΔT on the LEC section of the test heater versus coolant air velocity using corrugated carbon fiber veil prototype test piece. Measurements taken with various sizes of PGS placed underneath heater.

We are currently developing prototypes focused on the development of assembly tooling, module handling, and thermal and mechanical tests. Prototypes will undergo vibration tests to understand mechanical stability. Mechanical dummy silicon (40 μm unpatterned silicon) is in hand to construct a quarter disk mechanical prototype. We expect thermo-mechanical dummies (40 μm silicon encapsulated in 25 μm and 50 μm thick Kapton layers with a 5 μm thick Cu trace layer) at the end of the calendar year to create a thermo-mechanical prototype.

The bench tests will be paired with ANSYS structural and fluent simulations to understand the performance under air flow and the structural integrity of the disk. This will also need to be accompanied by bench tests and simulations that include the disc support ring and the outer ring.

E&D status and outlook – FPCs: The development of the flexible printed circuits (FPCs) for the ePIC SVT adopts an iterative approach where a sequence of prototypes will inform the evolutionary development of the final design. The activity on the FPC started in September 2023 and it is progressing as part of Work Package 3 “Electrical Interfaces”. The first iteration of prototypes is underway. This started with targeting an initial design for OB L4. A definition stage captured the design requirements for powering, data transmission and geometrical factors until March 2024. This was followed by a design stage and then by an order submission to RPE LTU (Ukraine). The first set of prototypes are currently being manufactured. The prototypes from RPE LTU will be tested at Daresbury Laboratory and at the University of Oxford. They will also be distributed to other interested sites. In parallel, the community of institutes interested in FPCs started to grow. Since 09/05/2024, the WP3 community started to have monthly meetings with representatives from BNL, Daresbury Laboratory, LANL, LBNL and the University of Oxford. LBNL started to evaluate prototypes from Omni Circuit Board (Canada). LANL also approached a third supplier called Q-Flex Inc. (USA) to procure low level prototypes. The aim is to evaluate the capabilities of three different supplier to manufacture FPCs with aluminium conductors. Signal and power integrity of the FPCs will be tested and the performance over samples of different suppliers compared. A key requirement is signal attenuation for the high speed differential transmission lines (10 Gb/s). Wire bonding and single point Tape Automated Bonding (spTAB) are being evaluated as potential interconnection techniques in ongoing and future prototypes.

E&D status and outlook – Powering: The need to regulate voltages for the MOSAIX sensors

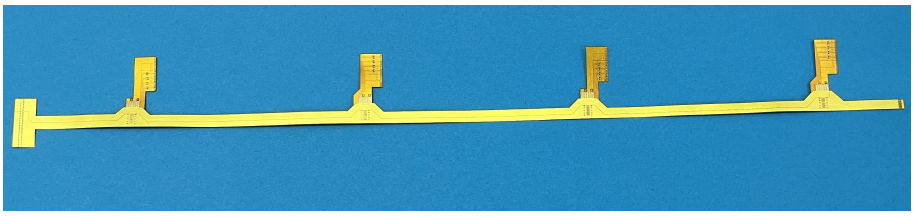

Figure 8.18: An example of a low technology readiness level prototype for the FPC of the outer barrel (layer4). Prototype made by RPE LTU.

as close to the IB (to minimise losses) dictates the need for a(t least one) powering board. Considerations for the design and development of these boards are ongoing; this includes deciding how many regulation stages give the best balance between power losses (fewer stages is likely to mean longer lengths of the most lossy cables, when delivering low voltage and high current), versus additional material in the detector volume (more stages equals more high material powering board, and the final voltage regulation is likely closer to the active area of the IB).

Conceptual powering schemes were developed and used to define specifications for the AncASIC and FPC designs for the OB and Disks. Requirements are being iterated based on limitations introduced by these designs so that they can be iteratively improved. Testing and confirmation of requirements will occur as prototypes become available; this includes:

- Verifying output voltages and current capacity of the individual SLDOs.
- Verifying output voltages of NVGs.
- Daisy-chaining AncASICs to verify serial powering chain performance.
- Quantifying performance of the FPCs in terms of current carrying capacity and voltage-drop along the conductor lengths.
- Combining the above elements to test full serial powering chain prototypes (1 FPC feeding current to 4 AncASICs, each loaded with an EIC-LAS-like structure).

E&D status and outlook – Powering: Work on readout electronics has mainly concentrated on testing evaluation boards of the various components being considered for SVT readout: lpGBT, VTRx+, radiation tolerant FPGA PolarFire, optical FireFly. As part of the ITS3 work-package responsible for readout (WP6) we follow closely the developments in ITS3, since a lot of the electronics for SVT is modeled after ITS3 designs. An initial prototype for the Fiber Aggregator Board was discussed and is now under development using a commercial FPGA board (ZCU102) mated with the optical FireFly FMC card to provide up to 8 fiber inputs and multiple fiber outputs. The VLDB+ board from CERN (containing both lpGBT and VTRx+ was used setup a full chain starting from a Skyworks clock generator board as a stand-in for the Global Timing Unit (GTU), a Xilinx ZCU102 board running lpGBT-FPGA firmware as a stand-in for the FELIX board, and the VLDB+ board as the RDO. A measurement of the jitter of the clock recovered by the lpGBT showed demostrated adequate performance of this chain to provide a low-jitter clock to the sensors.

Together with Nikhef and Utrecht University, we are currently developing a test system for the serializer chiplet of the ER1 prototype submission. This serializer is a prototype for the 10Gbps serializer to be deployed in the Left End Cap of the final ITS3 sensor. The test system consists of an FMC card which contains the bonding pads for the serializer chiplet, as well as various drivers and connectors including the possiblity to drive the high-speed signal onto a Flex-PCB to test the signal integrity over those traces. The FMC card itself will connect to a commercial Xilinx FPGA board for pattern generation and checking.

Another prototype development is the "MOSAIX Mock-up" board currently being designed at ORNL consisting of an FMC daughter card which contains the various Readout components (2 data VTRx+ and an lpGBT / VTRx+ combination for the slow controls interfaces. It will interface to a ZCU102 board where firmware will simulate the responses to slow controls commands, while also allowing to simulate data packets to be sent over the up to 8 fiber optic lines of the 2 VTRx+ interfaces in order to develop both data acquisition protocols and slow controls interfaces of the Readout Electronics to the MOSAIX sensor without the need of an actual MOSAIX sensor.

E&D status and outlook – Cooling: Our prior work has shown that foam can be an important factor in the cooling and thermal performance of staves and disks. This is an integral part of the OB stave design and is being pursued as an option for under the LEC in the disk design. Both will be tested using thermal and thermo-mechanical dummies with upcoming prototypes.

The final air cooling system will be designed based on the overall air volume of the SVT. Current estimates put the total air volume around 1000 cfm total, which would require a pressurized system. The air will be pressurized before entering the ePIC detector volume and then regulated down to various pressures as required by the different parts of the SVT (e.g. OB design requires air above 1 atm).

Simulations from LBNL and Jlab have shown that during beam-pipe bake-out a 5 mm distance from the beam-pipe can keep the silicon below 30 °C with air flow below 10 m/s. However, air flow between the beam-pipe and L0 brings down the temperature of the beam-pipe and can affect ability to reach the 100 °C required inside. Studies are ongoing to determine what hot gas temperature is needed to bring the beam-pipe to temperature and what effect that has on the silicon. We also plan to study if airflow only between L0 and L1 is sufficient to keep the detector below the current 30 °C requirement as this will help mitigate the effect of the air cooling on the beam-pipe itself. Simulations will be paired with thermo-elastic studies in a climate chamber that will study cycling, longevity, and assess the point of failure.

Other activity needed for the design completion: We are continuing our testing characterization of the products from the ITS3 sensor development sequence. We are currently preparing for the first tests on MOSAIX at CERN, in collaboration with ITS3, using a high-frequency wafer probe setup that we are jointly developing. Laboratory tests of thinned and diced wafers are also being planned, as well as beamtests and irradiation efforts.

The AncASIC will be manufactured in a different process than the MOSAIX and EIC-LAS sensors. We are readying an initial MPW submission in this 110 nm process and are planning for its testing and validation. Test structures and the main functional modules of AncASIC, the SLDO, NVG and Slow Control, will undergo irradiation to verify their correct functioning in the expected radiation environment.

Status of maturity of the subsystem:

Environmental, Safety and Health (ES&H) aspects and Quality Assessment (QA planning): We will follow and adhere to all applicable ES&*H* standards during the development, construction, installation, and ultimately commissioning and operation of the SVT. Hazards include those associated with adhesives, carbon composites, flammables, wafer-probing and wire-bonding, use of radioactive sources, testbeams, and irradiation facilities, and electrical safety. Where possible, we will work across institutions to implement standardized controls and mitigations, as well as documented safety procedures.

System tests in the development phase of the SVT are integral to our Quality Assessment. Quality Control forms an integral part of WBS and schedule during construction and assembly.

Construction and assembly planning: The L0-L1 half-barrels will be manufactured in Italy by INFN: the current plan is to have a main assembly site in Bari and a second one in Padova currently being equipped. The L2 production half-layers will be built in the US. Both construction activities will include a final QC step of the corresponding complete assembly: this will include operation with air-cooling to verify thermal performance and testing of readout and control lines. After a successful pass of the QC step, L0-L1 half-barrels and L2 half-layer will be shipped to BNL. The global IB mechanics will be produced by INFN in Padova, undergo a QC step based on a metrological survey and finally shipped to BNL. At BNL the L0-L1 half-barrels and L2 half-layers will be assembled to the global mechanics to form complete IB half-barrels. All the connections to services (powering, cooling and readout) will be put in place to allow a final QC step.

Modules and staves for the OB layers will be manufactured in the UK. Currently we plan to manufacture modules at two sites, Birmingham and Daresbury Lab. This production includes electrical bonding of the sensors and ancillary ASICs to the bridge FPC. Module construction concludes with a QC on the completed module before shipping to the stave loading sites. Stave production, which comprises manufacture of the stave composite structures, and gluing of modules onto the structures and electrical bonding of the bridge FPCs to the main FPCs. These production steps will be performed at Oxford and RAL. Again, the final step of the stave construction will be a QC of the completed stave. This will comprise operation with internal air cooling to verify thermal performance, operation of control lines and readout of modules. After successful pass of these QC steps, staves will be shipped individually to BNL. At BNL staves will be mounted on the support half-cones from the inside, starting with the outermost layer L4. This involves mechanical connection, connection of the air supply, and dressing of the FPCs and mounting of the RDOs on the outside of the support cones. After the mounting of the L4 staves they will be tested, and after that the same procedures will be repeated for the inner OB layer, L3.

Disks and their modules will be produced and assembled in the US. LBNL, Purdue, and LANL are expected to be disk assembly sites, with LBNL and Purdue also serving as module assembly sites. Assembly of modules includes gluing of sensors to carbon composite structures, as well as electrical connection (wire or tab bonding) to a bridge FPC and the AncASIC. Modules will undergo QC before being assembled onto disk structures. The corrugated carbon composite disk structures and module flat sheets will be produced at LBNL and shipped to LANL and Purdue. Disc support rings will be produced by an outside vendor, validated at LBNL, then shipped to disk assembly sites. Disks will be assembled in halves, first on one side and then the other. Disk assembly includes gluing modules and common bus FPCs onto the front and rear sides of the discs and making electrical connections. QC is planned for each corrugated row assembly and then again after completion of the front and rear sides of each disk. Disks will be shipped in halves to BNL, where they will be installed into the larger SVT assembly. Disks are the last piece to be installed, after the IB and OB. Assembly will occur from the inner disks outward. ED0 and HD0 will be mounted to the SVT support cones. ED2–4 and HD2–4 will be mounted to the support cylinder. ED1 and HD1 could be mounted to either and will be iterated with global mechanics. Installation must include the dressing of the services, connecting of the air supply, and mounting of the RDOs. Each half disk will be tested after installation.

We plan to produce the outer global support structures at Purdue and/or LBNL. Readout will be led by ORNL with testing at multiple sites.

Collaborators and their role, resources and workforce: (Placeholder:) The SVT currently has collaborators at 20 institutions with the main institutional roles and resources outlined above.

Risks and mitigation strategy: The SVT depends crucially on its sensors, the ITS3 sensor used in the IB and the ITS3-based EIC-LAS used in the OB, EE, and HE, since they form the only known way to meet the full performance requirements within ePIC. Their development is ongoing and presents a risk. Together with the project we have identified two branchpoints, which are both based on schedule delays:

1. the ITS3 schedule remains compatible with the EIC project schedule, but EIC-lAS development is delayed,
2. the ITS3 schedule is delayed and becomes incompatible with the EIC project schedule.

If the first branchpoint were triggered, the SVT OB will be replaced with two MPGD barrel layers derived from the outer MPGD tracker, specifically its innermost (micromegas) layer. The SVT EE and HE will in this case each be replaced with in total up to seven near-identical MPGD disks, specifically based on the existing uRWELL disks. If, in addition, the second branchpoint were triggered, the SVT IB will be replaced by two or three layers based on the existing ITS2 sensor, as used in the ALICE and sPHENIX experiments, without EIC-specific modifications.

Additional Material

8.3.3.2 The MPGD trackers

Requirements

Requirements from physics: Micro-Pattern Gas Detector (MPGD) technologies have been chosen to complement the Si based tracking layers. MPGDs are relatively fast detectors able to provide precision space point measurements with good timing resolution, while also maintaining the overall conservative material budget that is required of the ePIC detector [23]. MPGDs will play a role in pattern recognition, ensure the central tracking system covers the required full pseudorapidity range $-3.5 \leq \eta \leq 3.5$, and aide in PID reconstruction.

The EIC collider is expected to deliver collisions with bunches crossing every ∼10ns [24], which will require the MPGD detectors to provide timing resolutions $\mathcal{O}(10\ ns)$ to separate events from adjacent bunches. For ep collisions of 10×275 GeV, the DIS physics rate is expected to be around 500 kHz, while hadron and electron beam gas backgrounds rates are estimated to be 32.6 kHz and 3177.25 kHz, respectively [5]. These rates are well within the rate capabilities of MPGDs. Combining the timing information from the MPGDs with information from the Si detectors should allow pattern recognition algorithms to discriminate between physics and background signals. In addition to providing hit information with good timing resolutions, the MPGDs will provide additional hit points needed for robust track reconstruction. Early simulations showed that the number of hit points used in the track reconstruction reduced from around 6 hits near $\eta = 0$, to only 3 hits at $|\eta| > 3$, due to tracks moving out of the acceptance of some of the Si layers. ePIC endcap gaseous trackers, (μRWELL-ECT) were implemented to recover additional hits at larger η values. Figure 8.20 shows the average number of hits per event in the current ePIC tracking detector as a function of η for different momentum ranges. In this configuration the ePIC tracker measures at least 5 hits per event over the region ($|\eta| < 3.5$).

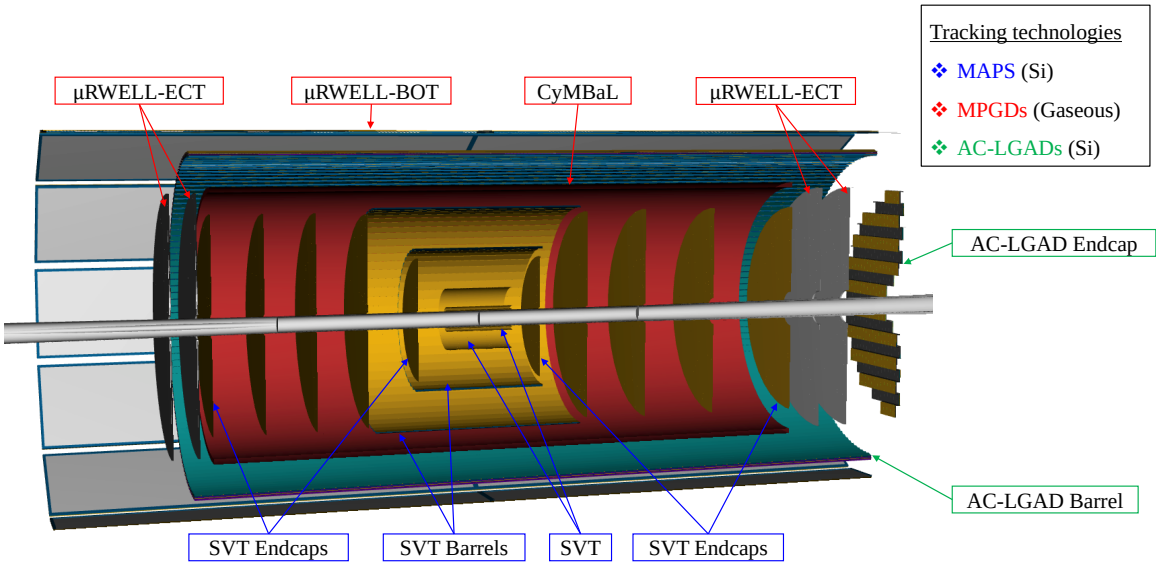

Figure 8.19: ePIC Tracking Subsystems

Finally, as detailed in the Yellow Report [23], the hpDIRC requires the track entering the PID volume to have good angular resolution (0.5 mrad at p = 6 GeV) in order to meet its performance requirements. This will be accomplished by providing the hpDIRC with precision hit points just before a particle enters its volume via ePIC barrel outer tracker, (μRWELL-BOT) and exits to the first tracking layer of the barrel imaging calorimeter.

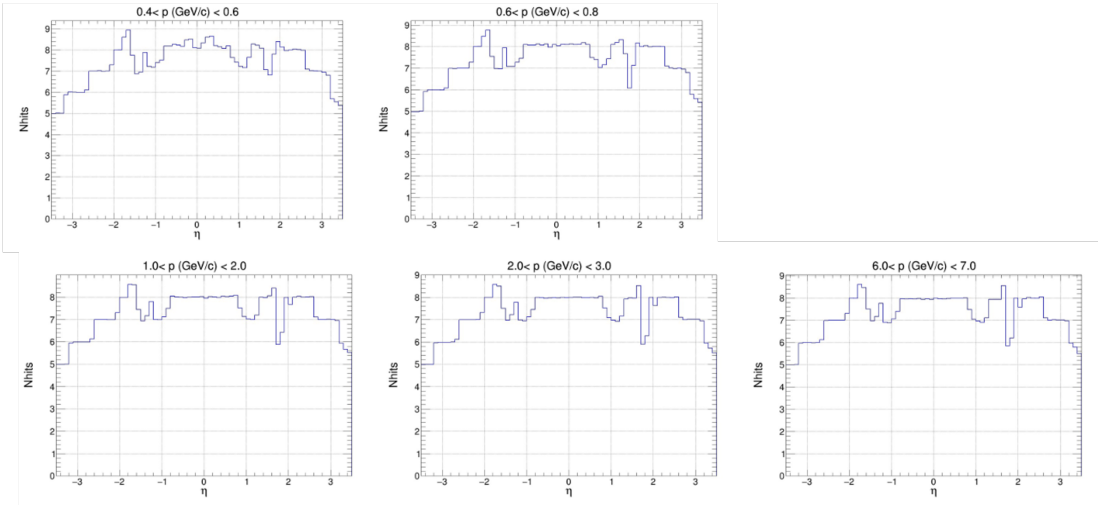

Figure 8.20: Total tracker hits vs. η for various momentum ranges.

Requirements from Radiation Hardness: Detailed simulation on radiation dose in ePIC has been performed. Fig. 8.21 shows the estimate of hadron and EM radiation doses in ePIC simulation

along with location of MPGD layers [5]. Table 8.5 shows the maximum estimated radiation dose from various sources for MPGD trackers at various locations with 10 years of running at top machine luminosity and 100% detector and accelerator efficiency based on e+p PYTHIA simulation.

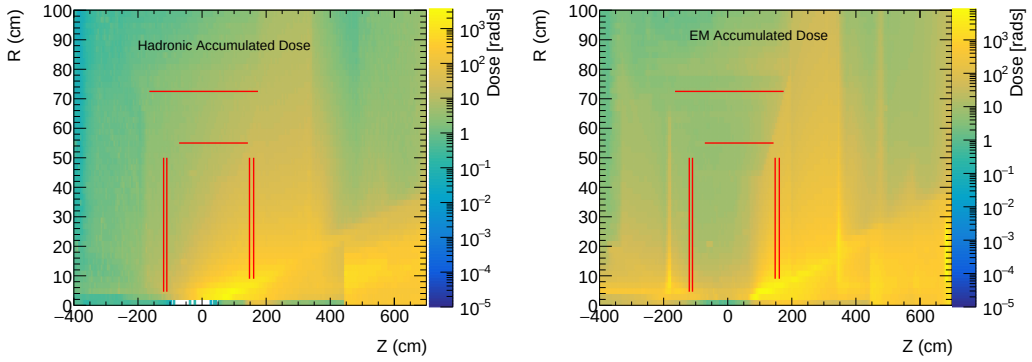

Figure 8.21: (*left*) EM radiation and (*right*) Hadron radiation dose estimate for minimum bias PYTHIA e+p events at 10x275 GeV at top machine luminosity for 6 months of running at 100% machine and detector efficiency [5]. The locations of MPGD trackers are shown by red lines [25].

MPGD tracker	EM Radiation dose [krads]	Hadron Radiation dose [krads]	1 MeV neutrons equivalent fluence [cm^{-2}]	1 MeV protons equivalent fluence [cm^{-2}]
CyMBaL	0.22	0.15	2.7×10^{10}	2.0×10^{10}
μRWELL-BOT	0.3	0.1	2.8×10^{10}	4.2×10^{9}
electron ECT	0.064	0.03	1.1×10^{10}	1.7×10^{9}
hadron ECT	0.87	0.23	3.0×10^{10}	8.5×10^{9}

Table 8.5: Maximum dose of radiation by different sources at MPGD tracker layers for e+p minimum-bias event at 500 kHz event rate for 10 years EIC running with 6 months run time per year and 100% efficiency [5].

The MPGD trackers in ePIC will experience low radiation dose and based on past experience with MPGD trackers in various experiments [26–28] there will be negligible aging issues. The electronics based on SALSA and also DC-DC converter, which will be mounted on the detector back end, are radiation hard as is shown by electronics group for ePIC in section 8.3.10 of this document.

Requirements from Data Rates: Table 8.6 shows hit rate per unit area for each MPGD subsystem in ePIC which is far lower than rate capability of MPGD detectors [29, 30]. Table 8.7 shows the maximum hit rate experienced by a channel for various MPGD trackers in ePIC [5]. The rates are low enough for ASIC developed for MPGDs which can handle rate of 100 kHz/channel.

Justification The requirements cited above drives the necessity of using MPGD trackers at various locations of ePIC. MPGDs can be built over large area and their ability to handle higher rates

MPGD tracker	DIS e+p rate [Hz/cm^2]	Hadron beam gas rate [Hz/cm^2]	Electron beam gas rate [Hz/cm^2]
CyMBaL	26.37	14.33	5.5
μRWELL-BOT	9.82	5.33	1.7
electron ECT	144.68	78.63	437
hadron ECT	1326.36	720	201

Table 8.6: Hit rate per unit area of various MPGD trackers for e+p DIS events at 10×275 GeV with $1.54 \times 10^{34} cm^2 s^{-1}$ luminosity scaled from e+p DIS events at 18×275 GeV and $1.54 \times 10^{33} cm^2 s^{-1}$ luminosity, 10 GeV electron beam gas and 275 GeV hadron beam gas

MPGD tracker	DIS e+p events [Hz]	Hadron beam gas [Hz]	Electron beam gas [Hz]
CyMBaL	3.68	0.05	4.78
μRWELL-BOT	2.76	0.04	4.78
electron ECT	9.2	3.56	102
hadron ECT	101.2	4.39	39.88

Table 8.7: Maximum hit rate by a single channel of various MPGD trackers for e+p DIS events at 10×275 GeV with $1.54 \times 10^{34} cm^2 s^{-1}$ luminosity scaled from e+p DIS events at 18×275 GeV and $1.54 \times 10^{33} cm^2 s^{-1}$ luminosity, 10 GeV electron beam gas and 275 GeV hadron beam gas

with moderate spatial resolution makes them excellent candidate for large size trackers.

Device concept and technological choice: The MPGD trackers are based on two different technology and are described in the following.

Subsystems description: CyMBaL. The role of the ePIC Cylindrical Micromegas Barrel Layer (CyMBaL) is to wrap around the SVT in its entire length to provide an additional hit point. Consequently, the main requirement is to have as little as possible acceptance gaps. In order to limit the impact on particle reconstruction in the outer detectors, CyMBaL has to be light in material budget, possibly less than $X/X_0 \sim 1\%$. The requirements in space resolution are still to be finalized, but CyMBaL is expected to provide hit points with about 150 μm uncertainty. In order to help the track finding, the time resolution is expected to be of the same order of magnitude of the bunch spacing, i.e. ∼10 ns.

CyMBaL (Figure 8.22a) is composed as a set of 32 Micromegas tiles arranged in a way to ensure full coverage in φ (8 modules) and in z (4 modules). The space envelop assigned to CyMBaL spans the range between 55 cm and 60 cm in radius and it is asymmetric in the longitudinal direction, covering the range -105 cm $< z <$ 143 cm. CyMBaL is designed in two symmetric halves that meet at $z = 19$ cm (due to the asymmetric keeping zone). In each half, the 16 modules are arranged in two cylinders, the inner one (in $|z|$) sitting at a radius of 55 cm and the outer one at 57.5 cm.

In order to limit the complexity of the detector production, the design is aiming at limiting the

differences among the modules, possibly having only a single design for the module PCBs that will be assembled with different bending radii.

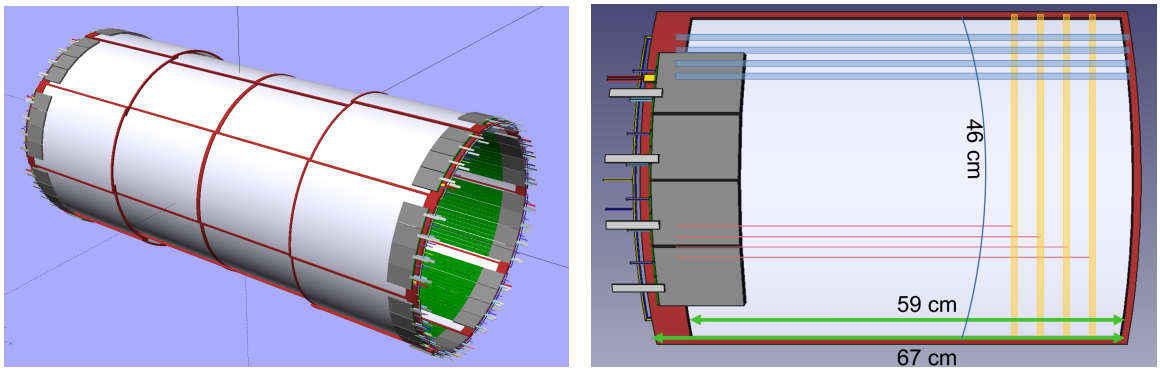

(a) **(b)**

Figure 8.22: (a) CyMBaL CAD model showing the assembly of the 32 modules. (b) CAD model of a CyMBaL module. The light blue represents examples of readout strips measuring the $r \cdot \varphi$ coordinate (called Z-strips as they run along the z axis). The light yellow represents examples of readout strips measuring the z coordinate (called C-strips as they are arcs of a cylinder). The light red lines represent examples of trail lines to bring the C-strip signals to the FEBs. For the explanation of the services see the text.

The preliminary design of a CyMBaL module is shown in Figure 8.22b. A module is a cylindrical tile 48 cm wide (equivalent to about 50 degrees in the azimuthal direction) and 67 cm long, and the active region is about 46×59 cm^2. The sensor is based on the bulk resistive Micromegas technology [31] with a 3 mm conversion gap. The signal will be readout by orthogonal strips to provide a two dimensional information of the position of the charged particle crossing the sensitive area. The strips running along the longitudinal direction (therefore called Z-strips) will provide the $r \cdot \varphi$ measurement of the hit and they will be directly routed to the connector area. The strips running along the azimuthal direction (C-strips, C for cylindrical) will provide the z information of the hit and they will need be connected with vias to routing trails to bring the signals to the connectors. The pitch of the readout strips will be $\sim$ 1 mm and the resistive layer will allow the charges to be shared among neighboring strips for a better centroid reconstruction. The total number of strips per module will be 1024 and they will be readout by four FEBs, each one equipped with 4×64-channels SALSA chips.

The frame will consists of carbon fiber hollow square beams and arcs of about 3 mm in size. Being hollow, these beams not only will provide the mechanical rigidity and support for the detector, but also will be used to distributed the gas inside the detector.

Subsystems description: μRWELL-BOT. The ePIC MPGD Barrel Outer Tracker (μRWELL-BOT layer) is the outermost gaseous tracking layer installed in the barrel region of ePIC central tracker. The detector sits right at a radius of 72.5 cm right in front of the high performance DIRC (hpDIRC) as shown in the layout at the top left of Fig. 8.23. The tracker is split in two sectors (Z-sector) along the beam axis z. Each Z-sector is consists of 12 μRWELL-BOT rectangular modules ((φ-modules) arranged in dodecagon shape to cover 2π acceptance in the azimuthal direction (φ) as shown in the top right of Fig. 8.23. The μRWELL-BOT φ-modules are designed to match the hpDIRC acceptance in both z and φ as shown on the bottom right of Fig. 8.23. Mechanical constraints associated to the detector support frames as well as the very limited space available for

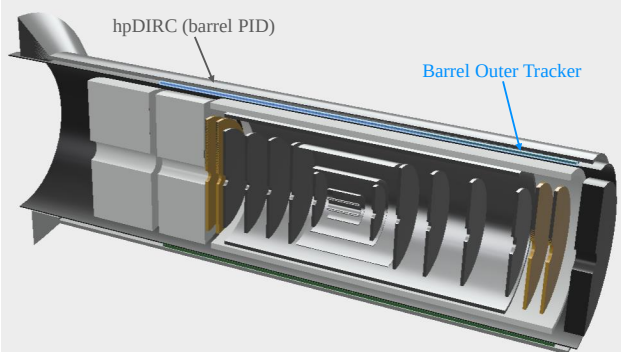

μRWELL-BOT Tracker in ePIC central detector

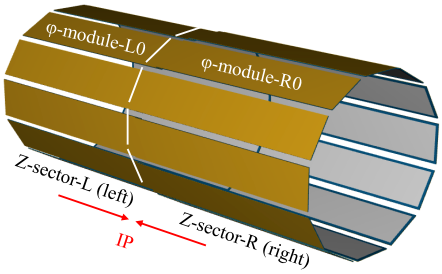

μRWELL-BOT tracker in dodecagon arrangement

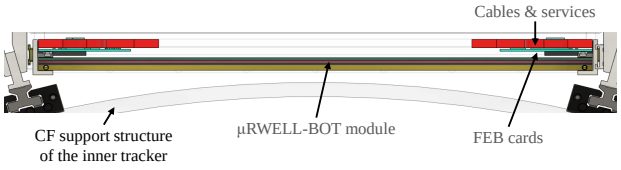

Front view of μRWELL-BOT module

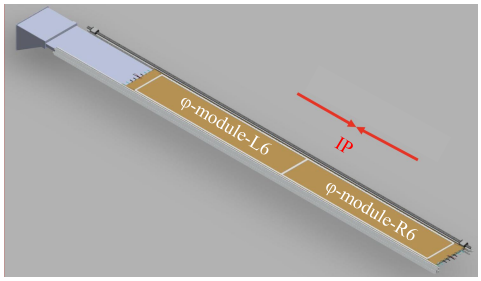

μRWELL-BOT module acceptance match with hpDIRC bar

Figure 8.23: μRWELL-BOT in ePIC central detector frame

integration in the ePIC detector support frames result in an acceptance gap of ∼13% in φ and ∼1% in z.

For the μRWELL-BOT φ-modules, thin-gap GEM-μRWELL hybrid detector technology (see Appendix section **??**) was chosen to satisfy the detector requirement in term of position and timing resolution as well as detector efficiency and operation stability. Proof of concept and preliminary performance results on small size prototypes tested in beam at Fermilab in 2023 are also reported in Appendix section **??**. The design of the full size μRWELL-BOT module prototype based on the thin-gap GEM-μRWELL technology is presented in Appendix section **??** as part of the Project Engineering Design (PED) effort to develop the engineering test article μRWELL-BOT module based on thin-gap GEM-μRWELL technology.

Subsystems description: μRWELL-ECT. Monte Carlo simulations show that the endcap regions of the ePIC detector experience the highest backgrounds in the experiment and charged particle tracking requires several hit points in the $|\eta| > 2$ region for good pattern recognition. To optimize the ePIC baseline tracker design, two planar Micro-Pattern Gaseous Detectors (MPGD) disks, with a central hole for the beam pipe are located both in the hadronic and the leptonic sectors (see the right drawing of Figure 8.24). The ECT disks geometrical envelope is reported in Table 8.8. It takes into account the integration constraints within the ePIC detector and the beam pipes dimensions. As shown in the left drawing of Figure 8.24, the hadron and lepton beam pipes slightly diverge from the interaction point, therefore the ECT inner radii are calculated taking into account the envelope radii and their center offset, the hadron beampipe forming a larger angle with the z axis. For simplicity the inner radius if fixed by the largest of the two values calculated for the disk located at the larger z position at each endcap region. As a result the two lepton disks located closer to the interaction point, will have a smaller inner radius than the two hadron disks (4.65 cm vs 9 cm) as they are located closer to the interaction point, while the outer radii of 50 cm are equal for all the four disks and are fixed by the available volume inside the ePIC detector. The ECT disks envelope

MPGD Disk	Longitudinal location z (cm)	Outer Radius (cm)	Inner Radius (cm)	Outer Active Area Radius (cm)	Inner Active Area Radius (cm)
HD MPGD 2	161	50	9	45	10.5
HD MPGD 1	148	50	9	45	10.5
LD MPGD 1	-110	50	4.65	45	6
LD MPGD 2	-120	50	4.65	45	6

Table 8.8: The ECT disks geometrical envelope and active areas dimensions.

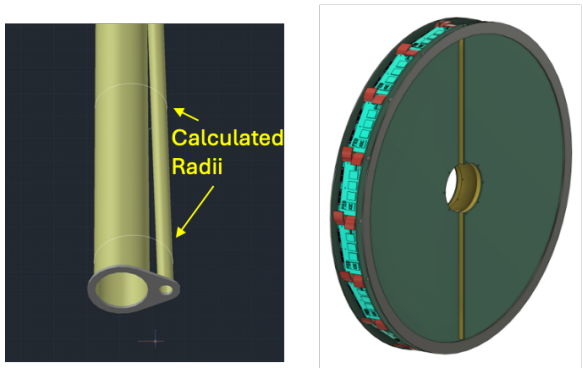

Figure 8.24: Left: Hadron and lepton beam pipes slightly diverge from the interaction point. The ECT inner radii are calculated taking into account the envelope radii and their center offset, the hadron beampipe forming a larger angle with the z axis. Right: layout of a couple of μRWELL-ECT disks.

also includes the MPDG gas frames of 1.5 cm thickness, and a 3.5 cm outer service ring, to locate services and electronics front-end boards. The resulting active area dimensions of the disks are also reported in Table 8.8 and the corresponding angular and pseudorapidity acceptances are reported in Table 8.9. The final active ranges in pseudorapidty are $2.0 < \eta < 3.3$ for the hadron sector and $-3.6 < \eta < -1.7$ for the lepton sector, compliant with the tracking requirements. A GEM-μRWELL

MPGD Disk	$\lvert\theta\rvert$ min (deg)	$\lvert\theta\rvert$ max (deg)	$\lvert\eta\rvert$ min	$\lvert\eta\rvert$ max
HD MPGD 2	3.7	15.5	2.0	3.4
HD MPGD 1	4.0	16.9	1.9	3.3
LD MPGD 1	3.1	22.1	1.6	3.6
LD MPGD 2	2.8	20.4	1.7	3.7

Table 8.9: The ECT disks angular and pseudorapidity acceptance.

hybrid technology with XY 2D readout has been chosen to match all the performance requirements (see paragraph 8.3.3.2. Figure 8.25 shows the schematics of the hybrid GEM-μRWELL detector. A 3 mm drift region, where the primary ionization charge is produced, is located between the cathode and the GEM foil. A 3 mm transfer gap is located between the GEM foil and the μRWELL foil. The cathode and the 2D readout PCB are supported by a 3 mm thick honeycomb structure to minimize

the detector material budget. The 2D strip read-out using a Compass-like scheme is also shown, where the charge is collected by XY orthogonal strips located on two different printed circuit board (PBC) layers. The strip widths of the two coordinates must be optimized (in a ratio of about 1:3) to balance the signal amplitude in the two dimensions, since the upper layer strips screen the charge collected on the lower ones.

The XY Cartesian readout scheme was preferred over the Rφ geometry for two reasons: i) the high radial strip density at the center hole and ii) the possibility offered by the XY geometry to route all the strips to connectors located on the outer service ring. The cathode and the 2D readout PCB are supported by a 3 mm thick honeycomb structure to minimize the detector material budget, which amounts to 0.85%X/X_0 in the active region.

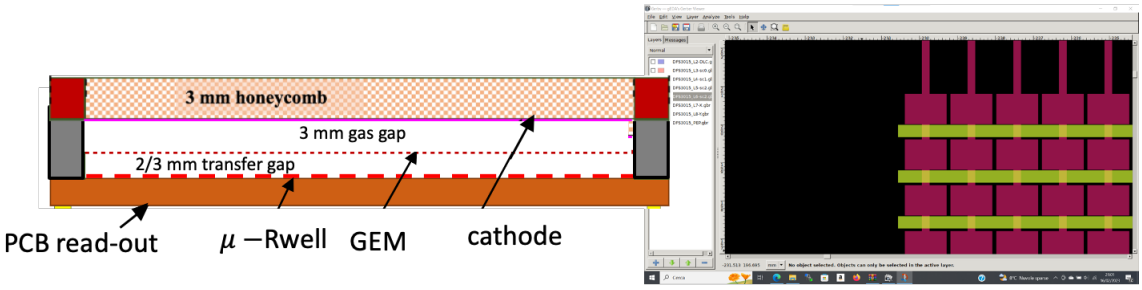

Figure 8.25: Left: schematics of the hybrid GEM-μRWELL detector. A 3mm drift region, where the primary ionization charge is produced, is located between the cathode and the GEM foil. A 3 mm transfer gap is located between the GEM foil and the μRWELL foil. The cathode and the 2D readout PCB are supported by a 3 mm thick honeycomb structure to minimize the detector material budget. Right: 2D strip read-out using a Compass-like scheme.

Subsystems description:FEE. To meet the requirement of streaming readout new front-end chips for MPGD trackers in ePIC are being developed by Sao Paulo Universities and CEA Saclay IRFU. The chip, known as SALSA, has the following characteristics :

- 64 channels with large input capacitance range, optimized for 50-200 pF, reasonable gain up to 1nF
- Large range of peaking times: 50-500 ns.
- Large gain ranges: 0-50 to 0-5000 fC.
- Large range of input rates, up to 100 kHz/ch.
- Reversible polarity.

Other components. The **gas mixing unit** will be a critical component of the MPGD trackers. The mixing unit preferably will use Mass Flow Controllers based on Proportional-Integral-Derivative (PID) control systems. Furthermore, the mixing unit should be able to mix either two or three different inert gases depending on the final composition of the operating gas. The preferred mixture for CyMBaL is Ar-isobutane (95:5), however if concern is raised for flammability of this gas mixture then a three gas mixing unit will provide the possibility of adding third gas (preferably CO_2) at the expense of isobutane. This will help in maintaining stability (due to the isobutane component),

make the gas faster and non-flammable (due to the CO_2) component. Additionally **sensors** will be installed to monitor the temperature, pressure and humidity close to MPGD modules and if possible also to monitor temperature of incoming and outgoing gas to give an idea of heating of gas volume inside detector itself. The **High Voltage Power Supplies (HVPS)** are another important component for the subsystem to bias the detector. Preferably each HV electrode associated with each MPGDs will be powered by individual HVPS channel which will also have the capability of monitoring current drawn by each MPGD layers, preferably having current resolution of few nA and extremely low ripple ($< 5mVpp$) to reduce noise from HVPS. There is also possibility of using **voltage divider** to bias MPGD modules in place of using individual HV channel from HVPS to bias the modules.

Performance The MPGD tracking detectors share 2D spatial resolutions performances better $\simeq$ 150 μm, timing resolutions of the order of $10 - 20$ ns, rate capability better than $10\,kHz/cm^2$, and detectors response not impacted by temperature instabilities, which may be compensated in the calibration procedures. The radiation hardness of the components material is able to sustain doses as reported in Table 8.5. The specific performances of each MPGD tracker subsystem are reported in the following.

CyMBaL. The CyMBaL design aims at providing complete azimuth (φ) coverage. Along the longitudinal direction where the two halves of the system meet, only $\sim$3 cm will not be covered. CyMBaL modules are expected to provide a hit spatial resolution around 150 μm with a time resolution of $10 - 20$ ns.

μRWELL-BOT. The barrel outer tracker will provide hit space point resolution better than 150 μm on average in the eta range of $-1 \leq \eta \leq 1$ and 100 μm in the azimuthal direction and a timing resolution of $\sim$10 ns. The tracker has an acceptance gap of 15% along φ because of space constraints imposed by the limited space in the ePIC detector. The tracker will operate at a nominal efficiency of $\sim$95%. As shown in 8.6 and 8.7, the anticipated particle rate per unit area and per readout channel is very low and will not pose any challenge in term of tracking performance, safety operation and long term stability of the μRWELL-BOT trackers for the lifetime of the ePIC detector.

μRWELL-ECT. The MPGD-ECT disks are designed to provide intrinsic spatial resolution for perpendicular tracks less than $150\mu m$. Technological solutions and data analysis procedures exist to guarantee similar performances also for inclined or curved tracks. The active area of the detector has a material budget less than 1% in units of radiation length (X_0) and will cover all azimuthal angels in the polar region specified in Table 8.9. A time resolution in the $10 - 20$ ns range is achievable using the gas mixtures described in section 8.3.3.2. A single disk efficiency of $\simeq$ 96–97 % is required to provide 92–94 % combined efficiency for two disks in the same region.

Implementation

Services. The MPGD tracking detectors subsystem are divided in different modules, each one requiring: gas supply lines and outlet, front end boards (FEB) connected to 5-line optical fibers (VTRX+) for data transfer to the RDO, low voltage lines (four lines for each FEB: one pair for the 1.8 V and one for the 3.3 V.), high voltage cables, temperature and humidity sensors and cooling in

and out lines. Studies on the type of cooling and possible implementation in a serialize distribution will be done in synergy with the other subsystem of ePIC.

The service requirements for each MPGD tracking subsystem is summarized in Table 8.10.

Subsystem	**CyMBaL**	**μRWELL-BOT**	**μRWELL-ECT**
Number of Modules	32 Micromegas tiles	24 GEM-μRWELL φ-modules	4 GEM-μRWELL disks
Gas supply lines per module	1 in / 1 out	1 in / 1 out	8 in / 8 out
Number of FEB per module	4	14	32
Low voltage lines per module	16	56	128
High voltage lines per module	2	1 (or 4)	16
Cooling lines per module	1 in / 1 out	1 in / 1 out	4 in / 4 out
VTRX+ lines per module	4	14	32

Table 8.10: Services requirements for the three MPGD tracking subsystems.

Subsystem mechanics and integration.

CyMBaL. CyMBaL integration and mechanics rely on the central tracker global support structures. CyMBaL modules will be connected to the support structure.

μRWELL-BOT. μRWELL-BOT integration and mechanics (see **??**) rely on the outer barrel support structures. Support structure connecting the carbon fiber tube and EM-Cal will serve as μRWELL-BOT and HP-DIRC support structure.

μRWELL-ECT. The outer 5 *cm* wide ring of each disk hosts all the services listed in Table 8.10. The FEB are mounted perpendicularly to the disks, occupying the longitudinal region between them.

Because of the divergence of the beam pipes, the disks cannot longitudinally slide along them but need to be shaped in sectors to be mounted around the pipes. Moreover, as the width of the Cu-kapton foil base material for the MPGD detectors restricts one dimension to about 550 mm, an implementation of the endcap trackers would consist of two half-circular disks with "D-shaped" cut-outs for the beam pipe, eventually sub segmented in four quadrants. As sketched in Figure 8.26, the disks integration and mechanics rely on the central tracker global support structures, using the same layout of the Silicon trackers. The MPGD-ECT disk are the most outer elements in the endcap region and the last to be installed in the mounting scheme of the tracking system.

Calibration, alignment and monitoring: The three MPGD subsystems will generally follow similar calibration, alignment and monitoring procedures. There are two main calibration tasks that have been identified. The first is to determine the optimal HV settings for the MPGDs, which will be determined through efficiency scans. These scans will be performed prior to data taking campaigns and after changes in running conditions (e.g. changes in gas composition). The second

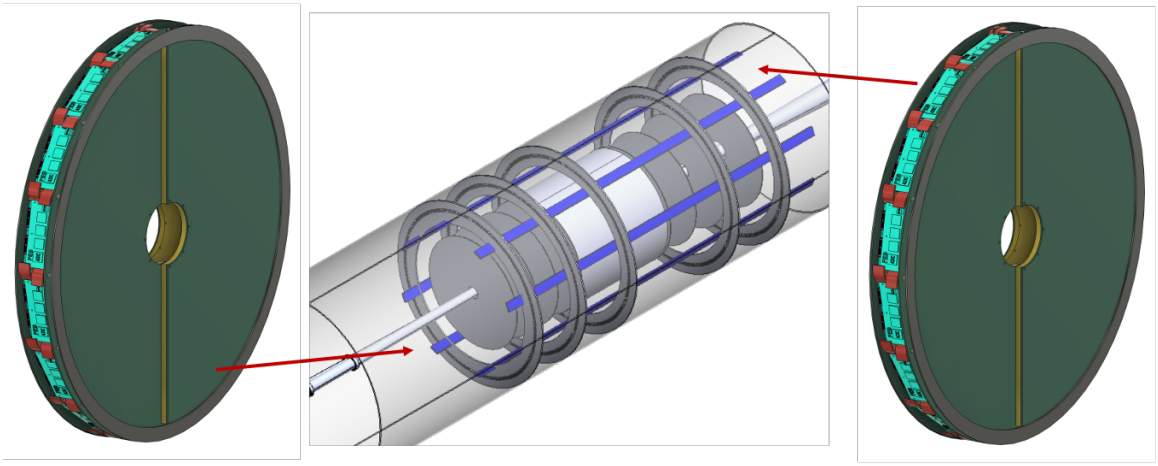

Figure 8.26: Integration of the MPGD-ECT disks in the ePIC detector

calibration task is to determine pedestal values and the common noise to be subtracted from the ADC samples, which will be determined through dedicated calibration runs. To meet the overall ePIC tracking performance precise knowledge of the tracking detector positions will need to be known. The alignment of the MPGD modules will be surveyed and entered into a database before integration. This information will be used to establish a starting point for the software alignment, which will be based on track reconstruction with and without magnetic field applied and will involve all of the ePIC tracking detectors. To assure that the MPGD detectors are performing optimally there are several criteria that will be monitored, which include the gas composition, the environmental conditions near the MPGDs (e.g. temperature, humidity and pressure), currents drawn by the MPGD layers from the power supply and general detector performance. Changes in the environmental conditions can be addressed by adjusting the detector gain via a feedback loop. The currents drawn by each high voltage channel will be read out and logged with a frequency of about 1 Hz. Additionally, we will need to monitor and log the low voltage currents and FEB temperatures. Not only will this allow us to monitor for abnormal values, but also implement automatic safety measures should a particular value fall outside of an acceptable range. Finally, during data taking we will monitor basic detector performance parameters such as hit occupancy maps, 2D efficiency, signal amplitude and timing distributions will be constantly monitored.

Status and remaining design effort.

CyMBaL. The resistive Micromegas technology has been extensively used in nuclear and particle physics experiments. In particular, 1D-readout cylindrical Micromegas tiles are in use at JLab in the Barrel Micromegas Tracker (BMT) of the CLAS12 experiment since 2017 [32], in experimental conditions which are more challenging than those expected at the EIC. The main focus of the ongoing R&D is to upgrade the BMT technology to 2D readout. In order to limit the number or readout channels, the R&D also focus on exploiting the charge sharing thorough the resistive layer and using $\sim$1 mm pitch readout strips. Several combinations of strip readout patterns together with layers of different resistivity have been tested in a beam test in MAMI in 2023. Further studies are ongoing with the cosmic rays test bench in Saclay and an additional beam test at CERN is planned for 2025. The production of cylindrical tiles is being refurbished using the BMT PCBs and a first completed detector is expected to be tested in Fall 2024. In parallel, the design of a CyMBaL

module prototype has begun and its production is expected to be completed by summer 2025.

μRWELL-BOT. The R&D phase for the development of the μRWELL-based trackers for EIC detector was completed in summer 2023 and transitioned into project engineering design (PED) effort to develop the full size thin-gap GEM-μRWELL engineering test article as a beta version of pre-production φ-module of μRWELL-BOT tracker in ePIC detector. The design effort including the CAD drawings of all mechanical parts i.e. frames and support structures as well as the sensitive devices such as the GEM foil, the μRWELL and the U-V strip readout PCB is in advanced stage (see **??**) and expected to be completed by the end of 2024. The fabrication of the full size engineering test article will take place during the first half of 2025. The second half of the year 2025 will be dedicated to a full characterization of the prototype on a cosmic test bench setup and in beam at the CERN NA H4 beam test area including test in its 1.5 T GOLIATH magnet to study the performance of the detector in a magnetic field strength similar to the one expected from the ePIC magnet. The PED effort to develop the μRWELL-BOT module including a detailed review of the design choices and options, the timeline and outlook for the completion of the engineering test article effort in anticipation of the module production phase is described in detail in **??**

μRWELL-ECT. Disk design and modules segmentation is ongoing. The choice of the connectors will have in impact on the final strip pitch and the total number of read-out channels for each disk: usage of Hirose connectors (140 pins for 126 channels) would limit the maximum number of connectors and read-out channels if compared with obsolete Panasonic ones. Segmentation of the disks in four quadrants may avoid the use of a support structure for the GEM foil. A final decision on the final layout will be based on the results of prototype testing. Figure 8.27 shows some design details under investigation.

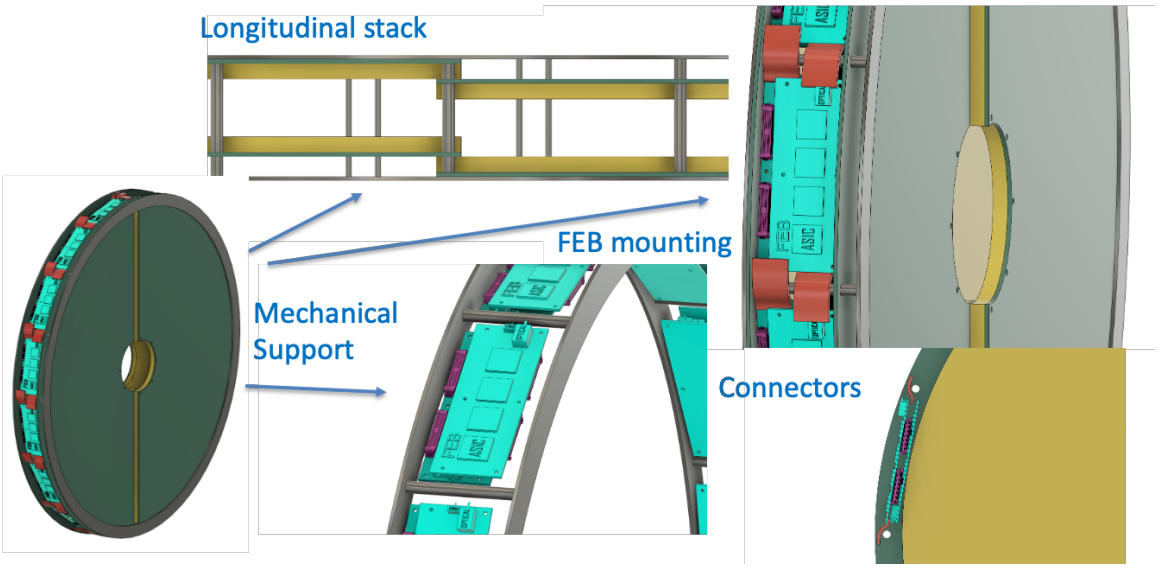

Figure 8.27: Design details of MPGD-ECT disks

Environmental, Safety and Health (ES&H) aspects and Quality Assessment (QA planning). Considering MPGD consortium is composed of international collaboration so each

production site for module assembly will follow guidelines of their local government to be in compliance with ES&H requirements. This include minimizing wastes during assembly procedure and disposal of harmful wastes in safe manner as directed by local government alongwith general electric and mechanical safety. During final integration of the detector subsystem at BNL , scientists and technicians will follow DOE guidelines as directed by BNL ES&H department.

The Quality Assessment protocol will cover the entire production lane of MPGD detectors. The readout PCBs will be assessed for mechanical precision and electrical continuity. The resistive layers will be checked for uniformity, During each step of the assembling, electrical continuity and high voltage capability of the different electrodes will be tested. Once the assembly of the module is finished, the module is checked for gas leakage and HV stability before bringing it outside of the clean rooms. Each finished detector will be then tested with cosmic rays in dedicated test benches. In these tests, the main parameters that will be studied for each module are the noise levels and the number of dead channels, efficiency and effective gain uniformity over the detector active area . A database will be used to log all the information and results for each produced module.

Construction and assembly planning. Each of the MPGD detectors share a similar construction, assembly and QA timeline for having the detectors arrive at BNL in late 2029. This general timeline is shown in Fig. 8.28. More detailed timelines can be found in appendix **??** for μRWELL-BOT

The construction and assembly of the MPGD subsystems will take place at various places. CEA-Saclay will be the main production site for CyMBaL modules, while the readout PCBs will be produced by industry partners. At Saclay, all the remaining parts of the production process will be realized. The resistive layer will be added using serigraphy and the low-tension micromesh will be added using the bulk process [33], which will be performed in the Saclay MPGD Lab. The curving and mechanical integration of the final detector will be done in a dedicated clean room.

CERN will serve as the primary source for μRWELL and GEM foils, as well as the readout PCBs for the μRWELL-BOT and μRWELL-ECT detectors. Other components, such as the frames, will be produced by industry partners. The production of the μRWELL-BOT and μRWELL-ECT modules will be spread out over several productions sites. Jefferson Lab, Florida Institute of Technology and University of Virginia responsible for the μRWELL-BOT modules, while INFN and Temple University will build the μRWELL-ECT modules. A set of technical documents will be developed for each MPGD sub-detector, ensuring that all modules are produced under consistent conditions, using appropriate infrastructure, and following standardized procedures for construction and quality control testing. Each production site will procure and inspect the components separately. It is crucial that all production sites are equipped with suitable clean room infrastructure for the construction and assembly of their respective μRWELL modules, as well as identical instrumentation for a standardized component inspection and module characterization. Each of the institutes will be responsible for the construction and characterization of their respective μRWELL modules (+ spares). The essential equipment needed for each institute are listed in Tab. **??** of appendix **??** for the μRWELL-BOT modules, and Tab. 8.11 for the μRWELL-ECT modules. Each institution will leverage its existing MPGD infrastructure (clean room and detector lab and existing equipment) to minimize instrumentation costs but will upgrade where needed to meet the more demanding requirement of μRWELL technology assembly.

Collaborators and their role, resources and workforce.

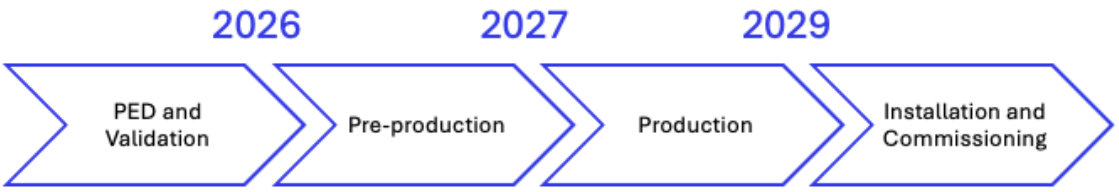

Figure 8.28: General overview ePIC MPGD tracker construction and assembly timeline.

CyMBaL. CyMBaL design, production and tests will be lead by CEA Saclay. The details of the workforce will be added in appendix before the next draft.

μRWELL-BOT. Three institutes — Jefferson Lab, Florida Institute of Technology, and the University of Virginia will participate in the construction, assembly, and characterization of μRWELL-BOT φ-modules to ensure timely mass production. They will collaborate to develop a set of technical documents, ensuring that all modules are produced under consistent conditions, using appropriate infrastructure, and following standardized procedures for construction and quality control testing. All components of a μRWELL-BOT φ-module will be designed by Jefferson Lab, however, each production site will procure and inspect the components separately. It is crucial that all three production sites are equipped with suitable clean room infrastructure for the construction and assembly of μRWELL-BOT φ-modules, as well as identical instrumentation for a standardized component inspection and module characterization.Each of the three institutes will be responsible for the construction and characterization of eight μRWELL-BOT φ-modules (+ spares). The essential equipment needed for each institute are listed in Tab. **??** of appendix **??**. Each institution will leverage on its existing MPGD infrastructure (clean room and detector lab and existing equipment) to minimize instrumentation costs but will upgrade wherever possible to meet the more demanding requirement of μRWELL technology assembly. The personnel effort, expressed as a percentage of research time over the duration of the project, at each institute is provided in tables **??**, **??**, **??** of appendix **??**.

μRWELL-ECT Two institutes — Temple University and INFN Roma Tor Vergata — will participate in the design, production, assembly, and characterization of μRWELL-ECT disks, with the engineering support from Jefferson Lab and the collaboration of INFN LNF MPGD group lead by Gianni Bencivenni, inventor of the μ-RWELL technology. INFN Roma Tor Vergata will focus on the two hadron disks while Temple University will be in charge of the lepton disks. Each of the two institutes will be responsible for the construction and characterization of 4-8 μRWELL-ECT modules, depending on final design. The essential equipment needed for each institute are listed in Tab. 8.11. Wherever possible, existing equipment from the collaborating groups will be utilized to minimize instrumentation costs.

Risks and mitigation strategy. Based on past experiences with MPGD technology following risks and mitigation strategies are identified.

- Delay in production of MPGD foils at CERN is the biggest risk. Considering this it has been decided to place procurement request well in advance to provide enough time to procure

Table 8.11: Main equipment required in the production site and availability at sites

Equipment	**Purpose**	**INFN Roma Tor Vergata**	**Temple** bf University
ISO7 cleanroom	Inspection & Assembly	y	y
Stretcher system	Construction process	y	n
Ultrasonic Cleaner	GEM frame prep	n	y
Fume hood	GEM frame prep	y	y
Microscope	GEM visual inspection	y	y
Giga-Ohm insulation meter	GEM electrical inspection	y	n
HV box	GEM electrical cleaning	y	n
Oven	Construction process	y	n
Electronic instrumentation	Module characterization	y	n
Gas supplies	Module characterization	y	n
Shipping containers	Transport b/w sites	y	n

the MPGD foils. Additionally there is possibility of using additional person power and also prepare additional set up for assembling each module in each assembly sites so that at least 2 modules are assembled at the same time.

- Minor risk of higher humidity content within the MPGD modules is possible however it can be mitigated by flowing gas at higher rate.
- It is possible that the gain provided by any of the MPGD module after installation in experimental hall is lower than what has been estimated during QA. This can be mitigated either by increasing the content of primary ionized gas in gas mixture or increasing the high voltage on MPGD electrodes without affecting detector stability.

Additional Material Add text here.

8.3.4 Particle Identification

In addition to tracking and calorimetry, Particle IDentification (PID) is a crucial component of the ePIC experiment's physics program. The identification of stable particles is achieved either by analyzing the way they interact, or by determining their mass measuring their velocity and momentum simultaneously. The difference in interaction is primarily used for identifying leptons, photons and neutral hadrons, which leave very different signatures in the electromagnetic calorimeters. Charge hadrons cannot be distinguished by their interaction in the calorimeter, but their velocity can be measured using dedicated time-of-flight and Cherenkov detectors. All dedicated ePIC PID detectors discussed in this section measure the velocity, β, of the particle and thus allow to determine its mass. In short, they tie together $\vec{p}$, β, and m. In a second step this PID information can of course also be used in a refit of the particle's trajectory. The knowledge of the particle type and its mass does improve the multiple scattering evaluation and serve as a further constraints.

ePIC has stringent requirements on its PID capabilities as detailed in the Yellow Report [7]. The two-dimensional histogram in Fig. 8.29 illustrates the simulated yield of charged hadrons as a function of momentum and pseudorapidity, η, over the range $-5 < \eta < 5$ at the highest EIC energy

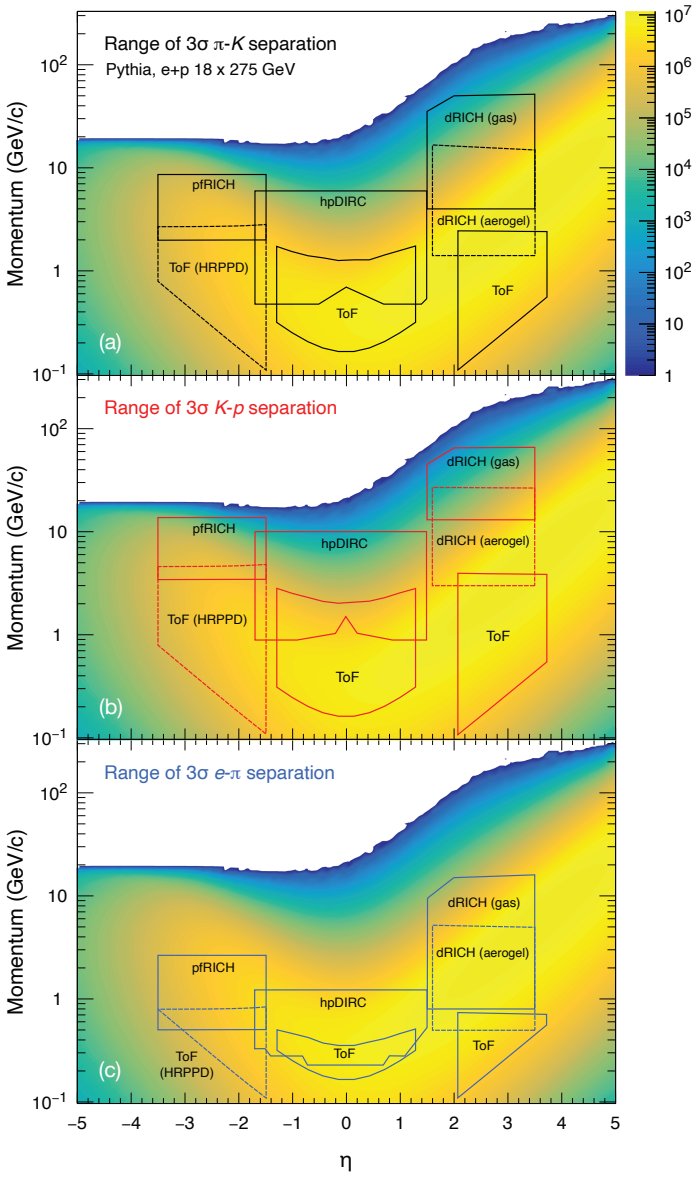

Figure 8.29: The histogram shows the relative yield of charged hadrons from Pythia simulations for 18×275 GeV ep collisions as a function of momenta and pseudorapidity, η. The contours indicate the 3σ separation region of the different ePIC PID subsystems for π/K (a), K/p (b), and e/π (c), respectively.

of $\sqrt{s} = 141$ GeV. Studies of the key semi-inclusive and exclusive processes define the upper limit requirements for 3σ separation of $\pi/K/p$ for different pseudorapidity regions [7]:

- $p \leq 7$ GeV/c for $-3.5 < \eta < -1.0$
- $p \leq 6$ GeV/c for midrapidity $-1.0 < \eta < 1.0$
- $p \leq 50$ GeV/c for the forward region or $1.0 < \eta < 3.5$

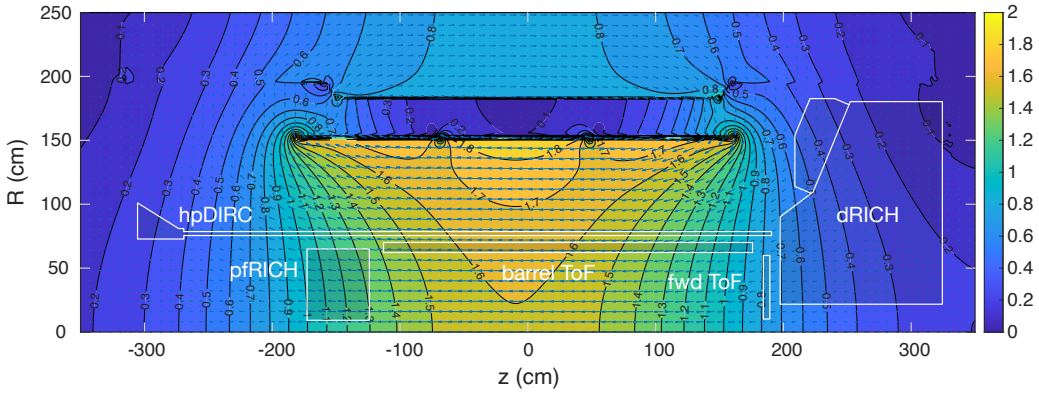

Figure 8.30: EPIC magnetic field map with the PID detector envelopes overlaid. Shown is the 1.7 T setup.

Pure and efficient kaon identification is particularly relevant to semi-inclusive DIS studies, where quark flavor tagging provides critical insights into the transverse momentum distribution and potentially the orbital angular momentum of the strange sea quarks. Kaon identification is also needed to reconstruct charmed hadrons, which are sensitive probes of gluon distributions in protons and nuclei.

Achieving the PID goals of the ePIC experiment requires multiple detection technologies tailored to specific momentum and pseudorapidity ranges. Cherenkov radiation detection is the primary method at higher momenta but is limited in its low-momentum reach. After the Yellow Report, it was realized that improving low-momentum PID is critical for light vector meson and charm meson/baryon reconstruction. To address this, Time-of-Flight (ToF) detectors based on finely pixelated AC-LGAD sensors were added in the barrel (0.5×10 mm pixels) and forward region (0.5×0.5 mm pixels). In addition to PID they will additional hits for tracking. The η-dependence of the momentum spectrum along with space constraints necessitate different technologies in the forward, backward, and barrel regions. The solution chosen by ePIC involves:

- A dual radiator RICH (dRICH) in the forward region utilizing aerogel and gas radiators, a set of focusing mirrors, and instrumented by SiPMs.
- Additional low-momentum PID in the forward region is achieved by an AC-LGAD based ToF that also provides an additional layer of tracking points.
- A large radius high-performance DIRC (hpDIRC) in the barrel, which adds focusing to the original DIRC design.
- The hpDIRC is complemented by an AC-LGAD ToF detector at smaller radius. The AC-LGAD layer provides PID information for low momentum particles that do not reach the hpDIRC or are too slow to leave Cherenkov signal in it.
- A proximity-focusing aerogel RICH (pfRICH) to cover the electron endcap region. This design features minimal material budget and provides additionally excellent ToF through its novel HRPPD photosensors.

Figures 8.29 illustrates the achieved coverage in the η vs. p plane of the various PID subsystems. The contours indicate the 3σ range for e/π, π/K, and K/p-separation, respectively. This unprecedented wide coverage of PID in momentum and over a wide range of η makes ePIC a truly unique

collider detector. As shown, the PID systems provide, in addition to hadron PID, a significant contribution to the e-identification and its purity (e/h). When combined with the EM calorimeters, these subsystems will provide excellent suppression of the low-momentum charged-pion backgrounds, which otherwise limit the ability of the EMCal to measure the scattered electron in kinematic reagion where it does not provide sufficient e/h separation.

ePIC's Cherenkov detectors, dRICH, pfRICH, and hpDIRC, must overcome various challenges related to their respective photosensors. One is the strong magnetic field that rules out the use of conventional photomultipliers. Figure 8.30 shows the realistic ePIC magnetic field for the 1.7 T setup with highlighted Cherenkov PID detectors envelopes. In the region of the hpDIRC detector plane, where the MCP-PMTs will be located, the magnetic field is at a level of 0.2-0.3 T. The field at position of the pfRICH HRPPD sensors is about 1.2 T and the field at the dRICH is 0.3-0.6 T.

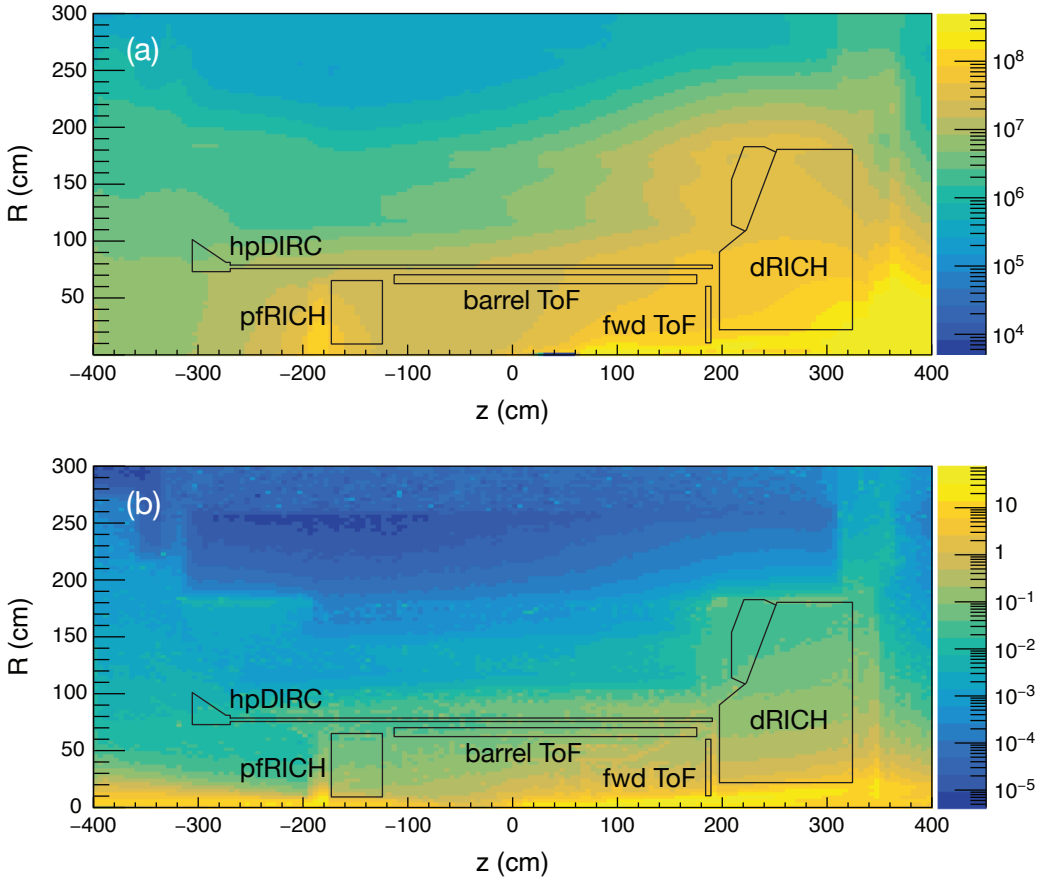

Figure 8.31: (a) Estimates of the 1-MeV neutron equivalent fluence in $\mathrm{cm}^{-2}/\mathrm{fb}^{-1}$ and (b) the sum of electromagnetic and charged-hadron doses in $\mathrm{rads}/\mathrm{fb}^{-1}$ integrated in 1 fb^{-1} equivalent Pythia events for 10×275 GeV ep collisions. The values shown are averaged over the azimuthal angle.

Another significant challenge is the sensors' sensitivity to radiation, particularly in the forward region where the dRICH is located. Figure 8.31 depicts the radiation map for ePIC with the PID subsystem contours. Shown are the estimates of the 1-MeV neutron equivalent fluence and (b) the sum of electromagnetic and charged-hadron dose simulated with 10×275 GeV ep Pythia events.

SiPMs, while ideal in terms of quantum efficiency and wavelength sensitivity, do suffer from increased dark currents due to radiation exposure. However, cooling during operation and thermal annealing have been demonstrated to mitigate this issue [34, 35]. Other photosensors used, show enough radiation hardness (HRPPD) or are situated in less radiation-intensive areas (MCP-PMT).

In the following subsection the different PID subsystems in ePIC are discussed in detail. Subsection 8.3.4.1 discusses the ToF systems, followed by 8.3.4.2 on the pfRICH, **??** describes the hpDIRC and we end with details on the dRICH system in 8.3.4.4.

8.3.4.1 The time-of-flight layers

Requirements and Justifications

Requirements from physics: The ePIC detector is designed to provide charged particle identification for $e^{\pm}$, $\pi^{\pm}$, $K^{\pm}$ and $p(\bar{p})$ over a wide range of three-dimension momentum space (η and p_T). For specific physics justification, readers are referred to the physics sections; instead, specific PID requirements can be found in the overview of the particle identification preceding the present section. With a single-hit timing resolution of 35 ps from the Barrel TOF (BTOF) and 25 ps from the Forward TOF (FTOF), the AC-LGAD TOF detector system can provide particle identification for charged particles up to a few GeV. E.g., π-K separation at the 3σ level for $p_T < 1.2$ GeV/c for $-1.2 < \eta < 1.6$, and $p < 2.5$ GeV/c for $1.9 < \eta < 3.6$, respectively. By combining the PID information for low-momentum particles from the TOF detectors and high-momentum particles from the Cherenkov detectors, ePIC will have excellent PID capability over a wide momentum range in a nearly 4π acceptance, which is crucial to achieving the goals of the EIC physics program. Besides precise timing resolution, AC-LGAD sensors can also provide precise spatial resolution, thus aiding track reconstruction and momentum determination. The timing and spatial resolution requirements and the material budget requirements are evaluated in the ePIC MC simulation framework to find the optimal configuration. The BTOF and FTOF layouts are shown in Fig. 8.32. Table 8.12 summarizes the current specifications of the timing and spatial resolutions, material budgets, spatial coverage, channel counts, and dimensions. Figure 8.33 shows the performance of the TOF detector in the form of $1/\beta$ as a function of particle momentum p for ep DIS events from PYTHIA+GEANT4 simulation. The TOF detector, combined with the other ePIC PID detectors, is crucial to demonstrate that ePIC's PID performance can meet the requirements.

Subsystem	Area (m^2)	dimension (mm^2)	channel count	timing σ_t (ps)	spatial σ_x (μm)	material budget (X/X_0)
Barrel TOF	12	0.5*10	2.4M	35	30 ($r \cdot \phi$)	3%
Forward TOF	1.1	0.5*0.5	3.2M	25	30 (x, y)	5%

Table 8.12: Required performance for physics and proposed configurations for the TOF detector system. The Barrel TOF consists of strip sensors with a pitch of 0.5 mm in the azimuthal direction and a length of 1 cm along the beam direction, while the Forward TOF consists of pixel sensors with a pitch of 0.5 mm.

Requirements from Radiation Hardness: The radiation fluence and dose at ePIC are significantly less than in the LHC experiments. The maximum fluence foreseen for the lifetime of the TOF

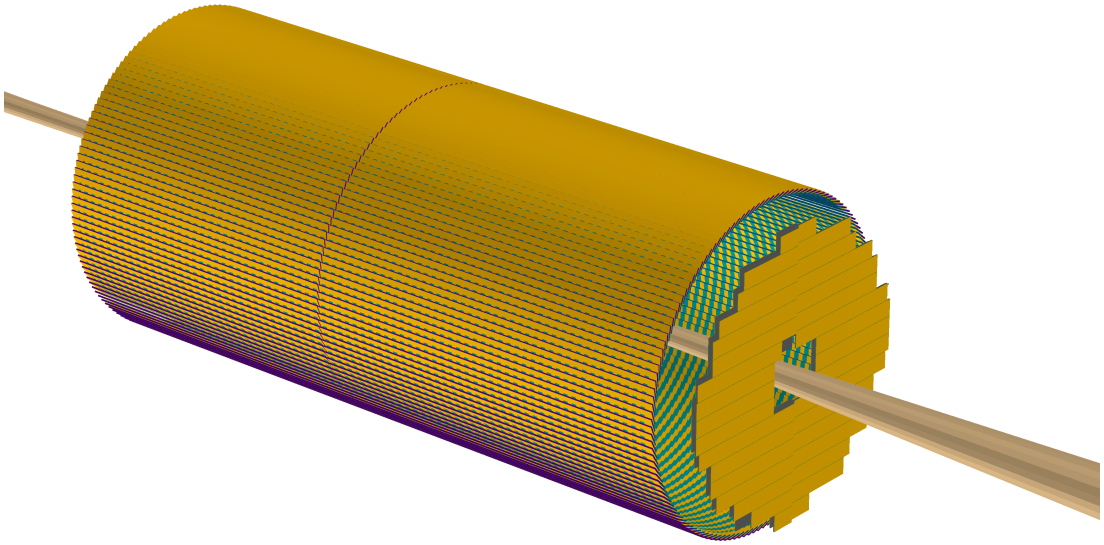

Figure 8.32: Geometries of BTOF with strip sensors and FTOF with pixel sensors.

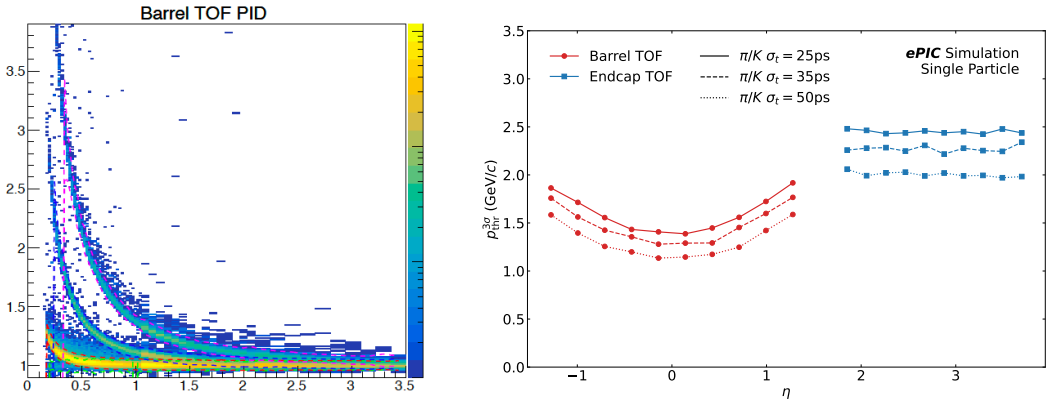

Figure 8.33: BTOF $1/\beta$ as a function of momentum (p) in the simulation performance with PYTHIA DIS events (left). Upper limits on the 3σ particle separation from BTOF and FTOF as a function of pseudorapidity (right).

detectors will be $< 5 \times 10^{12}$ n_{eq}/cm^2, as seen in Fig. 8.34 and Tab. 8.13. Here, the highest fluence between raw and 1 MeV n_{eq}/cm^2 fluence was considered, as the standard NIEL correction is not applicable for some effects in AC-LGAD radiation damage.

Much work has been done to characterize and improve the radiation resistance ofAC-LGAD gain layers to meet the requirements at the LHC [36] (up to 2.5×10^{15} 1MeV n_{eq}/cm^2). Because of the sensitivity of the sensor performance to the value of the N+ sheet resistance (a feature absent from the conventional AC-LGADs used for the LHC), AC-LGADs may be significantly less radiation tolerant than their conventional cousins. Indeed, N-type doping is known to be particularly sensitive

to hadronic irradiation, with N-bulk sensors inverting to P-bulk even before an exposure of 1×10^{14} is accumulated. Furthermore, LHC AC-LGAD detectors are designed to run at -30 ^{o}C to reduce the post-radiation leakage current, while in the ePIC, the sensors will be operated at room or slightly lower temperatures throughout the experiment's lifetime. The leakage current increase due to radiation damage has to be low enough to avoid thermal runaway in the system; that is, temperature increase triggers additional dark current in positive feedback. That is related to the cooling system extracting the heat of the sensor combined with the power dissipation from the readout chip. This is especially important for the far forward and endcap regions where the chips are bump-bonded on top of the sensors, and the thermal connection with the cooling system is sub-optimal.

Therefore, a radiation exposure run was performed before the ePIC AC-LGAD design was finalized. To probe the radiation effect from ionizing and non-ionizing particles, several sensors from HPK and BNL were irradiated at the FNAL ITA facility (400 MeV protons) and the TRIGA reactor in Ljubljana (MeV-scale neutrons). The radiation exposure was done in steps, allowing potential charge-collection pathologies, should they exist, to be mapped out to develop models and corrections. By studying the sensor performance before and after irradiation, the change in N+ resistivity can be characterized, and this particular risk can be addressed. Sensors irradiated with 1 MeV neutrons were received in the Summer of 2024 and subsequently tested. The results are encouraging, as seen in the following sections. Sensors irradiated at the FNAL ITA facility are still cooling down from the activation. They will likely be available for testing in early 2025.

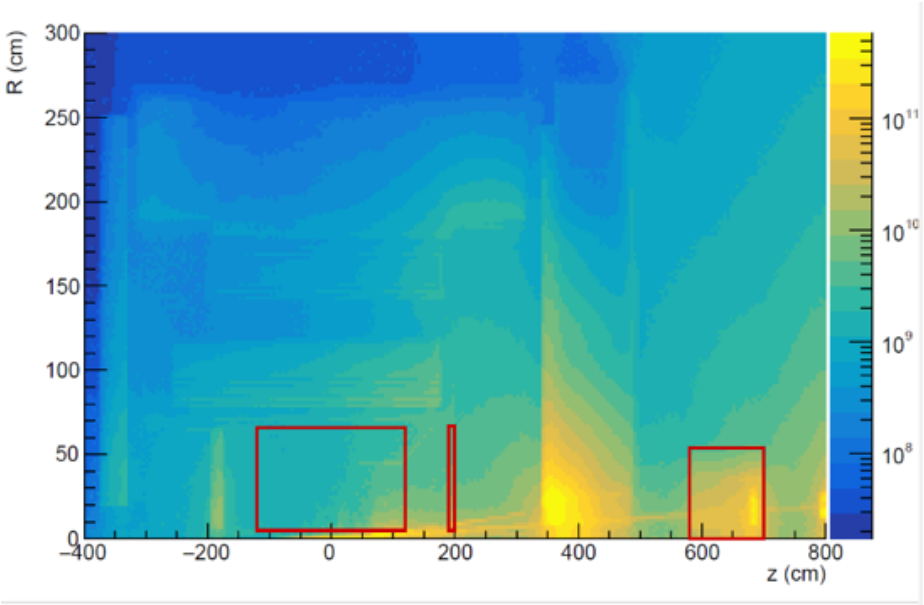

Figure 8.34: Fluence accumulated for 6 months at 100% time, corresponding to one year of data taking, the fluence has to be multiplied by the assumed 10 years of lifetime of the ePIC detector. Red squares highlight the barrel, endcap, and B0 tracker detectors. Simulation from Fluka.

Requirements from Data Rates: As the sensors and ASICs differ between the BTOF and FTOF, the rate requirements are presented separately for both sub-components. On top of that, the phase space coverage is different (mid-rapidity vs forward rapidity), which mandates different particle rates and background calculations.

RAW fluence			
System	Average	Min	Max
Barrel	5.4×10^{10}	3.4×10^{10}	5.9×10^{11}
End-cap	1.3×10^{11}	5.1×10^{10}	1.6×10^{12}
B0 trackers	3.9×10^{11}	3.3×10^{10}	1.8×10^{12}
NEQ fluence			
System	Average	Min	Max
Barrel	3.6×10^{10}	1.1×10^{10}	1.3×10^{12}
End-cap	1.2×10^{11}	3.2×10^{10}	8.4×10^{11}
B0 trackers	4.5×10^{11}	2.7×10^{10}	4.2×10^{12}

Table 8.13: RAW and NEQ fluence per system for the lifetime of the ePIC experiment, assuming 10 years of data taking at 50% time.

BTOF: The BTOF simulations show an average of 5 charged particles per ep collision at the highest center of mass energy. At a 500 kHz collision rate, this amounts to a 2.5 MHz particle rate on the surface of the BTOF barrel. BTOF contains 2.4 million channels, which give an average hit frequency per channel of 1 Hz. Due to charge sharing of the AC-LGAD strips, a particle is expected to generate signals on a maximum of 3 strips/channels of the readout ASIC.

FTOF: The FTOF simulation shows an average of 2 charged particles per ep collision at the highest center of mass energy. At a 500 kHz collision rate, this amounts to a 1 MHz particle rate on the surface of the FTOF disk. Since FTOF is expected to contain 5.8 million channels, the average hit frequency per channel is 0.2 Hz. Due to charge sharing of the AC-LGAD pixels, a particle hit is expected to generate signals on a maximum of 3×3 pixels/channels of the readout ASIC.

Electronics Noise: Noise measurements have consistently shown a rate of 30 Hz per channel. Such a noise rate is achieved with a 5σ cut and is deemed to be even somewhat pessimistic but is the number that is planned to be used during these calculations.

Data Rates: A typical CERN-developed ASIC's zero-suppressed data format will be assumed, which is: 32 bits header, Nx32 bits of channel data (ADC, TDC, ch Id), and 32 bits trailer. Such data formats are used in, e.g., HGCROC, which is a precursor to our expected ASICs.

For BTOF, the expected signal rate of bits per second per ASIC is 1 Hz (particle rate) $\times$ 5 $\times$ 32 (bits for 3 hits) $\times$ 64 (channels) = 10 kbps, while the noise rate is 30 Hz (noise) $\times$ 3 $\times$ 32 (bits for a single hit) $\times$ 64 (channels) = 185 kbps. Summing up these two contributions, the total data rate reaches 195 kbs per ASIC. Since an RDO reads out 128 ASICs per half stave, a rate per RDO (or fiber) of 24 Mbps is expected. For the entire BTOF, which contains 288 half staves, a total rate requirement of 7 Gbps is expected.

For FTOF, the expected signal rate of bits per second per ASIC is 0.2 Hz (particle rate) $\times$ 11 $\times$ 32 (bits for 9 hits) $\times$ 1024 (channels) = 72 kbps, while the noise rate is 30 Hz (noise rate) $\times$ 3 $\times$ 32 (bits for a single hit) $\times$ 1024 (channels) = 3000 kbps. The per-ASIC data rate arrives at 3.1 Mbps by summing up these two contributions. In the worst case of 28 ASICs per RDO (or fiber), it reaches 87 Mbs per fiber link to DAQ. In the total FTOF sub-detector of 212 RDOs, 18 Gbps is reached.

These rates are very small and well within the reach of the ASIC and interconnects, as well as the electronics and DAQ fiber interfaces. The data rates are dominated by the electronics noise, which can be controlled by raising or lowering the ASIC's various ADC or TDC thresholds, thus adjusting the system performance even ASIC-to-ASIC if required.

Subsystem description:

General device description: The BTOF consists of 144 tilted staves, each of which is made of two half staves with a total length of around 270 cm sitting at a radial position of around 65 cm. Strip sensors are mounted on low-mass Kapton flexible printed circuit boards (FPCs) and are wire-bonded with frontend ASICs. The FPCs are glued onto mechanical structures made from low-density carbon fiber (CF) materials, bringing power and input/output signals to the sensors and ASICs. The heat generated by the frontend ASICs is removed by an embedded aluminum cooling tube in the CF structure. The FTOF consists of detector modules made from pixel sensors bump-bonded with frontend ASICs. These detector modules are mounted from both sides onto a thermally conductive supporting disk with embedded liquid cooling lines located around 190 cm away from the center of the experiment. Since the irradiation flux at the EIC is much smaller than that at the LHC, it is assumed that the radiation damage will not be a concern; therefore, the sensors can be operated at room temperature.

Sensors: The sensors identified for the TOF timing layers are AC-coupled Low-Gain Avalanche Diode (AC-LGAD), a relatively new sensor technology that can provide both exceptional position resolution and timing resolution [2,37–39] while maintaining low channel density. In AC-LGADs, the signal produced by charged particles in the sensor active volume is amplified via an internal p+ gain layer near the sensor surface. The signal is induced on a continuous resistive n+ layer on top of the p+ gain layer, which is AC coupled to patterned metal readout electrodes, which are on the sensor surface and separated by a dielectric layer from the n+ layer. The internal signal amplification and thin active volume enable precise timing measurement, while charge sharing among neighboring electrodes can provide precise position measurement. AC-LGADs will be used for TOF PID and tracking in the BTOF, FTOF, and far forward detectors.

The BTOF will employ strip sensors 1 cm long with a pitch of 500 μm and a metal electrode width of 50 μm (a larger pitch up to 1000 μm is also under investigation). The sensor thickness will likely be 50 μm to reduce the input capacitance to the preamplifiers, but 30 μm thick strip sensors are also under investigation. The full sensor size will be 3.2×2 cm^2 with 1 cm segments. The FTOF will use pixel AC-LGADs with a pitch of 500 μm and metal electrode size of 50 μm (a large pitch up to 1000 μm and electrode size of 150 μm are also under investigation). The thickness of the pixel sensors will likely be 20 μm to maximize the time resolution reach, as the input capacitance is not a concern for small pixels. Nevertheless, 30 μm thick pixel sensors are also under investigation. The full-size sensor will be 1.6×1.6 cm^2 with 0.5×0.5 mm^2 pixels. A summary of the geometry is in Tab. 8.14. Studies on smaller-scale devices are presented in [2,37] and in the following sections. Different thicknesses and geometry were investigated in the scope of the eRD112 effort, and the best results obtained are shown in Sec 8.3.4.1. Full-size strip sensor prototypes have been produced for the first time in the most recent HPK fabrication and are received at the time of writing. Procurement of the full-size pixel sensor prototypes is still in progress. A complete evaluation of the full-size prototype sensors is expected by mid-2025.

System	Size	Type	Pitch	Ch/sensor	Thickness
Barrel	3.2x2 cm	Strips	500 μm x 1 cm	128	50 μm
End-cap	1.6x1.6 cm	Pixels	500 μm x 500 μm	1024	20 μm
B0 trackers	1.6x1.6 cm	Pixels	500 μm x 500 μm	1024	20 μm

Table 8.14: Baseline BTOF, FTOF and B0 AC-LGAD geometries.

Frontend Electronics (FEE): The FEE for AC-LGAD-based detectors is focused on the development of two different ASICs and service hybrids with performance and requirements aimed at the barrel (strips) and endcap (pixels), respectively. Different ASICs for the two subsystems are necessary since the geometry, integration method, and requirements differ between BTOF and FTOF. An ASIC featuring a Constant Fraction Discriminator (CFD) chip is being developed at Fermilab for the BTOF, focused on optimizing the analog frontend design to read out AC-LGAD strip sensors with large input capacitance. Two versions of the ASICs, FCFDv0, and FCFDv1, featuring single- and multi-channel preamplifier and CFD, respectively, have been fabricated and tested. The new versions, FCFDv1.1, with further improvement to the frontend design tailored to 1 cm AC-LGAD strip sensors, and FCFDv2, with digital readout, are under development with an expected delivery date in early 2025 and 2026, respectively.

The EICROC project by the French group is instead focused on designing an ASIC for reading finely-pixelated AC-LGAD sensors, optimized for the pixel-based AC-LGADs detectors at ePIC such as B0, OMD, Roman Pots, and FTOF. The first version, EICROC0, is a 4×4 channel ASIC with 0.5×0.5 mm^2 pixel size, featuring components like a trans-impedance preamplifier, 10-bit TDC for timing, 8-bit ADC for amplitude measurement, and an I2C slow control interface. It is designed for low capacitance and sensitivity to low charges (2 fC), operating with 1 mW per channel and targeting 30 ps timing and 30 μm spatial resolution. The prototype is currently under testing.The next version, EICROC1, expected in early 2025, will feature a 32×32 channel configuration to study power distribution; it will be followed by the final 32×32 channel version for full-scale implementation. This will be followed by EICROC2, the final 32×32 channel version, projected for full-scale implementation by the end of 2026. EICROC2 will have a digital backend compatible with the ePIC DAQ system. Tab. 8.15 summarizes the current baseline ASICs for the different timing layers.

System	ASIC	Time Res.	Input C.	Hybridization
Barrel	FCFD	35 ps	10s pF	wire bonds
End-cap	EICROC	20 ps	100s fF	bump bonds
B0 trackers	EICROC	20 ps	100s fF	bump bonds

Table 8.15: Readout chips BTOF, FTOF and B0 AC-LGAD geometries.

The service hybrids (SH) consist of a readout board (RB) and a power board (PB). A schematic design of a service hybrid is shown in Fig. 8.35 for FTOF and serves 3 modules or 12 sensors/ASICs. The readout board aggregates data from multiple ASICs to an lpGBT (from CERN) transceiver chip via e-links. Then, it converts to optical signals via a VTRx+ chip (from CERN) to be transmitted to the backend data acquisition system. The lpGBT and VTRx+ are designed for HL-LHC and have proven to be sufficiently radiation-hard for the EIC environment. The VTRx+ has one uplink up to 10 Gbs (for receiving clock and control signals), and four downlinks (for data transmission), each up to 2.56 Gbs, and it can transmit data up to four lpGBTs. The readout board also hosts interface connectors for the module board (as described later) and the power board, as well as for input LV and HV cables. The power board provides low voltages for ASICs (1.2 V), lpGBT (1.2 V), and VTRx+ (2.5 V and 1.2 V) on the readout board from the DC-DC converters. The CERN bPOL48V module is chosen as the main converter, which takes an input of 15 V and converts it into 1.2 V and 2.5 V. As illustrated in Fig. 8.35, the RB is on top of the PB and sensor module. The PB directly contacts the cooling structure, facilitating efficient cooling of heat dissipating from the DC-DC converters. The SH has three different types with different lengths, serving 3 (12), 6 (24), and 7 (28) modules (sensor/ASICs). This will provide the most efficient coverage

of a circular-shaped disk while minimizing the number of cables and fibers. The example shown in Fig. 8.35 is the shortest version (about 100 mm long) which serves 3 modules. The latest layout design for the FTOF disk is shown in Fig. 8.32 (right), where different colored boxes indicate different types of SHs. Prototyping of the SH is in an advanced stage. A pre-prototype readout board (ppRDO), based on an Xilinx FPGA chip and a commercial SFP+ optical transceiver, has been developed and is under testing. The first prototype RB and PB using the CERN chips will be under development soon and will be based on a similar existing CMS endcap timing layer (ETL) detector design.

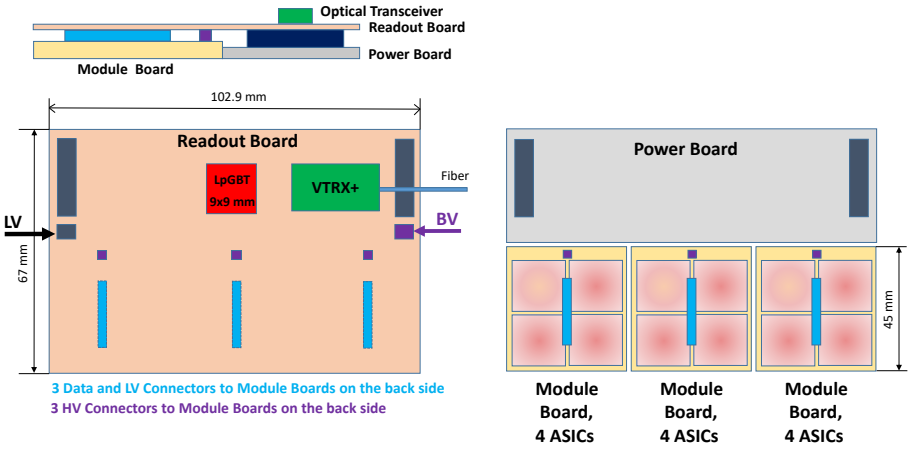

Figure 8.35: A schematic design of service hybrids for FTOF, which serves 3 modules or 12 sensors/ASICs.

Flexible Printed Circuit boards: A Flexible Printed Circuit (FPC) will read data and distribute power to the sensors and ASICs. A material budget of 3% X/X_0 is required in the acceptance region, meaning the FPC material should be as lightweight as possible. Additionally, the FPC must be up to 135 cm in length. To meet these stringent requirements, careful consideration of the FPC material is necessary, as signal loss is expected with such a long FPC, especially if using polyimide, a standard material in FPCs. The sPHENIX experiment encountered a similar challenge with their Inner Tracker (INTT, also a silicon sensor tracker). It successfully addressed the issue using Liquid Crystal Polymer (LCP) instead of polyimide as the dielectric material. This technology will be adopted for the TOF sub-detector as well.

BTOF stave design: Barrel staves are divided into two half-staves, with services and connections coming from the outer side. The half-staves comprise a support structure with an integrated cooling pipe, flexible printed circuit (FPC), sensors, and ASICs. Sensors and ASICs will be mounted on both the top and bottom sides of the half-stave, making it double-sided, with enough overlap to achieve 100% coverage in the stave direction. The lateral overlap and tilting ensure 100% coverage in the direction parallel to the staves. There are 64 sensors and 64-128 ASICs on each side of the half-stave in total. The number of ASICs depends on the final design; each ASIC will serve either one sector for one sensor or one sector for two sensors.

FTOF module design: A schematic design of the module for FTOF is shown in Fig. 8.36. Each module consists of 2×2 AC-LGADs sensors and ASICs glued together. The unit is covered by a module PCB board (MB), which provides LV power (1.2 V) and transmits the data of ASICs via a board-to-board connector to the RB. In addition, the MB also has an HV

connector for the RB to provide the HV to the AC-LGAD sensors. The ASIC readout will be wire-bonded to a metal pad near the edge of the module on the side facing the baseplate and cooling structure, as illustrated in Fig. 8.36 (right). The AC-LGAD sensors and ASICs will be connected via bump bonding. The dimensions shown are preliminary and will be adjusted as the prototyping progresses. In the current design, the AC-LGAD sensors are placed underneath the ASIC. The motivation is to have the sensor as close as possible to the cooling structure to ensure a lower and stable temperature, which has been proven essential for achieving optimal time resolution with a narrow range of temperature gradients. An alternative option would be to swap the ASIC and sensor layers, which has the advantage of more efficiently dissipating the heat primarily generated by the ASIC. A final choice will be made as the prototype progresses, especially after realistic thermal performance studies have been carried out.

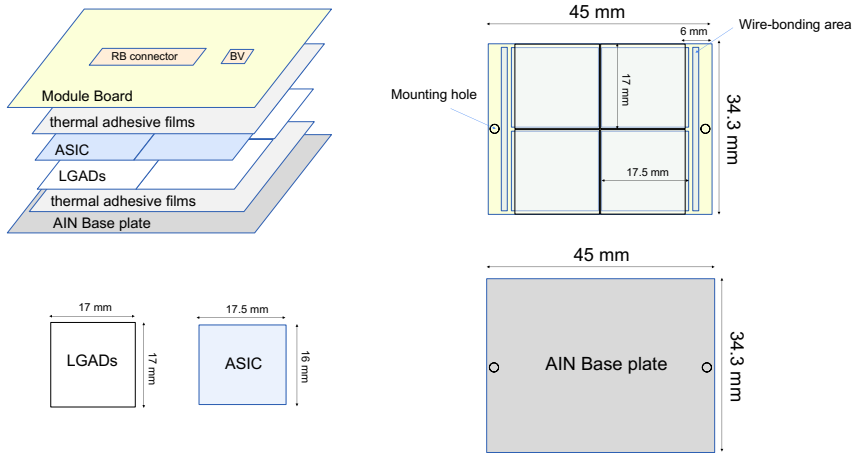

Figure 8.36: A schematic design of the module for FTOF, which consists of 2 × 2 AC-LGAD sensors and ASICs.

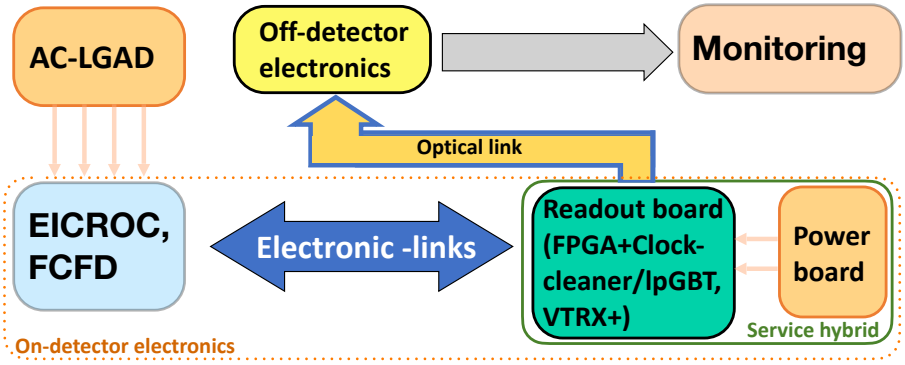

Figure 8.37: Schematic of the AC-LGAD subsystem readout chain. Each component is undergoing design, (pre-)prototyping, testing under various environments, and customization to meet the specific requirements of individual subsystems.

Performance The AC-LGAD systems, including the BTOF, FTOF, and far-forward systems (Roman Pots, OMD, and B0 tracker), share a common readout chain that is currently under development. Performance evaluations are conducted in various laboratory environments as part of ongoing R&D efforts. A schematic of the full readout chain is shown in Fig. 8.37. The effort can be divided into two parts: 1) integrating the sensors with ASIC and 2) developing the readout and power boards.

The Fermilab team has been developing an ASIC targeting the AC-LGAD strip sensors for BTOF. Studies have shown that a Constant Fraction Discriminator (CFD) could provide a better timing resolution for small signal amplitudes from AC-LGAD than a leading-edge discriminator [40]. The first single-channel CFD-based ASIC (FCFDv0) wire-bonded to a DC-LGAD sensor achieved around 35 ps timing precision during test beams, where the dominant contribution is expected from the intrinsic resolution of the AC-LGAD sensor. A 6-channel prototype (FCFDv1) was developed for AC-LGAD sensors, demonstrating around 11 ps jitter in charge injection and around 50 ps time resolution with 0.5 cm AC-LGAD strip sensors during test beams. Ongoing efforts focus on optimizing the frontend design for 1 cm AC-LGAD strip sensors for the BTOF.

Assemblies of 4×4 AC-LGAD pixel sensors with 500×500 μm^2 pixelation and 30 μm thickness, and 4×4 EICROC0 ASICs, were completed by the BNL, IJCLab, OMEGA, and Hiroshima groups on test-boards developed by IJCLab/OMEGA. Testing included scans of the analog and digital components using charge injection and beta particles from a Sr-90 source, resulting in a measured jitter of 8-9 ps for charges above 20 fC. Both wire-bonded and flip-chip assemblies were developed for various characterizations. Additional tests using Transient Current Technique (TCT) laser scans were conducted to map out charge distribution, and various tests are still ongoing.

ORNL is developing flexible Kapton PCBs for TOF applications, where sensors and mock-up ASICs will be glued to the stave and wire-bonded at UCSC and then co-cured onto a composite structure at Purdue for evaluation. Flip-chip options will be available soon, aiming to support low-cost sensor-ASIC hybridization techniques.

In FY24, BNL, LBNL, and Rice developed a prototype board (ppRDO) for precise clock distribution and ASIC integration for AC-LGAD systems. Key milestones, including schematic designs, part orders, PCB layout, and initial testing, were completed ahead of schedule. Firmware development and performance tests on clock cleaning, jitter, and power distribution are ongoing. The collaboration aims to continue in FY25, focusing on developing a readout board (RBv1) and power board (PBv0) for AC-LGAD systems, supporting the TOF applications, and ensuring DAQ compatibility. The ppRDO includes three components: an FPGA, a clock cleaner, and an SFP+ module. Future versions will adopt an lpGBT to replace the FPGA, clock cleaner, and a VTRx+ to replace the SFP+ module, improving performance, radiation hardness, and integration.

Implementation

Services: Electric power is distributed to the detector components via the Power Board (PB), which is part of the Service Hybrid (SH). The SH also includes the functionality of the Readout Board (RDO). In the case of BTOF, one SH supports 64 sensors and 128 ASICs, with SHs placed on both sides of the stave. For FTOF, several types of SHs are used, covering 12, 24, or 28 sets of sensors and ASICs. The SH is distributed on the mechanical and support disk, together with sensor modules.

Low Voltage (LV) and High Voltage (HV) cables are connected to the PB, where multiple DC-DC converters step down or adjust the voltages as needed. HV is applied to groups of multiple sensors

subsystem	item	quantity	diameter (mm)	lengths (m)	description
BTOF	288 FEE LV s.hybrid dist.	24	20	15–25	Rack to Panel, 8AWG(24 AWG sense pairs)
BTOF	FEE LV	72	6.3	8	panel-to detector, Alpha-PN: 2424C SL005
BTOF	FEE HV	18	14	15–25	Rack to Dist. Panel
BTOF	FEE HV	144x2	1.5	8	panel to sensor
BTOF	cooling tubes	144x2	5	> 2.6	supply/return from panel to stave (Aluminum)
BTOF	cooling tubes	4x2			supply/return to panel
FTOF	132FEE/ sHybrids, service feeds	44	10.0	25	LV,rack-to-detector LV-dist,14AWG TC,w/24AWG-sense wires
FTOF	132FEE/ sHybrids, dist.	44	9	3	18 AWG TC, 6 cond.dist. panel-to s.hybrids
FTOF	FEE HV	212	2.42	10	panel to sensor
FTOF	cooling tubes	2x2	5		supply/return from panel to detector (Aluminum)
FTOF	cooling tubes	2			supply/return to panel

Table 8.16: Summary of BTOF and FTOF low voltage and high voltage power supply cables to distribution panels and then to the detector FEE (the exact numbers are being checked at the time of writing).

rather than distributed individually to each sensor. The size of each sensor group is determined by the design of the sensors and the electronics. Table 8.16 summarizes the services (cables and tubes) necessary for the TOF detectors.

A liquid cooling system is employed to control the temperature of the detector. For the BTOF stave, one or two cooling pipes are integrated into the stave sandwich structure, with liquid flowing in one direction along the length of the stave. In FTOF, a winding liquid pipe is integrated into the support sandwich structure. The flow rate and pipe diameter are determined by the amount of heat generated and the detector's performance requirements; thermal finite element analysis determines the design. The pressure must remain below the surrounding air pressure to ensure safe operation. Fig. 8.38 shows a single BTOF stave with cooling pipe (left) and half of the FTOF structure with cooling pipes (right). Possible cooling liquid choices are either water or the NOVEC 7200 engineered fluid [41].

Subsystem mechanics and integration: Both the BTOF and FTOF detector systems are supported by their own support structure, which is integrated and supported by the global support

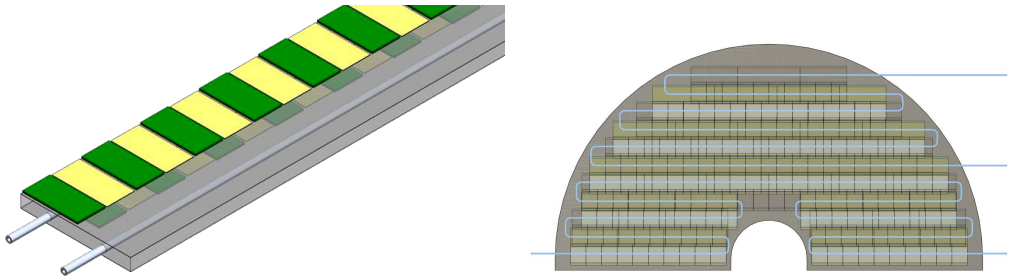

Figure 8.38: schematic drawings of the cooling pipes in one BTOF stave (left) and half of the whole FTOF (right). Each BTOF stave has one input line and a return line, while the FTOF has a total of 4 input lines and 4 return lines.

tube (GST). The BTOF is a barrel geometry time-of-flight detector system located at a radius of 63 cm from $z = -117.5$ cm to $z = +171.5$ cm along the beam direction as shown in Fig. 8.39. The BTOF detector subsystem has a dedicated 7.5 cm space in the radial direction, and similarly, the FTOF subsystem has a dedicated 7.4 cm space along the beam direction. Three engagement rings (each 5 mm width) are made from composite materials and support the BTOF detector - they are supported by the GST. A first concept was developed for a BTOF stave mounting mechanism employing the engagement rings by clips with staves at an 18° angle. Staves are individually removable to ease maintenance. The FTOF detector is designed in two half-disc structures, or dee's, that are kinematically mounted to the GST. Services (readout, power, cooling) of the BTOF are routed to both ends of the barrel, while those of the FTOF are routed to the outer radius, and all are supported by the GST. Table 8.17 lists the positions of the BTOF and FTOF relative to the global ePIC geometry.

subsystem	z_{min} (cm)	z_{max} (cm)	inner radius (cm)	outer radius (cm)	stave angle
Barrel TOF	-117.5	171.5	62	69.5	18^o
Forward TOF	185	192.5	10.5	60	0

Table 8.17: The BTOF is designed with a barrel geometry surrounding the beam pipe and interaction point, while the FTOF is a disk geometry perpendicular to the beam direction on the hadron side (positive z).

Calibration, alignment and monitoring: **Calibration and alignment:** For spacial calibration and alignment, the TOF layer is essentially treated as a layer of the overall tracking system. Therefore, spacial alignment will be carried out as part of the entire tracker. This is typically based on the match between tracks reconstructed in other layers of the tracking, then extrapolated to the TOF and the hits in the TOF. By combining the information from many tracks, high precision can be achieved.

To exploit timing in the reconstruction of the charged tracks, the different TOF channels must be synchronized to a precision of a few picoseconds. The absolute time calibration (or phase shifts relative to the beam clock) is not a particular concern, as all the event reconstruction relies on the relative time between tracks within the same collision event. The time offsets of the TOF channels can be intercalibrated using all the tracks collected online through a fast reconstruction stream. The distribution of the reconstructed time at the vertex of these tracks – assuming they are pions

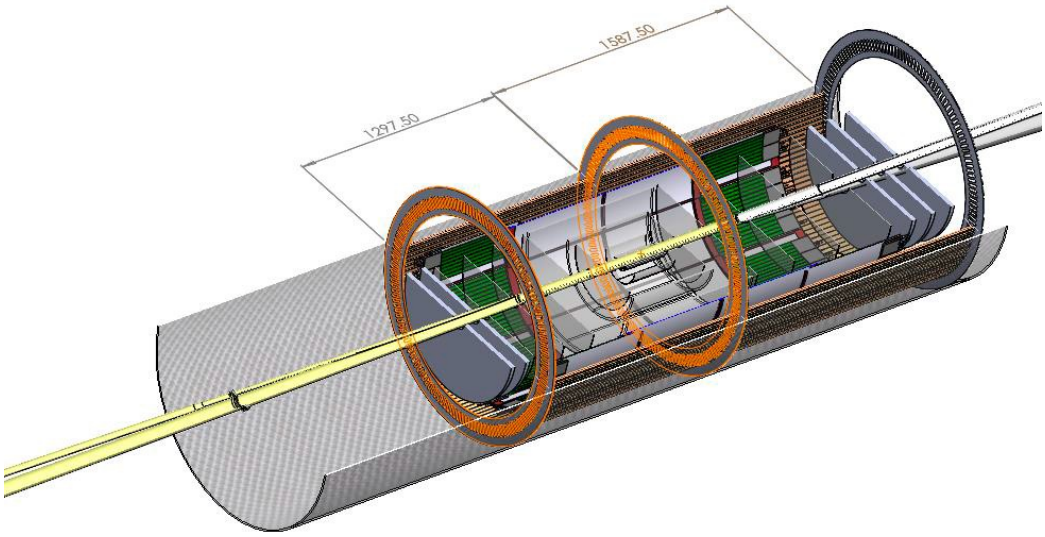

Figure 8.39: BTOF supporting mechanical structure with engagement rings situated and supported by the EPIC global support tube structure (GST). The width of each of the three engagement rings is 5 mm.

– should have an rms spread of approximately 50 ps, including the time spread of the luminous region and detector resolution. The mean time of this distribution over many tracks provides the reference calibration points. Non-pion particles will contribute to the tail of the distribution, which can be cleaned up using an iterative procedure. These calibrations can be made available for the prompt reconstruction of the events and updated frequently.

Monitoring: In the readout scheme of the TOF, a common clock is distributed to the individual channels belonging to the same service hybrid. The time stability of the clock distribution can be monitored with a precision of a few picoseconds every second.

Status and remaining design effort: eRD112 and eRD109

eRD112: Sensor R&D effort A brief summary of eRD112 activities is reported in this section, for a more detailed review of the sensor development effort consult the 2024 eRD112 report document. HPK sensors from the 2023 production have been tested at the Fermilab test beam facility; the results are summarized in Ref. [2]. HPK strip sensors from the latest full-size production were received in the fall of 2024 and are currently being characterized; HPK pixel sensors from the same production will be received by the end of the year. A summary of the best results is shown in Fig. 8.40. The same HPK production was tested in the laboratory with focused laser TCT and showed similar results as reported in Ref. [38]. The presented strip sensors (Fig. 8.40, left) show a constant time resolution of around 35 ps, which is within the requirements for the ePIC TOF (see Table. 8.12). The strip reconstructed position resolution is between 10-20 μm, which is also within the ePIC TOF requirement of 30 μm. The best result for pixel sensors (Fig. 8.40, right) shows a homogeneous time resolution of 20-25 ps, well within the ePIC TOF requirements. The position resolution is 20-70 μm across the device; the charge-sharing mechanism allows for precision recon-

struction between metal electrodes, but the resolution is significantly worse for hits directly on the metal electrodes.

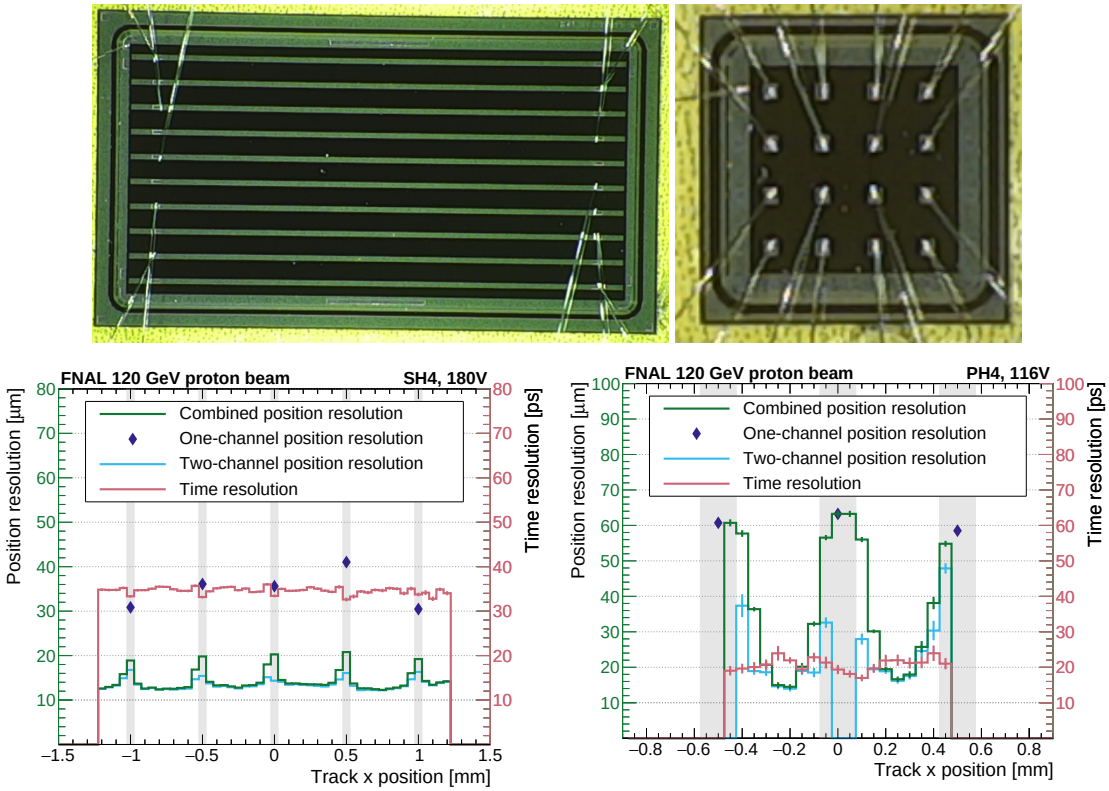

Figure 8.40: Left: Picture and beam test results for HPK strip sensor, 1 cm long, 500 μm pitch, and 50 μm metal electrode width. Right: Picture and beam test results for HPK pixel sensor, 4x4, 500 μm pitch, and 150 μm metal electrode width. Sensors were read out by an FNAL 16ch board, plots from Ref. [2].

The position resolution requirement for the FTOF is 30 μm. Therefore, pixel technology needs to be refined to meet the requirements. The new HPK production (expected by the end of 2024) includes smaller electrode sizes and larger gaps between electrodes, which could provide good reconstruction across the sensor. However, it was observed that a larger gap decreases the total S/N between electrodes, which might degrade the overall performance of the sensors. Results from a BNL production provide a promising alternative to square metal pixels. The S/N is better across the sensor for a cross-shape electrode given the same central metal shape, allowing for better reconstruction using charge sharing. HPK did not include cross-shape geometry in the latest production, but it might be included in the next one. Another producer of cross-shaped AC-LGADs is Fondazione Bruno Kessler (FBK). The FBK prototypes were investigated with a laser TCT, and a similar behavior was observed for cross-shaped devices [39].

The sensors irradiated at the Triga Reactor with 1 MeV neutrons were received in Spring 2024 and characterized both for electrical proprieties (capacitance and current over-voltage) and with the laser TCT station. Gain degradation can be probed with measurements of capacitance over voltage by identifying the gain layer depletion point (V_{GL}). Figure 8.41 (left) shows the change in the gain layer for the irradiated HPK AC-LGADs from several wafers, with different n+, oxide, and active thickness, up to 1×10^{15} Neq. In the region of interest for ePIC ($< 10^{13}$ Neq), the gain layer is

unchanged. The charge-sharing proprieties after irradiation were tested in the laboratory using a focused IR laser. As seen in Fig. 8.41 (right), the spatial response of the sensor is unchanged after irradiation up to 5×10^{14} Neq. The current increase in the irradiated HPK sensors is also negligible until $< 10^{13}$ Neq, as shown in Fig. 8.41 (bottom). The measurements were done at room temperature; therefore, no cooling will be necessary to reduce the dark current, which would increase the sensor power dissipation in the ePIC. In conclusion, no change in the behavior of the sensors is expected during the lifetime of the ePIC detector due to radiation damage.

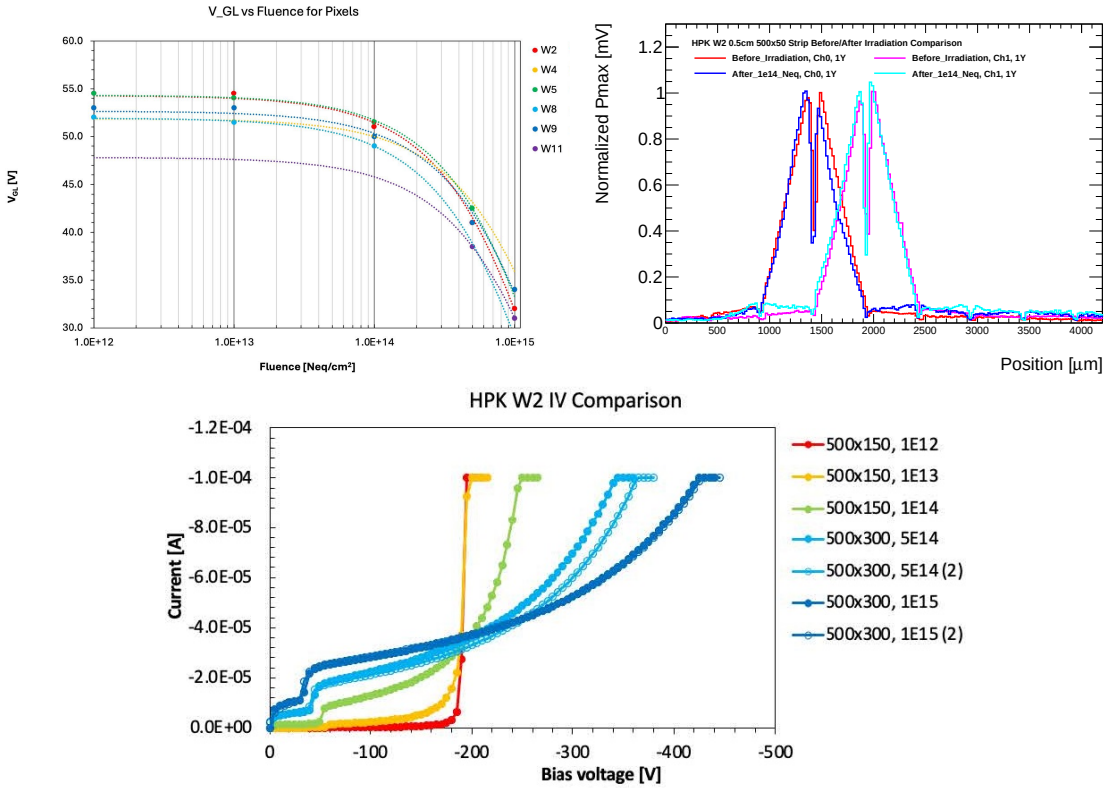

Figure 8.41: Left: Degradation of the gain layer for AC-LGADs of several wafers (with different n+, oxide, and active thickness) from HPK latest sensor production, showing no change in gain layer doping up to 10^{13} Neq, which is an order of magnitude over the ePIC TOF radiation requirement. Sensors were irradiated at the TRIGA reactor (Lubjiana) with 1 MeV neutrons. Right: Normalized comparison of response profile of two nearby strips for two HPK 0.5 cm length, 500 μm pitch, 50 μm strip width: one before irradiation and one after 1×10^{14} Neq. Even if the total signal is degraded, the charge-sharing profile will remain unchanged. Bottom: Current over voltage measurement for irradiated HPK sensors.

eRD109: readout R&D effort A more detailed review of the electronics development effort can be found in the 2024 eRD109 report document. In the following section, a brief summary will be provided.

The Fermilab team has continued the development of the FCFD ASIC prototype and, in FY23, has designed the first multi-channel prototype with this approach, labeled FCFDv1. Numerous technical improvements were implemented based on the experience with FCFDv0, aimed at addressing the stability and performance of the system. The FCFDv1 ASIC was submitted for production in September 2023 and received in January 2024. A specialized readout board was designed to ac-

commodate the FCFDv1 connected to a 0.5 cm HPK AC-LGAD strip sensor. Initial performance measurements were done using internal charge injections performed with an LGAD-like signal. With input capacitance ∼3.5 pF (mimicking AC-strip input capacitance), a jitter of around 11 ps was achieved, as shown in Fig. 8.42 (left). Test beam campaigns were performed in June 2024 to study the performance of the FCFDv1. The newly introduced amplitude readout was found to function well, and results show 100% efficiency when combining neighboring strips. The time resolution measured from the beam test was around 50 ps. A further design improvement is foreseen in FCFDv1.1 to accommodate a 1 cm AC-LGAD strip sensor and improve the timing resolution.

The development of the EICROC0 chip is proceeding as planned. In 2024, an updated PCB ("2024" PCB) was designed by the OMEGA group in France. This updated PCB features improved testability and grounding, as well as the removal of supplementary PLLs. The chip shows good homogeneity between channels and jitter below 35 ps for an injected charge of >4 fC, both for the preamplifier and for the discriminator output, as seen in Fig. 8.42 (left). A large correlated noise still remains with the updated "2024" PCBs (already observed in the "2023" PCB), which leads to large TDC jitters, over 50 ps, when by design, the TDC jitter is expected to be of the order of 10 ps. Nevertheless, the intrinsic performance of the preamplifier, the TDC, and the ADC, taken individually, agrees with the design and within the ePIC detector specifications.

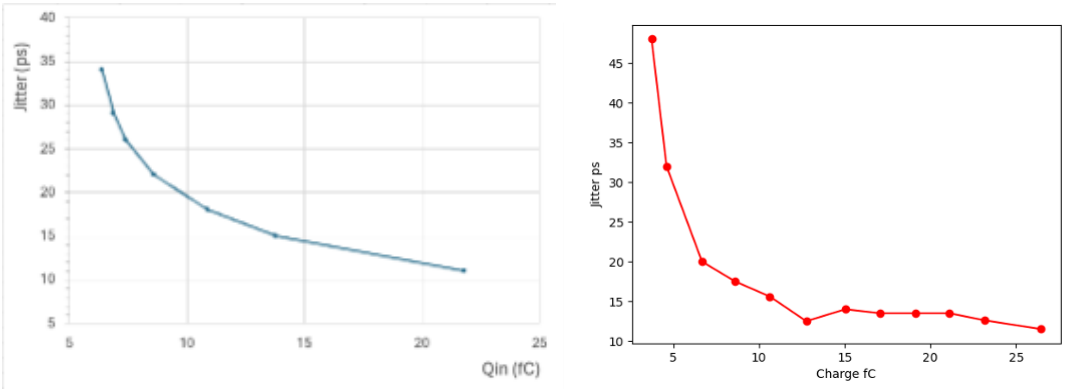

Figure 8.42: Left: FCFD Jitter measurements with 3.5 pF input capacitance and charge injection. Right: EICROC Discriminator jitter versus the injected charge, determined from data on an oscilloscope. Plots from the eRD112 and eRD109 2024 reports.

The development of a pre-prototype readout board (RDO) with high-precision clock distribution has been completed. Figure 8.43 shows a picture of the ppRDO. It is connected with the CMS ETL module board v0, which consists of the full-sized ETROC2 chip for testing purposes. The ppRDO will be evolved into the prototype RB for the FTOF next, which consists of lpGBT and VTRx+ chips instead of FPGA and SFP+. Those efforts will be carried out under engineer designs as described later.

E&D status and outlook: E&D activities

Thermo-Mechanical demonstrator: The fabrication of a demonstrator stave following the double-sided design, as seen in Fig. 8.45, is ongoing. The demonstrator will be a thermal/mechanical demonstrator of the assembly procedure and chip/sensor power dissipation. A mock-up stave, see example in Fig. 8.44, will be co-cured with a readout flex with a cooling pipe in the center. A series of Si heaters and full-size HPK sensors from the latest production will be glued to the stave, then

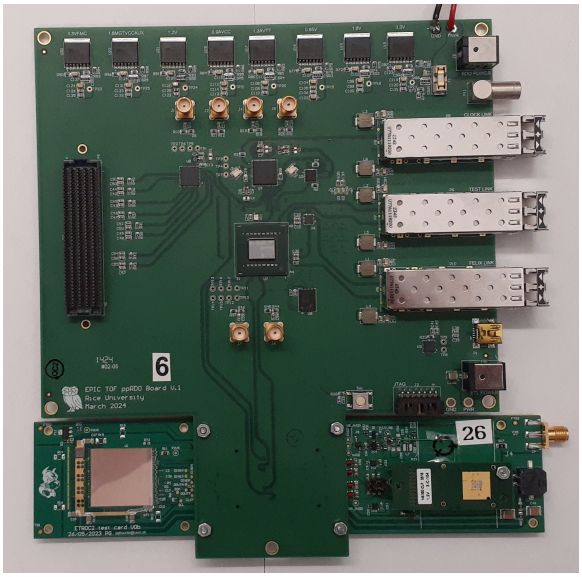

Figure 8.43: Picture of ppRDO connected with CMS ETL module board v0 for testing.

wire-bonded together and to the readout flex. The demonstrator will probe the power dissipation, the temperature gradient across the stave, and the mechanical assembly procedure. Demonstrator results are expected by Q1 2025.

Figure 8.44: Assembled BTOF stave prototype at Purdue.

Environmental, Safety and Health (ES&H) aspects and Quality Assessment (QA planning): We also carried out QA long-term and stress-test reliability studies of AC-LGADs as a stepping-stone towards studies on AC-LGADs. The tests were conducted in an ambient chamber at various environmental conditions. We kept the sensors under bias voltage over periods of weeks, at different temperatures, ranging from -60° to +80° C, and under different humidity conditions. Under these extreme conditions, we carried out I-V scans. At intervals of time between temperature cycles, we also collected signals from β particles from a Sr-90 source at room temperatures to study any deterioration in noise or charge collection. The results were presented at an IEEE conference. While we saw an impact of humidity and temperature on current and breakdown voltage, the sensors recovered their original performance in subsequent cycles. In addition, we also studied the impact of passivation on sensors to minimize charge build-up and early mortality. We confirmed that passivation is critical to minimize the impact of humidity on sensors and prevent early mortality. Such tests were critical after issues had been observed in silicon sensors used for tracking detectors in other experiments, such as those at the HL-LHC. As part of our QA strategy, we also sent BNL-made AC-LGADs to colleagues of UNM to have them irradiated at various fluences in a proton beam at ITA, in a gamma beam at SANDIA and with neutrons at the TRIGA reactor. The first results are shown in the previous sections.

For both sensors and readout chips, it is imperative to evaluate the yield of the test productions to adjust the final production orders. The QA plans to evaluate the yield of the sensor productions are as follows: each produced sensor will be tested in the laboratory in a probe station with simple current over voltage (IV) and capacitance over voltage (CV) tests. AC-LGADs have a single point of DC connection on the n+, so only 1 or 2 needles are necessary for the test; a probe card is not necessary for QA. The IV test will allow us to check the current level and the breakdown voltage for each produced device; the current level has to be $\ll 1\,\mu$A, not to introduce power dissipation issues. The breakdown voltage of all devices has to be within 10% spread to avoid issues in the HV distribution. The CV test will probe the gain layer depletion voltage and demonstrate that all devices have homogeneous gain. For LHC prototypes [36] as a reference, the gain homogeneity was within 1% spread. A selection of devices from the full production will be characterized by mounting them on analog frontend boards with laser TCT and at test beam facilities to ensure the homogeneity of the charge-sharing response.

To evaluate the yield of the chip (EICROC, FCFD) productions, a sample of chips from each batch will be tested and probed for homogeneity in all the channels using a calibration input. All channels have to be within 10% (spread) of homogeneity. A selection of chips will be coupled (wire bonded or bump bonded) with a matching working sensor and mounted on a prototype PCB to probe correct and homogeneous operation in a realistic configuration. Then, the boards will be tested with a laser TCT or at test beam facilities.

Once the state of sensors, readout chips, and flex is advanced, a fully loaded demonstrator stave is envisioned. The mounting procedure will already be tested during the assembly of the thermo-mechanical demonstrator. The full demonstrator will then be tested with radioactive sources in a laboratory or at test beams.

Construction and assembly planning: The BTOF detector has a cylindrical shape consisting of 144 tilted staves. These staves are assembled at designated sites within Class-7 or higher clean rooms before being transported to BNL for final construction. Each stave is approximately 270 cm long and is divided into two half-staves of 135 cm each. A half-stave includes a support structure with an integrated cooling pipe, a flexible printed circuit (FPC), sensors, and ASICs. The sensors and ASICs are mounted on both sides of the half-stave, with 64 sensors and 128 ASICs on each side. Wire bonding is used to connect the ASICs to the sensors and electronics. Only components that pass various quality inspections — such as visual checks, metrology, and electrical tests — proceed to the assembly stage. During the half-stave assembly, one FPC is glued onto the support structure; see Fig. 8.45(a). To ensure precise alignment, a specialized tool is used featuring pins and holes that guide the placement of the FPC and the correct application of glue. After assembly, the staves undergo both electrical and mechanical tests. Subsequently, sensors and ASICs are installed on the FPC surface using alignment tools similar to those used during the FPC mounting process, as shown in Fig. 8.45(b). These tools help position the components and apply adhesive. Electrical connections are verified, and in Fig. 8.45(c), the ASICs are bonded to the sensors using wire bonding, followed by wire encapsulation. Two support structures with wire-bonded sensors, ASIC, and FPC (front and back side), are attached to each other as in Fig. 8.45(d). The final round of testing is conducted after completing the installation on both sides (Fig. 8.45(e)). Fully tested staves are then shipped to BNL for integration into the global support structure of the ePIC detector, which contains 144 slots for precise alignment of the staves within the global coordinate system.

The FTOF is constructed in a double-sided disk shape by populating modules with dimensions indicated in Fig. 8.36. Each module includes 4 sensors, 4 ASICs, a module board, and an aluminum-nitride (AlN) base plate, which acts as a thermal conduit to the cooling system. The modules are connected to a service hybrid (SH) that consists of a power board (PB) and a readout board (RB). As

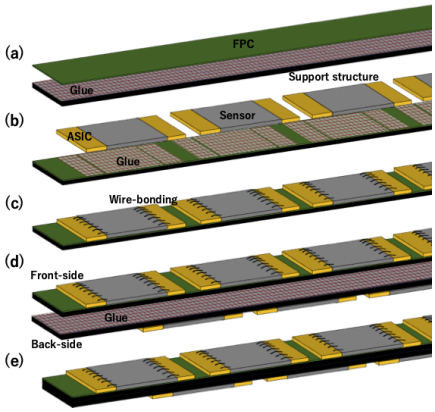

Figure 8.45: Assembly process of BTOF stave. The drawing is not to scale.

mentioned earlier, three different configurations of SH are used, depending on the number of modules being supported: 3 modules (RB3), 6 modules (RB6), and 7 modules (RB7). There are about 780 modules in total to patch the disk shape. Sensor and ASIC are connected by bump-bonding. The module board is connected to the ASICs through wire bonding and has a connector to interface with the RDO. Assembly of the modules occurs in Class-7 (or higher) clean rooms, while the PB and RB can be assembled under standard conditions. The assembly of each module begins with the connection of one sensor to one ASIC using bump-bonding technology (Fig. 8.46(a)). Automated machines are used for sensor and ASIC placement, alignment, and bonding. After bonding, the electrical performance of the sensor-ASIC hybrids is tested. Following this, 4 sensor-ASIC hybrids are mounted on the module board, using a dedicated tool to ensure precise alignment (Fig. 8.46(b)). Thermal adhesive films are placed between the hybrids and the module board to ensure efficient heat dissipation. Once mounted, the ASICs are wire-bonded to the module board, and the wires are encapsulated for protection. After the bonding process, the AlN base plate is attached to the opposite side of the hybrid (Fig. 8.46(b)), with thermal adhesive films again used between them to aid heat transfer. The thermal adhesive films are also put between them. The modules undergo thorough quality checks before moving on to SH assembly. The RBs and PBs are manufactured using standard circuit board techniques and come with dedicated connectors for integration. SHs are available in configurations supporting 3, 6, or 7 modules, with the RB and PB connected via dedicated interfaces (Fig. 8.46(c)). Once assembled (Fig. 8.46(d)), the modules and SHs are tested for connectivity and performance. After passing all tests, the modules and SHs are shipped to BNL, where they are attached to the disk-shaped support structure. Specialized tools ensure the accurate placement of the components. Modules and SHs are mounted on both sides of the support structure to eliminate acceptance gaps between sensors. A fixture maintains the required clearance between components when installing the modules and SHs on the opposite side. Finally, the fully assembled disk is installed into the ePIC detector.

Collaborators and their role, resources, and workforce: Table 8.47 shows the participating institutes with their roles, the contact person, and potential commitments. This shows substantial participation by the international collaborators outside of the U.S.. We also anticipate substantial funding support from international collaborators for the BTOF detector.

Risks and mitigation strategy: Our R&D results (eRD112) show that the performance of the tested sensors would meet physics requirements for the TOF subsystems. Those studies were done

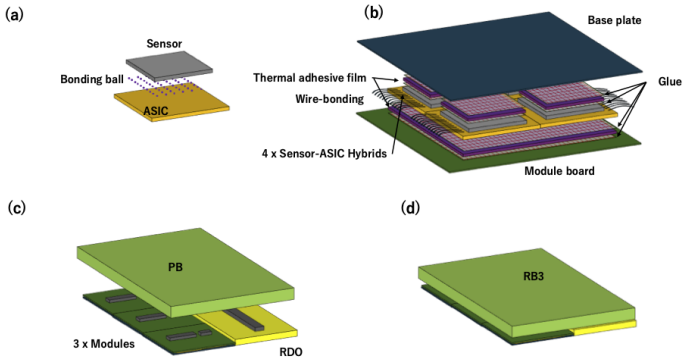

Figure 8.46: Assembly process of FTOF modules. RB3 type is shown as an example. The drawing is not to scale.

with smaller chip dimensions. The production for the R&D study with a full-size sensor chip is underway. There is a potential risk that the performance of sensors with larger sizes would be worse. The mitigation is to reduce the sensor size.

The HPK sensors for R&D (eRD112) are of a small quantity. Mass production would be a risk in terms of chip yield and schedule delay. The mitigation is to explore other possible production sites (Taiwan/FBK).

FCFD ASIC design (eRD109) currently has analog signal readout only. The design and test of the digitization component is underway and is expected to have a first pass early next year. Additional resources may be needed to mitigate potential schedule delays and cost increases. In addition to the baseline chips, EICROC and FCFD, third-party ASICs are also taken into consideration: FAST (INFN Torino), AS-ROC (Anadyne Inc. and UCSC), and HPSoC (Nalu and UCSC). The most advanced one is the High-Performance System-on-Chip (HPSoC) ASIC, designed by Nalu Scientific [42], in close collaboration with SCIPP, and fabricated in 65 nm CMOS by TSMC. HPSoC includes a fast analog frontend and, unique to all other current AC-LGAD readout ASICs, will capture the full signal waveform at a sampling rate of 10-20 GS/s. Together, these are expected to address the EIC goal of 25 ps timing resolution or better per measured space point. V2b of the chip has a working digital backend and is currently under review.

We have performed heat conductivity and cooling simulations, as well as tests on the cooling capacity (currently with PED funding). Those show promising outcomes for meeting the cooling needs. The potential risk is that the cooling capacity is insufficient to maintain a stable and relatively uniform temperature. A possible mitigation strategy is to use different materials for cooling pipes with better heat conductivity and higher flow rates.

Schedule The schedules for BTOF and FTOF projects have been incorporated into the overall EIC project schedule. A major inter-dependence of the schedule is the sensor and ASIC designs. In the preproduction phase, 10% will be made in six months, during which quality and procedures will be confirmed. Then, during the production phase, the remaining 90% will be produced in two years.

Additional Material

Institute	Contact Person	NOW (TDR->Project)
Brookhaven National Laboratory	Prithwish Tribedy tribady@bnl.gov	DAQ readout chain readout, sensor-ASIC integration, sensor with FF AC-LGAD; EICROC testing
Fermi National Accelerator	Artur Apresyan Artur.Apresyan@cern.ch	FCFD ASIC (no ePIC)
OMEGA	Dominique Marchand dominique.marchand@ijclab.in2p3.fr	EICROC
Los Alamos National Laboratory	Xuan Li xuanli@lanl.gov	
Rice University	Wei Li wl33@rice.edu	B/FTOF FEE?, Backend electronics (postdoc) , simulation and reconstruction
Oak Ridge National Laboratory	Oskar Hartbirch hartbricho@ornl.gov	sensor-ASIC integration, frontend electronics (waffle probing), module assembly
Ohio State University	Daniel Brandenburg Brandenburg.89@osu.edu	BTOF/FTOF: module assembly; backend electronics
Purdue University	Andreas Jung anjung@purdue.edu	Module assembly
Univ. of California, Santa Cruz	Simone Mazza simazza@ucsc.edu	Sensor, sensor-ASIC integration, module assembly (no in-kind)
University of Illinois at Chicago	Olga Evdokimov mailto:evdolga@uic.edu	
Hiroshima University	Kenta Shigaki shigaki@hiroshima-u.ac.jp	FTOF EICROC testing, sensor testing (30%), simulation
RIKEN	Yuji Goto. goto@bnl.gov	BTOF: module assembly
Shinshu University	Kentaro Kawaide kawade@shinshu-u.ac.jp	Sensor testing, simulations
University of Tokyo	Taku Gunji gunji@cns.s.u-tokyo.ac.jp	DAQ streaming readout
South China Normal University	Shuai Yang syang@scnu.edu.cn	
Univ of Sci. and Tech. of China	Yanwen Liu	
Indian Institute of Tech., Mandi	Prabhakar Palni prabhakar.palni@unigoa.ac.in	FTOF Module Assembly/QA, sensor testing
National Inst. of Sci. Edu. Res.	Ganesh Tambave ganesh.tambave@niser.ac.in	Module Assembly
National Central University		FF AC-LGAD (sensor QA)
National Cheng-Kung University	Yi Yang yiyang@ncku.edu.tw	Mechanics and cooling systems
National Taiwan University	Rong-Shyan Lu rslu@phys.ntu.edu.tw	FF AC-LGAD; module assembly
Univ. Técnica Federico Santa María		Simulations
LBNL	Zhenyu Ye yezhenyu2003@gmail.com	BTOF ASIC testing; SH
Kent State University	Zhangbu Xu zxu22@kent.edu	Simulation, readout test, machine shop (in-kind)
Nara	Takashi Hachiya hachiya@cc.nara-wu.ac.jp	BTOF module assembly/validation/FPCB

Figure 8.47: Collaboration institutions and their potential responsibilities.

Low-voltage and High-Voltage power supplies Each service hybrid module will be powered by a radiation and magnetic field tolerant DC-DC regulation board as part of the hybrid module and mounted to the cooling plate. The minimum efficiency of the regulator board should be $\geq$ 70.0%. Input power to the DC-DC board is delivered from rack-mounted Wiener PL500 series power supplies to source 15 V DC $\pm$ 3.0%. The current demand from the rack-mounted PSU should not exceed 80.0% of the manufacturer's rating. Each channel of the PSU will have over-current fuse protection. The power-cable size is selected to operate at 125% of the total continuous maximum load. The estimated power consumption and LV cable feed size for each detector is designated as follows: Forward TOF system LV power: 6.0 kW (400 A). LV power feeds from the platform: Custom two-conductor 12 AWG tray-rated cabling with embedded low-voltage twisted-pair sense wires.

Barrel TOF system LV power: 15.0 kW (1,000 A). LV power feeds from the platform: Custom two-conductor 8 AWG or 10 AWG (depending on LV segmentation) tray-rated cabling with embedded low-voltage twisted-pair sense wires. Custom-enclosed LV power distribution PCBs will be installed at the detector side and outside the inner detector volume. A disconnect is required for each LV output port of the distribution box. Power distribution to the service hybrids will be config-

ured not to exceed 10.0% channel segmentation from the rack-mount power control. Multi-channel ISEG ESH series power modules will provide up to negative 500 VDC bias at a current of 10 mA per channel. Multiconductor cables terminated with REDEL connectors or individual coax cables terminated with SHV connectors will feed an enclosed HV distribution box. The HV bias cabling to the detector hybrids will be carried over a multi-drop cable configuration to service the sensor hybrids in small groups.

Schedule Although there are still many uncertain elements at this stage, the latest schedule is shown in this section. The overall progress of development depends heavily on the advancement of the sensor. For instance, since the ASIC blueprint is based on the sensor's features, the ASIC design cannot be completed before the sensor development is finalized. This was the first principle we used to set up the schedule.

At least three sensor prototypes will be produced. The first prototype, the full-size sensor prototype, has already been manufactured by HPK. Based on the characteristics of this sensor, the FCFDv2 and EICROC2 ASICs will be developed. Based on our experience, we can also expect that the time required to fabricate the sensor and the ASIC will be 4 months from submitting the design to delivery. It could be up to 6 months for the ASICs. Additionally, prototypes of the Service Hybrid (SH), electronics (FPC for BTOF and module board for FTOF), and support structure will be created based on this sensor and ASIC.

Next, the design for the second full-size sensor prototype will incorporate improvements identified from the first prototype. The design will start 2 months after starting the first sensor validation. The design of the next ASICs (FCFDv3 and EICROC2_v1) will begin as soon as the sensor design is finalized. The SH, FPC, and stave support structure will also be developed in conjunction with this sensor and ASIC. Some sensor characteristics can be estimated based on accumulated knowledge, which might allow certain designs to be completed simultaneously.

The second full-size sensor prototype will be the last, but we will make another prototype as a backup and make final adjustments for mass production. Depending on the budget, additional sensor and ASIC prototypes may be ordered.

During the development phase, assembly was carried out as soon as the other components became available. However, there will be a time lag between the arrival of components and the start of assembly in the preproduction and production phases. This is because additional time is required for quality assurance (QA) and quality control (QC) procedures before the components can be shipped to the dedicated assembly sites. As a result, the preproduction and production phases will begin two months later than other phases.

particle identification Figure 8.48 shows an example of a single-particle response simulation of $1/\beta$ as a function of particle momentum for BTOF and FTOF performance.

8.3.4.2 The proximity focusing RICH

Requirements

Requirements from physics: Particle identification capabilities in the electron going endcap region of the ePIC detector ($-3.5 \leq \eta \leq -1.5$) will be provided by a proximity focusing ring

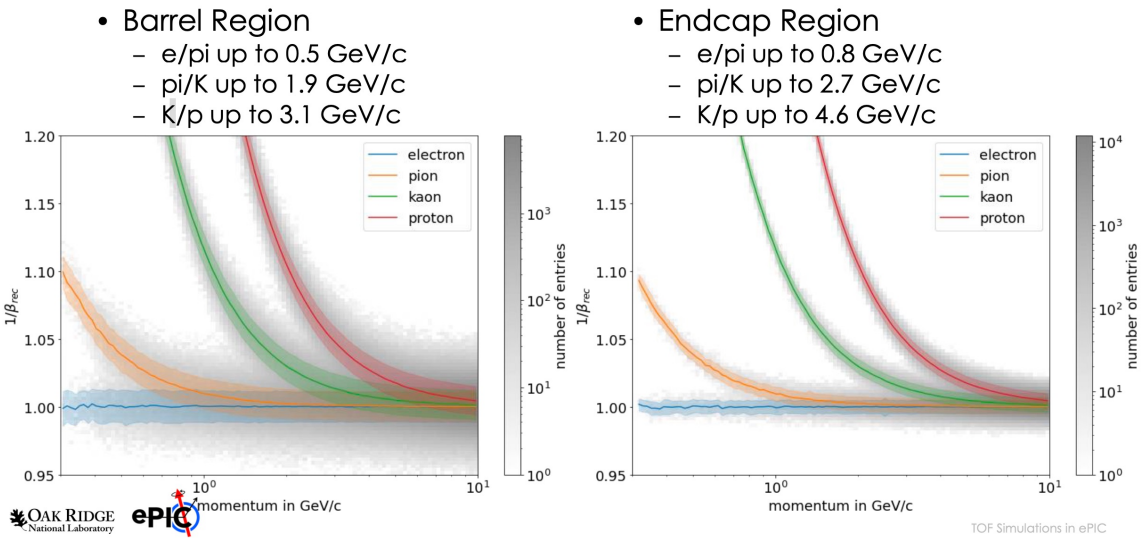

Figure 8.48: simulation of $1/\beta$ as a function of particle momentum for BTOF and FTOF performance.

imaging Cherenkov detector (pfRICH). Driven primarily by the requirements from SIDIS measurements, the pfRICH will need to provide 3σ separation or better between pions, kaons, and protons for momenta $p < 7$ GeV/c. The pfRICH will also play a critical role in electron-hadron separation for momenta below roughly 3 GeV, where hadron distributions are at their maximum and the electron ID capabilities of the backward EM calorimeter will not be sufficient to achieve the overall required electron purity. In addition to electron and hadron identification, the excellent timing resolution of the pfRICH photosensors, High Rate Picosecond Photon Detectors (HRPPDs), will allow the pfRICH to provide a high quality t_0 reference for the barrel and forward endcap time-of-flight detectors.

Requirements from Radiation Hardness: The beam induced charged particle background impacts the pfRICH mainly via excess photons produced in the aerogel and fused silica windows of the HRPPD photo sensors. A fraction of the incoming photons are converted to photo-electrons (PE) by the photocathode according to its quantum efficiency. The amplification of PEs produces ions which drift towards the photocathode. These ions can react with or even sputter the photocathode material which leads to degradation of its quantum efficiency. HRPPD gains can also be affected by the desorption of ions from surfaces.

To estimate the flux of ion back flow during the expected life span of the detector, a simulation study was performed, combining the rates from DIS events and beam gas interactions. A mass-dependent minimum energy cutoff was applied so that only particles that would produce Cherenkov radiation in the aerogel plane or HRPPD window would be considered. Each particle producing Cherenkov photons in the aerogel (n = 1.04) was assumed to produce ≈ 10 photons, while ≈ 100 photons were assumed from the HRPPD window (n = 1.4) after factoring in the QE.

Convoluting an expected operating gain of 10^5 with a running period of 26 weeks/year and a luminosity of 10^{34} cm^{-2}s^{-1} yields a yearly estimate for accumulated charge of up to 0.011 C/cm^2 on the photocathodes of sensors closest to the beam line. For a running period of 10 years, this will result in 0.11 C/cm^2, or 1.1 C/cm^2 if one assume a higher gain of 10^6 to compensate the aging over

time. It should be noted that the estimate of particle flux is based on realistic simulations for beam gas and DIS events. Furthermore, the rates and running period are overestimated which gives a safety factor of around 2 from the most plausible scenario. Studies to evaluate the degradation of QE with the accumulated charge are underway.

Requirements from Data Rates: Previous data rate estimates need to be compared to rate studies above. Will add text when complete.

Justification

Device concept and technological choice: The operation of a generic proximity focusing RICH detector is based on a very simple set of principles. A charged particle passing through a thin layer of radiator (often aerogel with an appropriate refractive index) with a velocity higher than the speed of light in that medium emits Cherenkov light (photons) at an angle which is solely determined by the particle mass, momentum, and refractive index of the radiator. The 3D momentum of the particle is typically provided by a tracking system. If the average refractive index of the radiator is also known, measurements of the Cherenkov light emission angle can determine the particle mass, thus allowing identification of different particle species, e.g. distinguishing electrons, pions, kaons, and protons.

The ePIC pfRICH was designed as a conceptually simple detector, based on proven principles, providing a high degree of performance that is practically uniform over the whole available angular acceptance in η and ϕ. In order to reach the performance requirement of 3σ separation or better of $\pi/K/p$ for momenta $p < 7$ GeV/c, the pfRICH design was optimized in the following ways: (1) the proximity gap length was maximized as much as possible within the volume available in ePIC; (2) the radiator thickness was taken to be small enough to reduce the contribution to the single photon angular resolution to below $\sim$5 mrad, yet produce enough photons per track to robustly reconstruct the Cherenkov angle; (3) the HRPPD pixellation was chosen such that it contributes at most $\sim$2 mrad to the angular resolution; and (4) the acrylic filter cuts off all UV light produced in the aerogel below $\sim$ 300 nm, where the $dn/d\lambda$ dependency is strongest. In addition to satisfying the PID requirements in the backward direction, the small material budget of the pfRICH design minimizes the impact on the the resolution of the endcap electromagnetic calorimeter which sits directly downstream.

Subsystem description:

General device description: The layout of the proposed ePIC pfRICH detector is shown in Fig. 8.49. It consists of a 1.3 m diameter and $\sim$49 cm long cylindrical vessel with the outer and inner walls made from a lightweight honeycomb carbon fiber sandwich and front and rear plates made of a carbon fiber reinforced plastic (CFRP). The vessel sits 123.6 cm from the nominal interaction point. Forty-two 2.5 cm thick aerogel tiles of a trapezoidal shape are installed in individual opaque compartments in a container mounted on the upstream side of the vessel. A thin acrylic filter is installed immediately after the aerogel container. The vessel is continually flushed with dry purified nitrogen. Sixty eight HRPPD photosensors are installed in individual slots in the rear CFRP mounting plate with their fused silica windows facing the aerogel. Inner and outer conical mirrors cover the cylindrical sides of the vessel in order to increase the η acceptance of the Cherenkov photons produced in the aerogel radiator.

Readout boards equipped with four 256-channel EICROC ASICs are mounted on the rear ceramic anode plates of each of the HRPPDs.

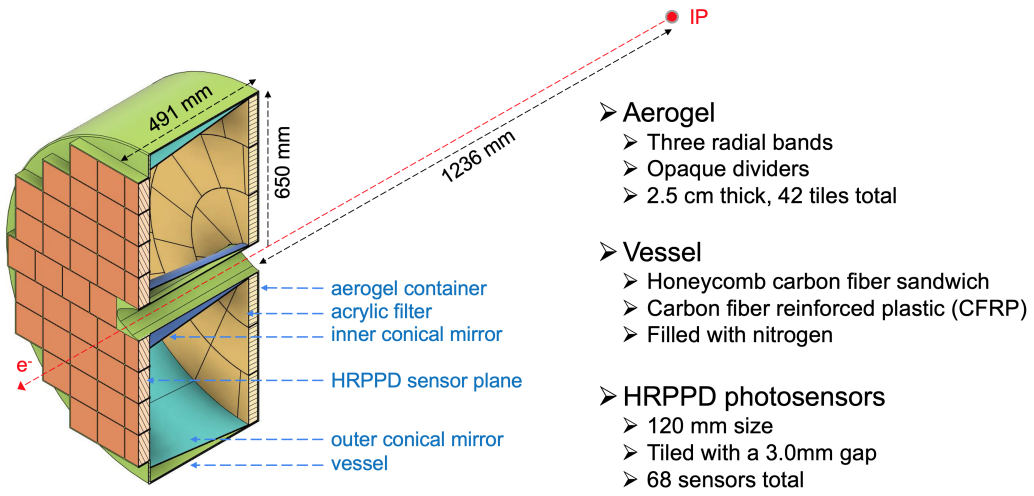

Figure 8.49: The proposed pfRICH detector. See the text for more details.

Sensors: An improved version of the Micro-Channel Plate Photomultiplier Tubes (MCP-PMTs) manufactured by Incom Inc. [43], the so-called High Rate Picosecond Photon Detectors, will be used as the photosensor solution. The sensor dimensions will be 120 mm x 120 mm, with a 104 mm x 104 mm fully efficient active area in the center (75% geometric efficiency) and will have slightly tapered 5 mm thick UV-grade fused silica windows, and 3 mm thick multi-layer ceramic anode base plates. A DC-coupled variety of these sensors will be used, with the inner side of the anode base plate patterned into 32 x 32 square pixels, corresponding to 1024 channels per sensor, and a pitch of 3.25 mm. The sensors will be equipped with a UV-enhanced high quantum efficiency (QE) bialkali photocathode, with peak values exceeding 30% at 350 nm (see left and center panels in Fig. 8.50) [44]. The HRPPDs will be fitted with a pair of 600 μm thick MCPs with a pore diameter of 10 μm, open area ratio in excess of 70%, and bias angle of 13 degrees in a conventional chevron configuration. These will be operated at an amplification voltage of up to $\sim$700 V to comfortably achieve an overall detector gain above 10^6 if needed. HRPPDs will have a single photon Transit Time Spread (TTS) of $\sim$30-40 ps (right panel of Fig. 8.50). The anode base plates will be manufactured from multi-layer High Temperature Co-fired Ceramic (HTCC) by Kyocera (Japan). They will have a custom design, matching the uniform 32 x 32 pixellation on the inner (vacuum) side of the sensor, short shielded traces inside of the ceramic stack, and a pattern of square pads with a smaller pitch on the outer side, matching the readout PCB design.

FEE: Each sensor will be equipped with four 256-channel EICROC ASICs [45], designed by the OMEGA group [46], each serving one quadrant of the sensor. EICROC ASICs will be built via a 130 nm technology process, with an expected power consumption of 1-3 mW/channel [45]. They will provide a Time of Arrival (TOA) and an ADC measurement with a dynamic range of 1 pC for each pixel, which should be sufficient for both single photon hits (both imaging and timing) and multi-photon hits (timing only) at a moderate HRPPD gain of a few times 10^5. The ASICs will be able to measure the TOA with a resolution better than 20 ps per pixel assuming detector capacitance on the order of $\sim$10 pF, leading edge length of the HRPPD signal below 500 ps, and collected charge of a few dozens fC achieved by tuning the MCP gain [46]. These ballpark parameters seem to be easily within reach for pfRICH

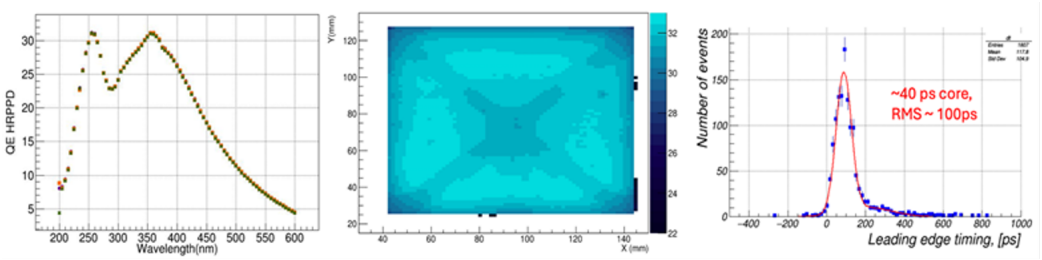

Figure 8.50: PLACEHOLDER Left: EIC HRPPD QE as a function of wavelength. Center: QE map in the full active area at a wavelength of 365 nm. Right: Single photon timing resolution (PiLas picosecond laser pulse jitter not unfolded.

HRPPD sensors.

The ASICs will be bump bonded to the readout PCB in a "flip-chip" fashion to minimize the parasitic capacitance of the traces inside of the PCB stack. Preliminary estimates show that in such a scheme, where four 16 x 16 primary pixel arrays with a pitch of 3.25 mm are first "compressed" to a 2.0 mm pitch inside the HRPPD ceramic base plate and then further reduced to a 500 μm pad size in the readout PCB stack in order to ultimately match the EICROC ASIC pitch, the combined pad and trace capacitance should not exceed 10 pF. This is well within the expected operating range of the ASICs.

Each ASIC will be connected via a dedicated copper link to its respective readout unit (RDO), located on the outer circumference of the rear side of the pfRICH vessel. Each RDO will serve 16 EICROC ASICs, for a total of 17 RDOs. The RDOs will then be connected to a single Data Aggregation Module (DAM). The DAM board is envisioned to be a FrontEnd LInk eXchange (FELIX) board [47] installed in the DAQ. The RDO will be connected to the DAM via a high speed optical link capable of at least 5 Gb/s throughput. The RDOs will follow the same design used by the ePIC pixelated AC-LGAD detectors. These boards will utilize lpGBT for aggregation of ASIC data and VTRX+ to provide the fiber interfaces. The RDO should deliver timing signals synchronized to the beam crossings with jitter $<$ 5ps.

Other components: In addition to the vessel structure and sensors described above, two other components will be critical to the pfRICH: the aerogel radiators and mirrors. The pfRICH will be equipped with aerogel tiles produced by Chiba Aerogel Factory Co., Ltd. [48] with a nominal refractive index, $n \sim 1.040$ and a thickness of 2.5 cm. The aerogel will be cut using a water jet technique into trapezoidal tiles providing a required radial and azimuthal segmentation with minimal dead area. This type of aerogel will replicate the performance of the material used in the Belle II experiment [49], and in particular, will be very transparent in the near UV range, with an absorption length and Rayleigh scattering length in excess of 5 mm down to $\sim$275-300 nm. The aerogel tiles will be installed in segmented containers (slots) with $\sim$500 μm thick walls and held in place with a thin filament. The container walls will be opaque to suppress stray photons leaking out of the aerogel tile side facets, which are not expected to be of a high optical quality after water jetting.

The pfRICH will also utilize three types of mirrors to increase the active acceptance of the detector. The outer mirror cone consists of 12 segments approximately 40 cm in length which sit just inside the outer wall of the pfRICH vessel. These mirrors will recover Cherenkov photons from charged particles with large polar angles which pass through the aerogel but would exit the vessel before reaching the sensor plane. Similarly, a set of inner mirrors which wrap around the beam pipe and surrounding support structures will reflect photons emitted by small angle charged particles (close to $\eta \approx -3.5$) back onto the sensor plane. Finally,

small pyramidal mirrors will be placed on top of the HRPPD side walls to reflect (funnel) photons hitting this area back into the sensor acceptance. The mirrors themselves will have a reflectivity of approximately 90% for wavelengths between 300 and 600 nm and will be produced at Stony Brook University using an evaporator with the CFRP substrate material provided by Purdue University.

Performance

Monte-Carlo simulations: The performance of the pfRICH design was studied using a custom simulation and reconstruction software suite. The geometry of the detector, along with other relevant characteristics such as the ePIC magnetic field map, aerogel optical properties, mirror reflectivity, and HRPPD quantum efficiency were modeled in GEANT4 v10.05.p01 [50]. The reconstruction made use of the Inverse Ray Tracing (IRT) library, which is part of the ePIC software stack [51], and a ROOT [52] based data structure providing access to all photo-electron, track, and event level quantities.

Parameters relevant to the performance of the pfRICH were determined by simulating single particles thrown at a variety of energies and angles. On average, roughly 11 Cherenkov photons were detected from particles at the saturation momentum, which is in agreement with first principles estimates taking into account a realistic sensor quantum efficiency. The working acceptance of the detector, defined as the region in which the ratio of tracks producing at least one detected photon over the total number of tracks is greater than 80%, was found to cover $-3.5 < \eta < -1.5$. Single photo-electron (SPE) and track level resolutions in the working acceptance were also determined, with the SPE resolution being roughly 5 mrad and independent of momentum, while the track level resolution improved with the number of detected photons and reached a value of 1.7 mrad.

The algorithm for event based reconstruction of the Cherenkov angles was validated using multi-particle simulations. The reconstructed Cherenkov angle (in units of mrad) as a function of particle momentum (in units of GeV/c) is shown in the left panel of Fig. 8.51 and compared to the theoretical expectations for a given mass hypothesis. It is seen that the reconstructed angles and theoretical expectations are in good agreement, confirming that the event based reconstruction is performing well. This plot also shows that the Cherenkov saturation angle is approximately 295 mrad. The N_σ separation count between the electron-pion and pion-kaon hypotheses as a function of momentum are shown in the middle and right panels of Fig. 8.51, respectively. It is seen that 3σ separation is possible up to roughly 2.5 GeV/c for electron-pion and 9 GeV/c for pion-kaon hypotheses. Performance was found to be relatively uniform across the whole acceptance of the detector.

One of the main purposes of the pfRICH detector is to identify low momentum scattered electrons in the backward direction. Specifically, it will help with separating the electrons from π^- mesons, which are expected to dominate in the pfRICH acceptance. Using PYTHIA-6 e+p collisions at 18×275 GeV, it was shown that the pfRICH will provide good π^--electron separation for $p < 2$ GeV/c and decreasing separation power for momenta up to ~ 5 GeV/c as seen in Fig. 8.52.The pfRICH detector therefore plays an important role in the ePIC detector, allowing identification of the scattered electrons in kinematic region not accessible by other detectors.

Another important utilization of the pfRICH is hadron identification in the backward region in SIDIS studies. For that reason, the ability to separate π, K, and p hadrons was studied using simulation of e+p collisions at 18×275 GeV in PYTHIA-8. Specifically, the expected purity of leading K^- mesons was evaluated and was shown to be close to 100% up to hadron

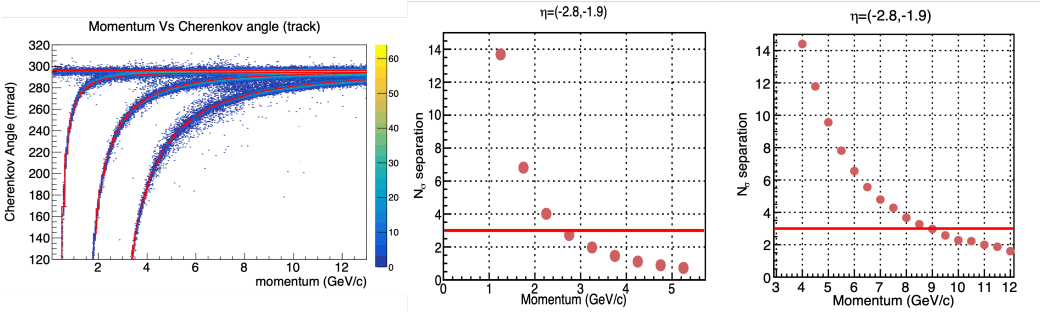

Figure 8.51: PLACEHOLDER (Left) The reconstructed Cherenkov angle for electrons, pions, kaons, and protons as a function of momentum. (Middle) N_σ separation between the electron and pion hypotheses as a function of momentum. (Right) Same as the middle panel, for pion and kaon hypotheses.

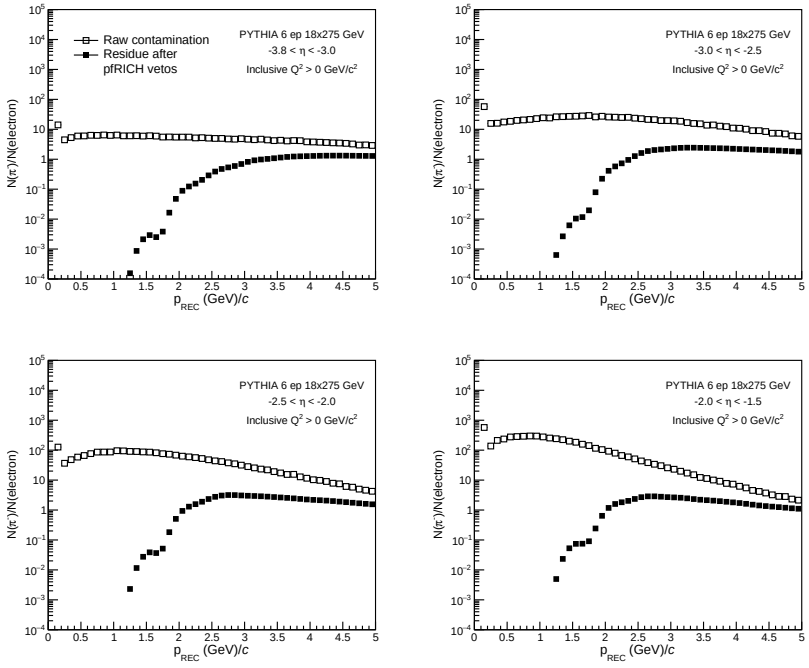

Figure 8.52: PLACEHOLDER Yield ratios of π^-/e_{scat} before (open black squares) and after (black full squares) pfRICH veto on π^- in PYTHIA 6 e+p collisions at 18×275 GeV for four η bins, covering full pfRICH η acceptance.

momenta of $p < 6\,\text{GeV}/c$. This means that pfRICH will play an important role in SIDIS studies as it can efficiently distinguish various hadron species in a wide momentum range.

Hardware component evaluation: Hydrophobic silica aerogel manufactured by the Aerogel Factory [48] will be used for the radiator in the pfRICH detector. Three hydrophobic aerogel tiles, with nominal dimensions of 11 cm × 11 cm × 2.5 cm, density of 0.14 g/cm^3, and refractive index of 1.04, were ordered from the Aerogel Factory to verify and assess their refractive index and transparency, two aerogel properties which are critical to the detector's

performance. The refractive index was determined at Temple University by measuring the deflection of the refracted light exiting the corners of the aerogel (see QA section). The refractive index measured by Temple University (n_{TU}) and the Aerogel Factory (n_{AF}) were found to be in agreement, with a typical value of $(n_{TU} - n_{AF}) \,/\, (n_{AF} - 1) \sim 2\%$. The optical transparency was evaluated by measuring the transmittance as a function of wavelength. Transmittance curves for each tile were measured by the Aerogel Factory using a monochromator and spectrometer (Hitachi U-4100) [53], at BNL using a monochromator and spectrometer (Hitachi U-3210), and at Temple University using a LED and spectrometer setup which provides measurements at four discrete wavelengths (see left panel of Fig. 8.53). These three sets of measurements were found to be consistent with each other within the quoted errors. A sufficiently high transmittance of about 68.5% at 432 nm was found when averaging the results from three different measurements over the three produced aerogel tiles at Temple. The wavelength dependent transmittance measurements were used to extract additional information such as clarity, transmission length, and scattering length.

The mirrors will be produced by the pfRICH subsystem collaboration members, with substrates fabricated at Purdue University and coating performed at Stony Brook University. Optimization of the substrate and coating procedures is ongoing with a number of mirror samples being produced with different substrate manufacturing techniques, coating chamber settings, and coating material thickness. The reflectivity of the various mirror samples was evaluated at BNL using a dedicated test stand. The best performing mirror sample, manufactured using a ∼12 kilo-angstrom thickness aluminium coating, showed a measured average reflectivity of 0.89 for wavelengths between 300 and 600 nm (see right panel of Fig. 8.53).

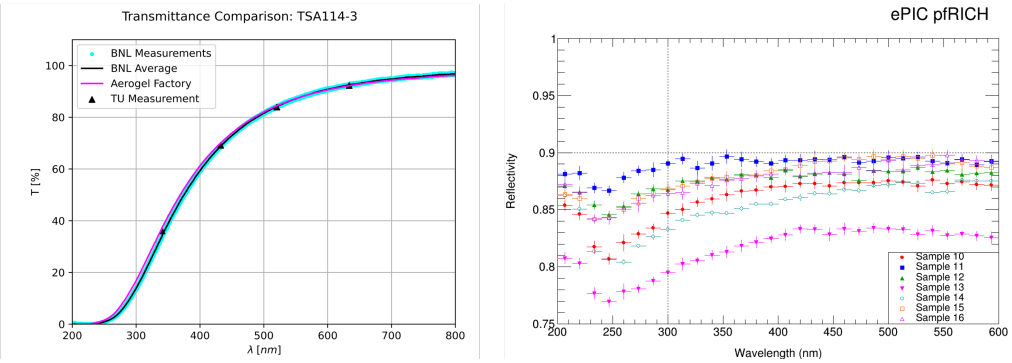

Figure 8.53: PLACEHOLDER Left: Aerogel transmittance as a function of wavelength for factory, BNL, and Temple University measurements. Right: Mirror sample reflectivities as measured at BNL as a function of wavelength.

Implementation

Services: Services relevant for the pfRICH include High Voltage (HV) and Low Voltage (LV) systems to operate the photosensors and power the front-end electronics, respectively, a cooling system to regulate the temperature of the electronics and sensors, and a gas system to maintain the proper environment inside the pfRICH vessel.

The HV and LV modules will be located on the electronics platform, about 15 meters away from the pfRICH detector, in a low Total Ionizing Dose (TID) environment. Therefore, standard off-the-shelf units can be used. The high-voltage system will consist of 340 individual stackable negative HV

channels. Twenty three CAEN A1515BV 16-channel 1.4kV/1mA floating ground modules [54] will be used. The HV modules will be housed in a pair of CAEN SY4527 mainframes [55], equipped with additional 1200 W power module boosters. Each of the twenty three modules will be connected to an enclosed box distribution PCB installed on the rear side of the pfRICH vessel. The box is fed from individual 15 m long multi-conductor high voltage cables. For the HV interconnect, CERN-approved 52-pin Radiall cable connectors and receptacles will be used throughout the system. The distribution PCB will arrange five of the isolated channels of the A1515BV in a manner to provide five individual stacked voltage levels and a common ground referenced return to each HRPPD. The respective five bias levels and ground will be connected to the pads on the rear side of the HRPPDs via narrow profile Teledyne Reynolds shielded 26 AWG coaxial cables, conductive vias in the Front End Board (FEB) stackup with a matching pad pattern, and custom Samtec compression interposers.

The EICROC ASICs will require 1.2 V low-voltage power. Under the assumption of up to 3 mW/channel power dissipation this corresponds to 3 W power (or up to 2.5A current) per photosensor FEB. Accounting for other electronics components present on such a FEB, and providing a 20% safety margin, we estimate the total power consumption to be less than 300 W for the whole system. This number is used as input for designing the cooling system discussed below. We will be using a single Wiener MPOD Mini LX crate with a MPOD-C controller and four MPV4008I1 4-channel LV modules [56]. One Low Voltage channel will serve four FEBs. 15 m long tray rated 10 AWG jacketed cables with 20AWG (sense wires) will run between the electronics platform and a LV distribution panel on the rear side of the pfRICH vessel. From there, 18 AWG multi-conductor cables will distribute power to the individual FEB cards.

The pfRICH cooling system will consist of several off-detector components and a few on-detector thermal interfaces and assemblies. The primary heat dissipating components will be the ASICs, which are anticipated to produce just over 1 W each (4 W per module), or about 300 W for the 68 total modules. In addition to the ASICs, the sensors are anticipated to dissipate just under 1.5 W each or 100 W total. Conservatively, the total power output will be roughly 400 W. Following the geometry, each row of sensors will have its own pair of titanium cooling tubes directly over the ASICs. The pair of tubes that contact the same row of sensors will be in series, and all rows will be in parallel with each other. The tubes will be attached to aluminum plates with thermal epoxy, and a gap pad between the plate and ASIC will maximize thermal contact. Using a stock tube of 0.25" OD and 0.218" ID and maintaining a minimal temperature gradient in the water allows the mass flow rate to be calculated. From there the Reynolds number and pressure drop can be determined, confirming the viability of the system. Additionally, a finite element analysis (FEA) was performed to confirm the water temperature difference and determine the thermal gradient across the various components. With the described configuration, the sensors reach a maximum temperature of about 32 C in the analysis.

The three primary off-detector elements of the cooling system are a Polyscience chiller, Chilldyne circulator, and a distribution panel. The Polyscience chiller will allow the water to be slightly colder than room temperature, or about 15 C, which is the lowest recommended temperature without nearing the dewpoint in the interaction region. The unit is also capable of flowing about 10 liters per minute (lpm), dissipating about 800 W at that temperature and maintaining the temperature within +/-0.1 C. The Polyscience chiller would be paired with a Chilldyne negative pressure system capable of circulating water at about 8 lpm and $\sim$10 psi. It offers a significant advantage over a positive pressure solution, as if there is a leak in the system, it will draw air into the tube instead of letting water out and potentially damaging electrical components.

The gas system for the pfRICH detector is designed to circulate dry nitrogen at precise pressure and flow rates to remove moisture from within the pfRICH chamber. High-purity nitrogen (H_2O

$<$ 3 ppm) will be supplied from cryogenic sources. To provide secondary protection, moisture traps such as silica gel dryers will be installed near the nitrogen source. The system will maintain both the required moisture levels and gas purity by ensuring that it is sufficiently gas tight and that the chamber is kept at a slight overpressure (4 mbar) above atmospheric pressure, preventing any infiltration of ambient air. A 0.5 μm filter will be added near the source to capture dust particles. A standby nitrogen source will be available to ensure continuous operation in the event of a primary source failure. To manage fluctuations in the source pressure, a digital pressure outlet controller will be used. Additionally, nitrogen flow will be regulated by a non-pressure-limiting digital mass flow controller. The nitrogen flow rate is expected to allow several complete volume exchanges per hour, with the precise rate to be finalized later.

Pressure inside the chamber will be controlled using a tank blanketing pressure regulator, which maintains a positive internal pressure relative to varying atmospheric conditions. An overpressure protection bubbler will serve as a safeguard against excessive pressure within the chamber. To ensure uniform nitrogen distribution and prevent localized air pockets, nitrogen will be introduced into the chamber at two locations near the top side of the pfRICH vessel, closer to the aerogel plane, and exhausted through two openings near the sensor plane at the bottom. All exhausted gases will be vented outside the experimental area. The entire gas system will undergo pressure testing at 1.5 times the operating pressure to ensure integrity. For monitoring and troubleshooting, pressure gauges and transmitters will be installed, with critical data such as chamber pressure and flow archived for reference.

Subsystem mechanics and integration: The shell that creates the volume of the detector will be made primarily of carbon fiber to optimize the radiation length in ePIC. Specifically, the sensor plane is intended to be made from a bulk carbon fiber layup at approximately 14.7 mm thick at its thickest point. The bulk carbon fiber will be molded and CNC-cut to allow for individual sensor frames and staves to be bonded in-place to create 68 sensor pockets along this plane of the detector. Each individual HRPPD sensor will be added into the sensor plane from the outside of the vessel and sealed in each of the sensor pockets with a face seal. The overall plane will be sealed to the cylinder at the outer and inner walls using a tightly spaced bolt-pattern and an o-ring groove on the upstream end of the sensor plane to accommodate another face seal.

On the upstream end of the vessel, the aerogel plane will be made from a carbon fiber honeycomb layup around 1/4" thick. The outer and inner circumferences of the aerogel plane will house a sealing ring made from bulk carbon fiber and an o-ring groove to create a face seal. Attached to this aerogel plane will be a web of carbon fiber that creates radial rows of pockets for the aerogel to be placed in. These tiles will be held into the pockets using a thin transparent line strung across the opening in order to contain them in place.

The cylindrical portion of the vessel is comprised of identical end rings on the upstream and downstream end that house the threaded bolt holes and sealing surfaces for the sensor plane and aerogel plane face seals. These end rings are approximately 3/4" (on the bolting surface) and 1" in thickness (in the z-direction). They are made from bulk carbon fiber and contain threaded inserts that are placed by CNC-machining the insert locations and bonding and threading them into place. The rest of the cylinder is made from single sheets of carbon fiber on the inside and outside of the vessel, as well as a 3/4" nomex honeycomb layer in between.

The inner wall of the cylinder is created in a similar manner to the outer wall, namely a honeycomb construction with the end rings embedded into both ends for bolting and sealing to the aerogel and sensor planes. However, the shape of the inner wall is made such that there is 5 mm of clearance (radially) from the beam pipe flange that the pfRICH will need to pass by to be installed in ePIC. This makes the shape of this inner wall similar to an egg or an avocado.

Lastly, the conical mirrors are designed such that they are attached solely to the sensor plane. This is being done to ensure that the mirrors can be controlled in relation to the sensors and will be unaffected by manufacturing misalignments and tolerance stack-up issues throughout the rest of the vessel. As such, they will hang cantilevered perpendicular the sensor plane for both the inner and outer mirrors. The outer mirrors will be concave and the inner mirrors will be convex. The construction will be a combination of a molded, bulk carbon fiber base with a bonded lexan sheet on top of it (which will have been deposited with a mirror film).

Once the pfRICH has been fully assembled and ready to be placed in the overall ePIC detector, it will be moved around the assembly hall on a cart. The cart will integrate lifting eyelets for the installation of the pfRICH into ePIC, rails identical to its final location, and wheels to transport, store and work on the detector when it is out of the barrel. This tooling will allow us to lift the cart with the pfRICH secured in place with the crane in the detector hall, position it against the barrel, align the rails, and transfer the pfRICH into its final position by translating it along the z-axis.

Calibration, alignment and monitoring: A laser-based system will be used to monitor the pfRICH performance throughout its operational life. The purpose is to monitor, on a pixel-by-pixel basis the single photon timing resolution, the single photon pulse hight amplitude (HRPPD gain), HRPPD QE, and the relative delays between channels on a few ps level. The system will also monitor the reflectivity of the conical and pyramidal mirrors. To measure the timing resolution, an array of six fibers is introduced inside the detector volume from the aerogel side which casts a broad profile of low-intensity light onto the sensor plane such that each HRPPD pixel accumulates some number of single photon hits after a given number of laser pulses. The distance between a given fiber tip and an HRPPD pixel (minimum of 40 cm) defines the flight time for photons emitted from this fiber, hence the distribution of reconstructed flight times will reveal the timing resolution for this single pixel. Similarly, a separate array of six fibers is arranged such that emitted photons reflect off of the outer mirror surface before impinging on the HRPPDs. In this case, the single photon counting rate is monitored for any degradation over time, which would indicate the deterioration of either the photocathode quantum efficiency or mirror reflectivity, or both.

The pfRICH monitoring system deploys a picosecond PiLas laser which produces a 405 nm laser beam with a nominal $\sim$ 45 ps pulse width. The beam is coupled to a custom 1-to-14 optical fiber splitter by Thorlabs, that evenly distributes the light into arrays of fibers routed into the detector vessel. Two additional fibers are connected to silicon photodiodes to provide laser signal quality verification and an initial timestamp (t_0). A custom-sized 5 mm $\times$ 5 mm engineered diffuser is used to generate a uniform 50° square pattern to optimize the intensity profile emitted from each fiber. Additionally, a fiber delay line is added to each fiber branch to provide the ability to easily separate out in time photons originating from a given fiber. In all, there are three sets (segments) of fibers downstream of the splitter that deliver photons from the laser to the detector vessel: delay fibers, long extension fibers, and fibers mounted permanently inside the detector vessel. Finally, multiple fast photodiode sensors are used to sample the laser light before and after the splitter to monitor the light output intensity and the timing performance.

A relative alignment of the conical mirror segments inside of the vessel, and surface mapping will be performed on a fully assembled detector (up to the front wall removed) prior to the installation in ePIC, by using a 3D scanning system which is being built now for the purposes of first article mirrors QA assessment. The vessel as a whole will be aligned in ePIC after the installation, following a generic procedure developed by EIC engineers for all detector subsystems. Appropriate survey targets will be mounted on the rear and barrel sides of the vessel if required.

Status and remaining design effort: As shown in the previous text, the present pfRICH design fully meets the EIC Yellow Report requirements and subsequent amendments (see performance section):

- Pseudorapidity coverage from -3.5 to -1.5 in the electron-going endcap
- π/K separation on a 3σ level up to 7 GeV/c in this whole acceptance
- $\sim$20 ps timing reference for ePIC ToF subsystems in the barrel and the forward endcap by combining single photon signals from aerogel and signals from multi-photon flashes of Cherenkov photons produced by charged particles in HRPPD fused silica windows

R&D effort: The pfRICH design is based mostly on proven technologies, therefore, the remaining R&D effort is fairly small. FY25 R&D activities (partly funded through eRD110 consortium) will be limited to HRPPD aging studies, which will be performed at JLab and INFN Trieste.

E&D status and outlook: Several engineering design activities and first article productions described earlier in the text in more detail have been performed in FY24, and will continue into FY25:

- Full size mirror production and quality assessment
- First article pfRICH vessel outer shell production
- Adjustments of the production process of CFRP-based parts, mirror substrates and HRPPD pockets in the sensor plane in particular
- Fine tuning of the aerogel refractive index and bulk uniformity measurement procedure
- HRPPD sensor design modifications required after the first batch was produced
- HRPPD performance confirmation in the $\sim$1.7 T magnetic field typical for a pfRICH location in ePIC

Other activity needed for the design completion: The readout backplane design cannot be fully completed at this stage because of the unavailability of a final design iteration of the anticipated ASIC chip (EICROC) in either of its low channel count configurations (64, 128 or 256 channels).

The performance of the pfRICH in its anticipated configuration needs to be confirmed in a beam test for both Cherenkov photon imaging and timing in the whole momentum range required for e/π, π/K and K/p separation. Such a beam test will be performed with electron and hadron beams at Fermilab in Spring 2025, with an extensive use of first article components (outer vessel shell, aerogel, mirrors, HRPPDs).

Status of maturity of the subsystem: The design of the pfRICH subsystem is in a fairly mature state. As described in previous sections, the pfRICH consists of a cylindrical vessel with two endcap plates, an aerogel tile plane, an HRPPD sensor plane with onboard electronics, mirrors and a number of subsystems (HV and LV, cooling, gas, light monitoring). Engineering design of all of these components (except for the HRPPD ASIC backplane for reasons explained in section 3.4.3) is by now sufficiently advanced to be more than 60% ready by the CD-2 EIC Project phase at the end of 2025.

Environmental, Safety and Health (ES&H) aspects and Quality Assessment (QA) planning: The environmental, safety, and health impacts of the pfRICH subsystem are expected to be minimal. When installing and integrating the pfRICH into the overall detector, all applicable safety standards (i.e. OSHA, Critical Lift procedures, etc.) will be followed and adhered to. Furthermore, the composition of the vessel itself consists mainly of carbon fiber, epoxy, and plastic and any (small) excess can be retained for future use or disposed of via standard waste streams. The operation of the detector will require a modest 400 watts of cooling power and the working gas is pure nitrogen which does not pose any greenhouse concerns.

The individual HRPPDs, mirrors, and aerogel tiles used in the pfRICH will all undergo rigorous quality assessment (QA) checks to ensure that their operation and/or properties are within acceptable limits. Beyond the testing done by the manufacturer, the performance of individual HRPPDs will be evaluated using test stands located at BNL, JLab, and possibly Yale University. While the details of the test stands differ, they all consist of a light-tight enclosure to house the HRPPD, a fiber-coupled light source (either a pulsed laser or a monochromator), an optical assembly to focus the light onto the sensor, power supplies, and readout electronics. The gain uniformity, quantum efficiency, photon detection efficiency, and dark count rates will be determined over the entire active photosensor area. In addition, the use of a Menlo Systems Elmo 780 femtosecond laser at BNL will allow precision determination of the timing characteristics of the sensors.

The reflectivity of the mirror samples produced at SBU is determined using a dedicated test stand at BNL. The setup consists of a monochromator light source, dark box, optical assembly, and motorized sample and sensor mount. Light from the monochromator is fed via fiber to the optical assembly where a beam splitter directs a fraction of the light to a reference photodiode and passes the remaining beam to focusing elements and then on to the mirror and measurement photodiode. The mirror sample and measurement photodiode sit on independently rotating platforms allowing measurements at a variety of angles. The mirror reflectivity is determined by taking the ratio of the photodiode current with and without the mirror present. Variations in the monochromator light source intensity are corrected using the reference photodiode. This stand is designed to evaluate mirror test samples with a maximum size of several square centimeters. Detailed QA and mapping of the detector mirrors will be performed *in situ* before the pfRICH vessel is sealed during final assembly. A dedicated 3-D scanner will be constructed for this purpose utilizing the techniques developed with the sample test stand.

The aerogel quality assessment will be performed at Temple University and include assessments of the refractive index, transparency, uniformity and mechanical specifications. So far, the refractive index has been determined by measuring the deflection of the light passing through the corner of the aerogel tile, following the proceedure described in Ref. [57]. Work is currently underway to develop a setup and approach that is based on measuring changes in the polarization between the light incident on the aerogel and the light that is reflected from its surface. This would allow for localized refractive index measurements to ensure not only the aerogel has the proper mean refractive index, but also its uniformity across the whole tile. Transparency QA will make use of wavelength dependent transmittance measurements carried out using a newly commissioned and validated UV/VIS LED-spectrometer system. The transmittance data will be fitted with the Hunt Formula [58] to extract aerogel properties such as the scattering surface coefficient and clarity, as well as the wavelength dependent properties which include the transmittance, transmission length, and scattering length. The density will be calculated by measuring the aerogel mass using a precision scale (100 μg) and volume via caliper and touch probe. Reference jigs can be made to ensure that the aerogel mechanical specifications such as the side-to-side length, tile height, and surface planarity variations are within acceptable ranges.

Construction and assembly planning: The pfRICH has been designed such that it can be fully assembled and inserted into ePIC in one piece. Individual components such as vessel walls, sensor and aerogel planes, mirrors, HRPPDs, and aerogel tiles will be manufactured and tested at various locations and then shipped to BNL for final assembly. It is envisioned that final subsystem assembly will take place in a cleanroom or dedicated lab space within the physics building at BNL. Once assembled, the pfRICH will be transported by truck roughly 1.3 miles to the experimental hall where it will be integrated with the other ePIC subsystems.

The assembly of the pfRICH itself will proceed via the following general steps: (1) assemble the aerogel plane by fastening it to the outer and inner walls, (2) place the sub-assembly such that the upstream end is facing down, (3) add aerogel tiles and aerogel retaining system into the aerogel plane, (4) pre-assemble most of the sensor plane by affixing the inner and outer mirrors and any vessel services (i.e. inner gas tubing, laser monitoring system, etc.) to the sensor plane, (5) lift the sensor plane over the rest of the vessel and lower the sensor plane and mirrors into place, (6) fasten the sensor plane to the subassembly at the inner and outer walls, completing the cylindrical vessel, (7) systematically insert and secure the individual HRPPD modules into the back of the sensor plane, (8) lift the completed pfRICH, rotate it into its operating position, and install it onto the transportation/storage cart.

Collaborators and their role, resources and workforce: The pfRICH Detector Subsystem Collaboration (DSC) member institutions, as well as other affiliated groups are listed in Tab. 8.18, along with their anticipated commitments.

Table 8.18: Institutions contributing to the pfRICH effort and their roles, resources, and participating workforce. Starred entries indicate no institutional commitment.

Institution	Role	Workforce	Resources
Brookhaven National Lab	Project Lead HRPPD and mirror testing Gas Systems DAQ Detector and physics simulation	5 staff	HRPPD test stands (pico/femtosecond laser, dark box with translation stages, high-performance scope, wavefor digitizers) Mirror test stand (monochromator) Sample temperature control chamber
Chiba University*	Connection to aerogel factory	N/A	Aerogel production equipment
Duke University	Detector modeling	1 staff	
INFN Genova*	HRPPD B-field studies	1 staff	
INFN Trieste*	Detector modeling HRPPD aging and B-field studies	1 staff	HRPPD test stand (laser, dark box, waveform digitizers)
Jefferson Lab*	Mechanical design EIC Project support HRPPD testing	2 staff	HRPPD test stand (laser, dark box, translation stages, digitizers)
Ljubljana University & JSI*	Expert input on detector design	N/A	
Mississippi State University	Laser monitoring system	1 staff, students	
Purdue University	Vessel and mirror fabrication	2 staff, students	Machine shop and fabrication lab
Stony Brook University	Vessel fabrication Mirror coating	1 Post-doc, students	Mirror coating chamber Vessel form
Temple University	Aerogel testing and QA	1 staff	Aerogel test stand
University of Debrecen	HRPPD backpland design and fabrication	1 staff	
University of Glasgow	MCP-PMT evaluation	1 staff, students	MCP-PMT test stand (laser, dark box, cosmic ray stand, electronics)
Yale University	Software support HRPPD QA	1 staff, students	HRPPD test stand (dark box with translation stages, digitizers)

Risks and mitigation strategy: A number of risks has been identified in the past, and mitigation strategies developed.

A reliable large area highly pixelated photosensor with a high quantum efficiency and single photon timing resolution better than ∼50 ps is a core component of the pfRICH design. The pfRICH team, together with the EIC eRD110 consortium (Photosensors) has been routinely working with one of the two manufacturers remaining on the market (Incom Inc.) for several years to help the company re-design their HRPPD sensors so they fully meet EIC specifications. The ongoing evaluation of the first seven EIC HRPPDs produced in 2024 shows that overall quality, as well as reproducibility of parameters verified so far (quantum efficiency in particular) meet the requirements. As a fallback photosensor solution, we consider Photek Auratek MCP-PMTs. Such a PMT has been ordered already, and its performance will be evaluated against the pfRICH detector needs in FY25.

Aerogel tiles of required quality can be produced in a very few places worldwide. The pfRICH team, together with the EIC Project, has been routinely working with the Aerogel Factory in Japan over the last two years, to make sure the quality and production capacity meet our requirements. A technical lead of the Chiba Aerogel Factory in Japan is also a member of the pfRICH DSC, see Fig. **??**. Our simulations show, that in case Aerogel Factory cannot produce sufficiently large tiles to cover the whole front wall of the vessel in a configuration with three radial bands as shown in Fig. 8.49, one can resort to using tiles of a readily available size up to 145 mm in a four-band configuration, with an acceptable loss of performance caused by additional dead area introduced by an extra row of radial spacers between the tiles.

Additional Material Additional material will be provided on a number of subjects, including:

- pfRICH performance from simulation
- π/k/p and e/h separation performance
- Aerogel and mirror test stand results
- Fabrication procedures
- Test stand details

8.3.4.3 The high performance DIRC

Requirements

Requirements from physics: The PID system in the central section of the ePIC detector must provide at least 3 standard deviations of separation of π/K up to 6 GeV/c, and contribute to low momentum e/π identification.

Requirements from Radiation Hardness: The anticipated radiation dose in the hpDIRC optics and its potentially sensitive readout electronics are predicted to be modest. These estimates are based on minimum-bias 10×275 GeV e+p events from PYTHIA. The maximum machine luminosity over a six-month period of annual operation at 100% machine and detector efficiency for a total of 10 years was assumed. Under these conditions, the total dose from electromagnetic and hadronic radiation is expected to be less than 100 rad. The 1-MeV-neutron-equivalent fluence is expected to reach 10^{10} neutrons per cm^2.

Requirements from Data Rates: The expected hit rate of 25 kHz per cm^2 for the hpDIRC was estimated using detailed Geant4 simulations, incorporating the Pythia event generator. This estimation assumes the baseline MCP-PMT sensors, which typically have a dark count rate of approximately 1 kHz per mm^2, or 0.09 kHz per pixel.

Justification

Device concept and technological choice: A radially compact detector based on the DIRC (Detection of Internally Reflected Cherenkov light) principle, a specialized type of RICH counter, is appropriate. It employs solid, long, rectangular-shaped radiators made of synthetic fused silica, which also serve to guide the Cherenkov photons to outside the central region for readout. This design allows the active radiator section to remain radially compact, minimizing its impact on the performance of neighboring systems and simplifying the system integration.

The photons are recorded by an array of pixelated photon sensors mounted on the back of the expansion volume. As a result of the excellent optical finish of the optical components, the emission angle of Cherenkov photons with respect to the particle track is maintained during the photon transport via the total internal reflection. This angle can be reconstructed for each track from the measured position of the photon on the detector surface and the measured arrival time of each photon.

The general concept of a barrel DIRC detector was first successfully demonstrated by the BaBar DIRC and followed by several other experiments worldwide. The ePIC high-performance DIRC (hpDIRC) takes advantage of the lens-based focusing concept of the PANDA Barrel DIRC, and has also several other advancements to meet the performance requirements of the Electron-Ion Collider (EIC). The hpDIRC concept for ePIC was developed as part of the EIC generic R&D program performed by the EIC PID collaboration (eRD14) and direct EIC Project R&D eRD103 with the focus on extending the momentum coverage well beyond the DIRC counter state-of-the-art at that time.

Subsystem description:

General device description:

The baseline design of the ePIC hpDIRC detector, as implemented in a detailed and test beam-vetted Geant4 simulation, is shown in Fig. 8.54. It is divided into twelve optically isolated sectors, each composed of a bar box and a readout box. These 12 sectors surround the beamline in a 12-sided polygonal barrel with an inner radius of about 760 cm. Each bar box includes ten radiator bars, each made of synthetic fused silica and with a length of 4880 mm and a cross-section of 17 mm $\times$ 35 mm. The bars are placed side-by-side, separated by small air gaps, inside the light-tight bar box. Mirrors are attached to one end of each bar to reflect the Cherenkov photons towards the other (readout) end. At the readout end they exit the bar and are focused by a 3-layer spherical lens on the back surface of the prism which serves as an expansion volume.

Bars:

The baseline ePIC hpDIRC design envisions that the 120 long bars needed will be composed of three repurposed BaBar DIRC bars and one shorter new bar manufactured by industry. The number of bar boxes and bars per box has been optimized to the width of the BaBar DIRC bars while maximizing the azimuthal acceptance of the hpDIRC. This approach assumes that the BaBar bars can be safely extracted from the Babar boxes without compromising their

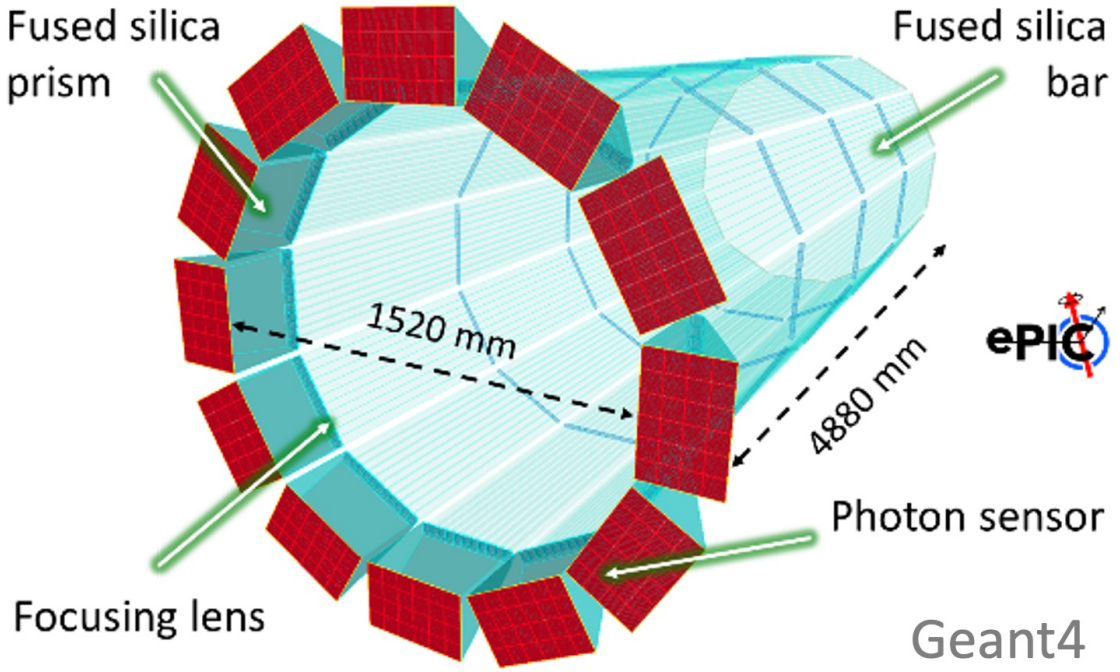

Figure 8.54: ePIC hpDIRC geometry in the Geant4 standalone simulation.

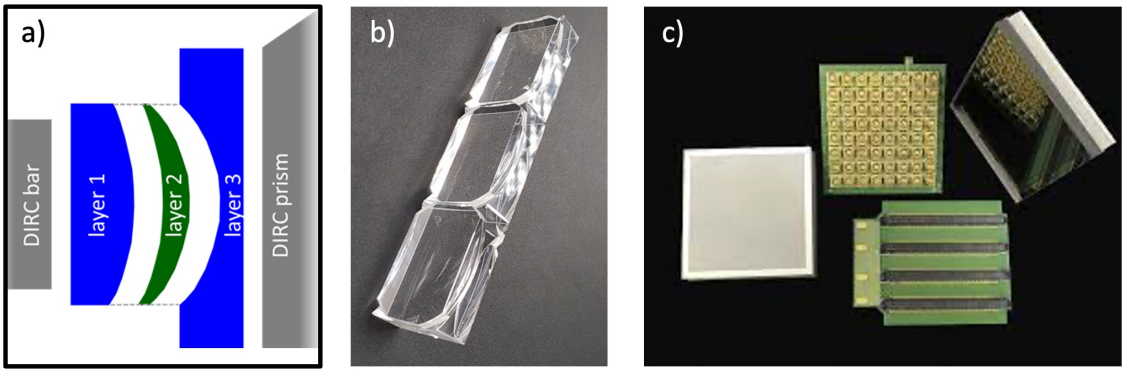

Figure 8.55: a) Schematic of the side view of one hpDIRC section and an exploded view of the 3-layer lens. b) Photo of prototypes of the 3-layer spherical lenses. c) Photec AuraTek MAPMT253.

optical and mechanical integrity. The disassembly and evaluation of the BaBar bar boxes are currently underway. Final information on the availability of Baber bars for ePIC is expected by Spring 2025.

Lenses:

The 3-layer spherical focusing lens is a novel component of the hpDIRC and is essential for achieving the PID performance ePIC requires. The lens design, shown in Fig.8.55, avoids the dramatic photon loss caused by air gap transitions in standard lens systems. It does this by focusing Cherenkov light through refraction at the interface between synthetic fused silica

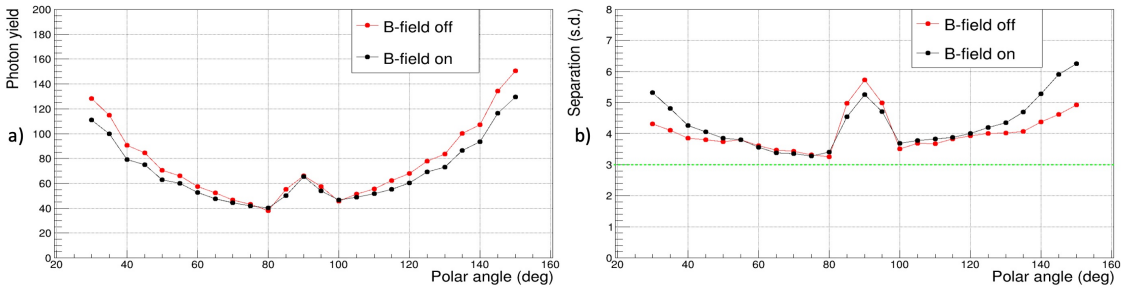

Figure 8.56: The expected performance of the hpDIRC as a function of the particle's polar angle in terms of photon yield (a) for pions and π/K separation power (b). These results are based on a standalone Geant4 simulation of 6 GeV/c particles.

and a high-refractive-index material, such as sapphire or lanthanum crown glass. A thin layer of the high-refractive-index material is sandwiched between two layers of synthetic fused silica, with carefully optimized radii of curvature on all spherical surfaces. This design combines defocussing and focusing transitions to form a flat detector plane that accommodates a wide range of photon angles, matching the layout of the sensor array on the expansion volume prism. Several prototypes using different materials for the middle layer have been produced by the optical industry, and examples of these three prototypes are shown in Fig.8.55b.

Prisms:

The prism expansion volume is made of synthetic fused silica, has a 32° opening angle, and dimensions of 237 mm × 350 mm × 300 mm. The detector plane of each prism is covered by an array of 24 sensors shown in red in Fig. 8.54.

Sensors:

The photosensors attached to the rear of the prism record the positions and arrival times of the Cherenkov photons. In the baseline design of the hpDIRC, commercial microchannel plate photomultiplier tubes (MCP-PMTs) with a pore size of 10 µm or smaller were assumed. A pixel size of 3.2 mm was chosen based on Geant4 simulations as a balance between cost, performance, and expected availability as the sensor technology for the hpDIRC. Lifetime-enhanced 2" MCP-PMT tubes are commercially available from Photonis and Photek with suitable DC-coupled anode configurations. The simulation utilized Photonis Planacon XP85122 MCP-PMTs, incorporating realistic sensor characteristics including photon timing, collection efficiency, and quantum efficiency. With the termination of the production of the Photonis PMTs, the Photek MAPMT 253 sensors shown in Fig. 8.55 are now the leading candidates for the hpDIRC. These share the same footprint and are expected to exhibit similar properties to the Photonis tubes.

FEE: Fast ASIC-based readout systems are being developed by the EIC project to meet the demands of various ePIC detector systems. For the hpDIRC, the readout electronics must be capable of detecting small signals (on the order of a few millivolts) from MCP-PMTs while maintaining excellent single-photon timing resolution. Additionally, the electronics need to match the channel density and sensor footprint, as they will be directly coupled to the back of the sensor to minimize distance and achieve optimal timing precision. The two leading candidates for hpDIRC readout are EICROC and FCFD, which are discussed in detail in Section XXX.

Performance Figure 8.56 presents the expected performance based on standalone Geant4 simulation studies. The plots illustrate particles that are fired over a range of polar angles but with an azimuthal angle fixed at zero degrees (so perpendicular to one of the middle bars). The black points represent the photon yield and separation power for 6 GeV/c charged pions and kaons as a function of polar angle with the magnetic field enabled, while the red points display the same data with the magnetic field disabled.

The number of detected Cherenkov photons per particle (plot a) ranges from 40 to 150, depending on the polar angle. The sharp increase in photon yield at steeper forward and backward angles is due to the longer track lengths in the fused silica bars, with an asymmetry in forward/backward yields resulting from photon loss along longer propagation paths at smaller polar angles. The peak in the photon yield near a polar angle of 90° occurs because a larger fraction of the photons satisfy the total internal reflection criterion near perpendicular incidence, compared to slightly larger or smaller angles.

The "separation power" for both particle hypotheses (plot b) is obtained from Gaussian fits to the log-likelihood differences between pairs of particle hypotheses. It is calculated as the difference between the means of the two Gaussians divided by the arithmetic average of the two widths. The slightly improved performance for polar angles above 100° is due to shorter photon paths, resulting in higher photon yields and reduced chromatic dispersion in the bar material.

Similar studies were conducted for electron-pion (e/π) separation, which is primarily the responsibility of the Electromagnetic Calorimeter. However, the hpDIRC can further improve the performance at low momentum. At lower momenta, multiple scattering is severe, but assuming ePIC achieves the tracking resolution described in the Yellow Report, the hpDIRC can provide a 3 standard-deviation separation power up to 1.2 GeV/c. The expected particle identification (PID) performance of the hpDIRC thus surpasses the ePIC PID goal, achieving more than 3 standard deviations of separation power for e/π identification up to 1.2 GeV/c and π/K separation up to 6 GeV/c across the entire polar angle range.

Performance Systematic Studies Most of the hpDIRC performance studies were conducted using a particle gun, providing precise control over the parameters under investigation while covering the entire required angular and momentum ranges. Detailed studies examined a range of azimuthal angles to measure the performance across the full width of the bar box. While a moderate performance deterioration was observed in some of the non-central bars, the system maintained the required 3-standard-deviation separation power. The effect of the magnetic field on hpDIRC performance was found to be negligible, as confirmed through simulations that incorporated a realistic ePIC magnetic field map.

Additionally, studies using Pythia-generated physics events were performed to assess the frequency and effect of multiple tracks per event within a single bar and hpDIRC module. Even in the extremely rare cases where two or more particles are very close in momentum, polar, and azimuthal angles within a single event, the impact on performance was found to be moderate, demonstrating the robustness of the hpDIRC system.

Most studies were based on an assumed angular tracking resolution of 0.5 mrad at 6 GeV/c. However, the simulation software is prepared to import and integrate a more detailed tracking parametrization when it becomes available.

Detailed hpDIRC PID Look-Up-Tables (LUTs), including the threshold mode, were generated using Geant4 simulations. These LUTs are now employed to streamline physics analyses without the need for full reconstruction.

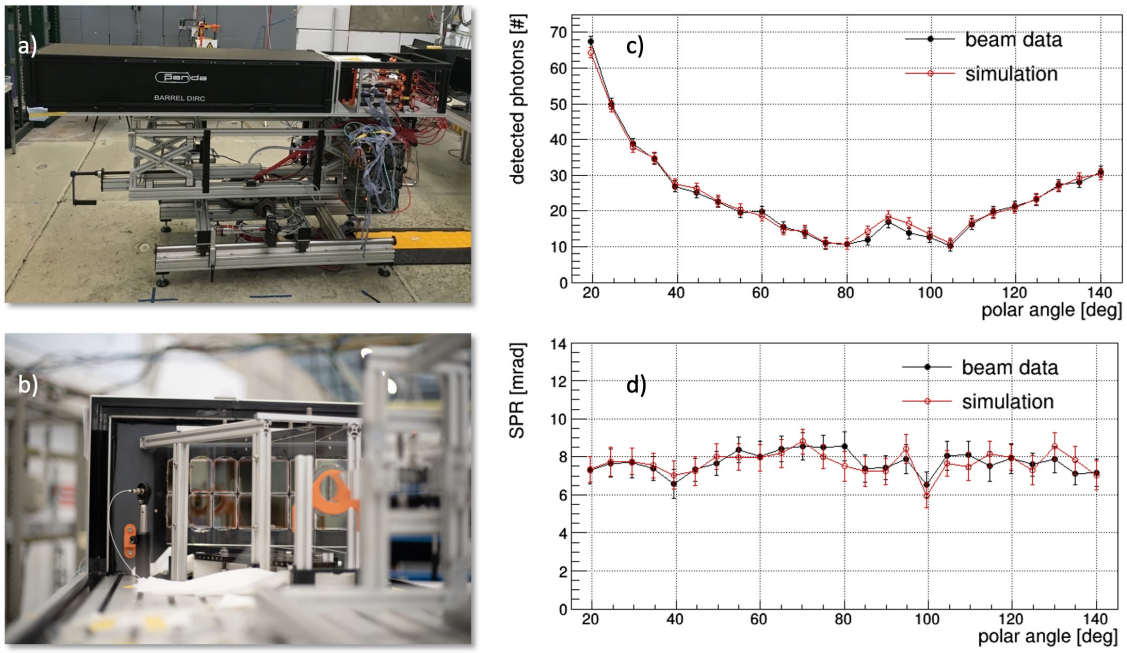

Figure 8.57: Photographs of the PANDA Barrel DIRC prototype (a), including a close-up of the readout section (b) taken during the CERN test beam. Performance plots illustrate the comparison between simulated and experimental data for photon yield (c) and single photon Cherenkov angle resolution (SPR) (d).

Simulation tools and validation A detailed standalone Geant4 simulation, featuring realistic geometry and material properties, was developed in collaboration with the PANDA Barrel DIRC group and validated through modular prototype tests using particle beams at CERN. The simulation incorporates measured values for MCP-PMT quantum efficiency, collection efficiency, and timing resolution. It also accounts for the coefficient of total internal reflection of the DIRC radiator bars as a function of photon energy, the bulk transmission of the bars, glue, and lenses, as well as the wavelength-dependent refractive indices of the materials used, the photocathode, and the reflectivity of the mirrors. Background contributions from hadronic interactions and delta electrons in the bar, along with effects from MCP-PMT dark noise and charge sharing between anode pads, were also simulated.

All relevant resolution factors for hpDIRC performance are modeled using Gaussian smearing with conservative resolution assumptions. The total timing precision per photon, including sensor and readout electronics, is assumed to be 100 ps, and the angular resolution of the ePIC tracking system at the hpDIRC radius is assumed to be 0.5 mrad for particles with a momentum of 6 GeV/c.

Figure 8.57 presents photos of the modular PANDA Barrel DIRC prototype along with results obtained during the 2018 test beam campaign at CERN. Although the PANDA prototype differs significantly from the ePIC hpDIRC in terms of geometry (single bar), slower readout electronics, and lower-quality sensors with larger pixels, the studies and results are highly valuable for hpDIRC development. The same software used for all ePIC hpDIRC performance studies was employed to successfully reproduce the PANDA prototype test beam results. As shown in Fig. 8.57c and d, the agreement between the simulation and experimental data is excellent

Reconstruction methods The hpDIRC utilizes two primary reconstruction methods for identifying particles based on Cherenkov photon detection: geometric reconstruction and time-based imaging reconstruction. These methods translate the detected photon patterns into meaningful physical information, particularly the Cherenkov angle, which allows direct particle identification.

Geometric reconstruction in DIRC detectors is based on determining the Cherenkov photon direction from the mutual location of the radiator's readout end and the pixel hit by the photon. This method allows direct geometrical reconstruction of the Cherenkov angle for each detected photon by utilizing both the photon's direction and the beam particle's direction. Photon directions in the prism are pre-calculated using full simulations, taking into account the optical materials, and stored in look-up tables (LUT). Discrete ambiguities arise due to photon reflections within the optical system, but these can be reduced by applying a cut on the difference between the expected and measured photon arrival times. The geometric method relies on the photon position, and only uses timing information to suppress background noise. The geomtrical method also provides key performance variables such as the single-photon Cherenkov angle resolution and the yields of signal and background photons.

The time-based imaging reconstruction method greatly enhances the particle identification (PID) by fully utilizing both the timing and position information of the detected photons. This method compares the measured photon arrival times against expected distributions for each particle hypothesis, stored as probability density functions (PDFs) derived from experimental or simulated data. For each photon, a time-based likelihood is calculated, which is then combined with the Poissonian PDF of the number of detected photons to provide the likelihood. Unlike the geometric reconstruction, the time-imaging method is suitable for both narrow-bar and wide-plate radiators, offering better separation power between the particle species. This method achieves the best resolution and allows for the most effective corrections of distortions.

Implementation

Subsystem mechanics and integration: The hpDIRC consists of two primary sub-assemblies: the readout section and the bar section. Both sections are composed of 12 boxes made of carbon fiber reinforced polymer (CFRP), with varying thickness depending on the stresses expected in different regions.

The readout section includes the fused silica expansion prism, readout sensors, and front-end electronics. The expansion prism has an angle of 32° and maximum dimensions of 300 mm in length, 352 mm in width, and 237.5 mm in thickness. The MCP-PMTs are coupled to the 352 mm x 237.5 mm back face of the prism using an optical interface. The sensors and associated readout electronics are mounted onto a 3D-printed frame. The rear of the readout box is sealed with a light-tight plate with ports for cables, fibers for calibration lasers, and monitoring cameras. Dry nitrogen gas is flowed through the readout box to keep the prism's surface clean and free from dust and condensation. To maintain stable temperatures and cool the electronics, water circulates through tubing thermally coupled to the heat sources.

The bar box is composed of a top and bottom shell with overall dimensions of 4627 mm in length, 368 mm in width, and 31.25 mm in height. Figure 8.58a shows a dimensioned view of the *XY* cross-section of the hpDIRC bar box. The thicker part of the carbon fiber shell on the sides will be used during installation to slide in the bar box and hold it in place. The carbon fiber thickness is 1.5 mm across the width and 3 mm across the height.

Each bar box contains 10 long radiator bars, lenses, and mirrors. The radiator bars are 35 mm

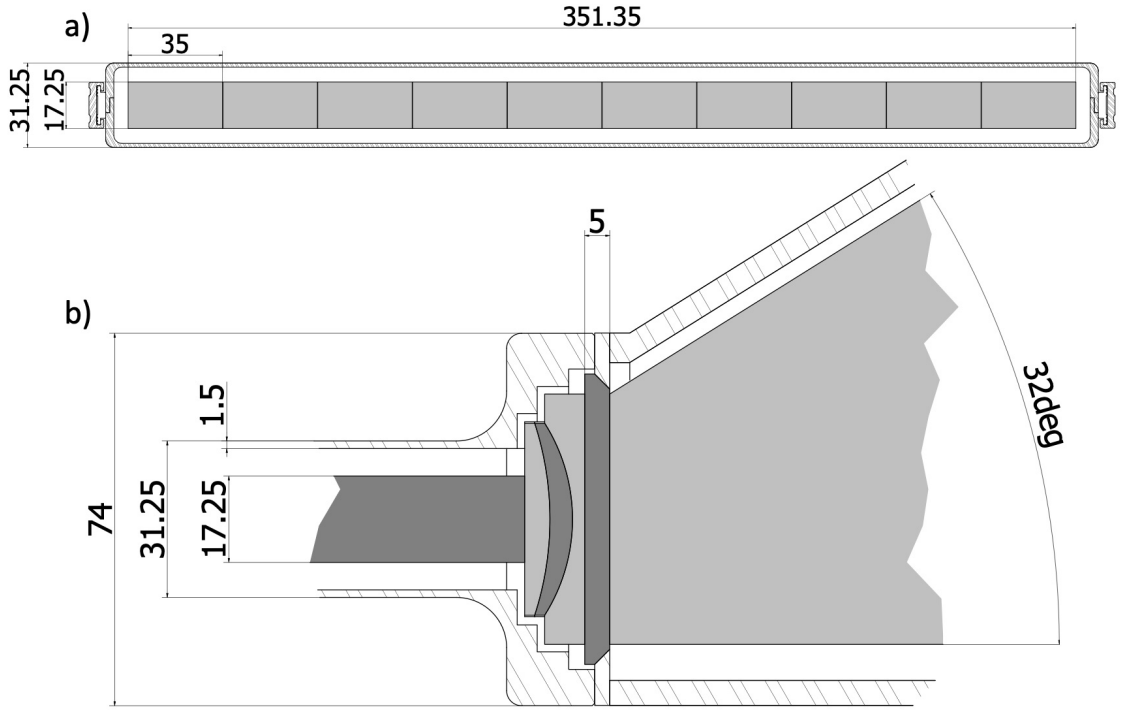

Figure 8.58: Technical drawings of the ePIC hpDIRC detector, showing the XY cross-section of the bar box (a) and the YZ cross-section of the connection between the bar box and the readout box (b).

wide, 17.25 mm thick, and 4580 mm long, spaced 0.15 mm apart using shims to ensure optical isolation. Each long radiator bar is made up of four shorter bars bonded together with an optically transparent adhesive, similar to the BaBar DIRC construction. Three of the shorter bars, each 1225 mm long, are repurposed from the BaBar experiment, while the fourth is newly manufactured to meet the ePIC total length requirement of 905 mm.

At one end of each long bar, a 3 mm-thick flat mirror reflects photons back toward the readout end. At the opposite end, a three-layer lens is attached to the bar using the same adhesive used to join the short bars. The lens-mirror-bar joints are kept in compression by adjustable spring plungers located behind the mirrors, which reduce stress on the joints and prevent movement during installation or operation. The spring system also compensates for differential thermal expansion and contraction rates between the bars and the bar box. Each short bar is supported by two pairs of fixed nylon buttons along its length, which minimize stress on the glue joints and reduce photon loss by reducing contact with the radiator surface. Eight support pairs are evenly distributed along each long bar's length, with adjustable spring buttons pressing the bars against the fixed buttons to maintain secure positioning while preserving the optical isolation. Similar support mechanisms are used for the 17.25 mm-thick end of the bars, where all 10 bars are pressed against a single set of fixed buttons. To handle the additional stress at the button locations and accommodate holes for the spring buttons, the CFRP is locally thickened at these points. Like the readout boxes, the bar boxes are also flushed with dry nitrogen to protect the radiator bars' surfaces, with nitrogen introduced at the mirror end and vented near the lenses.

The hpDIRC consists of 12 bar boxess and 12 readout boxes. The lenses at the bar box end are coupled to a thin window that seals the box, while this window is in turn connected to the prism

in the readout box using an optical interface during final installation. The readout box, including the prism, is compressed against the bar box window to form a tight optical seal. Figure 8.58b is a dimensioned view of the XZ cross-section of the connection between the bar box and the readout box. The 5 mm thick window between the 3-layer lens and the prism represents an initial design, which may be adjusted following further studies of strains and forces acting on the system.

The hpDIRC is positioned radially just inside the Barrel Electromagnetic Calorimeter (EM Calorimeter) and just outside the outer Micro-Pattern Gas Detector (MPGD) within the ePIC detector. Both the bar boxes and the MPGD are supported by the EM Calorimeter via rails mounted on triangular brackets extending radially inward from the calorimeter's inner surface.

Installation: During installation, the bar boxes are placed on a specialized lifting fixture, allowing them to be rotated into their final orientation before being transferred along rails into their designated positions. The readout boxes are supported by an external ring attached to the Hadron Calorimeter via a series of legs. Each readout box is aligned with its corresponding bar box using specialized brackets and rails, which allow the readout box to be slid into position, compressing the optical interface and forming the connection. This rail system also enables the readout boxes to be removed without disturbing the bar boxes if necessary.

Services: Gas and Moisture Control: To maintain a low-moisture environment for the bars, dry nitrogen gas from liquid nitrogen boil-off will flow through each box. The nitrogen gas will be monitored for humidity and filtered through a molecular sieve and mechanical filters to remove particulates. Some of the input N_2 gas will leak from the bar boxes, also helping to keep the bar box slots in the mechanical support structure free of condensation.

Power Supply and Monitoring: Both high- and low-voltage supplies will be provided for each MCP-PMT sensor. A control and monitoring system will be implemented for the readout and bar box sections. The high voltage required for each MCP-PMT will be supplied by commercially available multichannel power supply modules in crates located outside the experiment.

The low-voltage power supplies, which regulate power to the front-end electronics (FEE), need to be placed as close as possible to the detector, in racks dedicated to the hpDIRC system. A modular, multichannel approach—similar to the high-voltage system is planned for the control and monitoring of voltages, currents, and onboard temperatures for all FEE boards. The low voltage levels will range from 1 to 48 V, with currents reaching several Amperes.

Cooling System: The highly integrated FEE design generates a significant amount of heat in the compact readout unit. This heat will be extracted by a water cooling system, and the necessary supply lines are included in the mechanical design of the readout boxes, although further optimization is required.

Environmental Monitoring: Standard commercial devices will monitor environmental parameters such as temperature and humidity at various locations inside the hpDIRC volume to ensure optimal performance and safety.

Calibration, alignment and monitoring: Time Calibration: To achieve the time resolution required for the hpDIRC, it is essential to eliminate time offsets between pixels, which may arise from differences in cable lengths and pixel-to-pixel variations within the photon sensors. A laser monitoring system will be employed to provide channel-by-channel time-zero information, which will be stored in a database. This data will be used to accurately calibrate the photon arrival times

for all pixels.

Optical Calibration and Alignment: The exact positioning of the optical components will be determined during the hpDIRC DIRC installation, using a laser and precise survey marks. The reconstruction of the Cherenkov angle, based on the hit pattern on the MCP-PMT array, depends on the accurate relative positions and orientations of all optical elements, including the photon sensors and their individual pixels.

In-Beam Calibration and Alignment: After installation in the ePIC detector, the alignment of the hpDIRC will be verified using beam data. Samples of muons, pions, kaons, and protons identified by other ePIC sub-detectors or through kinematic fitting will be used to calibrate the hpDIRC's measured Cherenkov angles.

Geometric reconstruction will then be used to calculate the Cherenkov angle per photon for each track and sensor pixel. Any deviation between the measured and expected Cherenkov angles in the calibration samples will be utilized to develop a correction function or multi-dimensional lookup table. This information will be stored in the configuration database to correct for residual misalignment and optimize the performance. A similar procedure was successfully employed in the BaBar DIRC, where a 10% improvement in Cherenkov angle resolution was achieved by applying per-photon corrections based on a dedicated particle calibration sample.

Status and remaining design effort: Preparations for the hpDIRC are progressing in line with the overall project schedule. In the chart shown in Figure 8.59, the top few lines highlight the major milestones of the project from the present day to the start of the experiment and CD-4 approval. Below these milestones is a detailed breakdown of key work packages, including the optical components, readout system, and mechanical design. The hpDIRC is expected to be fully ready in advance of the installation deadline, with a substantial time contingency built into the schedule.

The length of the ePIC barrel necessitates a "light guide section" to direct photons from the active part of the hpDIRC bars to the expansion volume prism, where they are imaged. In the baseline hpDIRC design, shorter bars with the same cross-section as the narrow bars are used, as shown in Figure 8.60a for one module.

Figure 8.60b illustrates an alternative hybrid design, featuring a single wide plate in the light guide section that replaces the narrow bars. The primary motivation for this geometry was potential cost savings, but it also introduced additional opportunities. For instance, the choice of lens type became a question: should it be a set of spherical lenses matching each narrow bar or a single large cylindrical lens? Furthermore, where should the lens be positioned: after the light guide section as in the baseline design, or before the prism expansion volume, or even earlier, between the narrow bars and the plate to initiate the expansion sooner?

Detailed simulation studies of these configurations led to the selection of a geometry featuring a set of spherical 3-layer lenses with an optimized shape, placed before the light-guide plate, as the leading candidate for the alternative design. Figure 8.61 compares the performance of this alternative design (red points) with the baseline design (black points). The wide plate alternative shows a significant performance improvement for particle tracks with polar angles below 80°, comparable performance for polar angles above 100 degrees, and a slight reduction in performance for tracks around 90° and above 145°s. Despite these reductions, the separation power in the lower-performance regions remains above the required 3 standard deviations, making this hybrid design a promising alternative. However, this geometry has not yet been experimentally validated and would require further investigation before it could replace the current baseline design.

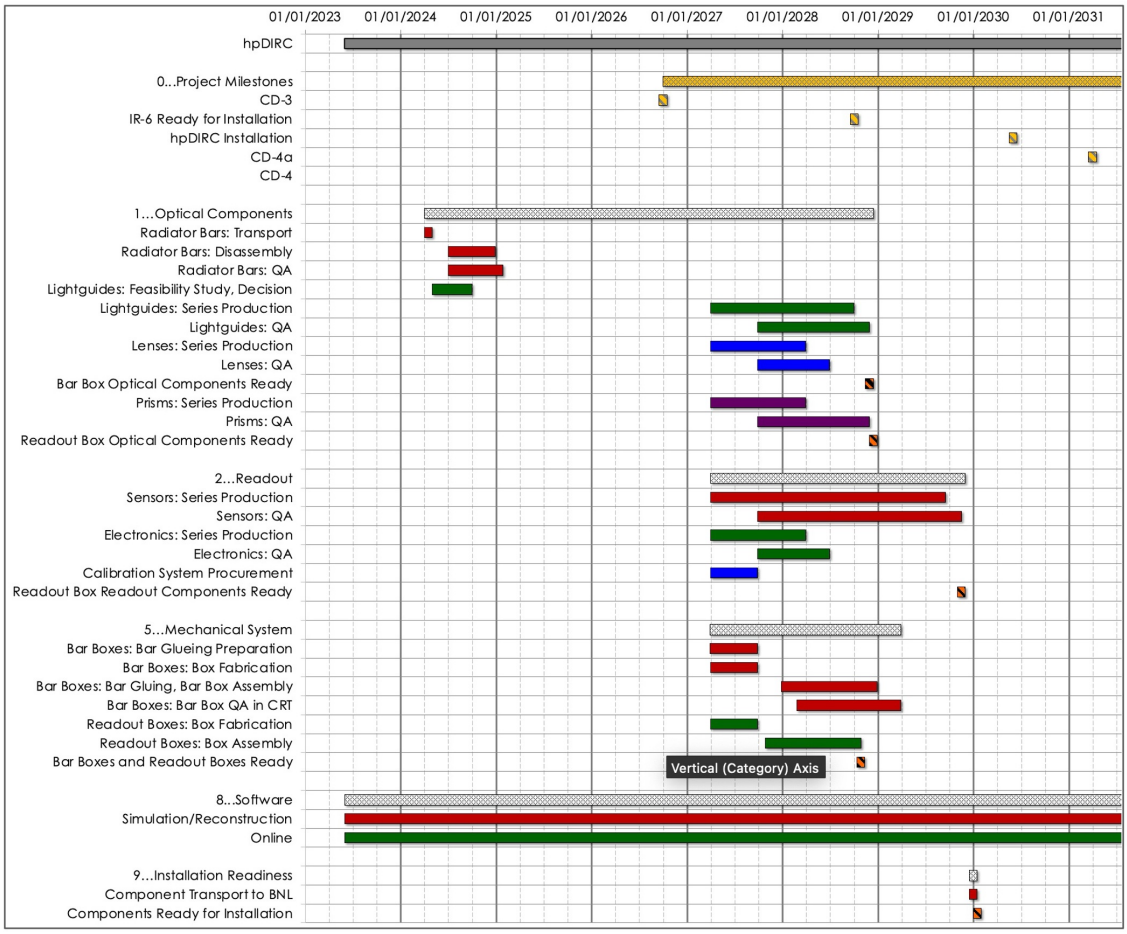

Figure 8.59: ePIC hpDIRC schedule chart alignment with EIC Project schedule

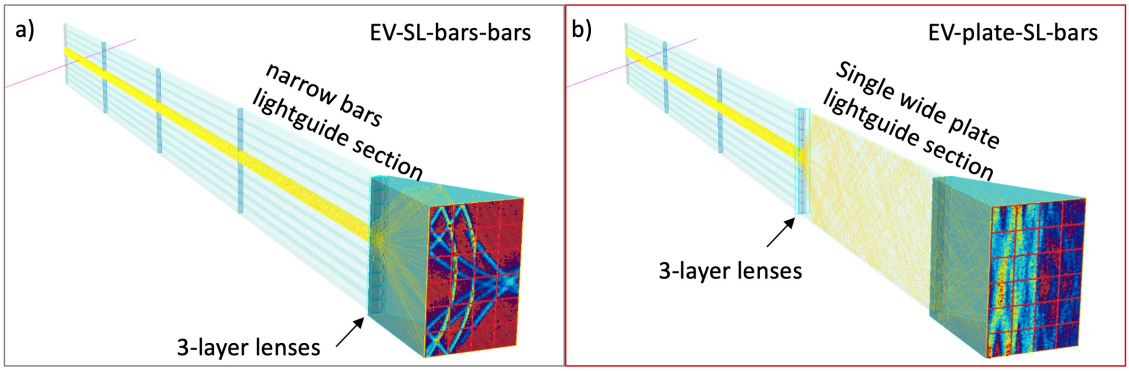

Figure 8.60: Event displays of a single module of the hpDIRC narrow bar baseline design geometry (a) and the narrow bar with wide plate hybrid geometry (b), illustrating an example of the accumulated hit pattern from charged pions, based on the standalone hpDIRC Geant4 simulation package.

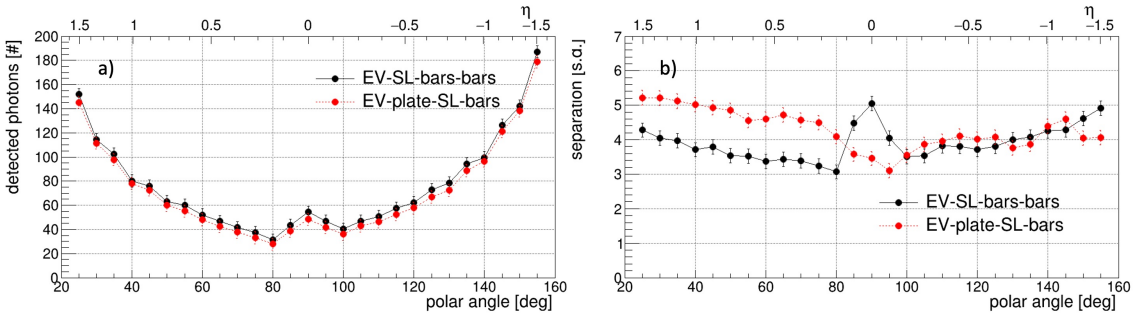

Figure 8.61: Performance comparison between the hpDIRC narrow bar baseline design geometry (black points) and the narrow bar with wide plate hybrid geometry (red points) in case of photon yield (a) for pions and π/K separation power(b) based on a standalone Geant4 simulation for particles with a momentum of 6 GeV/c.

Remaining R&D effort: The primary objectives of the remaining hpDIRC R&D are to validate new, untested components, ensure their successful integration into the hpDIRC system, and to optimize the final design. Ultimately, the goal is to achieve a validated, cost-efficient hpDIRC design for the ePIC detector, which will be demonstrated through a vertical-slice prototype in the Cosmic Ray Telescope (CRT) setup. Several critical aspects of the hpDIRC design still require thorough study and verification to guarantee the necessary performance, mitigate risks, and explore new opportunities.

Additional R&D projects with a direct impact on the hpDIRC include eRD109 (focused on readout and ASIC designs) and eRD110 (focused on photosensors). The development of compact readout electronics for fast single-photon detection, using high-density sensors, must be completed and integrated into the hpDIRC prototype to validate the performance of a cost-optimized design for particle identification (PID).

The final hpDIRC prototype will assess the optimized sensor arrangement and explore a potential new focusing approach within a hybrid design, as shown in Fig. **??**, which combines a narrow bar with a wide plate. This configuration offers significant cost-reduction potential, but it has not yet undergone experimental testing. Additionally, the reuse of BaBar DIRC bars, another key cost-saving measure, is currently being explored with support from Jefferson Lab and the EIC Project, as discussed above.

Environmental, Safety and Health (ES&H) aspects The hpDIRC system is designed to operate without the use of any flammable gases or cryogenic liquids, which eliminates the risks associated with these hazardous substances. Both the bar boxes and readout boxes will be purged using boil-off dry nitrogen, which will flow at a rate of a few liters per hour per box. This method ensures that the environment inside the boxes remains dry and free from contaminants, contributing to the system's safety and reliability.

In terms of electrical hazards, the sensors employed in the hpDIRC require high voltages, reaching up to 2.5 kV. To prevent the risk of electrical shock, the high-voltage (HV) connections will be completely inaccessible during normal operation. Furthermore, the HV module will be keyed off, ensuring that only trained personnel will be allowed to operate it, providing an additional layer of safety in the system's design.

The hpDIRC will also utilize a class 3B Helium-Cadmium (HeCd) laser pulser for the calibration of

Figure 8.62: Photos of available setups developed during the hpDIRC R&D program that will be used for future QA of 3-layer lenses with laser setup at ODU (a), bars and other optics at Jefferson Lab (b) and readout chain including sensors and electronics and other hpDIRC components in hpDIRC prototype at CRT at SBU (c).

sensors and electronics. Since lasers pose a radiation hazard, special precautions will be taken: the laser will be fully enclosed within optical fibers to prevent exposure, and only trained personnel will be authorized to operate the laser.

For the cooling of the readout electronics, a chilled liquid will be used, though the specific details of the liquid have yet to be determined. To avoid the risk of a chemical leak, the cooling liquid will circulate at sub-atmospheric pressure, which helps prevent potential leaks.

The entire hpDIRC system will comply with all applicable Environment, Safety, and Data (ES&D) standards and Occupational Safety and Health Administration (OSHA) regulations. This commitment to compliance ensures that the system adheres to the highest safety protocols, protecting both the equipment and the personnel involved in its operation.

Quality Assessment (QA planning: The quality assurance (QA) plans for the hpDIRC components and modules prior to construction are centered around a combination of process control at the vendor sites and extensive in-laboratory measurements. The radiator bars and light guides will undergo vendor-provided QA to assess their mechanical properties. Following this, a laser scanning system at JLab will be used to monitor the internal photon transport efficiency of either the repurposed BaBar DIRC bars or the newly produced DIRC bars. This will directly ensure that the optical performance of the bars meets the ePIC DIRC standards.

For the sensors and electronics testing, laser pulser systems will be deployed at CUA, JLab, or USC (to be determined) to perform measurements including gain, quantum efficiency, collection efficiency, and dark count rate. These tests will verify the operational integrity and performance of the sensors.

The lenses will be evaluated at the laser laboratory at ODU, where the shape of the focal plane will be carefully analyzed to ensure proper optical alignment and focusing. Prisms will be subjected to vendor-provided QA, followed by further checks at WSU to confirm their specifications. Similarly, the bar boxes and prism boxes will undergo QA at the vendor sites, with additional testing and validation at SBU.

Once the DIRC modules are fully assembled, including the coupling of the bar box to the readout box (a vertical slice), the Cosmic Ray Telescope at SBU will be used for testing. This will ensure that the assembled DIRC modules function as intended before final integration.

After installation of the DIRC module in ePIC, a picosecond laser pulser calibration system will be employed to fine-tune the system. Cameras will also be used to continuously monitor the optical coupling between the sensors, prisms, and lenses, ensuring that the entire optical system is correctly aligned and operational throughout the experiment. These comprehensive QA measures are critical to ensuring the high-performance operation of the hpDIRC system in the ePIC experiment.

Construction and assembly planning: In the current plan for the ePIC hpDIRC construction, the assembly will take place at three different locations. The bar boxes will be assembled at Jefferson Lab, utilizing the existing infrastructure developed for the disassembly of the BaBar bar boxes and the quality assurance of the bars. Short bars will be glued together to form ten long bars per bar box, with 3-layer lenses attached, and will then be mounted inside their carbon fiber shells. The readout boxes will be assembled at Wayne State University, incorporating newly acquired expansion volume prisms, as well as readout sensors and electronics previously validated at USC. Once both the bar boxes and readout boxes are assembled, they will be transported to BNL for initial alignment and matching before their final installation into the ePIC detector.

Collaborators and their role, resources, and workforce: The hpDIRC system collaboration (DSC) consists of a core group of institutions that have long-standing experience with DIRC counters, having contributed to the BaBar, GlueX, PANDA projects, and the EIC DIRC R&D program. Many of these groups have been involved in these efforts since 2011, bringing a wealth of expertise to the development of the hpDIRC system for the ePIC detector. This collaborative network is expected to expand, with few expressions of interest (EoIs) from various institutions interested in contributing to different aspects of the project closer towards constriction. The process of aligning expertise and interest with system priorities is already underway, ensuring that the work is distributed efficiently.

Among the key collaborators, Jefferson Lab together with CUA have been handling the transport and disassembly of BaBar DIRC bar boxes and validating the quality of the disassembled bars. They will continue this effort with the optional quality assurance (QA) of new bars or plates for the light guide section. Jefferson lab has expressed interest in continuing this support with an extension to the gluing of bars and lenses and final assembly of the bar boxes

Stony Brook University (SBU) is preparing an important QA tool with their Cosmic Ray Telescope. The initial plan is to use it for incremental integration of new components into the hpDIRC prototype like disassembled BaBar bars, sensors, and electronics, but eventually, it will be used for validation of full bar box modules. Old Dominion University (ODU) will contribute by evaluating the focal plane of the lenses and conducting QA procedures, ensuring the optical components meet the required standards.

On the sensor side, USC will handle QA and tests related to the readout chain, ensuring the sensors operate within specified parameters. Wayne State University (WSU) will oversee the assembly

and QA of the readout boxes, another critical component of the system. Finally, institutions like CUA, GSI, William & Mary, and WSU are heavily involved in simulation and reconstruction efforts, which are essential for optimizing the performance and integration of the hpDIRC system into the overall ePIC detector framework.

This broad collaboration, with specific responsibilities assigned to various expert groups, ensures that all components of the hpDIRC system are developed and tested by specialists, assuming more junior workforce like graduate students and postdoctoral researchers can be added through external grants.

Risks and mitigation strategy: The disassembly of the BaBar bar boxes is in an advanced stage of preparation, with the process set to begin soon. Immediately after disassembly, the quality of the legacy BaBar bars will be evaluated to determine their suitability for use in the ePIC hpDIRC. A decision on their usability is expected by early Summer 2025. If new radiator bars are required, a vendor will need to be identified, and the procurement and production process initiated. Based on the current production timeline for PANDA Barrel DIRC radiator bars, the production of new bars for ePIC is still possible within the project schedule.

Both the baseline commercial MCP-PMTs and HRPPDs require testing and evaluation, which are being prepared by different groups. These tests will be conducted in parallel to ensure the necessary sensors are available within the required time before installation. The development of ASIC-based readout electronics is being coordinated by the EIC project, with two parallel solutions under consideration.

Additional Material Add text here.

8.3.4.4 The dual radiator RICH

Requirements The dual radiator Ring Imaging Cherenkov (dRICH) detector is part of the particle identification system in the foward (ion-side) end-cap of the ePIC detector and complements the forward time-of-flight system and calorimetry, see Fig. **??**. The dRICH has to provide acceptance in the pseudo-rapidity range defined by the ePIC beam pipe and the barrel detector and to operate within the limited envelope allowed by the rest of the compact and hermetic ePIC detector. Distinctive features of the detector are: use of aerogel and gas radiators to extend the covered momentum range, usage of solid-state photomultiplier (SiPM) to ensure single photon detection capability in high and not-uniform magnetic field, non-conventional optics with curved active surfaces and compact readout electronics to fit into ePIC.

Requirements from physics: The dRICH is required to provide continuous hadron identification from $\sim$ 3 GeV/c to $\sim$ 50 GeV/c, and to supplement electron and positron identification from a few hundred MeV/c up to about 15 GeV/c. Such an extended momentum range imposes the use of two radiators, gas and aerogel, with a common imaging system to ensure compactness and cost-effectiveness. The radiator gas must ensure π/K separation at 3-σ level up to 50 GeV/c in the most forward region, namely for $\eta > 2$. The aerogel radiator must cover the intermediate momentum interval, bridging the upper limit of the time-of-flight ($\approx$ 2.5 GeV/c) to the Cherenkov threshold of the dRICH gas ($\approx$ 12 GeV/c). These requirements dictate the prescriptions on the refractive index and the radiator chromaticity in the sensitivity region of the photosensors. The dRICH has to provide open acceptance in the ePIC forward pseudo-rapidity range $1.5 < \eta < 3.5$. To provide proper light focalization within the due volume, the dRICH active area is located behind the shadow of the barrel detector and its support ring, close to the MARCO solenoid coils. In this region, see Fig. **??**, the $\approx 1T$ strong and not-uniform ePIC magnetic field imposes the use of unprecedented detectors (SiPM).

Requirements from Radiation Hardness: The radiation sensitive components (sensor and front-end electronics) of the dRICH detector are concentrated in a region of moderate radiation level, below O(10^{11}) cm^{-2} n_{eq} of maximum integrated fluence where n_{eq} is a 1-MeV neutron equivalent particle, see Fig. **??**. Close to the beam line, where the integrated dose can reach a value of 15 krad, only radiation tolerant materials reside like silica aerogel [59].

Requirements from Data Rates: The SiPM sensor features an intrinsic significant dark count rate, currently of the order of 50 kHz/mm^2 at room temperature, that indefinitely increases with the radiation damage. To mitigate this effect, the dRICH sensors are operated at low temperature (less than -30 C) and regularly annealed at high temperature (up to 150 C), in order to never exceed a maximum 300 kHz dark rate per channel. The latter value corresponds to a conservative limit taken to preserve the detector performance requirements for Physics and it is supported by present simulation studies that confirm the particle-identification capabilities of dRICH are unaffected.

Justification The specifications outlined above largely define the main technological choices: the momentum range dictates radiator refractive indexes that can be reliably met only by aerogel and gas, while the ePIC environment, space and magnetic field, imposes sensor characteristics that can only be met by SiPM.

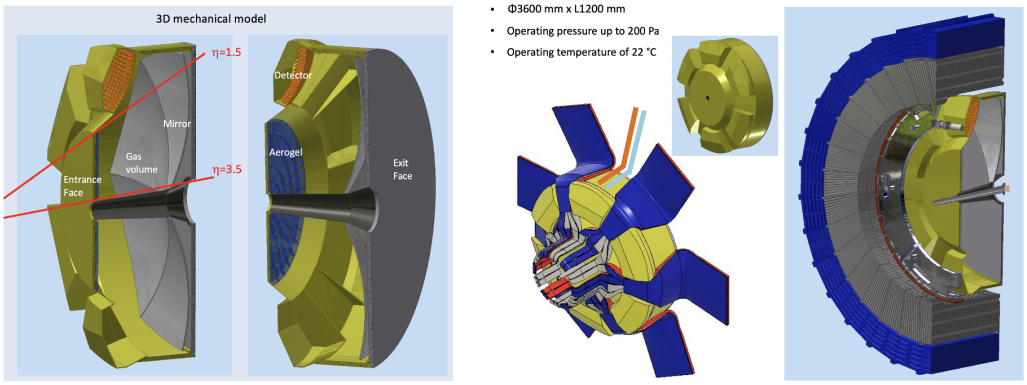

Figure 8.63: (Left) dRICH detector model with highlighted the major components. (Right) dRICH inside the ePIC services lines at the barrel HCAL end point.

Device concept and technological choice: The dRICH is a ring-shaped detector fitting inside the ePIC forward endcap, see Fig. 8.63. The essential components are a layer of aerogel radiator, a volume of gas radiator, and an array of mirrors focalising the Cherenkov light into compact areas instrumented with photo-sensors. The detector is designed in a modular way, with 6 sectors around the beam line of equivalent mirror set and detection area.

The aerogel radiator is a amorphous solid network of SiO_2 nanocrystals whose density regulates the refractive index and chromaticity [3]. The use of silica aerogel for RICH detectors is well established. It is available with refractive indices in the range 1.006–1.08 in between gases and liquids. The current manufacturing methods succeeded in improving the attenuation length Λ (λ = 400 nm) from 20 mm (aerogel used in HERMES) to 50 mm (aerogel for CLAS12 and BELLE-II). The selected aerogel radiator has refractive index n = 1.026 at $\lambda = 400\,nm$. The chromatic dispersion has been measured during the R&D phase to be $dn/d\lambda = 6 \cdot 10^{-6}\,nm^{-1}$ at 400 nm wavelength. Aerogel is typically produced in tiles of few cm thickness: in order to minimize edge effect, the dRICH tile side should be greater than 18 cm, approaching the word record value of 20 cm. The shape and surface flatness of the tiles are important parameters to consider for ensuring optimal PID performance. Typically, due to the fabrication process, aerogel tiles exhibit a slight meniscus shape. Measurements taken during the R&D phase on aerogel samples provided by Aerogel Factory Co. Ltd revealed deviations from the ideal parallelepiped shape by a few tenths of a millimeter, along with a thickness variation between the center and the edges of a similar magnitude. Based on the measurements conducted so far, this deviation from the ideal shape does not impact PID performance. Additionally, the manufacturer, Aerogel Factory Ltd (Chiba, JP), has confirmed that improvements in both flatness and thickness uniformity are feasible.

The selected reference gas radiator is hexafluoroethane (C_2F_6) (Appendix xxx), which matches the requirements being characterized by refractive index n = 1.00086 and excellent chromatic dispersion $dn/d\lambda = 0.2 \cdot 10^{-6}\,nm^{-1}$ at light wavelength $\lambda = 350\,nm$ [60].

The selected refractive indexes dictates a minimum thickness of 4 cm for the aerogel and O(1) m for the gas in order to ensure enough photon yield. Mirror focalisation is necessary to minimise the consequent uncertainty on the Cherenkov photon emission point. Being inside the detector acceptance, the mirror structure is made of carbon fiber reinforced polymer (CFRP) to ensure the necessary stiffness while being light. In order to preserve the Cherenkov angle information the mirror surface should have excellent optical quality, i.e. few nm roughness and better than 0.2 mrad angular precision (reflecting in a point-like image with more than 90% of the light intensity concen-

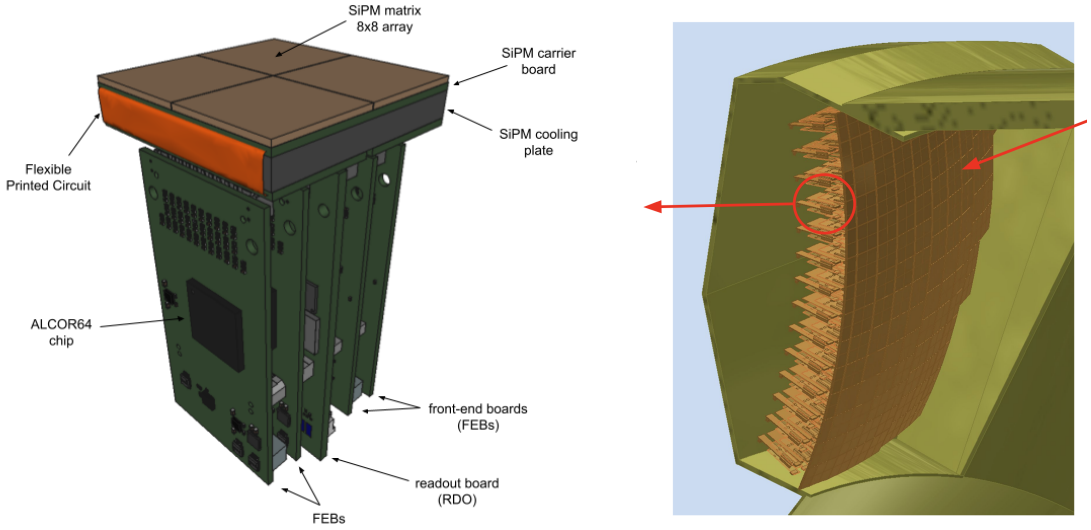

Figure 8.64: (Left) CAD model of the dRICH photodetector unit (PDU) module with its major components. (Right) dRICH detector box model with 208 PDUs forming a curved active surface.

trated in a disk smaller than 2.5 mm). The single mirror dimension is limited to a ≈ 1 m maximum diagonal when accounting for realistic forming mandrel and coating chamber dimensions. In the dRICH mirror array, the radius of curvature should be replicated within 1% of the nominal value.

The dRICH photon detector surface is shaped over a sphere of radius ~ 110 cm to best approach the 3D focal surface of the mirror array. The Silicon Photomultiplier (SiPM) sensor technology is selected for the photon detector. It ensures superior single-photon counting capability inside the ePIC magnetic field and compact dimensions suitable for tessellating a shaped active surface. The single SiPM sensor has a $3 \times 3\,\mathrm{mm}^2$ area to provide the necessary spatial resolution with an intrinsic time resolution better than 150 ps. The SiPM sensors are grouped into 8×8 arrays in a buttable arrangement to minimize the dead area, which are eventually mounted side-by-side to form a 16×16 array defining the 256 channels of the dRICH photodetector unit (PDU). The selected front-end ASIC is ALCOR, a 64-channel chip with coupling and rate capability optimized for SiPMs, and a ToT architecture with better than 50 ps LSB [1] resolution in order the SiPM-ALCOR readout chain could achieve an overall time resolution better than 200 ps RMS. To minimize the volume within the dRICH envelope and to maximize the active area, the photodetector is organized in compact photodetector units (PDU). The PDU integrates 256 SiPM channels with the ALCOR TDC readout provided by four front-end boards (FEB), one readout board (RDO) to interface with the ePIC data aquisition (DAQ) and detector control (DCS) systems. In addition, the PDU is designed to allow sub-zero cooling of the SiPMs as well as high-temperature annealing operations. Figure 8.64 (left) shows the conceptual design of the PDU and its main components. The present dimensions of the PDU concept are approximately $52 \times 52 \times 140\,\mathrm{mm}^3$.

Figure 8.65: (Left) dRICH aerogel model. (Right) dRICH mirror model [placeholder].

[1] Least Significant Bit

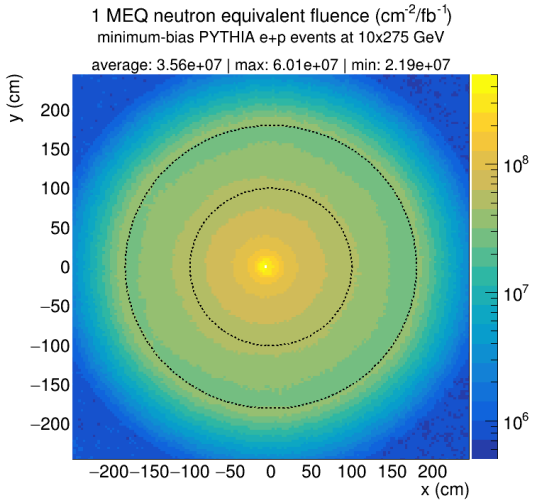

Figure 8.66: Transverse map of the expected 1-MeV equivalent neutron fluence per 1 fb^{-1} of integrated luminosity in e+p interactions at the maximum EIC center-of-mass energy at the location of the dRICH photodetector ($210 < z < 260$ cm). The average, maximum and minimum values within the region of the dRICH photodetector ($100 < R < 180$ cm, indicated by the dashed lines) are reported.

Subsystem description:

General device description:
Because at ePIC the electron and hadron beam collide at an angle of 25 mrad, the common beam pipe cross-section is off-axis at the dRICH location and increasing in area with the distance from IP, imposing an asymmetric layout of the inner components, see Fig. 8.65. The aerogel wall is composed by five rings of tiles, each shaped in order to fit inside a 0.2 mm thin aluminum supporting structure. In each sector, focalization is provided by a compound of five mirrors covering a total area of about 2 m^2 with an optimized radius of curvature around 2200 mm. Six independent spherical active surfaces with curvature radius around 1100 mm, each made of 208 PDUs for a total of 53k readout channels, are mounted inside detector-boxes that provide thermal insulation, cooling for the electronics and connections to the services. Given the gas radiator open volume, the Cherenkov photons can be reflected into different detectors depending on the parent charged particle kinematics. The aerogel and photo-detector are separated from the radiator gas by transparent septa, and immersed in a dry (e.g. purged N_2) atmosphere to minimize contaminant absorption and prevent moisture formation. The mirrors are supported by a light carbon fiber structure that is mechanically decoupled from the vessel and allows fine alignment adjustments by means of pizezo-electric motors.

Sensors:
The silicon photomultiplier (SiPM) [61, 62] is chosen as the sensor technology for the dRICH photodetector. The main baseline specifications demand sensors with a 3×3 mm^2 single-channel active area, single photon detection over a broad spectral range from 300 to 900 nm and very high overall photodetection efficiency $> 40\%$ at the peak sensitivity wavelength $400 < \lambda_{peak} < 450$ nm (see Table 8.22 in Additional Material for the full list of the baseline parameters and specifications of the SiPM sensor devices for the dRICH photodetector). SiPMs fulfil the dRICH requirements being cheap and versatile devices with excellent

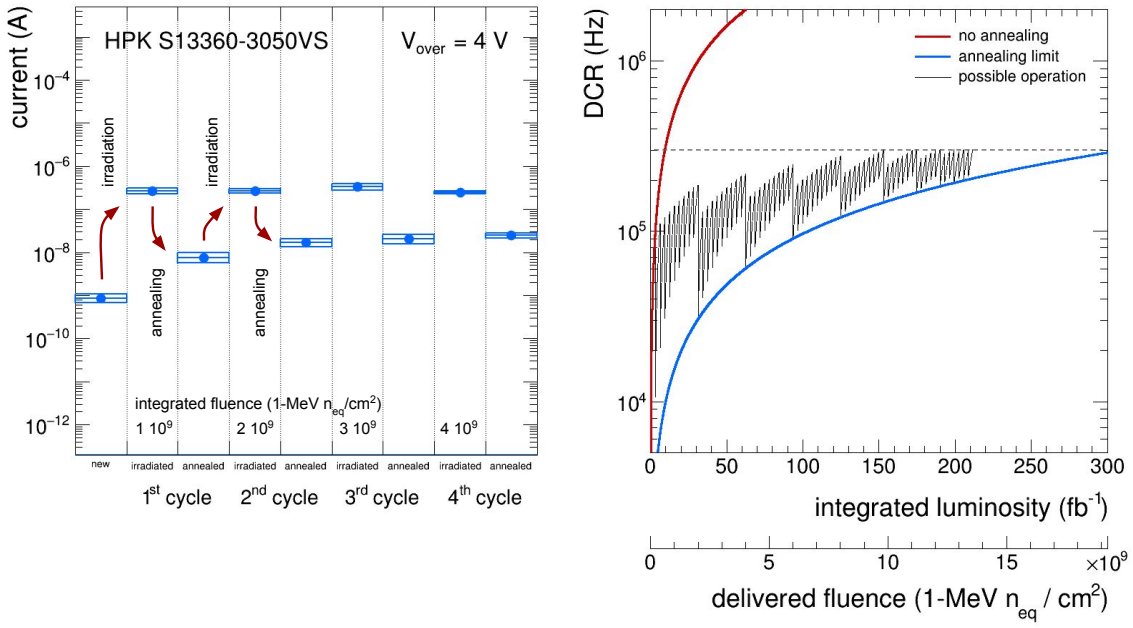

Figure 8.67: (Left) Dark current measurements on sample SiPM sensors for the studies of repeated irradiation-annealing . (Right) Projected increase of the DCR of SiPM as a function of the integrated luminosity (delivered fluence). The "no annealing" and the "annealing limit" curves show the limits of possible operations. The dashed line indicate the desired maximum DCR threshold.

photodetection efficiency (PDE) and time resolution. Their single-photon performance is unaffected by high magnetic fields [63, 64], which makes SiPM the only photosensor that can efficiently operate in the field configuration at the dRICH photodetector location in the ePIC experiment, see Fig. **??**. SiPM sensors on the other hand have very high dark count rates (DCR) and are not radiation tolerant. The DCR in SiPM is mostly of thermal origin and it reduces significantly by lowering the SiPM temperature, typically halving every 7-10°C in new sensors [65]. Radiation damage in SiPM is mainly due to displacement damage in silicon, which causes a significant DCR increase and reduces the effectiveness of cooling [66]. At the moderate radiation levels expected at the location in the dRICH, no significant change in the SiPM parameters (PDE, gain, quenching resistor R_{quench}, pixel capacitance C_{pixel}, breakdown voltage V_{break}) is observed [67]. SiPM cooling is important to keep the DCR low and it becomes crucial after radiation damage [68], as the increase in DCR would be such to make SiPM unusable as single-photon detectors, otherwise. In the dRICH, the SiPMs will be operated at subzero temperature of T = -30°C, or lower. A cooling block is placed in thermal contact with the back-side of the printed-circuit board hosting the SiPMs (carrier board). Cooling fluid in the cooling block will be circulated through a closed loop by a dynamic temperature control system circulating thermostat to regulate and maintain the SiPMs at low temperature The circulating thermostat system will also be used to circulate fluid at high temperature (T = 100°C, or higher) to provide heat during SiPM annealing. Therefore a low-viscosity silicone fluid is particularly suitable for cold and heat transfer. The radiation damage on SiPMs increases moderately with the integrated luminosity. At the location of the dRICH photodetector a maximum (average) fluence of Φ_{eq} = 6.0 (3.6) 10^7 cm^{-2}/fb^{-1} 1-MeV equivalent neutrons (n_{eq} in the following) is expected from e+p interactions at the

highest center-of-mass energy of the EIC (Figure 8.66). Beam-induced background from proton beam-gas events at 35 kHz are expected contribute with a maximum (average) of Φ_{eq} = 3.7 (1.6) 10^6 cm^{-2}/fb^{-1} n_{eq} at the location of the dRICH photodetector, bringing the total maximum (average) expected radiation damage to Φ_{eq} = 6.4 (3.7) 10^7 cm^{-2}/fb^{-1} n_{eq}. As shown by the "no annealing" curve in Figure 8.67 (right), the SiPM DCR is expected to increase with the integrated luminosity at a rate of 31.8 (18.6) kHz/fb^{-1}, reaching a DCR of 300 kHz after an integrated luminosity of approximately 9.5 (16.1) fb^{-1}. These values are based on measurements performed on Hamamatsu S13360-3050 sensors operated at V_{over} = 4 V at T = -30°C., more details in Additional Material.

Annealing of SiPMs can be achieved exploiting the Joule effect []. When a SiPM is forward biased, the microcells composing the device behave as directly polarized diodes connected to their quenching resistors. The current flowing through the resistors eventually heat up the entirety of the sensor. In the dRICH, SiPM annealing will be performed up to temperatures of T = 150°C in "forward-bias mode". The actual annealing temperature and annealing time will be tuned during detector operations according to the DCR reduction needs and available experiment down time. During the R&D phase it was shown that the "forward-bias mode" approach can cure approximately 97% of the radiation damage. It is therefore expected that a residual irreducible radiation damage (residual DCR) will build up during the dRICH lifetime. As shown by the "annealing limit" curve in Figure 8.67 (right), the SiPM residual DCR is expected to increase with the integrated luminosity at a rate of 950 (560) Hz/fb^{-1}, reaching a residual DCR of 300 kHz after an integrated luminosity of approximately 310 (530) fb^{-1}. In the dRICH, SiPM annealing will be performed with a technical implementation of the "forward-bias mode" which needs to be integrated both into the SiPM power-supply system, the front-end and control electronics, cooling and the temperature monitoring system. As previously mentioned, the circulating thermostat system used for low-temperature operation of the SiPM will be operated in heating mode to warm up the SiPM cooling plate during high-temperature annealing. This will allow one to perform the "forward-bias annealing" by delivering a lower current to the SiPM, as as fraction of the heating power is delivered by fluid. Nonetheless the required power to perform "forward-bias annealing" at once over the full dRICH detector is excessively large. Therefore annealing operations will be segmented in space and time across the dRICH detector and will be performed during periods with no Physics beam and depending on the DCR needs. As can be see from Figure 8.66 the sensors closer to the beam line will experience a radiation damage almost a factor 3 larger than those father from the beam line and will likely require a more frequent annealing. The "possible operation" curve in Figure 8.67 (right) shows a potential scenario for the DCR evolution for SiPM sensors closer to beam pipe (worst case). This is based on an operation model where more frequent (every $\sim$ 3 fb^{-1}) softer annealing cycles at lower temperature and/or of shorter duration, delivering a DCR reduction of 10×, are interleave by less frequent (every $\sim$ 30 fb^{-1}) full annealing cycles to reduce DCR as much a possible. A limit in the operation scenario is reached when the annealing is not capable to keep the DCR below the desired threshold or when the annealing frequency become too high. As it can be seen from Figure 8.67 (right), beyond an integrated luminosity of $\sim$ 200 fb^{-1} to keep the DCR below the 300 kHz threshold requires to perform full annealing cycles every $\sim$ 5 fb^{-1}, which is not obviously a practical operation scenario anymore. Some or all of the SiPM sensors might be needed to be replaced at that stage with new ones or with SiPM sensors of improved performance and radiation hardness in a future upgrade of the dRICH photodetector. One has to keep in mind though that the 300 kHz limit is a conservative value that is connected to the present level of dRICH reconstruction and could be relaxed in future. Moreover, the model shown in Figure 8.67 (right) is based on measurement on Hamamatsu S13360-3050 sensors operated at V_{over} = 4 V in a climatic chamber at T = -30°C. Possible

SiPM operation in ePIC at a lower V_{over} of 3 V and at a lower T of $-40°C$ will allow one to achieve lower DCR overall.

FEE:
The ALCOR (A Low Power Chip for Optical Sensor Readout) ASIC, developed by the electronics laboratory of INFN Torino, is the baseline option for the readout of the dRICH SiPM sensors. The architecture of ALCOR and its key specifications are described in Section **??***Readout Electronics and Data Acquisition*, here only some specific EIC-driven features are discussed as well as the integration of the ALCOR ASIC in the dRICH front-end electronics. The main goal of ALCOR is to provide single-photon time tagging of the incoming signals, while being able to cope with the SiPMs inherently high DCR: a maximum DCR value of 300 kHz/ch is expected before an annealing cycle is performed. A good time resolution, better than 200 ps RMS, is required to perform DCR suppression via time gating at both hardware and software levels. A programmable hardware shutter, implemented inside the digital logic of ALCOR, can be enabled to filter out-of-time DCR and provide a significant bandwidth reduction to the system. The time window of interest is controlled off-chip by the RDO FPGA and can be adjusted using in-pixel programmable delays to compensate timing offsets among the 64 channels. With a time window of approximately 2-3 ns, considering that the EIC bunch crossing period is about 10.15 ns, data can be reduced by a factor of 3 or 5. One important point is that the shutter will be needed only when DCR becomes higher due to SiPMs taking radiation damage over time. Therefore, the first period of ePIC data taking can be used to optimize the shutter calibration. The ASIC will be integrated inside a BGA package, providing a compact and robust solution to be assembled on the FEB. A 16×16 mm^2 flip-chip ball grid array (FC-BGA), with 256 balls and 1 mm ball pitch, is the option chosen for the ASIC packaging since it offers more interconnections and better performance w.r.t. standard packaging techniques and matches well with the pixel-matrix geometry of the ALCOR ASIC. A 3D model of the FEB is shown in Fig. 8.68. Each FEB hosts one ALCOR BGA device and several components to ensure a stable and safe operation of the system. Linear regulators are employed to provide clean power supplies to the chip and are coupled to I2C interface and current monitors to control the regulators and prevent potential damage from over-current conditions. The FEB incorporates a dedicated PCB section for SiPMs bias voltage routing and also a circuit to enable the SiPM forward-biasing when annealing cycles are carried out. AC-coupling between the SiPM sensors and ALCOR inputs has been chosen to isolate them when the SiPMs are operated in forward bias. Several connectors, mounted on the FEB, provide the interface towards the RDO and the other FEB boards of the same PDU as well as towards the SiPMs carrier board and the LV-HV services.

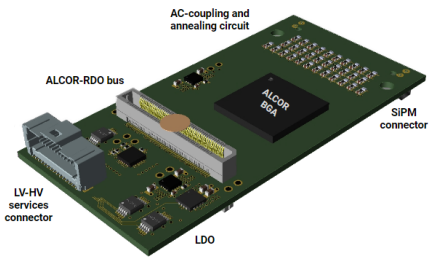

Figure 8.68: 3D model of the dRICH FEB.

Other components:
The radiator gas in the RICH vessel is controlled by the gas radiator system (Fig. 8.69). Its main tasks are, during detector operation, (i) providing well controlled pressure conditions

in the 12 m^3 RICH vessel to avoid relevant pressure difference at the vessel walls and at the fused silica windows; (ii) removing oxygen and water vapor contaminates, in order to prevent building up impurities due to air leaks entering the gas system; (iii) performing detector vessel filling with hexafluoroethane before a data taking period and radiator gas recovery at the end of the period; the filling/recovery is from/to the storage tank. The main components of the radiator gas system are two oil-free compressors, working in parallel, which continuously extracts gas from the vessel at constant rate in order to ensure the gas circulation, a pressure sensor installed on top of the radiator vessel for continuous monitoring of the internal relative pressure and to dictate the opening level of a flow control valve on the input line, adjusting the opening so to preserve the relative pressure inside the vessel. Oxygen and water vapor traces are removed by filtering cartridges with molecular sieves and Cu-catalyst, which are permanently in series in the circulation system. The vessel is flushed with nitrogen during the shutdown periods. Nitrogen and hexafluoroethane separation during filling and recovery is under study and two options can be envisaged: (i) the use of osmosis via dedicated membranes or (ii) via a two-step procedure: replacing nitrogen with carbon dioxide and then performing distillation at -35^oC. Hexafluoroethane is a greenhouse gas and, therefore, the residual C_2F_6 present in the nitrogen/carbon dioxide cannot be vent out: it must be collected and trapped for disposal with a dedicated recovery system. The control of the whole radiator gas system is performed via a Programmable Logic Controller (PLC). More details are provided in Additional Material.

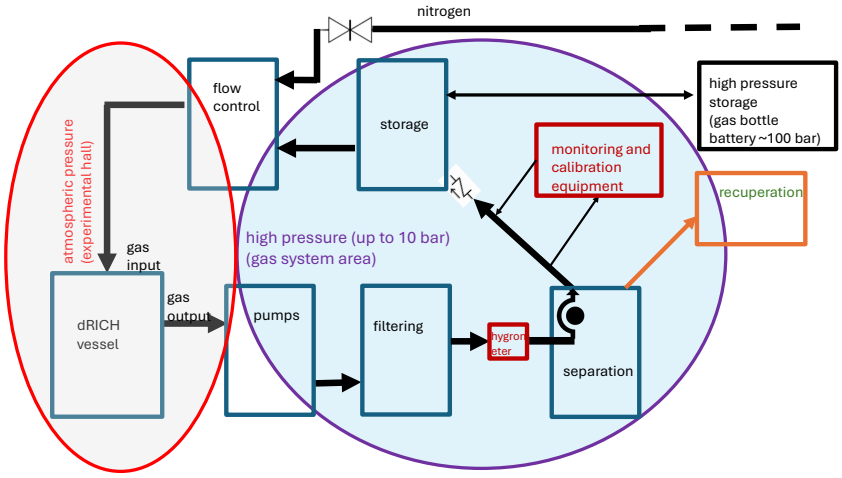

Figure 8.69: Block diagram of the dRICH gas system [graphically, a preliminary version].

Performance

For each recorded dRICH hit, the photon path is reconstructed taking into account the charged particle trajectory and the focalising optics of the detector, in order to provide an estimate of the Cherenkov angle at the emission point. The combined information of all the Cherenkov photons associated to a charged particle concur to a precise determination of its velocity (beta) and, knowing the momentum from the ePIC spectrometer, its mass. The dRICH model is part of the ePIC simulation framework and allows complete performance studies taking into account quality of the track reconstruction, bent trajectories (by magnetic field) and multiple scattering. To bypass the complexity of such a framework, some specific study can be anyway performed with private or simplified simulation chain. The laboratory characterization and the numerous test-beams have

provided detailed inputs for modeling in a realistic way the single components and global detector response. In the dRICH, the contributions to the single-photon (SPE) angular resolution have a different weight depending on the radiator. The dRICH has been designed in order to keep most of the contributions to the SPE angle resolution below 0.5 mrad, see Fig. 8.70, a value dictated by the tiny Cherenkov angle difference between pions and kaons at 50 GeV/c in the radiator gas. The single SiPM readout channel has been limited to 3×3 mm^2 area. The MARCO coils and the dRICH position has been optimized in order to minimize the bending inside the radiator gas volume. The tracking resolution is assumed to cope with the same constrain. Note that combining N photons the angular precision scale with a maximum $N^{-1/2}$ factor only in case of a completely uncorrelated information, a condition that is not valid for the bending and tracking contributions. The uncertainty on the emission point is not an issue for a few cm layer of aerogel, but is critical for a 1 m long gas volume, expecially within the limited space available in ePIC for the optics: this remains the major contribution to the SPE resolution of the radiator gas despite the mirror focalization and the curved dRICH detector surface. As the present model assumes a single radius for the dRICH mirros, optimized for the forward rapidity region to boost the high-momentum reach, the resolution worsens with the polar angle increase. This is not a problem, because the average particle momentum decrease as well loosing the performance requirement. The chromatic error is well under control for gas but is the largest contribution to the angular resolution for the aerogel. This derives from the intrinsic nature of the radiator in conjunction with the quantum efficiency characteristic of the photosensor. The chromatic uncertainty limits the aerogel momentum reach to something above 15 GeV/c, a value well above the Cherenkov threshold of kaons in gas, high enough to provide the wanted overlap between the measured ranges of the two radiators.

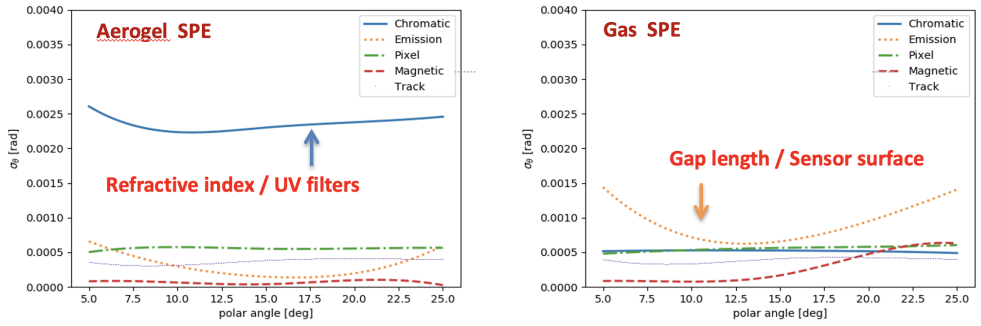

Figure 8.70: (Left) Contributions to the single-photon angular resolution for aerogel. (Right) Contributions to the single-photon angular resolution for radiator gas.

The number of emitted photons varies with the pseudo-rapidity due to the different path of the particle within the radiators. The mean number of recorded photons is about 18 for the radiator gas and 12 for the aerogel for a particle with momentum well above the Cherenkov threshold. In average, few charged particles per event are expected to hit the detector, see left panel of Fig. 8.71. With a proper pattern recogition and photon path reconstruction, the information of the two radiators can be combined to extend the momentum coverage of ePIC PID from the TOF $\approx$ 2.5 GeV/c upper momentum limit to above 50 GeV/c, see central panel of Fig. 8.71. In the forward direction with optimized focalization, an identification efficiency greater than 95 % at a corresponding 5 % percent mis-identification probability, is achieved, see right panel of Fig. 8.71. As expected from the resolution study, the momentum reach is reduced with the pseudo-rapidity, in accordance wth the kinemartics of the particles expected from physics reactions.

Implementation

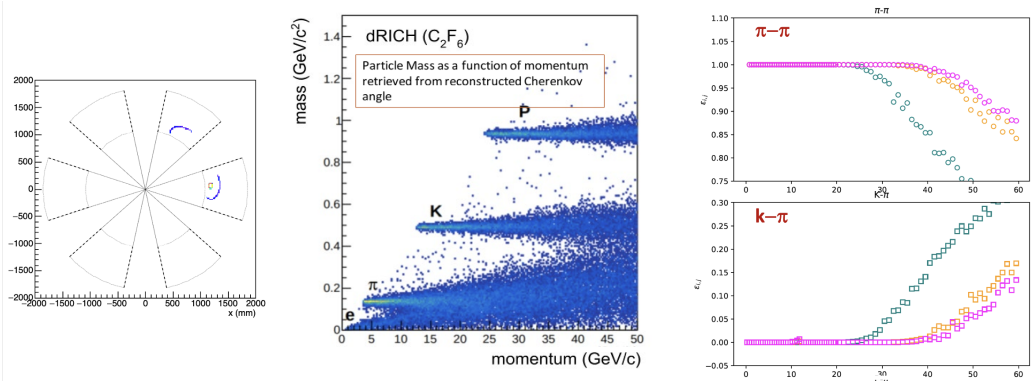

Figure 8.71: (Left) Event display. (Center) Reconstructed mass vs momentum. (Right) Pion identification efficiency and pion to kaon mis-identification probability as a function of momentum in three bins of rapidity.

Services:

The dRICH services are grouped into power lines for sensors, electronics and slow control monitors, gas lines for the radiator gas volume, the aerogel inert gas volume, and cooling lines for the sensors and electronics. Table 8.19 shows a list of the power services for the dRICH photodetector. 18 19″ wide/8U mainframes (approximately $50 \times 40 \times 70$ cm^2 each) capable to host 16 boards each are needed to accommodate the low-voltage and high-voltage boards. The primary power-supply channels will serve multiple modules at the same time, with a typical grouping of 1024 SiPM channels. Nonetheless, further segmentation is implemented on the detector electronics, reaching a low-voltage power segmentation of 64 SiPM channels and a high-voltage power segmentation of 32 SiPM channels. The circulating thermostat system should be capable of circulating approximately 50 l/min of fluid at a maximum pressure of 1.5 bar in a broad temperature range (from -60°C to 120°C). Possible commercial systems are available, but more time is needed to better investigate the options. It is expected that a potential circulating thermostat system with the desired characteristics will require space in the experimental hall for a volume of approximately $1.3 \times 0.8 \times 1.6$ m^3. Manifolds are needed to split the fluid from the thermostat into 6 loops, each feeding one dRICH photodetector box. A solution without manifold and 6 smaller independent thermostat unit for each dRICH sector will be investigated as a possible optimization. Insulated pipes will be needed to transport the fluid from the thermostat to the detector, and back. The insulation must guarantee no frost and no water condensation on the pipes when operating at the lowest temperatures and is also required to limit transport losses in heating/cooling capacity. Cooling for the front-

Name	Voltage (V)	Current (A)	Channels	Boards	AWG gauge
Analog	1.4	10.0	312	39	10
Digital low	1.4	8.5	312	39	11
Digital high	2.7	6.0	312	39	12
Master panel	5.0	5.2	6	1	13
SiPM bias	64.0	1.3	12	2	19
Annealing	12.0	3.2	1248	156	15

Table 8.19: List of the voltage services to the dRICH electronics, indicating the number of primary power-supply channels and boards as well as the cross-section of the cables (AWG). The number of power-supply boards is defined assuming to use commercial 8-channel low-voltage boards.

end electronics is required to remove the approximately 15 kW of heat generated by the dRICH photodetector ($\approx$ 2.5 kW in each of the six photodetector boxes). Force-air circulation in the boxes with diffusers are being studied as a possible effective solution. It is important that the air-cooling system for the FEE electronics provides dry air with a dew point of T = -70°c or lower, well below the SiPM operating temperature. A system based on forced circulation of gaseous nitrogen might be well suited also to ensure an inert environment inside the detector boxes. Gaseous nitrogen will be used to maintain the aergoel in a clean and inert environment. The radiator gas system and its related monitoring equipment require a surface of about 15 m^2, in order to host 5 racks of instrumentation, the gas storage tank and a support for the spectrophotometer. This surface includes the space needed by the operators. Various sections of the gas system operate at a 2-3 bar pressure, while the cell to measure and monitor the gas transparency operates at 10 bar. Some gas bottles at typical high pressure (100-150 bar), organized in a battery, have to be included to provide the radiator gas at filling and house it when recovered. The pipelines connecting the gas system to the vessel are 70 m long with a diameter of 10 cm.

Subsystem mechanics and integration:
The dRICH structure can be described by two disks, one entrance window of 0.9 m radius supporting the aerogel radiator and one exit window of 1.8 radius mounting the mirror system, connected by two ring-shaped structures, one shell that mounts the six detector boxes and one inner pipe surrounding the ePIC beam pipe. All the elements are made in composite materials. The pipe and shell are made by a carbon fiber reinforced polymer (CFRP) bulk to provide support strenght. The two windows are a sandwich of two carbon fiber skins and a core honeycomb to limit the material budget to about 1% of radiation length each. The shell and detector boxes are shaped in order to allow the passage of all the services of the inner barrel detectors, see left panel of Fig. 8.72. The dRICH services are concentrated on the shadow of the detector boxes and do not interfere with the routing of the others. A dedicated scaffolding would be realized to allow the installation of the detector, and the roll-in and roll-out movements to the service position without interference with the beam pipe to preserve the beam vacuum, see central and right panel of Fig. 8.72. The dRICH is suspended inside ePIC via brakets connected to the HCAL barrell.

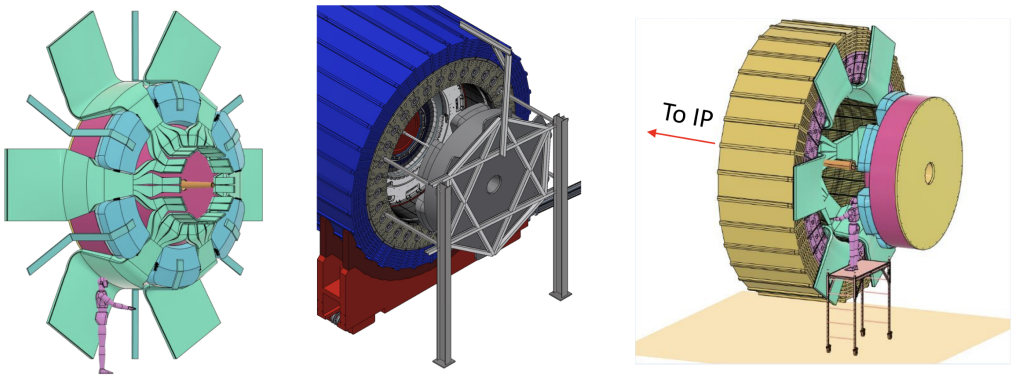

Figure 8.72: (Left) Service routing around the dRICH. (Center) Installation tool. (Right) Maintenance position.

Calibration, alignment and monitoring:
Dark counts in SiPMs are indistinguishable from photon-induced signals and owing the large SiPM DCR there is no need of a dedicated system to evaluate the functioning of any given readout chan-

nel. A measurements of the DCR as a function of the front-end electronics discrimination threshold can provide information on the signal amplitude. This technique can be used at different bias voltages. Using solely the dRICH readout system it is possible to measure the signal amplitude as a function of the bias voltage, hence to obtain information on sensor functioning and its breakdown voltage at different operation conditions. Timing calibration of the SiPM sensors can be achieved with a picosecond pulsed laser light system. The light from the laser is brought inside the dRICH volume via optical fibres. The light from the laser directly impinges on a diffuser that eventually illuminates the full area of one dRICH photodetector sector. At least one laser-fibre-diffuser system is needed for each dRICH sector. The time delay due to the different path of photons from the diffuser to the SiPM that detects the light is known and can be corrected to achieve a relative calibration of the times of SiPMs within the same sector. Absolute timing calibration can then be achieved with collision data. Samples particles from physics reactions can be used to perform fine adjustment of the calibration costants. Electron particles identified by other ePIC subsystems can be used to correct residual misalignment or calibrate the radiator refractive index thanks to the saturated Cherenkov rings. Known particles from meson decays (Λ, ϕ, K_S, ...) identified by kinematics criteria can be used to verify the parameters of the dRICH reconstruction and the consequent PID performance. The calibration and monitoring equipment of the radiator gas and gas system (see Additinal Materialism) includes a set of temperature sensors placed inside the dRICH vessel and equipment on-line in the gas circulation loop. A commercial hygrometer and a commercial oximeter, a transparency measurement system by a commercial spectrophotometer equipped with a high pressure ($\approx$ 10 bar) cell and a Jamin interferometer setup complete the set of the equipment. The interferometer, complemented with temperature and pressure sensors, will provide in real-time the refractive index of the gas in the vessel. The refractive index measurement has a twofold role: during filling/recovery, it monitors the hexafluoroethane level in the vessel, during operation it will provide in real time the refractive index of the radiator gas to make possible quasi on-line data reconstruction as foreseen in the ePIC streaming read-out model.

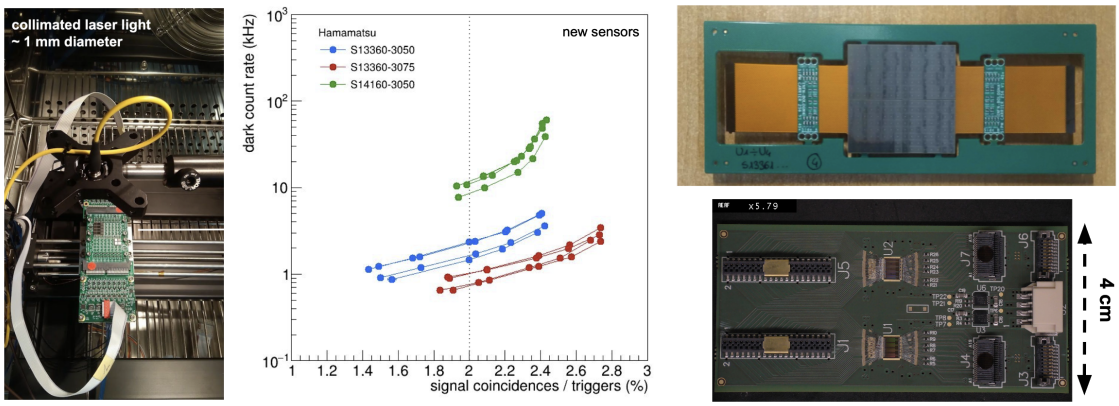

Figure 8.73: (Left) Test stand for SIPM characterization. (Center) Performance comparison between different SiPM models. (Right) Prototype version of the SiPM carrier board (top) and FEB (bottom).

Status and remaining design effort:

R&D effort:

SiPM sensors. A station has been realized to characterize the SiPM sensors inside a climatic chamber to control the working temperature, see left panel of Fig. 8.73. The readout chain

is based on ALCOR to reproduce the ePIC configuration. Such a station allowed detailed performance comparison between SiPMs of different manufacturers and types, and different ageing due to radiation and annealing, e.g. see central panel of Fig. 8.73. The R&D results on photosensors reported here are those obtained with Hamamatsu S13360-3050 sensors operated at V_{over} = 4 V in a climatic chamber at T = -30°C, unless otherwised specified. Nonetheless, the qualitative features of the results are valid also for other types of sensors. Irradiation tests and laboratory measurements on SiPM candidate samples show that after irradiation with a fluence of $\Phi_{eq} = 10^9$ cm^{-2} n_{eq} the DCR increases by approximately 500 kHz with respect to the DCR measured when new [35]. The dark current and the DCR of irradiated SiPM decreases by almost two order of magnitudes when placed in a thermostatic chamber at T = 150°C for 150 hours ("oven annealing"). Further tests performed to simulate a realistic experimental situation where SiPMs experience repeated irradiation and annealing cycles (see left panel of Figure 8.67) show that each irradiation cycle produces a consistent DCR increase (approximately 500 kHz for a 10^9 cm^{-2} n_{eq} irradiation) and a consistent residual DCR (approximately 15 kHz for a 10^9 cm^{-2} n_{eq} irradiation) remains after an "oven annealing" cycle. The fraction of damage cured by the "oven annealing" cycle is of approximately 97% of each newly-produced irradiation damage. The residual damage of 15 kHz/10^9 n_{eq} builds up after each irradiation-annealing cycle and seems to be irreducible within the details of this annealing protocol. The "oven annealing" protocol is not a practical approach for a central-barrel detector in a collider experiment, because of the limited access and because it would entail the removal of the sensors from the photodetector to place them the thermostatic chamber to perform annealing. Irradiation tests and laboratory measurements show that the "forward-bias annealing" mode can cure radiation-induced damage on SiPM (see left panel of Figure 8.74) to the same effectiveness level as the one measured for the "oven annealing" with a residual damage of approximately 3%. The benefit of the "forward-bias annealing" is significant: an extended SiPM sensors lifetime that can be achieved over the delivered radiation damage without the need to directly access the detectors in the experimental cavern. The fraction of damage, measured as dark current reduction, depends on the annealing temperature and the duration of the annealing. Higher temperatures and longer annealing times lead to more effective annealing. On the other hand, a limit seems to be reached already at T = 150°C and annealing at a higher temperature of T = 175 C does not lead to improved current reduction. Self-heating of the SiPM happens also when reverse biased, although given that the reverse I-V characteristics of SiPM is non-linear and depends on the illumination state, currents can increase with less control making the reverse-bias annealing intrinsically more dangerous than forward-bias annealing. Laboratory measurements performed so far show that one can increase the temperature of the SiPM with respect to the temperature of the SiPM carrier board proportionally to the power delivered by the forward-bias current. Figure 8.74 (right panel) shows that, as expected, the increase of SiPM temperature linearly depends on the annealing power and it is the same at different values of circulating thermostat temperature. It is therefore sufficient to monitor the temperature of the SiPM carrier board and deliver the needed annealing power to have control of the SiPM temperature during "forward-bias annealing" and keep the process safely under control. Laboratory measurements reported here are performed in an open environment at room temperature. With the circulating thermostat temperature set at T = 100°, we reach a SiPM annealing temperature of T = 150° with approximately a power of 0.5 W/sensor, which corresponds to a forward-bias current of approximately 60 mA/sensor. With the SiPM placed in a closed environment as the in dRICH photodetector box, one would expect a lower power needed that will be measured during detector construction. Laboratory measurements of the variation of the SiPM PDE as a function of the annealing temperature and annealing time show that for annealing temperatures up to T = 150° there is no observation of a significant degradation of the PDE up to annealing times of 150 hours. On the other hand, annealing

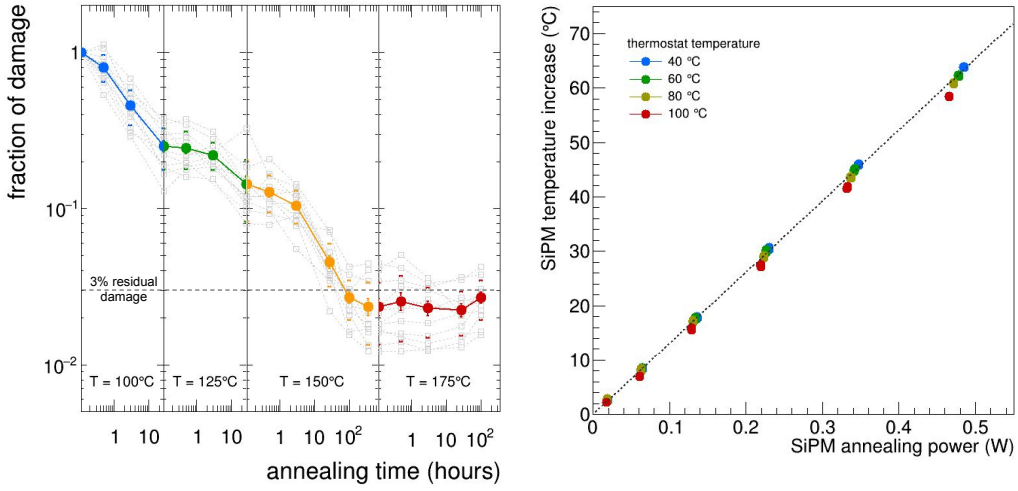

Figure 8.74: (Left) Fraction of residual irradiation damage measured on multiple SiPM candidate samples after "forward-bias annealing" cycles at increasing temperature and integrated annealing time. The measurements are shown for individual sensors (gray points) and as averages (coloured points, uncertainty of the average and RMS are indicated on the plot). (Right) Temperature increase of the SiPM sensor with respect to the temperature of the SiPM carrier board as a function of the "forward-bias annealing" power at different temperature values of the circulating thermostat system.

at a temperature of T = 175° seem to cause a degradation of the transparency of the silicone protective window of the SiPM, which causes a decrease in the PDE to approximately 80% of the initial value after 150 hours. As already discussed, annealing at temperatures higher than T = 150° does not bring any advantage for what concerns DCR reduction. More studies will be done, but at the time of writing annealing at T = 150° can be considered safe for the expected dRICH operations.

FE Electronics. ALCOR has been extensively used within the ePIC dRICH Collaboration since 2021. The current version of ALCOR incorporates 32 channels, arranged in a 8×4 pixel matrix. It has been tested coupled to different SiPM models assessing its single-photon time-tagging capability and time resolution. A prototype version of the SiPM carrier and FEB board have been developed, see right panel of Fig. 8.73. The SiPM carrier provides electrical connections via thin kapton cables in order to bypass the sensor cooling plate. The prototype FEB hosts two 32-channel ALCOR chips which are directly wire-bonded on the PCB. It has been designed using specifications close to the ones for the final FEB, i.e. having the same dimensions and incorporating the same number of channels (64). It is served by a master-logic board that provide bias control and temperature monitor. These boards have been extensively used for the 2023-2024 dRICH activities, including two successful beam tests. ALCOR has been tested for radiation hardness with results showing only some small degradation on the TDC performance after a total ionizing dose (TID) of 300 krad, which is O(100) times the expected TID in ePIC. These results confirm that the technology is sufficiently radiation tolerant to be used in the ePIC dRICH environment and that no special design techniques have to be adopted for the new version of ALCOR. The single-event upset (SEU) cross section has been measured to be $3.3{\cdot}10^{-15}$ cm^2/bit for the pixel configuration registers and $8.5{\cdot}10^{-14}$ cm^2/bit for the periphery configuration registers, which is signifi-

cantly higher because these registers are not triplicated in the current version of ALCOR. From these results we can expect a mean time between failure due to SEU of about 190 hours for the entire dRICH detector.

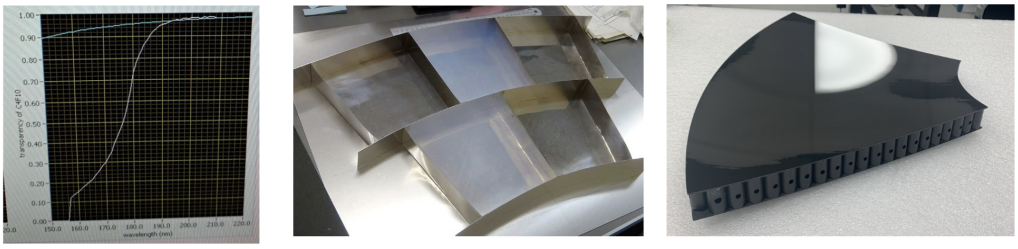

Figure 8.75: (Left) C_2F_6 measured transmittance. (Center) Aerogel large tiles assembling as obtained at BELLE-II [3]. (Right) Mirror demonstrator with an optimized dRICH core structure.

Radiator gas. The transparency in the near-UV benchmark region (most sensitive to the gas quality and contaminants) has been measured with a monochromator at CERN, resulting in values above 98% for a 1.6 m coloumn of gas at wavelengths grater than 200 nm, see left panel of Fig. 8.75. The measurement has been done with a gas that was stored into bottles for about 4 years, indicating an excellent preservation with time.

Aerogel. Several measurements were performed to optically characterize the aerogel. The transmittance of silica aerogel is a measure of how much light passes through the material without being absorbed or scattered. Silica aerogel consists mostly of air. Indeed, it has a unique structure made of a three-dimensional network of interconnected nanopores, with diameters ranging from 2 to 50 nm, which allows visible light to pass through the material with minimal scattering or absorption. Specifically, in aerogel, light undergoes Rayleigh scattering, which is the elastic scattering of light by particles much smaller than the wavelength of the light. The transmittance is typically highest in the near-infrared region, where the absorption of radiation by the silica network is minimal. Its dependence on the radiation wavelength is usually defined by the Hunt formula [69] which assumes a λ^4-dependence of Rayleigh scattering cross section. In silica aerogel, the low absorption is due to the absence of impurities or defects in the silica network that could trap and dissipate the energy of the photons. Additionally, silica aerogel can be hydrophobic or hydrophilic. The tiles tested are highly hydrophobic, which means that they repel water and other liquids. This property helps to maintain the material's transparency even in humid or wet conditions. The aerogel scattering and absorption capability can be assessed through the transmission length as follows: $1/\Lambda_T = 1/\Lambda_{scat} + 1/\Lambda_{abs}$.

We have characterized several 10×10 cm^2 and 5×5 cm^2 aerogel tiles produced as a spin-off the BELLE-II development in a broad range of refractive indexes. Table 8.23 reports a list of the tested samples, where for each tile its refractive index and expected thickness in the thinnest point of its meniscus geometry are reported. On each tile transmittance was measured on 15 different sampling points, to provide information on the dependence of the transmittance on the thickness as well as on the light wavelength (in a range from 250 to 800 nm). The maximum discrepancy along the tile is of the order of $\approx$ 0.3%, the transparency homogeneity is quite good. Transmittance as a function of the wavelength of a single tile was considered as the average of the transmittance value at each sampling point. The average transmittance was fitted by the extended Hunt formula suggested in [69] to extract scattering and absorption lengths. The results are presented in Fig. 8.80 for a tile with n = 1.03, which shows that the transmission length is nearly equal to the scattering length,

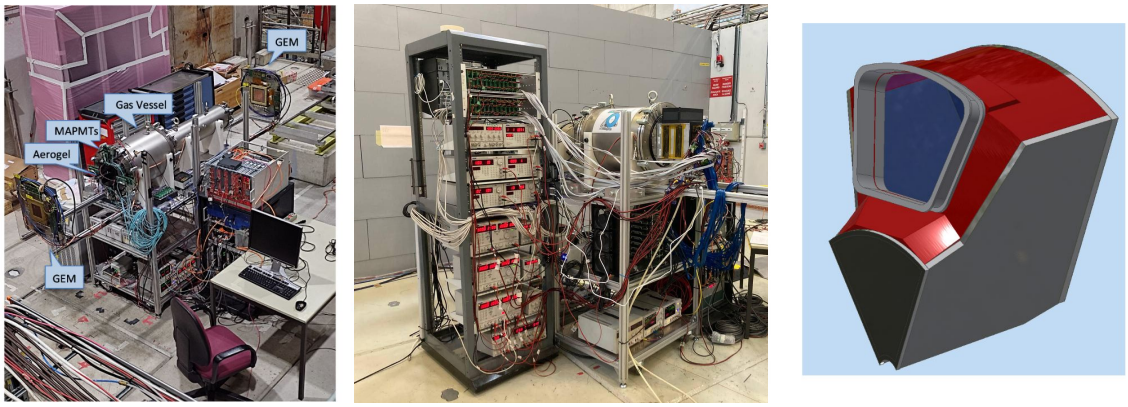

Figure 8.76: (Left) Baseline prototype with reference detector at the SPS-H8 beam line of CERN. (Center) First ePIC-drive detector box under test at the PS-T10 beam line of CERN. (Right) Real-scale prototype model mimicking the basic dRICH construction unit (sector).

whereas the absorption length is considerably higher. Therefore, the contribution of absorption can be considered negligible. A comparison of the results from all the tested tiles can provide valuable insights into the impact of the refractive index on the optical properties of the aerogel, see Fig. 8.81. The transmittance measurements reveal that the tiles with a refractive index close to n=1.03 exhibit higher transmittance length values at 400 nm compared with tiles of higher or lower refractive index, see Fig. 8.82. In the metrology laboratory at CERN, the thickness and flatness of the tile have been also measured. The measurement has been executed on a tile with n = 1.03 using the touch probe system (force applied = 2 g). The measuring system is the LEITZ PMMC with $\pm$ 0.3 μm of precision. There is a variation in thickness from the center to the edges, of the order of 0.4 mm, and a different planarity in the two faces, one 0.7 mm, the other 1.27 mm. In general the tiles have the shape of a dome.

Mirror. A mid-size demonstrator (of 60 cm diagonal) has been realized with dRICH specifications, see right panel of Fig. 8.75. The CFRP core structure has been optimized for preserving the surface shape accuracy and a light body: it adopts the light LHCb structure in the center, and the stronger CLAS12 structure on the edges. Before coating, the point-like source image test measures a D0 value, that represents a global surface quality estimator, of 1.8 mm, better than the specification of 2.5 mm. The same test indicates a radius of 2254.1 mm, slight above the request to be within 1% of the nominal 2200 mm value.

Prototyping. A baseline prototype has evolved in time to serve the dRICH R&D development for few years, see left panel of Fig. 8.76. The gas vessel is a cylinder made of vacuum standards, to allow an efficient and safe gas exchange. The entrance flange can mount an external dark box separated from the inner gas volume by a UV-transparent lucite foil (or quartz window). An aerogel tile with possible additional UV filters, plus an array of alternative sensors and readout electronics, can be inserted into the dark box. Two mirrors inside the vessel have optimized focal lenghts to image the Cherenkov light from the two radiators onto the limited active surface. The major achievements obtained during several test-beams have been the validation of the dual-radiator concept, the validation of the C_2F_6 gas radiator (see left panel of Fig. 8.77), the optimization of the aerogel refractive index (see central panel of Fig. 8.77), the performance study of the SiPM-ALCOR readout chain (see right panel of Fig. 8.77), and the development of an EIC-driven readout plane. A partially equipped EIC-driven plane has been realized in time for the October '23 test-beam with Hamamatsu S13360-3050 SiPM sensors of standard 50 μm pixel pitch, see left panel of Fig. 8.78. The plane

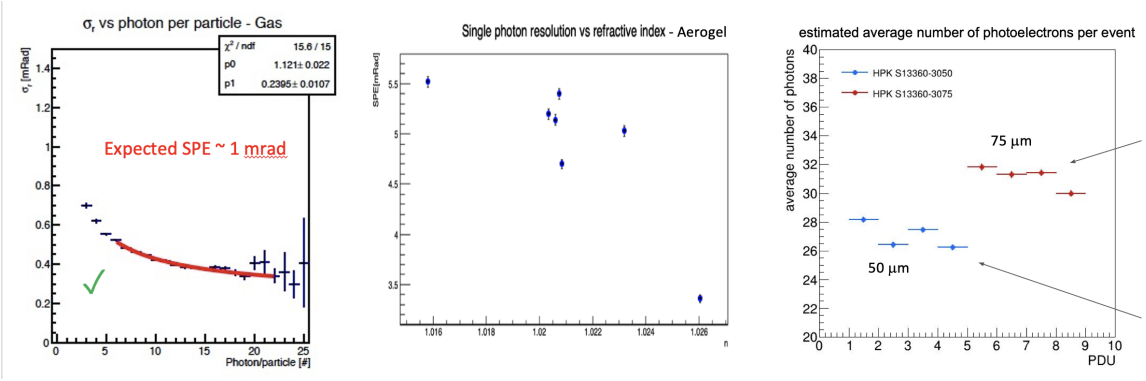

Figure 8.77: (Left) Cherenkov angular resolution obtained for C_2F_6 as a function of the recorded number of photons. The SPE values is consistent with expectations. (Center) SPE angular resolution measured on aerogel as a function of the refractive index. The expected resolution is obtained for an index greater than n=1.025. (Right) Comparison in photon yield of sensor with different SPAD size. All the measurements are obained with the dRICH prototype.

has been complemented for the test-beam in May 2024 with sensors of 75 μm pixel pitch, to verify the potential benefit in timing and photon detection efficiency. This has allowed for the first time a full ring coverage, an essential requirement for precise radiator performance study and effective signal over background study, see central panel of Fig. 8.78. An effective interplay between the two radiators at intermediate energies has been demonstrated, see right panel of Fig. 8.78. The new detector box has allowed a preliminary study of the thermal gradients and possible effects on the gas performance, indicating that the possible temperature gradient of few degrees induced into the gas volume by the cool sensor plane can be largely mitigated by a gas re-circulation or by a double window.

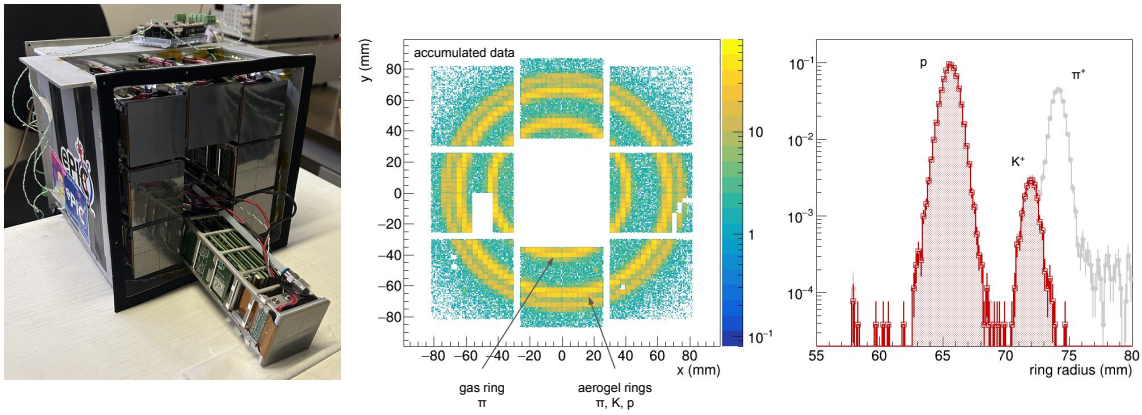

Figure 8.78: (Left) Prototype PDU and assembled detector plane. (Center) Cumulated ring imaging. (Right) dual-radiator interplay for a mixed hadron beam at 10 GeV/c: After the gas information is used to tag pions (clear histogram), an effective separation between kaon an proton is provided by the aerogel (shaded histogram).

E&D status and outlook:

A new version of the ALCOR ASIC is currently being designed to extend the number of

channels to 64 and integrate the chip inside a BGA package, aiming to enhance the scalability of the readout system and meet specific EIC-driven requirements. The ASIC package will use FC-BGA technology with 256 balls and 1 mm ball pitch. Since no re-distribution layer (RDL) is available for the 110 nm technology in which ALCOR is fabricated, a dedicated 10-layer 1.27 mm thick substrate in bismaleimide-triazine (BT) resin material is currently being designed. This BT epoxy provides a more advanced and reliable solution w.r.t. many FR4 grade materials, while being also commonly available from multiple vendors. In particular, its higher thermal conductivity and lower z-axis coefficient of thermal expansion (CTE) values make it more suited to cope with repeated thermal cycles, in which CTE mismatches may induce mechanical stress on the BGA solder joints. The new version of ALCOR will also include some internal design revisions. A programmable hardware shutter is being implemented to filter out-of-time DCR and thus significantly reduce the data throughput. The asynchronous digital shutter is implemented in ALCOR pixel logic using the external test-pulse signal and will be provided by the RDO board. Inside the ASIC programmable delay chains, with 4 configuration bits at channel-level (LSB $\simeq$ 350 ps) and at the chip periphery (LSB $\simeq$ 100 ps), allow the compensation of the offsets between different pixels and columns. In addition, the front-end will feature an increased bandwidth amplifier to improve the system time resolution while keeping the same power consumption and also an hysteresis circuit in the discriminator stage to avoid unwanted re-triggering on the SiPM signals slow tail, occurring when operating with very low thresholds. To improve its overall SEU tolerance, the new version of the ASIC will implement triple modular redundancy (TMR) also for the periphery registers as well as error-correcting Hamming encoding for the finite-state machines (FSM). Further irradiation tests are foreseen in 2025-2026 on ALCOR final version to fully validate the front-end electronics in terms of radiation tolerance for all of its components. The tape-out is scheduled during the first months of 2025. A thorough electrical characterization of this version of ALCOR, the first one assembled in a BGA package and including all the features required for the dRICH application, will be carried out to validate its new functionalities and measure its performance in order to complete the E&D activity and go ahead with the ASIC mass production which is foreseen in 2026.

The development of the final front-end boards takes advantage of the work done for the prototype version in terms of space constraints, readout scheme and components selection. To finalize their layout several design optimization are required: define the best segmentation and routing to provide the bias voltage to the SiPMs, optimize the AC-coupling circuitry between ALCOR and the SiPM sensors, include the annealing circuit required to operate the SiPMs in forward-bias, distribute the power lines and optimize the control and monitor protocols. In addition, all components that will be mounted on these boards need to be tested to verify their radiation hardness. The design of the final version of the SiPM carrier, FEB and master-logic boards will be completed in 2025 while the mass production is expected during 2026.

For the radiator gas, it is required to complete the design of the gas system and finalize the layout of the monitoring equipment. Each of these activities assumes an engineering study and its validation by laboratory studies. The remaining E&D activity is expected to be completed by the end of 2026.

An increase of the aerogel tile volume is instrumental to minimize the edge effects and contain the cost. During the R&D phase, tiles with side up to 15 cm and thickness up to 2 cm were realized. A feasibility study is ongoing to increase these limits towards a side of 20 cm or a thickness of 3 cm to support the successful assembling scheme adopted at BELLE-II, see central panel of Fig. 8.75. The aerogel production efficiency should be evaluated in conjunction with the optical quality obtained. This engineering work is expected to take time and not be completed before the end of 2026.

Coating of the CFRP mirror substrate should be realized and compare with the benchmark

performance obtained with the same materials at CLAS12. This work will be completed by mid 2025.
A real-scale prototype is being realized with composite materials and a realistic geometry (mimicking a dRICH sector). This is instrumental to validate the mechanical elements and study the assembling details (e.g. of transparent septa), the mechanical stability, the gas tightness, and the thermal aspects. One of the major goals of the real-scale prototype is also to reproduce the final ePIC working conditions, mount an extended readout plane with the designed RDO board, operate demonstrators of the optical components as results of the ongoing developments, and optimize the performance in a realistic off-axis optics configuration. To this end, a test-beam is planned for mid 2025.

Other activity needed for the design completion:
Slow control, interlock and the calibration LED/laser system design is not started yet.

Status of maturity of the subsystem:
The R&D activity has been focused on the most innovative aspects of the detector that present technological challenges. These are the SiPM for single-photon detection in a strong magnetic field, a compact readout electronics to fit into the ePIC envelope and the use of two radiators to extend the momentum reach. The remaining effort is substantial, but is connected to more consolidated technologies, with possibly the only exception of the gas separation system for the peculiar C_2F_6 gas.

Environmental, Safety and Health (ES&H) aspects and Quality Assessment (QA planning:
Standard slow-control and interlock procedures will be implemented to control power and cooling while monitoring gas flow, humidity and temperature. The cooling system is complemented by a buffer tank to allow air flow and heat removal from the detector boxes in case of a failure of the recirculating system. The gas volume is maintained at +1 mbar with respect the atmospheric pressure on the top, with a consequent +5 mbar overpressure defined by the hydrostatic pressure of the radiator gas on the bottom, by means of pressure regulators connected to an UPS station and a two-way bubbler. Hexafluoroethane is non-flammable and it has limited toxicity, when below 1000 ppm level and for short exposure time [ref to be added]. In case of a major damage of the supply pipeline or of the vessel itself, 12 m^3 of hexafluoroethane at atmospheric pressure from the vessel (0.02% of the hall volume) will mix with the air present in the experimental hall, requiring the implementation of standard ODH procedures. Hexafluoroethane has a high Global Warming Potential (GWP): 12400 for a horizon time of 100 years [70] and it is, therefore, included in the group of GreenHouse Gasses (GHG). Environment protection imposes that GHGes are not released in the atmosphere. This is obtained by using them in closed circuits, where leakages are minimized, and by collecting and sending for disposal the fraction of gas purged during circuit filling and gas recovery at the beginning and at the end of an operation period, respectively. Both closed circuit gas circulation and purged gas trapping are characterizing elements of the dRICH radiator gas system design. The maximum expected leakage rate during operation is about 20 m^3 / year assuming six-month operation. Experience in quality assurance protocols has being gained in parallel with the R&D activity. For each critical component two stations are being organized to provide essential QA and redundancy, with a (third) station able to supports in-deep characterization on samples and serve as backup, see Table 8.20. The QA activity will be supported by manpower from all the dRICH groups. Essential QA parameters will be measured: integrity, refraction index, transparency, dimensions, and planarity of the aerogel; leak rate of the gas system (after completion); refractive index and transparency of the radiator gas (with the monitoring equipment of the gas system); dark count rate and PDE for the sensors; electrical connections, bias levels and data rate for the readout; dimensions, weight, reflectivity and D0 (point-like source image brigthness) for the

Component	QA station 1	QA station 2	QA detail and backup
Aerogel	Temple U.	BNL	INFN-BA
Gas	BNL		INFN-TS
Mirror	JLab		Duke U.
Sensor (SiPM)	INFN CS-SA-CT	INFN-TS	INFN-BO
Readout	INFN-BO	INFN-FE	INFN-TO

Table 8.20: Planned quality assurance (QA) stations, organized in order to provide redundancy and support specific characterization studies.

mirrors.

Annealing of SiPM will be performed during technical stops and/or during the annual stops of the EIC machine. All the dRICH front-end electronics (FEE) will not be powered, with the exception of a few components needed to monitor and control the annealing operations. An interlock-based sistem will inhibit the FEE power-supply units during annealing. The circulating thermostat system used to cool the SiPMs will be switched to heating mode to reach a temperature of up to T = 100°C. A slow heating ramp of < 1 °C/minute will be employed to reduce thermal stress on the system. The dRICH photodetector boxes will be thermally insulated as much as possible to reduce heat leaks into neighbouring detectors while performing annealing. It is expected that the inner volume of the detector box can reach a temperature of T = 100°C and will be monitored with temperature sensors. Temperature sensors will be placed on the outside of the photodetector boxes to monitor the external environment. Annealing of the whole dRICH photosensors at once requires up to 160 kW of power and will not be performed as such. Only a fraction of the dRICH SiPMs will perform annealing at a given time, to limit the total amount of power needs to about 20-40 kW. This is a similar to the total power consumption of the FEE during normal operations and the same safety procedures apply. Annealing power will be distributed evenly across the dRICH SiPM. In case of a power outage, the annealing current will be promptly removed from the SiPMs and their temperature will promptly drop to the temperature of the thermostat. The latter will eventually slowly cool down.

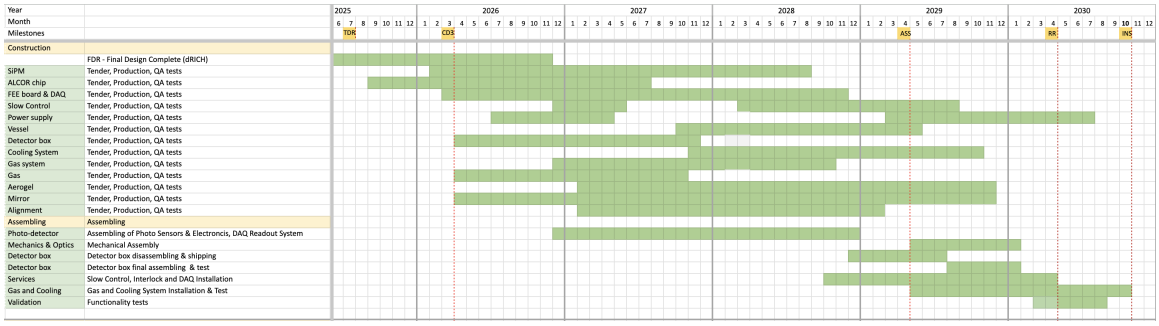

Figure 8.79: Construction plan

Construction and assembly planning:

The construction and assembling plan assumes to compress all the necessary tasks in a short time period in between the presently known EIC milestones: start with CD3 (at the beginning of 2026) and completion 6 months in advance of installation (in October 2030). This results in an aggressive schedule in terms of manpower and funding profile. The 6 months contingency time before installation will be used to perform functionality tests, and complete the services in the experimental

hall at IP6. The assembling of 1248 PDUs comprising SiPM sensors and cooling, front-end electronics and RDOs, and their integration with the services inside six detector boxes will be staged over 2 years (mainly 2027 and 2028) by the dRICH DSC in Italy. This organized effort requires a timely procurement, starting with the ALCOR chip (wafer and packaging) followed by sensors, readout electronics, and box mechanics. Cooling infrastructure and DAQ system are expected to run in parallel to the detector box construction and be mainly covered by the EIC Project. First articles of DAQ, power supply and slow control could be used for the initial functionality tests of each single detector box, but the main effort on such services is concentrated on a later stage of the plan during assembling at BNL. The detector boxes will be completed in time to be shipped to BNL and mounted on the dRICH in the second half of 2029. The dRICH vessel construction, a joint venture of the dRICH DSC and the EIC Project, will start in 2028 in order to be ready for detector assembling mid 2029. Mirror production is expected to take 2 years and is staged as soon as possible, subject to the funding profile of the EIC Project, to reduce the sole source risk. The engineering of the aerogel production is expected to extend beyond the TDR, with the consequent production led by the dRICH DSC not happening before 2027 and lasting for at least 2.5 years. An early procurement of the C_2F_6 gas by the EIC Project is planned in order to reduce the risk of a market price increase. The principle design of the radiator gas system will be completed by the end of 2026 by the dRICH DSC. The executive drawings and the system realization by the EIC Project engineering team supported by adequate technical personnel is expected during years 2027 and 2028. The layout finalization and validation of the monitoring equipment will be completed by the end of 2026, while its realization is by the end of 2027 by the dRICH DSC. This equipment will be interfaced with the gas system in 2028, via synergistic effort between the EIC Project engineering team and the dRICH DSC. This combined group will perform the QA assessment of the gas system in 2029.

Collaborators and their role, resources and workforce:
INFN has agreed on a substantial in-kind contribution and the corresponding workforce has taken corresponding responsibilities in the construction within the DSC. The INFN in-kind will cover the design, production and quality assurance cost of the SiPM sensors, of front-end ASIC (ALCOR), of the front-end board (FEB), of the readout boards (RDO) as well as the assembly of the above components in a compact Photo Detector Unit (PDU), including the cooling circuitry and related mechanics. It will cover the cost of the realization of the six detector boxes (containing the PDU of each sector) with the control panels and the electronic services attached (for HV/LV/daq links routing). It will contribute to the design and realization of the main vessel, the design/supervision of the powering and monitoring systems, the dRICH tagging system and data filtering in streaming mode, see Sec. **??** , and to the definition of specifications and quality assurance (QA) of all the other components and services (i.e. gas, power and cooling plants). The availability of the essential local resources as mechanical and electronic workshops and laboratory space have been negotiated. **INFN-FE** (IT): is coordinating the DSC activity and is leading the mechanical design. The group will lead the design and production of the vessel in collaboration with the EIC Project and will take care of the realization of the detector boxes and corresponding control panels for the 6 sectors. The assembly of the detector boxes is expected to happen in its laboratories. **INFN-BO** (IT): the group is leading the activity on photosensors (SiPM) and data-acquisition. It will be responsible of the procurement of SiPM, design and production the readout boards (RDO) and coordinate the integration of the various elements of the PDU. The PDU will be assembled in BO and tested/validated before being moved to INFN-FE for the installation in the detector boxes. **INFN-BA** (IT): the group is leading the aerogel activity. It will coordinate the mass production and the quality assurance (expected to be operated in the US at Temple University and BNL). **INFN-CS-SA-CT** (IT): this cluster of units will work on the QA of SiPM and front-end boards prior of the PDU assembling. They will equip test stations in SA and CS for this purpose. **INFN-GE** (IT): is carrying out a feasibility study

(and if successful, the realization) of a dRICH tagger to filter the SiPM data stream. **INFN-LNS** (IT): the group will contribute to the mechanical design effort. **INFN-RM1/RM-TV** (IT): the RM1 group (and one staff person of RM-TV) has extensive experience on AI algorithm running on FPGA. They will develop algorithm for pattern recognition and data reduction on FELIX cards and the interface with the signals received by the dRICH tagger or from ePIC via GTU. **INFN-TO** (IT): the group is leading on the design, test and production of the front-end ASIC ALCOR. The group will produce the chips and the front-end cards (FEB) mounting the ALCOR, and coordinate the quality assurance tests of the chip and FEB. **INFN-TS** (IT): the group is leading the radiator gas activity. It will lead the design of the gas system and develop a continuous monitor system (critical to maintain a good chromaticity). It will also develop a test station of SiPM (with smaller capacity with respect to the CS-SA-CT cluster). **DUKE U.** (US) is leading the mirror activity. It will coordinate the mirror production, expected to happen in the States, the corresponding QA activity, and the coating process that possibly will be realized at Stony Brook. **Jefferson Lab** (US) is contributing to the mechanical design and developing tools for mirror characterization. **Brookhaven Lab** (US) is contributing to the mechanical design and integration study. It will lead the infrastructure (installation tools, services, safety control) realization with its design authority and technical resources. **Stony Brook** (US) is developing mirror coating capability. **Temple U.** (US) is developing an aergel quality assurance facility. **M.S.Ramaiah U.** (India) is contributing to the simulation and performance study. **NISER** (India) is contributing to the performance study. **Haryana and Karnataka U.** (India) have started contrinuting to the performance study. Secondments of personnel from all the DSC groups will be organized to support the QA activity in US and the assembling phase at BNL. The EIC Project is expected to cover the procurement effort that can be more efficiently based on US, and all the safety, infrastructural and integration aspect that require specific engineering background. This include the cost of the gas, of the mirrors, of the installation tools, of the power-supply systems , of the cooling plant and the gas plant, and of the FELIX cards receiving the data from the RDO.

Risks and mitigation strategy:

The major risk of the dRICH gas radiator is the banning of the hexafluoroethane or more severe restriction on its usage, that can also result in increased cost or difficult procurement. The only alternative option to preserve the dRICH performance would be an eco-friendly gas with very similar refractive index, an option not available in nature at atmospheric pressure. Argon at ≈ 3 bar absolute pressure mimics with great accuracy the hexafluoroethane characteristics. It is also non-expensive, non-toxic and non-flammable. R&D is being performed within the EIC generic R&D program to establish the validity of this approach as risk mitigation strategy. Radiation damage reduces the lifetime of the SiPM as good photodetector for the dRICH performance. Estimates of the radiation level on the dRICH photodetectors are expected to be accurate. The DCR model shown in Figure 8.67 (right) is for the sensors experiencing the largest radiation levels (closer to the beam line) and for detector operation at V_{over} = 4 V and T = -30°C. Operation at lower V_{over} = 3 V and/or lower temperature T = -40°C would reduce the DCR without loss in performance, hence allowing one to accommodate larger integrated radiation levels (up to a factor 2-3) than those reported in the figure. The addition of small thermoelectric cooling (TEC) modules will be evaluated as a potential approach to boost the cooling performance, allowing one to reach an even lower operation temperature of T = -50°C and avoid possible dishomogeneities. Current R&D on new SiPM technologies for improved performance and radiation hardness are being followed up as a risk mitigation strategy and as a potential upgrade for the dRICH photodetector in the late 2030's or in the early 2040's. For two components, optical aerogel and carbon-fiber mirror, there is only one known supplier able to deliver the wanted specifications at the present stage. An early procurement should limit the risk of a market discontinuity. Within the ePIC RICH Consortium, the recently initiated R&D on mirrors at Purdue University are being followed up as potential sources of risk mitigation in the long term period, if the adaptation to the dRICH needs

will be proven feasible. DSC members are part of the recent DRD4 initiative, that aims to create a worldwide collaborative environment to favor new technological breakthroughs in Cherenkov particle identification and photon detectors. Within DRD4, there are many development areas of interest for the dRICH program, in particular gasses or mixtures alternative to the greenhouse fluorocarbon gasses and radiation hard SiPM.

Additional Material Planning of additional material for the gas radiator system/monitoring equipment:

- Radiator Aerogel:
  - aerogel characterization in lab and beam tests;
  - details of the aerogel support and purging;
- Radiator Gas:
  - Hexafluoroethane characteristics;
  - Detailed description of the gas system;
  - Options for gas separation during filling and gas recovery operations;
  - Trapping system to collect hexafluoroethane in the purged gas;
  - Jamin interferometer for refractive index measurement;
  - Measurement of the transparency with the spectrophotometer;
  - Oxygen and water vapor contamination: measurement and removal;
  - High-pressure Ar R&D;
- Mirror:
  - mirror characterization in lab and beam tests;
  - details of the mirror structure;
  - details of the mirror support;
  - details of the mirror alignment;

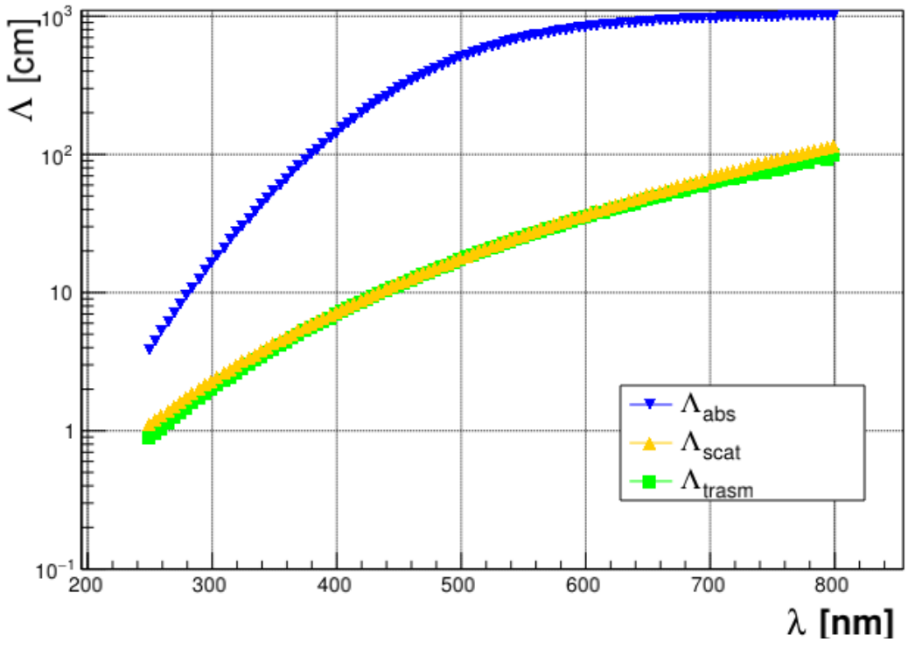

Figure 8.80: Transmission, absorption and scattering length curves as a function of the wavelength for the tile with $n = 1.03$.

4291 In the following the specifications of the main dRICH components are tabulated.

Detector element	Abbreviation	Elements/sector	Total elements
Photodetector box	PDB	1	6
Master panel board	MPB	26	156
Photodetector unit	PDU	208	1248
Silicon photomultiplier	SiPM	53248	319488
SiPM sensor arrays		832	4992
Readout board	RDO	208	1248
Front-end board	FEB	832	4992
ALCOR chips		832	4992

Table 8.21: Main elements of the dRICH photodetector system with the indication of number of elements per sector and the total.

Parameter	Value	Notes
Package type	SiPM array	
Package dimension	$< 26 \times 26$ cm^2	
Mounting technology	surface mount	
Number of channels	64	
Matrix layout	8×8	
Channel size	3×3 mm^2	
Fraction of active area in package	$> 85\%$	
Microcell pitch	50 - 75 μm	
Protective window material	silicone resin	radiation & heat resistant
Protective window refractive index	1.55 - 1.57	
Spectral response range	300 to 900 nm	
Peak sensitivity wavelength (λ_{peak})	400 - 450 nm	
Photon detection efficiency at λ_{peak}	$> 40\%$	
Breakdown voltage (V_{break})	< 60 V	
Operating overvoltage (V_{over})	< 5 V	
Operative voltage (V_{op})	< 64 V	
Max V_{op} variation between channels	< 100 mV	at T = $-30°$C
Channel dark count rate (DCR)	< 50 kHz	
DCR at T = $-30°$C	< 5 kHz	at T = $-30°$C
DCR increase with radiation damage	< 500 kHz/10^9 n_{eq}	at T = $-30°$C
Residual DCR after annealing	< 50 kHz/10^9 n_{eq}	at T = $-30°$C
Terminal capacitance	< 500 pF	
Gain	$> 1.5\ 10^6$	
Recharge time constant (τ)	< 100 ns	
Crosstalk (CT)	$< 5\%$	
Afterpulsing (AP)	$< 5\%$	
Operating temperature range	-40 to 25°C	
Single photon time resolution (SPTR)	< 200 ps FWHM	

Table 8.22: Baseline specifications of the SiPM sensor devices for the dRICH photodetector. All parameters are defined at room temperature (T = 25°C) and at the operating voltage V_{op}, unless otherwise specified.

Tile	Refractive index @405 nm	Nominal thickness (mm)
1	1.03	20.7
2	1.03	20.8
3	1.03	20.1
4	1.03	20.5
5	1.03	20.4
6	1.03	10.0
7	1.03	10.0
8	1.04	20.3
9	1.04	20.5
10	1.04	20.3
11	1.04	20.4
12	1.04	20.5
13	1.05	20.5
14	1.05	20.7
15	1.05	20.6
16	1.05	20.6
17	1.05	20.8
18	1.005	20.0
19	1.005	20.0
20	1.005	20.0

Table 8.23: Tiles list. Tiles from 1 to 17 were produced at the High Energy Accelerator Research Organization (KEK) in Japan and delivered in March 2021 [6], except tiles 6-7 which belongs to a 2000 production manufactured by Matsushita Electric Works (Japan).

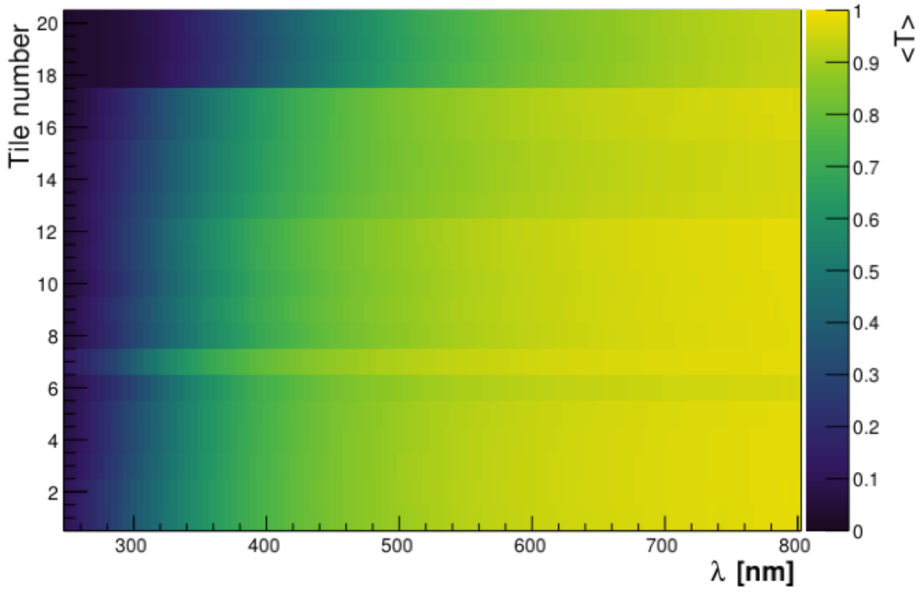

Figure 8.81: Transmittance as a function of the wavelength for all the tiles.

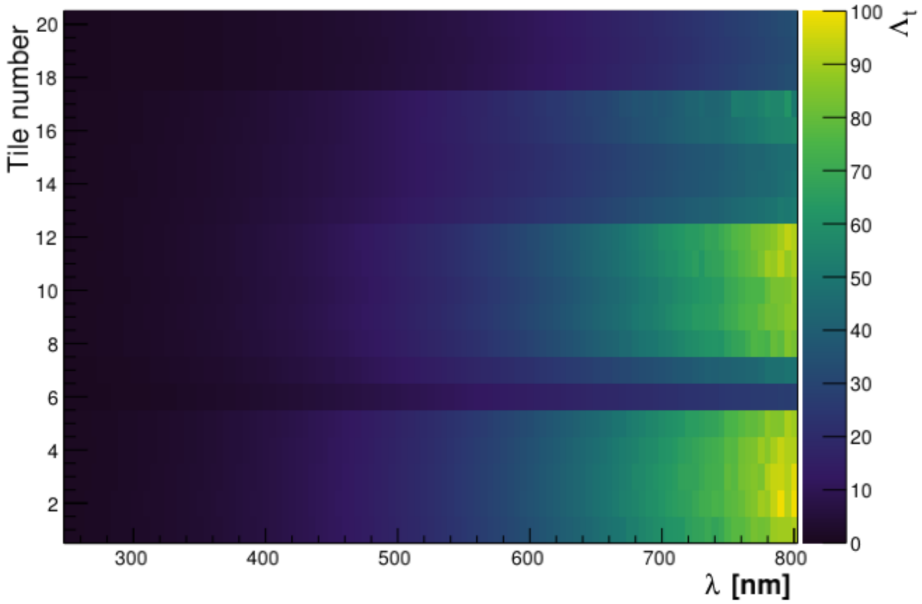

Figure 8.82: Transmission length as a function of the wavelength for all the tiles.

8.3.5 Electromagnetic Calorimetry

Add text here.

8.3.5.1 The backward endcap electromagnetic calorimeter

Requirements

Requirements from physics: The electron-end-cap calorimeter will cover a dynamic energy range of 0.1–18 GeV for electromagnetic showers of the scattered electron based on e+p Pythia simulations at 18x275 GeV^2. The EEMC is a high-resolution ECal designed for precision measurements of the energy of scattered electrons and final-state photons in the electron-going region. The requirements for energy resolution in the backward region is driven by inclusive DIS where precise determination of the scattered electron properties is critical to constrain the event kinematics.

An excellent energy resolution of $\sigma_E/E \approx 2\%/\sqrt{E} \oplus 1\%$ is required for the backward endcap electromagnetic calorimeter.

Requirements from Radiation Hardness: The EEEMCal detector must operate at a radiation level of $\sim$3 krad/year (30 Gy/year) electromagnetic and 10^{10} n/cm^2 hadronic at the EIC top luminosity

Requirements from Data Rates: Add text here.

Justification

Device concept and technological choice: The EIC physics program requires high-precision detection and identification of the scattered electrons emitted in the electron-going direction, as well as final-state photons. The backward endcap electromagnetic calorimeter (EEEMCAL) provides a compact solution with excellent energy resolution over a large dynamic range and with high granularity. The EEEMCAL meets the experiment requirements of fast timing to handle an interaction rate up to 0.5×10^6 Hz and acceptable radiation hardness up to $\sim$3 krad/year (30 Gy/year) electromagnetic and 10^{10} n/cm^2 hadronic at the EIC top luminosity. Furthermore, the EEEMCAL achieves the required clean electron identification for energies greater than 2 GeV with a rejection factor better than 10^4 when combined with other detector subsystems. The EEEMCAL has been reviewed and passed the EIC Project detector technical review of electromagnetic calorimetry in December 2022.

A drawing of the EEEMCal mechanical design is shown in Figure 8.83. The EEEMCAL will be located at a distance of 175 cm from the EIC interaction point where it is installed around the beam line in a roughly cylindrical geometry. The particles of interest impinge on the front face of the detector and pass through a radiator with adapted geometrical dimensions to contain the major part of the electromagnetic shower. The produced scintillation photons are detected at the back of the radiator by means of an array of Silicon PhotoMultipliers (SiPMs) and readout with back- and front-end electronics. The entire detector is enclosed in a mechanical structure that also provides services like thermal monitoring and cooling and light monitoring. The entire assembly weighs on the order of three tons, which is consistent with the specifications of the EIC experimental area.

Based on extensive simulation studies, the preferred material for the EEEMCAL radiator is lead tungstate (PWO), an extremely fast, compact, and radiation-hard scintillator providing sufficient luminescence yield (15 - 25 photoelectrons/MeV) to achieve good energy resolution. This material

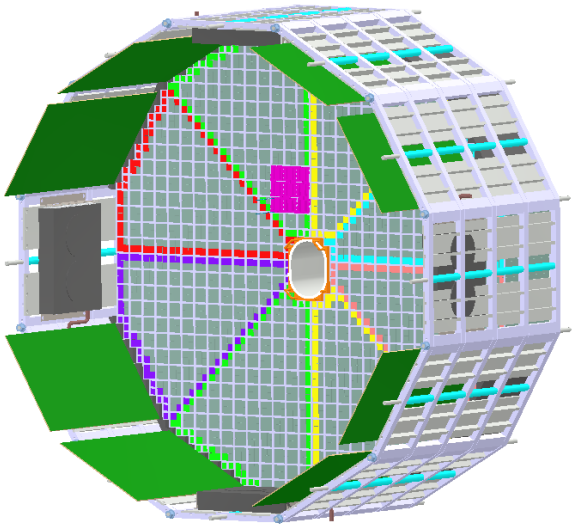

Figure 8.83: CAD drawing of the EEEMCAL. The small gray shapes are the scintillating crystals. The SiPM photosensor matrices are grouped over four crystals and indicated by the pink area. The green rectangles are part of the backend electronics. The dark gray rectangles and circles on the circumference are part of the cooling system.

has been the most common precision calorimetry method of choice for hadron physics measurements with electromagnetic reactions, such as at multiple setups at JLAB and also at PANDA/GSI. To achieve good energy resolution including the so-called constant term typically requires 20 or more radiation lengths (X_0). For PWO in the EEEMCAL we have $22X_0$ (20 cm). The transverse block dimensions are matched to the Moliere radius to capture the major part of the transverse shower. The measured energy resolution for PWO is $\sigma_E/E \approx 2\%/\sqrt{E} \oplus 1\%$ [71]. To pinpoint the electron scattering kinematics, the EEEMCAL provides a position resolution of ∼2mm at 1-3 GeV with a granularity of 2 cm. The technology for mass production of PWO crystals that guarantees the needed homogeneity of the whole calorimeter has been well established with recent experiments, most recently with the Neutral Particle Spectrometer at JLab [72,73].

An effective way to read out the EEEMCAL is through SiPMs that offer several advantages, e.g., a high gain and a medium photodetection efficiency of about 50%. Furthermore, SiPMs can be operated in the magnetic field of order few hundred Gauss expected at the location of the EEEMCAL. Individual devices are grouped into an array to maximize surface coverage of the PWO blocks. In a recent beam test campaign, the readout concept was validated to work well with a Streaming Readout setup, the method of choice envisioned for the EIC [74].

Subsystem description:

General device description: In the EEEMCal the PWO crystals are arranged in the mechanical support structure (Fig. 8.84). This provides the infrastructure to attach the readout components, cooling system, and cables, as well as the installation fixtures to mount the detector in the experimental hall. The support for the crystals is provided by a frame that is installed in the mechanical structure. Photosensors are located at the backend of the crystals. Mechanical grating in the mechanical structure allows the attachment of the SiPM PCBs there. The crystals are stacked with carbon fiber plates at front and back that allow one to guide the crystal

into position. The cooling system provides thermal stabilization, which is important for crystal performance. Based on initial thermal calculations, this stabilization can be achieved with a combination of internal and external cooling aided by airflow.

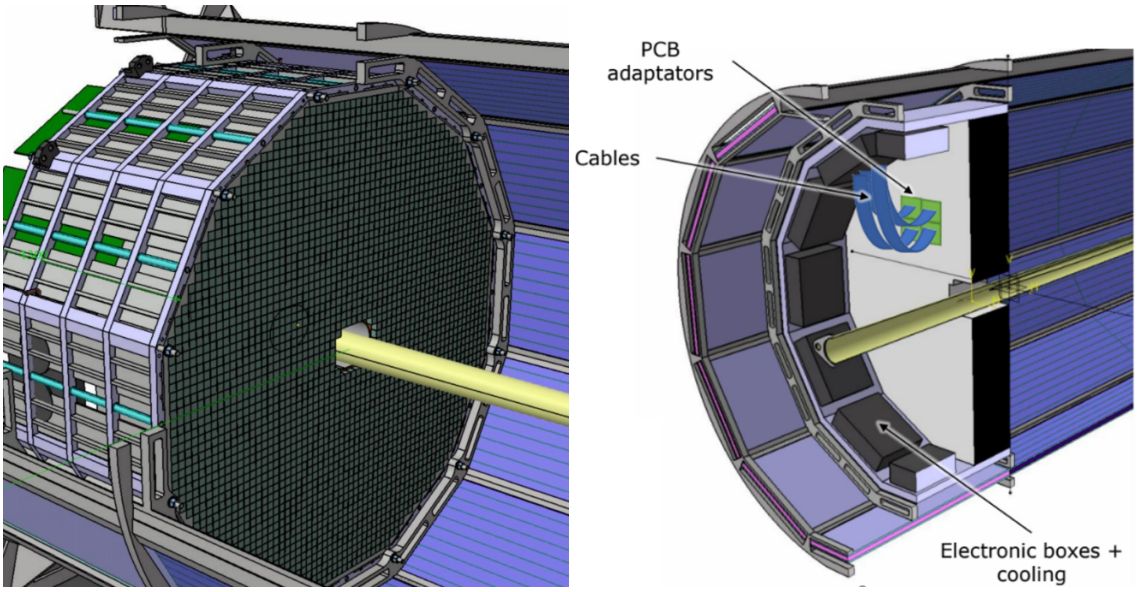

Figure 8.84: Conceptual design of the ePIC electron endcap electromagnetic calorimeter support.

Sensors: Hamamatsu S14160-1315 SiPMs have been identified as the optimal choice for the EEEMCal. Their gain of $3.6 \cdot 10^5$ and relatively low dark current rate (0.7 MHz) allow the measurement of very small signals, close to the single photo-electron (Fig. 8.85, left), while its high pixel density provided by a 15-μm pixel pitch provides very good linearity over several orders of magnitude (Fig. 8.85, right).

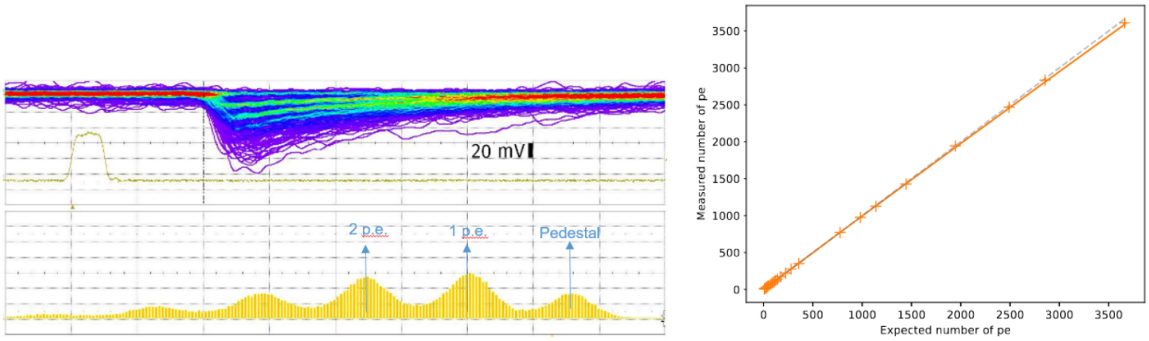

Figure 8.85: Left: waveform (top) and integrated signal (bottom) showing single photo-electron signals in Hamamatsu 15 um pixel SiPMs. Signals are produced with a low-intensity LED. Right: Linearity measurement, showing 2% linearity up to 3500 photo-electrons.

FEE: All calorimetry in ePIC will use SiPMs for their readout. However, the number of channels and input signals and capacitance varies greatly from detector to detector. The require-

ments of the EEEMCal are particularly stringent in terms of energy resolution, which in particular requires the detection of low energy signals (down to 5 MeV per crystal). The readout should provide sufficient dynamic range to accommodate for signals of energy up to 18 GeV.

A discrete readout solution based on commercial devices is currently the baseline for the forward and backward ECals. However, a readout based on the existing H2GCROCv3 chip (developed for the CMS HGCAL) is currently under investigation for the backward ECal. It presents many advantages, in addition to exploiting the synergies with most of the other calorimeters in ePIC. Using an ASIC in the readout of the calorimeter is a very cost effective, more radiation tolerant and cooler (i.e. consuming less power) solution. The H2GCROCv3 chip was developed by the Omega group for the primary use for the High Granularity Calorimeter (HGCAL) for the CMS detector at LHC, making it a great fit for any calorimeter readout. The ASIC requirements for the EEEMCal are very low noise level, low power consumption and very good ($< 1\%$) linearity throughout a very large dynamic range. The chip also has a current conveyor where each channel's bias voltage can be fine-tuned from the ASIC itself. A variation of the H2GCROCv3 chip (CALOROC) is currently under development by OMEGA in order to make it compatible with EIC.

Other components: Add text here.

Performance Our group has performed extensive simulations of the detector performance in the ePIC geometry, including a realistic material budget in front of the detector, which directly affects its resolution and PID capabilities. Figure 8.86 shows the performance of two key parameters: the energy resolution and the pion rejection factor. Results fulfill the physics requirements as outlined in the Yellow Report [7] and NAS study [ref].

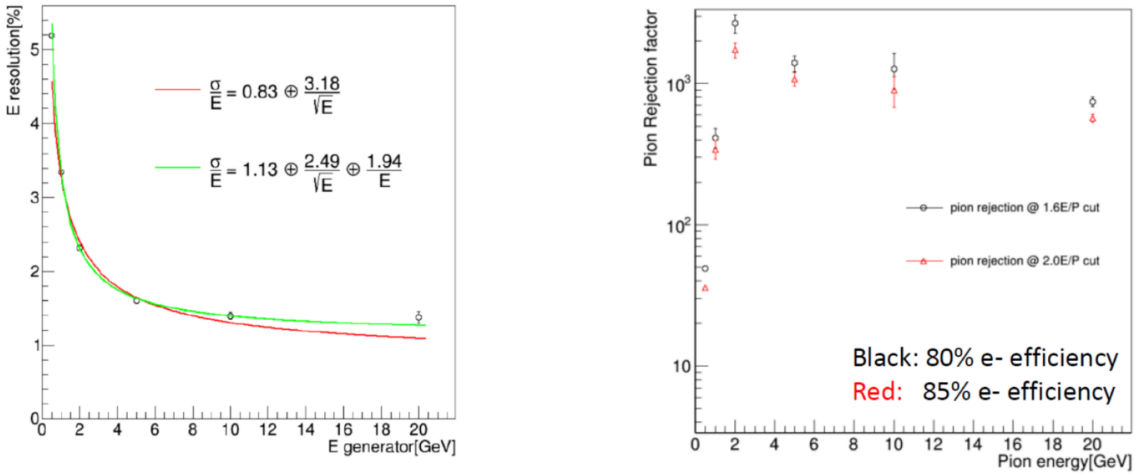

Figure 8.86: EEEMCal simulated performance using the ePIC detector framework including all materials. Left: energy resolution as a function of the incident particle energy. Right: pion rejection factor as a function of energy and different values of electron efficiency.

Implementation The EEEMCAL project has been organized into a well-defined Work Breakdown Structure (WBS). The WBS contains the work necessary to complete the project scope and will form the basis of planning, executing, and controlling project activities. The WBS ensures that

WBS	WBS Title	WBS description
2.00	EEEMCAL Project	Construct the EEEMCAL. The EEEMCAL is an electromagnetic calorimeter for measurement of the inclusive process physics in the electron-going direction at the EIC
2.01	Radiator	Radiation detectors consisting of scintillating crystals (PWO) and thin reflector sheets. These provide the detection of energetic electrons
2.02	Photosensor	Photosensors consisting of multi-pixel photon counters grouped into an array to maximize surface coverage of the PWO blocks.
2.03	Mechanical	Mechanical structure including installation fixtures and a cooling system providing thermal stabilization, which is important for crystal performance.
2.04	Signal Processing/DAQ	Signal Processing/DAQ providing the front-end electronics to transmit the signals to the data analysis modules
2.05	Simulation/Software	Simulations/Software providing the software libraries and infrastructure foundation for extracting the physics from the detector

Table 8.24: EEEMCAL WBS Structure

no portions of the estimate are omitted. The level of the WBS reflect a logical breakdown of the work by major system as shown in Table 8.24.

The baseline schedule for the EEEMCAL Project is shown in Fig. 8.87. The EEEMCAL project aims at the beginning of the window of installation at BNL. The installation window dates are October 2028 to June 2030.

Services: $PbWO_4$ crystals are sensitive to temperature changes with a variation of 2%/°C in light output. Thus, the specification is to keep the crystal temperature stable within ± 0.1 °C. To ensure this stability the additional heat generated by the electronics needs to be removed and the following cooling structures are being considered. As internal cooling structure several machined copper blocks with internal coolant circulation will be used around the beam pipe. To reduce the spatial extend support structures the EEEMCAL consortium is moreover planning to use cooling plates in between the readout cables which are linked to the support structure surrounding the EEMC with tubes. This system is composed of 12 plates with a 5-8 mm spacing in which water can be circulated. The cooling near the crystals will likely not be enough to meet specification. These challenges could be overcome by outside cooling with standard cooling blocks with airflow in front of the electronics or additional cooling added at the back of the assembly.

Subsystem mechanics and integration: The EEEMCAL installation fixtures are shown in Fig. 8.88. They include a mechanical structure that mounts the detector and positions it in the EIC experimental hall at the appropriate height above ground. The structure is envisioned to ride on rails for the installation. The rails could be on the floor as shown, but could also be within the

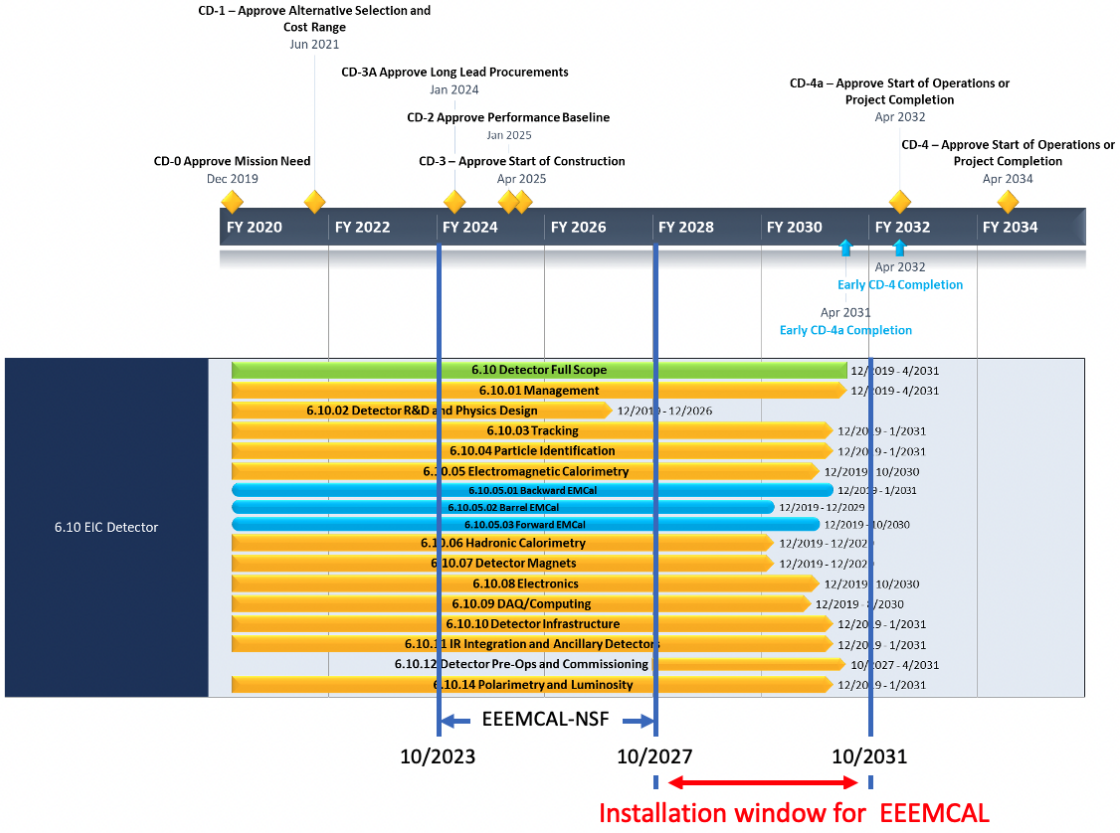

Figure 8.87: EEEMCAL integrated schedule.

cylindrical structure. In the latter case the outer structure would be bolted to the floor. Having the rails extend from the cylindrical structure has the advantage that it would not require rails on the floor of the experimental hall, which could interfere with other hall infrastructure, e.g., the magnet.

Calibration, alignment and monitoring: Add text here.

Status and remaining design effort:

R&D effort: Add text here.

E&D status and outlook: Add text here.

Other activity needed for the design completion: Add text here.

Status of maturity of the subsystem: Add text here.

Environmental, Safety and Health (ES&H) aspects and Quality Assessment (QA planning): Quality Assurance (QA) is an integral part of effective project management and will be employed throughout the design, procurement, and construction of the project. An EEEMCAL

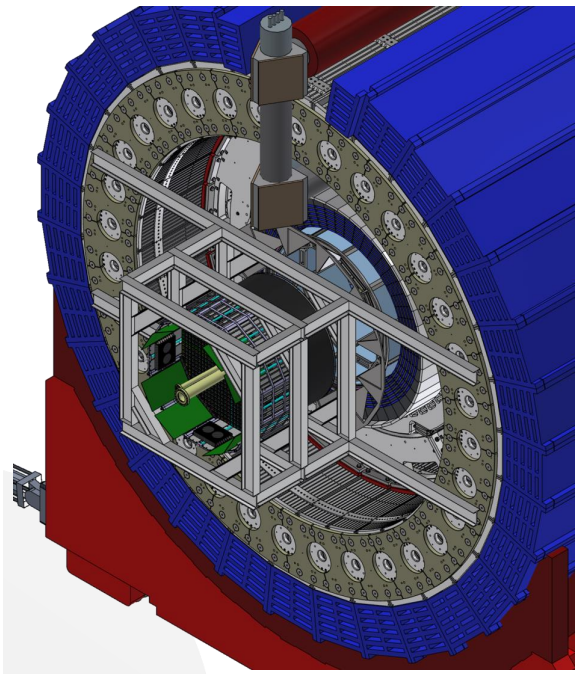

Figure 8.88: EEEMCal installation fixtures that allow for installing the detector safely into the ePIC detector barrel.

Project-specific Quality Assurance Plan has been developed to establish all applicable QA requirements for the design, construction, and operation of the EEEMCAL, consistent with the EIC Quality Assurance Plan that implements the ten criteria defined in DOE Order 414.1D.

Construction and assembly planning: Upon completion of its construction and initial testing, the EEEMCAL will be situated at BNL. The EEEMCal collaboration leaders will coordinate the required equipment readiness for experiment and final integration of the EEEMCAL into the EIC beamline with the EIC Project Management, the ePIC collaboration, and the BNL and JLAB Technical leads. This is necessary for successful integration. For example, a special external support frame will be provided, installed, and surveyed by the BNL technical staff for this purpose. All installations and the integration of the EEEMCAL will be handled by BNL technical staff with expert's assistance to ensure appropriate interfacing of infrastructure and fulfillment of installation and operation protocols.

Once installed in the EIC experimental hall the EEEMCAL will be operated and maintained by the EEEMCAL team and its stakeholders in collaboration with technical teams at BNL. The normal operating resources will be provided by BNL. The physics resources to operate and maintain the EEEMCAL will be provided through research grants. These resources are critical for tasks that are not directly related to the construction of the calorimeter, but instead to the integration of the EEEMCAL into the ePIC detector. Examples include developing readout software and trigger algorithms, implementing online GUIs and the slow controls interfaces required to operate and monitor the detector during data taking, as well as designing clustering algorithms and calibration tools and integrating them into the ePIC workflow.

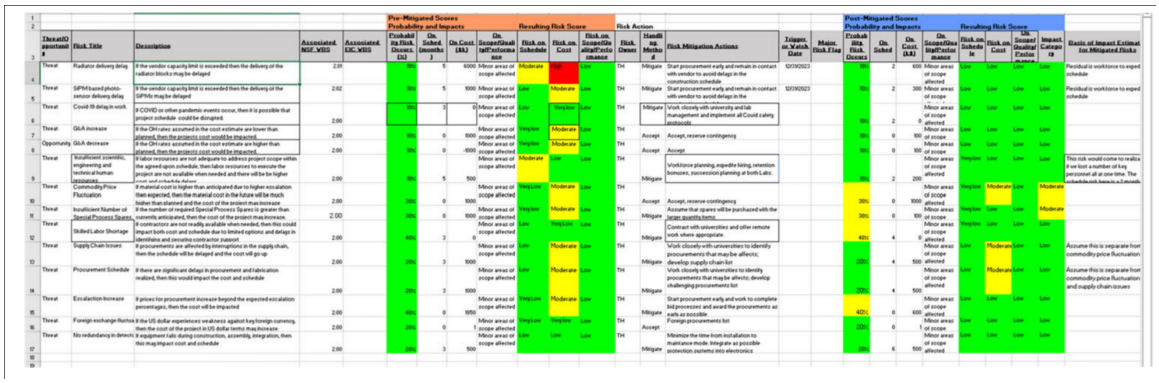

Figure 8.89: Screenshot of the EEEMCal Risk Management Plan and registry.

Collaborators and their role, resources and workforce: Add text here.

Risks and mitigation strategy: Risk planning details are included in the Risk Management Plan and the Risk Registry (see Fig. 8.89). The EEEMCAL Risk Registry is a living document used and updated throughout the life of the project. The EEEMCAL Risk Registry is reviewed and updated monthly by the EEEMCAL Project Team and the Risk owners to reflect any reassessment of risks and opportunities to the project. It contains 14 risks and opportunities. Post mitigation, two of them are considered moderate impact due to the probability of occurrence and impact on cost, schedule, or scope, based on the Risk Matrix analysis. There are two risks on cost with a moderate risk score, but due to the low probability of occurrence, they are in the low-impact category. Post mitigation all risks on schedule and scope are in the low-impact category. In general, the schedule risks are relatively very modest relative to the schedule of the full EIC-DOE project.

Additional Material Add text here.

8.3.5.2 The barrel electromagnetic calorimeter

Requirements

Requirements from physics: The Barrel Electromagnetic Calorimeter (BEMC) must meet the stringent physics requirements set by the EIC program. It needs to identify scattered electrons and measure their energy, particularly in high Q^2 events, and also detect decay electrons from vector or heavy flavor meson decays, and DVCS photons (G-DET-ECAL-BAR.1). Electron identification, including electron-pion separation, is required up to 50 GeV and down to 1 GeV (F-DET-ECAL-BAR.1), with an energy resolution better than $10\%/\sqrt{E} \oplus$ (2–3)% (P-DET-ECAL-BAR.1). Additionally, the BEMC must provide photon reconstruction from 100 MeV to 10 GeV (F-DET-ECAL.9, F-DET-ECAL-BAR.2). The system must also achieve photon-pion discrimination (γ/π^0 separation) up to 10 GeV, with the ability to distinguish two showers with an opening angle down to 30 mrad (P-DET-ECAL-BAR.3). Furthermore, the BEMC will assist with muon identification (G-DET-ECAL-BAR.3) and provide a charged tracking point behind the DIRC to help with charged hadron PID (P-DET-ECAL-BAR.4), with a spatial resolution of less than 150 μm. Lastly, the system must have sufficient dynamic range to detect MIP signals (P-DET-ECAL-BAR.5).

Requirements from Radiation Hardness: The BEMC must be designed to operate in an environment where it may experience radiation levels of up to about 3.9×10^9 1-MeV neutron equivalent per cm^2 per year of running (6 months), corresponding to full luminosity and background conditions (F-DET-ECAL.6). All components, including sensors, electronics, and structural materials, must be sufficiently radiation-hardened to maintain performance under these conditions. This includes ensuring that the sensor response, energy resolution, and position reconstruction capabilities remain stable throughout the detector's operational lifetime.

Requirements from Data Rates: The BEMC and its readout technology must be designed to handle the high event rates expected at full luminosity, ensuring stable performance under expected background conditions, including radiation doses and neutron flux (F-DET-ECAL.6). The system must provide sufficient timing resolution to accurately discriminate between different bunch crossings (F-DET-ECAL.10), ensuring precise event separation and minimizing pile-up effects. The chosen detector and readout technologies must be capable of processing the high data rates without compromising performance or data integrity. Expected rates in the BIC are presented in the Performance paragraph.

Justification

Device concept and technological choice: The ePIC BEMC is called the Barrel Imaging Calorimeter (BIC). The BIC combines two proven technologies to meet the stringent requirements of the EIC physics program. The first is a lead-scintillating fiber (Pb/ScFi) sampling calorimeter read by Silicon Photomultipliers (SiPMs), providing robust energy measurement through light collection, based on the well-established GlueX Barrel Calorimeter (BCAL) design. This technology offers a reliable solution for high-resolution energy measurements, benefiting from its extensive use in other experiments.

The second is a silicon tracker comprising AstroPix, a monolithic active pixel sensor (MAPS) based on an HV-CMOS technology, which is interleaved with the Pb/ScFi layers to provide precise 3D

imaging of calorimeter shower development. This hybrid approach enables excellent spatial resolution and position reconstruction, critical for separating particle showers and achieving the necessary photon and electron identification capabilities. The AstroPix sensors, developed for the NASA space mission AMEGO-X, offer low power consumption, radiation tolerance, cost-effectiveness, and scalability, making them ideal for large-area applications in a high-radiation environment.

This combination of Pb/ScFi for energy resolution and AstroPix for spatial resolution was chosen to balance performance, cost-effectiveness, and long-term reliability under the expected operational conditions at the EIC.

Subsystem description: The Barrel Imaging Calorimeter (BIC) consists of 48 trapezoidal sectors, with End-of-Sector Boxes (ESBs) at each end for readout. The calorimeter spans about 17.1 radiation lengths (X_0) at central pseudorapidity, with the first layer being an AstroPix imaging layer, which provides a tracking point behind the DIRC. Each sector has six slots for AstroPix imaging layers, separated by about 1.43 X_0 of Pb/ScFi at $\eta = 0$. In the baseline configuration, slots 1, 3, 4, and 6—counting radially outward—are filled with AstroPix sensors, while slots 2 and 5 are designated for future upgrades. Figure 8.90 presents the overall structure of BIC and its sectors and Fig. 8.91 shows the imaging AstroPix layers components. Sketch of mechanical envalopes of the ESB is presented in Fig. 8.92. Table 8.26 summarizes the structure of AstroPix and Pb/ScFi layers of the BIC.

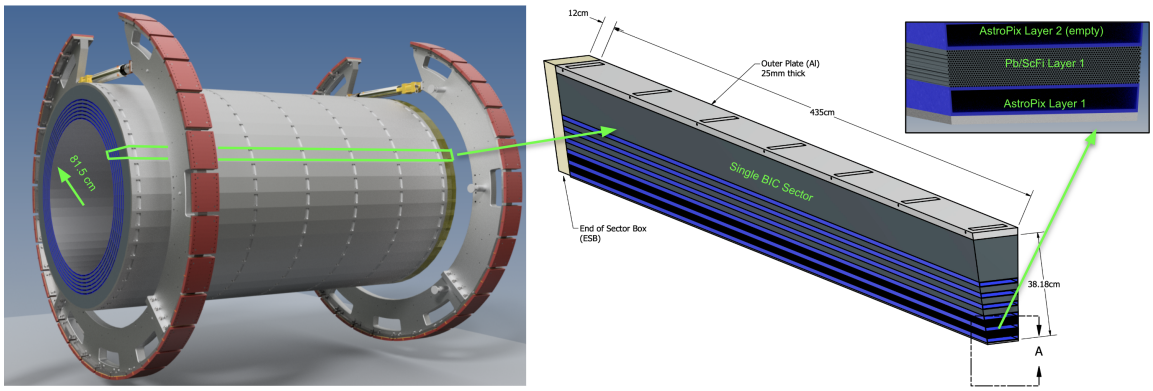

Figure 8.90: Drawing of the Barrel Imaging Calorimeter with its 48 sectors. The central drawing shows the structure of a single sector, featuring interleaved Pb/ScFi layers and slots for trays holding AstroPix chips, followed by the Pb/ScFi bulk section. On the right, a zoomed view of the first radially layers is presented.

Scintillating fibers for Pb/ScFi: The Pb/ScFi calorimeter system is based on the GlueX model with fibers positioned parallel to the z-direction with 2-sided readout for energy measurement and position reconstruction along the fiber. We will use scintillating fibers with 1 mm diameter embedded in lead and glue to provide reliable energy measurement through light collection. For the scintillating fiber parameters refer to Tab. 8.29.

Sensors for Pb/ScFi: The light from the scintillating fibers is subdivided into 12 rows of 5 columns per sector-end by light guides, which are optically coupled with cookies to the SiPMs. These sensors have a 50 μm pixel pitch to optimize dynamic range and photon detection efficiency. For the SiPMs parameters refer to Tab. 8.28.

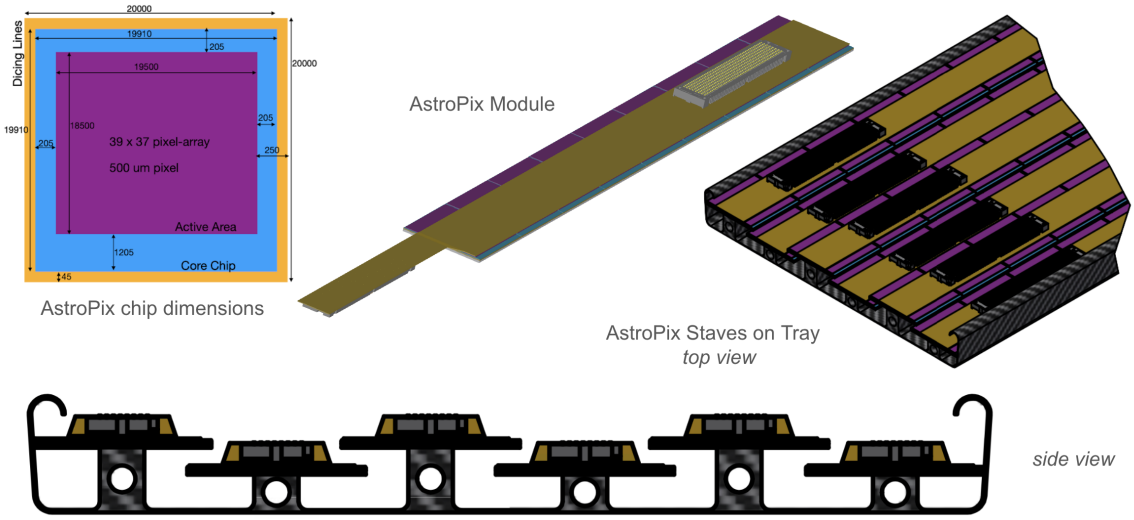

Figure 8.91: Components of Barrel Imaging Calorimeter imaging AstroPix layers.

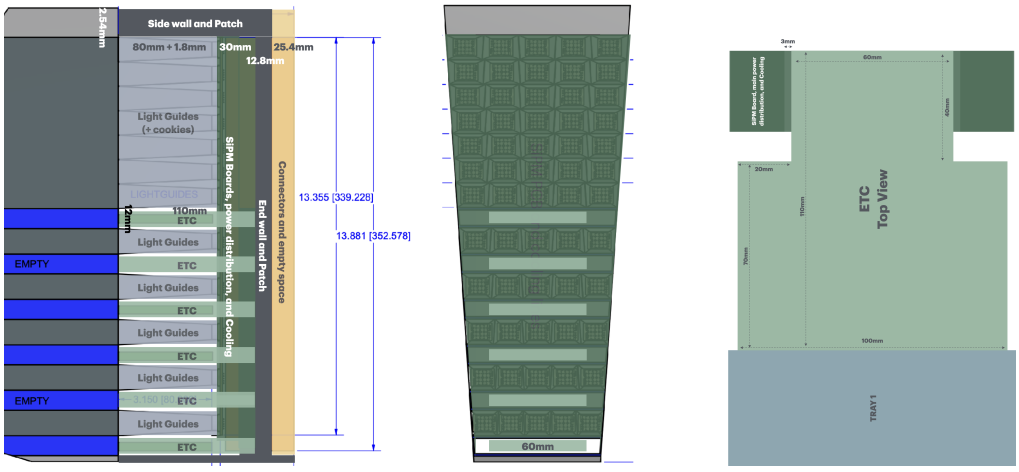

Figure 8.92: Sketch of the mechanical envelopes for the BIC End-of-Sector Box. Left: Side view in the middle of a sector. Center: Rear view cutout at the SiPM PCB Right: Top view of the AstroPix readout FPGA (End-of-Tray Card).

FEE for Pb/ScFi: The FEE for the Pb/ScFi system, based on the CALOROC ASIC, processes the signals from the SiPMs. It provides sufficient time resolution for determining the z-position of events within the scintillating fiber, while maintaining low noise and high radiation tolerance.

Sensors and modules for imaging layers: The imaging layers use AstroPix monolithic silicon sensors with a 500 μm pixel pitch, interleaved with the Pb/ScFi layers. The 9 daisy-chained AstroPix sensors are glued on a base plate and read out on a flexible PCB to form a module, providing high-resolution spatial information for 3D imaging and particle identification. For the AstroPix chip parameters refer to Tab. 8.27.

Staves and trays: Each stave is formed by daisy-chaining 12 AstroPix modules. A tray holds 6–7 staves based on the layer position, with each tray being half of the sector length and read

out at its respective end in the ESB. This modular structure allows for flexible scaling and future upgrades to the system.

End-of-Tray Card (ETC): The ETC functions as the RDO unit in the ePIC DAQ scheme. It manages signal processing, data formatting, and communication with the DAM, ensuring efficient and reliable data flow from the sensors. Note that within the module-stave-tray design, the ETC communicates directly with each 9-chip module.

Detector parameters	Value
Active length (z-direction)	435 cm
Inner radius	82.5 cm
Number of sectors	48
η coverage	$-1.71 \lesssim \eta \lesssim 1.31$
Radiation length X_0	1.45 cm
Total depth in X_0	from 17.1 ($\eta = 0$) to 42 ($\eta = -1.55$)
Molière radius	4.5 cm
Total sampling fraction of Pb/ScFi layers	about 9.5%, see Fig. 8.93
Total sampling fraction of AstroPix layers	$< 0.4\%$
ScFi diameter	$\varnothing$ 1 mm
ScFi radial separation	1.22 mm (between fiber centers)
ScFi azimuthal separation	1.35 mm (between fiber centers)
Light guide length	5 cm
Number of light guides	60 per sector per side
Monitoring system	Blue LED, one LED per light guide
SiPMs	1.2×1.2 cm^2 arrays, 50 μm pixel
Number of SiPMs	60 arrays per sector per side

Table 8.25: Selected BIC Parameters.

Performance The BIC has been designed to meet the stringent energy and particle separation requirements of the EIC scientific program. The performance of the BIC and its components has been simulated through a combination of detector simulations, beam tests, and bench measurements. Key metrics, such as energy resolution, angular resulution, and particle identification have been carefully studied to ensure the detector meets or exceeds the required specifications. The results presented here highlight the detector's capabilities and its ability to operate efficiently under EIC conditions.

Energy resolution: We estimated the energy resolution of the Pb/ScFi layers based on detailed simulations in various rapidity ranges and photon/electron energies. The energy resolution for photons extracted from the Gaussian core of a Crystal Ball fit to the expected energy losses in Pb/ScFi is presented in Fig. 8.93 (a) and the results of the fitted stochastic and constant terms a and b of the energy dependence $\sigma/E = a/\sqrt{E} \oplus b$ are presented in Tab. 8.30. The stochastic term of around 5.8–6.6%/$\sqrt{E}$, with the constant term of 0.6–1.2%, depending

AstroPix layer (radially out)	Number of staves per sector	Number of modules per sector	Number of chips per sector
1	6×2	144	1296
2	-	-	-
3	7×2	168	1512
4	7×2	168	1512
5	-	-	-
6	7×2	168	1512

Pb/ScFi layer (radially out)	Number of ScFi sublayers radially	Thickness in X_0	Readout channels per sector
1–12	17	about 1.43	5×2

Table 8.26: AstroPix and Pb/ScFi layer parameters. The first table presents the parameters for the AstroPix layers, while the second table outlines the Pb/ScFi layer configuration. Radially outward, the calorimeter begins with AstroPix layer 1, followed by interleaved Pb/ScFi and AstroPix layers. Beyond AstroPix layer 6, the bulk section of the calorimeter consists of Pb/ScFi layers 6–12.

Parameter	Specification
Pixel size	500 μm x 500 μm
Power usage	< 2 mW/cm^2
Energy resolution	10% @ 60 keV
Dynamic range	25-700 keV
Passive material	$< 5\%$ on the active Si area
Time resolution	3.125 ns
Si Thickness	500 μm
Active area per chip	2 cm x 2 cm

Table 8.27: AstroPix chip parameters for BIC.

on rapidity, satisfy the detector requirement of energy resolution better than $10\%/\sqrt{E} \oplus 2$–3%. The sampling fraction, defined as energy deposited in the scintillating fibers divided by the true energy of generated photons is presented in Fig. 8.93 (b). Our energy performance results align well with beam test data using a positron beam at Jefferson Lab. See the Additional Material for more details, including results on the contribution of the low-energy tail of the energy loss.

Angular resolution: We estimated the angular resolution for photons using the AstroPix layers, based on detailed detector simulations for various rapidity ranges and photon energies. We extracted the difference between the true and reconstructed polar (θ) and azimuthal (ϕ) to estimate the FWHM resolution. In the current reconstruction algorithm, the angles are reconstructed from the hit with the maximal energy deposit in the AstroPix layer where the shower started. The resolutions for θ and ϕ are presented in Fig. 8.94. The results indicate a small dependence of the angular resolution on η. In all regions, the angu-

Parameter	Specification
Active Area	3 mm x 3 mm (4 x 4 array) Preassembled array covering 1.2cm x 1.2cm
Pixel Size	50 μm
Package Type	Surface Mount
Peak Sensitivity	450 nm
PDE	$\sim$ 50%
Gain	$>\sim 2 \times 10^6$
DCR (Dark Count Rate)	Typ.: $\sim$ 500 kHz / SiPM Max: $<$ 1.5 MHz / SiPM (DCR applies to each SiPM in the 4 x 4 array)
Temperature Coefficient of Vop	$<$ 40 mV/C
Direct Crosstalk Probability	$<\sim$ 7%
Terminal Capacity	$\sim$ 500 pF / SiPM (Applies to each SiPM in the 4 x 4 array)
Vop Variation within a Tray	$<$ 200 mV
Recharge Time	$<$ 100 ns
Fill Factor	$>$ 70%
Protective Layer	Silicone (n $\sim$ 1.5-1.6)

Table 8.28: SiPM specifications for BIC.

Parameter	Specification
Light yield	$>$ 3.5 photoelectrons (measured using Sr-90 source with blackened opposite end)
Diameter	1.00 ± 0.01 mm (RMS $\leq$ 0.02 mm)
Attenuation length	$>$ 4 m (for blue light)
Batch-to-batch variation of light yield	$<$ 15%
Batch-to-batch variation of attenuation length	$<$ 10%
Emission spectrum	Blue-green light
Scintillation decay time	$<$ 3 ns
Total length	4900 km
Delivery method	In canes, length of fibers 4.55 meters $\pm$0.01 m

Table 8.29: Scintillating fiber specifications for BIC.

lar resolution remains well below 0.1 degrees, which is on the level of single pixel resolution. The example fit of the θ resolution in the rapidity region of $-0.88 < \eta < -0.4$ gives (0.040 ± 0.004) deg$/\sqrt{E} \oplus (0.016 \pm 0.003)$ deg. The ϕ resolution is worse than the θ resolution due to the smearing of shower particles by the magnetic field. Overall, the results show significantly better performance than what can be achieved with any tower-like calorimetry systems and fulfills the requirements for the barrel electromagnetic calorimetry for the EIC.

η range	$a/\sqrt{E}$ [%]	b [%]
$(-1.7, -1.3)$	6.60 ± 0.03	0.66 ± 0.04
$(-1.3, -0.88)$	6.11 ± 0.01	1.24 ± 0.01
$(-0.88, -0.4)$	5.91 ± 0.02	1.24 ± 0.02
$(-0.4, 0)$	5.85 ± 0.01	0.88 ± 0.02

Table 8.30: Fitted energy resolution parameters for photons in BIC for different η ranges.

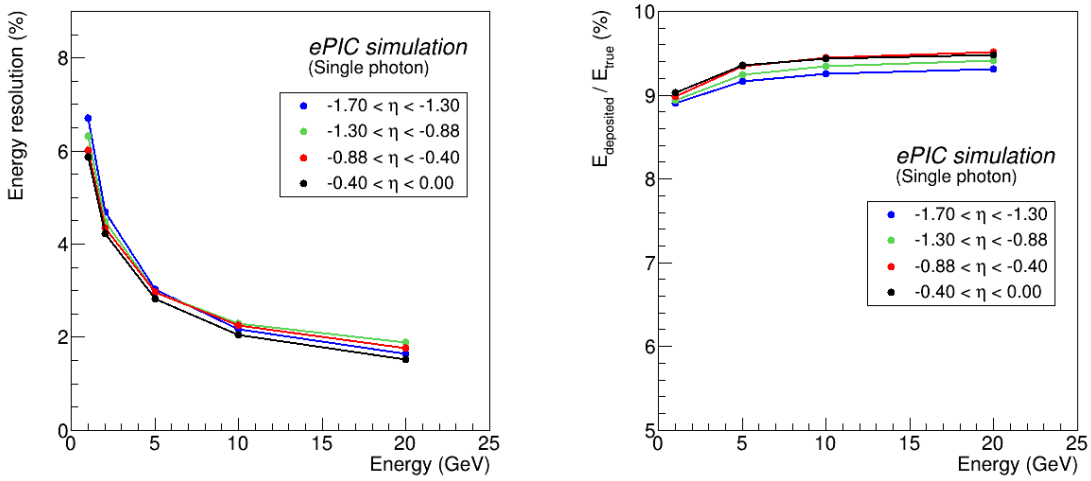

(a) (b)

Figure 8.93: (a) Simulated energy resolution in from Pb/ScFi extracted as a σ of the Gaussian core of the Crystal Ball fit to the energy deposits of photons in different rapidity ranges at BIC. Repository to be added. (b) Sampling fraction for photons, defined as energy losses in scintillating fibers divided by the true photon energy, as a function of photon energy in different rapidity ranges. Repository to be added.

Electron-pion separation: The design of the barrel calorimeter aims to provide high π^-/e^- separation, particularly in the momentum region below 5 GeV. The AstroPix layers capture snapshots of electromagnetic and hadronic showers, allowing for the reconstruction of a 3-dimensional profile of the shower development, supported by the longitudinal energy profiles from the Pb/ScFi layers. Charged pion rejection is carried out in a two-step process. First, an E/p cut is applied to the cumulative energy deposit in the Pb/ScFi layers. This cut is deliberately loosened to ensure high electron efficiency. The "cleaned" samples, following the E/p cut, are then fed into a classification neural network for inference. We used a 10-layer Visual Geometry Group-style Convolutional Neural Network using the combined AstroPix and Pb/ScFi detector response. The network utilizes energy and position features from both technologies capturing energy and spatial shower details. Future improvements may come from using more advanced reconstruction techniques based on Graph Neural Networks or Point Clouds. The charged pion suppression factor for $\eta = 0$ rapidity is shown in Fig.8.95 (a), for a target 95% electron efficiency. The rejection exceeds 10^3 at low to mid energies, where rejection is most critical. For comparison, results where all six imaging layers are instrumented

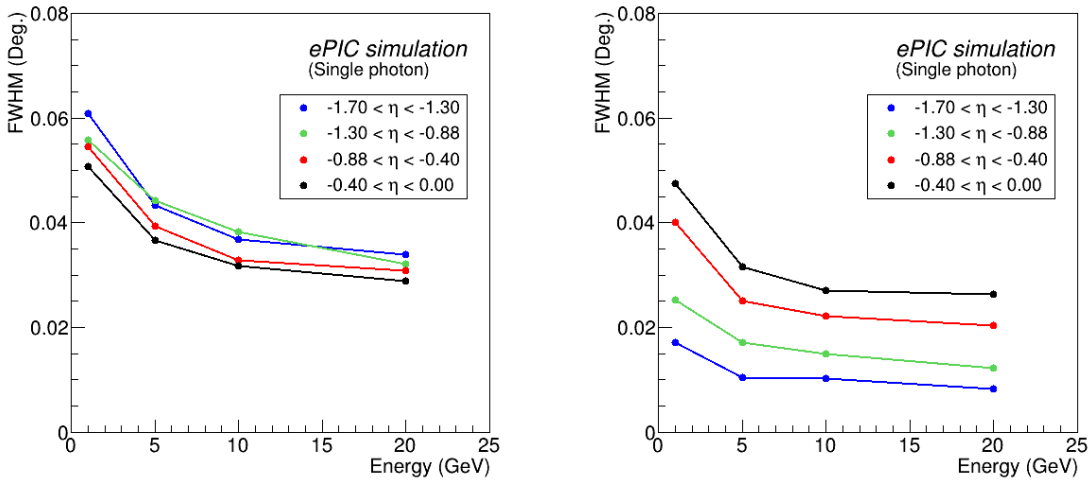

Figure 8.94: Simulated angular resolution for photons at different energies for the ϕ (a) and θ (b) angles reconstructed form the maximal-energy pixel from the first AstroPix layer where the shower started. The resolution is taken as FWHM from the distribution of the difference between true and reconstructed angle. Repository to be added.

are also presented.

Photon-π^0 separation: The upper limit of the probability of merging two γs from a π^0 decay into one cluster at $\eta = 0$ is shown in Fig. 8.95 (b). Neutral pions decaying into two γs were simulated with various momenta. In different calorimeter technologies based on tower geometry, as outlined in the EIC Yellow Report [7], the separation criterion requires that the two γs be separated by at least one tower size. However, for the BIC technology, which uses granular position information from AstroPix, a different criterion has been established. The probability of merging two γs was determined using a separation of 6 times the FWHM of the shower profile, measured at the third imaging layer (where more than 90% of photons with energies above 0.5 GeV register at least one hit), providing a conservative estimate. The upper limit for γ/π^0 separation is expected to be well above 10 GeV, based on studies incorporating AstroPix's position resolution and shower profile data. Additionally, initial results from a neural network approach for neutral pion identification, similar to the e^-/π^- studies but simplified, were applied using full detector simulations. Preliminary results suggest a π^0 rejection of approximately 82% at 90% photon efficiency for 10 GeV particles, based on the current status of model training.

Low-energy response: We evaluated the performance of the BIC for detecting MIPs through simulations using 5 GeV muons at various rapidities. The deposited energy per readout cell, represented by the most probable value of the MIP peak, was extracted from simulations with Kuraray fibers that meet the FDR fiber specifications. This was compared against the 4-sigma pedestal peak from S14161-3050-04 SiPM array simulations, which also fulfill FDR specifications. Even with the dark count rate corresponding to the irradiation level of 1×10^9 1-MeV neq/cm^2 (performed for ePIC by the INFN Bologna group) at 5°C, the MIP signal remains well-detectable with a 4-sigma cut on the pedestal. Figure 8.96 shows the extracted

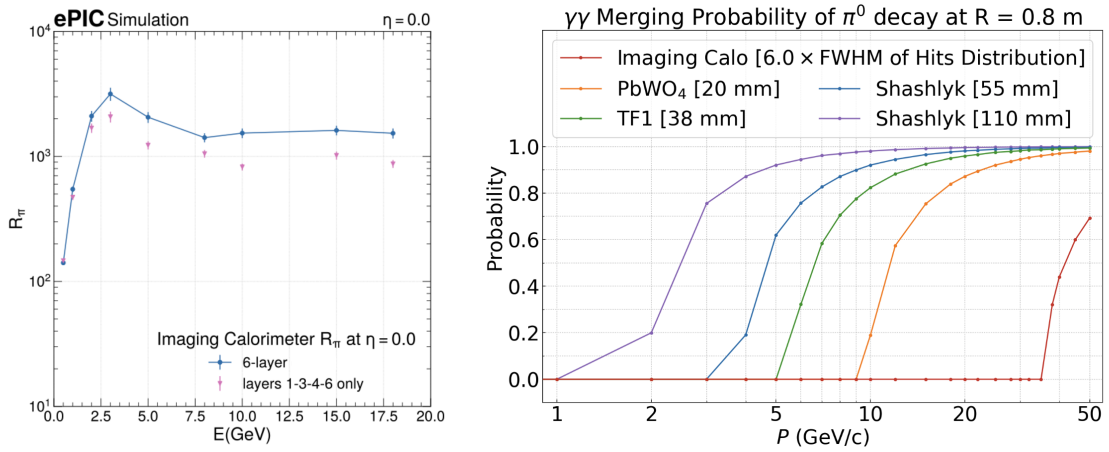

(a) (b)

Figure 8.95: Simulated performance on particle identification from BIC. (a) The charged pion suppression factor for $\eta = 0$ rapidity for 95% electron efficiency as a function of particle energy E. Pink points show the baseline performance where slots 1, 3, 4, and 6, counting radially, of imaging layers are filled with AstroPix trays, blue points show performance with 6 imaging layers. Repository to be added. (b) Upper limit on cluster merging at $\eta = 0$ (shortest distance for particles to travel about 80 cm) from 2 photons from π^0 decay at particular π^0 momentum P. For calorimeter technologies based on tower geometry from [7] the separation by at least one tower size is required. For BIC the separation based on shower profile was assumed (see text). Repository to be added. (To be replaced by the NN results with full simulation when ready)

most probable value (MPV) of the MIP peak in terms of the number of photoelectrons (nphe) for muons at $\eta = 0$, which is the case where we observe the least photoelectrons from muons due to the combination of the distance the light has to travel in the fibers and the energy muons deposit at this angle in one Pb/ScFi layer. The pedestal 4-sigma value is marked in red. An example pedestal and MIP signal spectrum for 9 and 12 phe MIP signals, showing the worst-case scenario for the back Pb/ScFi layer of the BIC, is also presented. The BIC demonstrates the capability to detect minimum ionizing particles for calibration purposes in the Pb/ScFi layers, with the MIP peak from 5 GeV muons remaining well-separated from the pedestal, even after realistic irradiation doses. This separation is maintained through careful application of threshold cuts in each channel, ensuring that the MIP signal remains distinguishable from the noise. If necessary, we can lower readout thresholds, as the ASIC provides enough headroom, and employ a coincidence logic (e.g., requiring two neighboring readout cells to fire) for further zero suppression to ensure stable MIP performance over the lifetime of the detector. Investigations of SiPM performance at (higher) room temperature (performed for ePIC by the UC Riverside group) at irradiation levels of 1×10^{10} 1-MeV neq/cm^2, when folded in our simulations, give the pedestal sigma of approximately 9 phe, and at 1×10^9 1-MeV neq/cm^2, of about 5.4 phe. However, the irradiation results in general do not fully represent the expected dark noise level under typical operating conditions, as the irradiation dose corresponding to years of operation was applied in a much shorter timeframe. Consequently, these measurements do not account for effects like self-annealing. Further studies are necessary to better understand long-term performance.

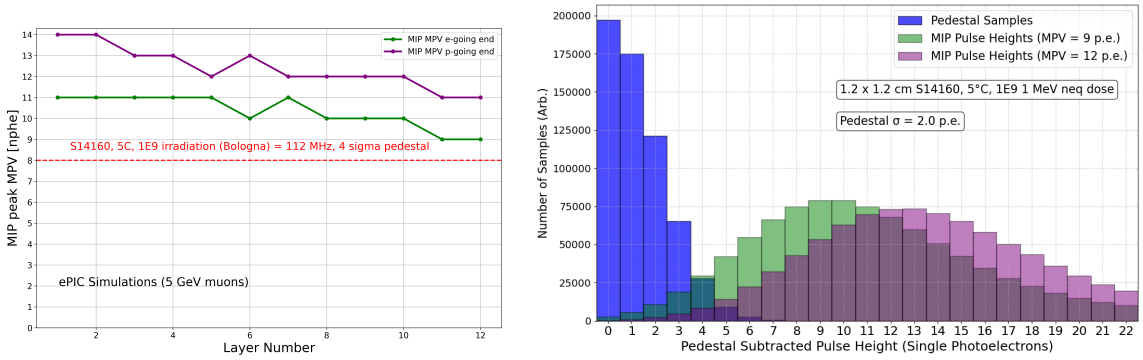

(a) (b)

Figure 8.96: Simulated performance on MIP response in BIC. (a) The most probable value of the MIP peak in terms of the number of photoelectrons for 5 GeV muons at $\eta = 0$ at each of the BIC layers. The red line corresponds to 4 sigma of the pedestal simulated with realistic S14160 family SiPM responses at 7 degrees Celsius, irradiated with a dose of 1×10^9 1-MeV neq/cm^2. The green line corresponds to the electron-going end, while the purple line corresponds to the proton-going end readout cells. Repository to be added. (b) An example spectrum of the pedestal and MIP pulses at 9 and 12 phe signals, showing the worst-case scenario from plot (a) for the back Pb/ScFi layer of the BIC at $\eta = 0$. Repository to be added.

AstroPix sensor performance: The AstroPix chip has been extensively tested in both bench and beam environments. The AstroPix_v3, the first full-size chip with a 500 µm pixel pitch and row-and-column readout (35 rows and columns in a strip-like format), has demonstrated strong performance, as summarized, for example, in [75]. Key tests included a noise study and a radiation source test. In the noise study, less than 0.5% of the pixels exhibited a noise rate exceeding 2 Hz, with the chip's dynamic range starting at 25 keV, allowing thresholds over 200 mV above the baseline. These results meet the BIC's requirements for low energy thresholds and masked pixel yield. The radiation source test, using isotopes with calibration points ranging from 22.2 keV to 122 keV, as shown in Fig. 8.97, showed that 44% of pixels met the 10% energy resolution requirement at 59.5 keV, and 92.4% of pixels achieved the required 25 keV sensitivity for BIC. Although the AstroPix_v3 chip is not fully depleted, it demonstrated promising performance. The upcoming AstroPix_v5, designed with a dynamic range extending to 700 keV, is expected to meet energy resolution requirements for all pixels.

AstroPix beam test results: We used beam tests at Fermilab to further validate the AstroPix_v3 chip in both single- and double-layer configurations. In the single-layer test, data collected with a 120 GeV proton beam was used to match corresponding row and column hits, using matching timestamps and ToT to reveal a hit map that showed the proton beam profile presented in Fig. 8.97. Although the AstroPix_v3 has a daisy-chained row and column readout and does not yet have an individual pixel buffer (which is implemented in AstroPix_v4 and higher), it demonstrated a precise hit-pixel reconstruction. In the double-layer configuration, two daisy-chained layers of AstroPix_v3 were tested, successfully reading events in coincidence and pinpointing hit-pixel locations, providing a proof-of-concept for layer integration in a beam environment.

The characterization of AstroPix_v3 is ongoing, with specific tests designed to meet the ePIC detector requirements. Results show that the chip is well-suited for the BIC and aligns with project goals. Remaining improvements, including enhanced dynamic range and energy resolution, will be addressed in the upcoming AstroPix_v5, which is expected to be fabricated

by early 2025.

Simulation performance validation: We validated the simulation performance of BIC and its components using a combination of bench tests and beam tests at the FTBF and at Hall D in Jefferson Lab. We present more details on select benchmarks of realistic simulation results against measurements in the supplemental material.

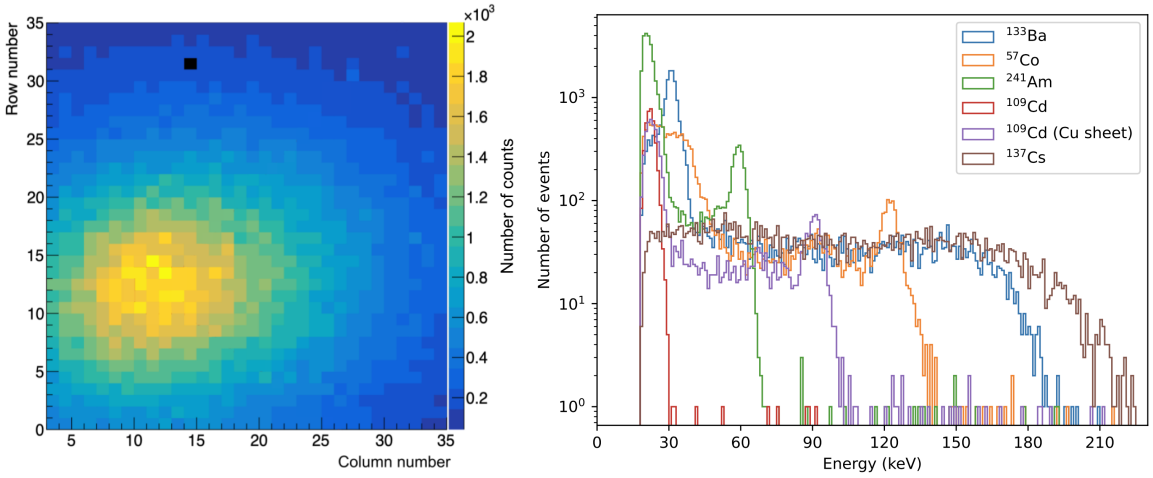

(a) (b)

Figure 8.97: (a) Beam hit map recorded in the 120 GeV proton run in Fermilab Test Beam Facility with a AstroPix_v3 chip. The masked pixel has been marked in black. Repository to be added.(b) Calibrated energy responses form an example pixel of a AstroPix_v3 chip. Plot from [75].

Data Rates: Based on global ePIC studies on rates from signal and backgrounds [76], the maximum channel rates for the Barrel Imaging Calorimeter are as follows. For electron-proton DIS at 18×275 GeV where $0 < Q^2 < 1$, luminosity is $1.54 \cdot 10^{33}$ cm^{2}s^{-1} and collision rate is 83 kHz, the highest rate per channel is 0.66 Hz for the imaging layers and 0.5 Hz for the Pb/ScFi layers. The total hit rates are about $2 \cdot 10^6$ Hz for the imaging layers and $4 \cdot 10^6$ Hz for the Pb/ScFi layers. In background simulations, the highest channel rates are achieved for the hadron beam background at 10×275 GeV, reaching approximately 10 Hz for the imaging layers and 8 Hz for the Pb/ScFi for the hottest channel, and about $9 \cdot 10^6$ Hz for the imaging layers and $1.5 \cdot 10^7$ Hz for the Pb/ScFi layers for the total hit rate. For the 10 GeV electron beam background, the maximum channel rates are about 4.8 Hz and 8.0 Hz, respectively. The total hit rates are about $2.4 \cdot 10^6$ Hz for the imaging layers and $3.1 \cdot 10^6$ Hz for the Pb/ScFi layers. These numbers come from the ePIC Background Wiki, but they are not consistent with the numbers from Jeff. We will be able to specify the rates in Gbps or GBps when we understand this discrepancy.

Implementation

Subsystem mechanics and integration: The 48 BIC sectors are arranged in a self-supporting Roman arch configuration. Once assembled, the full calorimeter is supported by the solenoid cryostat support rings. In the hadron-going direction a small gap must be bridged between the end of

the BIC and the support ring, while in the lepton-going direction the system slightly overhangs, creating a cantilevered structure.

A BIC sector consists of six carbon fiber frames for the imaging layers, interleaved with five single layers of a Pb/ScFi matrix (each 17 fibers tall), followed by a bulk segment consisting of seven Pb/ScFi matrix layers. The back of the sector consists of an aluminum support plate with connectors designed to link the sectors together, affix the ESB, and integrate with the global BIC support structure. The sector is constructed as a monolith, with all components epoxied together to ensure structural integrity.

The inner face of each BIC sector consists of a 0.5 cm thick aluminum plate, designed to connect the inner support rails to the detector. The inner support rails hold the inner detector support structure, maximizing the use of available space while avoiding obstruction of the ESBs (the readout boxes), ensuring that individual imaging layers can be added or removed as necessary for future upgrades or servicing. Hence, the BIC plays a critical role in supporting the overall inner detector structure.

Detailed FEA to validate the mechanical integrity of the sector design is ongoing. The design of the support that connects the BIC to the solenoid cryostat support rings is still under development, ensuring it meets the mechanical stability requirements while maintaining accessibility to readout electronics and other critical components.

Calibration, alignment and monitoring: The BIC calibration approach treats the Pb/ScFi and AstroPix imaging layers as two separate systems, each calibrated independently. For the Pb/ScFi calorimeter, we will follow well-established in-situ calibration methods, starting with MIP-based calibration, then refining with meson decays, electrons, and kinematic techniques derived from experiences with GlueX and HERA experiments. The energy calibration is further refined using decay photons from neutral pion events ($\pi^0 \to \gamma\gamma$).

For the AstroPix layers, the calibration process occurs in three steps. First, an absolute pixel energy calibration is performed during stave assembly using a radioactive source. Next, in-situ position and alignment calibration will be conducted similarly to standard tracker procedures, utilizing cosmics. Finally, the overall imaging cluster energy calibration will be matched with the Pb/ScFi calorimeter, leveraging the energy reconstruction methods described above.

Metrology will be used for alignment during installation, though very precise alignment is not critical, given the calorimeter's purpose. Cosmic and physics events will be used to calibrate the relative positioning of detectors and sensors, ensuring accurate reconstruction.

Calibration stability during operation will be ensured by using LED-based relative light monitoring systems for continuous monitoring, along with additional checks on linearity and timing using both cosmics and dedicated calibration runs.

Services: The Pb/ScFi part of BIC, which utilizes SiPMs, requires two LV lines (plus ground) of 1.2 V and 2.5 V for each H2GCROC3-based front-end board (FEB), along with one HV line (plus ground) operating at less than 50V for biasing SiPMs. The system features a total of 5,760 readout channels distributed across 48 sectors, with one FEB per sector per side, each managing 60 readout channels. Each FEB is connected to the RDO through four lines: two data lines, one clock line, and one slow control line, and 1 RDO maintains 24 FEBs.

For the AstroPix sensor layers, the LV services include two 1.8 V to power the analog and the digital part of the chip and the HV of 200-400 V distributed to each stave. Each stave within an AstroPix tray connects to the data acquisition system through an FPGA-based End-of-Tray Card (ETC, one

per tray) connected to DAM via an optical link. In total, each sector will include 27 staves per side. The ETC will be powered through Power over Ethernet (PoE) within the control cable.

The SiPMs require cooling to maintain a temperature of 7°C. Each ESB will have in/out lines for cooling water and a dry air or N_2 system to prevent condensation. The estimated heat load per ESB is projected to be under 100 W, necessitating effective heat management. Liquid water cooling will be utilized for the SiPMs, their readout boards, and the ETCs. AstroPix sensors are highly heat efficient, consuming less than $2\,mW/cm^2$. The baseline cooling strategy involves thermal coupling to dissipate heat through the staves and trays, with cooling occurring at the edges along with the ETCs. If additional cooling is required, circulating liquid through the staves will be employed as a mitigation measure. A preliminary cooling design is expected by May 2025 as part of the Cooling FEA in the PED phase.

Status and remaining design effort: High-level schedule for the BIC design and production phase is available in Additional Material (See Fig. 8.98).

R&D effort: The R&D efforts for BIC focus on demonstrating the combined performance of Pb/SciFi and AstroPix in EIC-like environments. This involves measuring higher than GlueX energy response up to about 10 GeV, benchmarking high-energy electron and pion simulations, testing AstroPix in high-rate environments, and integrating the Pb/SciFi with AstroPix sensor layers. In FY23, responses to 6 GeV positrons in 60 cm long Pb/ScFi prototype were measured in Hall D of Jefferson Lab, showing a constant term of about 2%, consistent with simulations. The Baby BCAL was commissioned with proton, pion, and electron beams during a June 2024 FBTF test, where data collected allowed for pion simulation benchmarking. A proof-of-concept synchronization of AstroPix with Baby BCAL was achieved by triggering on the AstroPix analog signal. With extensive data from previous AstroPix tests in FY23, the R&D is ready for multi-layer beam tests, to be conducted in early FY25 pending delays at Fermilab Test Beam Facility.

E&D status and outlook: The Project Engineering Design phase of our project that started with granting the funding to the participating institutions starting Q4 2024, encompasses a detailed roadmap for the design, testing, and integration of key components for BIC. Early milestones focus on the design and development of the Pb/SciFi sector, including short and long test articles and the structural framework needed for housing these components. Alongside this, efforts are directed toward the design and prototyping of the end-of-sector box, which includes light guide and light monitoring systems integration. The tracking layer, which features AstroPix sensors, undergoes simultaneous development. This includes performance characterization of the AstroPix chips, module design and assembly, and testing of components such as bus tapes and end-of-tray cards. By mid-PED-phase, both the Pb/SciFi and tracking layers will undergo rigorous integration testing to ensure seamless functionality within the full detector system. The final phase focuses on validating the designs and performing full integration testing of staves, modules, and tracking layers. Quality control procedures will be established for each component, ensuring that everything meets performance specifications before final assembly. The PED phase is expected to finish in Q1-Q2 FY26.

Other activity needed for the design completion: Within the small-scale R&D and design funding in Korea, a focused effort is underway during the period from August 2024 to April 2027, covering the PED phase and pre-production phase. The primary objectives include the development of testing and assembly systems for the AstroPix chip, particularly emphasizing automatic wafer testing and module assembly. Additionally, this work involves

designing the readout box for the Pb/SciFi system and producing test modules to conduct performance studies.

Status of maturity of the subsystem: The maturity of BIC is currently estimated to be between 30% and 60%, depending on the specific component. The entire BIC underwent an incremental Preliminary Design Review (PDR2) in September 2024. Scintillating fibers and SiPMs have reached the final design stage, as they are classified as long-lead procurement items. Recognizing the extensive requirements for these materials—around 4900 km of scintillating fibers and a large quantity of SiPMs for ePIC—the project identified the need for early procurement. The Final Design Reviews (FDR) for both the scintillating fibers and SiPMs were successfully passed in September 2023. The first portion of the scintillating fibers was included in CD3a, with further procurement scheduled for CD3b. Vendor selection is nearly complete, and the first long-lead orders are expected by Spring 2025.

Construction and assembly planning:

Pb/ScFi Sectors Construction: The production of Pb/ScFi sectors will take place at Argonne, where there will be two production lines. The sectors will be constructed by embedding scintillating fibers in lead sheets, arranged in a stepped "Mayan pyramid" configuration, following the GlueX model. Carbon fiber frames will be integrated with the sector as it is built, with each frame assembled from two C-channel-like sides and a top and bottom plate. The sector construction process will proceed at a pace of 0.5 to 1 matrix layer per day, with the ability to build two sectors in parallel. Once a sector is fully assembled, it will be sent to an external machine shop for precise machining. Upon return to Argonne, the sector will undergo metrology and QC before being prepared for shipment to BNL.

ESB Manufacturing: The construction process for the ESB is still in development. ESB construction will include large-scale SiPM testing, SiPM mounting, light-guide manufacturing, light-monitoring system integration, construction of structural and cooling components, and manufacturing of electronics boards. There will be at least two ESB production sites: one in Canada at U. Regina and one in Korea. As the procedure is finalized, further details on assembly and integration will be specified.

AstroPix Wafers: The AstroPix sensors will be fabricated at the AMS foundry. Due to the large scale of the detector, automatic wafer-level testing will be conducted at two sites: PNU (South Korea) and Argonne. This testing will ensure the functionality of each chip before dicing, including IV-CV measurements, ASIC performance, noise levels, and defect detection early in the production process. After testing, the wafers will be diced into individual AstroPix chips.

AstroPix Modules and Trays: AstroPix chips will be assembled into modules at three production sites: Argonne, UC Santa Cruz, and PNU (South Korea). Each module will consist of nine daisy-chained AstroPix chips, readout on flexible PCBs. After assembly, each module will undergo initial testing to ensure proper chip-to-chip communication, pixel functionality, and noise levels. Modules that pass this stage will be integrated into staves, with 12 modules per stave. To keep the production process scalable and efficient, only one flavor of stave will be used across the entire system. The staves will then undergo additional QC testing. Once validated, the staves will be integrated into trays. There are two flavors of trays: one for the first imaging layer and the other for layers 3, 4, and 6. The hadron-going side and the lepton-going side trays of the detector are mirror images of each other. Each tray will contain 6 staves in layer 2 and 7 staves in the outer three layers. These trays will then undergo final QC prior to shipping to BNL. The entire production and QC procedure is designed to catch

any defects early and ensure that the trays are fully operational before final integration into the BIC sectors.

Assembly Planning: The assembly of the BIC will follow a carefully planned sequence. Upon arrival at the integration site, the Pb/ScFi sectors will be unpacked and prepared for assembly. The first step will involve attaching the light guides to the sectors. Once the initial sectors have been prepared, we can begin the barrel assembly while continuing to unpack and attach light guides to the remaining sectors. The BIC barrel will be assembled next to the solenoid and then inserted into the solenoid using existing sPHENIX tooling. Following the installation of the barrel, the imaging layer trays will be inserted using specialized tooling that is still under development. After all trays are installed, the electrical and cooling connections will be made, and the rest of the ESB will be installed to complete the installation. This phased approach ensures that all components are properly integrated before the system is brought online for testing.

Quality Control (QC) Planning: QC will be implemented at multiple stages of the BIC production and assembly process to ensure system integrity and performance. The system, particularly the imaging layers, is designed with both modularity and scalability in mind, allowing for efficient production, easier upgrades, and reworkability. Key QC procedures include:

Pb/ScFi Sector Assembly: The Pb/ScFi sectors will undergo thorough inspection during assembly. Scintillating fibers and lead sheets will be inspected for defects before embedding. After each matrix layer is completed, visual and metrological inspections will ensure proper alignment and uniformity. Final metrology checks will be performed after external machining to confirm dimensions prior to shipment.

AstroPix Wafer Testing: Automatic wafer-level testing will be conducted to assess chip functionality, including chip performance, noise levels, and defect detection. Once tested, wafers will be diced, followed by additional metrology and electrical/non-electrical QC on individual AstroPix chips to ensure reliability before moving to the module assembly phase.

Module and Tray QC: Modules will be assembled from AstroPix chips and undergo functional tests to verify chip-to-chip communication, pixel functionality, and noise levels. Defective modules will be identified and replaced before progressing to stave assembly. Staves will be tested for electrical continuity, power consumption, and thermal performance under load. QC for staves and trays will use the actual End-of-Tray Card (ETC) readout electronics to perform these tests. Once integrated into trays, final testing will check for alignment, electronic connectivity, and cooling performance, ensuring that trays operate as intended under operational conditions.

ESB QC: SiPMs will undergo rigorous testing to ensure proper photon detection efficiency, dark count rates, and timing precision before being integrated into the ESB. ESB integration with the sector first article will test the complete system, including electrical connections, data acquisition, and cooling systems, to ensure seamless functionality with the Pb/ScFi sectors.

Final Integration and Barrel Assembly: After attaching light guides to the Pb/ScFi sectors, alignment and metrology checks will be conducted during barrel assembly to ensure sector and tray alignment within tolerances. Electrical and cooling system checks will be completed post-installation to confirm proper functionality. System-wide tests, including cosmic ray runs and electronic readout, will validate the entire system before commissioning.

Environmental, Safety and Health (ES&H) aspects The BIC design incorporates standard safety and environmental practices across all production sites. We will strive for standardized safety protocols while adhering to internal work planning and control processes at each institution to identify hazards, implement mitigations, and document safety procedures. Main hazards associated with the BIC include:

Lead handling: The handling of lead sheets for the Pb/ScFi matrix requires careful consideration. We are working closely with experts to determine the appropriate safety steps. These steps may include specific protocols to mitigate any hazards and the potential enrollment of personnel in continuous health monitoring programs to ensure long-term safety.

Epoxy usage: Standard procedures for handling, mixing, and applying epoxy will be followed, with work conducted in fume hoods to ensure safety. Part of our PED work aims to deploy a custom mixing nozzle to reduce air contaminants and epoxy waste while improving consistency in the application process.

Scintillating fibers: The fibers are made of flammable polystyrene, and with the total fiber mass exceeding 3.9 tons, proper fire safety measures and storage protocols are essential.

Pinch/nip hazards: Automated systems, such as robots for wafer probing, pick-and-place, and glue application, present pinch hazards. Controls, such as PPE, gloves, guards, and procedures, will be in place to mitigate these risks.

Crush hazards: The use of presses and swaging equipment introduces crush hazards during assembly processes. Strict safety protocols, including the use of guards and operator training, will mitigate these risks.

Radioactive sources: The use of radioactive sources for calibration introduces additional handling requirements, and proper shielding and storage protocols will be implemented as necessary.

Electrical safety: Electrical safety procedures will also be applied for all electronics and power systems associated with the BIC production tooling and detector components.

Collaborators and their role, resources and workforce: The full BIC WBS org chart is available in Additional Material (see Fig. 8.102). BIC is supported by a diverse and robust international collaboration, with institutions from the United States, Canada, Korea, and Germany. These collaborators bring together a wealth of expertise and resources, working collectively to advance the development of the BIC.

In the United States, several institutions play a key role across multiple aspects of the project. Argonne National Laboratory is leading several crucial areas, including the design and assembly of modules and staves, sector production, cooling systems, and system testing and QC, while also overseeing the software, simulation, and benchmarks. Oklahoma State University leads efforts on stave bus assembly, and the University of California, Santa Cruz (UCSC) supports module design and assembly efforts. NASA Goddard Space Flight Center (GSFC) contributes via the ETC components, ensuring that electronic testing is integrated into the system.

Canadian institutions play a critical role, especially in the production and quality control of ESB. The University of Regina contributes to multiple efforts, including the QC of scintillating fibers, SiPM integration, light guides, and electrical design, while also contributing to the system's demonstration and testing. The University of Manitoba provides leadership in cooling system development and supports the SiPM integration efforts. Mount Allison University focuses on ESB production, aiding in the overall electronics support infrastructure.

Korean institutions are heavily involved in various production, design, and testing processes. Collaborators from Kyungpook National University (KNU) support both electronics and SiPM integration. Yonsei University plays a key role in the sector production process and testing, while Sungkyunkwan University (SKKU) focuses on sector development and production. Pusan National University (PNU) leads efforts on wafer testing and supports software development and simulation. Additionally, Hanyang University, Korea University, and other Korean institutions provide significant contributions across assembly, installation, and testing.

The Karlsruhe Institute of Technology (KIT, Germany) provides essential AstroPix chip support.

Risks and mitigation strategy:

A potential risk in the production of AstroPix chips is related to the feasibility of using 12-inch wafers, which offer a more modern and cost-effective solution. However, if this option proves unviable, we will need to use 8-inch wafers, increasing costs. This is budgeted in the risk registry.

The schedule has sufficient time built in to accomodate an additional iteration of AstroPix beyond v6 if needed.

Risks on production-delays due to the availability of scintillating fibers and SiPMs were mitigated through CD3a/b long-lead procurement ensuring the timely availability of these components.

As outlined in the Construction and assembly planning paragraph, in the default scenario, sector production will take place at Argonne using two production lines, with one staffed by Korean collaborators. ESB production and quality control will be managed by Canada and Korea. Wafer testing will occur in both Korea and the US. AstroPix module and stave production will be distributed across three or more sites in the US and Korea. Depending on the level of in-kind funding, the baseline plan is to produce four to six layers. In the unlikely event of no in-kind funding from Canada and Korea, the project will cover all sector production labor costs, including Korean collaborators, and consolidate production to a single ESB site (Canada) and a single wafer testing site (US). AstroPix module/stave production will be limited to two sites in the US, requiring an increased workforce at each site or potentially facing a one-year delay to deliver the four baseline layers.

Additional Material

Subsystem description

- More detailed description of subsystems: sector, ESB, tray, module, chip
- More details on AstroPix chip with timelines
- More details on SiPMs
- More details on readout scheme ETC and CALOROC

Schedule

- High-level BIC Schedule in Fig. 8.98.

Parameter	AMEGO-X Mission Requirements	BIC Requirements
Pixel size	500 μm x 500 μm	same
Power usage	< 1.5 mW/cm^2	~ 2 mW/cm^2 acceptable
Energy resolution	10% @ 60 keV	same
Dynamic range	25-700 keV	same
Passive material	$< 5\%$ on the active Si area	same
Time resolution	25 ns	3.125 ns (available in v5)
Si Thickness	500 μm	same

Table 8.31: Comparison of AstroPix requirements for AMEGO-X and BIC.

Performance

Realism of simulations

- Geometry implementation description
- How light response is simulated: folded in measurements of nphe/GeV, fiber attenuation length, simulations of light guides and optical cookie, SiMP PDE and simulations
- Comparison of data from beam tests and simulations benchmarking their realism: response to electrons and pions

The realistic BIC geometry was implemented, including a detailed Pb/SciFi matrix with scintillating fibers embedded in lead and glue, following the GlueX model. The AstroPix layers were implemented as staves, with AstroPix chips placed in realistic dead areas, and materials accounted for the sensors, electronics, cables, insulation, glue, and support structure. Realistic digitization and reconstruction were applied. For the Pb/SciFi component, an effective model for light attenuation in the fibers, photoelectron statistics, light guide efficiency, and SiPM thresholds was implemented based on beam and bench measurements as well as optical simulations. For AstroPix, each digitized readout unit corresponds to one pixel, while for the Pb/SciFi component, each readout cell covers the area of one light guide with an attached SiPM.

Energy response

- Evaluation of the energy response tail
- Simulated energy response to electrons
- Energy resolution for low energy photons
- Energy resolution from FTBF FY24 beam test.

The contribution of the low-energy tail of the energy losses was quantified by calculating the difference between the area under the fitted Crystal Ball function and that of its Gaussian core marked in red in Fig. 8.99 (a). The tail contribution to the overall energy loss area is shown in Fig. 8.99 (b) and (c) for electrons and photons, respectively. The results of energy resolution and total sampling fraction as a function of energy for electrons is presented in Fig. 8.100.

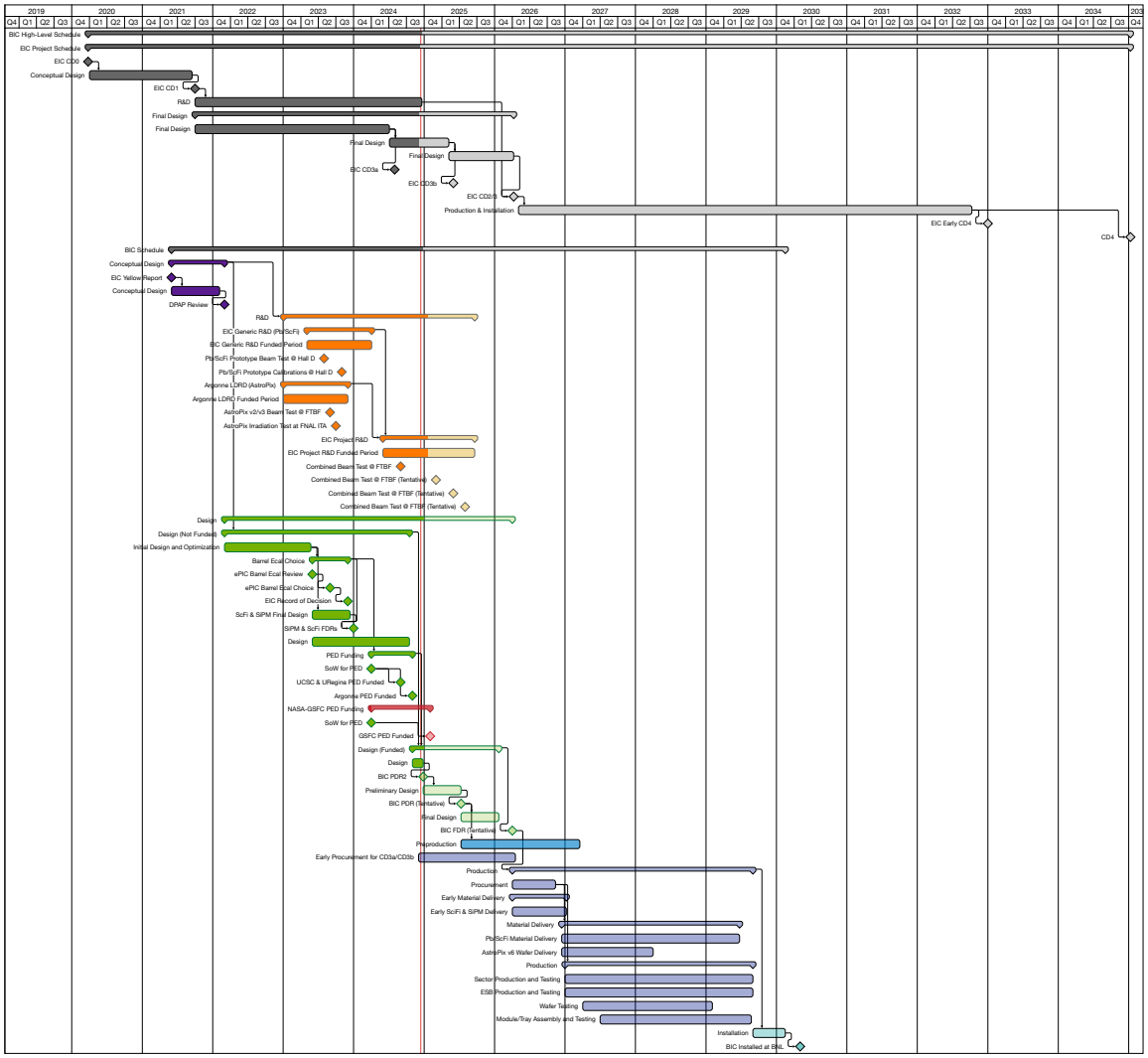

Figure 8.98: Barrel Imaging Calorimeter high-level schedule for design and production phases. (Updates expected)

Energy response to both electromagnetic and hadronic showers has been also tested in the beam test environment with a 60 cm long and 15.5 X_0 deep Pb/ScFi bulk-section prototype based on GlueX BCAL geometry, termed *Baby BCAL*. At Hall D of Jefferson Lab, Baby BCAL was exposed to 3-6 GeV positrons hitting it at different impact angle and position depending on beam energy. Figure 8.101 (a) presents the measured energy resolution measured in those conditions. Note that the highest energy points reflect positrons hitting the prototype close to the end and at the impact angle that causes partial shower leakage. At Fermilab Test Beam Facility, Baby BCAL was exposed to mixed electron-pion-muon beam at energies of 4, 6, 8 and 10 GeV. The energy response to pion beam has been benchamrked in simulation of Baby BCAL implemented in ePIC environment, same as used for the BIC simulations. Fig. 8.101 (b) shows comparison between collected data and simulations benchmarking their realism.

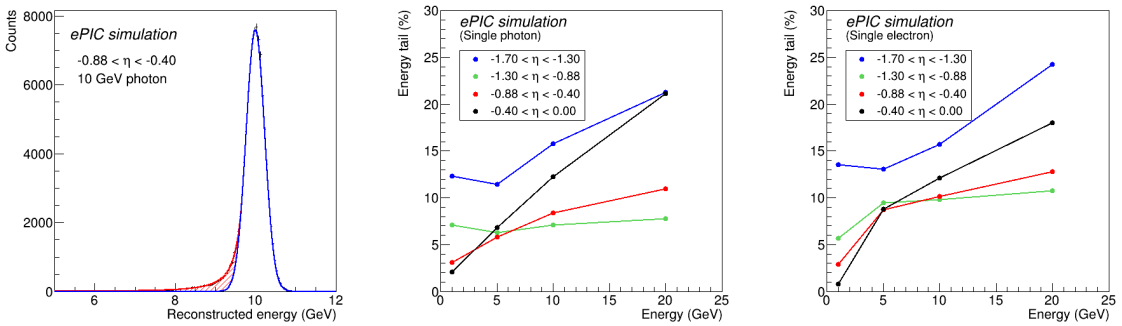

(a) (b) (b)

Figure 8.99: (a) Simulated energy losses in scintillating fibers of BIC for 10 GeV photons in the rapidity range $-0.88 < \eta < -0.4$. The distribution has been fitted with the Crystal Ball function; the Gaussian core of the function is marked in blue, and the power-law tail area is marked in red. (b) Percentage contribution of the low-energy tail–red area in plot (a)–to the overall area under the Crystal Ball fit to the energy losses of photon in Pb/ScFi as a function of photon energy and rapidity. (c) Same as (b) but for electrons.

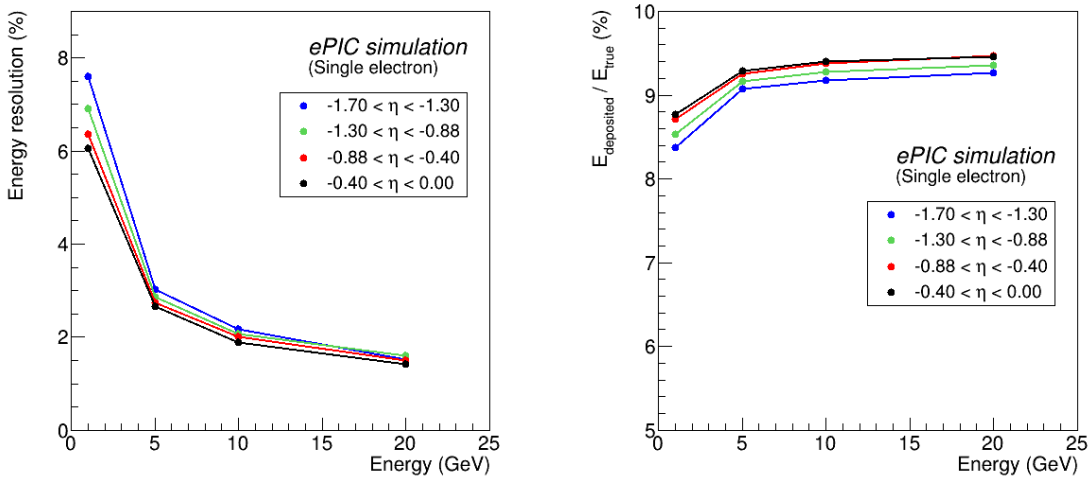

(a) (b)

Figure 8.100: (a) Simulated energy resolution in from Pb/ScFi extracted as a σ of the Gaussian core of the Crystal Ball fit to the energy deposits of electrons in different rapidity ranges at BIC. (b) Sampling fraction for electrons, defined as energy losses in scintillating fibers divided by the true photon energy, as a function of photon energy in different rapidity ranges. (To be replaced with matching η regions and adjusted y-axis)

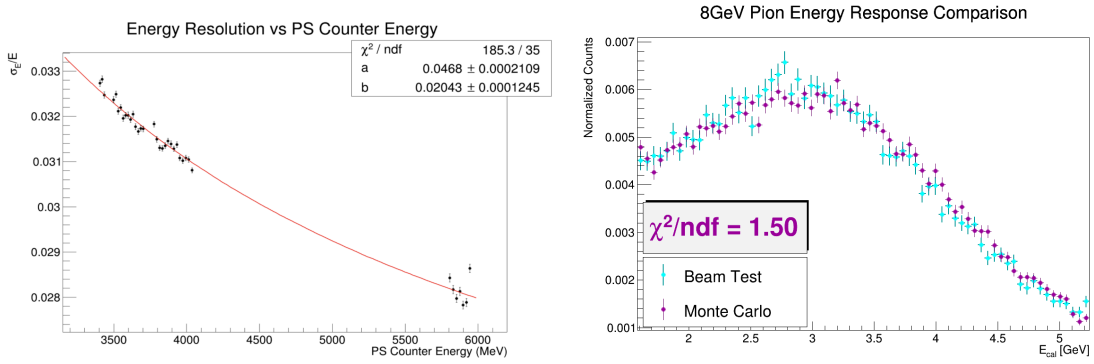

(a) (b)

Figure 8.101: (a) Preliminary energy resolution of Baby BCAL exposed to 3–6 GeV positrons at Hall D of Jefferson Lab, with varying impact angles and positions depending on beam energy. The highest energy points correspond to positrons striking near the end of the prototype and at angles causing partial shower leakage. Red line shows the fitted function $\sigma/E = a/\sqrt{E} \oplus b$. Repository to be added (b) Preliminary energy response of Baby BCAL to an 8 GeV pion beam at the Fermilab Test Beam Facility. The plot compares the collected data (light blue) with simulations (purple) implemented in the ePIC environment, as used for BIC simulations, benchmarking the realism of the simulation model. Repository.

Particle identification

- More details about the NN methodology
- Performance for different rapidity ranges and electron efficiencies
- Muon detection efficiency

For our π^-/e^- separation studies, we utilized a 10-layer Visual Geometry Group (VGG)-style Convolutional Neural Network (CNN) to process combined data from the AstroPix and Pb/ScFi parts of the calorimeter. This CNN architecture consists of 5 convolutional layers interspersed with 2 pooling layers, followed by 3 fully connected (dense) layers. Each event is formatted into an input array with dimensions $N_{\text{layers}} \times N_{\text{hits}} \times N_{\text{features}}$, where 4 primary features: energy deposit, η, ϕ, and radial position of the hit inside the calorimeter, to capture both energy deposition and spatial information about the particle shower.

We trained the network using supervised learning with a data set composed of a 10:1 ratio of pions to electrons. This ensured a sufficient number of pions remained after applying the energy-over-momentum (E/p) cut, which was crucial for training accuracy. Each training cycle consisted of 20 epochs, with data split into 70% for training, 10% for validation, and 20% for testing. On average, between 100,000 and 200,000 events were included in each training set, drawn from over 2TB of official singles productions simulations.

The CNN's performance is measured with uncertainties based on binomial statistics, providing robust estimates of classification accuracy. A similar but simplified approach was used for neutral pion identification. Initial results demonstrate promising pion rejection rates, which could be further enhanced by implementing algorithmic improvements. Future iterations of the model may explore Graph Neural Networks or Point Clouds to better capture the spatial and relational data inherent in these complex events.

MIP measurement capability

- More details about the SiPM simulations
- Performance for different rapidity ranges

Services and subsystem mechanics and integration

- More details about integration and services

Calibration, alignment and monitoring

- More details about calibration

Status and remaining design effort:

- Detailed timeline on R&D and PED efforts

Environmental, Safety and Health (ES&H) aspects and Quality Assessment (QA planning:

- Remaining details on ES&H

Construction and assembly planning:

- Full construction plan with sites, FTEs, yelds, etc

Collaborators and their role, resources and workforce:

- Full org chart

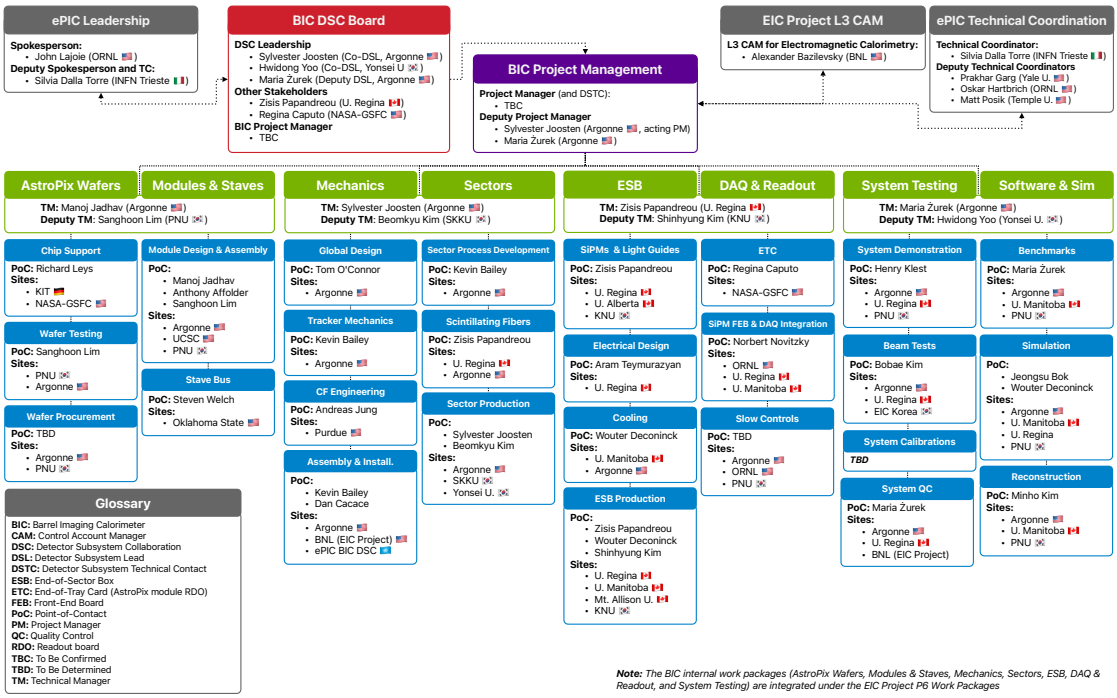

Figure 8.102: Barrel Imaging Calorimeter org chart. (Updates expected)

8.3.5.3 The forward endcap electromagnetic calorimeter

Introduction The ePIC forward electromagnetic calorimeter (fEMCal) is part of the hadron end-cap calorimeter system, complementing the forward hadronic calorimeter. Complete calorimetric coverage in ePIC is essential for detecting photons and electromagnetically decaying mesons, which are crucial for reconstructing parton-scattering kinematics through jets and to identify DVCS photons. fEMCal provides full azimuthal coverage within a pseudorapidity range of approximately $1.4 \lesssim \eta \lesssim 3.9$. At lower pseudorapidity, fEMCal overlaps with BEMC, ensuring continuous coverage by electromagnetic calorimeters in the hadron side of the ePIC detector. Coverage at higher pseudo-rapidity is restricted due to mechanical limitations (clearance required to accommodate the accelerator beam pipe).

The design requirements for the fEMCal were established through extensive studies of various detector concepts proposed for the EIC over the past decade. These concepts originated from the designs presented in the EIC White Paper [8] and Yellow Report [7], evolving through the ECCE [11] and ATHENA [12] proposals and culminating in the ePIC detector concept discussed here. It was concluded that an energy resolution of approximately $12\%/\sqrt{E} \oplus 2\%$, along with high granularity needed to distinguish single photons from DVCS events and photon pairs from π^0 decays up to 50 GeV, would meet the EIC's measurement objectives.

Though numerous electromagnetic calorimeter technologies were considered, as noted in the EIC Yellow Report [7], the stringent space limitation in ePIC detector (an integration length of only 27 cm along the Z-axis for fEMCal) ruled out all but one technology for the fEMCal: WScFi. This technology, developed during the generic EIC detector R&D program [77], has also been successfully implemented in the recently constructed barrel electromagnetic calorimeter of the sPHENIX experiment [78], which is comparable in scope with the ePIC fEMCal.

Some of the key requirements and parameters for the fEMCal are summarized in Tab. 8.32. The most critical challenges include the limited integration space and the need for a very large dynamic range, approaching 7000:1. Radiation doses and neutron fluxes are not expected to pose significant challenges for current technologies. For instance, the forward calorimeter system (FCS) constructed for the STAR experiment at RHIC has been successfully operational since 2021 under conditions—both in terms of radiation and neutron flux—similar to those anticipated at the highest luminosities of the EIC. The choice of photodetectors and front-end readout electronics for the fEMCal is partially based on the readout system developed for the STAR FCS.

Device concept and technological choice: Figure. 8.103 depicts the front face of the ePIC hadron end-cap in its closed position, which is divided into two halves to allow access to the inner ePIC detectors in its open position. The end-cap features 1,145 fEMCal installation blocks, each of which is mounted to a one-inch-thick steel plate situated between the hadronic and electromagnetic calorimeters. Each installation block comprises 16 fEMCal towers and weighs approximately 18 kilograms, bringing the total weight of the fEMCal to around 21,000 kilograms. A 0.250 mm air gap separates each fEMCal installation block to accommodate production and installation fixtures tolerances. The readout system for the fEMCal is located at the front face of the blocks, ensuring easy access to the electronics. Cables and utilities run horizontally along each row of blocks to the perimeter of the fEMCal, where they bunched and passed through few openings in the light-tight external shell and connected to the RDOs positioned on the sides of the hadron end-cap.

Each fEMCal installation block is composed of four "production blocks," with each production block consisting of a 2×2 arrangement of towers. All production blocks are identical, and precise mechanical tolerances are ensured by using identical production molds fabricated to high toler-

Table 8.32: Some requirements on performance of fEMCal and its parameters

Parameter	Requirements	Comments
Geometrical Acceptance	$1.4 \lesssim \eta \lesssim 3.9$	$R_{out} \sim 190$ cm, $Z_{frontface} \sim 341$ cm
		Hole for the beam pipe $30 \times 30\ cm^2$
Integration envelope	R_{max}=205 cm, Depth = 27 cm	
E_{min} in a single tower	15 MeV	Minimal shower energy 50 MeV
E_{max} in a single tower	100 GeV	18×275 GeV, ep
Maximum rate in a single tower	10 kHz	E_{thr}=15 MeV, 10×275 GeV ep
		500 kHz collision rate
Radiation doses	15 kRad	Integrated over 10 years
Neutron fluxes	4×10^{11} n/cm^2	1 MeV eq, integrated over 10 years
Energy resolution	$\lesssim 12\%/\sqrt{E} \oplus (2)\%$	Verified in the test beams
γ/π^0 separation	up to 50 GeV	$\sim 5\%$ mis-identification at 50 GeV
Depth	23 X_0	Minimize leakages
Detector parameters	**Units**	**Comments**
X_0, R_m	7 mm, 19 mm	Rad. length, Moliere radius
f_{samp}	2%	e/h $\simeq$1 above 10 GeV
Scintillating Fibers	$\varnothing$ 0.47 mm	Single clad sc. fibers
Light yield	$\sim$ 1600 pixels/GeV	Test beam results.
Transverse size of tower	2.5 cm $\times$ 2.5 cm	Matches R_m
Transverse size of installation block	10 cm $\times$ 10 cm	Block of 16 towers
Total number of towers	18320	
Photodetector	S14160-6015PS	Four 6×6 mm^2 SiPMs per tower
		15 um pixels size
Monitoring system	Blue LED	LED integrated on SiPM board.
		One LED per four towers

ances, within a few tens of micrometers. The epoxy layer between production blocks is typically less than 100 micrometers thick. These thin epoxy layers, along with air gaps between installation blocks, represent the only dead material within the fEMCal volume. These dead zones have a negligible impact on the overall performance of the fEMCal.

The primary reason for using tungsten powder and scintillating fiber technology for fEMCal is that it is the only practical method to meet the stringent requirements outlined in Tab. 8.32. Specifically, the desired energy resolution with extremely compact tower dimensions can only be achieved by combining a small sampling fraction with a high sampling frequency. This high sampling frequency is attained by using 780 thin, 0.47 mm diameter scintillating fibers in each tower, arranged in a staggered pattern with a center-to-center distance of approximately 0.955 mm. Both the fiber diameter and spacing were optimized through Monte Carlo simulations to ensure fEMCal is nearly compensated and maintains the required energy resolution. Tungsten powder is used as the base material for the absorber structure to make the technology viable in practice. A set of specifications for tungsten powder and scintillating fibers for ePIC were established during generic detector R&D program for EIC and experience of constructing sPHENIX barrel EMCal utilizing WScFi technology.

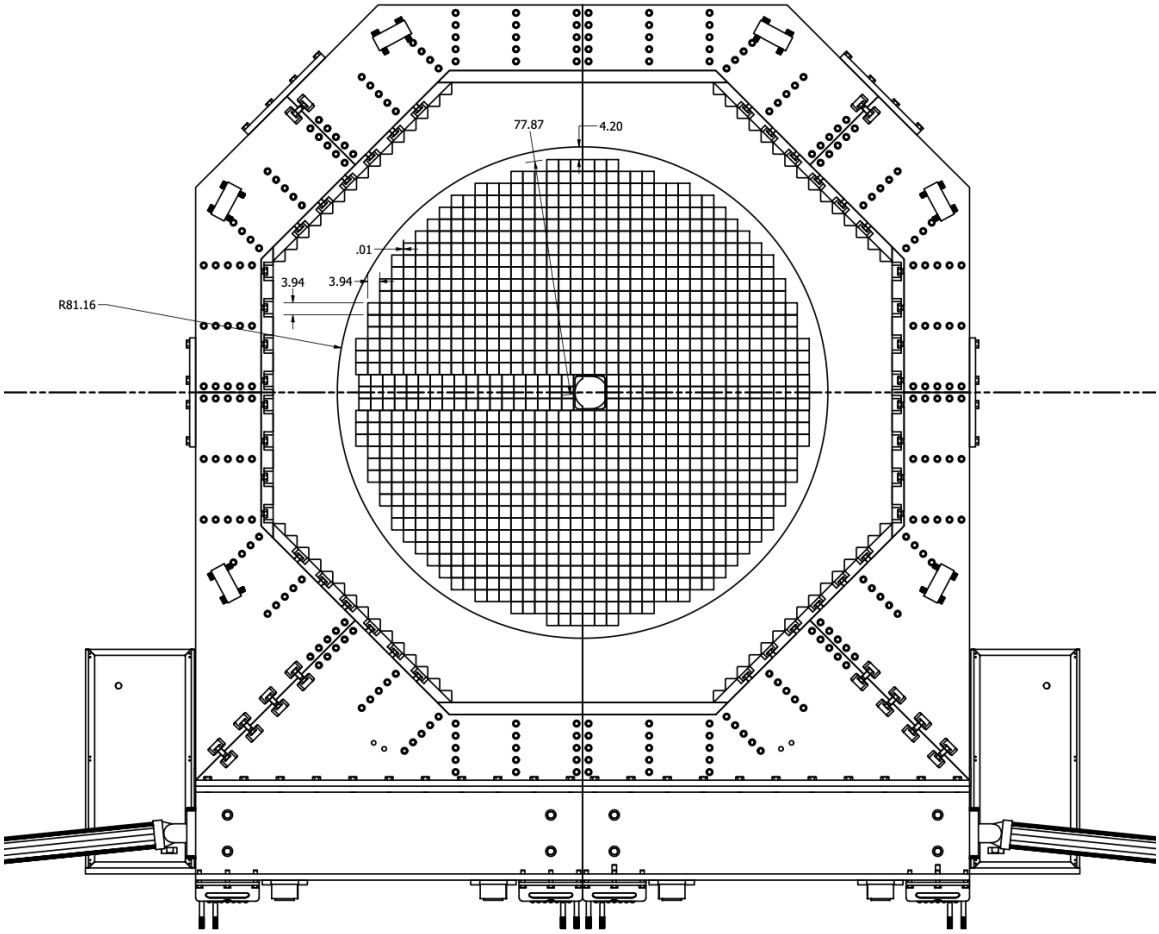

Figure 8.103: The front face of the ePIC hadron end-cap.

Despite the apparent simplicity of fiber calorimeters, constructing them is not straightforward. Detector components must be produced with extremely tight tolerances to maintain uniformity. Historically, techniques like extrusion, machining, or rolling were used to manufacture absorber plates, but these processes were complex and often required the creation of specialized machinery and tools. Building fiber calorimeters has traditionally been a labor-intensive process, with individual detector elements being handled one at a time, driving up costs compared to scintillating plate detectors. Moreover, traditional methods face challenges with increasing sampling frequency, as thinner absorber layers and fibers become more difficult to produce and manage. For example, construction and assembly techniques for H1 fiber calorimeter detailed in [79].

Our approach differs in that we first create a matrix of fibers and then pour the absorber material into the matrix. Unlike previous methods, this technique eliminates the need to handle individual calorimeter elements separately. Fig. 8.104 shows a matrix of scintillating fibers and image of tungsten powder used to build fEMCal prototypes. This powder has a particle size distribution of 90% between 70 and 160 microns, a tap density of 11.5 g/cm^3, and a purity of W $\geq$ 99.9%, with Fe, Ni, and Co combined at $\leq$ 0.1%. Additionally, this tungsten powder exhibits excellent fluidity, a crucial property for our application. The only operation required for the absorber material is measuring the correct amount of powder before pouring it into the fiber matrix.

Figure 8.104: Matrix of scintillating fibers prepared to build production fEMCal blocks and SEM image of tungsten powder.

The second key element is a straightforward method for forming the scintillating fiber matrix. This matrix is defined by a set of precision brass meshes produced via photo-etching. These meshes have mechanical tolerances of 30 microns on their overall dimensions for 300-micron thick meshes and about 15 microns for the center-to-center distances between the holes for the scintillating fibers. The fibers are cut to the desired length using a thermo-cutter, which melts the fiber ends to form small drops that act as stoppers, preventing the fibers from slipping through the mesh holes. Once the meshes are stacked, approximately 500 fibers at a time can be dropped into the container holding the meshes, and with slight tapping, the fibers will flow through the set in seconds. For our recent prototypes, a trained student could form a fiber matrix for a 2x2 tower production block with 3,120 fibers in around 30 minutes.

The total production volume of scintillating fibers for the forward EMCal (fEMCal) is 3,000 km. Only two companies, KURARAY and Luxium (formerly St. Gobain, BICRON), are capable of producing the necessary fibers. Both companies' fibers were previously used to construct and beam-test several WScFI EMCal prototypes for the EIC, with St. Gobain fibers also utilized by the sPHENIX collaboration for their barrel EMCal. Recently, Luxium optimized the composition of their standard BCF-12 fibers specifically for the shorter 17 cm fibers required for fEMCal, resulting in a 20% improvement in light yield compared to their standard fibers. This was achieved by adjusting the concentrations of primary and wavelength-shifting fluors, bringing them to the same performance level as KURARAY fibers. Tab. 8.33 outlines the technical specifications and requirements for the fEMCal fibers.

To create a scintillating fiber matrix, it is essential that the fibers remain straight when placed into the mesh framework. Fibers processed from spools tend to retain a bend due to "memory," which leads to significant friction between fibers flowing through a set of meshes, which complicates the assembly process. Among suppliers, only Luxium agreed to a delivery method that addresses this issue, making them the sole provider of fibers for the fEMCal. These scintillating fibers are a long lead procurement item, with a pre-production batch expected to arrive at ePIC by the end of 2024,

Table 8.33: Requirements and Technical specifications for fEMCal scintillating fibers.

Parameter	Requirements	Comments
Light Yield (LY)	$\geq$ 8000 photons per MeV	Acceptance QA with Sr90 source
		Compared to a standard sample
Nominal Diameter	0.47 mm $\pm$ 0.0094 mm RMS $\leq$ 0.02 mm	QA sampled on 10% boxes
		100% at ramp-up prod. stage
Attenuation Length	$\geq$ 3 m	QA with UV LED
Batch-to-batch LY variation	$\leq$ 10%	QA with Sr90
Emission spectrum	Blue-green light	To match QE of SiPMs
Scintillation Decay Time	$\leq$ 3 ns	Bunch structure at EIC
Delivery Method	In cans, length of fibers +2%, -0%	Length $\geq$ 1 m, increment 20 cm

followed by monthly deliveries of the remaining fibers. Both the production and acceptance sites will adhere to agreed-upon QA and acceptance protocols to ensure that the fibers meet fEMCal specifications. Some of these QA steps are outlined in Tab. 8.33.

The concept of using tungsten powder as an absorber was briefly explored by the UCLA group in 2003, when they constructed and tested a small electromagnetic prototype at SLAC. At the time, the tower structure required a thin-walled brass container to hold the dry powder and fibers in place. However, this assembly technique proved imperfect, leading to significant transverse non-uniformities in detector response due to variations in the sampling fraction and potential displacement of fibers during packing. A compact calorimeter demands strict mechanical tolerances and a highly uniform internal structure to achieve theoretical energy resolution. To address these issues, we introduced intermediate meshes to secure fibers along the towers and developed a vacuum-assisted method to infuse epoxy into the tungsten powder/fiber assembly. Once assembled, the structure becomes rigid, eliminating the need for external containers and dead material in the tower. The homogeneity of the WScFi structure was verified by cutting multiple samples on small pieces which were analyzed and was found to exceed 1%. The mechanical properties of the WScFi structure were measured and they are comparable to construction steel.

This refined technique, with slight variations, was then employed in constructing the sPHENIX barrel EMCal and all recent fEMCal R&D prototypes.

Light Collection scheme and Photosensors The light collection scheme and photosensor setup adhere to the general requirements outlined in Tab. 8.32. The back of each installation block features a thin layer of optical epoxy (1.8 mm thick) mixed with 10% TiO_2, which acts as a diffuse optical reflector for the scintillating fibers and provides a surface for bonding the 13 mm-thick aluminum "strong back." This strong back plate is then bolted to the steel interface plate connecting the EMCal and HCal. On the front side of the installation block, a 21 mm-long light guide (LG) plate is attached. Made from a single piece of optically clear cast acrylic, this LG plate has 64 trapezoidal light guides to direct light from the fibers to the SiPMs. The front and back views of the LG plate with SiPMs attached can be seen in Fig. 8.105. The light collection efficiency of this setup is approximately 80%, which is sufficient to detect 15 MeV in a single tower, corresponding to 24 fired pixels. However, due to the short length of the light guide (typically much longer in fiber calorimeters), light "mixing" from individual fibers is minimal, resulting in spatial non-uniformities in light collection at the 10% level, as measured with a point light source.

The chosen photodetector for the fEMCal is the SiPM (Silicon Photomultiplier). Over the past 15

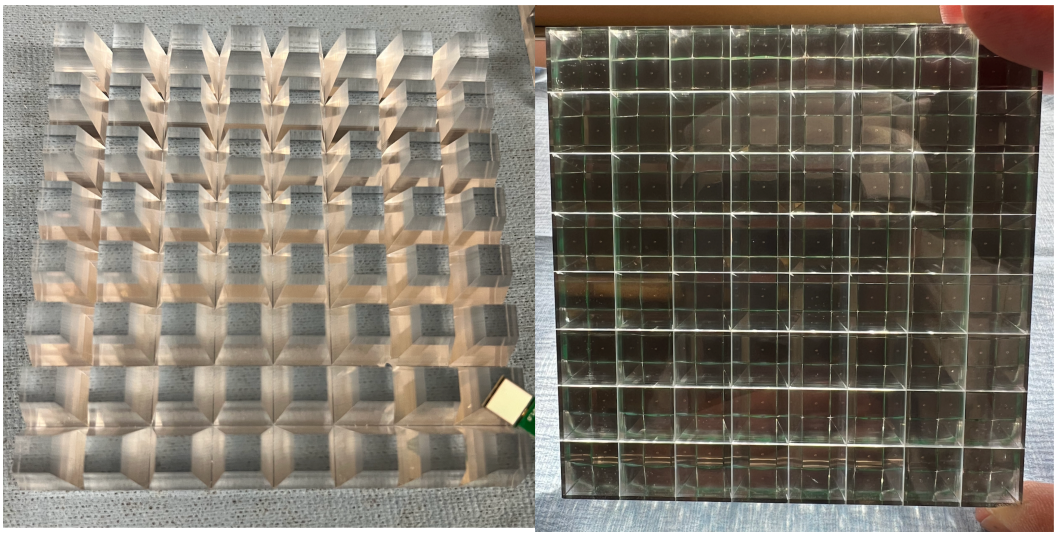

Figure 8.105: Front and back wievs of LG plates with installed SiPMs.

years, extensive R&D programs across the globe—including the generic detector R&D program for the EIC—have worked to bring SiPM technology to a mature and reliable level. Today, hundreds of thousands of SiPMs are in use in various high-energy physics and nuclear physics experiments. These detectors are extremely compact, robust, and well-suited for calorimetry readout in moderate radiation environments, such as the forward region of the ePIC detector, as shown in Tab. 8.32. The failure rates of SiPMs in calorimeter operations at facilities like JLab, BNL, and CERN have been remarkably low, typically less than 0.1%. Notably, the STAR Forward Calorimeter System (FCS) experienced zero SiPM failures during three years of operation under conditions similar to those expected in the high-luminosity EIC. Although neutron-induced damage will lead to increased leakage current and noise levels, these effects remain within tolerable limits. For example, it is anticipated that the equivalent noise level for fEMCal at ePIC will rise to around 6 MeV after 10 years of operation, particularly in areas near the beam pipe. This projection is based on scaling from the results observed in the STAR FCS. After this period, replacement of some of the SiPM boards near the beam pipe may be necessary. These considerations informed the design of the fEMCal readout system, ensuring a straightforward integration with the detector. The technical specifications and performance details of the SiPMs for the fEMCal are summarized in Tab. 8.34.

Mechanical Integration The mechanical integration, installation procedures, and structural tests for the fEMCal were validated using installation blocks at BNL. These blocks were produced following the final production protocols and using the same components that will be used for the actual installation. Structural tests on smaller samples demonstrated that the safety factor for the proposed mounting scheme is greater than 48. A full structural test Fig. 8.106 was conducted by mounting an installation block on a mockup plate and applying five times the expected load. The deflections at the readout end of the fEMCal block were measured to be less than 100 um, confirming that each installation block is self-supporting and does not exert any load on the blocks beneath it. Simple installation fixtures were designed, and the installation procedures were verified to ensure safety. Specifically, it was crucial to confirm that the fEMCal blocks could be safely installed with the SiPM-carrying boards glued to the LG plates. The tests confirmed that the blocks can be

Table 8.34: Requirements and Technical specifications for fEMCal SiPMs.

Parameter	Requirements	Comments
Active Area	6 mm × 6 mm	Efficiency of light collection, E_{min}15 MeV
Pixel Size	15 or 20 um	Dynamic Range, E_{max}100 GeV
Peak Sensitivity	$\sim$ 420 nm	Match scintillating fibers spectra.
PDE	$\geq$ 30%	Efficiency of light collection, S/N
Gain	$\sim 2\times10^5$	at 3 V overvoltage, S/N
DCR	$\leq$ 3000 kcps	at 3 V overvoltage, 25 C, S/N
Temperature Coefficient	$\leq$ 40 mV/C	Stability, Uniformity
Direct Cross Talk	$\leq$ 1%	
Terminal Capacitance	$\leq$ 2.5 nF	FEE coupling
Packing Granularity	Multiple of 4 per tray	4 SiPMs per tower at same V_{op}
V_{op} variation within a tray	$\pm$ 0.02 V	Uniformity of response

safely mounted onto the hadron end-cap without causing any damage to the SiPM boards.

Figure 8.106: Structural and installation tests at BNL.

Performance The performance of the fEMCal prototypes has been tested in several test beams at FNAL over the past few years, initially as part of the generic detector R&D for the EIC and later as part of the ePIC R&D program. In the summer of 2024, one installation block featuring the latest version of the light guide (LG) and SiPM readout was tested at FNAL. Energy scans were conducted at various impact angles covering the entire fEMCal acceptance range. As expected, some variation in response across the surface was observed, as shown in Fig. 8.107, due to the compact nature of the LG. However, this variation represents an improvement compared to earlier versions [80]. Position-dependent corrections, based solely on the data from fEMCal, were applied to account for non-uniformities. This method is similar to the approach used in the 2014 test [80] and for

the sPHENIX barrel EMCal. As anticipated, the uniformity of response improves with shallower impact angles. The energy resolution, shown in Fig. 8.107, corroborates previous measurements with this type of electromagnetic calorimeter [80] and aligns with the performance requirements outlined in Tab. 8.32. The measured absolute light yield is 1580 pixels/GeV.

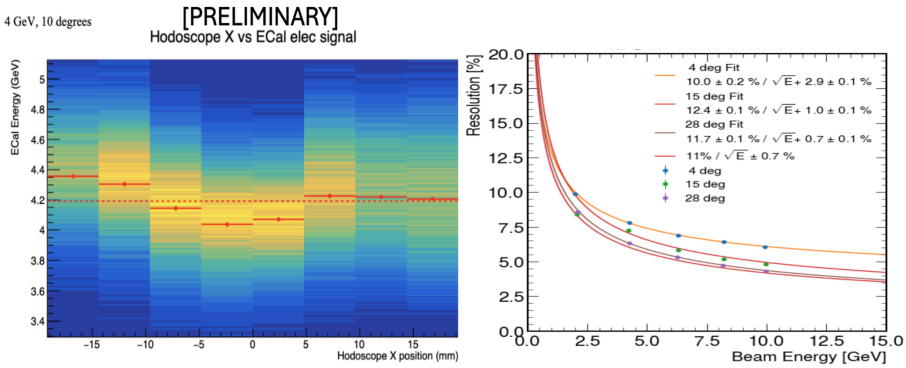

Figure 8.107: Response of calorimeter vs position in hodoscope (left panel). Energy resolution for different impact angles (right panel).

The remaining performance parameters were extensively tested using MC simulations, incorporating the full ePIC simulation chain with the latest detector geometry updates. A material scan indicated the presence of approximately 0.2 X_0 of "dead" material in front of the fEMCal in ePIC, but its impact on performance was found to be negligibly small. Simulations conducted with PYTHIA8, using minimal Q^2 cuts for all energy configurations at the EIC, examined occupancy, rates, and dynamic range. These studies informed the set of requirements listed in Tab. 8.32.

An initial investigation into γ/π^0 separation, based on the traditional shower shape analysis method outlined in the EIC Yellow Report (Fig. 11.46, [7]), revealed potential for improvement. A significant enhancement in γ/π^0 separation was achieved by applying machine learning algorithms. As shown in Fig. 8.108 (left panel), the misidentification rate at 60 GeV dropped to approximately 10%, compared to 80% with traditional methods [7].

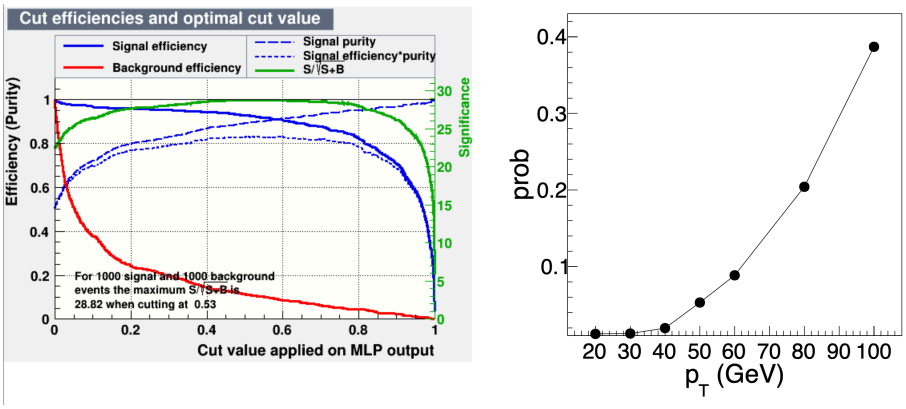

Figure 8.108: Signal (single photon) efficiency and background (merged di-photons) contamination for different cut value of the NN output for 60 GeV (left panel). Probability of misidentifying π^0 as a single photon vs energy (right panel)

Readout Electronics The fEMCal readout electronics face three primary challenges: achieving a large dynamic range of 7000:1, ensuring precise discrimination for streaming small signals (24 pixels) amidst dark counts of up to 45 GHz caused by radiation damage to SiPMs, and integrating everything within a compact space—around 5 cm for SiPM boards, front-end boards (FEBs), cooling, and cables. Tab. 8.35 summarizes requirements for the FEB.

Table 8.35: Requirements for the FEB

Parameter	Requirements	Comments
SiPM & overvoltage	4xS14160-6015PS, 2-3V	
Min signal	15 MeV (@ 1.6 pix/MeV)	
Max signal	100 GeV	
Hit rate	10 kHz	per channel
Charge reso.	$\sim$210%/$\sqrt{npix}$ $\oplus$ (0.9)%	contribute $\leq$10% of fEMCal resolution
Charge nonlinearity	$\leq$ 1%	
Time resolution	$\ll$ 10 ns	for $\geq$100 MeV signals only
SiPM bias voltage stability	$\leq$ 10 mV	including T compensation
Bias voltage setting range	33 to 47 V	sufficient for meaningful IV curve
Bias current range & mon. resolution	2 mA, $\leq$200 nA	4 SiPMs per tower at same V_{op}
LED drive control	var. amplitude, masks	fired by global command

Building on the successful design of the STAR FCS readout, fEMCal's readout system transfers SiPM signals to a low impedance load, shapes and amplifies the resulting voltage, and digitizes the waveform. Hits are detected in the digital waveform via threshold crossing (which may be filtered). In streaming readout mode, regions of interest in the digital waveform are identified, timestamped, and sent to an output FIFO/merging scheme, before being transmitted to the readout (RDO) board. At the RDO, data from up to 16 FEBs are buffered, merged, and sent to the DAM. Feature extraction, converting raw waveform samples to estimated pulse amplitude and timing, may be done either at the FEB or RDO level to reduce data volume. If hardware feature extraction is not used, this will be performed during preliminary online analysis.

Waveform digitization for fEMCal will operate at either 39.4 MSPS or 49.25 MSPS. The digitization clock must be phase-locked to the beam bunch crossing clock at 98.5 MSPS to extract hit timestamps in real-time within the streaming DAQ system. Sampling at 98.5 MSPS is not feasible due to power and FPGA resource constraints. To meet the 15 MeV readout threshold and achieve the dynamic range, the ADC resolution must be 14 bits. The analog waveform will be shaped before digitization to achieve a peaking time of approximately $2.8/f_{SAMPLE}$, which ensures less than 1% error in pulse amplitude measurement while minimizing noise from dark count pileups. For instance, a 57 ns peaking time is optimal at 49.25 MSPS.

The FEB will individually regulate bias voltage for each tower, providing temperature compensation for each SiPM board (covering 2 × 2 towers) and monitoring current with built-in protective current limits. Each tower's four SiPMs will be connected in parallel, sharing a common bias voltage, requiring precise matching of the breakdown voltages (V_{BR}) among the four SiPMs to ensure uniform gain. The bias regulation circuits, developed from the STAR Forward Calorimeter, have proven effective, though radiation sensitivity in a voltage reference IC was noted. To mitigate this, fEMCal's bias regulator will use a remote reference on the power distribution boards, ensuring the required 0.03% stability. Less critical internal voltage references require only 1% stability. The bias regulation channels provide sharp current limiting to protect the SiPMs from overload, maintaining 10 mV bias voltage stability up to the current limit (2 mA).

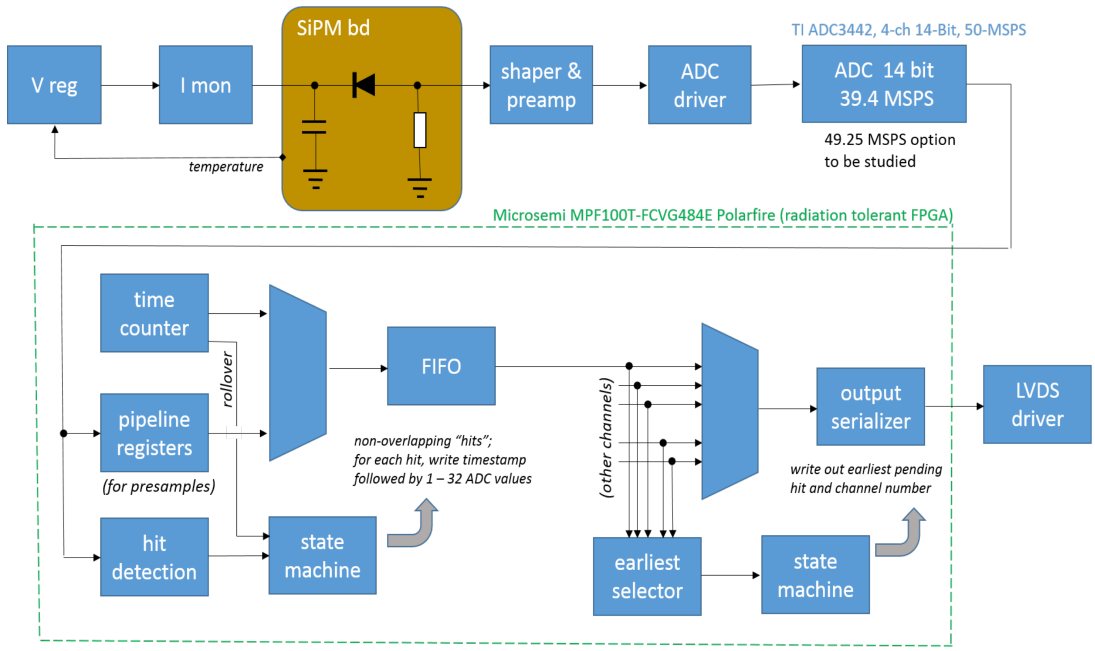

Figure 8.109: fEMCal front end electronics.

Signal routing from the SiPM boards to the FEBs is achieved through board-to-board connectors, eliminating the need for cables. These connectors can accommodate mechanical tolerances of +/- 0.5 mm between the FEB and SiPM boards and overlap with space allocated for the cooling water tube. Should radiation damage impact the innermost FEBs, a backup plan would route SiPM signals via 2m coaxial cable bundles to FEBs mounted at the block periphery.

Connections between the FEBs and RDO will use shielded Cat6 Ethernet cables, routed horizontally through the FEB rows and out of the magnet to racks housing the RDOs. One rack will be placed north of the north detector half, and another south of the south detector half. Cable lengths are estimated at 15 meters, and it has been confirmed that LVDS signals can be properly received at 200 Mb/s over this distance, meeting performance requirements.

Each rack will also house a Wiener MPOD crate with low-voltage (LV) power supplies, with one crate serving the north half and one for the south half of the detector. Each FEB will require approximately 250 mA at +16 V, 180 mA at -2 V, and up to 67 mA (depending on SiPM radiation damage) at +50 V.

The FEBs will be cooled conductively via a copper bracket attached to the main board (housing the ADCs, FPGA, and power supply circuits) and connected to a water cooling line. The water line will consist of standard ¼ inch (potentially 3/16 inch) diameter copper tubing. A negative pressure system will mitigate the risk of water leaks. Two rows of FEBs will be served by a single water line in a U-shaped loop, with no fittings at each FEB, only at the loop ends. Reliable flare fittings will be used for the connections. Custom water manifolds, located in the "service gap" at the outer perimeter of the calorimeter blocks, will manage water distribution. The arrangement will likely consist of two supply and return manifold sets—one for the upper and one for the lower half of the detector.

Each water circuit will need to cool about 750 W of power from 148 FEBs, requiring chillers with at least 1.5 kW capacity for each half of the detector. One chiller will serve the north half and another

the south, cooling two water circuits each.

Slow controls for fEMCal will fall into two categories: hardware registers on the FEBs (communicated through DAQ software and the DAM/RDO) and controls for commercial equipment such as the water chillers and power supplies (Wiener MPOD), connected via Ethernet. SoftIOC interfaces will manage EPICS variables, providing GUI control, logging, and alarms.

Tab. 8.36 summarizes the control and status registers for the FEB.

Table 8.36: Control and status registers on the FEB

Function/description	Qty per FEB	R/W	Notes
SiPM bias voltage (base)	32	R/W	
Bias temp. comp. slope	1	R/W	
actual compensation	8	R	i.e. temperature
SiPM current monitor	32	R	extra diagnostic info
input LV supply monitor	2	R	
FEB temperature monitor	3	R	
FEB & SiPM board serial numbers	9	R	read once at startup
firmware revision	1	R	read once at startup
firmware update interface	1	R/W	maintenance use only
hit threshold channel mask	32	R/W	
hit detection options registers	4	R/W	
LED firing mask	1	R/W	
hit scalers	32	R	
fifo overrun scalers	32	R	
ADC configuration interface	1	R/W	might be internal use only

Calibration The fEMCal faces the hadron beam, and at mid to high energies, its signals will predominantly come from photons produced by π^0 decays. Tower-by-tower absolute energy calibration of the forward electromagnetic calorimeter will be performed by reconstructing π^0 mesons through the invariant mass of two photons from π^0 decays. It is expected that π^0 calibration for each tower can be achieved in approximately one day of data collection, followed by semi-online analysis using only forward fEMCal data. The method involves associating reconstructed π^0 mesons with the tower showing the highest response, adjusting the tower's gain based on the π^0 mass location, and repeating the process over several iterations. This technique has been successfully implemented in forward calorimeters at RHIC, including the STAR FCS.

Electrons from DIS events, combined with tracking information, can be used to cross-check the calibration. However, this approach requires a large dataset and will be performed offline. Additionally, Minimum Ionizing Particle (MIP) signals from hadrons can be utilized for calibration at the low-energy end. For high energies, where the two photons from π^0 decays are too close together for the forward EMCal to distinguish them, η mesons can be used to verify energy non-linearity.

Monitoring system An LED system will be installed on the FEE boards to illuminate four towers using a trigger pulse. The LEDs will be preselected to provide equal light output to the towers, serving as a critical monitoring system. This will be essential for initial testing during installation, verifying mapping, and ensuring long-term stability of the detector, SiPMs, and FEE board gain,

as well as detecting any potential radiation damage. A dedicated short LED run will be performed daily to monitor the calorimeter's performance.

Additionally, the current and voltage on the FEE boards will be continuously monitored. Periodic I-V curve measurements will be conducted, on a weekly or bi-weekly basis, to assess the health of the SiPMs and FEE boards.

Status and remaining design effort:

R&D effort: eRD106 will be completed in early 2025 with finalizing analysis of the test beam data.

E&D effort: Detailing of mechanical design, and formalizing production drawings.

Other activity needed for the design completion: Produce and test first versions of final design FEB and SiPM boards.

Status of maturity of the subsystem: $\sim 70\%$

Environmental, Safety and Health (ES&H) The project will strictly adhere to all Environment, Safety, and Health (ES&H) regulations to ensure the safety of personnel, the integrity of the equipment, and the protection of the environment throughout the construction and operation phases. Comprehensive risk assessments will be conducted for all activities, including the handling of hazardous materials, electrical components, while implementing proper controls to minimize exposure to risks. Personnel will receive specialized training in safety protocols and emergency response procedures, and regular audits will be conducted to ensure compliance with ES&H standards. Additionally, the design of systems such as power management will prioritize environmentally friendly practices, incorporating energy-efficient technologies and minimizing waste and emissions. Continuous monitoring of environmental impact and adherence to radiation safety guidelines will be maintained to ensure the long-term safety and sustainability of the project.

Collaborators and their role, resources and workforce: Collaboration plays a pivotal role in the success of this project, as it brings together a diverse group of experts from various institutions, each contributing specialized knowledge and skills. The development of the fEMCal detector, for instance, relies on coordinated efforts between physicists, engineers, and technicians working on different aspects such as design, testing, and integration. Collaborative efforts ensure that challenges in areas like electronics, cooling systems, and data acquisition are addressed through shared expertise and innovative problem-solving. Additionally, partnerships with other research labs, such as BNL and international institutions, allow for the exchange of ideas, the pooling of resources, and the sharing of key R&D advancements. This collaborative environment fosters a culture of learning and inclusivity, which is critical for the project's long-term success, allowing it to meet both scientific and technical goals.

8.3.6 Hadronic Calorimetry

Add text here.

8.3.6.1 The backward endcap hadronic calorimeter

The backward hadronic calorimeter, here called **nHCal** (meaning Negative-eta/Neutral Hadronic Calorimeter), is a tail catcher calorimeter to be installed in the electron-going negative-z direction. As illustrated in the ePIC detector schematic 8.3, the nHCal is surrounded by an outer collar, backed by a flux return plate and has an oculus ring placed in front. Experience from the H1 experiment at HERA demonstrates the need for such a calorimeter for low-x measurements [81, 82].

Requirements

Requirements from physics: The main requirements for nHCal originate from physics processes in events with low Q^2 and low $x \sim 10^{-3} - 10^{-2}$ as well as high inelasticity y. This requires the acceptance of $-4.14 < \eta < -1.18$.

The processes of interests include diffractive vector meson overproduction $J/\psi \rightarrow \mu^+\mu^-$, $\phi \rightarrow K_L K_S$, $\phi \rightarrow K^+K^- \rightarrow \mu^+\mu^-$ and diffractive dijets. It will be also used as a veto for jet studies with neutral energy component and help in scattered electron identification along with backward EMCal. Finally, it will be used as a hadron beam background veto for dRICH in conjunction with LFHCAL for which a good timing resolution is required. In order to measure vector meson production with muons a good μ/π separation of tracks with MIP signal in calorimeters is required. Low-energy neutron detection for neutral jet identification demands low hit thresholds to achieve greater than 90% detection efficiency for 2 GeV neutrons. Moreover, neutral clusters must be identifiable after charged hadron correction, necessitating track matching and cluster position resolution capable of distinguishing showers separated by 30 cm. This resolution is achievable with tiles of up to 25 cm size.

Requirements from Radiation Hardness: In general, the radiation dose in the electron endcap area is expected to be low. A study was performed and summarized by ePIC background study group [83].

The low radiation dose compared to the forward region makes the use of SiPMs and FEE safe. SiPMs are required to maintain a low dark count rate after 10 years of operation. This is possible with the selected Hamamatsu S14160-1315PS model. Radiation tests [0] show that non-avalanche starts to increase above the level of 10^{-10} MEQ neutron fluence, which is expected to be reached after 10 years of operation.

Requirements from Data Rates: Data rates were studied by considering the following sources:

- Deep Inelastic Scattering (DIS)
- Synchrotron Radiation
- Electron Beam Gas

bkg. type	hit rate in detector [kHz]	max single channel hit rate [kHz]
DIS	$\sim 10^3$	1.23324
Synchrotron rad.	$\sim 2 \cdot 10^1$	-
e+gas	403.899	6.6448
h+gas	$\sim 7 \cdot 10^2$	0.303781

Table 8.37: Maximum expected background rates for backward HCal. The assumed threshold is 170 keV.

- Hadron Beam Gas

The values are taken from background studies found here:

- `https://wiki.bnl.gov/EPIC/index.php?title=Background`

Justification

Device concept and technological choice: Sampling calorimeter design featuring 10 layers of steel absorber and plastic scintillator tiles was selected as nHCal, because of low cost and simplicity. SiPMs and WLS fibers are going to be used for the light collection. The design, similarly to LFHCAL, is inspired by CALICE [0] collaboration, which allows mass production and easy handling of same type of detector modules.

Subsystem description:

General device description:

The nHCal is planned to be a sampling hadronic calorimeter with 10 layers of alternating steel and plastic scintillator, 4 cm and 0.4 cm thick, respectively. This arrangement provides compensation. The structure of the calorimeter will be a flattened cylinder with an outer radius of 276 cm cm and an inner radius of 14 cm to accommodate the hadron and electron beam pipes. The total thickness along the beam direction will be 45 cm. The detector will be placed at a position of -395 cm from the interaction point in the electron-going direction. The plastic scintillator layer will consist of tiles with a size of 10 cm $\times$ 10 cm(TBD). Two light collection solutions are under consideration: either the use of WLS fibers with SiPM readout or the SiPM-on-tile design, similar to that used for the LFHCAL, which was developed by CALICE [0]. The SiPM-on-tile approach is feasible with smaller tiles near the beam ($\eta \sim -4$), while larger tiles will require the WLS+SiPM combination. Tiles and absorber plates will be assembled into modules inspired by LFHCAL modules, with dimensions of 10 cm $\times$ 20 cm $\times$ 45 cm in the y, x, and z directions, respectively.

Sensors:

The Hamamatsu S14160-1315PS SiPMs will serve as light sensors. They will either be connected to the WLS fibers or placed directly on the tiles.

FEE:

The HGCROCv3 will be used as a Front-End Electronics (FEE) system, similar to other calorimetry systems in ePIC. The FEEs will be placed in front of the modules.

Other components:

The nHCal will also feature a calibration system based on LEDs as well as a temperature monitoring via sparsely place temperature sensors. This is described in more detail in 8.3.6.1.

Performance: The performance of the nHCal was studied using single particle simulations in dd4hep with GEANT4 used for particle transport. Neutron detection thresholds were evaluated against kinetic energy and integration time. Figure 8.110 illustrates the neutron detection efficiency as a function of energy threshold and integration time. Good performance is achieved with 100 ns integration time, and further increases offer minimal improvement. Additionally, a low threshold of $0.25E_{MIP}$ already provides a good detection efficiency 70% at 300 MeV.

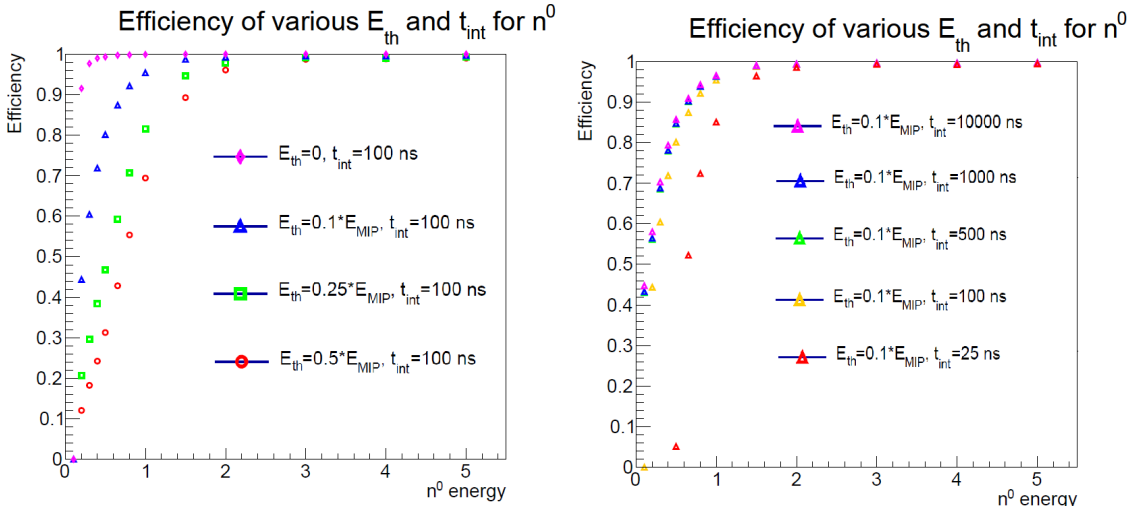

Figure 8.110: Left: Neutron detection efficiency vs. kinetic energy E_{kin}, dependence on threshold as a fraction of MIP energy deposit. Right: Same as left, but showing dependence on integration time.

Studies of e/h response with e/π simulation show that the ratio of steel and scintillator achieves compensation within uncertainties as presented in Fig. 8.112.

Simulated DIS events: One of the basic studies is a check of energy and momentum distributions going into backward HCal. This study used DIS $e+p$ events at $18+275$ GeV with $Q^2 > 1\,\text{GeV}^2$. The Fig. 8.113 shows total energy E and p distributions of each particle species in the nHCal acceptance $-4.0 < \eta < -1.0$.

Energy and momentum distributions of particles within nHCal acceptance in $e+p$ DIS events at $18+275$ GeV with $Q^2 > 1\,\text{GeV}^2$ were studied using the full official simulation of the ePIC detector. These distributions are presented in Fig. 8.113 as well as versus η in Fig. 8.114, Fig. 8.115 and Fig. 8.116. This analysis was used to determine the average energy of neutrons and optimize the detector geometry and thresholds.

Vector meson reconstruction: Vector meson reconstruction and acceptance were studied in $e+p$ and $e+A$ events using a standalone Sartre simulation, focusing on exclusive diffractive pho-

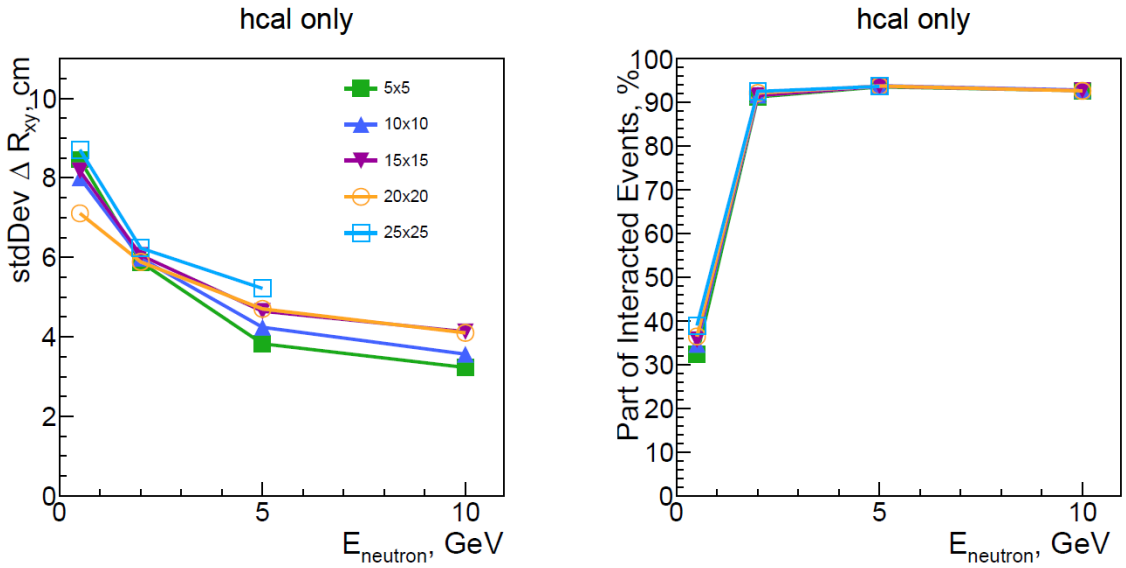

Figure 8.111: Position resolution R_{xy} and cluster efficiency vs. E for different tile sizes.

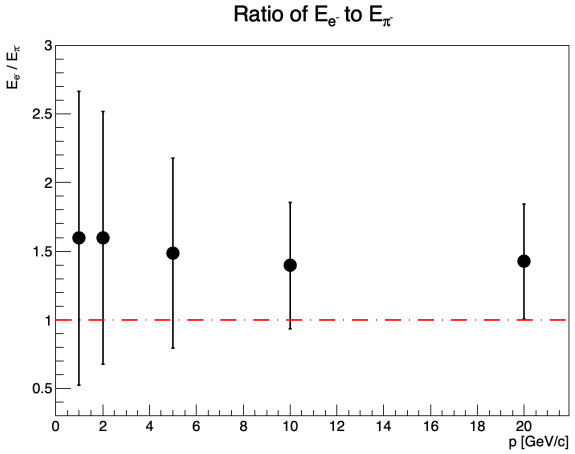

Figure 8.112: Ratio of e/π response vs. E.

toproduction. A large fraction of the J/ψ cross section was found to be produced in the backward direction, highlighting its importance. It should be noted that the J/ψ study is one of the major goals of EIC, as listed in the Yellow Report [23]. The acceptance of J/ψ is shown in Fig. 8.117 versus $-t$, Bjorken x_{BJ}, and Pomeron x_P. The figure also illustrates the acceptance when decay daughters are measured in different hadronic calorimeters. A similar study was performed for $e + A$ collisions and is presented in Fig. 8.118. Studies of $\Phi \to K^+K^-$ were also performed as shown in Fig. 8.119 for $e + p$ and in Fig. 8.120 for $e + A$ collisions. These studies indicate that nHCal is needed to measure J/ψ and ϕ in events with $x \sim 10^{-3}$ and lower.

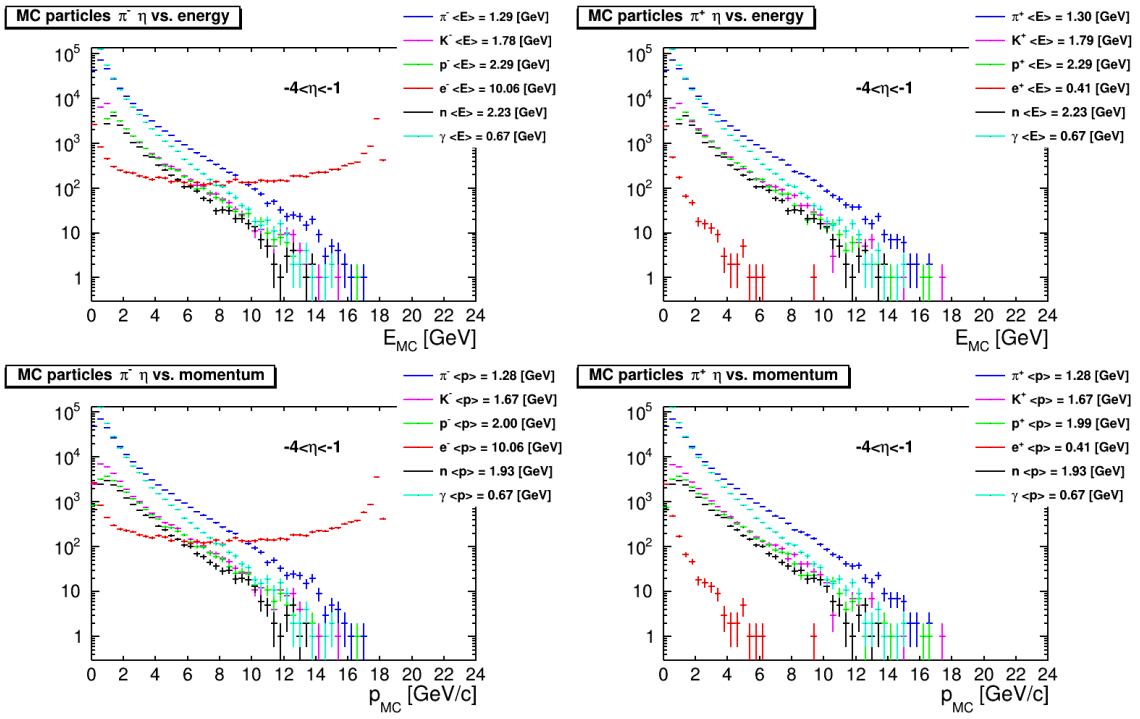

Figure 8.113: Top: Primary, generated particle E distributions in nHCal acceptance $-4.0 < \eta < -1.0$. Bottom: Primary, generated particle p distributions in nHCal acceptance $-4.0 < \eta < -1.0$.

Jets with neutral component: Another purpose of the nHCal is to help identify jets with neutral energy component, especially low energy neutrons of around $E = 2.23\,\text{GeV}$ total energy. This is an average neutron energy as indicated by the DIS study mentioned above. By selecting charged only jets and vetoing those containing neutral hadrons, the jet energy resolution can be improved. This was studied with a full ePIC simulation and track matching to MC particles or clusters using MC information. The jet energy resolution for the cases of inclusive (squares) and charged-only jets (triangles) is compared in Fig. 8.121. Results show a $\sim$ 20% improvement in jet energy resolution with the nHCal present.

Diffractive dijet measurement: Diffractively produced dijets [0] are a key area of study for the nHCal. Preliminary studies indicate that 1.8% of diffractive dijet events contain one of the jets in the nHCal acceptance. This increases to 4.8% for jets shared between nHCal and barrel HCal. Such events have $x \sim 10^{-3}$, so are important to study the structure of protons and nuclei. This is illustrated in Fig. 8.122 vs. Bjorken x and inelasticity y for different number of jets with thrust axis in the nHCal acceptance.

Scattered electron identification: The nHCal will augment the backward EMCal in scattered electron identification, by increasing the e/π rejection.

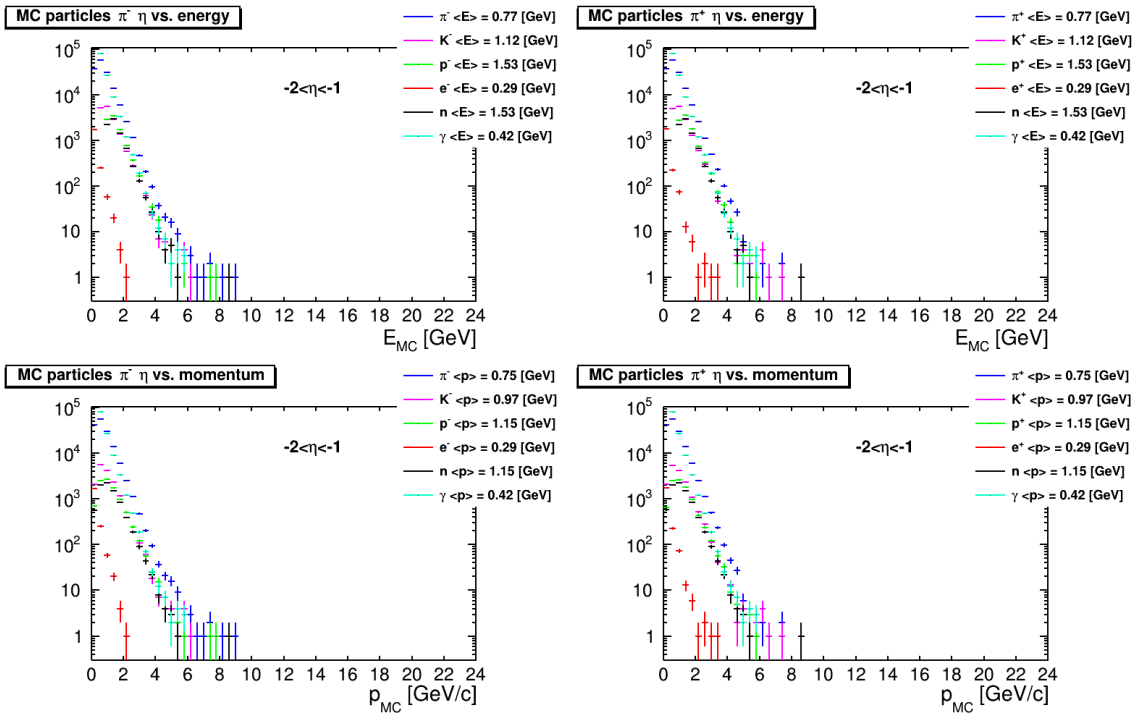

Figure 8.114: Top: Primary, generated particle E distributions in $-2.0 < \eta < -1.0$ range. Bottom: Primary, generated particle p distributions in $-2.0 < \eta < -1.0$ range.

Hadron beam background veto for dRICH: Another important function of the nHCal is to serve as a hadron beam background veto along with the LFHCAL. Such background is problematic for dRICH. Experience from STAR experiment shows that 30% of events may be due to background. Further studies need to be performed in order to understand the impact of beam background.

Cluster reconstruction: Clusters are reconstructed using the standard island clustering algorithm [0, 0]. To distinguish between charged and neutral clusters, track-cluster matching must be employed. The neutral energy component is obtained by subtracting the expected energy of charged particles, determined from the momentum measurement via tracking. The overlap of clusters was studied using two-particle simulations of neutrons and pions with $E = 1$ GeV. This is illustrated in Fig. 8.123 as a function of x, y position of the reconstructed clusters. The legends indicate the emission angles of the neutrons and pions.

Initial studies show that neutron and pion clusters can be distinguished when separated by ≈ 30 cm or ≈ 4.5 degrees.

Implementation

Services: All services will be provided through the service gap in front of the endcap, including power supply cables for the FEEs and SiPMs, as well as data connections to the FEEs. Depending on the final chosen granularity of the nHCal readout channels, it will have to be investigated whether

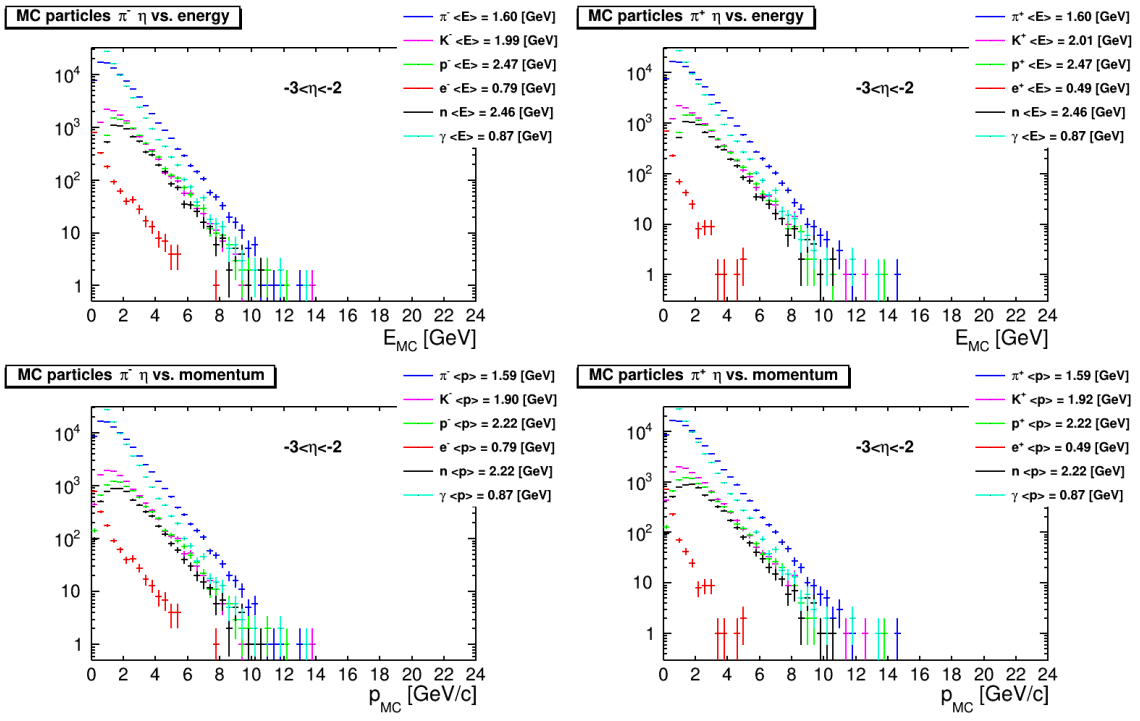

Figure 8.115: Top: Primary, generated particle E distributions in $-3.0 < \eta < -2.0$ range. Bottom: Primary, generated particle p distributions in $-3.0 < \eta < -2.0$ range.

a small cooling system to dissipate the heat produced by the ASICs will have to be integrated, similarly to the LFHCAL as described in Subsec. 8.3.6.3.

Subsystem mechanics and integration: The backward HCal modules will be stacked on top of each other similarly to the LFHCAL. Communication with the calibration system will be handled by the HGCROCv3 ASIC on FEE board through I^2C.

Calibration, alignment and monitoring: Calibration will be performed using LEDs on the tiles or additional clear fibers to guide laser/LED light (similar to the STAR EEMC calibration system) to the scintillator tiles. The system will enable the simulation of custom shower shapes, similar to the LFHCAL. The response will be studied and used to calibrate the SiPM gains by adjusting the bias voltage to compensate for variations in response, differences between SiPMs, and potential radiation damage to the SiPMs and tiles. This approach allows for system monitoring during operation.

Alignment will be performed during assembly. During operation, physics events and cosmic rays will be used to study the relative position of the calorimeter with respect to the trackers. We will follow standard alignment procedures used in many collider experiments.

Since SiPM gains are sensitive to temperature variations, a temperature monitoring system with thermocouples will be employed. These only need to be placed coarsely, as SiPMs generate very little heat. Additionally, the absorber steel, with its high thermal conductivity, will help distribute

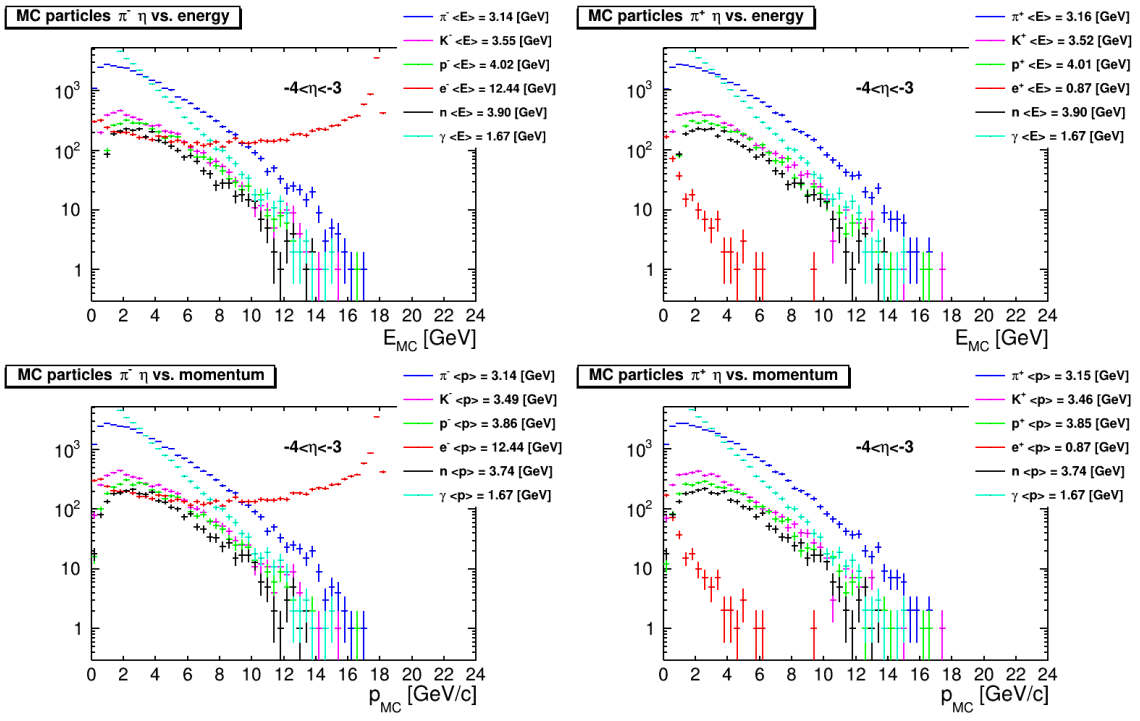

Figure 8.116: Top: Primary, generated particle E distributions in $-4.0 < \eta < -3.0$ range. Bottom: Primary, generated particle p distributions in $-4.0 < \eta < -3.0$ range.

heat over large volume.

Status and remaining design effort:

R&D effort: Finalize simulations and confirm optimal tile size.

E&D status and outlook: Design of support structures to follow the confirmed tile design.

Other activity needed for the design completion: Finalize simulations to confirm the tile size and design.

Status of maturity of the subsystem: Technologies and design are mature. Dependent on the outcome of performance simulations.

Environmental, Safety and Health (ES&H) aspects and Quality Assessment (QA planning): We will follow standard ES&H procedures observed at all participating institutions. Quality of the tile, fiber and SiPM interfaces as well as optical isolation will be tested after assembly of individual modules. This will be performed with the calibration system of the nHCal.

Construction and assembly planning: The 294 nHCal modules will each contain 2×10 scintillator tiles and 10 steel absorber plates. They will be produced using electron beam welding

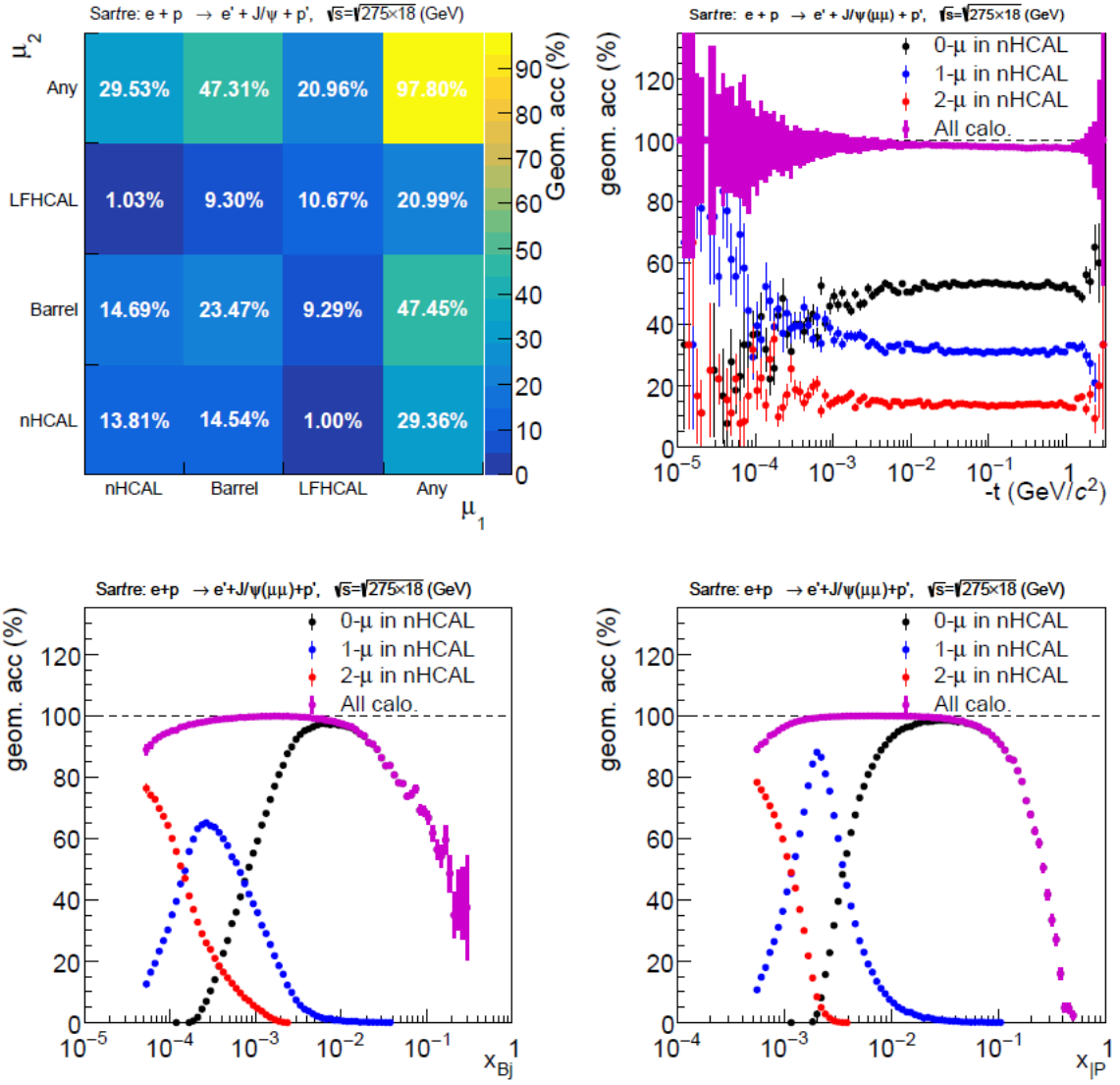

Figure 8.117: Acceptance of photoproduced $J/\psi \rightarrow \mu^+\mu^-$ in $e + p$ collisions at $18 + 275$ GeV. Top left: Acceptance vs. μ_1 and μ_2 hitting different HCals. Top Right: Acceptance vs. $-t$ for different number of μ in nHCal. Bottom Left: Acceptance vs. Bjorken x_{bj} for different number of μ in nHCal. Top Right: Acceptance vs. Pomeron x_P for different number of μ in nHCal.

technique in a vacuum. The modules will be assembled in a similar way as it is described for LFHCAL.

The tiles will be wrapped in a highly reflective foil using a machine being developed for CMS collaboration or by hand with the help of students.

Collaborators and their role, resources and workforce: Add text here.

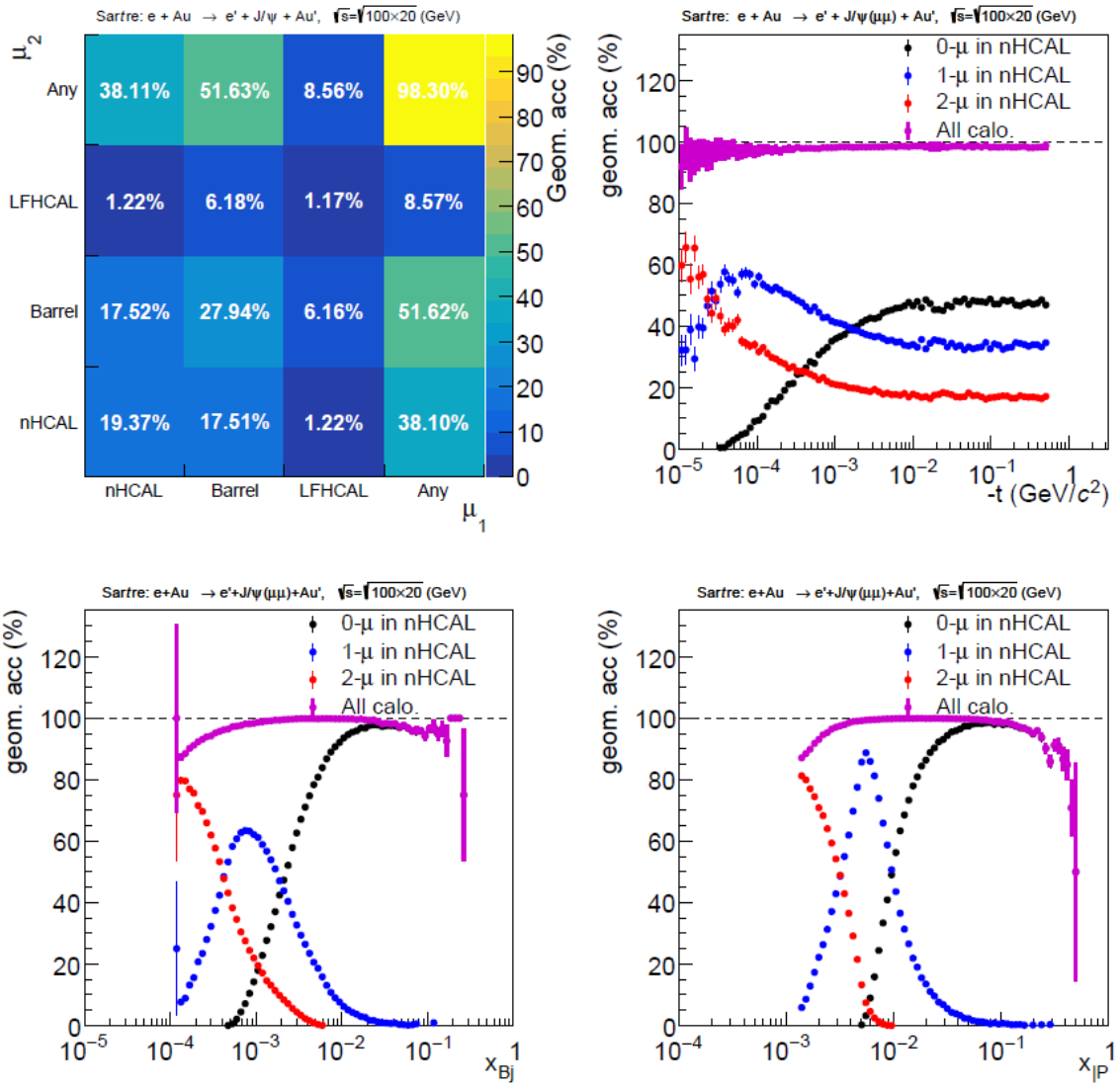

Figure 8.118: Acceptance of photoproduced $J/\psi \rightarrow \mu^+\mu^-$ in $e+p$ collisions at $20+100$ GeV. Top left: Acceptance vs. μ_1 and μ_2 hitting different HCals. Top Right: Acceptance vs. $-t$ for different number of μ in nHCal. Bottom Left: Acceptance vs. Bjorken x_{bj} for different number of μ in nHCal. Top Right: Acceptance vs. Pomeron x_P for different number of μ in nHCal.

5486 **Risks and mitigation strategy:** Each nHCal module needs to be tested before assembly to
5487 make sure that the LEDs, SiPMs and connectors work properly.

5488 **Additional Material** Add text here.

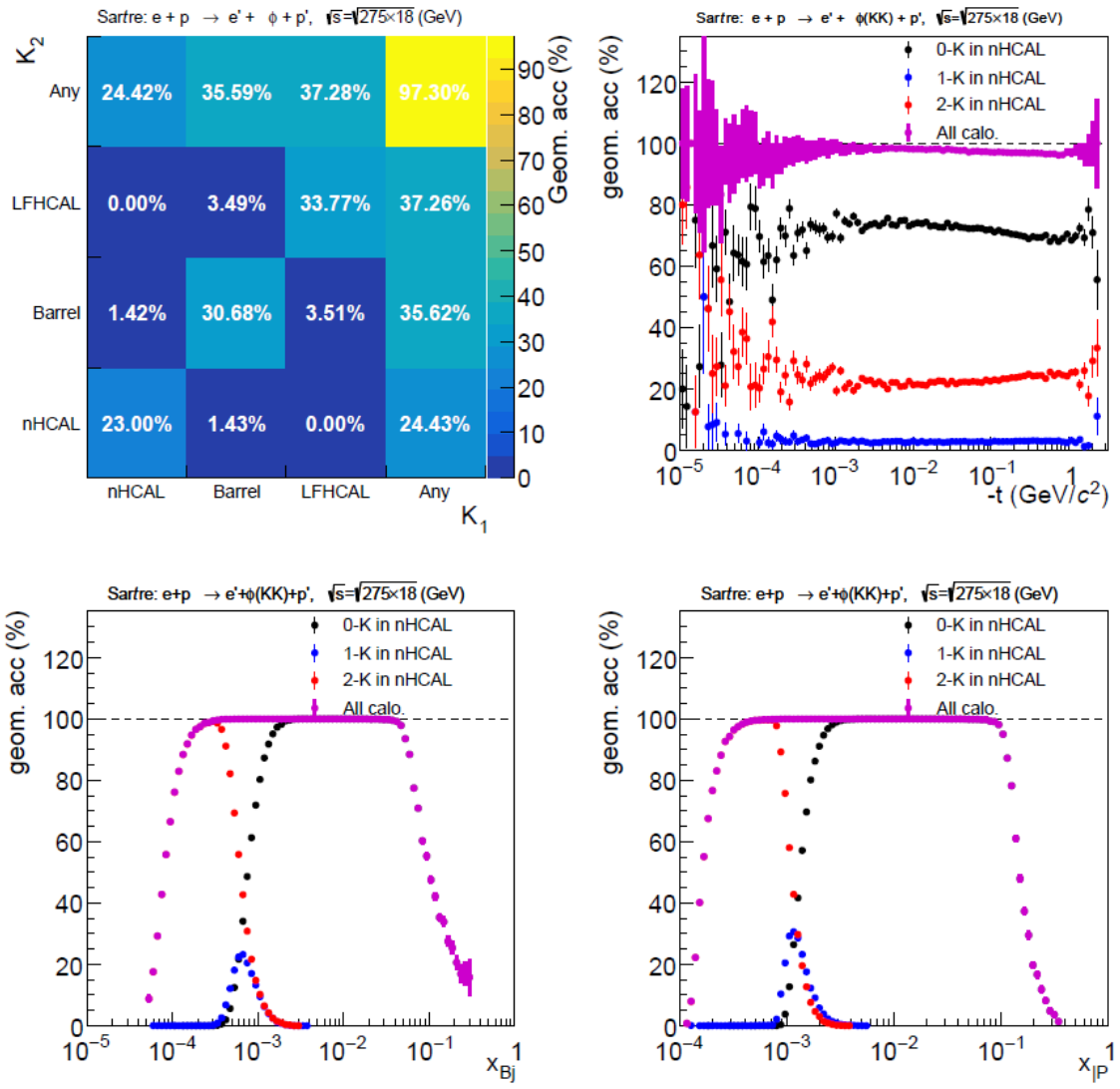

Figure 8.119: Acceptance of photoproduced $\Phi \to K^+K^-$ in $e+p$ collisions at $18+275$ GeV. Top left: Acceptance vs. K_1 and K_2 hitting different HCals. Top Right: Acceptance vs. $-t$ for different number of K in nHCal. Bottom Left: Acceptance vs. Bjorken x_{bj} for different number of K in nHCal. Top Right: Acceptance vs. Pomeron x_P for different number of K in nHCal.

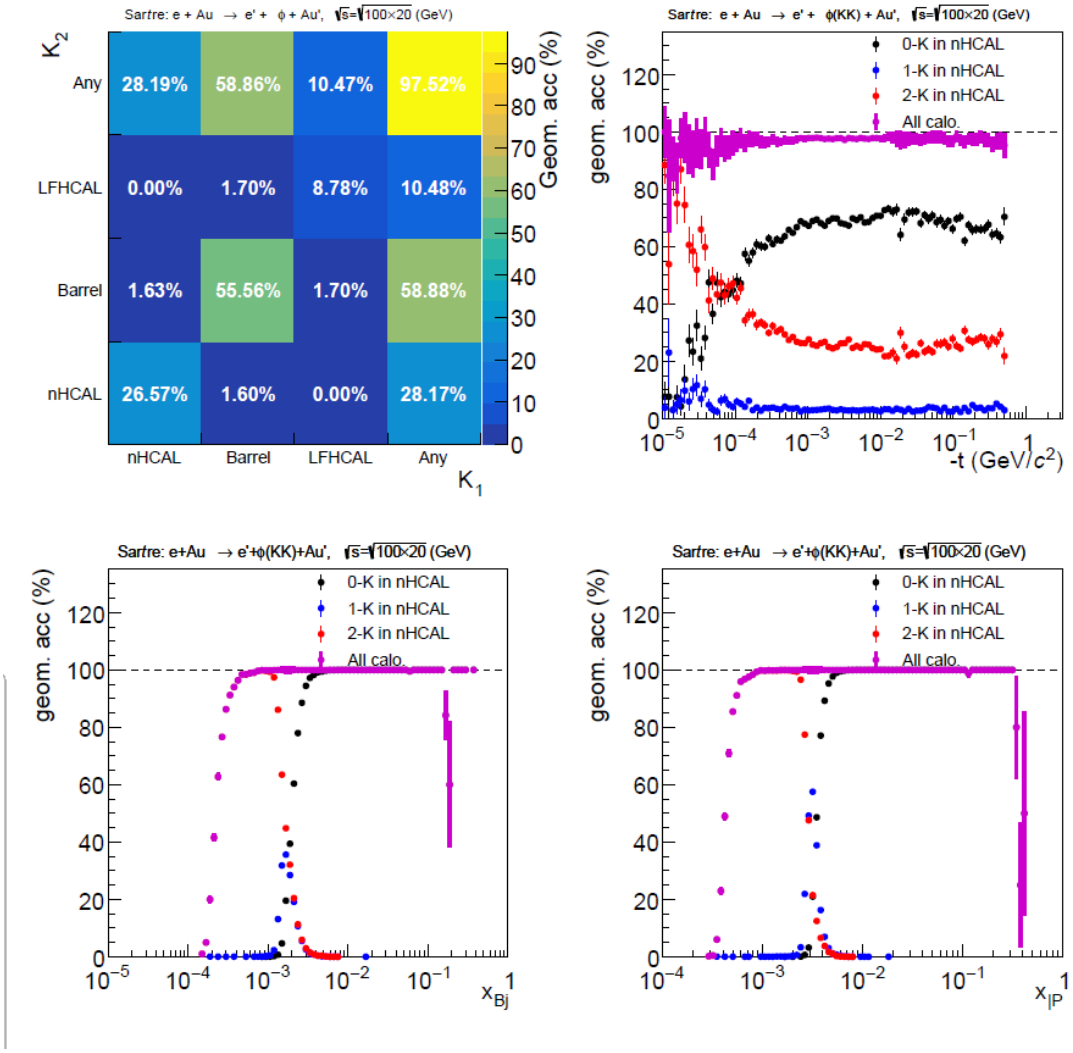

Figure 8.120: Acceptance of photoproduced $\Phi \to K^+K^-$ in $e+p$ collisions at $20+100$ GeV. Top left: Acceptance vs. μ_1 and μ_2 hitting different HCals. Top Right: Acceptance vs. $-t$ for different number of K in nHCal. Bottom Left: Acceptance vs. Bjorken x_{bj} for different number of K in nHCal. Top Right: Acceptance vs. Pomeron x_P for different number of K in nHCal.

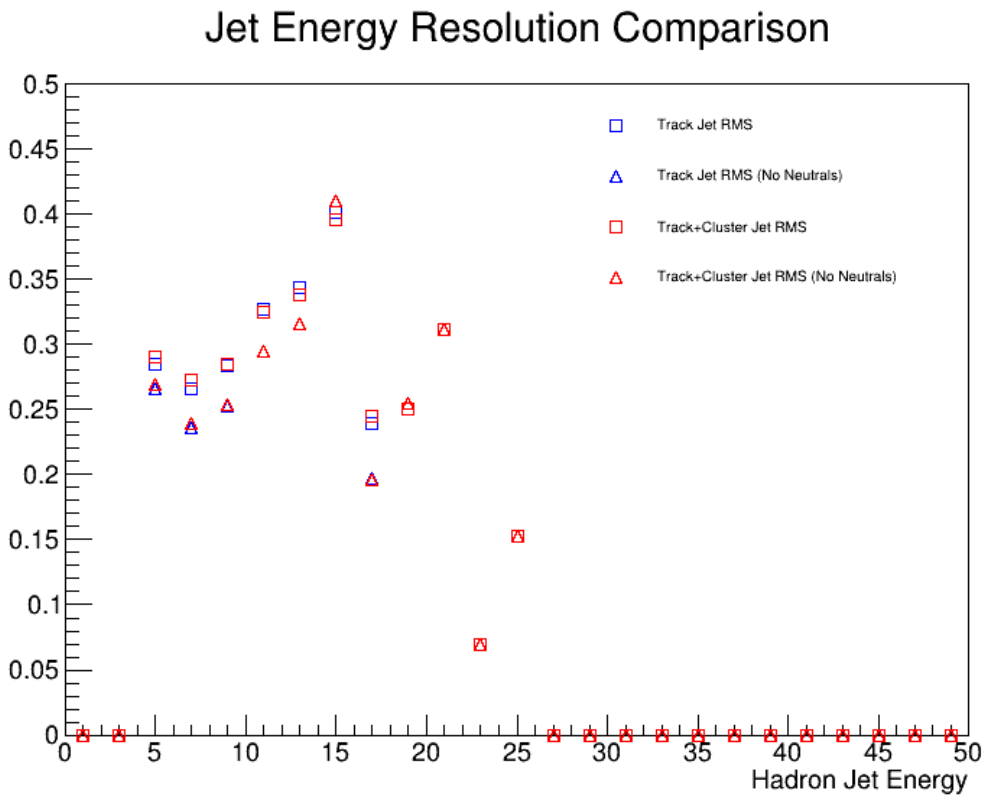

Figure 8.121: Energy resolution of jets vs. jet energy E compared for inclusive jets(squares) and jets with neutral veto(triangles). Track only jets(blue) are also compared to track and nHCal cluster jets(red).

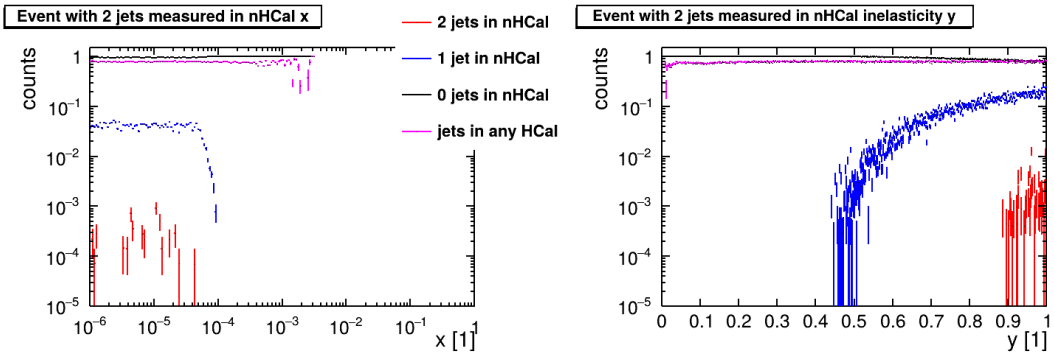

Figure 8.122: Left: Acceptance vs. x for 2, 1 and no diffractively produced jets with thrust axis in nHCal acceptance. Right: Acceptance vs. inelasticity y for 2, 1 and no diffractively produced jets with thrust axis in nHCal acceptance.

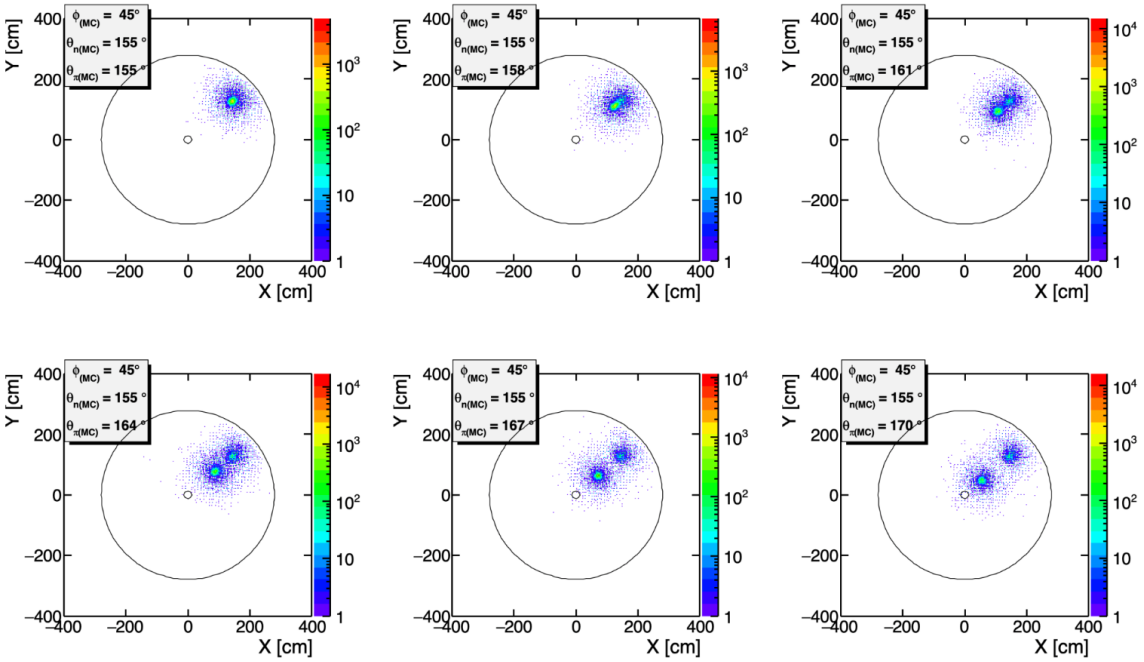

Figure 8.123: Position of the reconstructed clusters in x, y for 2-particle position resolution study.

8.3.6.2 The barrel hadronic calorimeter

Requirements The yellow report states that the energy resolution of the mid-rapidity hadron calorimeter should be $85\%/\sqrt{E/\mathrm{GeV}} + 7\%$. This requirement is driven by single jet measurements. While approximately 90% of the jet energy will be measured in the high precision tracking and electromagnetic calorimetry, the hadronic calorimeter is crucial for capturing the neutral hadron contribution. Figure 8.124 demonstrates the significance of the neutral hadron component.

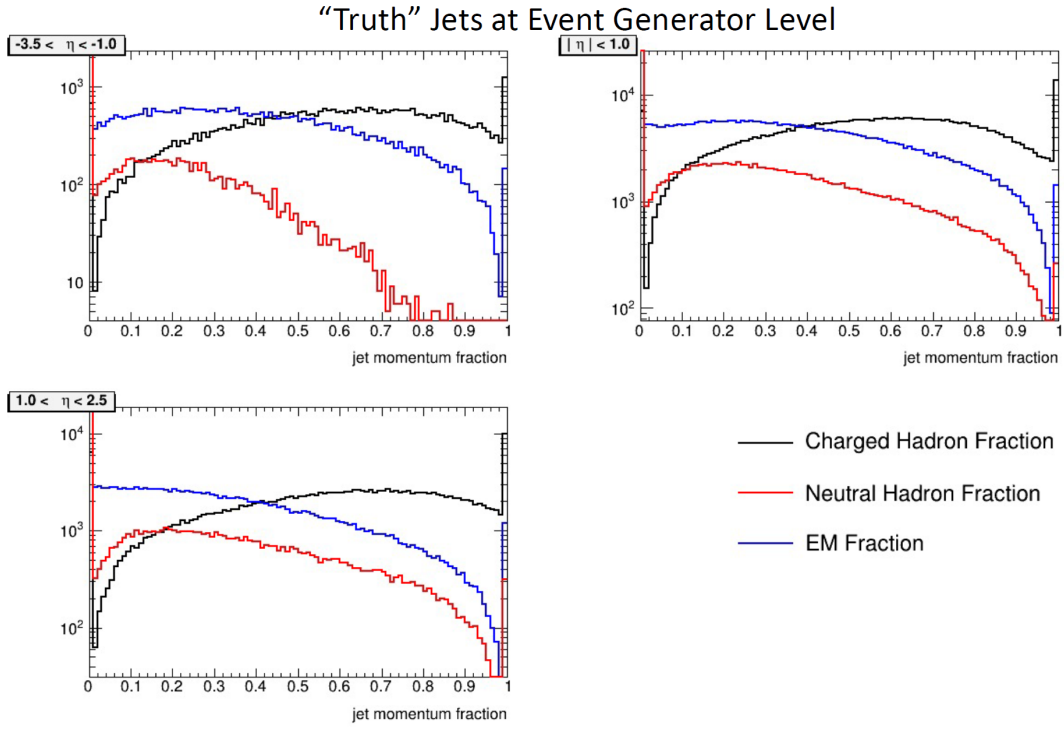

Figure 8.124: Jet charged and neutral Fractions: The charged (black lines), neutral EM (blue lines), and neutral hadron (red lines) fractions of jets at the truth level in $\eta \in (-3.5, 1.0)$ (upper left panel), $|\eta| < 1$ (upper right panel), and $\eta \in (1.0, 3.5)$ (lower left panel). This illustrates that while jets are dominated by charged and neutral EM particles, there are still a distinct population of jets at central rapidity with a substantial neutral hadronic component.

A simple inclusion of the HCal energy does not necessarily improve the energy measurement due to the energy smearing of neutral particles. However, the HCal can serve as a neutral veto to select jets without neutral hadrons, providing optimal energy resolution, as demonstrated in Fig. 8.125.

Requirements from Radiation Hardness: Compared to LHC detectors, the various subsystems of the ePIC detector have moderate radiation hardness requirements. The Yellow Report states that at the calorimeters, the radiation level will be up to ≈ 3 krad/year electromagnetic and $10^{11} n/\mathrm{cm}^2$ hadronic at top luminosity. However at the BHCal, the radiation level will be only 10 rad electromagnetic and 0.1 rad hadronic, orders of magnitude lower than, *e.g.*, at the fHCal.

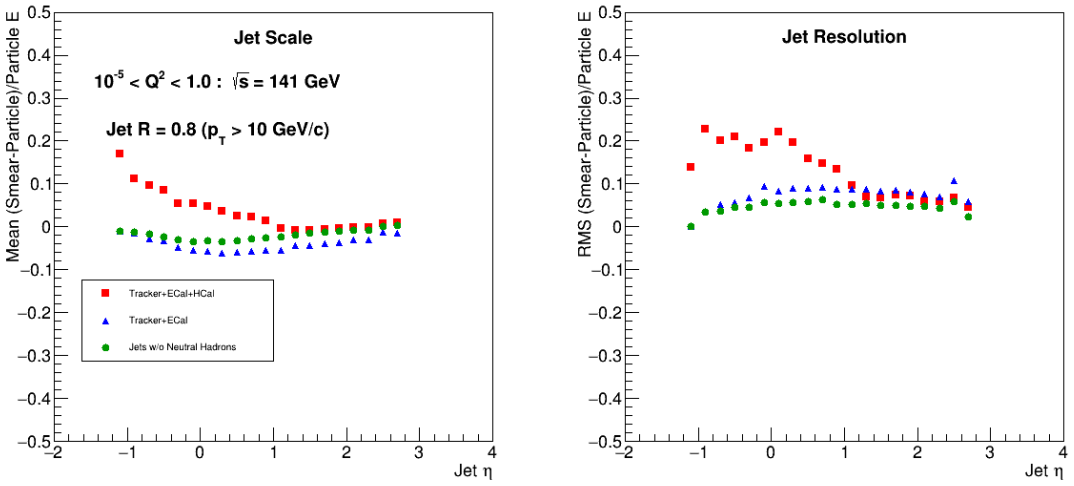

Figure 8.125: Demonstration of the effect of selecting only jets which do not contain a neutral hadron (green circles) on the jet energy scale (left) and resolution (right) as compared to the cases when all subsystems are used in jet finding (red squares) and when HCal information is excluded (blue triangles). Detector simulation and reconstruction was carried out using a fast simulation using Delphes. Figure 8.57 from the EIC Yellow Report.

The on-detector electronics (SiPMs, H2GCROC3) are radiation tolerant. While the read-out boards (RDOs) contain FPGAs and are therefore radiation sensitive, they will be positioned well outside the detector, eliminating concerns about single event upsets (SEUs). The neutron fluence will be low enough not to pose an issue for the SiPMs. It is also lower than in sPHENIX, where the dark current increase after the first year of operation was consistent with expectations. Since H2GCROC3s are used in other calorimeter systems as well, there is no concern regarding their performance in the BHCal.

Justification

Device concept and technological choice: The sPHENIX outer HCal, which was demonstrated to have a single particle energy resolution of $75\%/\sqrt{E} \oplus 14.5\%$, will be repurposed for the EIC. It generally satisfies the requirements described in the previous section. The constant term of the energy resolution may be further improved by reading out the individual scintillator tiles instead of grouping them in towers.

The absorber material for the central hadronic calorimeter will also serve as the flux return for the solenoid magnet. Additional absorber will be added to the existing sPHENIX HCal steel plates to further contain the magnetic field.

Subsystem description:

General device description: The sPHENIX Outer HCal will be used as the basis of the ePIC

Barrel HCal. The sPHENIX OHCal design was developed and optimized through a series of simulation and prototype studies. The sPHENIX hadronic calorimeter system consists of two longitudinal compartments of calorimeter, one inside the solenoid, which serves both to measure the longitudinal development of electromagnetic showers thus providing additional discrimination between electrons and hadrons beyond determination of E/p in the electromagnetic shower, and as the first nuclear interaction length of the hadronic calorimeter. In the ePIC design, the electromagnetic calorimeter will occupy the space before the magnet. Consequently, only the sPHENIX Outer HCal will be adopted in ePIC.

The basic calorimeter concept is a sampling calorimeter with tapered absorber plates tilted from the radial direction to provide more uniform sampling in azimuth. Extruded tiles of plastic scintillator with embedded wavelength shifting fibers are interspersed between the absorber plates and read out at the outer radius with silicon photomultipliers. The tilt angle is chosen so that a radial track from the center of the interaction region traverses at least four scintillator tiles as shown in Figure 8.126.

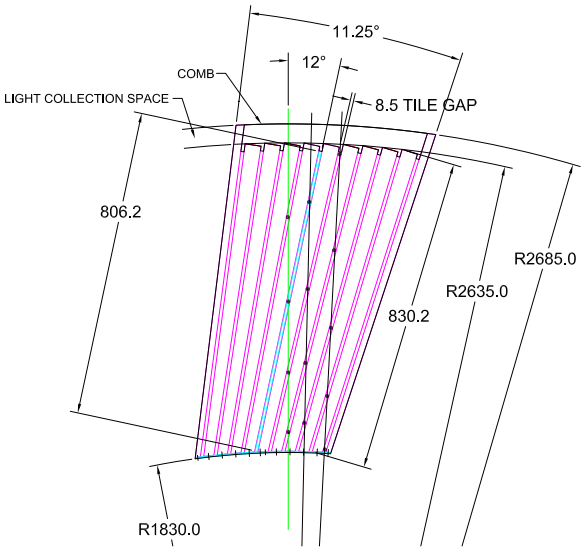

Figure 8.126: Transverse cutaway view of an sPHENIX Outer HCal module, showing the tilted tapered absorber plates. Light collection and cabling is on the outer radius at the top of the drawing.

Each tile has a single SiPM. In the sPHENIX design, the analog signal from five SiPMs are combined at a single preamplifier channel to form a calorimeter tower. In ePIC, each SiPM will be read out individually. Twelve tiles span 1.1 units of pseudorapidity in each direction as shown in Figure 8.127. Therefore the overall segmentation is $\Delta\eta \times \Delta\phi \sim 0.1 \times 0.02$.

Scintillator description:

The properties of the HCAL scintillating tiles are listed in Table 8.38. There are 12 differently shaped tiles which span half of the η range of the detector. The detector is mirror-symmetric in η except in the region where the chimney for the cooling of the magnet reduces the depth of the HCal.

A wavelength shifting (WLS) fiber is embedded in each tile to direct the light to the SiPM. The Kuraray single clad fiber was selected due to its flexibility and longevity which are critical for the multiple fiber bends in the design. The routing of the fiber was carefully designed

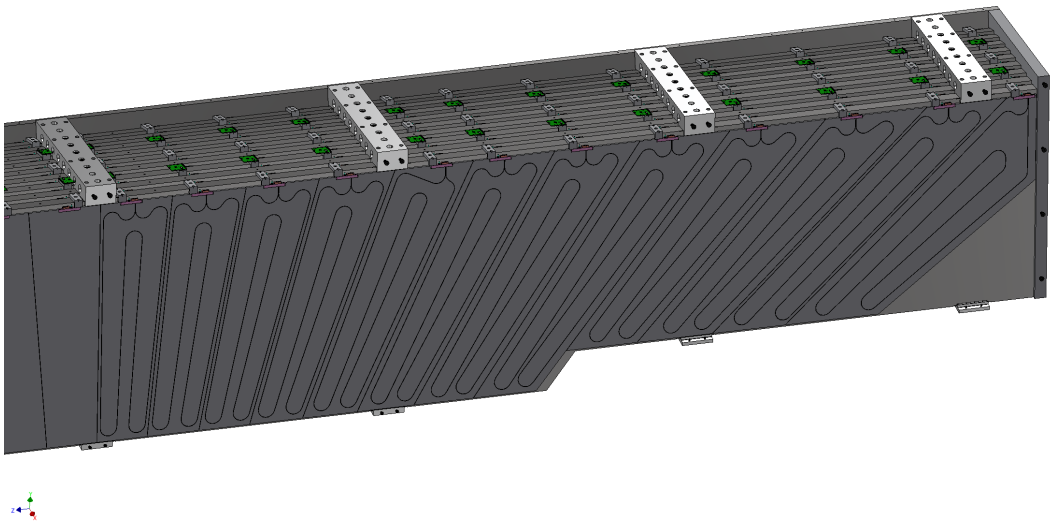

Figure 8.127: Scintillator tiles in a layer of the Outer HCal.

Component	Description
Plastic	Extruded polystyrene
Scintillation dopant	1.5% PTP and 0.01% POPOP
Reflective coating	Proprietary coating by surface exposure to aromatic solvents
Reflective layer thickness	50μ
Wrapping	one layer of 100 μ Al foil, one layer of 30 μ cling-wrap, one 100 μ layer of black Tyvek
Attenuation length in lateral (with respect to extrusion) direction	$\sim$2-2.5 m
Wavelength shifting fiber	Single clad Kuraray Y11
Fiber size	1 mm round
Fiber core attenuation length	$>$ 2 m
Optical cement	EPO-TEK 3015

Table 8.38: Properties of HCal scintillating tiles.

to maximize the uniformity of light collection across the various tile shapes and avoid light leaks in the bends.

The Kuraray single clad fiber was chosen due to its flexibility and longevity which are critical in the geometry with multiple fiber bends. The properties of the HCAL wavelength shifting fibers are listed in Table 8.39

The fiber routing was designed so that any energy deposited in the scintillator is within 2.5 cm of a WLS fiber to minimize the pathlength of the light through the tile to the fiber and maintain uniformity in the response of energy depositions throughout the tile and across

Property	Description
Fiber diameter	1.0 mm
Formulation	200, K-27, S-Type
Cladding	single
Cladding thickness	2 percent of d (0.02 mm)
Numerical Aperture (NA)	0.55
Emission angle	33.7 deg
Trapping Efficiency	3.1 percent
Core material	polystyrene (PS)
Core density	1.05 g/cc
Core refractive index	1.59
Cladding material	Polymethylmethacrylate (PMMA)
Cladding density	1.19 g/cc
Cladding refractive index	1.49
Color	green
Emission peak	476 nm
Absorption Peak	430 nm
Attenuation length	$>$ 3.5 m
Minimum bending radius	100 mm

Table 8.39: Properties of Kuraray Y-11 (200) wavelength shifting fibers.

various tile shapes. In addition, the bend radius of any turn in the fiber has been limited to 35 mm based. These parameters on the fiber routing where based on T2K and the sPHENIX R&D experience with test tiles. Since there are 12 different tile shape, the routing for each tile shape was uniquely designed to satisfy these conditions.

The two ends of a fiber are brought to the outer radius of a tile where a small plastic holder carries a 3×3 mm SiPM at 0.75 mm from the end of the polished fibers.

Table 8.40 summarizes the major design parameters of the HCAL, which is illustrated in Figure 8.126.

The Outer HCAL SiPM sensors and electronics are to be arranged on the outer circumference of the detector which reduces the radiation exposure of the SiPMs.

Sensors: The SiPMs used in sPHENIX will be replaced with newer S14160-3015PS Hamamatsu SiPMs. The SiPMs are still 3 mm X 3 mm and will be attached to a board that will fit in the same plastic connectors used in sPHENIX to mount the SiPM to the tile. Each SiPM will be read out individually via the CALOROC. The electronics developed for the BHCal is similar to other calorimeters and are described in a separate section.

LED system: Each tile has a fiber that can be illuminated by an LED. The fibers will extend to the edges of the detector where the electronics are also stationed.

Performance The performance of the BHCal for ePIC has been studied in simulation as well as tested through the experience of the HCals in sPHENIX. Thus far the sPHENIX HCal system has performed very well in Au+Au and p+p collisions. One concern with using SiPM sensors is the potential radiation damage in high energy collisions. The radiation exposure causes an increase in the leakage currents and the measured noise. The leakage current measured in the commissioning

Parameter	Units	Value
Inner radius (envelope)	mm	1820
Outer radius (envelope)	mm	2700
Length (envelope)	mm	6316
Material		1020 low carbon steel
Number of tiles in azimuth ($\Delta\phi$)		320
Number of tiles in pseudorapidity ($\Delta\eta$)		24
Number of electronic channels		$320 \times 24 = 7680$
Number of modules (azimuthal slices)		32
Total number of absorber plates		$5 \times 64 = 320$
Tilt angle (relative to radius)	$^\circ$	12
Absorber plate thickness at inner radius	mm	10.2
Absorber plate thickness at outer radius	mm	14.7
Gap thickness	mm	8.5
Scintillator thickness	mm	7
Module weight	kg	12247
Sampling fraction at inner radius		0.037
Sampling fraction at outer radius		0.028
Calorimeter depth	λ	3.8

Table 8.40: Design parameters for the Barrel Hadronic Calorimeter w/o additional absorber, based on the sPHENIX Outer Hadronic Calorimeter.

run for sPHENIX shows that leakage currents even an extrapolated are well below the limit. This is expected since the large amount of material in front of the SiPMs reduces their radiation exposure.

Fig. 8.128

Simulations demonstrate the energy deposition for muons and DIS events. For muons, a clear MIP peak is observed as shown in 8.129. In contrast, energy distributions for DIS events are shown in 8.130.

The resolution of calibrated single pion energies is shown in Figure 8.131.

Additional placeholders demonstrating the BHCal performance are included in Figures 8.132 to 8.142.

Implementation

Subsystem mechanics and integration: The BHCal is the outermost central detector and will need to be installed first. The steel serves as the flux return for the solenoid magnet.

Calibration, alignment and monitoring: The sPHENIX HCal was primarily calibrated using cosmic ray measurements. In addition to cosmic ray measurements LEDs are used to monitor the tiles. These monitoring systems will be crucial for properly calibrating the detector over time to account for aging effects of the tiles and radiation damage to the SiPMs.

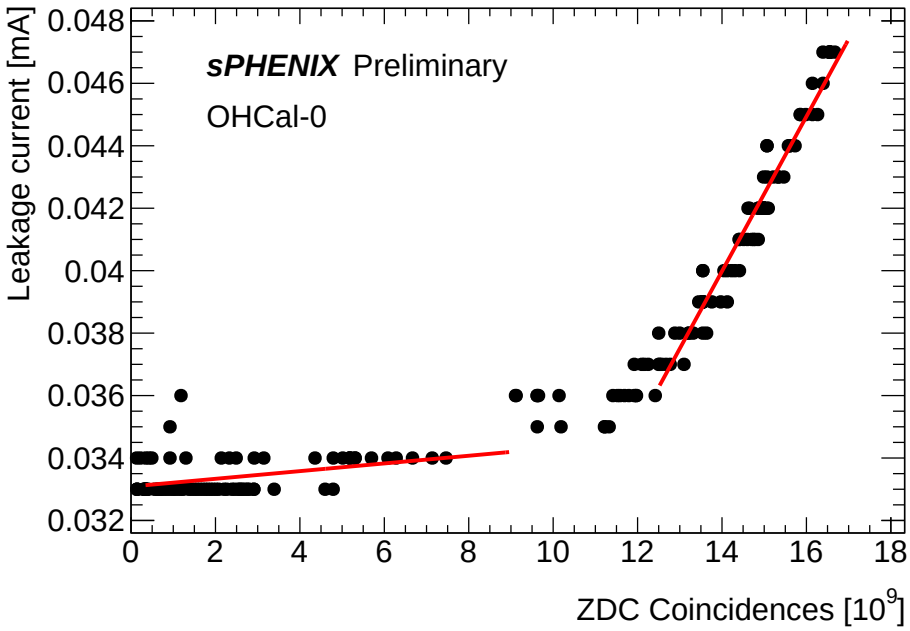

Figure 8.128: Leakage current in HCal measured once per fill as a function of total number of ZDC coincidence hits

Status and remaining design effort:

R&D effort: The basic design is set by reusing the sPHENIX outer HCal. However, the electronics and details of the LED system are still being developed. There are plans to utilize the sPHENIX prototype, which was used to demonstrate the energy resolution from beam tests, to test the readout of individual tiles instead of tiles. Related simulation studies are also underway. Additional tests include measuring the potential noise for longer cables to transmit the signal from the SiPM to HGCROCs located at the end of the sector.

Environmental, Safety and Health (ES&H) aspects and Quality Assessment (QA planning):

Construction and assembly planning: After RHIC running concludes, sPHENIX will be disassembled. When a sector of the outer HCal is removed from sPHENIX, the tiles within the sector will be extracted. The tiles will be shipped to Georgia State University (GSU) and University of New Hampshire (UNH) where test stands are ready to quantify the response of the tiles tiles to cosmic rays and record their relative performances. These initial tests proved to be very useful in the initial calibration procedure in sPHENIX. For sPHENIX these tests were also crucial in the quality assessment procedure which required that the tile performance deviate no more than 20% from the mean for that tile shape. Similar performing tiles were also grouped together into towers for calibration purposes.

After the tiles have been tested, they will be shipped back to BNL to be installed in the new sectors. Additional material will have been added to the sPHENIX steel sectors. Stefan Bathe from

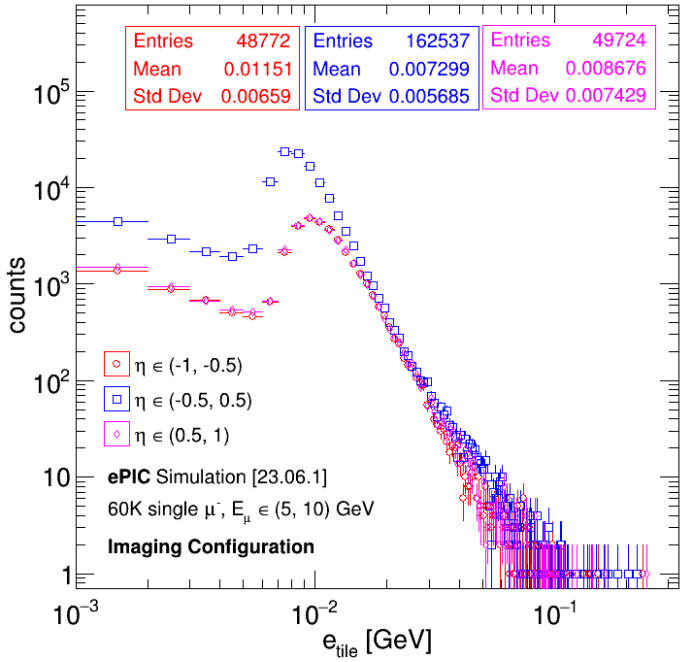

Figure 8.129: Muon energy deposited on tile: energy deposited on a given scintillator tile (i.e. the sum of G4 hits for a tile) by single GeV/c μ^- with energies between 5 and 10 GeV/c as a function of μ^- pseudorapidity. Distributions were simulated using the 2023.06.1 simulation geometry. A clear MIP peak is observed.

Baruch College will oversee the assembly process at BNL. He served as the level 3 manager for the sPHENIX HCals and likewise oversaw the assembly of the inner and outer HCals for sPHENIX. After inserting the tiles in the proper sector locations, an SiPM will be connected to each tile. The cables will be installed and connected to a test setup for the electronics to confirm that each tile can be readout. Cosmic ray tests of each sector will also be performed which will confirm the relative tile by tile calibration factors.

Collaborators and their roles, resources and workforce: Derek Anderson from Iowa State University has been leading the simulation efforts for the BHCal. He has help trained collaborators at UNH and GSU to work on tasks associated with needed simulation studies and software development.

The Baruch College and GSU groups led by Bathe and Connors respectively have extensive experience working with the sPHENIX HCals. They will oversee the assembly and tile testing procedures for the ePIC BHCal as they did for sPHENIX. Additionly, UNH, BNL and others will be extremely important for ensuring the assembly timeline is achieved. Norbert Novitzky from Oak Ridge National Laboratory is developing the electronics and is collaborating with members of the BNL group that conducted the sPHENIX R&D to test the electronics with the sPHENIX HCal prototype.

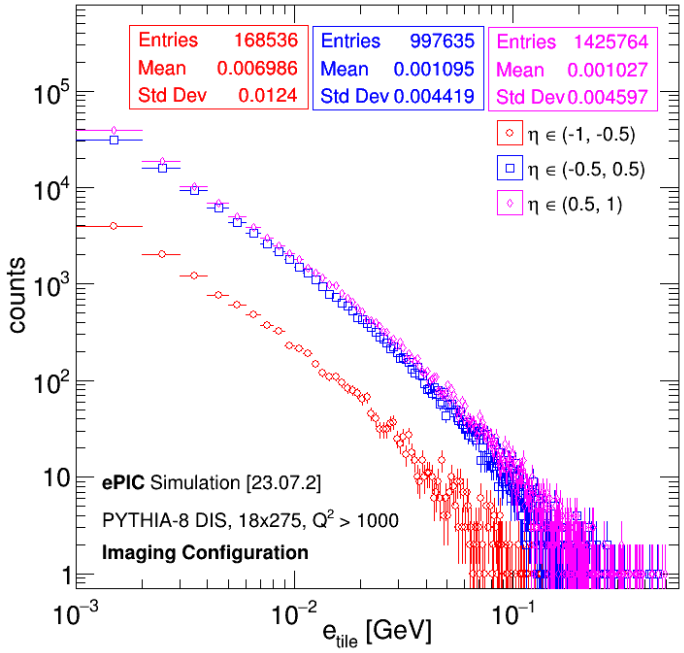

Figure 8.130: DIS energy deposited on tile: energy deposited on a given scintillator tile (i.e. the sum of G4 hits for a tile) in 18×275 NC DIS events for $Q^2 > 1000$ GeV^2 for all particles in the events as a function of their pseudorapidity. Distributions were simulated using the 2023.07.2 simulation geometry.

Risks and mitigation strategy: The BHCal depends on previously tested technologies which minimizes the risks associated with it. A limited number of spare tiles exist at Georgia State University in case any tiles are damaged. There are two ways we can monitor the tiles once they are installed into EPIC. The LED system is useful for quickly testing the tiles on a regular basis while the cosmic ray studies require a long time to collect sufficient data.

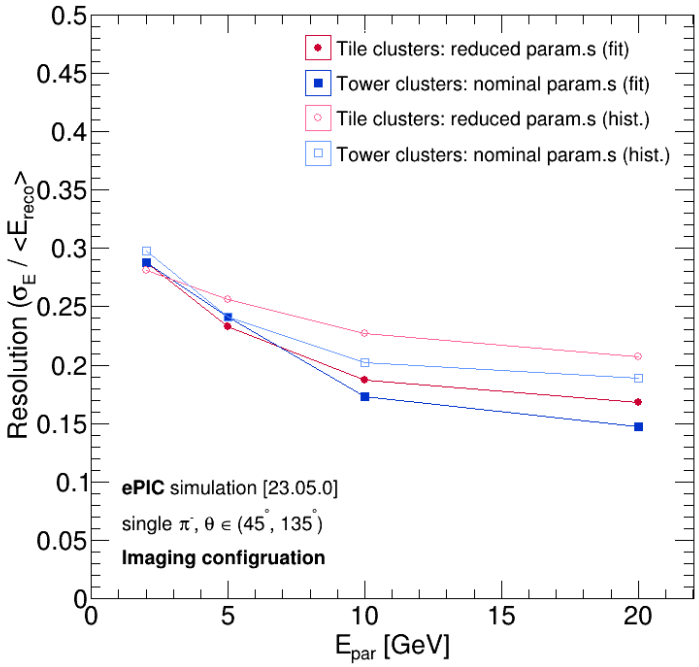

Figure 8.131: Resolution of calibrated single pion energies: Resolution of calibrated single π^- energies. Distributions were simulated using the 2023.05.0 simulation geometry. Red markers indicate the output of the calibration using tile-based clusters from the BHCal, while blue markers indicate the output of the calibration using tower-based clusters from the BHCal. The closed markers indicate the resolution as obtained by comparing the mean of a gaussian fit to the calibrated energies vs. the particle energies, while the open markers indicate the resolution as obtained by directory comparing the mean of the calibrated energies vs. the particle energies. Calibration is carried out by the LD model.

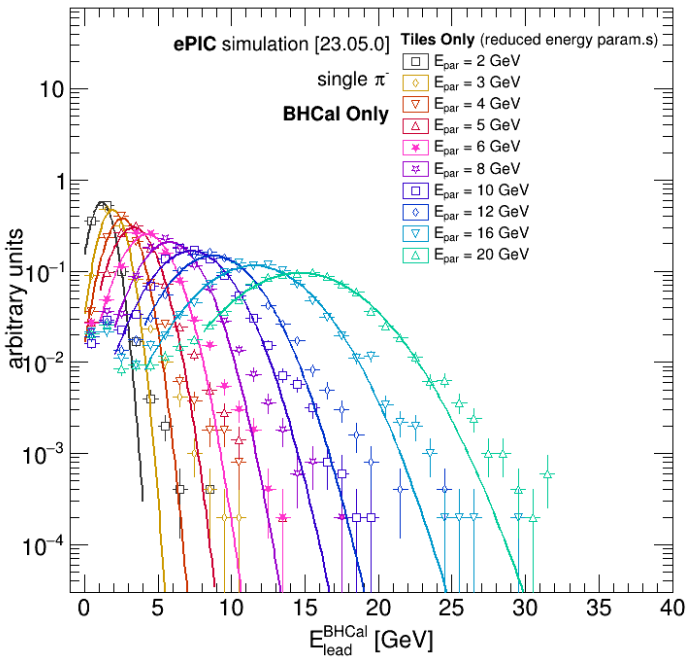

Figure 8.132: Single pion energies in only BHCal: reconstructed energy of leading (highest energy) BHCal cluster for 2 (black) - 20 GeV (light blue) single π^- in the BHCal *only*. Distributions were simulated using the 2023.05.0 simulation geometry. Clusters are formed from individual tiles. Solid lines are guassian fits. Energies are "uncalibrated" in the sense that they have only been corrected for the sampling fraction.

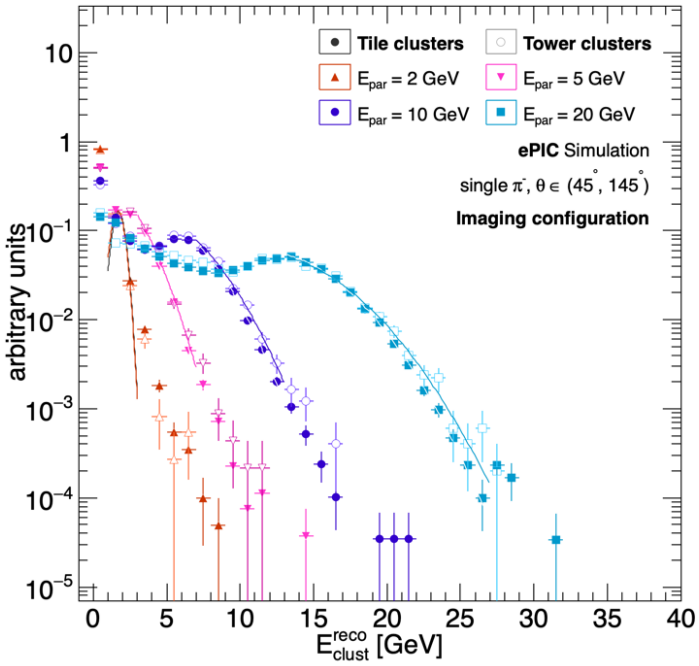

Figure 8.133: Uncalibrated single pion energies: reconstructed energy of all BHCal clusters for 2 (orange), 5 (pink), 10 (purple), and 20 GeV (blue) π^- with θ between 45° and 145°. Distributions were simulated using the 2023.05.0 simulation geometry. Closed markers indicate clusters formed from individual tiles, and open markers indicate clusters formed from towers (5 tiles). Solid lines are gaussian fits, but aren't relevant for this particular plot. Energies are "uncalibrated" in the sense that they have only been corrected for the sampling fraction.

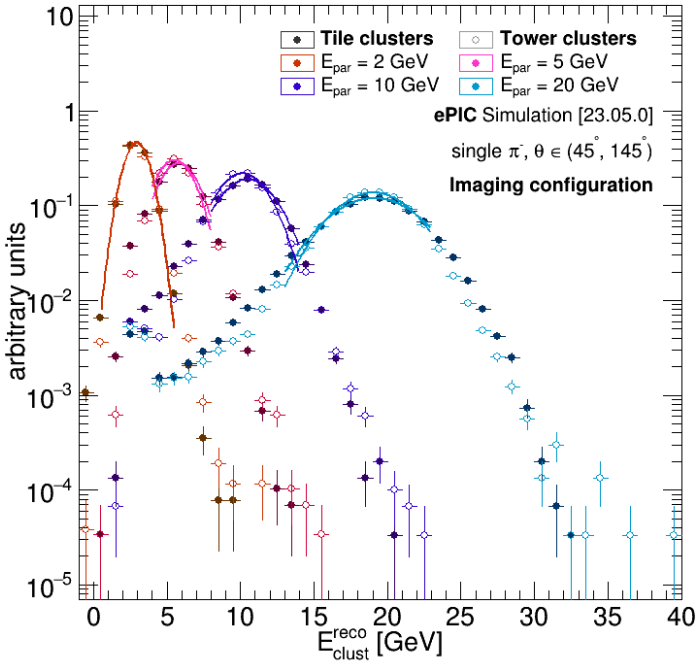

Figure 8.134: Calibrated single pion energies: calibrated energy of single 2 (orange), 5 (pink), 10 (purple), and 20 GeV (blue) single π^- with θ between 45° and 145°. Distributions were simulated using the 2023.05.0 simulation geometry. Closed markers indicate clusters formed from individual tiles, and open markers indicate clusters formed from towers (5 tiles). Solid lines are gaussian fits. Energies are calibrated, i.e. the output of a regression by a Linear Discriminant (LD) ML model as implemented in TMVA. The LD model is trained on the energy, pseudorapidity, azimuth, and no. of hits (constituent cells) of the leading (highest energy) BHCal and BIC (ScFi + imaging) clusters as well as on the sum of energy in the 6 imaging (AstroPix) and 12 ScFi (Scintillating Fiber) layers of the BIC.

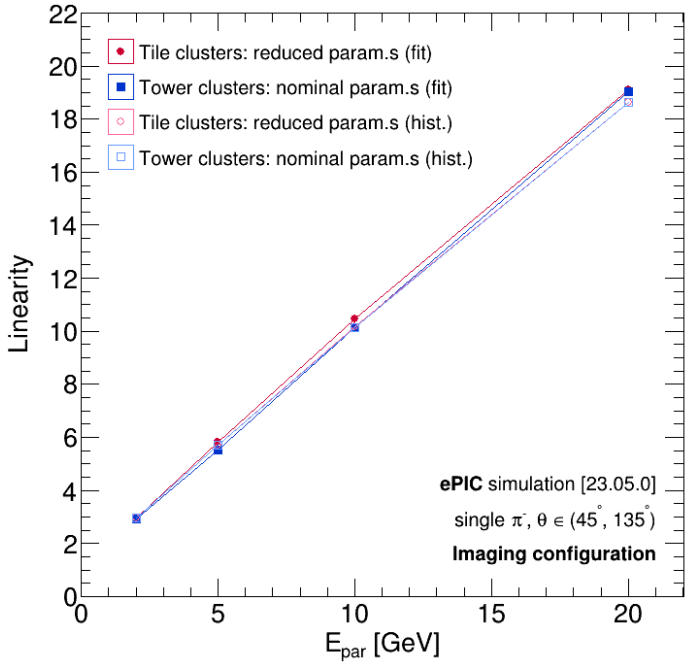

Figure 8.135: Linearity of calibrated single pion energies: Linearity of calibrated single π^- energies. Distributions were simulated using the 2023.05.0 simulation geometry. Red markers indicate the output of the calibration using tile-based clusters from the BHCal, while blue markers indicate the output of the calibration using tower-based clusters from the BHCal. The closed markers indicate the linearity as obtained by comparing the mean of a gaussian fit to the calibrated energies vs. the particle energies, while the open markers indicate the linearity as obtained by directory comparing the mean of the calibrated energies vs. the particle energies. Calibration is carried out by the LD model as was done in fig. 8.134.

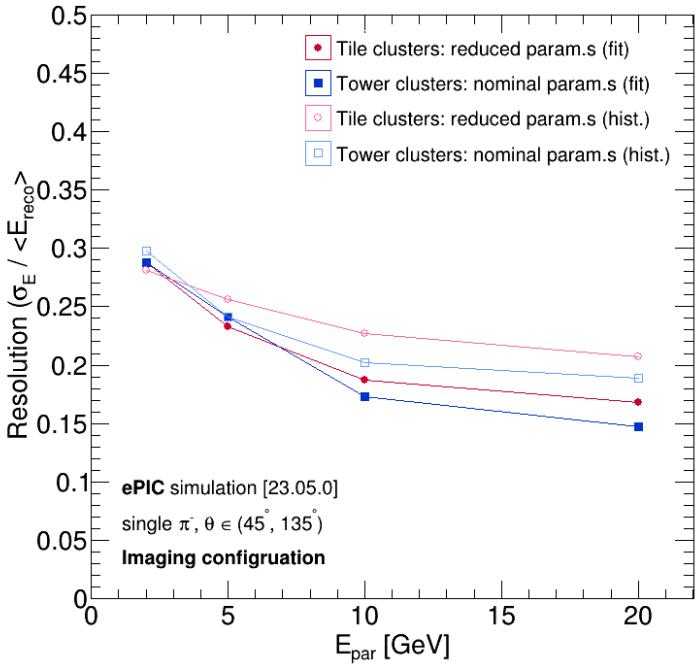

Figure 8.136: Resolution of calibrated single pion energies: Resolution of calibrated single π^- energies. Distributions were simulated using the 2023.05.0 simulation geometry. Red markers indicate the output of the calibration using tile-based clusters from the BHCal, while blue markers indicate the output of the calibration using tower-based clusters from the BHCal. The closed markers indicate the resolution as obtained by comparing the mean of a gaussian fit to the calibrated energies vs. the particle energies, while the open markers indicate the resolution as obtained by directory comparing the mean of the calibrated energies vs. the particle energies. Calibration is carried out by the LD model as was done in fig. 8.134.

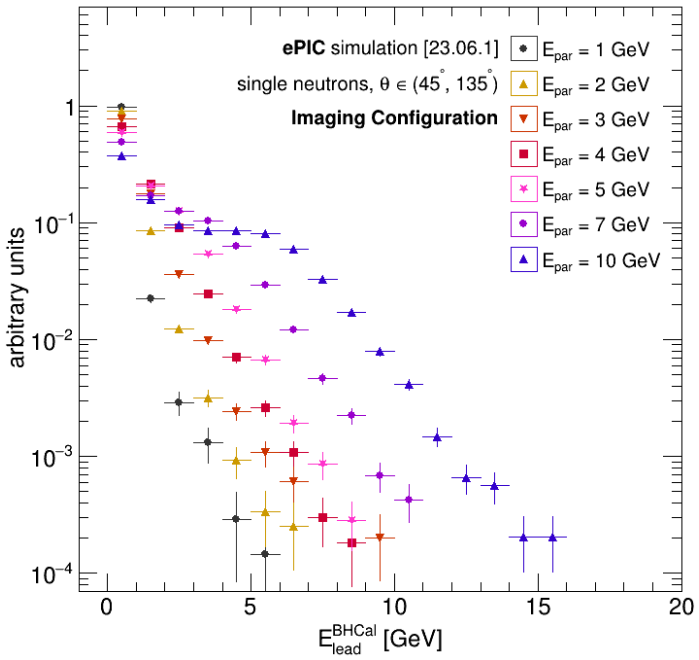

Figure 8.137: Uncalibrated single neutron energies: reconstructed energy of leading (highest energy) BHCal clusters for 1 (black) - 10 GeV (violet) single neutrons with θ between 45° and 145°. Distributions were simulated using the 2023.06.1 simulation geometry. Energies are "uncalibrated" in the sense that they have only been corrected for the sampling fraction.

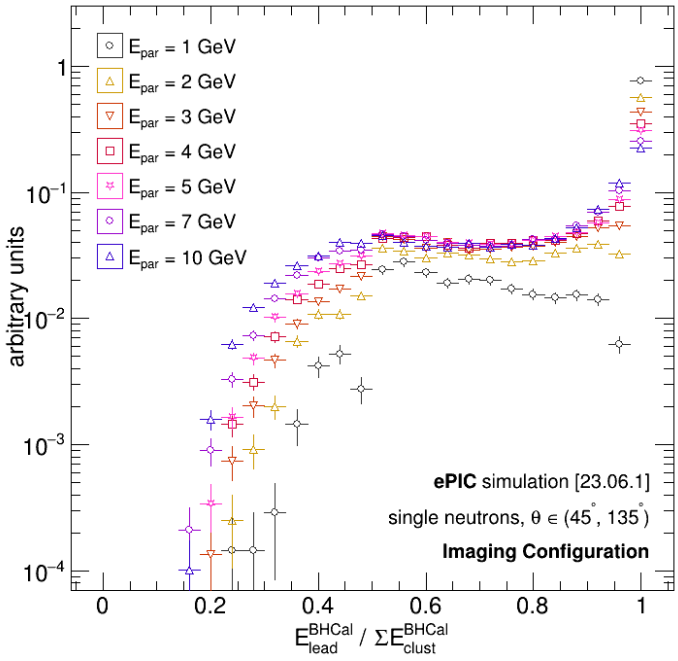

Figure 8.138: Uncalibrated single neutron energy fractions: fraction of the reconstructed energy of the leading (highest energy) BHCal cluster to the sum of all BHCal clusters for 1 (black) - 10 GeV (violet) single neutrons with θ between 45° and 145°. Distributions were simulated using the 2023.06.1 simulation geometry. Energies are "uncalibrated" in the sense that they have only been corrected for the sampling fraction. Demonstrates substantial cluster splitting for neutrons.

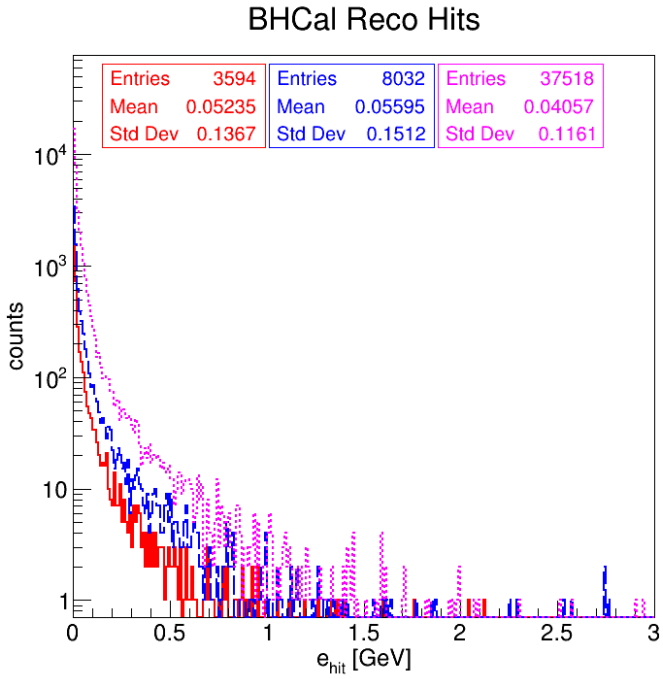

Figure 8.139: DIS reconstructed tile energy: the energy of reconstructed "hits" (i.e. the reconstructed energy of individual tiles) in the BHCal in 18 × 275 NC DIS events for $Q^2 > 1000$ GeV^2 for all particles in the events as a function of their pseudorapidity. Distributions were simulated using the 2023.06.1 simulation geometry. Demonstrates typical range of reconstructed energies on a tile-by-tile basis.

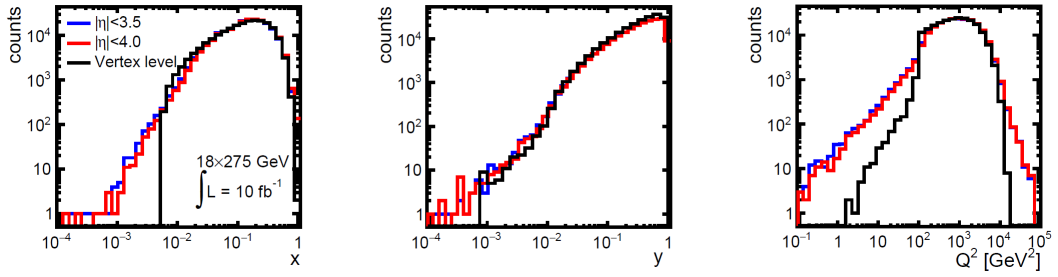

Figure 8.140: Jacquet-Blondel variables in CC DIS: DIS kinematic variables calculated using the Jacquet-Blondel method in 18 × 275 CC DIS events. The black lines indicate the distributions at the truth ("vertex") level, and the blue/red lines indicate the distributions at the reconstructed level: blue indicates a detector with an acceptance of $|\eta| < 3.5$, while red indicates a detector with an acceptance of $|\eta| < 4$. Detector simulation and reconstruction was carried out using a fast simulation using Delphes. Figure 8.21 from the EIC Yellow Report.

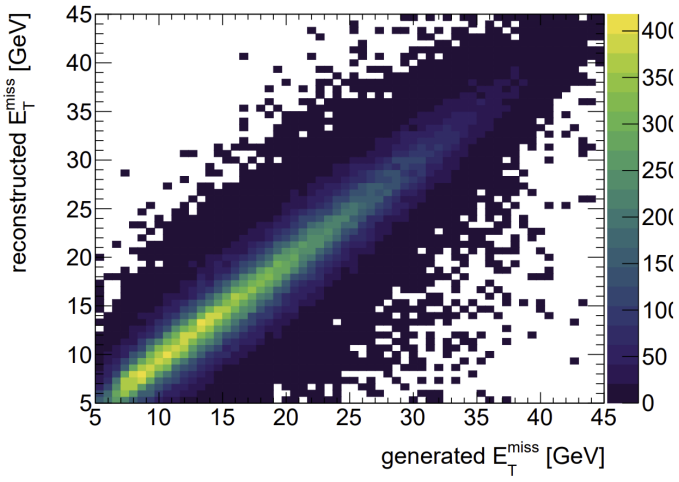

Figure 8.141: Truth vs. reconstructed $E_{\mathbf{T}}^{\mathbf{miss}}$: the truth (x-axis) vs. reconstructed (y-axis) $E_{\mathrm{T}}^{\mathrm{miss}}$ for 10×275 CC DIS events. Detector simulation and reconstruction was carried out using a fast simulation using Delphes. Figure 4 from arXiv:2006.12520.

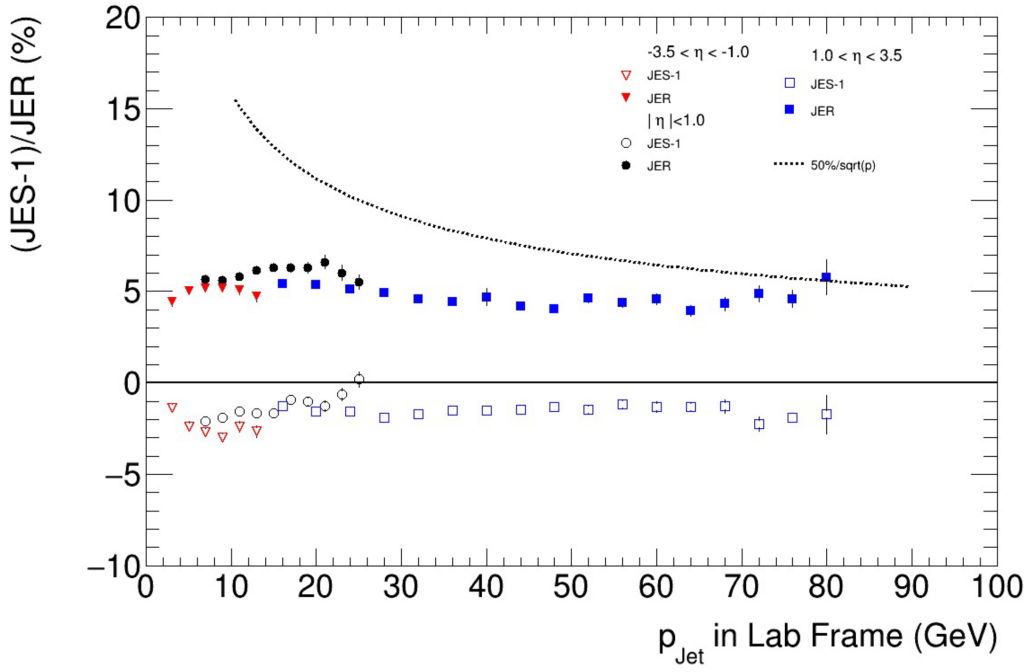

Figure 8.142: JES/R for full (tracks + ECal + HCal): The JES $-1 = \langle \Delta p/p \rangle$ (open markers) and JER (closed markers) plotted as a function of p_{jet} in the lab frame for jets in $\eta \in (-3.5, 1.0)$ (red points), $|\eta| < 1$ (black points), and $\eta \in (1.0, 3.5)$ (blue points). In the barrel region, jets are constructed from reconstructed tracks and ECal clusters *without* a nearby track. Neutral hadrons are included in the jets by smearing the particle energy by the measured energy resolution of the sPHENIX OHCal. Jets are reconstructed via the Centauro algorithm (R = 0.8) and transformed back into the lab frame. Jets are required to have at least 2 particles, and exclusively charged or neutral jets are rejected. From ECCE responses to the EIC DPAP Panel; received from John Lajoie in private communication.

8.3.6.3 The forward endcap hadronic calorimeter

Requirements

Requirements from physics: In electron-proton (ep) or electron-ion (eA) collisions, many highly-energetic hadrons are created in the process of probing the partonic structure of the target proton or ion using the electron. However, since the incoming proton/ion has a significantly larger kinetic energy than the incoming electron, most of the hadrons are emitted in the same direction as the hadron beam, into the hadron end cap, which is defined as the "forward" direction at the EIC.

Thus jets of particles, with single-particle energies of up to 150 GeV, are expected to reach the forward hadronic calorimeter, e.g. based on simulated PYTHIA events for e+p collisions at 18×275 GeV^2. Typical jets consist of 10-12 particles contained within a jet radius of $R = 1$, with R being the angular distance $\sqrt{\eta^2 + \phi^2}$. These jets also contain nontrivial substructure within this cone, which carries important information about QCD dynamics. Unfortunately, the tracking momentum and angular resolution worsens rapidly above $\eta = 3$. Because of this, the hadronic and electromagnetic calorimetry in that region are required to provide both excellent energy resolution and sufficient spatial resolution to resolve particles within the jets. Thus, the forward calorimeter system has to be finely-segmented and built with minimal dead space in between the towers. This design will provide shower containment for highly energetic particles while still providing good energy resolution down to low energies.

Requirements from Radiation Hardness: In the forward region the radiation dose the detector is exposed to varies significantly as a function of radius. Three different regions are considered:

A: $R > 1\,\text{m}$ which is exposed to less than $5 \cdot 10^9$ neq cm^{-2}year^{-1}

B: $0.2\,\text{m} < R < 1\,\text{m}$ which is exposed to less than $10^9 - 10^{11}$ neq cm^{-2}year^{-1}

C: $R < 0.2\,\text{m}$ which receives around 10^{11} neq cm^{-2}year^{-1}

The maximum radiation dose is received closest to the beam pipe and closest to the interaction point. Consequently, the primary concern will be the radiation hardness of the silicon photo multipliers (SiPM) within each layer and a secondary concern are the ASICs used to read out their signals and all other components for calibration or control, which will be sitting behind the calorimeter. It is not expected that the scintillator or steel will experience significant deterioration due to the radiation.

Requirements from Data Rates:

Justification

Device concept and technological choice: The ePIC forward HCal (LFHCal) will be a steel-plastic scintillator sandwich calorimeter, read out in transverse and longitudinally separated segments. The design is based on the SiPM-on-tile concept first introduced by CALICE collaboration [**?**], which is now being further developed for the CMS HGCAL upgrade [**?**]. The SiPM-on-tile

concept allows high readout granularities with low dead space in between scintillator tiles in a design that enables largely automated assembly of individual layer modules.

The LFHCAL baseline readout granularity has been adapted to satisfy the physics performance requirements of the EIC Yellow Report [7], leading to a readout granularity of 5x5 cm in transverse direction and about 10-20 cm in the longitudinal direction. The innermost section closest to the beam pipe will be populated by an high-granularity insert [0,0] with geometry tailored to maximize acceptance up to $\eta = 4.0$.

Figure 8.143 shows an overview of the LFHCal design and the main parameters are given in Table 8.41.

parameter	**LFHCal** **8M & 4M modules**	**insert modules**
inner x,y (R)	-20 cm $> x >$ 40 cm, -30 cm $> y >$ 30 cm	$R >$ 17 cm
outer R (x,y)	$R <$ 270 cm	-20 cm $> x >$ 40 cm, -30 cm $> y >$ 30 cm
η acceptance	$1.2 < \eta < 3.5$	$3.5 < \eta < 4.4$
tower information		
x, y	5 cm	$\approx$ 4.2 cm (layer 1-20) $\approx$ 6.5 cm (layer 21-60)
z (active depth)	120 cm	120 cm
z read-out	$\approx$ 8.4 cm	$\approx$ 8.4 cm
# scintillator plates	60 (0.4 cm each)	60 (0.3 cm)
# absorber plates	60 (1.52 cm)	60 (1.52 cm)
interaction lengths	5.8-6.5 λ/λ_0	5.8 λ/λ_0
# towers	8752	
# modules		2
8M	1058	
4M	72	
# read-out channels	7 x 8752 = 61264	$\approx$ 7000

Table 8.41: Overview of the calorimeter design properties for the LFHCal.

Subsystem description:

General device description: The LFHCal is positioned at $z = 3.68$ m from the interaction point, with a radius of about 2.7 m and a total depth of $\Delta z = 1.32$ m. It is constructed in alternating layers of 1.52 cm steel absorber and 0.4 cm plastic scintillator, see details in Table **??**.

The LFHCAL is largely constructed from mechanical assemblies housing 60 layers of 2x4 ("8M" modules) or 2x2 ("4M" module) tile layers. Alongside each assembly module, a multi-layer PCB picks up the analog pulses from each SiPM and passively transports them towards the end-face of the LFHCAL. This analog signal transport approach differs from the latest CALICE/CMS designs, where the signal is digitized with ASICs placed near the SiPMs. Similar to the approach first proposed in Ref. [0], it simplifies the SiPM-carrying boards, saves longitudinal space in the detector's active area, and eliminates the need for cooling to counteract heat generated by the ASICs. In order to reduce the number of readout channels of the

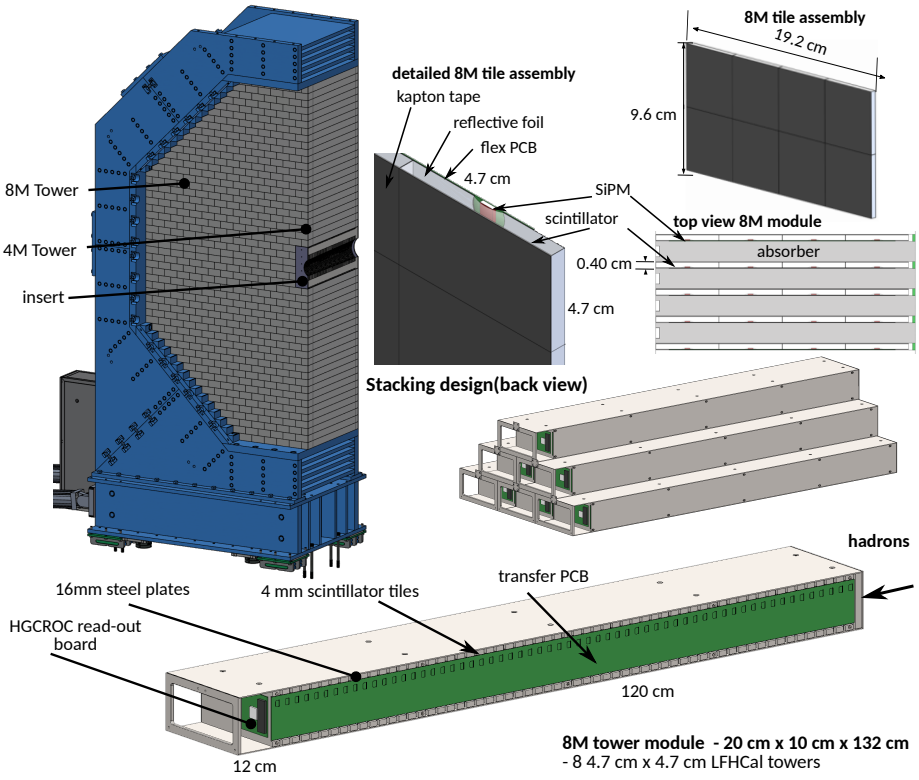

Figure 8.143: Renderings of the forward calorimeter assembly (top left), tile assembly of 8 scintillator tiles of the LFHCal with the SiPMs sitting in a dimple on each tile, detailed stacking example (middle right) and 8-tower module design (bottom).

LFHCAL, SiPM signals from tiles in 5-10 consecutive layers are summed up before digitization by the readout electronics placed on the rear end of the LFHCAL, facing away from the interaction point. Following [0], to increase the geometrical acceptance around the beam pipe and allow access to the scintillator layers during extended shutdowns for SiPM replacement or annealing, the modules surrounding the beam pipe are designed to be larger and include a conical cut-out for the beam pipe, as shown in Figure **??** (left).

The majority of the active scintillator layers are segmented into $5 \times 5 \times 0.4$cm tiles, individually wrapped in reflective foil, as depicted in Figure 8.145. The scintillation light generated in each tile is detected by a SiPM placed inside a circular "dimple" depression in the center of the tile. Tiles and SiPMs are assembled on thin, flexible printed circuit boards which carry the electrical signal of each SiPM to the side of an assembly module. In the insert region hexagonal tiles of two different sizes are used in order to maximize the acceptance and simultaneously reduce the number of read-out channels Consequently, the first 20 layers are equipped with hexagonal tiles of 4.2 cm width which are arranged in a staggered pattern repeating every four layers and the subsequent layers are tiled with hexagonal tiles of 6.5 cm width. This staggering pattern creates overlaps among neighboring cells, which can improve position resolution for hadronic showers when applied in sub-cell reweighting algorithms, such as HEXPLIT [0], or with AI/ML methods. In the insert region, each tile is read out separately to maximize the position resolution of individual showers and to facilitate cell-by-cell calibration and monitoring in high-radiation environments, where radiation levels are expected to be inhomogeneous in both radial and longitudinal positions.

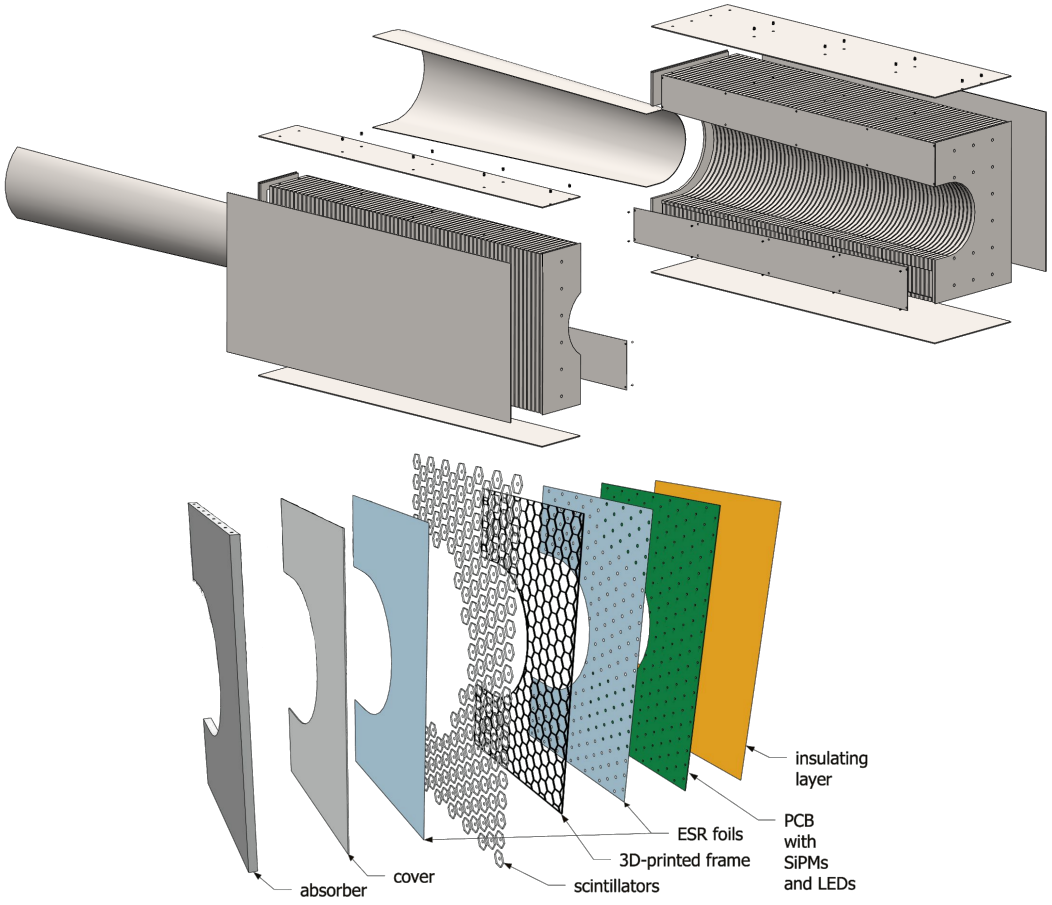

Figure 8.144: Renderings of the absorber structure for the insert modules surrounding the beam pipe (top) and their individual layer composition (bottom).

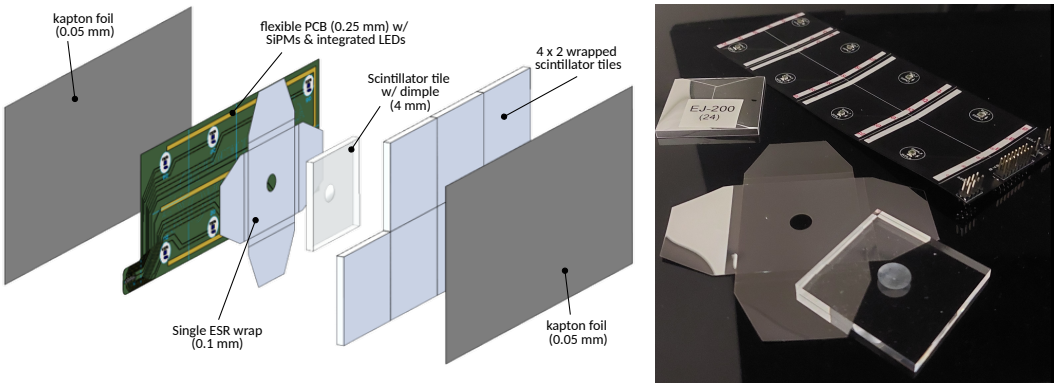

Figure 8.145: Left: Visualization of 8M-scintillator assembly with its individual components. Right: Samples of the individual components used for the 2024 test beam campaign.

The full LFHCal consists of 68264 readout channels. Out of these about 7000 channels are located in the insert modules and the remaining channels are contained in the 1058 ''8M" modules and 72 "4M" modules. They are grouped into 8752 towers of 5×5 cm^2 transverse size with each 7 read-out segments.

Scintillator: The majority of the LFHCAL will be instrumented with injection molded plastic scintillator tiles developed and produced by the Fermilab Scintillator Manufacturing Facility. While the lightyield of injection molded plastic scintillator is found to be 20-25% lower than that of otherwise comparable commercially available cast sheet plastic scintillators, injection molded scintillator tiles are at least one order of magnitude more economical on the scale of the full LFHCAL.

Only for the LFHCAL segments that will be exposed to the highest radiation doses ($R < 1$ m) and inaccesible during the yearly maintainance intervals tiles machined from cast plastic scintillator stock will be used to increase the lightyield in order to maintain enough signal-to-noise ratio to distinguish single MIP signals from the background noise.

Sensors: Simulations and test bench studies have shown that SiPMs with an active area of 1.3×1.3 mm^2 and pixel sizes around 20 µm (i.e. Hamamatsu S13360-1325PE or S14160-1315PS) will yield enough light yield, gain and dynamic range even after full irradiation over the whole projected lifetime of the LFHCAL. However, as neither the scintillator tiles nor the SiPMs are accessible after assembly, larger SiPMs with an area of 3×3 mm^2 (ie. Hamamatsu S13360-3025PE or S14160-3015PS) for radii below 1 m in order to provide an additional operational safety factor in the S/N ratio towards the end of its lifetime. For example, Ref. [0] demonstrated that an S14160-3015PS, operated at 40.5 V (≈ 2 V over-voltage), yields a most-probable value of approximately 60 photoelectrons per MIP when coupled with an EJ-212 scintillator cell with an area of 8 cm^2.

FEE: The electrical signals from all SiPMs in the LFHCAL are routed towards the end-face of the LFHCAL using a passive transfer board, where they are picked up by a summing board that forms analog sums of $5-10$ channels located consecutive layers of the same position. . The summed signals are then digitized by an ASIC based on the CMS HGCROC chip designed and produced by OMEGA. Each HGCROC can read out up to 72 individual SiPM channels. It features a 12bit ADC for low amplitude hit digitization, complemented by a 16bit time-over-threshold counter for larger amplitude signals. Individual signal arrival times are tagged with a 20 ps time-of-arrival counter. The HGCROC chip family features trimmable bias voltage in the range $0-2.5$ V for each input channel, greatly reducing the number of required high voltage power supply channels to operate the LFHCAL.

While the HGCROC chip family is well advanced in its design, it is designed for the externally triggered environment of the CMS experiment. A self-triggered variant of the HGCROC concept named CALOROC will be developed for the use in ePIC, which will natively support the ePIC streaming readout model. [**?**].

Performance The minimum requirements for the LFHCal performance are driven by the energy and position reconstruction of hadronic particles within a jet of $5-250$ GeV. These requirements, however, must be evaluated as a combined resolution of the electromagnetic and hadronic calorimeter responses, as a significant fraction of the energy may already be deposited in the electromagnetic calorimeter, which has an equivalent depth of one interaction length. Since these two calorimeters have different e/h values, their combination must account for this to achieve a linear response with optimal resolution. Moreover, as the hadronic calorimeter is not compensated at the hardware level (i.e., given its Fe/Sc design, the response differs for electromagnetic and hadronic

depositions, with $e/h \approx 1.2$), optimal energy reconstruction requires a shower-by-shower weighting approach. This is necessary because the electromagnetic content of hadronic showers varies on a shower-by-shower basis on an energy-dependent manner. This weighting procedure, dependent on particle energy and angle, is commonly referred to as "software compensation" or "offline compensation". As noted in Section 11.4.1 of the YR [7], this approach requires fine granularity in the hadronic calorimeter, including in the longitudinal direction. This was demonstrated in previous experiments, such as H1 at HERA, which used a Pb/Fe liquid argon calorimeter, and in test beams with the CALICE Fe/Sc calorimeter.

Rather than following a traditional minimization approach to achieve the weight functions to implement software compensation, we rely on AI/ML methods, which provid a more efficient and optimal way. Specifically, we used a graph neural network approach, following the method applied in EIC calorimetry studies in Refs. [0, 4], which builds on prior work by the ATLAS collaboration [0]. Similar advancements were recently presented by the CALICE collaboration using test beam data [0]. This graph network approach effectively implements software compensation through shower-by-shower weighting at the cell level, using the shower structure encoded in graphs to achieve a linear response that is independent of both energy and the electromagnetic energy fraction of the hadronic shower, thereby yielding optimal energy resolution.

Figure 8.146 shows the combined energy resolution of the forward electromagnetic and hadronic calorimeter for single pions within the primary acceptance of the LFHCal as a function of η, obtained using the aforementioned graph network approach. The resulting combined energy resolution of $\sigma_E/E = 27\%/\sqrt{E} \oplus 3\%$ surpasses the required resolution of $\sigma_E/E = (35-50)\%/\sqrt{E} \oplus (7-10)\%$, as specified in the YR.

The combined position resolution of the LFHCal and forward electromagnetic calorimeter for single pions can be found in Figure 8.147. Both the φ and θ resolution are found to be better than 4 mrad for pions with an energy larger than 5 GeV within the full acceptance. A mild energy dependence can be observed for the θ resolution increasing as a function of energy down to 2.5 mrad. For the φ no clear energy dependence can be claimed. While the θ resolution appears to be largely η independent, the φ improves with increasing η to better than 2.5 mrad

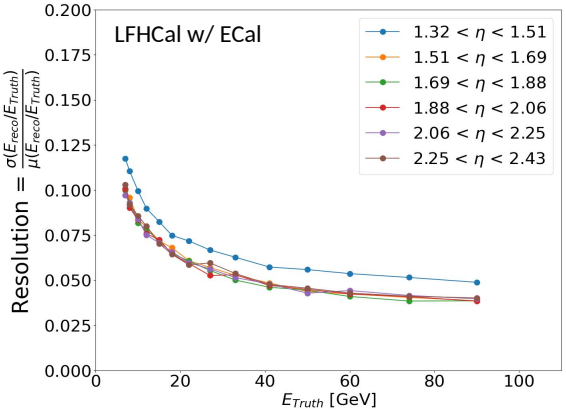

Figure 8.146: Combined energy resolution of the forward calorimeter system as a function of pseudo rapidity η for single pions, evaluated within the primary LFHCal acceptance. These results are obtained using the graph-neural network approach described in Ref. [4].

Implementation

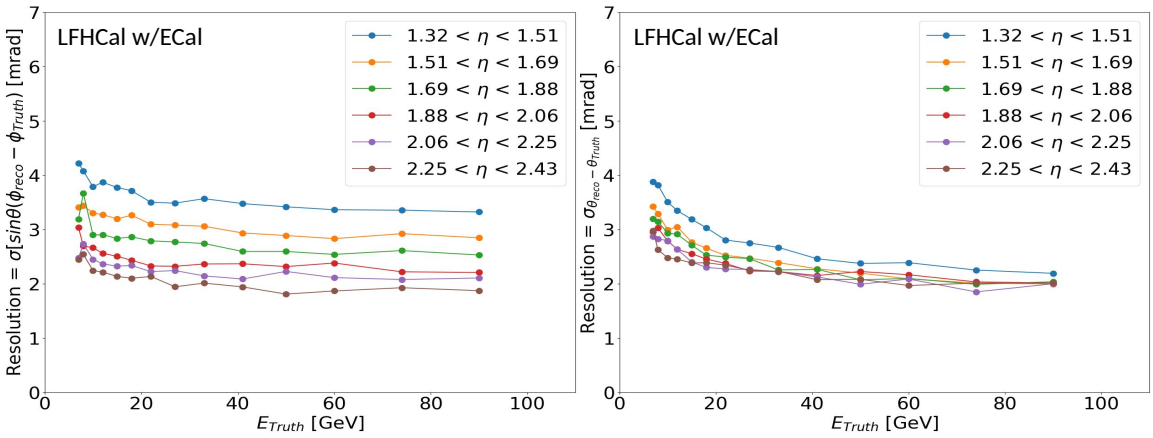

Figure 8.147: Combined position resolution of the forward calorimeter system as a function of pseudo rapidity η for single pions, evaluated within the primary LFHCal acceptance. These results are obtained using the graph-neural network approach described in Ref. [4].

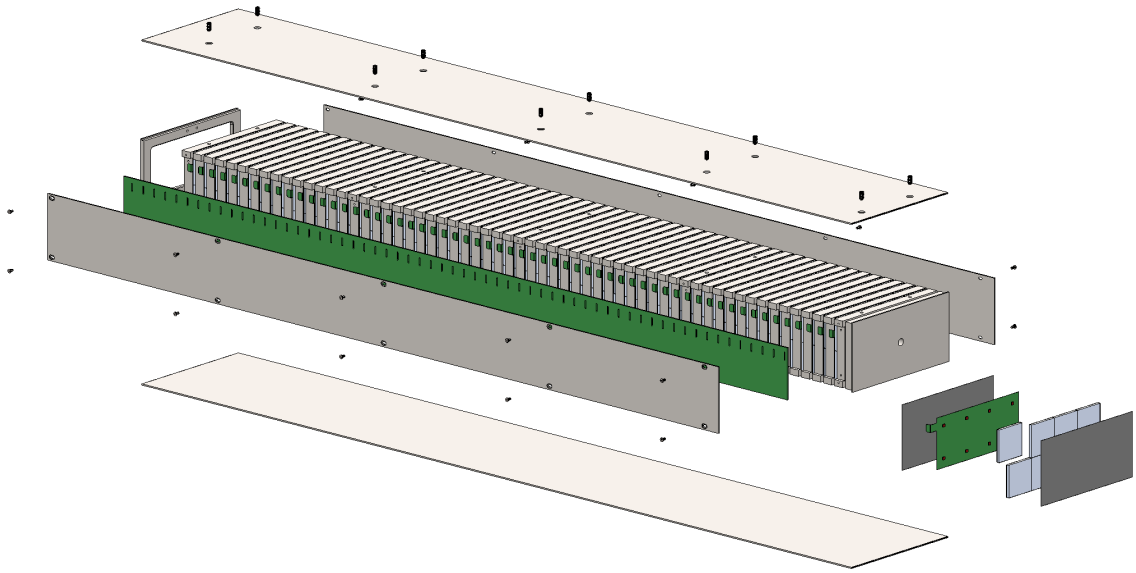

Figure 8.148: Visualization of the individual components of an 8M module.

Subsystem mechanics and integration: The primary construction component of the LFHCal are the 1052 8M modules, as depicted in Figure 8.148. These modules are constructed out of an electron beam welded and nickel-plated absorber structure out of AISI-1020 carbon steel, consisting of the 60 absorber plates, the front and back plate and the top and bottom plate. Inside the resulting slots inbetween the absorber plates 8M scintillator assemblies (Figure 8.145) are placed, which are connected to a long transfer PCB running along the side of the 8M module. The module is closed by two screwed side panels out of AISI 304 stainless steel. The read-out electronics is placed in a rear compartment of about $19.5 \times 9.5 \times 8.5$ cm^3, which is accessible from the rear though a cut-out window in the back plate.

The individual absober plates are welded on the top and bottom using alternating stich welds of

two times 63.5 mm and 88.78 mm length with a minimum penetration depth of 0.5 mm over the full length. For the front and back plates, as well as, the those plates to which the strong back for transportation is anchored the available maximum weld length is used to ensure maximum stability. Afterwards, the fully welded structure is nickel electroplated to reduce the effects of corrosion and the stainless steel side covers are installed. This production mechanisms allows for minimal distortions during construction and thus allows for a maximization of the available active detector surface.

The active layers are inserted and tested together with the long transfer board at the various assembly locations. The FEE-cards at the rear of each module can be installed during the same assembly process or could be mounted prior to installation at Brookhaven National Laboratory depending on the production readiness of the CALOROCs.

A similar construction procedure will be followed for the half sized 4M modules, where the staggering of the welds will not be necessary. For the two individual modules we envision the same construction technique, however, due to is weight and corresponding necessary rigidity it will most likely need to be welded also on the outer straight edge of each module to correctly disperse the load of the modules stacked on top of the respective inserts.

The LFHCal will be stacked in two half shells surrounding the beam pipe, as shown in Figure 8.149 (top), which are situated on rails and movable using Hillman rolers and linear actuators, which are detailed in the same drawing on the bottom. During assembly each module is lifted into place and then adjusted horrizontally and vertically using different sized stainless steel shims. Afterwards it is fixated in place using bracket at the rear of each module as seen in the detailed stacking pictures in Figure 8.143. Moreover, each module is bolted to the 2.54 cm plate covering the full front face of the each half of the LFHCal. This steel plate will simultaneously serve as mounting plate for the forward electromagnetic calorimeter.

Services: Apart from the SiPM sensors integrated into each scintillator tile layer, all active LFHCAL electronics are located on the end-face of the LFHCAL, fully accessible in between active beam runs of the EIC. As such, there are no significant bottlenecks in terms of maximum permissible occupied cross section of service channels.

The total number of readout ASICs is expected to be around 1000 at a power dissipation of an estimated 2 W per ASIC distributed over the entire end-face of the LFHCAL, which is cooled with a small liquid cooling system.

The overall cross section of low voltage supply cable conductors is estimated to be around 1000 mm^2 from the required current rating (up to 1kA at 2.5V), which can be supplied by a few units of off-detector low voltage power supplies in a common crate area with the appropriate air flow, mains power connection and electrical safety facilities.

The HGCROC readout ASIC supports channel-individual trimming of SiPM bias voltages, reducing the overall number of required high voltage bias supply channels. For the start of the operation of ePIC, we expect not more than 16 channels of high voltage supplies in the voltage range 50-80 V. When more significant adjustments to the bias voltages will have to be made due to the varying effects of radiation damage across the LFHCAL volume, more channels might have to be added.

Since the LFHCAL is planned to be assembled in two individual half-discs, all cables and other services are separated along the same axis and cannot reach across the central separation gap of the LFHCAL, which is either reflected in individual cable trees from the power supplies to individual halves of the LFHCAL, or potentially entirely separate power supplies located on different sides of the experimental hall.

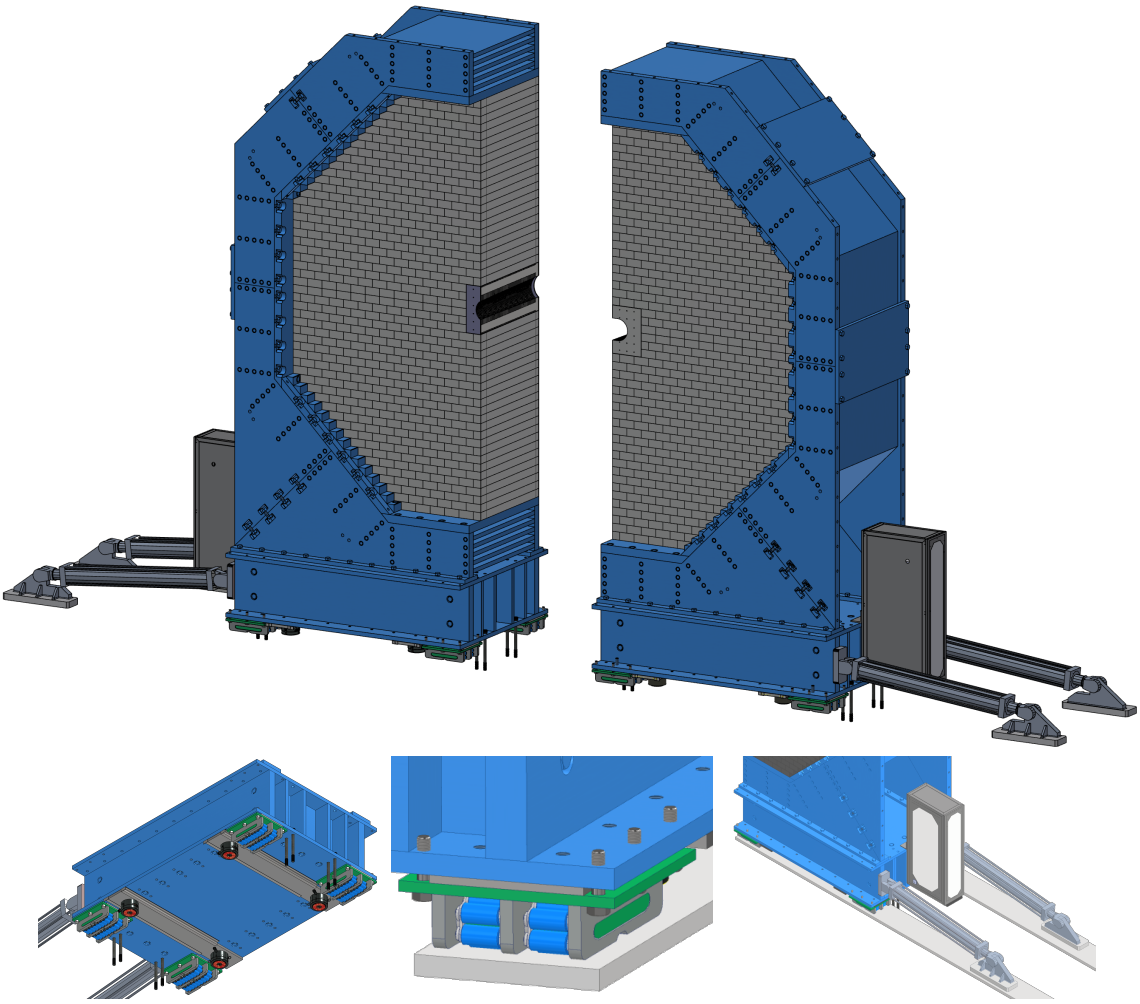

Figure 8.149: Visualization of the full LFHCal in its cradle (top) and details of its moving mechanism (bottom).

Calibration, alignment and monitoring: The gains of individual SiPMs will be monitored and calibrated by means of an integrated LED calibration system providing short, low amplitude flashes of light into each sensor. This gain calibration scheme does not depend on the exact amplitude of each LED pulse and is thus robust to changes in ambient conditions and very cost effective. The front-end electronics include a charge injection mechanism that can calibrate its own ADC and ToT scales with respect to each other.

Using the calibrations in sensor gain and readout electronics scales, the lightyield of each tower of summed scintillator tiles will be monitored from the deposits of minimum ionizing tracks produced in EIC collisions during the operation of the accelerator, as well as with cosmic muons in between run periods.

Initial parameters for module alignment will be provided from the metrology during and after the stack-up of the LFHCAL modules into the full LFHCAL detector. No significant relative movement of LFHCAL modules is expected during its lifetime, however the absolute position of each half-cradle will need to be validated each time the cradles are moved out and back into their positions.

Status and remaining design effort:

R&D effort: Add text here.

E&D status and outlook: Add text here.

Other activity needed for the design completion: Add text here.

Status of maturity of the subsystem: Add text here.

Quality Assessment (QA) and Control (QC) planning:

Environmental, Safety and Health (ES&H) aspects: The LFHCal design follow the best practices established within the national laboratories regarding standard safety and environmental concerns. We will strive to implement these practices at all production sites by standardizing the safety protocols, while adhering to local constraints and control processes specific to each institution. Consequently, for each site the potential hazards will be identified, mitigation strategy will be developed and the appropriate safety procedures will be documented.
The primary hazard during construction of the LFHCal have been identified as:

Handling of absorber structure: The different modules of the LFHCal range in weight from 74 kg up to 1.3 t. None of them should be lifted without a lifting fixture (strongback) and the appropriate lifting equipment for the respective weight. They will need to be uncrated for assembly and lifted on top an appropriate assembly table which can support the respective weight during installation and testing of the individual components. In particular, for the lifting operations specific protocols in compliance with the local safety rules will need to be established in order to prevent accidents.

Storage of absorber structure during assembly: While the modules are being assembled a large fraction of the 8M modules will need to be stored at the different assembly sites. Thus in order to mitigate excessive space requirements a storage solution which allows stacking of crate modules (2-3 crates) or similar solutions will need to be pursued. This will require additional safety measures to prevent collaps of the crates or other stacking previsions as well as lifting the modules accordingly in their crates.

Laser operation hazards: The ESR foil wraps will need to be cut with a laser-cutter. Controls and measures will be implemented to ensure the corresponding device cannot be operated without interlocks and following the laser safety guidelines of the respective institution.

Pinch/nip hazards: Automated systems, such as robots for wafer probing, pick-and-place, and glue application, present pinch hazards. Controls, such as guards and procedures, will be in place to mitigate these risks.

Crush hazards: The use of presses and swaging equipment introduces crush hazards during assembly processes. Strict safety protocols, including the use of guards and operator training, will mitigate these risks.

Radioactive sources: The use of radioactive sources for calibration introduces additional handling requirements, and proper shielding and storage protocols will be implemented as necessary.

Electrical safety: Electrical safety procedures will also be applied for all electronics and power systems associated with the LFHCal production tooling and detector components.

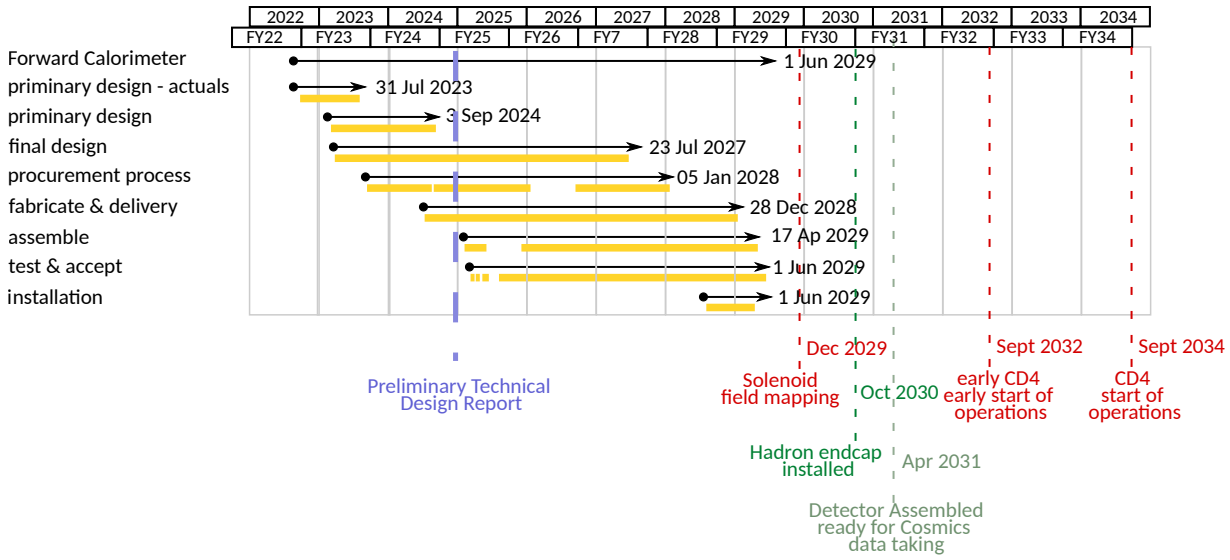

Figure 8.150: General timeline of the LFHCal design, construction and assembly.

Flammable liquid handling: For cleaning the different electrical components ethanol might be used, these bottles will need to be handled with care and their storage will follow the institutional safety protocols. Handling will only be done with appropriate gloves.

Construction and assembly planning: The LFHCal construction is divided into several phases, which are partially happening in parallel:

Absorber structure fabrication: The individual 8M, 4M and insert module absorber structures are assembled out of 66 individual pieces each, excluding screws, as seen in Figure 8.148. Out of these 64 pieces are welded together using electron-beam welding after having been preassembled and fixated in a specially designed jig for the weldment. It has been currently estimated that a maximum of 12-20 8M modules and 4M modules could be produced within a 5-day work week. The limiting factor being the availability of the large vacuum welding chamber and a full weldment cycle lasting about 2/hour per weldment. The weldments are afterwards electroplated with nickel to prevent corrosion and reduce the wearing on the outer surface due to transportation and handling. At full capacity this would require a full year of production time for the 1058 8M weldments not factoring in any delays in the supply chain. With the LFHCal also serving as flux-return for the MARCO magnet and the need to be available for the powering tests currently scheduled for December 2029, has led us to acquire the LFHCal modules as part of CD3-A and CD3-B long lead procurement starting in fiscal year 2024. In order to reduce the storage needs at the respective vendors and allow for a staggered further assembly the delivery of these modules will be done in badges of 50-100 modules during 2025 and 2026.

Scintillator layer assembly: The assembly of the individual scintillator layers for the 8M and 4M modules can be completely decoupled from the absorber structures fabrication. In order to assemble a single 8M-scintillator layer one fully equipped flexible SiPM-carrier board, 8 wrapped tiles and two layers of Kapton foil will be needed. For the main body of the LFHCal (1058 8M and 72 4M) modules a total of 63480 8M scintillator layers and 4320 4M scintillator layers will be required, leading to at least 525120 wrapped scintillator tiles.

About $10 - 12\%$ of the tiles will be produced out of cast sheets, while te remaining $\approx 90\%$ of the tiles will be injection molded out of scintillator plastic using the facilities at Fermilab. Producing all tiles out of cast material is cost and schedule prohibitive, despite having an about 20% higher light yield. The production time at Fermilab has been estimated to be about 6/month of nominal operations, which can be done in batches in order to reduce the storage overhead. The tiles produced using injection molding have to be degrated and subsequently wrapped in highly reflective foil (i.e. ESR foil). Given the tight tolerances of the LFHCal modules and the amount of tiles to be wrapped it is currently envisioned to perform the wrapping using a specifically designed tile-wrapping setup similar as for the CMS HGCAL.

Afterwards, the wrapped tiles are assembled into 4×2 or 2×2 scintillator assemblies backed by a flexible SiPM-carrier board and sandwiched into two adhesive sheets fo thin capton foil, as seen in Figure 8.145. The assembled layers are subsequently tested and packaged into groups of 60 assemblies to ease storage and assembly during the module assembly.

For the two insert modules each layer will need to be assembled individually due their unique shape and hexagonal tile arrangements. The around 7000 hexagonal will need to be painted on their edges individually with TiO_2-paint and then subsequently embedded in their 3D printed frame for each layer. The frame is mounted to a kapton backed SiPM carrier board which is covered with a precut ESR sheet in order to accomodate the SiPMs and LEDs for each tile. After installing another sheet of ESR-foil ontop of the scintillator layer the assembly is completed by a thin cover. Do due to their uniqui shapes and placements the insert module layers have to be assembled manually and then tested. These layers are constructed with a significantly larger rigidity than the 8M assemblies in order to allow for removal during the extended year end shutdowns and possible replacement of annihilation.

Module assembly and testing:

LFHCal assembly:

Collaborators and their role, resources and workforce: The full LFHCal WBS organizatorial chart is available in the additional material (Figure 8.151). The LFHCal consortium consists of a diverse list of institutions under the leadership of Oak Ridge National Laboratory (ORNL). Currently the majority of the leadership team is situated at ORNL, in particular regarding mechanical, electrical and read-out design as well as scintillator testing. System testing and Software and Simulation design are headed by Brookhaven National Laboratory (BNL) and the University of Riverside, respectively.

Risks and mitigation strategy:

Each LFHCAL scintillator tiles has to be wrapped in a suitable foil, ensuring the wrapping fulfills the requirement in light-tightness as well as geometric tolerances after wrapping. The LFHCAL tiles for lab tests and testbeam studies so far have been wrapped manually. The CMS collaboration is developing an automated wrapping machine, following two similar concepts at Northern Illinois University and DESY, Germany. We are in close contact with these groups and plan to adapt one of their designs to the needs of the LFHCAL design. If their final designs turns out to be unsuitable to wrap LFHCAL tiles, we will require additional R&D efforts to adapt the existing design to the LFHCAL or potentially develop our own. If all automated wrapping developments fail to produce reliable results, all tiles can be manually wrapped with the help of already existing 3d-printed and a sufficient number of e.g. students to perform the wrapping under supervision.

The readout ASIC of the LFHCAL (as well as other ePIC detectors) is expected to be based on the HGCROC design with modifications enabling a self-triggered streaming readout named CALOROC. In case the CALOROC developments are not successful, HGCROC can be operated to be quasi self-triggering by adding additional FPGA logic close to the readout electronics that locally generates external triggers based on the streaming trigger output that already exists in the HGCROC. This mitigation would require additional electronics on the LFHCAL end-face and greatly increase the number of differential data links required, which increases system complexity and cost.

Stacking the 1168 LFHCAL modules into two coherent half-discs requires each module to adhere to the defined tolerances after assembly. Ongoing tests of the electron-beam welding procedures achieve tolerances very close to the requirements, but scaling the production to the required volume still needs to be demonstrated and validated. If the tolerances for individual modules can not be ensured, more shimming is required during the module stackup.

A number of critical components of the LFHCAL are not accessible after the modules are stacked up into the full LFHCAL. All connectors and PCBs buried into the LFHCAL volume must thus be throughly validated for electrical and mechanical functionality and longevity. If certain connector types are found to be unsuitable e.g. in past and future testbeam campaigns, different connectors need to be selected or, if not possible, additional fastening mechanisms need to be introduced to ensure no readout channel is lost to bad or worsening connectors over the lifetime of the LFHCAL.

Additional Material

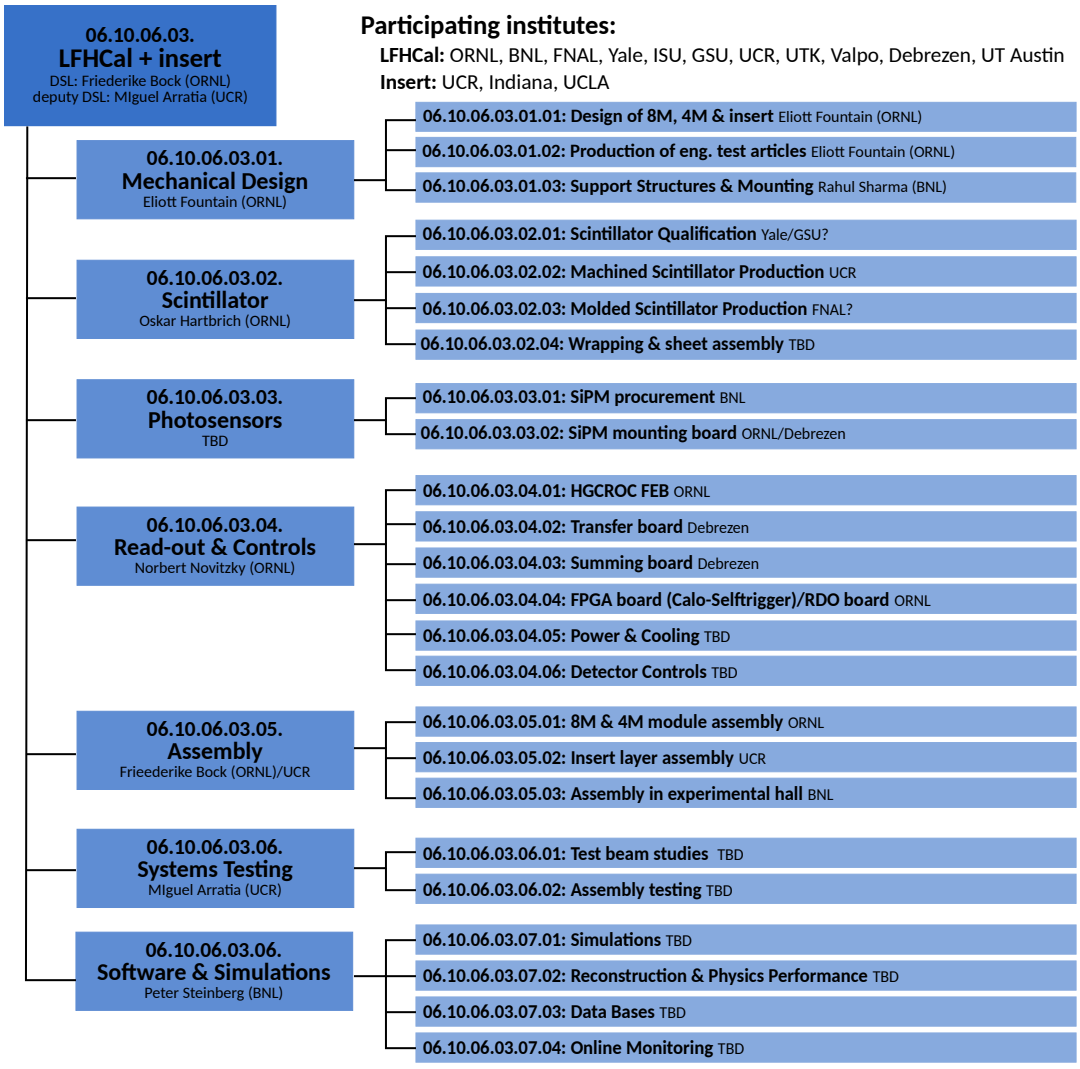

Figure 8.151: Organizatorial chart of the LFHCal & insert consortium, indicated by the numbers are the associated WBS structures.

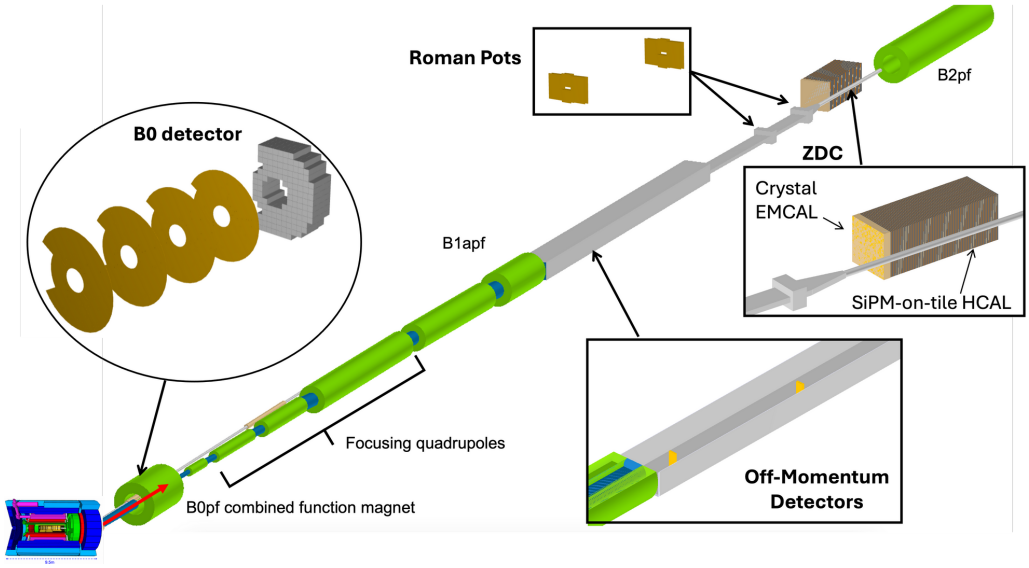

Figure 8.152: All four far-forward subsystems in the outgoing hadron beam direction. The green cylinders are accelerator dipole and quadrupole magnets.

8.3.7 Far forward detectors

The ePID far-forward detectors are required to enable essentially the entirety of the exclusive physics program at the EIC, where final-states involve protons, neutrons, photons, and various other particles at $\eta > 4.5$. There are four subsystems, all integrated with the outgoing hadron beamline between ∼5.5 and 39 meters from the interaction point. The far-forward subsystems are summarized in Fig. 8.152, and details are presented in subsequent subsections.

8.3.7.1 The detectors in the B0 bending magnet

Requirements

Requirements from physics: The B0 magnet bore will contain two detectors: a charged particle tracker and an electromagnetic calorimeter. Both will have acceptance covering the angular region from 5.5 to 20 mrad. Given the mechanical constraints imposed by the detectors' location in the magnet (and respecting the beam lines themselves) the detectors will be highly asymmetric for angles greater than ∼13 mrad. To maximize acceptance it's required that there be minimal dead areas in the instrumentation especially for angles less than ∼13 mrad. The tracker should have momentum resolution up to 6% for protons, and timing precision sufficient to deal with vertex smearing. The calorimeter should have a large dynamic range with sensitivity to both soft, O(100 MeV), and hard, O(100 GeV), photons. The energy resolution should be less than $8\%/\sqrt{E} \oplus 4\%$, with position resolution $\lesssim 10$ mm. We note that for some analysis use cases the calorimeter will function as a photon 'tagger' rather than an actual calorimeter, and so in some regions of acceptance (where the mechanical constraints are acute) this resolution may not be achieved but having the acceptance instrumented is still valuable.

Requirements from Radiation Hardness: The expected non-ionizing radiation dose at a longitudinal distance of 692 cm from the interaction point (near the fourth tracking layer and the front of the calorimeter) is approximately 3.1×10^{11}) 1 MeV neutron equivalent per square centimeter for 100 fb^{-1}. At this location the ionizing dose can reach O(100) kRad.

Requirements from Data Rates: Add text here.

Justification

Device concept and technological choice: The charged particle tracker will be composed of four layers instrumented with silicon. The layers are approximately equidistantly placed at distances between 590 and 690 cm from the interaction point, which given the field inside the magnet allows satisfactory proton measurement and momentum reconstruction. The electromagnetic calorimeter is composed of 135 scintillating $PbWO_4$ crystals, each one 2 x 2 x 20 cm^3 (the long direction is on the z axis). We note that the crystals are the same as those used in the EEEMCal.

Subsystem description:

General device description: Each tracking layer has a transverse layout to cover as much of the angular acceptance as possible given the mechanical constraints, as illustrated in Figure **??**. The crystals of the calorimeter are arranged in a similar way for the same reason.

Sensors: For the tracking detectors AC-coupled low-gain avalanche diodes (AC-LGADs) are chosen due to their capability to provide both high-precision space and time information. In order for the spatial resolution to meet the performance requirements charge sharing must be implemented in the reconstruction. We note that this technology is broadly in use within ePIC, and its particular implementation for the B0 detectors should be very similar to the Roman Pots/Off Momentum Detectors. For the calorimeter the $PbWO_4$ crystals produce light peaking at $\sim$ 420 nm, which will be read out by SiPM. Four 6x6 mm^2 SiPM will be used per crystal, 3 with 15 micron pitch and one with a 10 micron pitch (likely Hamamatsu S14160-6015PS and S14160-6010PS, respectively). The larger pitch SiPM have fewer pixels but higher efficiency making them appropriate for smaller signals, whereas the smaller pitch SiPM will be utilized for the higher energy particle signals.

FEE: Following the Roman Pots/Off Momentum Detectors, the ASICs will be readout using LPGBT in-place of FPGAs due to the high-radiation environment in which these detector will be located. AC-LGAD + ASIC modules will be connected to the LPGBT, which will be coupled to a VTRX+ to convert the signals to a fiber to send off to the DAW system. The electronics to process the SiPM signal are still to be worked out but expected to follow closely the scheme of the EEEMCal.

Other components: Add text here.

Performance The key physics task of the B0 tracker system is the measurement of protons, and this is summarized by the acceptance and transverse momentum resolution shown in Figure 8.153. The B0 calorimeter's acceptance for photons is shown in Figure 8.154. The calorimeter seeks to measure photons over a very large range. The performance of the detector, in particular the energy resolution, is shown separately for low and high energy photons in Figure 8.155. The higher energy

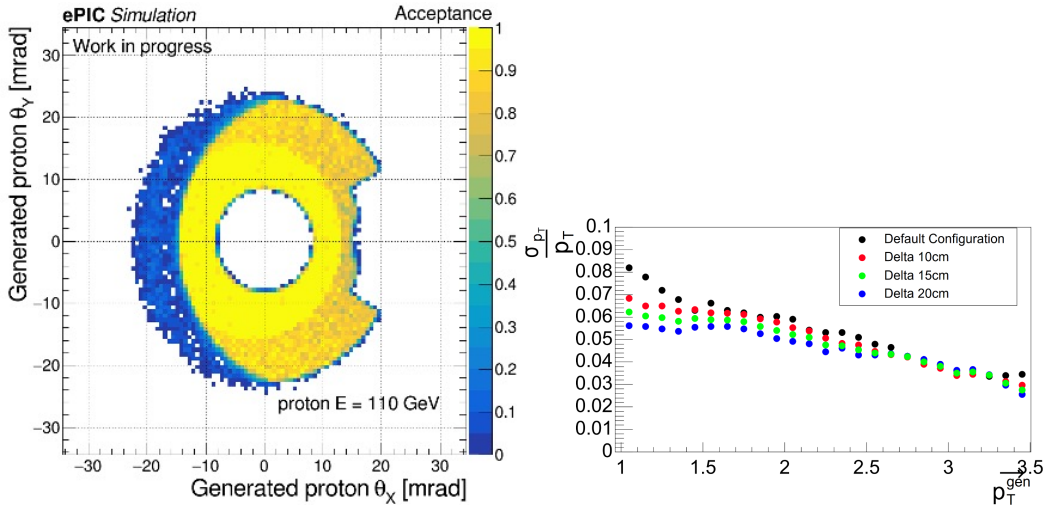

Figure 8.153: Left: The B0 tracker's acceptance of protons (E=110 GeV), as a function of θ_x and θ_y. PLACEHOLDER NEEDS TO BE REMADE W/REAL B FIELD Right: The p_T resolution for protons reconstructed in the B0 tracker. PLACEHOLDER NEEDS TO BE REMADE WITH FINAL LOCATIONS, FINAL TRACKING, PROPER LABELLING ETC

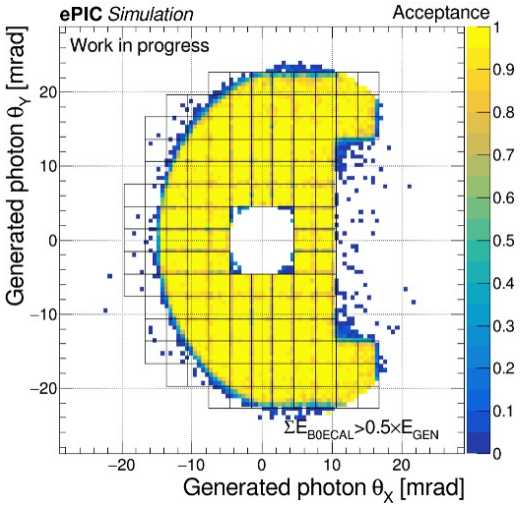

Figure 8.154: The B0 EM calorimeter's acceptance of photons with a substantial (for now half their energy) deposit in a calorimeter crystal.
PLACEHOLDER - SPLIT HARD SOFT, FIX CRYSTAL ALIGNMENT

photons are evaluated based on a signal to a single 10 micron pitch SiPM, whereas the lower energy photon performance assumes three 15 micron pitch SiPM per crystal.

Implementation

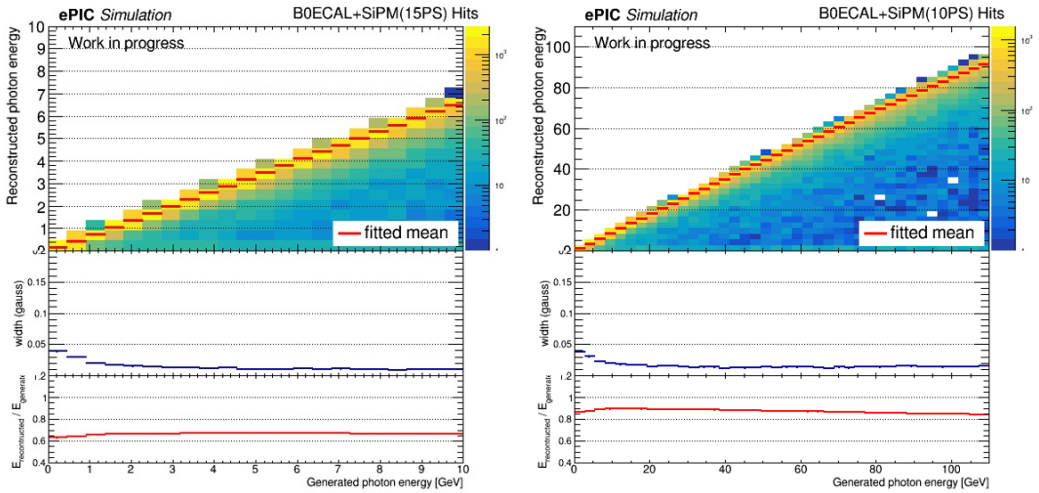

Figure 8.155: The energy reconstructed and associated resolution for the B0 EM calorimeter of photons with $\theta < 13$ mrad in the soft (left) and hard (right) energy reconstruction regimes.
PLACEHOLDER - zoom soft photon, update reflectivity

Services: For the trackers low voltage (∼3V) and high voltage (∼150V) supplies for the operation of the ASICs and the bias supply, as well as slow controls for the voltages and the DAQ system. The SiPM for the calorimeter need a bias of (∼5V) .The cooling system is still to be worked out, but is expected to be air based (unlike the in-vacuum challenge of the similar instrumentation for the Roman Pot/Off Momentum Detectors).

Subsystem mechanics and integration: The integration of the detectors into the B0 magnet bore is a significant undertaking. The space for the detectors (and services) is quite limited and the installation procedure introduces more constraints. After the vacuum valve is closed there is only about 10 cm of clearance in front of the magnet and this precludes installation of the 20 cm crystals. To address this difficulty, the crystals will be installed prior to closing the valve closing and the beam commissioning. At this point *only* the crystals will be installed to avoid the risk of damaging the other components during the commissioning. Following this the SiPM and electronics of the calorimeter will be installed. Both installations as well as the final positioning of the detectors will be via a rail system: detector components will be loaded onto the rails system outside the magnet and inserted in to it. We note that the detectors will be installed as sub-detectors not as monolithic pieces covering the entire acceptance.

Calibration, alignment and monitoring: Add text here.

Status and remaining design effort:

R&D effort: There is still work to be done for full detector operation. For the trackers especially demonstrating effective reconstruction using charge sharing and for the calorimeter the multi-SiPM readout. For both the trackers and calorimeter this includes optimizing the acceptance in concert with the installation procedure.

E&D status and outlook: Add text here.

Other activity needed for the design completion: Completion of the mechanical rail system is underway and this includes a final scheme of subdividing the detectors into sub-detectors accordingly.

Status of maturity of the subsystem: Add text here.

Environmental, Safety and Health (ES&H) aspects and Quality Assessment (QA planning): Add text here.

Construction and assembly planning: The tracking system should benefit from the BNL local expertise and production capabilities for AC-LGAD and from there 'directly' to installation readiness. The calorimeter sub-components may be prepared either on or off site, but in any case the final assembly can not be separated from the installation procedure.

Collaborators and their role, resources and workforce: The Israeli ePIC consortium (in particular BGU and TAU) are playing the main role in the detector development and this will continue through installation/operation. There is also very significant participation from BNL generally, and especially for the common AC-LGAD instrumentation.

Risks and mitigation strategy: For the trackers the largest risk is the necessity to utilize charge sharing in the reconstruction to obtain the needed momentum resolution. Other detection technologies have been considered to mitigate this risk (with smaller pixels) but to this point none has been identified as an appropriate alternative. For both detectors (and even more acutely for the calorimeter) the installation challenge risks limiting the detector acceptance.

Additional Material Add text here.

8.3.7.2 The roman pots and the off-momentum detectors

Requirements

Requirements from physics: Measurement of protons at various rigidities, with rigidity defined by ratio of the proton momentum to that of the beam itself, and with scattering at angles $<$ 5mrad requires detectors integrated directly into the hadron beamline in the form of Roman pots (RP). The Off-Momentum detectors (OMD) enable tagging and reconstruction of spectator protons from the breakup of light nuclei (e.g. deuterons and He-3), which produce protons at rigidities $<$ 65%, with deuterons producing protons at an average of $\sim$ 50% rigidity. For the Roman pots, achieving acceptance down to 0 mrad is impossible due to the presence of the hadron beam itself, so the low-θ (low-p_T) acceptance is essentially entirely driven by the focusing quadrupoles (machine optics) before and after the interaction point. For IP-6, the choice of low-β^* optics to maximize luminosity (so-called "high divergence") means the transverse beam size, $\sigma_{x,y} \approx \sqrt{\beta_{x,y}(z_{RP}) \times \epsilon_{x,y}}$, where $\beta_{x,y}(z_{RP})$ are the beta-functions in (x,y) at the Roman pots location and $\epsilon_{x,y}$ is the emittance for the machine, is larger, worsening the acceptance at the expense of luminosity. Generally, $10\sigma_{x,y}$ is the average "safe distance" for the Roman pots to operate. Conversely, a choice can be made to

reduce luminosity to improve low-θ acceptance at the Roman pots location, normally referred to as "high acceptance" optics. Given this set of operational parameters for the machine itself, it is required that the sensor packages have minimal dead area at the edges to take maximum advantage of the machine optics during data taking runs.

For resolution, the detectors must deliver p_T-resolution better than 10%.

Requirements from Radiation Hardness: Maximal radiation doses are shown to be ¡ 10^{12} 1 MeV neutron equivalent for NIEL radiation, while ionizing doses are around 1 krad for the Roman pots region of ePIC [will add plot here, or reference section on the radiation].

Requirements from Data Rates: Rates during normal operations, with expected vacuum of 10^{-9} mbar, are a few Hz/channel. However, the beam halo could potentially provide rates of 30-50kHz at $\sim 10\sigma$ from experience of Roman pots at STAR. While the EIC hadron beam will have many differences to the RHIC hadron beam, it's hard to estimate the full rate impact of the beam halo without an appropriate simulation. This is something to be done in the coming year as the machine develops.

Justification

Device concept and technological choice: The basic concept of Roman pots detectors for measuring protons near the beam is not new and has been employed at HERA, RHIC, and the LHC, among other collider facilities. In the case of the EIC, the Roman pots (and OMD) need to be able to make measurements with challenges different to those in previous facilities. Studies from the EIC generic R&D program, in particular eRD24, demonstrated that the RP detectors need to have both high spatial ($\sim 140\mu$m) and timing ($\sim$35ps) resolutions, a challenge to deliver with one subsystem. As silicon detector technology has advanced, an evolved version of the DC-coupled Low Gain Avalanche Diode (DC-LGAD) sensor, normally used for high-resolution timing detectors [Add reference here later], has come to the fore in the form of an AC-coupled version, known as the AC-LGAD. The AC-LGADs allow for pixilization and can meet the requirements of the RP and OMD subsystems, as was the goal of eRD24.

An additional challenge with operation of the RP and OMD systems is the operation of these detectors in vacuum. The subsystems themselves are large enough to prohibit use of the conventional "pot" vessels used to protect the detectors in other colliders, and therefore necessitate the inclusion of the sensor planes directly into the machine vacuum, providing unique challenges for cooling and shielding.

add figures of full detector layout here later when I have a better CAD picture to use.

Subsystem description:

General device description: The Roman pots and off-momentum detectors are both vacuum-based silicon sensors arranged into two stations for fully reconstructing protons at various magnetic rigidities, where rigidity here refers to the fraction of the momentum the proton has with respect to the steering dipoles design orbit momentum.

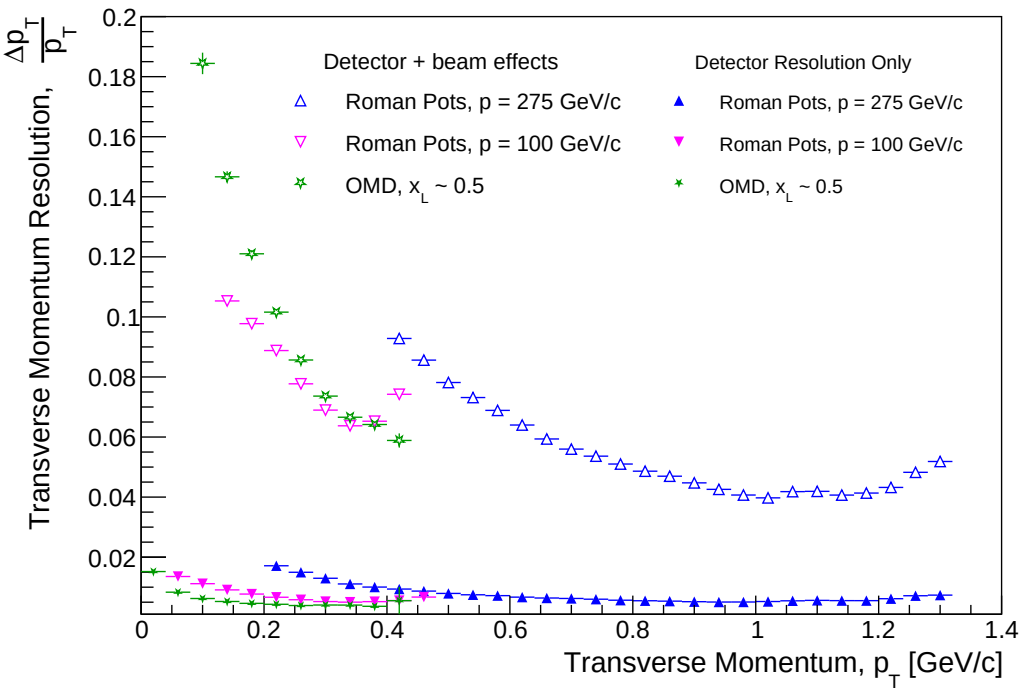

Figure 8.156: Summary of transverse momentum resolutions for the Roman pots and Off-Momentum Detectors. Contributions are separated by those induced by intrinsic detector choices (e.g. pixel sizes) and those from beam effects (e.g. angular divergence), which have an outsized impact on momentum measurements at very-forward rapidity. Will be replaced with DD4HEP version

Sensors: AC-coupled low-gain avalanche diodes (AC-LGADs) are the technology of choice for these two subsystems due to their capability to provide both high-precision space and time information. add references here for testbeam results on SENSORS.

FEE: ASICs will be readout using LPGBT in-place of FPGAs due to the high-radiation environment in which these detector will be located. Up to sixteen AC-LGAD + ASIC modules will be connected to a single LPGBT, which will be coupled to a VTRX+ to convert the signals to a fiber to send off to the DAW system. The stave design is aimed to have the minimal amount of components inside the vacuum to ensure smooth operations and ease of access during maintanence periods.

Other components: Design of the front-end board and power distribution is still in a very early stage for the RP and OMD systems.

Performance The performance of the Roman pots and Off-Momentum Detectors is summarized in Fig. 8.156. The overall momentum resolution is also affected by the detailed understanding of the hadron magnet lattice, which is used to be able extract the normal transfer matrices used to reconstruct momenta in Roman pots detectors. There is also a software solution in place using deep neutral networks to further improve the momentum resolution performance, especially for the off-momentum detectors.

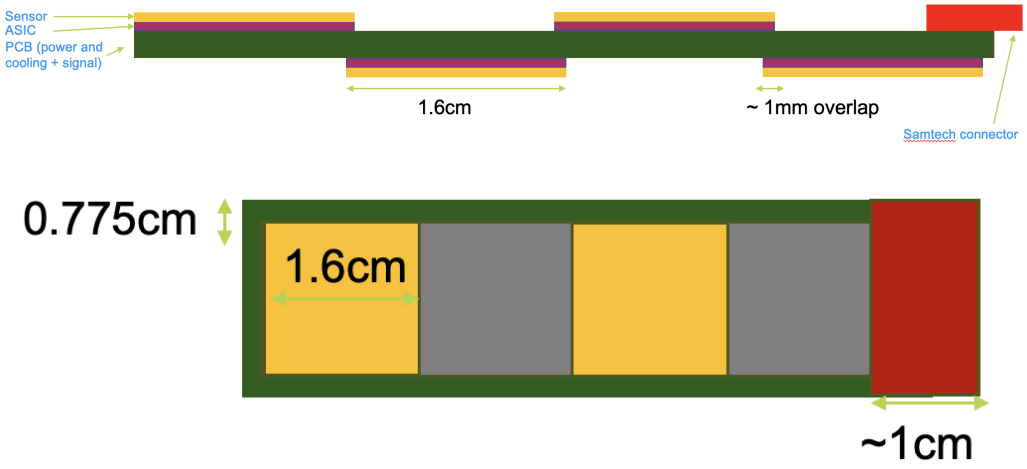

Figure 8.157: Strawman concept for the layout of the RP and OMD sensor staves. A 1x3 configuration is also being consider to reduce the size of the necessary Samtech connector for the staves, but more study is needed to assess impact of either choice, both in terms of construction feasibility and performance.

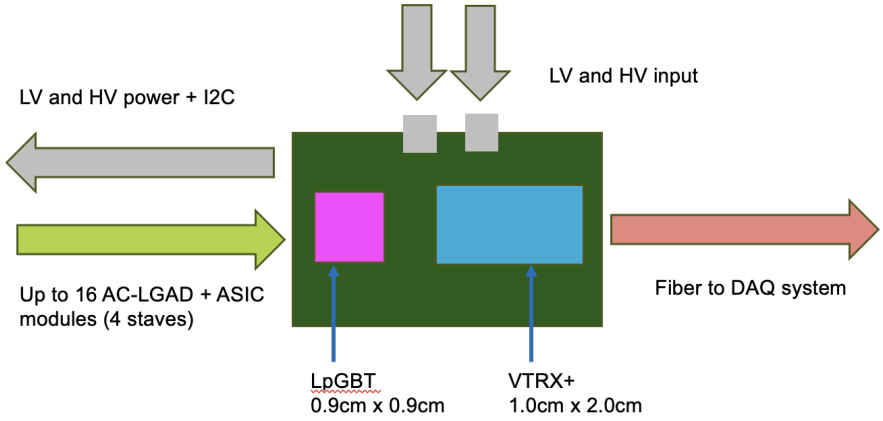

Figure 8.158: Strawman concept a readout board concept to communicate with and readout RP and OMD sensor staves. Work needs to be done to solve the issue of power distribution, and to ensure the EICROC ASIC can indeed be readout by the LpGBT.

Implementation The basic detector component will be a "stave" which contains 3-4 "modules" comprised of bump-bonded AC-LGADs and ASICs attached a PCB, arranged in a 1x4 or 1x3 layout with modules on either side of the PCB to enable partial transverse overlap of the sensors to cover the dead area at the edges (e.g. guard ring location). The staves are proposed to only contain the sensors and ASICs, plus cooling services, with all other services coming from a readout board place outside the vacuum which contains the LpGBT and VTRX+ components and power distribution. The details of the this concept still need to be properly worked out with engineering support, but strawman versions of these concepts can be found in Figs. 8.157 and 8.158.

Services: The Roman pots and OMD have the same essential needs for services, which include cooling using conductive strips coupled to an external chiller to allow cooling in-vacuum, low voltage (∼3V) and high voltage (∼150V) supplies for the operation of the ASICs and the HV bias supply for the sensor, and slow controls to control both voltages and the DAQ system, and also to control the moving stages necessary for the detector operations. There will also need to be communication between the slow controls and the machine for safety interlocks for fast beam abort systems, and for permits to enable motion control of the detectors when beam conditions are stabilized.

Subsystem mechanics and integration: The primary support systems only need to be able to support very light staves with 3-4 modules per PCB. However, the entire subsystem needs to be a on motor-driven rail system to enable movement near the hadron beam, especially in order to achieve acceptance at very-low $p_T \sim 0.2$ GeV/c.

Calibration, alignment and monitoring: AC-LGAD sensors will be calibrated with MIPs, while alignment of the detector systems will need to be carried out using beam-based alignment with dedicated, short, very-low luminosity runs, which enable the detectors to approach the beam much closer than the standard 10σ distance such that the beam halo itself can be seen on the sensor planes. This, combined with conventional survey information used to align the motion system to the machine should enable alignment at a level much less than 1mm.

Status and remaining design effort:

R&D effort: Much work is still needed to demonstrate full system operations with full size sensors + ASICs, and the cooling concept using conductive strips. As of now, only 4x4 channel versions have been tested.

E&D status and outlook: Engineering design is still very preliminary, but necessary design choices are being evaluated as engineering support becomes available.

Other activity needed for the design completion: The design of the front-end PCB which carries the sensors, ASICs, and necessary services needs to be carried out. Presently, only a strawman concept which will meet our requirements exists.

Status of maturity of the subsystem: The design maturity of the system will be at $\sim$ 60% by Q2 of FY25.

Environmental, Safety and Health (ES&H) aspects and Quality Assessment (QA) planning: Since these detectors are embedded directly into the machine vacuum, special considerations must be made for integration with the machine. We expect that the detectors will be interlocked against operation until permits are received from the machine, pending stable operations of the machine in terms of stable beam losses, collisions at the IP, and background conditions. The cooling system will also have to be integrated with the machine envelope and likely must pass an evaluation from the machine group.

Construction and assembly planning: Sensors and EICROC ASICs will be manufactured in different foundries, but bump-bonding of the sensors + ASICs can be done for the far-forward at BNL, since these detector subsystems are very small compared to other ePIC sub-systems. The assembly will have to take place in stages which include the following steps. First, preparation of

stave printed circuit boards and quality assurance testing to ensure traces pass continuity tests to the Samtech connectors will have to be carried out. In parallel, diced sensors need to be tested to ensure they can maintain bias voltage safely, and other electrical tests. ASICs will undergo similar tests to ensure they are ready for bonding into full modules. Once sensors and ASICs are prepped, modules of 32x32 channel size (one sensor, one ASIC) will be bump-bonded. Once sensors are bump-bonded, QA will need to be performed on the final modules before they are integrated into stave PCBs.

Collaborators and their role, resources and workforce: BNL and JLAB will take the primary role in constructing the Roman pots and Off-Momentum Detectors, with engineering support for cooling possibly supplied by IJCLab in France.

Risks and mitigation strategy: The primary risks to the successful construction of the Roman pots and OMD are late receipt of the final 32x32 channel EICROC ASICs and issues with the bump-bonding and construction of the final staves. There are additional risks related to machine integration.

Additional Material Will add sufficient reference to support documents as they are compiled.

8.3.7.3 The zero degree calorimeter

Requirements

Requirements from physics: The Zero-Degree Calorimeter (ZDC) plays an important role in many physics topics. The production of exclusive vector mesons in diffraction processes from electron-nucleus collisions is one of the important measurements. For the coherent processes, where the nucleus remains intact, the momentum transfer (t) dependent cross section can be related to the transverse spatial distribution of gluons in the nucleus, which is sensitive to gluon saturation. In this case, however, the coherence of the reaction needs to be determined precisely. Incoherent events can be isolated by identifying the break-up of the excited nucleus. The evaporated neutrons produced from the break-up in the diffraction process can be used in about 90% of the cases to separate coherent processes. In addition, photons from the de-excitation of the excited nuclei can help identify incoherent processes even in the absence of evaporated neutrons. Therefore, to identify coherent events over a wide t range, neutrons and photons must be accurately measured near zero degrees.
The geometry of the collision is important to understand the characteristics of each event in electron-nucleus collisions. It has been proposed that collision geometry can be studied by tagging it with the multiplicity of forward neutrons emitted near zero degrees. Determining the geometry of the collision, such as the "travel length" of the struck partons in the nucleus, which correlates with the impact parameters of the collision, is very useful in the study of nuclear matter effects. Determining the geometry of the collision will allow us to understand the nuclear structure with greater accuracy.

Requirements from Radiation Hardness: In the ePIC radiation doses and particle fluences, the ZDC neutron fluence is smaller than 10^{12} neutron/cm^2 for 6 month operation. It is not demanding, but degradation may occur for crystals and/or photon sensors due to radiation

Requirements from Data Rates: The dynamic range of the crystal calorimeter is a clear challenge. ∼100 MeV photons from e+A "quasi-coherent" reactions and ∼10-100 GeV photons possible from other exclusive processes (Λ decay, u-channel DVCS) should be covered.

Justification

Device concept and technological choice: Add text here.

Subsystem description:

Crystal calorimeter

General device description: The first section of the ZDC is designed with a layer of crystal calorimeter towers, each with 8 radiation lengths (X_0) thick. This layer is composed of 2×2 cm^2 crystals arranged in a 30×30 grid. LYSO is chosen as the crystal material for its high light yield and suitability for measuring low energy photons.

Sensors: The gain of SiPMs is on the order of 10^5 with an operational bias of 25–30 V, while for APDs (avalanche photodiodes), the gain ranges from 1 to 50. Given the high light yield of LYSO crystals, APDs are a more suitable choice to avoid signal saturation. However, an operational bias of 150-200 V is required. If SiPMs are selected as the photodetector, a filter would need to be installed between the crystals and photodetectors to reduce the light yield and prevent saturation.

FEE: Under consideration.

Other components: Under consideration.

Hadron calorimeter General device description: Add text here.

Sensors: Add text here.

FEE: Add text here.

Other components: Add text here.

Performance The first test beam experiment for crystal calorimeter prototype was performed in February 2024 using 50 to 800 MeV positron test beam at the ELPH facility (now the RARiS facility) in Tohoku University in Japan and its data analysis is underway. The prototype modules have been made by the Taiwan group. Two simulation calculations and evaluations are ongoing; Λ identification and low energy photon identification. Angular resolution is a common thread. It has been less emphasized early on, but absolute requirements for successful exclusive physics program should be given.

Implementation The ZDC implementation will benefit from a creative approach; for example, non-static configurations which can adapt to different running conditions. The crystal-calorimeter needs depend on physics channel. Some level of conflict in the final states and associated requirements. Having the ability to bring the crystal calorimeter in and out of configuration as needed, would provide clear benefit to specific physics needs.

Services: Add text here.

Subsystem mechanics and integration: Each LYSO crystal will be wrapped in ESR, a high-reflectivity foil. Each crystal tower, composed of a 5×5 array of crystals, will be either wrapped in aluminum foil or placed into an aluminum support structure to ensure stability. In total, there will be 36 towers. An additional thin aluminum support structure will be added around the crystal calorimeter for extra reinforcement.

The assembled crystal calorimeter will be housed in an aluminum container, which will be securely mounted to the table in the ZDC area using screws. This design allows for easy removal of the crystal calorimeter when necessary.

Calibration, alignment and monitoring: Precision cooling for the crystals and power cooling for the electronic readout will be achieved using water-cooling circuits. The cooling needs for individual crystals will be addressed through a thermal conduit extending from the crystal's rear face, through metal inserts, to the interface plate and support elements. A front thermal screen will also be installed to maintain the crystals at a controlled temperature.

The crystals will undergo pre-calibration using beam test facilities. In-situ calibration with physics events will be conducted using the process $\pi^0 \to \gamma\gamma$.

A light monitoring system will be implemented to continuously measure the relative light transmission and the full photodetector gains across all channels. Light pulses will be injected into each crystal to assess the optical transmission near the scintillation spectrum peak of LYSO crystals.

Status and remaining design effort:

R&D effort: Add text here.

E&D status and outlook: Add text here.

Other activity needed for the design completion: Add text here.

Status of maturity of the subsystem: Add text here.

Environmental, Safety and Health (ES&H) aspects and Quality Assessment (QA planning): The quality assurance for each crystal and the assembly of each crystal tower will be conducted in Taiwan. Each tower will undergo pre-calibration using beam test facilities before being assembled into the final detector in Japan, after which it will be shipped to BNL for in-situ installation.

Construction and assembly planning: Add text here.

Collaborators and their role, resources and workforce: Academia Sinica and National Central University in Taiwan will contribute to the R&D, assembly, beam tests, and operation of the ZDC crystal calorimeter. The Taiwan team will collaborate with a crystal producer in Taiwan for LYSO crystals and develop electronic readout circuits and mechanical support. Currently, the Taiwan team consists of three faculty members, five postdoctoral researchers, and three students.

Risks and mitigation strategy: Add text here.

Additional Material Add text here.

8.3.8 Far backward detectors

The luminosity system at the Electron-Ion Collider plays a critical role in achieving high-precision measurements in nuclear physics experiments. By determining, monitoring and optimizing the number of particle collisions, the luminosity system ensures that the collider operates at peak performance, enabling detailed exploration of the structure of matter. When electrons collide with protons or nuclei, Bremsstrahlung (BH) photons are generated, with a well know cross section []. This process thus provides us with the mean to indirectly determine the luminosity by accurate and precise determination of the Bremsstrahlung photons generated in the interaction region of the collider.

Accurately determining luminosity is essential for addressing the fundamental physics questions that underpin the construction of the Electron-Ion Collider. The Yellow Report specifies the EIC requirements for luminosity determination to be 1% in absolute uncertainty and 10^{-4} in relative luminosity [**?**]. This requirement will be fulfilled by two complementary detectors in the luminosity monitoring system: the Pair Spectrometer (PS) and the Direct Photon Detector (DPD). It was demonstrated at HERA – the first electron-hadron collider – that the bremsstrahlung process can be successfully used to precisely measure the luminosity of high-energy ep collisions (ZEUS achieved an absolute uncertainty of 1.7% [**?**, **?**]). The luminosity monitors designed for the EIC utilise the same approach with implementation that mitigates large systematic uncertainties.

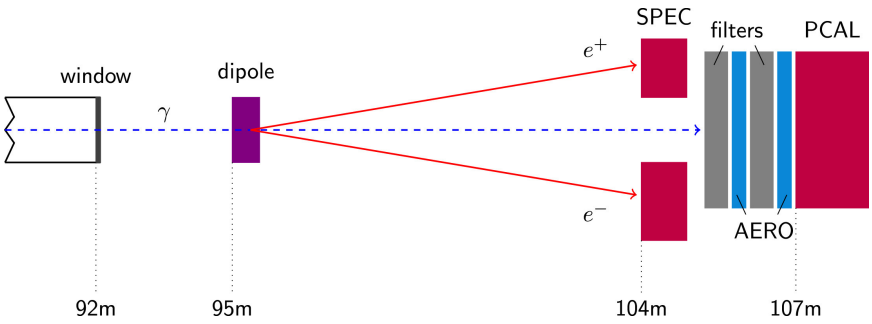

Figure 8.159: The layout of the luminosity monitor in the ZEUS experiment [**?**].

The two subsystems, Pair Spectrometer, and Direct Photon Detector, are sensitive to different systematic effects; on one hand the Direct Photon detector is placed downstream the photon beam with full acceptance, but within the synchrontron radiation fan and needs to be shielded. In addition, at nominal luminosities planned for the EIC several photons will hit the DPD in each bunch crossing. Thus the counting of bremsstrahlung photons is done through the total energy determination deposited in DPD and is associated with systematic uncertainties related to gain stability. On the other hand, the PS is outside the synchrontron radiation fan and overall rates can be controlled with a dedicated converter. The luminosity determination from the PS is sensitive to systematic effects related with the acceptance determination.

The PS and DPD detectors in the ZEUS luminosity monitor are shown in figure (8.159). The PS system consists of an analysing dipole magnet and two electromagnetic calorimeters, while the DPD system includes absorbing plates and an electromagnetic calorimeter. BH photons generated in the interaction region exit the vacuum chamber through a thick exit window. About 10% of these photons (depending on the window's thickness) undergo pair conversion into electron-positron

pairs, which are then detected by the PS calorimeters. The remaining unconverted photons are detected by the downstream DPD. Additionally, the luminosity monitor includes a collimator positioned just after the exit window to produce a uniform, narrow cone of photons and pair-converted particles. This simple steel block also protects the PS system components from direct synchrotron radiation (SR), BH radiation, and unwanted stray particles.

The PS was needed at ZEUS due to challenges introduced by upgrades to the HERA accelerator, which significantly increased luminosity and, consequently, the rate of BH events [**?**]. The stronger beam focusing and increased synchrotron radiation (SR) — radiation resulting from the bending of electrons by the magnet—led to a higher pile-up of photons in the DPD, increasing the uncertainty in luminosity measurements from 1% to 3% [**?**]. The PS, positioned outside the SR fan and unconverted photon flux, experienced a lower pile-up due to fractional pair conversion. This introduction reduced the uncertainties in rate measurement to 2% [**?**], and additionally both detectors were utilized to monitor real-time detector inefficiencies and manage systematic uncertainties.

8.3.8.1 The luminosity system

This ZEUS luminosity monitor design serves as a baseline for EIC but the expected luminosity at EIC will be about 10^2 to 10^3 times that of ZEUS [**?**]. This directly leads to several challenges faced during the upgrade of HERA, such as beam size effects (BSE), increased SR backgrounds, and higher pile-up from BH radiation, becoming much more pronounced at the EIC. In addition to these, the EIC will also feature electron beams colliding with a diverse range of hadron species, from protons to heavy nuclei like gold, lead, and uranium. This in turn dramatically increases the BH rates by a factor of Z^2, making pile-up at detectors even more difficult to manage. Furthermore, both the electron and light hadron beams will be polarized, adding another layer of complexity. In the following section, we will discuss these challenges in more detail and outline how the "upgraded" luminosity monitor of EIC will overcome them.

Beam Size Effect - The BH process in electron-proton collisions is notable for its extremely small momentum transfers between the radiating electron and the proton. It is kinetically possible for both particles to continue along their initial paths without angular scattering, while the BH photon is emitted in the direction of the electron's momentum. This specific configuration results in the smallest virtuality (Q^2_{min}) of the exchanged photon [**?**]. At high-energy colliders, this minimal photon virtuality becomes incredibly small. For instance, at HERA, the Q^2_{min} for a photon energy of 1 GeV can be as low as 10^{-8} eV^2. Consequently, the typical transverse momentum transfer ($q_\perp$) reaches values around 10^{-4} eV/c. Since the BH differential cross section is proportional to Q^{-4}, photon virtualities near Q^2_{min} dominates the process and allows for the approximation,

$$Q^2 = Q^2_{\text{min}} + q^2_\perp$$

and not to forget the scenarios with $q_\perp = 0$ is also feasible. Analyzing the process in impact parameter space reveals that these small $q_\perp$ values correlate to large impact parameters ($b = \hbar/q_\perp$), explaining the precision of Bethe-Heitler cross-section calculations in the Born approximation.

The derivation of the two-particle rate (R) relation with the collision luminosity (L) and cross-section (σ)

$$R = L\sigma \tag{8.1}$$

assumes both beams to be modeled as simple plane waves with a uniform impact parameter distribution. However, this assumption falls short when beams are strongly focused at the interaction point, as focusing suppresses large impact parameters. Consequently, the BH differential cross section is predominantly "over-sampled" at low impact parameters where the cross-section value is smaller. This results in an effective suppression of BH. This is particularly pronounced at lower photon energies, since typical $q_\perp$ is proportional to E_γ.

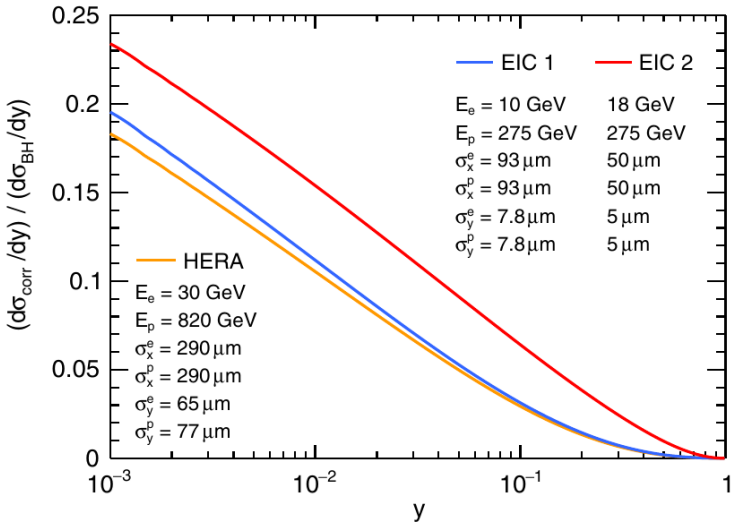

Figure 8.160: Relative suppression due to the BSE $(d\sigma_{corr}/dy)/(d\sigma_{BH}/dy)$ is shown as a function of $y = E_\gamma/E_e$ for three cases of collider parameters, HERA, EIC 1 & EIC 2. The corresponding beam energies and Gaussian lateral beam sizes at the interaction point are listed [**?**].

Relative corrections to the standard Bethe-Heitler cross-sections due to the BSE is shown in figure (8.160). Here the observed suppressed BH cross-section is related to the Bethe-Heitler cross-section as $(d\sigma_{obs}/dy) = (d\sigma_{BH}/dy) - (d\sigma_{corr}/dy)$. It is worth noting that even after higher beam energies at HERA, the BSE will be higher at EIC due to a stronger focused beam as evident from beam size parameters. In a recent study, the BSE is proposed to be corrected by a precise measurement of the BH spectra as a function of lateral beam displacements (indirectly the impact parameter) at the interaction point. This will be achieved using Van der Meer scans, commonly performed at hadron colliders. This involves systematically varying the beam positions and crossing angles to find the L as a function of lateral beam displacement, which can be described by the formula

$$L(B) = L(0)\exp\left(-\frac{B}{2(\sigma_1^2+\sigma_2^2)}\right)$$

Here, B represents the lateral displacement of one of the beams within either the horizontal or vertical plane, σ_1 and σ_2 are the two Gaussian widths in a given plane, often assumed to be equal, and $L(0)$ corresponds to the luminosity of nominal, head-on collisions. However, in the case of BH, its photon spectrum will also be modified in a very specific manner, reflecting the BSE.

High rate of BH radiation and SR background - The bunch crossing rate at EIC will be set to 100 MHz for 5 and 10 GeV electron beam and 25 MHz for 18 GeV electron beams [**?**]. When this rate is multiplied by the BH photon production rate per bunch crossing, as illustrated in Figure (8.161), the resulting photon rates reaching the detectors looks substantial. For instance, with a 5 GeV electron beam and a 41 GeV proton beam, the coincidence rate (the rate when both the pair converted pairs are detected simultaneously) at the Photon Spectrometer (PS) can reach approximately 90,000 photons per second. The BH photon rates during electron-nuclei interactions will be proportional to the square of nucleus's atomic number. Therefore for the same setup but 41 GeV Gold nuclei beams will result coincidence rate equivalent to $79^2 \times 90000 = 56 \times 10^7$ photons per second.

SR, similar to BH radiation, is emitted at very small angles ($\sim m_e/E_e$) relative to the instantaneous direction of an electron beam's motion. At the EIC, the electron beam exiting the interaction region passes through two quadrupole magnets, Q1eR and Q2eR, followed by a dipole magnet, B2eR. The electron beam passes through the center of the quadrapoles and consequently, the B2eR magnet is the sole source of direct SR impacting the far-backward region. [Calculation of SR rates at EIC? Comment quantitatively on how much sweeper helps in subsequent paragraph.]

To address the issue of high photon flux and its associated pile-up, as well as to mitigate the high SR background, the luminosity monitoring system has been redesigned to include two new components: a sweeper magnet and a thin converting foil, both positioned between the EW and the spectrometer magnet, as illustrated in Figure (8.162). The enormous BH radiation and SR pass through the exit window, resulting in substantial pair conversions. These converted particles are deflected by the Sweeper magnet, leading to a reduced photon flux, with a large percentage being BH photons. These photons then encounter a thin converter made of the same material as the exit window. This setup results in fewer pair conversions reaching the PS and an overall reduced photon flux to the DPD.

For electron beams at 10 and 18 GeV, the SR flux is substantial, with power reaching the exit window potentially exceeding 4 kW. To mitigate this, it was proposed to divide the dipole magnet into two segments. The first segment, relevant to luminosity detectors, has a magnetic field about four times weaker than that of B2eR. This modification is crucial to minimize the direct SR flux, which is vital for accurate luminosity measurements, as it influences both PS and DPD readings [**?**].

Beam Polarisation - The electron and light ion beams at the EIC will be polarized both longitudinally and transversely. A recent study investigated the impact of longitudinal beam polarization on the Bremsstrahlung cross-section in the low-q^2 region [**?**]. Numerical calculations revealed that the polarized component is significantly suppressed compared to the unpolarized component, by a factor of m_e^2/E_eE_p. Figure (8.163) illustrates the unpolarized component first calculated by Bethe-Heitler, alongside the polarized component. However, no calculation exists for transversely polarised beams and also with the effect of nuclear recoil.

Physical Constraints - The components of the luminosity monitoring system are placed within the beam tunnels and are therefore constrained by the beam pipes and the equipment required to maintain the beam, such as magnets and cooling systems. The majority of the system is located sixty meters back from the interaction region to provide sufficient space for the magnets and detectors to operate without interfering with the beam. The long air column between the exit window and the PS calorimeters is approximately 46 meters. The "unconverted" photon beam from the exit window undergoes pair conversions, which are quite significant (approximately 10%) and indeterminate during experimentation due to variability in air composition. Most of the unwanted

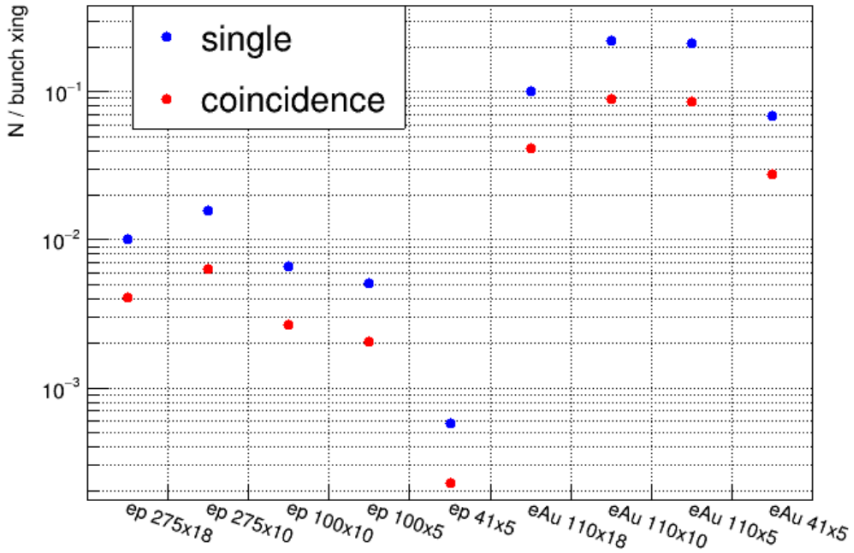

Figure 8.161: Rate of single and coincidence events for the PS detectors calculated by Dr. Gangadharan

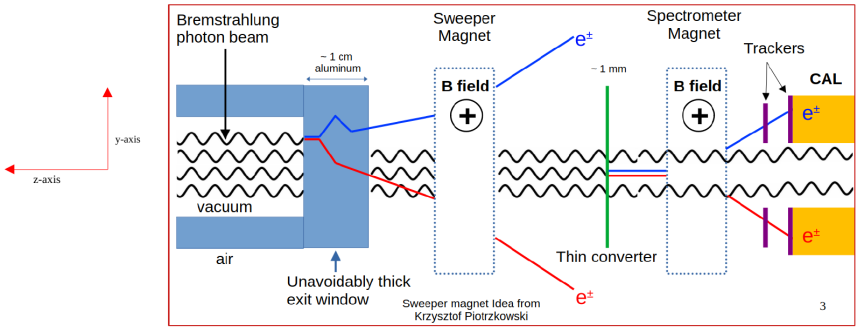

Figure 8.162: The layout of the luminosity monitor in the ePIC experiment of the EIC.

pair conversions occur between the exit window and the sweeper magnet and are swept away by the sweeper. To reduce pair conversions in the air column between the sweeper magnet and the spectrometer magnet, a helium or partial vacuum chamber will be installed between the magnets. The thin converter will remain at the same location but will be placed inside this vacuum chamber.

Add paragraph outlining requirements on magnets imposed by physical space limitations.

Systematic Uncertainties - The systematic uncertainty in the luminosity measurement at ZEUS was 1.7 %, and our goal is to reduce this value to below 1 %. Table 8.42 summarises the main systematic uncertainties that contributed to the ZEUS luminosity determination. In our current design, we ensure we mitigate the largest of these sources with the introduction of trackers for the PS, that would enable an accurate determination of the detector acceptance and beam size effects, and a sweeper magnet that allows us to have more control on the converted pair rates in the PS.

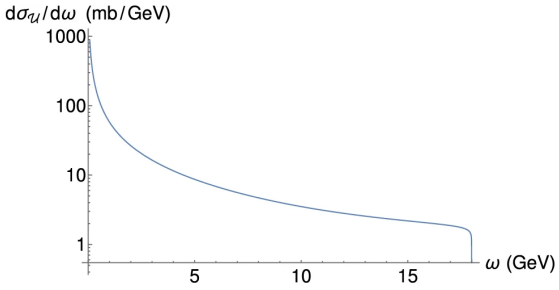

(a) Unpolarised Part

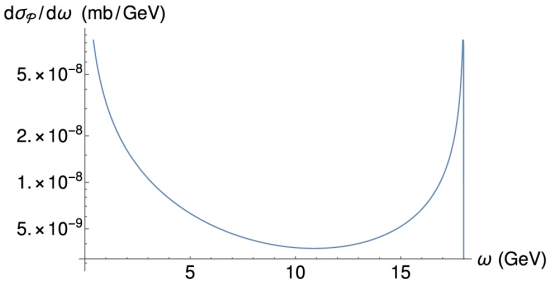

(b) Polarised Part

Figure 8.163: Unpolarised and polarised Bethe-Heitler Cross-Section. [**?**]

Source	DPD detector (%)	PS detector (%)
Acceptance	1.0	1.0
x-position of photon beam	1.2	1.2
Pair conversion in EW		0.7
RMS Cut Correction		0.5
Pedestal Shifts	1.5	
Pile up	0.5	
Total	2.2	1.8

Table 8.42: Summary of systematic uncertainties at ZEUS DPD and PS detector. [**?**]

Design and Components A two-level review of all the components of luminosity monitor is presented below. First, a short review on the component's material, location & dimension, and a longer version with detailed description of each component requirement, design with simulation or test-beam results. Note that all length measurements are in centimeters unless otherwise mentioned.

- Exit Window
  - Material - Aluminum
  - Location - (0.0, 0.0, - 1850.5)
  - Dimension - (4.0, 4.0, 1.0)
- Collimator

- Material - Stainless Steel
- Location - (0.0, 0.0, - 2260.0)
- Hollow Structure, Outer Dimension - (6.5, 6.5, 30.0), Inner Dimension - (4.832, 4.832, 30.0)

- Sweeper Magnet
  - 0.5 T horizontal magnetic field.
  - Location - (0.0, 0.0, - 5600.0)
  - Main Body Structure, Outer Dimension (75.972, 94.0, 120.0), Inner Dimension - (42.032, 61.262, 120.0)
  - Magnetic Coils Structure (How to describe ?)
- Photon Vacuum Chamber
  - Material - Pipe : Aluminum & End caps : Beryllium
  - Location - (0.0, 0.0, - 5800.0)
  - Pipe Structure, Outer Dimension (6.3119, 2π rad, 555.0), Inner Dimension (6.119, 2π rad, 555.0)
- Converter Foil
  - Material - Aluminum
  - Location - (0.0, 0.0, - 5800.0)
  - Disk Dimension - (6.119, 2π, 0.1)
- Spectrometer Magnet
  - Location - (0.0, 0.0, - 6000.0)
  - Main Body Structure, Outer Dimension (75.972, 94.0, 120.0), Inner Dimension - (42.032, 61.262, 120.0)
  - Magnetic Coils Structure (How to describe ?)
- PS Trackers
  - Type - AC-LGAD
  - Locations
    - Module 1 : Top (0.0, 15.76, - 6397.6) and Bottom (0.0, - 15.76, - 6397.6)
    - Module 2 : Top (0.0, 15.76, - 6407.6) and Bottom (0.0, - 15.76, - 6407.6)
  - Dimension - (18.06, 18.06, 0.044)
- PS Calorimeters
  - Type - Electromagnetic sampling (spaghetti) calorimeter
  - Material - Active : Scintillating Fiber (ScFi) and Passive : Tungsten (W)
    - Tungsten as powder, held together with optical epoxy.
  - Location - Top (0.0, 15.76, -6408.6) and Bottom (0.0, - 15.76, - 6408.6)
  - Dimension - (18.06, 18.06, 17.2)
- DPD Calorimeters

Exit window

- Needs exact study of its composition and irradiation studies.

Collimator

- Do we need any further study ?

Sweeper and Spectrometer magnet

- Mapping the magnetic field. Need info from magnet experts

Photon Vacuum Chamber

- need info from accelerator

The thickness of the exit window for electrons and positrons must be minimized to reduce material interactions. However, if a vacuum chamber is selected instead of helium filled, a minimum thickness of the exit widnow is required to withstand a pressure difference of 1 atm. The minimum thickness of beryllium should exceed 3 mm to ensure structural integrity under these conditions.

- Mapping the Pressure
- Study of exact composition and thickness of two end caps.

Converter Foil The converter foil is expected to operate in a vacuum, necessitating heat removal due to synchrotron radiation (SR). Heat removal from the converter can be achieved through the holder, utilizing one of two options: passive cooling or circulation of a coolant.

- Study of exact composition, thickness and radiation dose.
- Study of pair conversion percentage.
- How this will reduce the error in position resolution.
- Heat removal due to SR radiation.

PS Trackers

- PS trackers are required to reconstruct the vertex position at the conversion foil, which has a direct impact on determining acceptance. A vertex resolution of less than 6 mm is necessary to achieve an acceptance determination uncertainty of less than 1%.
- This has not been studied yet; however, since the PS system is located away from the IP and positioned behind collimators and magnets, and not within the BH cone, the radiation levels are expected to be manageable.
- AC-LGADs are chosen for their excellent position and timing performance. Due to the relatively small detection area and the fact that this technology is planned for FTOF, PS trackers will utilize a similar design.

- Initial studies with the nominal 500 μm pitch are expected to provide a 2 mm resolution at the vertex (conversion foil).

The tracking layers for the PS system are based on AC-LGAD technology with pixelated sensors. Each side will consist of two tracking layers, resulting in a total of four layers. AC-LGAD sensors will be placed on modules similar to the FTOF design. The pitch between the readout pads, set at 500 μm, is expected to provide approximately 70 μm position resolution at the detector plane and around 2 mm at the vertex (conversion foil). Current estimations indicate that, in order to achieve acceptance uncertainties below 1%, the vertex resolution in the dispersive direction must be less than 6 mm. With a 500 μm pitch, the number of readout channels is estimated to be about 130,000 per plane. To minimize the number of DAQ channels, the number of pixels in the non-dispersive direction could be combined.

PS Calorimeters The two electromagnetic calorimeters (CALs) used for the PS are of the sampling type, colloquially known as spaghetti CALs. The active component of the CAL consists of plastic scintillating fibers (ScFi), while the passive, or "hard," component is tungsten (W). The volumetric ratio of W to ScFi in each CAL is 4:1. The CALs are composed of 20 layers, with the fibers in alternate layers oriented parallel to either the x-direction or y-direction in the transverse plane. This alternating orientation in 10 layers along each direction aids in reconstructing the shower profile of hits, thereby enhancing the position resolution of hits. Each layer has a thickness of 0.86 cm and a transverse size of 18.06 × 18.06 cm^2. Additionally, the layers are segmented into three modules, each with a width of 6.02 cm. Each module contains well-distributed 448 ($14 \times 2 \times 16$) fibers. Finally, a group of 16 fibers forms a single channel for readout. Each readout will be associated with a silicon photo-multiplier (SIPM).

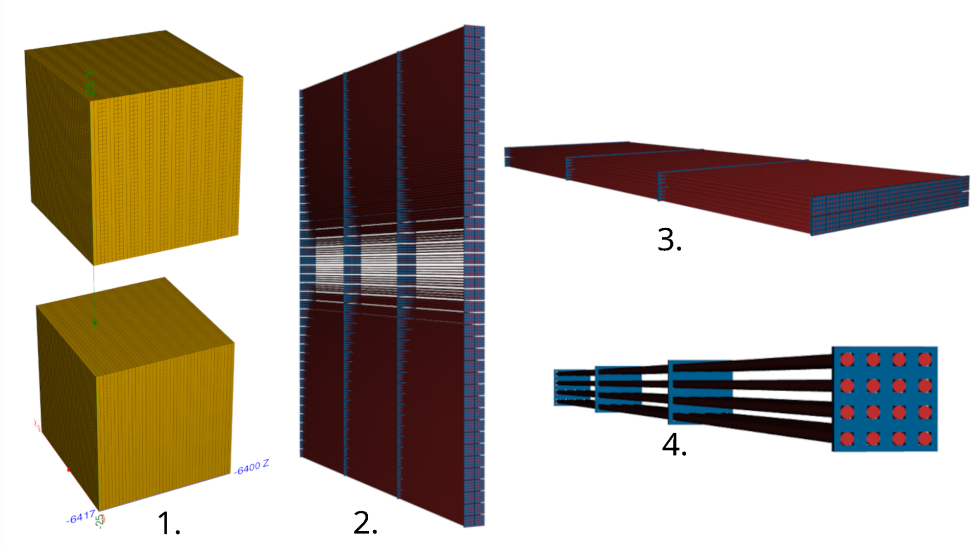

Figure 8.164: DD4hep implementation of PS Calorimeters.

The two PS CALs are symmetrically positioned in the vertical plane, perpendicular to the photon flux i.e., along the y-axis. The gap between the two CALs is approximately 3σ, which is sufficient for the detectors to not obstruct the final photon flux from reaching the DPD. The PS CALs serve the purpose of measuring the energy and the transverse coordinates of the pair-converted photons, which enables the reconstruction of the photon energy spectrum and thus the determination of the

beam luminosity.

The acceptance of PS system is effected by four major parts of the PS system.

- The collimator which obstructs some part of BH photons.
- The sweeper magnet which removes the pair-conversions from EW.
- The front end cap of the vacuum chamber whose pair-conversions are not detected in CALs.
- The fiducial areas of the CALs whose signals are rejected.

Plot the acceptance curve.

DPD

Collaborators and their role, resources and workforce: The main collaborating institutions for the PS calorimeter are York and Houston. The roles of each institution are outlined below -

- University of York, United Kingdom
  - Design and construction of calorimeters
  - Calorimeter simulation
  - Calorimeter reconstruction and analysis
  - DAQ and electronics for calorimeter
- University of Houston, Texas, USA
  - Calorimeter simulation
  - Calorimeter reconstruction software
  - Calorimeter design support
- Tel Aviv University, Israel
  - Design and integration of PS trackers.
  - Simulation.

The workforce at each institution is comprised of -

- University of York, United Kingdom
  1. Dan Watts, academic staff (20-25 % FTE)
  2. Nick Zachariou, academic staff (25-30% FTE)
  3. Mikhail Bashkanov, academic staff (10-15% FTE)
  4. Stephen Kay, PDRA (100% FTE)
  5. Alex Smith, PG Student (100% FTE)
  6. Pankaj Joshi, academic support staff (5% FTE)
  7. Julien Bordes, Geant4/simulation support (10-15% FTE)

8. Technical Support Staff
   - Electrical engineering
   - Mechanical engineering
   - CAD support

- University of Houston, Texas, USA
  1. Dhevan Gangadharan, academic staff (X% FTE)
  2. Aranya Giri, PG Student (100% FTE)
- Tel Aviv University, Israel
  1. Igor Korover, academic staff (15% FTE)
  2. Avishay Mizrahi, Mechanical engineer (50% FTE).

Note that where an FTE range is presented, this represents a min/max value.

Risks and mitigation strategy: Add text here.

Additional Material Add text here.

8.3.8.2 The low Q^2 taggers

Requirements The Low-Q^2 Tagger is required to measure the momentum of low-angle scattered electrons. The Tagger sits close to the electron beamline and consists of two modules - each with silicon trackers and a calorimeter. This is shown in Figure 8.165.

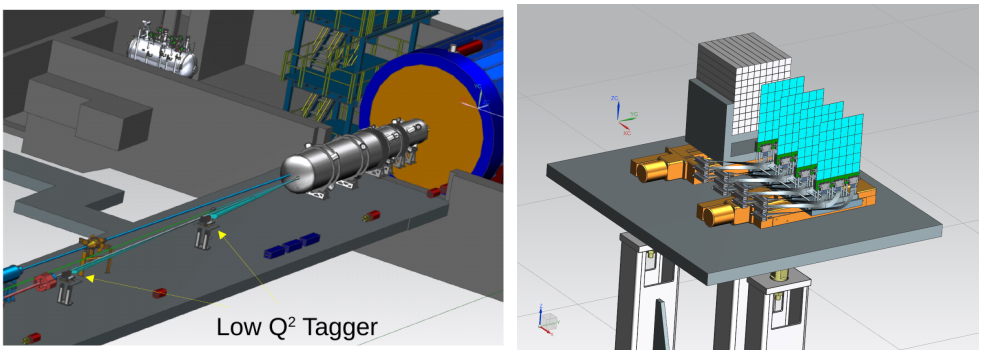

Figure 8.165: Left: Low-Q^2 taggers in relation to beamlines and central detector. Right: Tagger module with calorimeter and tracker from recent CAD model.

Requirements from physics: The acceptance for the low-Q^2 tagger should complement the central detector to reach the coverage close to the limits given by the divergence of the beam and beamline magnets. Low-Q^2 tagger will have one or more stations to cover the maximum momentum acceptance.

The Low-Q^2 tracking system shall have a spatial resolution providing a momentum resolution $<$ 5% with Q^2 acceptance between 0 and 0.1 GeV^2. The acceptance ranges of the Central Detector and Low-Q^2 Trackers as function of Q^2 and x are shown in Figure 8.166, and the positions and angular acceptances of the tracker are illustrated in Figure 8.167.

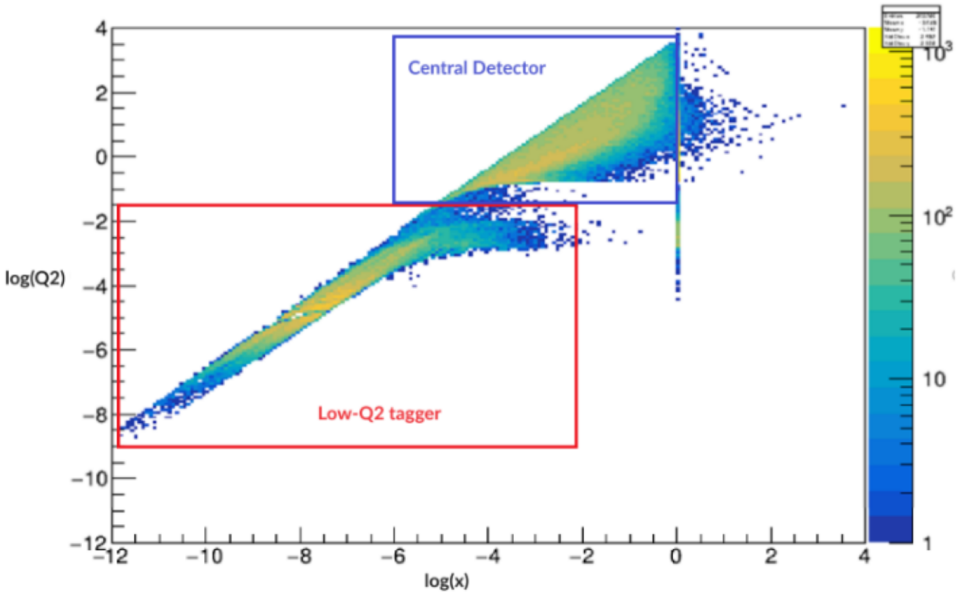

Figure 8.166: Acceptance ranges of the Central Detector and Low-Q^2 Trackers as function of Q^2 and x.

More on resolution here? Too much here on spectroscopy - maybe reduce and more from the ArXiv paper blurb. Or add other sections with other physics titles. I added two.

8.3.8.3 TCS

Add text

8.3.8.4 Vector Meson production

Add text

8.3.8.5 Spectroscopy

Reduce - only want to know how it influences the detector requirements. Electron-ion collisions, where the electron is scattered through a very shallow angle, correspond to the case where the exchanged photon is almost real. Such photoproduction processes are of interest in their own right, but also can enable a program of hadron spectroscopy. Furthermore, as the virtual photon flux is highest in this region, yields may be relatively high or rare states may be searched for.

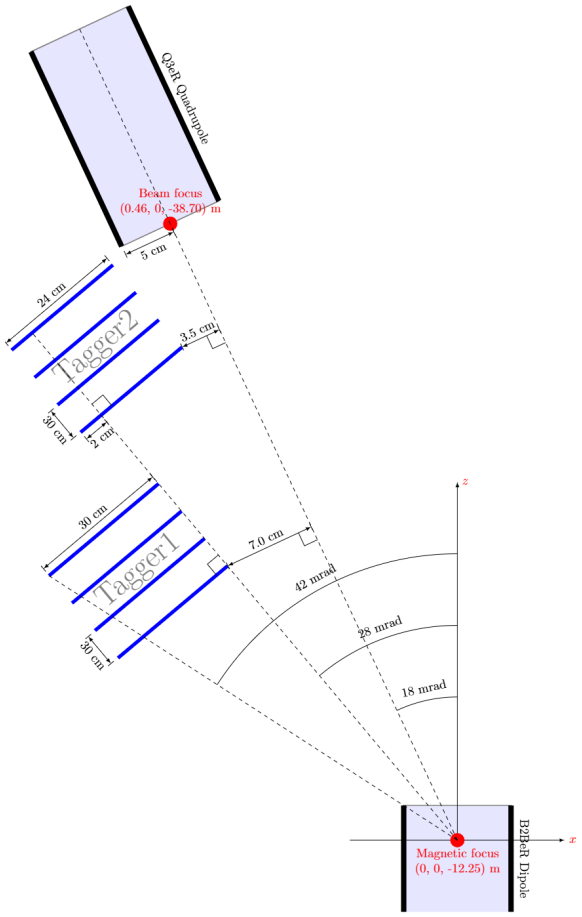

Figure 8.167: Low-Q^2 tagger coverage.

A topic of particular interest is the photoproduction of exotic charmonium-like mesonic states. Commonly refered to as XYZ spectroscopy, these states were originally seen in decays containing J/ψ mesons and additional products. Despite there being many missing charmonium states these states do not fit the quark model expectations in terms of numeracy, masses or widths. While the Z_c^+ states were manifestly exotic as their charge required additional constituent quarks to a $c\bar{c}$ pair.

The production cross section of these states is expected to be low, of order 1 nb and branching ratios to particles that can be detected can also be small. Therefore tagging a large fraction of the virtual photon flux is essential for making measurements of exclusive production of these states. The energy of the tagged photon can be used to determine the reaction invariant mass, W, and provide exclusivity discrimination when combined with the measured meson state from the central detector and hadron from the far-forward region.

Reconstruction of the azimuthal angle for the electron would provide an effective linearly polarised photon beam, with polarisations up to 1 when the tagger electron energy is close to the beam energy. Reconstructing this angle will be challenging and probably only possible with sufficiently high scattering angles. Provided this information alongside the virtual photon degree of polarisation, which will mainly depend on the measured energy, would allow additional constraints to be used in partial wave analysis of the meson decay allowing the production amplitudes to deter-

mined.

The Q^2 of the scattering is not directly of use for these reactions, however ultimately it can be used to reject bremsstrahlung electrons which would improve the analysis.

Count rate estimates were performed for a number of exotic states in [**?**] including branching ratio through to detected particles and using the models developed in [**?**] . To summarise for the charmonium-like XYZ states they are expected to be of the order 1000 per day at luminosities of $10^{34} cm^2 s^- 1$, while for double J/ψ or Z_b decays there may be 10s per day.

Given just providing evidence of the existence of these states in photoproduction would be a great result, as few of these states have been seen in more than one production mechanism, tagging efficiencies of 10% would be sufficient. However to perform detailed physics studies to determine quantum numbers and production amplitudes, which may provide insight into their exotic nature, or to measure rarer states such as the Z_b, large data samples would be required.

Requirements from Radiation Hardness:
The Low-Q^2 trackers are in the far backward region, where the incident flux is predominantly from bremsstrahlung electrons (MIPS). This means there is no requirement for a radiation hard classification for the trackers. However, the intensity is focused on a narrow band in the bend plane (see Figure 8.168), particularly close to the beam line, and trackers should be designed to *spread the load* by period vertical translation, and exchange of modules.

Requirements from Data Rates:
The Low-Q^2 system must operate at a full projected EIC luminosity.
The Low-Q^2 system must operate in extreme background conditions (synchrotron radiation, bremsstrahlung events and beam gas) at the levels specified by the simulation studies.
The Low-Q^2 trackers shall provide timing resolution sufficient to resolve 10 ns beam buckets.
The Low-Q^2 tagger will be able to measure the momentum of more than 10 electrons per bunch crossing.

The rate distributions, based on simulation, are illustrated in Figure 8.168. It is clear that the raw rates on the detectors are dominated by bremsstrahlung, with increasing intensity closer to the bend plane, and to the beam line. These results can be used to calculate the integrated data rates for DAQ and storage, and the bottom right plot can be used to estimate the maximum rate which the tracker must be able to handle, in terms of pixel, column, sensor and board. The rates are summarised in Figure 8.169.

Justification

Device concept and technological choice: As described above, the Low-Q^2 detector will consist of two separate taggers, each with a silicon tracker and a calorimeter. For the trackers, the positions and layer spacing are still to be optimised on the basis of simulations. The essential characteristics are angular resolution (since all other quantities are derived from polar and azimuthal angles), rate capability and background rejection. For pixel detectors, the angular resolutions relate to pixel size, or, more precisely, to the position resolution of the centroids of pixel clusters. From the simulations it is clear that 55 μm pixels (Timepix4 pixel size) would provide very good resolution.

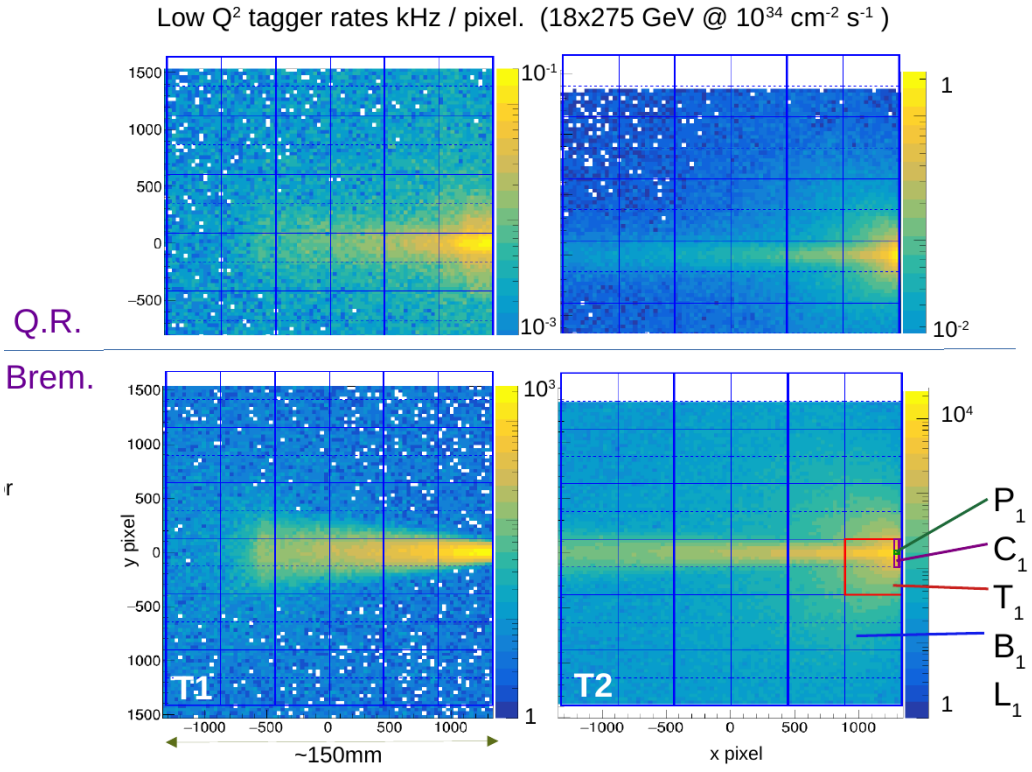

Figure 8.168: Hit rates on tracker layers for Quasi Real (Top) and bremsstrahlung (bottom) electrons, incident on Tagger 1 (left) and Tagger 2 (right), This design is based on layers with three carrier boards, each containing twelve Timepix4 hybrid sensors. The dashed lines indicated the centre lines of the Timepix4 ASICS, where the vertical columns terminate.

Bigger pixels would still provide acceptable resolution, but high segmentation is even more important for rate capability, where the efficiency for separating multiple tracks within a single event needs to be as high as possible: For an electron-proton collision event, at maximum lumonisity there are typically ten background bremsstrahlung electrons within the same beam bucket, each passing though all layers of a tagger and creating hits. Furthermore, in each layer there will be *singles* resulting from rescattering, or synchrotron radiation, together with hits from detector noise. However, we already have enough information to set some constraints on detector and readout technologies. We have used Timepix4 as the template for much of the development, and have had its dimensions, readout and rate capabilities as a strong influence in the development of the current design. However, where possible, we used *generic* pixel detectors - particularly in the Geant4 simulations, with the aim of being able to evaluate other current, or emerging, technologies.

It is already clear, both from a basic knowledge of the kinematics of bremsstrahlung and quasi-real events, and from preliminary simulations, that the intensity of electrons passing through the trackers will be distributed in a highly non-uniform way, with the bulk of the events close to the plane of the accelerator, and the flux increasing strongly towards the electron beamline. In particular, the rates on Tagger 2 are significantly higher than Tagger 1, with the hottest zone closest to the beamline (Figure 8.169). For an estimate of the relevant rates we focus on the bremsstrahlung distribution in Tagger 2 and superimpose a tracking layer geometry based on three boards, each consisting of 12 Timepix4 hybrids, as shown in Figure 8.168. The six Timepix4 detectors running

Maximum rates		
Pixel (P1)	70 kHz	
2 column (C1)	8 MHz	
Tpix4 (T1)	600 MHz	38 Gb/s
Board (B1)	1500 MHz	96 Gb/s
Layer (L1)	2500 MHz	160 Gb/s

Total integrated rates		
Tagger 1	2 GHz	130 Gb/s
Tagger 2	7 GHz	480 Gb/s
Total	**9 GHz**	**600 Gb/s**

Data buffered & filtered:	need a hadron in main detect	
Trigger rate: 500 kHz:	99.4% rejection (brem only)	
Data rate (signal):	4 Gb/s	
Data rate (incl BG and rand sample)	**<20 Gb/s**	To tape

Figure 8.169: Maximum and integrated rates for Low-Q^2 trackers.

across the centre of Tagger 2 take the bulk of the events, with the very highest on the one closest to the electron beam (T1). The small vertical offset between the centre of the board and the accelerator plane is to ensure that the centre line (dashed), where the top and bottom vertical 255 pixel columns meet, does not coincide with the very high rate band. The maximum rate estimates can be obtained by integrating over the relevant bins of the 2D histogram, and are shown in Figure 8.169. Although the dimensions of pixels and sensors are from Timepix4, these rates are *detector agnostic*, in the sense that they merely quantify numbers of electrons passing though the 55μm pixels in the tracking plane. After comparison with other technologies with other technologies proposed for the ePIC detector (MAPS, AC-LGAD) is became clear that Timepix4 is the only solution which can provide the required combination of rate capability, timing resolution and position resolution. The calorimeter ..... paragraph.

The final configuration and position of the Low-Q2 tagger is still to be decided, since it depends on the position and structure of the magnets and beamline configuration in the backward regions. These are not yet finalised.

Subsystem description Tracker :

There are two trackers, each consisting of four layers on pixel sensors. The sensors are mounted on carrier boards (12 sensors per board) which connect to a readout modules. Readout modules perform some presorting and pass data to cluster and tracking modules and data buffers. Tracks which are in coincidence with a hadron in the central detector are saved in the main DAQ readout.

Sensors: Timepix4 ASIC with Silicon sensor.

FEE: SPIDR4 readout to custom FPGA clustering and tracking modules.

Other components: Frame / infrastructure with cabling and cooling for layers with removable carrier boards. Cabling from boards to readout modules (housed below on platform).

Subsystem description Calorimeter: Main purpose of the calorimeter is direct energy measurement for cross check with energy obtained from trackers, where it is measured indirectly via ML methods. Also alignment and fake-track reduction will benefit from the use of the calorimeter.

General device description: In the initial running at lower luminosity when in-bunch pileup from Bethe-Heitler bremsstrahlung is relatively small it is assumed to share the same technology as luminosity pair spectrometer, i.e. scintillating fibers embedded in tungsten-powder epoxy (SciFi), read-out by SiPMs. General layout of the SciFi calorimeter is indicated in Fig. 8.170, giving tower arrangement of 4 layers. Total perpendicular size is given by the trackers. The towers are arranged perpendicular to shower axis. Fibers inner radius is 0.25 mm, fiber spacing is 1 mm. Optical photons are detected by SiPMs, shown as yellow rings at the end of each fiber. It is assumed that groups of 4x4 fibers in the same cell act as a single SiPM. Opposite ends of the fibers are ended by aluminum mirrors, shown as green caps.

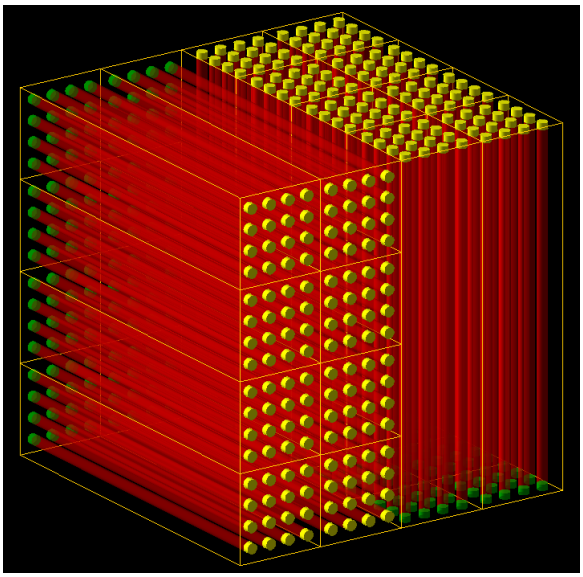

Figure 8.170: Layout of SciFi calorimeter.

For the case of nominal collider luminosity, reached in later runs, the in-bunch pileup from Bethe-Heitler bremsstrahlung will cause calorimeter rates to reach bunch crossing frequency, giving some signal every 10 ns at top luminosity for 10x100 GeV beams. Calorimeter technology will be shared with luminosity direct photon detector, where only Cherenkov fibers can fulfill the rate requirement. Expected energy resolution is shown in Fig. 8.171

Diameter for quarts fibers 1.5 mm, fiber spacing is 2.5 mm. The resolution is mainly driven by limited Cherenkov photon yields. Photon detection efficiency of 0.41 is included.

Sensors: SiPM, specific SiPM with fast capacitive coupling is required for nominal luminosity, possible example is Onsemi 30035 series.

FEE: fADC250 (flash ADC, 250 MSPS, 12 bit) for nominal luminosity

Other components: Add text here.

Performance Figures 8.172, 8.173 and 8.174 show the performance of the Trackers based on current simulation.

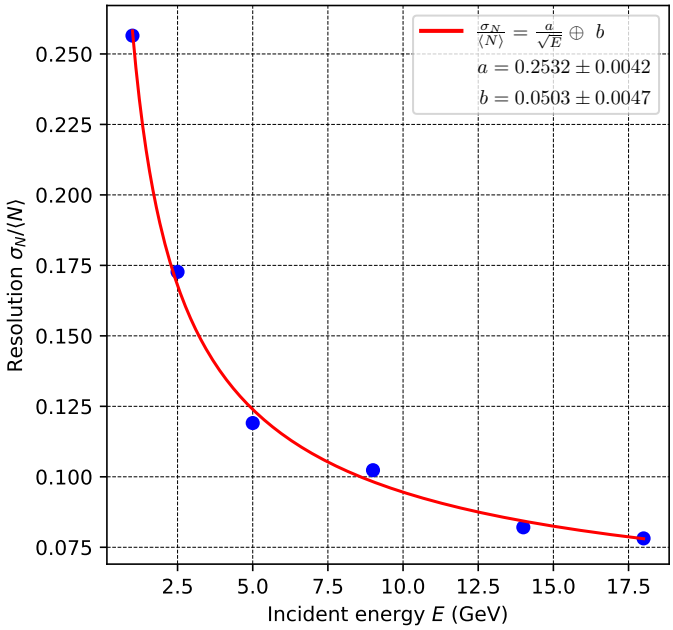

Figure 8.171: Energy resolution for Cherenkov fiber calorimeter.

Implementation

Services: No special services.

Subsystem mechanics and integration: The taggers are housed on platforms which need to be movable in vertical and horizontal (towards beamline) directions. Lower platform for readout modules in close proximity for readout modules. Bias and LV per board (24 total). Chiller (800W) per tagger.

Calibration, alignment and monitoring: Procedures for calibration and equalisation of individual sensors are already well established within the Medipix collaboration. These will be mapped to a dedicated Slow Controls interface for the tracker. Alignment and timing calibrations require tracks; they can be developed locally using cosmic rays and more rigorously tested in beam at Jlab or one of the European facilities.

Status and remaining design effort:

More a total effort not just R&D

R&D effort:
Electron tracker
Total expected from UK Infrastructure project in FTE years:
Academic 1.5
Senior Researchers 2.5

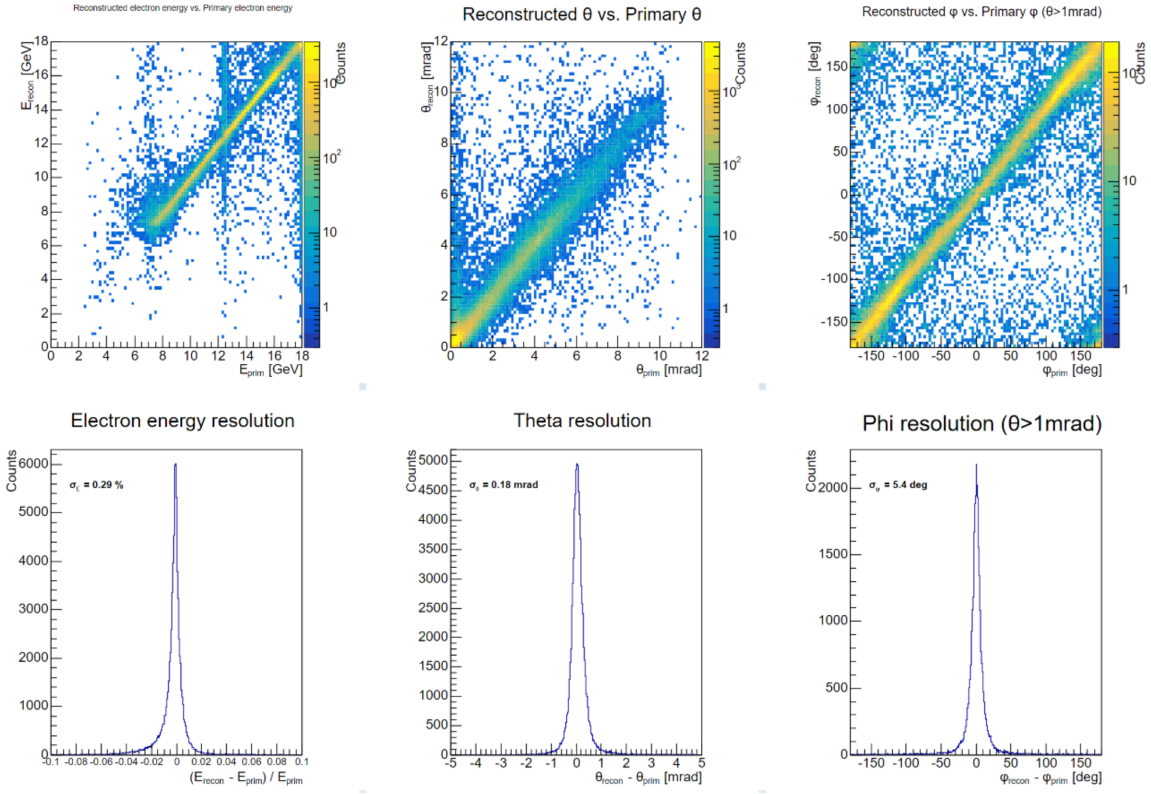

Figure 8.172: Top - Reconstruction of the initial electron energy, θ and ϕ angles from fitted tracks. Bottom - Integrated reconstruction difference.

Postdocs 10.0
Technical 3.0
PhDs 10
Additional Requirement: Postdoc 6 FTE Years

R&D status and outlook:
Electron tracker:
A test rig with SPIDR4 and Timepix4+Si sensors is complete, and fast readout tested. The development of prototype tracker with single sensor layers in progress. To be tested in stand-alone mode in Mainz, Dec24, with a further test using preliminary ePIC DAQ at Jlab in 2026. Carrier board for 12 x Timepix4 sensors to be developed and approved by Dec 2027. Procurement and fabrication of layers from Jan 2028 - 2030. Completion of taggers including mechanical infrastructure, cooling, readout to be completed in Glasgow by Dec 2030 with delivery to BNL Jan 31.

Other activity needed for the design completion
Final decision on positioning, layer dimensions and spacing is still to be made. The requires completion of designs for magnets, beamline and vacuum windows in the backward region.

Status of maturity of the subsystem:
Electron tracker

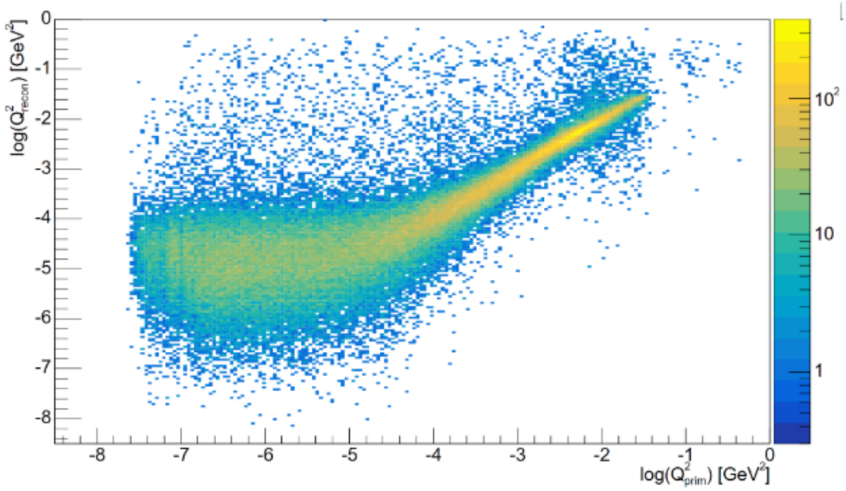

Figure 8.173: Reconstruction of the initial electron as a function of Q^2.

The Timepix4 sensor is well established, and is the latest in a series of detectors by the CERN Medipix collaboration. Current applications used the wire-bonded readout mode, but the TSV (through silicon vias) mode is in fast development, and we anticipate having a test setup within the next few months. The TSV mode is required to allow 4-side buttability, and fabrication of the layers with no dead space. The current readout uses SPIDR4 from the NIKHEF group in Amsterdam. We will collaborate with the developers to make an upgraded version of their carrier boards and readout to handle the data from the 12 sensor layer modules.

Environmental, Safety and Health (ES&H) aspects and Quality Assessment (QA planning): We will follow all procedures laid out by BNL and other labs where production test and development are carried out. During the engineering design phase, we will include production of mockups and engineering test articles to insure the proper functionality and quality, and will have full production chain tests for each sub-system.

For operation with HV and cooling we will ensure that these are mechanically secure and not a trip hazard, have proper warning signs and follow the lab procedures for electrical safety, and for operation near the beam-pipe and vacuum, anyone working near the far-forward/backward detectors will wear ear protection, and will post signage to that effect.

Construction and assembly planning: The tracker modules will be constructed assembled and tested in Glasgow as Work Package 2 (WP2) of the UK's EIC Infrastructure project. We will follow closely the fabrication and quality control procedures developed for the LHCb Velopix and ATLAS ITK detectors by the Glasgow experimental particle physics group.

Collaborators and their role, resources and workforce: The electron trackers are a *deliverable* within the UK's EIC Infrastructure project. The resources for constructing and delivering the trackers are expected to be mostly met by this. However, the project is still to be passed through a peer review panel and the costings for the tracker work package officially approved. As outlined

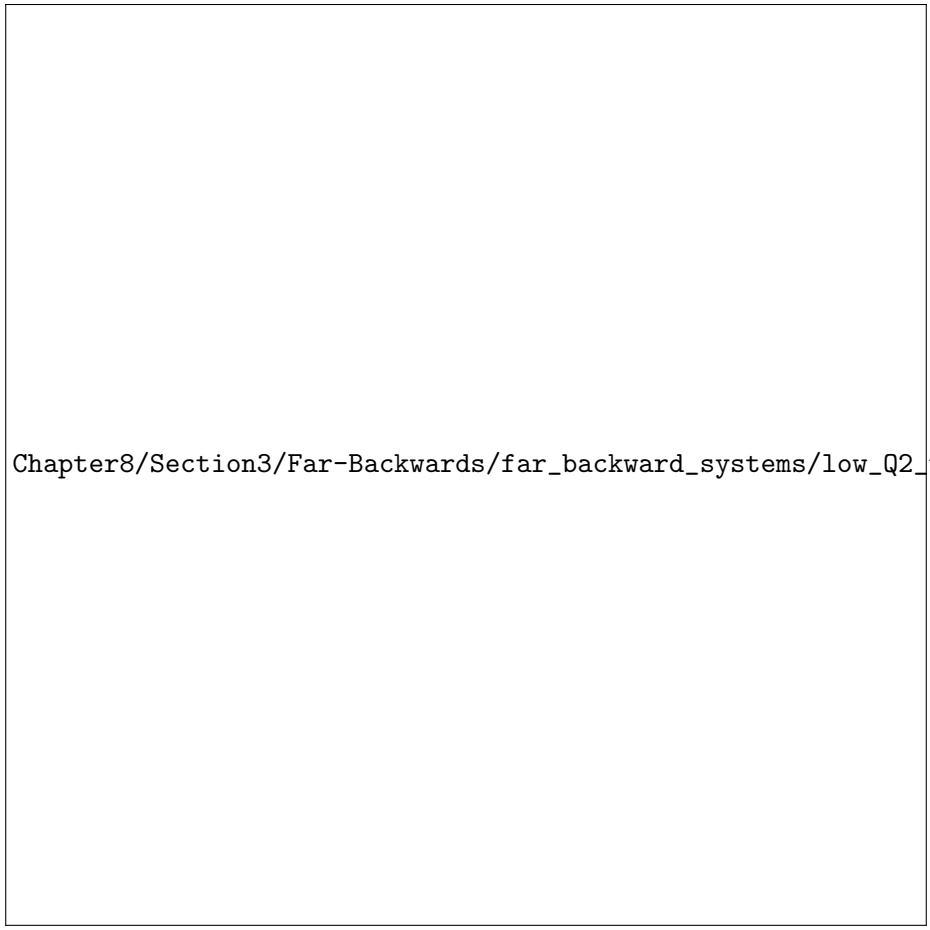

Figure 8.174: Acceptance as a function of Q^2 and $E_{e'}$.

above, we anticipate that we need and additional 6 FTE postdoc years for simulation, analysis and thermal modelling relating to detector development.

Risks and mitigation strategy: The Timepix4 tracker is being developed in close collaboration with colleagues in the Medipix collaboration. We will use suppliers and services recommended by them for wafers and production. For local production, fabrication and testing we have a team trained in bonding and quality control in case of staff changes. Our maximum rates have been calculated on the basis of EIC maximum proton luminosities, so in the initial running we will be well below capacity.

Additional Material Add text here.

8.3.9 Polarimeters

Add text here.

8.3.9.1 The electron polarimeters

Requirements

Requirements from physics: Add text here.

Requirements from Radiation Hardness: Add text here.

Requirements from Data Rates: Add text here.

Justification

Device concept and technological choice: Add text here.

Subsystem description:

General device description: Add text here.

Sensors: Add text here.

FEE: Add text here.

Other components: Add text here.

Performance

Implementation

Services: Add text here.

Subsystem mechanics and integration: Add text here.

Calibration, alignment and monitoring: Add text here.

Status and remaining design effort:

R&D effort: Add text here.

E&D status and outlook: Add text here.

Other activity needed for the design completion: Add text here.

Status of maturity of the subsystem: Add text here.

Environmental, Safety and Health (ES&H) aspects and Quality Assessment (QA planning): Add text here.

Construction and assembly planning: Add text here.

Collaborators and their role, resources and workforce: Add text here.

Risks and mitigation strategy: Add text here.

Additional Material Add text here.

8.3.9.2 The proton polarimeters

Requirements

Requirements from physics: Add text here.

Requirements from Radiation Hardness: Add text here.

Requirements from Data Rates: Add text here.

Justification

Device concept and technological choice: Add text here.

Subsystem description:

General device description: Add text here.

Sensors: Add text here.

FEE: Add text here.

Other components: Add text here.

Performance

Implementation

Services: Add text here.

Subsystem mechanics and integration: Add text here.

Calibration, alignment and monitoring: Add text here.

Status and remaining design effort:

R&D effort: Add text here.

E&D status and outlook: Add text here.

Other activity needed for the design completion: Add text here.

Status of maturity of the subsystem: Add text here.

Environmental, Safety and Health (ES&H) aspects and Quality Assessment (QA planning): Add text here.

Construction and assembly planning: Add text here.

Collaborators and their role, resources and workforce: Add text here.

Risks and mitigation strategy: Add text here.

Additional Material Add text here.

8.3.10 Readout Electronics and Data Acquisition

8.3.10.1 Requirements

The electronics and data acquisition systems are required to digitize and readout the data provided by the sensors of all ePIC detectors. The Electronics must tag hits with a time resolution sufficient to identify the bunch crossing (10.16 ns) and provide high resolution time references as stringent as 5 ps according the specific detector needs. The ePIC readout system must provide high data volume links to front end electronics up to 10 Gb/s for selected components. The readout system must provide very high live times, with the goal of zero-system wide deadtime in normal operation, despite the possibility of by-channel deadtime according the specific readout technology of each detector.

The Data Acquisition will group streaming data into time frames of O(0.6 ms). The readout systems are expected to digitize up to O(2 Tb/s) and must be capable of reducing this data volume to an output rate of O(100 Gb/s) using techniques to compress signal and remove noise with minimal impact to signal integrity. The data from all running detectors for each time frame will gathered together in a single buffer for transfer to the echelon 1 computing facilities located at BNL and JLAB for archive and analysis.

Detector Group	Channels					Det Fiber Down	Det Fiber Up	RDO	Fiber Pair (DAQ)	DAM	Data Volume (RDO) (Gb/s)	Data Volume (To Tape) (Gb/s)
	MAPS	AC-LGAD	SiPM/PMT	MPGD	HRPPD/ MCP-PMT							
Tracking (MAPS)	16B					183	5863	183	183	7	15	15
Tracking (MPGD)				164k		640	2560	160	160	5	27	5
Calorimeters	500M		100k					522	522	17	70	17
Far Forward		1.5M	10k					80	80	6	36	12
Far Backward	66M	128k	4k					60	82	14	301	16
PID (TOF)		6.1M				500	1364	500	500	14	50	12
PID Cherenkov			318k		143k			1283	1283	32	1275	32
TOTAL	**16.6B**	**7.7M**	**432k**	**164k**	**143k**	**843**	**9,787**	**2,788**	**2,810**	**95**	**1,774**	**109**

Figure 8.175: ePIC DAQ component count summary

Requirements from Physics The scientific mission of ePIC is reflected in the requirements of the Electronics and DAQ through the scale and technology of the ePIC detectors shown in figures 8.175 and 8.176. Large channel counts combined with low occupancy lead to the need for multiple levels of aggregation at the Front End Boards (FEB), the Readout Boards (RDO) and the Data aggregation and Manipulation Boards (DAM).

The performance of the EIC Collider also impacts the requirements of the readout system. The collision rates and background rates are detailed in section **??**. Two aspects are particularly important for the Electronics and DAQ.

The first is the maximum event rates, which we expect to be as high as 500 kHz for DIS, 3.2 MHz for Electron Beam Gas and 32 kHz for hadron Beam Gas. These rates are of primary interest within DAQ to estimate the data volumes which are described below.

The second consideration is that individual bunch crossing can have different polarization states. This implies that the luminosity and polarization of the beams must be tracked by bunch and produces the requirement that events must be associated to the bunch crossing from which they originated.

Requirements from Radiation Hardness The electronics installed in the ePIC detector will be subjected to significant radiation doses. Radiation doses are described in section **??**. Electronics placed in the central detector (SVT, eTOF, bTOF, and MPGDs) will utilize radiation hard components to minimize the effect of radiation.

Electronics must be chosen and placed to minimize failure rates. Transient failures such as single bit upsets (SEUs) must have a recovery process which automatically senses, initiates, and accomplishes recovery while running in order to avoid downtime. There are commercial IP cores available for FPGAs that can support recovery from simple SEUs. More complex (multi-bit) failures will require an automated reset and reload feature for FEBs and RDOs.

Requirements from Data Rates The triggerless readout of the ePIC detector uses zero-suppression to help manage the volume of data read out. The streaming model's sensitivity to noise, beam background, and collision data make the understanding of these effects critical. Collision, synchrotron radiation and beam gas backgrounds from both the electron and hadron beams have been studied extensively by the ePIC collaboration, and the methods are presented in section **??**. The hits have been converted to data volumes using our current understanding of zero suppression and data formats of each detector readout. Furthermore, the distribution of hits to each

Detector System		Channels	ASIC	FEB	RDO	Gb/s (RDO)	Gb/s (Tape)	DAM Boards	Readout Technology	Notes
Si Tracking:	Inner Barrel (IB)	1.8B Pixels	160	592*	24	2.36	2.36	1	ITS-3 sensors &	ASIC corresponds to VTRX+ counts
	Outer Barrel (OB)	5.0B Pixels	495	1870*	55	3.52	3.52	2	ITS-2 staves / w	FEB corresponds to detector fiber
	Backward Disks (EE)	4.7B Pixels	462	1744*	52	4.68	4.68	2	improvements	RDO is off detector Fiber aggregator
	Forward Disks (HE)	4.7B Pixels	462	1744*	52	4.68	4.68	2		
MPGD tracking:	Electron Endcap	16,384	256	64	16	2.86	0.58	1	uRWELL / SALSA	VTRX+ based FEB
	Hadron Endcap	16,384	256	64	16	4.01	0.80	1	uRWELL / SALSA	
	Inner Barrel	32,768	512	128	32	4.10	0.82	1	MicroMegas / SALSA	
	Outer Barrel	98,304	1536	384	96	15.81	3.16	2	uRWELL / SALSA	
Forward Calorimeters:	LFHCAL	63,280	1130	1130	74	18.54	2.47	2	SiPM / CALOROC	CALOROC:
	HCAL insert	8k	142	142	9	17.72	2.36	1	SiPM / CALOROC	56 Ch/CALOROC
	ECAL W/SciFi	18,320		574	72	14.75	7.36	2	SiPM / Discrete	16 CALOROC / RDO
Barrel Calorimeters:	HCAL	1,536	28	28	2	0.87	0.12	1	SiPM / CALOROC	
	ECAL SciFi/PB	5,760	102	102	4	11.45	1.52	1	SiPM / CALOROC	Discrete:
	ECAL ASTROPIX	500M pixels			340	1.25	1.25	8	Astropix	32 Ch/FEB,
Backward Calorimeters:	NHCAL	3,256	58	58	4	3.46	0.47	1	SiPM / CALOROC	8 FEB/RDO conservative (16 estimate).
	ECAL (PWO)	2,852		102	13	2.00	0.99	1	SiPM / Discrete	
Far Forward:	B0: Crystal Calorimeter	135		5	1	2.3	2.3	1	SiPM/APD / Discrete	
	4 AC-LGAD layer	688,128	672	168	42	12.75	2.1	1	AC-LGAD / EICROC	4 layer x 42 module x 4 EICROC x 1024 ch
	2 Roman Pots	524,288	512	128	32	14.53	2.1	1	AC-LGAD / EICROC	2 stations x 2 layer x 32 module x 4 EICROC x 1024 ch
	2 Off Momentum	294,912	288	72	18	3.53	0.7	1	AC-LGAD / EICROC	2 stations x 2 layer x 18 module x 4 EICROC x 1024 ch
	ZDC: Crystal Calorimeter	900		30	4	2.30	4.5	1	SiPM/APD / Discrete	
	HCAL	9,216	165	165	11	0.22	.22	1	CALOROC	
Far Backward:	2 x Low Q Tagger	66M pixels	3456	288	24	37	.3	10	Timepix4	Firmware Trigger to reduce output rate
	2 x Low Q Tagger Cal	420			1	-	-	1	SiPM / CALOROC	Low Q Calorimeter doesn't run at high luminosity
	2 x Lumi PS Calorimeter	3,360			1	19	7	1	SiPM / Discrete	
	2 x Lumi PS tracker	128k	1000	250	64	45	2	2	AC-LGAD: FCFD or EICROCx	
	Direct Photon Lumi Cal	100		24	24*	200	7	1	SiPM / fADC250	Direct Photon: commercial digitizer, no RDO
PID-TOF:	Barrel	2,359,296	18,432	288	288	15.95	4.79	8	AC-LGAD: FCFD or EICROCx	bTOF 128 ch/ASIC, 64 ASIC/RDO
	Endcap	3,719,168	3,632	212	212	33.92	7.34	6	AC-LGAD: EICROC	eTOF 1024 pixel/ASIC, up to 28 ASIC/RDO
PID-Cherenkov:	dRICH	317,952	4968	4968	1242	1240	13.5	30	SiPM / ALCOR	Worse case after radiation. Includes 30% timing window. Requires further data volume reduction
	pfRICH	69,632	544	68	17	24	12.5	1	HRPPD / FCFD or EICROCx	Firmware trigger
	DIRC	73,728	576	144	24	11	6	1	MCP-PMT / FCFD or EICROCx	

Figure 8.176: ePIC DAQ component counts

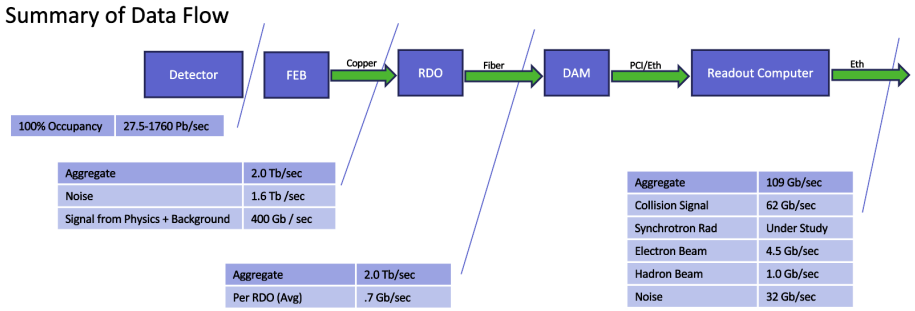

Figure 8.177: Expected worse case data rates contributions for the ePIC detector

Detector	Channel Max Hit Rate (Hz)	Noise To RDO (gbps)	Noise Per RDO (gbps)	Noise To Tape (gbps)	RDO (max) (gbps)	RDO_max / with Noise (gbps)
SiBarrelTracker	4.13E-04	3.25	0.06	3.25	0.00	0.06
SiBarrelVertex	5.22E-03	1.15	0.05	1.15	0.17	0.21
SiEndcapTracker	2.78E-03	6.02	0.06	6.02	0.23	0.29
BackwardMPGDEndcap	2.19E+02	1.74	0.11	0.35	0.42	0.52
ForwardMPGDEndcap	4.44E+02	1.74	0.11	0.35	0.86	0.97
MPGDBarrel	8.67E+01	3.26	0.10	0.65	0.04	0.14
OuterMPGDBarrel	1.29E+01	15.23	0.16	3.05	0.01	0.17
LFHCAL	2.10E+04	10.33	0.14	1.38	1.30	1.44
HcalEndcapPInsert	6.18E+04	1.31	0.15	0.17	2.78	2.93
EcalEndcapP	1.51E+05	0.78	0.01	0.35	2.69	2.70
HCcalEndcapN	7.81E+04	0.53	0.13	0.07	2.64	2.77
EcalEndcapN	8.07E+04	0.14	0.01	0.06	1.06	1.07
HcalBarrel	1.30E+03	0.25	0.13	0.03	0.08	0.21
EcalBarrelImaging	2.92E-02	0.32	0.00	0.32	0.01	0.01
EcalBarrelSciFi	1.52E+03	0.94	0.07	0.13	2.69	2.76
TOFBarrel	1.74E+00	13.59	0.05	4.53	0.01	0.06
TOFEndcap	8.34E-01	32.13	0.15	7.14	0.07	0.22
hpDIRC	2.35E+02	3.22	0.13	1.07	0.00	0.13
pfRICH	4.99E+02	3.05	0.18	1.02	0.00	0.18
dRICH	1.09E+02	1220.94	0.98	6.10	0.00	0.98
B0 Crystal Calorimeter	2.66E+05	0.00	0.00	0.00	0.00	0.00
B0 AC-LGAD	1.72E+01	5.95	0.20	1.32	0.00	0.20
RP	3.31E+01	4.53	0.21	1.01	0.00	0.21
OM	5.93E+00	2.53	0.21	0.56	0.00	0.21
ZDC Crystal Calorimeter	7.81E+04	0.02	0.00	0.02	0.00	0.00
ZDC HCAL	3.39E+01	0.20	0.02	0.20	0.00	0.02
DirectPhoton	2.00E+08	0.00	0.00	0.00	0.00	0.00
LowQ2Tracker	8.76E+00	0.04	0.00	0.04	0.00	0.00
LowQ2Calorimeter	0.00E+00	0.01	0.01	0.01	0.00	0.01
PairSpectrometerTracker	2.44E+02	0.74	0.07	0.25	0.00	0.07
PairSpectrometerCalorimeter	3.26E+04	0.07	0.07	0.07	0.00	0.07
Total		1334.01		40.67		

Figure 8.178: Maximum data volume per RDO with noise estimates.

Detector	Noise (Hz/channel)
ITS3, Astropix, Timepix	0.01
AC-LGAD	30
HRPPD	230
dRICH(initial)	3000
dRICH(Max)	300,000
All Others	4.5σ = 340

Table 8.43: Noise Estimates

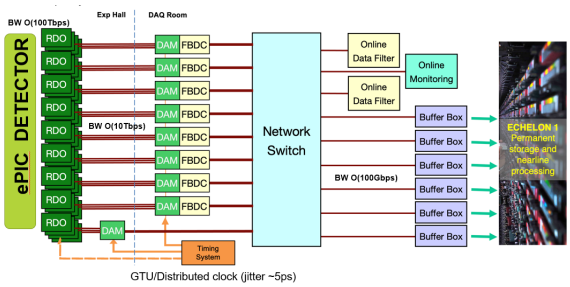

Figure 8.179: Schematic of the ePIC Streaming DAQ

component has been estimated by arbitrarily assigning readout components to the sensitive planes of the detectors in order to estimate the impact of potential bottlenecks.

The hit rate for the collision signal is taken from simulated hits for DIS events generated by the ePIC physics and detector simulations. The simulated data set was taken for 18x275 GeV collisions with $Q^2 > 0$ with luminosity $1.54x10^{33}$ cm^{2}s^{-1}. The collision rate was 83kHz, but the hit rates were scaled to the maximum rate of the EIC collider of 500kHz. Hadron and electron beam gas events were generated using the simulated vacuum profile after 10,000 Ah of pumping. Noise calculations are currently based on the ePIC detector group expert estimates and shown in table 8.43.

One additional factor that must be considered is dark currents in the SiPM detectors which increase with radiation damage. In particular, this issue affects the dRICH, in which the SiPM threshold must remain low enough to be sensitive to single photons. There are several features planned to reduce these dark currents including annealing, and implementation of timing windows to synchronise readout with collision times. These are described in section **??**. The DAQ system must be designed with the capability to manage the highest rates expected by the dRICH and must also apply filters to reduce the dRICH noise, either by applying a firmware trigger or by using specialized AI algorithms to determine which hits correspond to a dRICH physics signal.

Finally, noise is expected to be a potential issue in all other detectors as well. Generally, the noise level can be controlled with thresholds. The acceptable noise levels by detector is planned to be set according to the full data bandwidth requirements. The data volume expected, including collisions, background and noise for the worse case RDO by detector, is shown in table 8.178.

8.3.10.2 Device Concept and Technological choice: Streaming Readout

The ePIC readout system will implement a flexible, scalable, and efficient streaming DAQ as outlined by the EIC Yellow Report. This design will provide the advantages of streaming include the replacement of custom L1 trigger electronics with commercial off-the-shelf (COTS) computing, virtually deadtime-free operation, great flexibility in event selection using full event data along with offline analysis, and the opportunity to study event backgrounds in detail. These advantages come at the cost of greater sensitivity to noise and background. A schematic of the readout system is show in figure 8.179.

The components in the ePIC readout system are shown in figure 8.180. Readout will be accomplished using detector specific front end sensors and adaptors. Even though the organization of the front end electronics varies by detector needs the custom electronics of each system generically referred to as Front End Boards (FEBs). There is no global trigger system in ePIC, instead each FEB is required to self-trigger, providing a stream of hit data. Digitization and zero-suppression

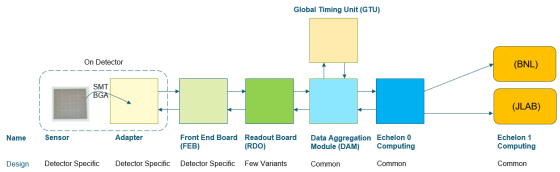

Figure 8.180: Components of the ePIC Streaming DAQ System

is typically handled with ASIC support. Each FEB has similar needs for clocks, configuration, and serial data links. These needs are provided by Readout Boards (RDOs). The RDOs also aggregate data from the FEBs. The RDOs are driven by either FPGAs or lpGBT. The RDO serves as an interface between custom, technology driven, readout schemes of specific detectors and the ePIC DAQ. While there are a number of variations of the RDOs depending upon the FEB technology, all of the RDOs support a unified ePIC DAQ fiber protocol. They distribute high-resolution time reference, configuration, and control to the FEBs and transmit hit data and monitoring information to the Data Aggregation and Manipulation Boards (DAM).

The DAM boards have significant processing available for implementing firmware triggers and other data reduction algorithms. They also provide further aggregation and function as the interface between the electronics and the first level of COTS computers called the Frame Builder Data Collectors (FBDC). The farm of COTS DAQ computers dedicated to readout, data reduction, logging, monitoring, QA and data buffering and transfer to data centers is integrated in the ePIC computing model and referred to as echelon 0.

Synchronizing the front end electronics and provide high resolution time reference to beam crossings is an important requirement of the streaming DAQ. The Global Timing Unit (GTU) is the interface to EIC collider controls. It receives the 98.5Mhz bunch crossing clock, orbit information, and beam polarization information and distributes it via the DAM boards to the RDOs and FEBs. The GTU is the only global source of real time information provided to the FEB/RDOs, so it must provide information a trigger system would normally provide. These functions include the ability to synchronize data from different detectors, to send flow control signals, to pass bunch information such as spin orientations and bunch structure, the ability to provide user defined signals for signaling special data formatting or calibration needs, and the ability to implement a hardware trigger for debugging or as a fallback option to solve unforeseen readout issues.

The communication between the RDOs, DAM, and GTU will use an unified data protocol serving four functions:

- The distribution of configuration information from the DAQ System to configure the RDOs, and to distribute configuration information to the FEBs via the RDOs using their serial links,
- The distribution of real-time control information to the RDO and FEBs,
- The distribution of a high-resolution beam crossing timing signal to the RDO and FEBs,
- The high performance ($\sim$10 Gb) transfer of hit data and monitoring information from the FEBs and RDO to the DAM boards.

8.3.10.3 Subsystem Description (components)

Readout Electronics and ASICS

Implementation	Detector/Sensor	Key Attributes
Discrete	Calorimeter/SiPM	COTS devices, 14-bit digitization
CALOROC	Calorimeter/SiPM	ASIC, 10-bit digitization
EICROC	AC-LGAD, pixel	ASIC, High-precision timing for Cd < 5 pF
FCFD	AC-LGAD, strip	ASIC, High-precision timing for Cd < 10 pF
ALCOR	dRICH/SiPM	ASIC, uses shutter for 1 p.e. sensitivity
SALSA	MPGD	ASIC, peaking time to 50 ns, includes DSP

Figure 8.181: ePIC Electronics and ASICs summary

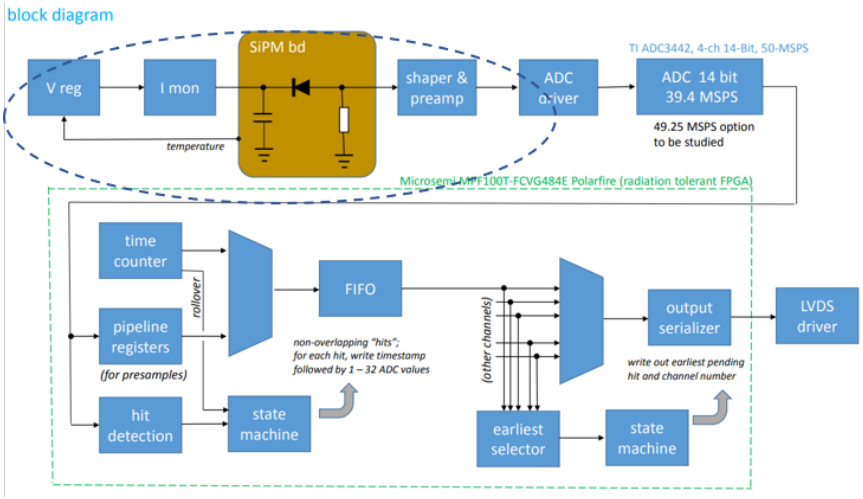

Figure 8.182: Discrete block diagram

Overview Readout electronics is being developed based on the sensor technologies. Common requirements among various sub-detectors have been identified to maximizing synergy. The readout electronics conforms to the ePIC streaming readout model with triggerless operation and serial interfaces. To facilitate calibration and debugging, capability for triggered operation is also implemented. The development of the readout electronics and ASICs are summarized in figure 8.181.

Discrete The Discrete readout implementation addresses the readout from calorimeters with SiPMs where high resolution digitization is required and commercial devices (COTS) are employed. The design and technologies will be validated for specific locations within the ePIC detector, where radiation hardness of COTS devices will need to be verified. The block diagram is shown in figure 8.182.

The circled area in fig. 8.182 delineates the Adapter section with SiPMs and bias circuitry; the remaining parts make up the FEB PCB, which includes signal conditioning, ADCs and readout logic. The Adapter and FEB PCBs are located at the detector, as a stack, and CAT6 cables are employed for serial interfaces. Key specifications are shown in figure 8.184. Prototypes of the Adapter and FEB PCBs are shown in figure 8.183.

CALOROC The CALOROC ASIC is currently under development to address readout from calorimeters with SiPMs and for which a 10-bit resolution digitization with wide dynamic range capabilities is applicable. The CALOROC design is based on the existing H2GCROC ASIC for SiPMs

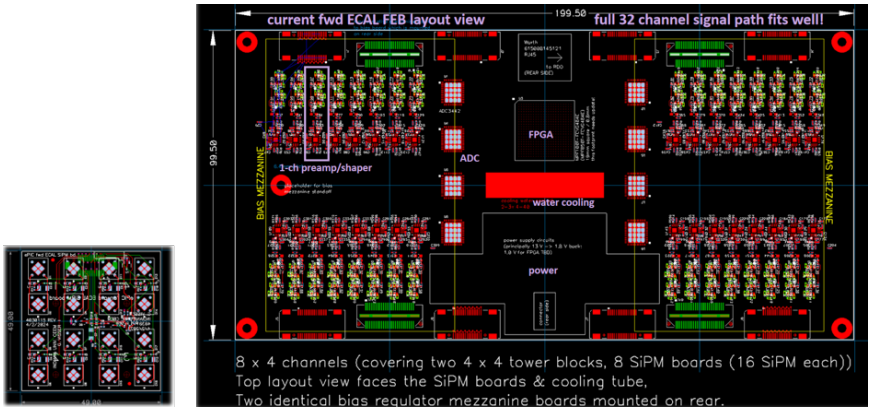

Figure 8.183: Discrete Adapter (left) and digitizer FEB PCBs

Function	Waveform digitizer with COTS devices
Channels	32
Digitizer	TI ADC 3422
Resolution	14-bit (12-bit also available)
Shaping	80 ns peaking time
FPGA	Microsemi MPF100T-FCVG484E Polarfire (Rad Hard)
Power	DC-DC converter (bPOL12V, bPOL48V, LTC36xx)
Cooling	Liquid
Cabling	CAT6

Figure 8.184: Discrete key specifications

with similar frontend and a backend, or digital section with interfaces, conforming to the needs of the streaming readout approach at the EIC. In parallel, tests with the H2GCROCv3 chip continue to provide input and validation into the design of the CALOROC ASIC. There are, however, two frontend variants being considered: CALOROC1A uses an ADC, a TOA and a TOT for wide dynamic range, similar to the H2GCROC; CALOROC1B uses a different frontend architecture making use of dual gain switching techniques to extend its dynamic range. The CALOROC block diagram is shown in figure 8.185 and its specifications summarized in figure 8.186.

EICROC The EICROC ASIC is currently under development to address readout from AC-LGAD pixel detectors with low detector capacitance (Cdin) and very stringent timing precision requirements. The EICROC design is based on the existing HGCROC ASIC for Si and PMTs with similar frontend and a backend, or digital section with interfaces, conforming to the needs of the streaming readout approach at the EIC, which is already being designed for the CALOROC. Main IP blocks consist of preamp, discriminator, TOA, ADC and TDC. The EICROC block diagram is shown in figure 8.187 and its specifications are summarized in figure 8.189. Figure 8.188 shows the EICROC timing performance with varying charge from input signals.

FCFD The FCFD ASIC is currently under development to address readout from AC-LGAD strip detectors with medium detector capacitance (Cdin) and very stringent timing precision requirements. The FCFD design implements the constant fraction discriminator technique for high precision timing without time-walk corrections. The backend, which is currently being considered, may be based on the existing ETROC ASIC or the EICROC development. The FCFD block diagram is

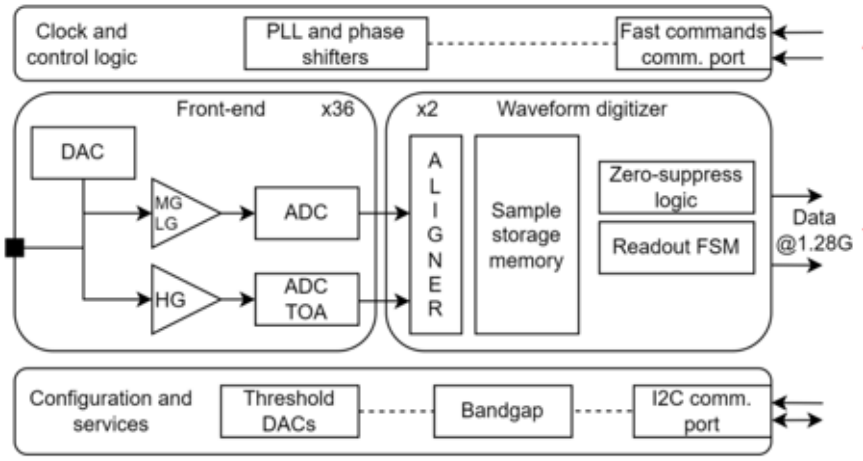

Figure 8.185: CALOROC block diagram

Function	Charge and timing digitization from SiPMs
Tech Node	130 nm CMOS
Channels	64
Cdin	500 pF – 10 nF
Digitization	Charge: 10-bit ADC, 15-bit TOT; Timing: <500 ps TOT (1 MIP)
Dynamic Range	Up to 12 nC
Clock	39.4 MHz operation from BX 98.5 MHz
Links	1260.8 Mbps @ 39.4 MHz, multiple
Power	10 mW/ch
Package	BGA
Rad Tolerance	Radiation hard

Figure 8.186: CALOROC Key Specifications

shown in figure 8.190 and its specifications are summarized in figure 8.192. Figure 8.191 shows the FCFD timing performance with varying charge from input signals.

ALCOR The ALCOR ASIC is currently under development specifically for the readout of the dRICH detector with SiPMs due to its single photo-electron sensitivity requirement. The ALCOR design includes trans-impedance amplification (TIA) with regulated common gate (RCG) bias for low noise, inhibit or shutter operation to limit contribution from dark-rate SiPM noise and TDCs to allow for single-photon tagging or time and charge digitization. The shutter function is a critical aspect of this ASIC and it is programmable for width and latency. The ALCOR Die and block diagram are shown in figure 8.193 and its specifications are summarized in figure 8.194.

SALSA The SALSA chip is an ASIC currently under development, foreseen to do the readout of the different MPGD trackers, namely the barrel cylindrical Micromegas, the barrel μRWELL and the end-cap μRWELL detectors. The purpose of SALSA is to amplify, shape and digitize signals coming from the MPGD detectors, and then perform basic data processing on the digitized samples before to transmit them to the next element of the data acquisition chain. It gathers in a single die a CSA pre-amplifier, a shaper and an ADC for each of the 64 channels, followed by a DSP which performs baseline corrections, digital shaping and a zero-suppression in order to reduce the

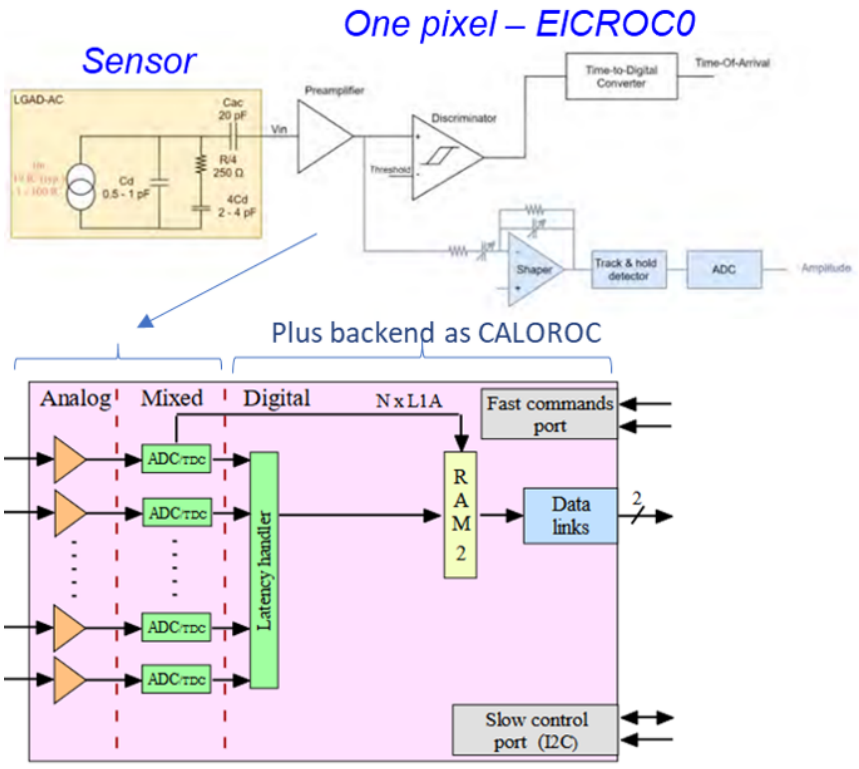

Figure 8.187: EICROC block diagram

output data bandwidth. Furthermore, to reduce data output even more, a peak finding algorithm is implemented to extract from samples information like amplitude and time of detected hits. It will be able to work both in the streaming readout environment foreseen at EPIC, and in a triggered environment.

The characteristics, performances and configurability of SALSA are designed to make the ASIC very versatile, being able to be adapted to several kinds of MPGD detectors and to several applications. It will be able to work with a large range of signal amplitudes, a large range of electrode capacitance and large range of signal rise times. Its target specifications are summarized in the Table 8.44.

Scope of the Effort The scope of the electronics and ASICs developments is summarized in figure 8.195, based on the number of readout channels, technologies employed and institutions developing these readout solutions.

It is noted that the pfRICH and the hpDIRC detectors benefit from the FCFD and the EICROC developments due to their timing precision requirements. The FCFD is, however, the nominal choice due to its lower channel density packaging for these applications with higher detector capacitances, which enable tailoring their timing performance via detector bias adjustment.

FEB components

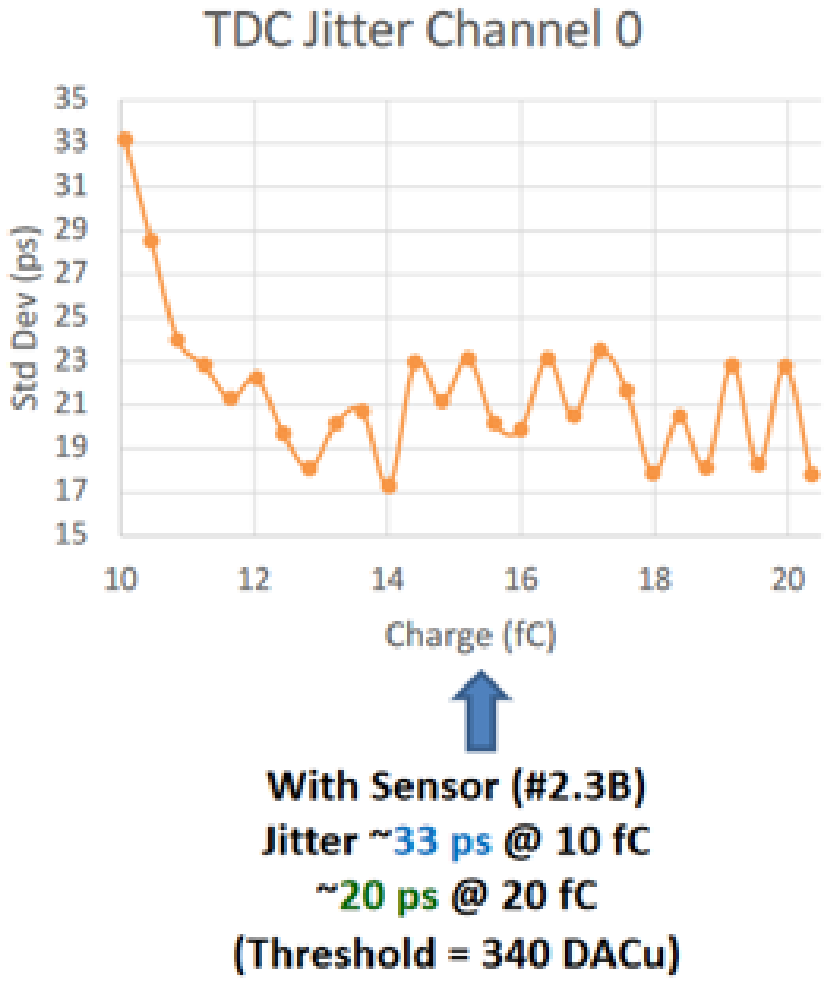

Figure 8.188: EICROC timing performance

Function	Timing digitization from AC-LGAD pixels
Tech Node	130 nm CMOS
Channels	1024 (32x32)
Cdin	1 – 5 pF
Digitization	ADC: 8-bit, TDC: 10b; Timing: 30 ps
Dynamic Range	1 – 50 fC
Clock	39.4 MHz operation from BX 98.5 MHz
Links	1260.8 Mbps @ 39.4 MHz, multiple
Power	<2 mW/ch
Package	Bump + wire bonds
Rad Tolerance	Radiation hard

Figure 8.189: EICROC Key Specifications

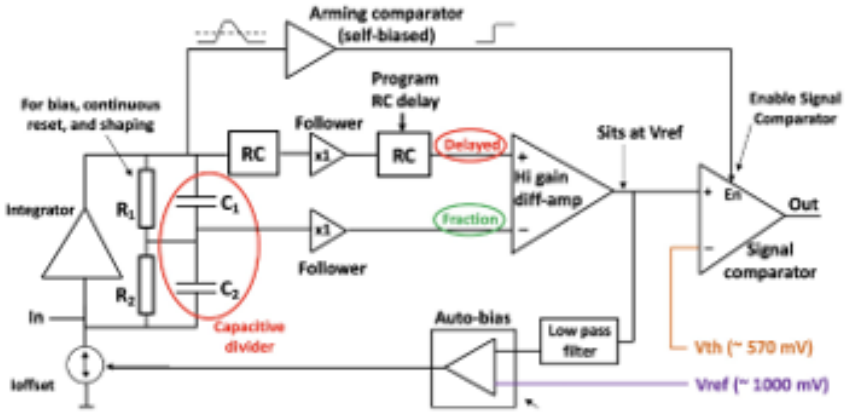

Figure 8.190: FCFD block diagram of the frontend

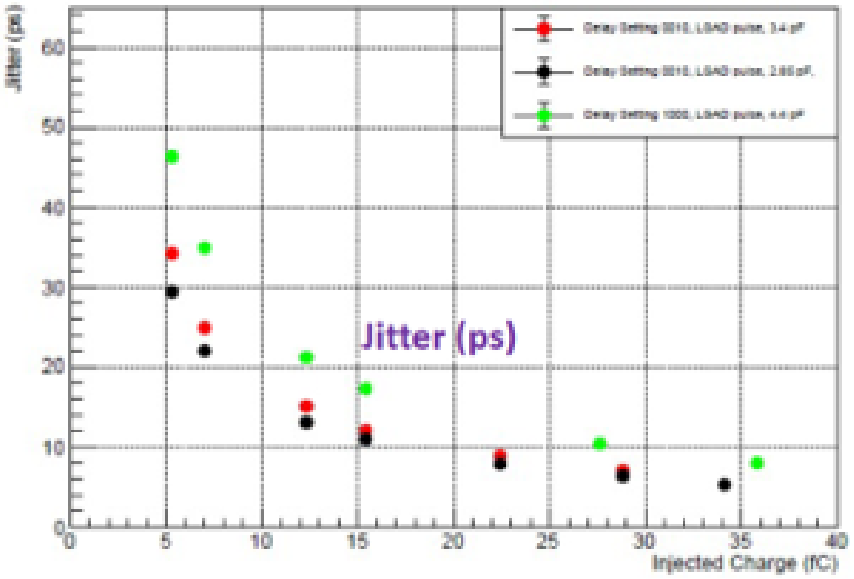

Figure 8.191: FCFD timing performance

Function	Timing digitization from AC-LGAD strips
Tech Node	65 nm CMOS
Channels	128
Cdin	<15 pF
Digitization	TBD; Timing: 10 - 30 ps
Dynamic Range	5 – 40 fC
Clock	39.4 MHz operation from BX 98.5 MHz
Links	1260.8 Mbps @ 39.4 MHz, multiple
Power	<2 mW/ch
Package	Bump + wire bonds
Rad Tolerance	Radiation hard

Figure 8.192: FCFD Key Specifications

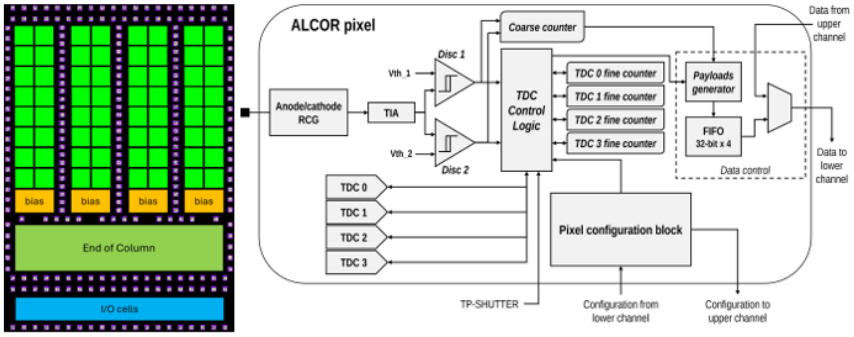

Figure 8.193: ALCOR Si Die (left) and block diagram

Function	Digitization from SiPMs with 1 p.e. sensitivity
Mode	Single-photon tagging or time and charge
Tech Node	110 nm CMOS
Channels	64 (8x8), dual polarity
Cdin	<1 nF
Digitization	20-40 ps TDCs, TOA + TOT; Timing <150 ps
Shutter	Width: 2–3 ns, programmable latency
Input Rate	<2.4 MHz (up to 5 MHz on single channel)
Clock	394.08 MHz operation from BX 98.5 MHz
Links	788 Mbps LVDS, SPI configuration
Power	12 mW/ch
Package	BGA
Rad Tolerance	Radiation hard

Figure 8.194: ALCOR Key Specifications

DC/DC converters DC/DC converters are employed throughout ePIC for the efficient distribution and regulation of the various sub-systems. The bPOL12V and bPOL48V DC/DC modules are selected for their radiation hardness and high magnetic field tolerances. Designs based on the LTC36xx family of devices will also be employed after proper validation.

lpGBT The low power Giga-Bit Transceiver (lpGBT) chip will be extensively used in ePIC subsystems to provide aggregation and serial communications of up to 2.5 Gbps. The lpGBT is radiation hard with Serializer/Deserializer (SERDES) functionality.

	# Ch	# Ch/ Unit	#ASICs/ Wafer	#Wafers	Node (nm)	Package	Institution
Discrete/COTS	24 k	32	NA	740 Digitizers	COTS	NA	IU
CALOROC	97 k	64	480	5	130	BGA	OMEGA/IN2P3/IJCL/ORNL
EICROC	5.2 M	1024	160	42	130	Wafer Bump	OMEGA/IN2P3/IJCL/CEA-IRFU/AGH
FCFD	2.6 M	128	180	149	65	Wire Bond	FNAL
ALCOR	318 k	64	800	8	110	BGA	INFN
SALSA	202 k	64	500	9	65	BGA	CEA-Saclay/U of Sao Paulo

Figure 8.195: Scope of the electronics and ASICs developments

Specification	Values	Remarks
Number of channels	64	
Input capacitance	50-200 pF	Reasonable gain up to 1 nF
Peaking time range	50 - 500 ns	
Max gain range	50 fC to 5 pC	
Max input rate	100 kHz/channel	Fast CSA reset
Signal polarity	Negative and positive	
ADC max sampling rate	50 MS/s	
ADC dynamics	12 bits	More than 10 effective bits
DSP processing	Baseline correction, filter, zero-suppression, peak finding	
Readout modes	Streaming readout, triggered	
Output data links	4 Gigabit links	1 only used at EPIC
Die technology	TSMC 65nm	
Die size	$\sim$1 cm^2	
Power consumption	$\sim$ 15 mW/channel	
Radiation hardness	Up to 300 Mrad and 10^{13} n_{eq}/cm^2	

Table 8.44: Main specifications of the SALSA chip.

VTRX+ The VTRX+ module is an electro-optical receiver/driver which will be extensively used in ePIC to interface to multi-mode optical fibers with MT optical connectors. One (1) receiver Rx (2.5 Gbps) and four (4) transmitters Tx (10 Gbps) are implemented. The VTRX+ is radiation hard and it is tolerant to high magnetic fields; it has a small footprint, has low power consumption and interfaces directly to the lpGBT transceiver devices.

RDOs The RDO aggregates ASIC information from the multiple front end boards. The RDO also has the function of delivering a high resolution clock (<=5 ps jitter) to the front end boards. This clock is reconstructed from the data downlink fiber. The final function of the RDO is act as the interface between the detector specific function of the ASICS to the global ePIC DAQ fiber protocol. This protocol labels bunch crossings, organizes time frames, uses user defined fast commands to communicate with the ASICs and provides the capabilities for firmware triggering and flow control.

However, several detectors: the SVT, the MPGD based detectors, and all AC-LGAD based readouts will make use of lpGBT or lpGBT-like aggregation using VTRX+ transceivers. The lpGBT aggregates ASIC information, and deliverers a high resolution reconstructed clock. However, it attempts to give a transparent interface to the ASICs. It does not have the capability of implementing the full ePIC protocol. For these RDOs the protocol will be implemented at the next level, either inside the DAM board or in a second level fiber to fiber RDO.

There will be several versions of the RDO depending on the needs of the specific detectors. The different RDO types are summarized in table 8.45

Target Detector	Input	Output	technology
TOF Pre-Prototype, Calorimeters	copper	SFP+ fiber	FPGA
dRICH	copper	VTRX+ fiber	FPGA
SVT, MPGD, AC-LGAD second level	fiber	fiber	FPGA
AC-LGAD	copper	VTRX+ fiber	lpGBT
Imaging Calorimeter (Astropix)	copper	fiber	FPGA
Low Q^2 Tagger (Spyder3 Board)	copper	up to 12 fiber	FPGA
Direct Photon Detector	copper	fiber	flash

Table 8.45: Types of RDO

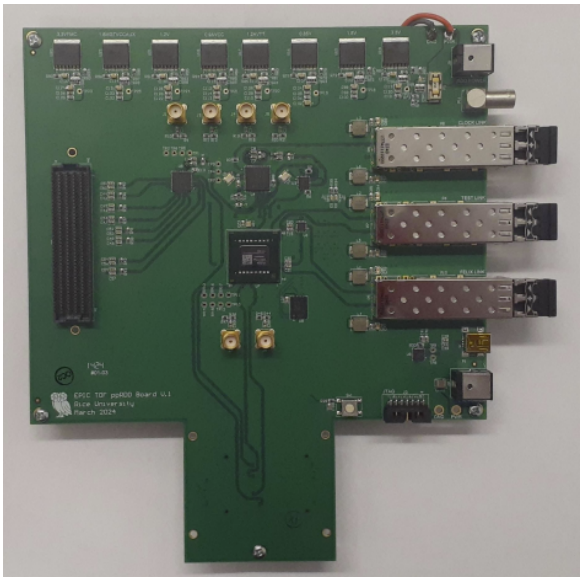

Figure 8.196: TOF pre-protype RDO

TOF pre-prototype RDO (FPGA based copper to SFP+ The TOF pre-prototype RDO was designed to use elements common to most ePIC detector RDOs. These elements include Xilinx Ultrascale+ Artix FPGA, SFP+ fiber optics interface, clock cleaner PLLs, and clock recovery. The pre-prototype has been produced and is undergoing measurements of power usage and clock jitter. The board is shown in figure 8.196.

dRICH RDO The dRICH RDO is part of the dRICH Photo Detector Unit PDU (see section **??**, 1248 PDUs will serve the dRICH). It provides read-out of four 64-channel ALCOR ASIC, installed each on a separate FEB. The space constraints are particularly demanding: the total RDO area is 40x9 mm^2 - quite similar to a credit card - requiring a devoted design, given the high integration of data buses and services within the PDU. The FPGA providing readout of the ALCOR is an AMD Artix Ultrascale+ AU15P-SBVB484, complemented by a PolarFire FLASH-based FPGA MPF050T-FCSG325. The latter will support remote programming and continuous scrubbing of configuration bits of the SRAM-based AMD FPGA, to protect against SEU. Given the space constraints and the need to curb power consumption (total RDO power is expected $\approx$ 4 W) the CERN-developed VTRX+ optical transceiver has been selected, directly connected to the AMD FPGA SERDES. The

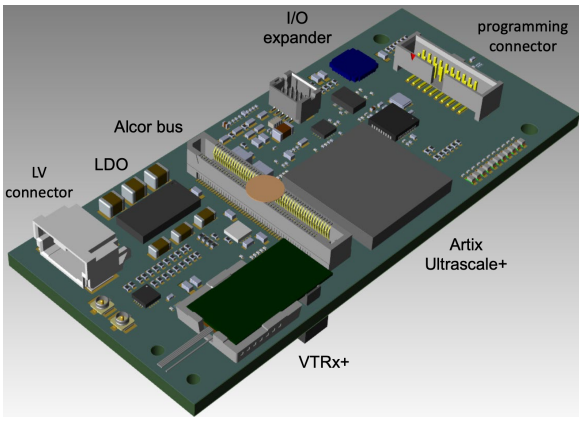

Figure 8.197: 3D model of dRICH RDO

maximum throughput per link (reached at maximum radiation damage before annealing) is foreseen not exceeding 2 Gbps, safely within VTRX+ specifications The ALCOR will be read out at 394 MHz, with a clock multiplier and jitter-attenuator (Skyworks Si5326) deriving this clock from the reconstructed EIC clock. A Microchip microcontroller provides power management and acts as watchdog against SEL. The first prototype of this card is under production and will be intensively tested during 2025, including irradiation tests. A 3D-rendering of the card is shown in Fig. 8.197.

Fiber to Fiber RDO The fiber to fiber RDO is to be used with lpGBT-like FEBs to convert the transparent ASIC interface to the ePIC DAQ protocol. They are also necessary to further aggregate the fibers, particularly in the case of SVT and bTOF large numbers of low-data utilization fibers are required.

lpGBT based copper to fiber RDO This RDO is yet to be designed, but is required for the lpGBT based readout of the inner detectors.

Astropix End of Stave Card (RDO) This RDO is to be developed by NASA for use with the Astropix sensors.

Low Q^2 RDO This is a RDO specifically for the low Q^2 taggers. It is expected to be an updated version of the Spyder3 board. These use the timepix sensor and have high potential data volumes, requiring several uplink fibers per RDO.

Flash based RDO The Flash RDO is a specialized interface for the Direct Photon Detector. This detector has only about 100 channels, but is expected to have very high occupancy, and as such the appropriate technology is to digitize all data at 200 MHz and stream it directly to the DAM boards which will summarize the information, writing out only the summed energy deposited each bunch crossing, or histograms of the bunch crossing energies according to bunch number.

DAM - Data Aggregation and Manipulation Hardware For the ePIC DAQ system the DAM boards will be used as the primary aggregation point for the "raw" detector data streams. Because

these boards are also the final aggregation points for the front-end (hardware managed) DAQ, there will need to be some well-defined but configurable algorithms for merging streams and managing potential congestion and data loss both for the incoming detector streams and the outgoing aggregated streams being queued up for online processing.

In Addition, the DAM boards will interface with the Global Timing Unit (GTU) hardware via a proprietary communication protocol that supports a synchronized EIC clock distribution to all subsystems and general DAQ/Run control and configuration. Finally, the DAM will act as the slow control interface for configuration and monitoring of all detector subsystem front-end boards (e.g. ASICs and other digitizing electronics).

We have identified an ideal candidate for the DAM hardware. An updated version of the FELIX board (Model FLX155) is currently being produced at BNL for ATLAS at the HL-LHC. Its features are substantial and the updated components ensure a longevity of production, performance and support that match very well with the EIC timeline. The board is built around the Xilinx Versal ACAP. This will facilitate using the board both as a PCIe device (supporting both PCIe Gen4 and Gen5 standards) in a server or as a standalone "smart" "aggregation" switch running a Linux OS. It can support up to 48 serial links to RDOs at the front-end running at speeds up to 25 Gbps as well as an LTI interface (8 fibers) supporting a high-resolution direct clock along with our GTU-DAM communication protocol. There is also a separate 100 Gb ethernet link off the board. A DDR4 RAM slot is available to support buffering and more complex algorithms for data reduction or interaction tagging. The board supports JTAG and I2C communications.

We expect to procure several FLX155 boards for testing and software/firmware development in 2025.

GTU - Global Timing Unit The design of the global timing distribution system (GTU) will be central to the operation of the streaming readout model. The timing system must provide signals to ensure that the data from different detectors can be synchronously aggregated. It must provide a copy of the accelerator bunch crossing clock (running at 98.5Mhz) to all front-end systems. A subset of these systems (e.g. TOF) will require a phase aligned system clock with a jitter of <5 ps in order realize required timing resolutions for these detectors (20-30 ps).

The GTU is also the only source of real time information provided to the FEB/RDOs, so it must provide information a trigger system would normally provide. These functions include the ability to synchronize data from different detectors, to send flow control signals, to pass bunch information such as spin orientations and bunch structure, the ability to provide user defined signals for signaling special data formatting or calibration needs, and the ability to implement a hardware trigger for debugging, calibration or as a fallback option to solve unforeseen readout issues.

Figure 8.198 shows a schematic layout based on required functionality of the GTU. The physical concept is shown in figure 8.199. The GTU will be custom rack-mounted hardware in the DAQ room with a base board and multiple plug-in optical interface modules. It will be based on a multi-FPGA architecture including a single Zync SoC FPGA supporting gigabit ethernet and a full Linux OS to facilitate both ePIC Run Control and other user-based applications. It will include an interface for the EIC Common platform (Clock, beam orbit and other collider information) and an interface for feedback from the local IP-6 beamline to support bunch crossing clock phase corrections

The jitter-cleaned and phase corrected clock then is fanned out for distribution to all DAM boards via a multi-fiber communications link (We intend to support up to 150 of these links for current needs as well as potential future requirements). In addition we plan to support up to 250 direct clock links to the RDO/FEB electronics. This is to mitigate potential limitations with the distribu-

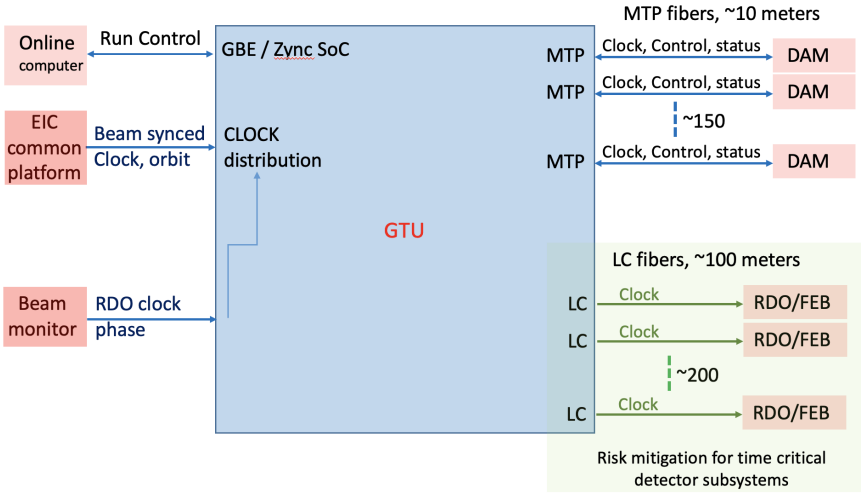

Figure 8.198: Schematic layout based for the GTU

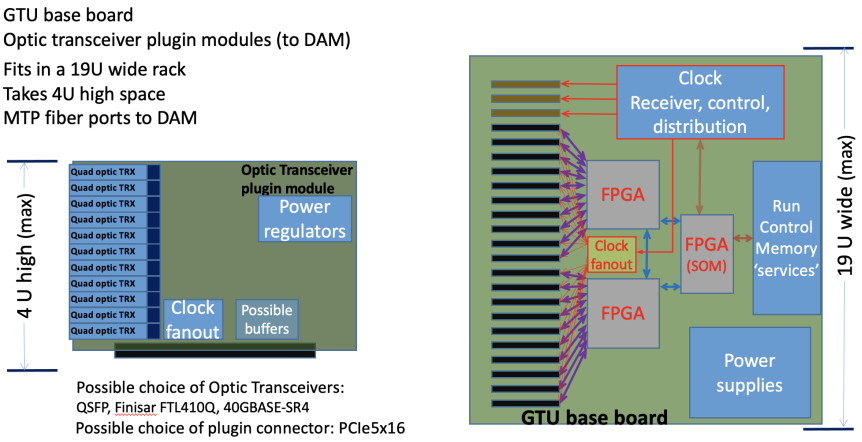

Figure 8.199: Physical concept for the fiber distribution for the GTU

tion of the low jitter (<5 ps) clock via the DAM path communication protocol.

Protocols The ePIC fiber protocol is used to communicate information between the GTU, DAM and RDO boards. The DAM to RDO communications are limited by the type of interface, and can be described in three categories as shown in table 8.47.

The ePIC fiber protocol depends upon a synchronous command structure (table 8.46 which simultaneously encodes fast commands, to be delivered to the RDO or ASICs with fixed latency relative to the bunch crossing and control information such as the current bunch crossing. The RDO acts upon delivered synchronous commands to provide headers defining the time frames, and to implement required features. The lpGBT provides a transparent fiber interface to the ASICs and does not have features capable of implementing the full ePIC DAQ protocol, so this functionality must be provided later in the chain, either in a second layer fiber to fiber RDO, or in the DAM board itself.

Decoded Synchronous Command Structure							
[0:7]	[8:15]	[16:23]	[24:31]	[32:39]	[40:47]	[48:55]	[56:64]
Flexible Command Data Encoding					FAST CMD		Comma
type	type specific				FAST CMD		Comma

Table 8.46: DAM/RDO Decoded Synchronous Command Structure. This structure is defined to allow continuous availability of the critical beam related bits and more rare commands. The data in the 40 bits worth of flexible command data encoding remains flexible but must contain enough control bits to select what structure it has. The "type", "type specific" division is an potential holding this flexibility

type	**clock (MHz)**	**downlink rate (Gb/s)**	**downlink word length** (ns)	**downline word width** (bits)
FPGA Standard	98.5	10	10.15	64
FPGA VTRX+	98.5	2.56	10.15	16
lpGBT VTRX+	39.4	2.56	25.375	64

Table 8.47: RDO downlink words

The maximum timeframe length, in bunch crossings will be defined to fit within 2^16, which implies a time frame length of ≈0.6 ms. This is also a convenient time as it corresponds to a manageable maximum time frame size of ≈10 MB. The need to support both the 10.15 ns EIC clock and the synchronized 25.375 ns clock support by cern lpGBT and CERN developed asics demands that time frame lengths be limited to multiples of 5 EIC clocks, if the time frame's are to be synchronized in time.

The features encoded in the Synchronous command protocol are

1. Synchronize bunch counters among all detector readouts
2. Define the time frame boundaries
3. Provide RDO and DAM Data processing flags
4. Configure ASICs and RDOs
5. Firmware based triggering
6. Flow control
7. Transfer Data
8. Transfer Slow Controls Data

Firmware Trigger One example of the operation of the protocol is in the firmware trigger to be implemented to reduce dRICH noise. It's important to note that the the firmware trigger under discussion is not (or not necessarily) a global trigger that would remove full events from the readout of the ePIC detector. Instead, this trigger is expected to affect only the data from particular detectors with unusually high data volumes. In this example, the dRICH.

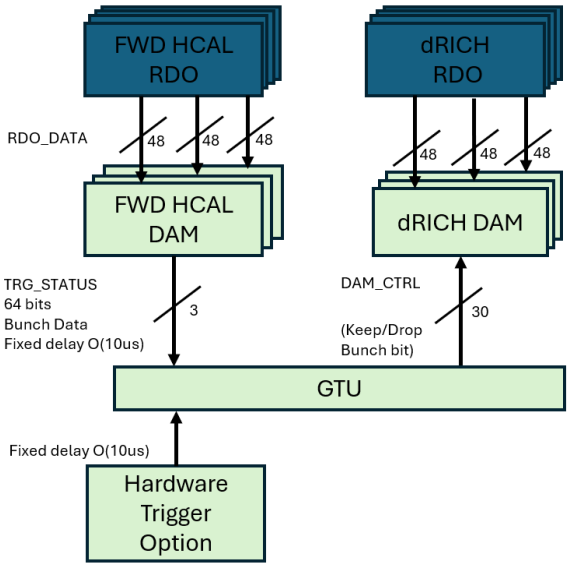

Figure 8.200: Operation of firmware trigger under assumption that the trigger decision for the dRICH depends upon data from fHCAL

The path of the commands sent is show in figure 8.200. Data arrives at DAM boards with 10us from digitization. It is stored in the DAM boards. After 10us FPGA based algorithms provide a description of the data (for example number of hits above a specified threshold) from each fHCAL DAM board. This information is encoded into 64 bits and sent to the GTU which aggregates data from fHCAL DAM boards and sends the keep/drop bunch bit to the dRICH DAM boards. The dRICH DAM boards drop or transmit data based upon this message. The decision comes after a fixed latency of about 11us which is very small compared to the buffering available on the DAM board.

Note that a similar approach can be implemented with a hardware signal into the GTU. In this case a fixed delay is applied to the hardware signal, but the decision mechanism uses the same data path.

dRICH data algorithms There are also additional schemes for implementing dRICH data reduction using only dRICH data or aggregated data from different sub-detectors. This is currently under investigation by the dRICH groups at INFN. One possibility would be to perform such reduction on the network of interconnected dRICH DAMS using the APEIRON framework [0] which implements a multi FPGA ML algorithm with deterministic time. The results of this calculation are transmitted to the GTU in the same manner as in the previous firmware trigger. The DAM buffering capacity is exploited in this scheme. Another possibility is to use instead, Online Data Filter algorithms in the servers receiving the aggregated data (see Fig. 8.179), exploiting xPU resources. Given the noise rate in the dRICH will increase with the radiation damage (see section **??**), this will provide an opportunity to develop and test carefully such systems

DAQ/Online Computing - Echelon 0 Table 8.48 outlines the planned resources for the ePIC detector DAQ and Online computing needs. This is based on the elements shown in the DAQ schematic in Figure 8.179. Several thousand fibers from the RDOs will be aggregated in the DAM

Resource	Totals
DAM/FELIX boards	136
EBDC Servers	92
DAQ Compute Nodes	108
File Servers (Buffer Box)	6

Table 8.48: DAQ Computing Resources

boards and presented to the Online Farm. To be clear each online farm node represents one multi-core server. The expectation is that they will minimally support 32-64 cores, and selected nodes will support PCIe-based GPUs and/or FPGAs in addition to the DAM boards in the FBDC (Frame Building Data Concentrator) nodes. The high performance DAQ network is expected to support 100/400 Gbps bandwidth connections. As the majority of the Online computing is expected to be COTS hardware, much of it will be acquired as late as is reasonable in the construction phase.

All Echelon 0 resources are fully dedicated to operation of the ePIC Detector and are included as part of the EIC Project. One open question under consideration, however, is to split these resources between the DAQ Room at IP-6 and the SDCC (BNL main data center) and to integrate them as a single enclave under ePIC control. There are several advantages to this configuration. First it will reduce the overall cost of infrastructure upgrades to the DAQ Room cooling systems. Also, having a subset of ePIC computing resources available in the SDCC will allow better network access to DAQ and electronics labs during construction (when the DAQ Room will not be available. Finally, during operations having DAQ tiered storage of production data in the SDCC will facilitate distribution of that data to both Echelon 1 processing sites (BNL and JLAB).

At the DAM stage the aggregated data streams will have substantial buffering and available network bandwidth for online processing that will be primarily focused on event identification and background/noise reduction. While we do not currently have solid estimates on the necessary computing resources to complete the required tasks, we have tried to provide conservative estimates of computing resources that would allow a full reconstruction of a 500 kHz trigger rate of events from similar scale detectors that exist now (e.g. GlueX and CLAS12 at Jefferson Lab and sPHENIX at RHIC). More likely the necessary computing resources for online filtering to get the expected data rates of O(100 Gbps) to files will be somewhat smaller.

Time Frame Building In the streaming model, the primary consideration is ensuring that enough bandwidth and buffering will be available to handle the digitized data at each stage of the DAQ. At the front-end stage time frames for the individual streams are created, managed and aggregated. Given current background and noise estimates the planned bandwidth off the detector to the DAM boards O(10 Tbps) should be more than sufficient.

Streams at the DAM boards will support time frames using a 16 bit bunch crossing counter which would represent a configurable time window of up to 65536*10.15 ns = 665 s. Although the front-end DAQ will be synchronized using a single common clock from the EIC, not all ASICS/digitizers at the FEBs will be running at the same frequency. Hence the timestamps coming from hits in different detectors will need to be wrapped in smaller "time slices" within the full time frame to establish an absolute time for each hit.

Time frames buffered at the DAM boards will be able to utilize the online farm to complete a full build of complete time frames with data from all detectors. Effectively N streams from the DAM boards will generate M<N streams of time frames containing the time frame fragments from the N

original streams. This will greatly facilitate additional event identification and processing at both the Echelon 0 and Echelon 1 stages.

Data Processing The ePIC readout system must support data reduction techniques. The implementation of firmware based triggering has already been described, but there are many additional techniques that might be implemented in echelon 0. These include zero loss techniques like aggregation of headers from ASICs or DAM board data. It could include standard or ML based compression techniques. It could involve analysis techniques such as cluster finding or track reconstruction. There could also be ML based noise reduction techniques. And there could be analysis done for specific purposes such as the creation of scalers for monitoring or collider feedback.

The framework for the code generating these features must allow the code to be shared with the offline software, for operational transparency, and for algorithm evaluation.

The results of the code must be incorporated into the time frame data using data formats that allow for independent data banks to co-exist. The policy of ePIC is expected to be to avoid dropping any data unless data volumes make it necessary. There should also be a sample of unprocessed data even if the readout of raw data banks are suppressed due to data volume limits. This implies that the write out of specific data banks be controlled by configurable prescales.

Configuration Databases Configuration information must be stored and made accessible to the ePIC Collaboration.

Slow controls interface to RDOs/FEBs The primary configuration and slow control communications interface to all the ASICs and other digitizing electronics (FEBs) will be through our proprietary data link between the DAM board and the RDOs. Our current plan is to take advantage of the Versal SoC FPGA dual-core ARM CorteX processor. ALL DAM boards will support a full LinuxOS and gigabit ethernet access. This will facilitate running an EPICS soft IOC as well as user-based server applications for local and remote communication with the front-end electronics.

Slow control communication on the DAM-RDO link must be bidirectional which means that slow control communications must share the link with streaming data coming from the detectors. The protocol must ensure that adequate bandwidth is available for digitized hits from the detector and slow controls readouts. The flow control provisions must enforce this requirement.

Software and firmware development of drivers and libraries necessary to access all the FEB "flavors" is supported as part of the Project. The majority of the FEBs will support standard I2C control communications.

Monitoring / Logging A unified system for centralized logging of informational and error messages is required. These messages should be ideally be available and archived in web-accessible form.

A unified system for monitoring of the real time behaviour and utilization of online components is also needed.

Interface to Echelon 1 As discussed in Section X (computing), the ePIC DAQ (Echelon 0) is an integral part of the computing system, and the output of the DAQ data triggers the calibration and reconstruction pipeline in Echelon 1, located at the computing centers of the host labs. From the

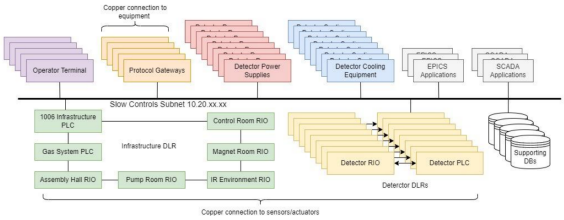

Figure 8.201: Proposed ePIC slow controls network topology

Scenario	Yearly Database Storage (TB)	Network Traffic (Mbps)
estimated	53.9	22.8
worst case	173.5	73.4

Table 8.49: Slow Controls data volume and network traffic

DAQ buffering disks, two identical copies will be sent to the buffer file system at the BNL SDCC via a dedicated fiber link and at the JLab Data Center via the 400 Gbps ESnet link, respectively. Each data center's data buffer has the capability of about three weeks' ePIC data taking to allow for multiple iterations of calibration jobs and reconstruction passes. Data will also be copied to permanent archival storage (presumably HPSS-like tape system), one copy at each site, which allows for reprocessing of the data in the future in case a problem identified in the prompt reconstruction pass or an improved reconstruction becomes available in the future. Nevertheless, in a steady state, the prompt calibration and production are expected to make the final analysis-ready data for physics working groups within days of the data taking, significantly expedited compared to many ongoing Nuclear Physics experiments.

Slow Controls There will be a myriad of slow controls information associated with both the EIC collider and the ePIC detector. These include various systems associated with the beamline, magnets, detector biases, gas flows, temperatures, pressures, etc… While the design and implementation of these slow control systems will be driven by the relevant subsystems they are associated with, it is the defined responsibility of the DAQ to provide software tools to facilitate the integration of all this information with the streaming physics data. This will include synchronizing the times associated with readout of slow control systems and the bunch-crossing clock that will be driving the DAQ system. Online slow control databases to support calibration and reconstruction processing will also be developed. Finally, a general network infrastructure in the experimental hall and control room, independent of the high performance DAQ network, will be provided to support integration of all slow control systems

A schematic of the proposed slow controls network topology is shown in figure 8.201. The implementation uses EPICS 7 on an ethernet network to control detector operation and read and archive conditions information. Allen-Bradley PLCs are to be used for controlling power to racks in the IR and for detector interlocks.

Resource requirements for the slow controls system were obtained by surveying detector managers. These resulted in approximately 500,000 channels to be read and stored. The yearly storage estimates and network traffic estimates are show in table 8.49.

Figure 8.202: DAQ/Computing schedule

8.3.10.4 Implementation

8.3.10.5 Calibration, alignment and monitoring:

During run time, predetermined calibration and alignment will be used in configuring the readout electronics and data reduction computing tasks. These calibration and alignment are managed by detector groups, extracted from dedicated prior-to-beam calibration runs, such as pedestal runs and zero field runs. When necessary, such as changes in detector condition, new calibration will be extracted and updated to be used in data taking. The calibration constant used will be archived in the run database and made available for reference in the offline analysis.

Constant monitoring for detector status and data pipeline healthiness is key to high-efficiency data taking and a successful run. We expect a multi-level of monitoring that includes monitoring the metrics on (1) detector statues (2) each stage of the data pipeline (3) sampled data content for decoding and analysis. In addition, in the Echelon-1 computing facility, full reconstruction will be performed for a small fraction of time frames expediently to provide holistic feedback of the experiment capability down to analysis level observable such as pi0 and K0s.

8.3.10.6 Status and remaining design effort:

R&D effort: ASIC R&D to continue through 2025

E&D status and outlook: The bulk of the engineering design efforts still required for the readout electronics are centered around the development of RDO and FEB designs needed to support all the detector subsystems. This information is needed to establish baseline costs and better define construction and testing schedules. Project Engineering design for a GTU engineering article can be completed prior to CD2/3. Finally, we expect to procure several FLX155 engineering articles in 2025 to support further timing and communication protocol testing and initial firmware development.

Status of maturity of the subsystem: Electronics and DAQ held a second PDR in June 2024. We expect to hold a third PDR in 2025 on track to an FDR in 2026. There are CD-3B items in the Electronics for VTRX+ and lpGBT. The FDR was held in June 2024, and will be presented during the CD-3B review in January 2025.

8.3.10.7 Environmental, Safety and Health (ES&H) aspects and Quality Assessment (QA planning:

8.3.10.8 Construction and assembly planning:

Figure 8.202 shows the current project schedule for DAQ/Computing. It is broken down into four general categories: Design/Procurement, Fabricate and Delivery, Test and Accept and Installation. Early in the construction phase there is a heavy focus on building and testing custom hardware (GTU, DAMs, RDOs) in order to facilitate detector subsystem testing and DAQ firmware/software development.

Once IP-6 infrastucture upgrades have been completed (DAQ and Control rooms, Wide Angle Hall), we can begin the main trunk fiber pulls into the hall and tunnels and install required patch panels and terminate fibers. At this time we can also start installation of the general IP-6 network infrastructure in the Hall, DAQ and Control Rooms.

Computing hardware procurement and installation are scheduled in three phases during the course of construction. Phase I at the beginning of construction will be for a small subset of machines for development and evaluation. They will be placed in both the DAQ/Electroncs development labs as well as in the SDCC. Phase II will be primarily in the DAQ Room as part of the DAQ subsystem installations and will provide the opportunity for full chain large scale testing of the DAQ as well as for detector subsystems as they begin to be installed at IP-6. Finally Phase III will be implemented at the end of the full ePIC detector installation as we have a better understanding of the required resources needed for inital Physics operation. This hardware will be installed at both the DAQ Room and in the SDCC which will define the full Echelon 0 enclave.

8.3.10.9 Collaborators and their role, resources and workforce:

The institutions specifically developing the readout electronics and ASICs are listed under the electronics section. Figure 8.203 lists the institutions which have expressed interest in participating in the design of various other parts of the readout chain. Formal agreements committing engineering and technical personnel have not been officiated.

8.3.11 Software and Computing

Requirements

Requirements from physics: Add text here.

Requirements from Radiation Hardness: Add text here.

Requirements from Data Rates: Add text here.

Justification

Detector System		Channels	SensorTechnology	Redout Technology	Institution
Si Tracking					
	3 vertex layers	7 m^2	MAPS	lpGBT, VTRX+	STFC, UK, ORNL
	2 sagitta layers	368 pixels	MAPS	lpGBT, VTRX+	STFC, UK, ORNL
	5 backward disks	5,200 MAPS sensors	MAPS	lpGBT, VTRX+	STFC, UK, ORNL
	5 forward disks		MAPS	lpGBT, VTRX+	STFC, UK, ORNL
MPGD Tracking					
	Barrel, e & H Endcaps	202 k	uRWELL, MicroMegas	SALSA	CEA, OMEGA, JLab
Forward Calorimeters					
	LFHCAL	63,280	SiPM	CALOROC	ORNL, Debrecen
	HCAL Insert	8 k	SiPM	CALOROC	ORNL, Debrecen
	pECAL W/SciFi	16,000	SiPM	Discrete	IU
Barrel Calorimeters					
	HCAL	7,680	SiPM	CALOROC	ORNL, Debrecen
	ECAL SciFi/Pb	5,760	SiPM	CALOROC	U Regina, ORNL
	ECAL Imaging Si ASTROPIX	500 M pixels	Astropix	Astropix	KIT,NASA (GSFC), ANL
Backward Calorimeters					
	nHCAL	3,256	SiPM	CALOROC	ORNL
	ECAL (PWO)	2,852	SiPM	Discrete	IU, EEEMCAL Consortium
Far Forward					
	B0: 3 Crystal Calorimeter	135	SiPM/APD	Discrete	IU, JLab
	B0: 4 AC-LGAD layers	688,128	AC-LGAD Pixel	EICROC	IJCLab, OMEGA, BNL, ORNL, Rice
	2 Roman Pots (RP)	524,288	AC-LGAD Pixel	EICROC	IJCLab, OMEGA, BNL, ORNL, Rice
	2 Off Momentum (OMD)	294,912	AC-LGAD Pixel	EICROC	IJCLab, OMEGA, BNL, ORNL, Rice
	ZDC: Crystal Calorimeter	900	SiPM/APD	Discrete	IU, JLab
	ZDC: HCAL	9,216	SiPM	CALOROC	ORNL, Debrecen, JLab
Far Backward					
	Low Q Tagger 1	33,030,144	Timepix4	Timepix4	U. Glasgow
	Low Q Tagger 2	33,030,144	Timepix4	Timepix4	U. Glasgow
	Low Q Tagger 1+2 Cal	420 (2x210)	SiPM	CALOROC	U. York
	2 Lumi PS Calorimeter	3,360 (2x1680)	SiPM	Discrete	U. York
	2 Lumi PS Tracker	128,000 (2x64,000)	AC-LGAD Strip	FCFD/EICROCx	FNAL, OMEGA, Hiroshima, NTU, ORNL, UIC, UH, Rice, KSU, Tokyo
	Lumi Direct Photon Calorimeter	100	SiPM	Flash250	AGH Krakow, JLab
PID-TOF					
	Barrel bTOF	2,359,296	AC-LGAD Strip	FCFD/EICROCx	FNAL, OMEGA, Hiroshima, NTU, ORNL, UIC, Rice, BNL, KSU, Tokyo
	Hadron Endcap fTOF	3,719,168	AC-LGAD Pixel	EICROC	IJCLab, OMEGA, BNL, ORNL, Rice
PID-Cherenkov					
	dRICH	317,952	SiPM	ALCOR, VTRX+	INFN (BO, FE, TO)
	pfRICH	69,632	HRPPD	FCFD/EICROCx	BNL, FNAL, JLab
	hpDIRC	73,728	MCP-PMT or HRPPD	FCFD/EICROCx	BNL, FNAL, JLab

Figure 8.203: Electronics and DAQ Resources

Device concept and technological choice: Add text here.

Subsystem description:

General device description: Add text here.

Sensors: Add text here.

FEE: Add text here.

Other components: Add text here.

Performance

Implementation

Services: Add text here.

Subsystem mechanics and integration: Add text here.

Calibration, alignment and monitoring: Add text here.

Status and remaining design effort:

R&D effort: Add text here.

E&D status and outlook: Add text here.

Other activity needed for the design completion: Add text here.

Status of maturity of the subsystem: Add text here.

Environmental, Safety and Health (ES&H) aspects and Quality Assessment (QA planning: Add text here.

Construction and assembly planning: Add text here.

Collaborators and their role, resources and workforce: Add text here.

Risks and mitigation strategy: Add text here.

Additional Material Add text here.

8.4 Detector Integration

Add text here.

8.4.1 Installation and Maintenance

Add text here.

8.5 Detector Commissioning and Pre-Operations

Add text here.

References

[1] A. Bacchetta, V. Bertone, C. Bissolotti, G. Bozzi, M. Cerutti, F. Delcarro, M. Radici, L. Rossi, and A. Signori, "Flavor dependence of unpolarized quark transverse momentum distributions from a global fit," *JHEP*, vol. 08, p. 232, 2024.

[2] Irene Dutta and Christopher Madrid and Ryan Heller and Shirsendu Nanda and Danush Shekar and Claudio San Martín and Matías Barría and Artur Apresyan and Zhenyu Ye and William K. Brooks and Wei Chen and Gabriele D'Amen and Gabriele Giacomini and Alessandro Tricoli and Aram Hayrapetyan and Hakseong Lee and Ohannes Kamer Köseyan and Sergey Los and Koji Nakamura and Sayuka Kita and Tomoka Imamura and Cristían Peña and Si Xie, "Results for pixel and strip centimeter-scale AC-LGAD sensors with a 120 GeV proton beam," 7 2024.

[3] M. Tabata *et al.*, "Silica aerogel radiator for use in the A-RICH system utilized in the Belle II experiment," *Nucl. Instrum. Meth. A*, vol. 766, pp. 212–216, 2014.

[4] F. T. Acosta, B. Karki, P. Karande, A. Angerami, M. Arratia, K. Barish, R. Milton, S. Morán, B. Nachman, and A. Sinha, "The optimal use of segmentation for sampling calorimeters," *JINST*, vol. 19, no. 06, p. P06002, 2024.

[5] ePIC, "Summary of epic background rates," 2024.

[6] M. Tabata, I. Adachi, H. Kawai, T. Sumiyoshi, and H. Yokogawa, "Hydrophobic silica aerogel production at kek," *Nuclear Instruments and Methods in Physics Research Section A: Accelerators, Spectrometers, Detectors and Associated Equipment*, vol. 668, pp. 64–70, 2012.

[7] R. Abdul Khalek *et al.*, "Science Requirements and Detector Concepts for the Electron-Ion Collider: EIC Yellow Report," *Nucl. Phys. A*, vol. 1026, p. 122447, 2022.

[8] A. Accardi *et al.*, "Electron Ion Collider: The Next QCD Frontier: Understanding the glue that binds us all," *Eur. Phys. J. A*, vol. 52, no. 9, p. 268, 2016.

[9] A. Accardi *et al.*, "Electron Ion Collider: The Next QCD Frontier: Understanding the glue that binds us all," *Eur. Phys. J. A*, vol. 52, no. 9, p. 268, 2016.

[10] "National Academies of Sciences, Engineering, and Medicine, An Assessment of U.S.-Based Electron-Ion Collider Science," *The National Academies Press,Washington, DC*, 2018.

[11] J. K. Adkins *et al.*, "Design of the ECCE Detector for the Electron Ion Collider," 9 2022.

[12] J. Adam *et al.*, "ATHENA detector proposal — a totally hermetic electron nucleus apparatus proposed for IP6 at the Electron-Ion Collider," *JINST*, vol. 17, no. 10, p. P10019, 2022.

[13] S. R. Klein, J. Nystrand, J. Seger, Y. Gorbunov, and J. Butterworth, "Starlight: A monte carlo simulation program for ultra-peripheral collisions of relativistic ions," *Computer Physics Communications*, vol. 212, pp. 258–268, 2017.

[14] D. W. Sivers, "Single Spin Production Asymmetries from the Hard Scattering of Point-Like Constituents," *Phys. Rev. D*, vol. 41, p. 83, 1990.

[15] D. W. Sivers, "Hard scattering scaling laws for single spin production asymmetries," *Phys. Rev. D*, vol. 43, pp. 261–263, 1991.

[16] E. C. Aschenauer, V. Batozskaya, S. Fazio, K. Gates, H. Moutarde, D. Sokhan, H. Spiesberger, P. Sznajder, and K. Tezgin, "EpIC: novel Monte Carlo generator for exclusive processes," *Eur. Phys. J. C*, vol. 82, no. 9, p. 819, 2022.

[17] "The electron-ion collider user group.".

[18] R. A. Khalek *et al.*, "Science Requirements and Detector Concepts for the Electron-Ion Collider: EIC Yellow Report," *Nucl. Instr. and Meth. A*, vol. 1026, p. 122447, 2022.

[19] "The epic collaboration website.".

[20] A. Collaboration, "Technical Design report for the ALICE Inner Tracking System 3 - ITS3 ; A bent wafer-scale monolithic pixel detector," tech. rep., CERN, Geneva, 2024.

[21] lpGBT Design Team, "lpgbt documentation – release," 2024.

[22] J. Troska *et al.*, "The VTRx+, an optical link module for data transmission at HL-LHC," 2017.

[23] D. H. et *al.*, "Science requirements and detector concepts for the electron-ion collider: Eic yellow report," *Nuclear Physics A*, vol. 1026, p. 122447, 2022.

[24] F. Willeke and J. Beebe-Wang, "Electron ion collider conceptual design report 2021," 2 2021.

[25] EIC, "Eic detector geometry," 2024.

[26] D. N. et *al.*, "Aging effects in the COMPASS hybrid GEM-Micromegas pixelized detectors," *Nucl. Instrum. Meth.*, vol. 1065, p. 169511, 2024.

[27] C. A. et *al.*, "Construction, test and commissioning of the triple-gem tracking detector for compass," *Nucl. Instrum. Meth.*, vol. A490, no. 1, pp. 177 – 203, 2002.

[28] T. Kawamoto, S. Vlachos, L. Pontecorvo, J. Dubbert, G. Mikenberg, P. Iengo, C. Dallapiccola, C. Amelung, L. Levinson, R. Richter, and D. Lellouch, "New Small Wheel Technical Design Report," tech. rep., 2013. ATLAS New Small Wheel Technical Design Report.

[29] M. P. et *al.*, "The μ-rwell: A compact, spark protected, single amplification-stage mpgd," *Nuclear Instruments and Methods in Physics Research Section A: Accelerators, Spectrometers, Detectors and Associated Equipment*, vol. 824, pp. 565–568, 2016. Frontier Detectors for Frontier Physics: Proceedings of the 13th Pisa Meeting on Advanced Detectors.

[30] E. F. et *al.*, "Resistive micromegas high-rate and long-term ageing studies at the cern gamma irradiation facility," *Nuclear Instruments and Methods in Physics Research Section A: Accelerators, Spectrometers, Detectors and Associated Equipment*, vol. 1042, p. 167423, 2022.

[31] M. C. et *al.*, "Development of micromegas detectors with resistive anode pads," *Nuclear Instruments and Methods in Physics Research Section A: Accelerators, Spectrometers, Detectors and Associated Equipment*, vol. 1003, p. 165268, 2021.

[32] A. Acker and others, "The CLAS12 micromegas vertex tracker," vol. 957, p. 163423.

[33] I. Giomataris, R. De Oliveira, S. Andriamonje, S. Aune, G. Charpak, P. Colas, A. Giganon, P. Rebourgeard, and P. Salin, "Micromegas in a bulk," *Nucl. Instrum. Meth. A*, vol. 560, pp. 405–408, 2006.

[34] M. Calvi, P. Carniti, C. Gotti, C. Matteuzzi, and G. Pessina, "Single photon detection with SiPMs irradiated up to 10^{14} cm^{-2} 1-MeV-equivalent neutron fluence," *Nucl. Instrum. Meth. A*, vol. 922, pp. 243–249, 2019.

[35] R. Preghenella *et al.*, "Study of radiation effects on SiPM for an optical readout system for the EIC dual-radiator RICH," *Nucl. Instrum. Meth. A*, vol. 1056, p. 168578, 2023.

[36] "Technical Design Report: A High-Granularity Timing Detector for the ATLAS Phase-II Upgrade," tech. rep., CERN, Geneva, 2020.

[37] C. Madrid, R. Heller, C. San Martín, S. Nanda, A. Apresyan, W. Brooks, W. Chen, G. Giacomini, O. Kamer Köseyan, S. Los, C. Peña, R. Rios, A. Tricoli, S. Xie, and Z. Ye, "First survey of centimeter-scale ac-lgad strip sensors with a 120 gev proton beam," *Journal of Instrumentation*, vol. 18, p. P06013, June 2023.

[38] C. Bishop, A. Das, J. Ding, M. Gignac, F. Martinez-McKinney, S. Mazza, A. Molnar, N. Nagel, M. Nizam, J. Ott, H.-W. Sadrozinski, B. Schumm, A. Seiden, T. Shin, A. Summerell, M. Wilder, and Y. Zhao, "Long-distance signal propagation in ac-lgad," *Nuclear Instruments and Methods in Physics Research Section A: Accelerators, Spectrometers, Detectors and Associated Equipment*, vol. 1064, p. 169478, 2024.

[39] L. Menzio *et al.*, "First test beam measurement of the 4D resolution of an RSD pixel matrix connected to a FAST2 ASIC," *Nucl. Instrum. Meth. A*, vol. 1065, p. 169526, 2024.

[40] S. Xie, A. Apresyan, R. Heller, C. Madrid, I. Dutta, A. Hayrapetyan, S. Los, C. Peña, and T. Zimmerman, "Design and performance of the fermilab constant fraction discriminator asic," *Nuclear Instruments and Methods in Physics Research Section A: Accelerators, Spectrometers, Detectors and Associated Equipment*, vol. 1056, p. 168655, 2023.

[41] J. D. Brandenburg *et al.*, "The STAR Forward Silicon Tracker," 7 2024.

[42] C. Chock, K. Flood, L. Macchiarulo, F. Martinez-Mckinney, A. Martinez-Rojas, S. Mazza, I. Mostafanezhad, M. Nizam, J. Ott, R. Perron, E. Ryan, H.-W. Sadrozinski, B. Schumm, A. Seiden, K. Shin, M. Tarka, D. Uehara, M. Wilder, and Y. Zhao, "First test results of the transimpedance amplifier stage of the ultra-fast hpsoc asic," *Journal of Instrumentation*, vol. 18, p. C02016, feb 2023.

[43] O. H. W. Siegmund *et al.*, "Advances in microchannel plates and photocathodes for ultraviolet photon counting detectors," *Society of Photo-Optical Instrumentation Engineers Proceedings*, vol. 81450J.

[44] C. J. Hamel *et al.*, "LAPPD and HRPPD: Upcoming Upgrades to Incom's Fast Photosensors,"

[45] "EICROC ASIC." `https://indico.bnl.gov/event/18539/contributions/73731/attachments/46348/78403/CdLT_EICROC_6mar23.pdf`.

[46] "Organization for Micro-Electronics desiGn and Applications." `https://portail.polytechnique.edu/omega/`.

[47] J. Anderson *et al.*, "FELIX: a PCIe based high-throughput approach for interfacing front-end and trigger electronics in the ATLAS Upgrade framework," *JINST*, vol. 11, no. 12, p. C12023, 2016.

[48] "Chiba Aerogel Factory Co., Ltd.." `https://www.aerogel-factory.jp/`.

[49] M. Yonenaga *et al.*, "Performance evaluation of the aerogel RICH counter for the Belle II spectrometer using early beam collision data," *Prog. Theor. Exp. Phys.*, no. 093H01, 2020.

[50] S. Agostinelli *et al.*, "GEANT4—a simulation toolkit," *Nucl. Instrum. Meth. A*, vol. 506, p. 250, 2003.

[51] "ePIC IRT Package." `https://github.com/eic/irt/tree/pfrich`.

[52] R. Brun and F. Rademakers, "ROOT - An Object Oriented Data Analysis Framework, Proceedings AIHENP'96 Workshop, Lausanne," *Nucl. Inst. & Meth. in Phys. Res. A*, no. 389, pp. 81–86, 1997.

[53] M. Tabata, I. Adachi, Y. Hatakeyama, H. Kawai, T. Morita, and T. Sumiyoshi, "Large-area silica aerogel for use as cherenkov radiators with high refractive index, developed by supercritical carbon dioxide drying," *The Journal of Supercritical Fluids*, vol. 110, pp. 183–192, 2016.

[54] "CAEN A1515BV 16-channel floating ground High Voltage module." `https://www.caen.it/products/a1515b/`.

[55] "CAEN SY4527 High Voltage mainframe." `https://www.caen.it/products/SY4527/`.

[56] "Wiener Mpod Low Voltage system." `https://www.wiener-d.com/power-supplies/mpod-lv-hv/`.

[57] A. Buzykaev, A. Danilyuk, S. Ganzhur, E. Kravchenko, and A. Onuchin, "Measurement of optical parameters of aerogel," *Nuclear Instruments and Methods in Physics Research Section A: Accelerators, Spectrometers, Detectors and Associated Equipment*, vol. 433, no. 1, pp. 396–400, 1999.

[58] A. J. Hunt, "Light scattering for aerogel characterization," *Journal of Non-Crystalline Solids*, vol. 225, pp. 303–306, 1998.

[59] S. K. Sahu *et al.*, "Measurement of Radiation Damage on Silica Aerogel Cherenkov Radiator," *Nucl. Instrum. Meth. A*, vol. 382, pp. 441–446, 1996.

[60] R. Abjean, A. Bideau-Mehu, and Y. Guern, "Refractive index of hexafluoroethane (C-2F-6) in the 300-nm to 150-nm wavelength range," *Nucl. Instrum. Meth. A*, vol. 354, pp. 417–418, 1995.

[61] C. Piemonte and A. Gola, "Overview on the main parameters and technology of modern Silicon Photomultipliers," *Nucl. Instrum. Meth. A*, vol. 926, pp. 2–15, 2019.

[62] L. P. Rignanese, P. Antonioli, R. Preghenella, and E. Scapparone, "SiPMs and examples of applications for low light detection in particle and astroparticle physics," *Riv. Nuovo Cim.*, vol. 47, no. 5, pp. 299–349, 2024. [Erratum: Riv.Nuovo Cim. 47, (2024)].

[63] R. Hawkes, A. Lucas, J. Stevick, G. Llosa, S. Marcatili, C. Piemonte, A. Del Guerra, and T. A. Carpenter, "Silicon photomultiplier performance tests in magnetic resonance pulsed fields," in *2007 IEEE Nuclear Science Symposium Conference Record*, vol. 5, pp. 3400–3403, 2007.

[64] S. España, L. Fraile, J. Herraiz, J. Udías, M. Desco, and J. Vaquero, "Performance evaluation of sipm photodetectors for pet imaging in the presence of magnetic fields," *Nuclear Instruments and Methods in Physics Research Section A: Accelerators, Spectrometers, Detectors and Associated Equipment*, vol. 613, no. 2, pp. 308–316, 2010.

[65] F. Acerbi *et al.*, "Cryogenic Characterization of FBK HD Near-UV Sensitive SiPMs," *IEEE Trans. Electron. Dev.*, vol. 64, pp. 521–526, 10 2016.

[66] S. Merzi, F. Acerbi, C. Aicardi, D. Fiore, V. Goiffon, A. G. Gola, O. Marcelot, A. Materne, and O. Saint-Pe, "Radiation Damage on Silicon Photomultipliers from Ionizing and Non-Ionizing Radiation of Low-Earth Orbit Operations," *Sensors*, vol. 24, no. 15, p. 4990, 2024.

[67] E. Garutti and Y. Musienko, "Radiation damage of SiPMs," *Nucl. Instrum. Meth. A*, vol. 926, pp. 69–84, 2019.

[68] T. Tsang, T. Rao, S. Stoll, and C. Woody, "Neutron radiation damage and recovery studies of SiPMs," *JINST*, vol. 11, no. 12, p. P12002, 2016.

[69] E. Nappi, "Aerogel and its applications to rich detectors," *Nuclear Physics B - Proceedings Supplements*, vol. 61, no. 3, pp. 270–276, 1998. Proceedings of the Fifth International Conference on Advanced Technology and Particle Physics.

[70] EU, "Regulation (EU) 2024/573 of the European Parliament and of the Council on fluorinate greehouse gases," *https://eur-lex.europa.eu/eli/reg/2024/573/oj*, 2024.

[71] M. Kubantsev, I. Larin, and A. Gasparian, "Performance of the PrimEx electromagnetic calorimeter," *AIP Conf. Proc.*, vol. 867, no. 1, pp. 51–58, 2006.

[72] T. Horn *et al.*, "Scintillating crystals for the Neutral Particle Spectrometer in Hall C at JLab," *Nucl. Instrum. Meth. A*, vol. 956, p. 163375, 2020.

[73] A. Asaturyan *et al.*, "Electromagnetic calorimeters based on scintillating lead tungstate crystals for experiments at Jefferson Lab," *Nucl. Instrum. Meth. A*, vol. 1013, p. 165683, 2021.

[74] F. Ameli *et al.*, "Streaming readout for next generation electron scattering experiments," *Eur. Phys. J. Plus*, vol. 137, no. 8, p. 958, 2022.

[75] Y. Suda *et al.*, "Performance evaluation of the high-voltage CMOS active pixel sensor AstroPix for gamma-ray space telescopes," *Nucl. Instrum. Meth. A*, vol. 1068, p. 169762, 2024.

[76] ePIC Collaboration, "Background studies - epic." `https://wiki.bnl.gov/EPIC/index.php?title=Background`, 2023. Accessed: 2024-09-28.

[77] O. D. Tsai *et al.*, "Results of \& on a new construction technique for W/ScFi Calorimeters," *J. Phys. Conf. Ser.*, vol. 404, p. 012023, 2012.

[78] C. A. Aidala *et al.*, "Design and Beam Test Results for the sPHENIX Electromagnetic and Hadronic Calorimeter Prototypes," *IEEE Trans. Nucl. Sci.*, vol. 65, no. 12, pp. 2901–2919, 2018.

[79] T. Nicholls *et al.*, "Performance of an electromagnetic lead / scintillating fiber calorimeter for the H1 detector," *Nucl. Instrum. Meth. A*, vol. 374, pp. 149–156, 1996.

[80] O. D. Tsai *et al.*, "Development of a forward calorimeter system for the STAR experiment," *J. Phys. Conf. Ser.*, vol. 587, no. 1, p. 012053, 2015.

[81] F. Aaron *et al.*, "Measurement of the proton structure function fl(x,q2) at low x," *Physics Letters B*, vol. 665, no. 4, pp. 139–146, 2008.

[82] R.-D. Appuhn *et al.*, "The h1 lead/scintillating-fibre calorimeter," *Nuclear Instruments and Methods in Physics Research Section A: Accelerators, Spectrometers, Detectors and Associated Equipment*, vol. 386, no. 2, pp. 397–408, 1997.

[83] "Radiation$_D$*oses*.".

"SiPM radiation hardness study." `https://indico.bnl.gov/event/24087/#17-further-rad-hard-studies-an`.

A. White *et al.*, "Design, construction and commissioning of a technological prototype of a highly granular sipm-on-tile scintillator-steel hadronic calorimeter," *Journal of Instrumentation*, vol. 18, p. P11018, nov 2023.

M. Salajegheh, H. Khanpour, U.-G. Meißner, H. Hashamipour, and M. Soleymaninia, "Determination of diffractive PDFs from a global QCD analysis of inclusive diffractive DIS and dijet cross-section measurements at HERA," *Phys. Rev. D*, vol. 107, no. 9, p. 094038, 2023.

E. Meschi, T. Monteiro, C. Seez, and P. Vikas, "Electron Reconstruction in the CMS Electromagnetic Calorimeter," tech. rep., CERN, Geneva, 2001.

"The algorithm for the PWO calorimeter." `https://www.jlab.org/primex/weekly_meetings/primexII/slides_2012_01_20/island_algorithm.pdf`.

M. Arratia *et al.*, "A high-granularity calorimeter insert based on SiPM-on-tile technology at the future Electron-Ion Collider," *Nucl. Instrum. Meth. A*, vol. 1047, p. 167866, 2023.

M. Arratia, B. Bagby, P. Carney, J. Huang, R. Milton, S. J. Paul, S. Preins, M. Rodriguez, and W. Zhang, "Beam Test of the First Prototype of SiPM-on-Tile Calorimeter Insert for the EIC Using 4 GeV Positrons at Jefferson Laboratory," *Instruments*, vol. 7, no. 4, p. 43, 2023.

S. J. Paul and M. Arratia, "Leveraging staggered tessellation for enhanced spatial resolution in high-granularity calorimeters," *Nucl. Instrum. Meth. A*, vol. 1060, p. 169044, 2024.

M. Arratia, L. Garabito Ruiz, J. Huang, S. J. Paul, S. Preins, and M. Rodriguez, "Studies of time resolution, light yield, and crosstalk using SiPM-on-tile calorimetry for the future Electron-Ion Collider," *JINST*, vol. 18, no. 05, p. P05045, 2023.

R. Milton, S. J. Paul, B. Schmookler, M. Arratia, P. Karande, A. Angerami, F. T. Acosta, and B. Nachman, "Design of a SiPM-on-Tile ZDC for the future EIC and its Performance with Graph Neural Networks," 5 2024.

"Point Cloud Deep Learning Methods for Pion Reconstruction in the ATLAS Experiment," tech. rep., CERN, Geneva, 2022. All figures including auxiliary figures are available at https://atlas.web.cern.ch/Atlas/GROUPS/PHYSICS/PUBNOTES/ATL-PHYS-PUB-2022-040.

S. Lai *et al.*, "Software Compensation for Highly Granular Calorimeters using Machine Learning," *JINST*, vol. 19, p. P04037, 2024.

R. A. et al., "Apeiron: A framework for high level programming of dataflow applications on multi-fpga systems," *EPJ Web of Conferences*, no. 11002, 2024.